Proceedings of the Canadian East Coast Workshop on Sea Ice, January 7-9, 1986

G. Symonds and I.K. Peterson (Compilers)

Atlantic Oceanographic Laboratory
Department of Fisheries and Oceans

Bedford Institute of Oceanography
P.O. Box 1006
Dartmouth, Nova Scotia
B2Y 4A2

June 1986

Canadian Technical Report of Hydrography and Ocean Sciences No. 73

Pêches et Océans   Fisheries and Oceans

Canada

87-03400/

Canadian Technical Report of Hydrography and Ocean Sciences

Technical reports contain scientific and technical information that contributes to existing knowledge but which is not normally appropriate for primary literature. The subject matter is related generally to programs and interests of the Ocean Science and Surveys (OSS) sector of the Department of Fisheries and Oceans.

Technical reports may be cited as full publications. The correct citation appears above the abstract of each report. Each report is abstracted in *Aquatic Sciences and Fisheries Abstracts* and indexed in the Department's annual index to scientific and technical publications.

Technical reports are produced regionally but are numbered nationally. Requests for individual reports will be filled by the issuing establishment listed on the front cover and title page. Out of stock reports will be supplied for a fee by commercial agents.

Regional and headquarters establishments of Ocean Science and Surveys ceased publication of their various report series as of December 1981. A complete listing of these publications is published in the *Canadian Journal of Fisheries and Aquatic Sciences*, Volume 39: Index to Publications 1982. The current series, which begins with report number 1, was initiated in January 1982.

Rapport technique canadien sur l'hydrographie et les sciences océaniques

Les rapports techniques contiennent des renseignements scientifiques et techniques qui constituent une contribution aux connaissances actuelles, mais qui ne sont pas normalement appropriés pour la publication dans un journal scientifique. Le sujet est généralement lié aux programmes et intérêts du service des Sciences et levés océaniques (SLO) du ministère des Pêches et des Océans.

Les rapports techniques peuvent être cités comme des publications complètes. Le titre exact paraît au-dessus du résumé de chaque rapport. Les rapports techniques sont résumés dans la revue *Résumés des sciences aquatiques et halieutiques*, et ils sont classés dans l'index annuel des publications scientifiques et techniques du Ministère.

Les rapports techniques sont produits à l'échelon régional, mais numérotés à l'échelon national. Les demandes de rapports seront satisfaites par l'établissement auteur dont le nom figure sur la couverture et la page du titre. Les rapports épuisés seront fournis contre rétribution par des agents commerciaux.

Les établissements des Sciences et levés océaniques dans les régions et à l'administration centrale ont cessé de publier leurs diverses séries de rapports en décembre 1981. Une liste complète de ces publications figure dans le volume 39, Index des publications 1982 du *Journal canadien des sciences halieutiques et aquatiques*. La série actuelle a commencé avec la publication du rapport numéro 1 en janvier 1982.

Canadian Technical Report of

Hydrography and Ocean Sciences No. 73

June 1986

PROCEEDINGS OF THE

CANADIAN EAST COAST WORKSHOP ON SEA ICE,

JANUARY 7 - 9, 1986

compiled by

G. Symonds

and

I.K. Peterson

Atlantic Oceanographic Laboratory
Department of Fisheries and Oceans

Bedford Institute of Oceanography
P.O. Box 1006
Dartmouth, Nova Scotia
B2Y 4A2

This workshop was supported (in part) by the
Federal Panel on Energy Research & Development (PERD)
and the Canadian Meteorological & Oceanographic Society (CMOS).

© Minister of Supply and Services Canada 1986
Cat. No. Fs 97-18/73E ISSN 0711-6764

Correct citation for this publication:

Symonds, G., and I.K. Peterson (Compilers). 1986. Proceedings of the Canadian East Coast Workshop on Sea Ice, January 7 - 9, 1986. Can. Tech. Rep. Hydrogr. Ocean Sci. No. 73: viii & 668 p.

PREFACE

Symonds, G., and I.K. Peterson (compilers). 1986. Proceedings of the Canadian East Coast Workshop on Sea Ice, January 7-9, 1986. Can. Tech. Rep. Hydrogr. Ocean Sci. No. 73: viii & 668 p.

The Canadian East Coast Workshop on Sea Ice was held at the Bedford Institute of Oceanography, January 7-9, 1986. Over 100 participants from Canada, the United States and Europe attended. Topics included ice climatology, ice and ice-ocean modelling, formation, movement and deformation of sea ice, icebergs, remote sensing and operational forecasting.

The papers and abstracts contained within these proceedings represent some of the current sea ice research and industry operations in ice covered waters. The purpose of the meeting was to bring together scientists and engineers to review the state-of-the-art ice research, to identify the major problems as perceived by both the scientific community and industry and to try to bridge the gap between basic research and the day to day requirements of offshore operations. From these proceedings, the reader can obtain an impression of the problems being addressed by scientists and engineers and judge to what extent the two groups compliment each other and where future efforts might be directed to the mutual benefit of both.

We gratefully acknowledge the presentations from the invited speakers; Dr. J.E. Walsh, R.E. Moritz, Dr. W.D. Hibler III, Dr. A.J. Semtner, Dr. R. Colony and Dr. A.S. Thorndike. Thanks also to the session chairpersons and to I. Peterson, D. Hendsbee and BIO staff who assisted in preparations before, during and after the meeting. This workshop was supported (in part) by the Federal Panel on Energy Research & Development (PERD) and the Canadian Meteorological and Oceanographic Society (CMOS).

PREFACE

Symonds, G., and I.K. Peterson (compilers). 1986. Proceedings of the Canadian East Coast Workshop on Sea Ice, January 7-9, 1986. Can. Tech. Rep. Hydrogr. Ocean Sci. No. 73: viii & 668 p.

Le Canadian East Coast Workshop on Sea Ice s'est déroulé du 7 au 9 janvier 1986, à l'Institut océanographique de Bedford. Plus de 100 participants du Canada, des États-Unis et de l'Europe ont pu s'y renseigner sur des sujets tels que la climatologie des glaces, la modélisation des glaces et de l'interaction glaces-océan, la formation, le mouvement et la déformation des glaces marines, la télédétection et les prévisions opérationnelles.

Les articles et les résumés contenus dans le présent rapport rendent compte de certaines des activités menées actuellement dans les secteurs de la recherche sur la glace marine et des opérations industrielles dans les eaux prises par les glaces. La rencontre susmentionnée avait pour but de réunir des scientifiques et des ingénieurs afin que ceux-ci puissent passer en revue les plus récentes découvertes dans le domaine de la recherche sur les glaces, définir les principaux problèmes rencontrés d'une part par la communauté scientifique et d'autre part par l'industrie, et tenter de réduire l'écart qui existe entre la recherche de base et les exigences quotidiennes associées aux opérations offshore. Le rapport qui suit donne un aperçu des problèmes dont ont discuté les scientifiques et les ingénieurs et indique jusqu'à quel point ces deux groupes se complètent et comment ils pourraient à l'avenir orienter leurs efforts vers leur intérêt mutuel.

Nous remercions sincèrement tous les conférenciers invités : MM. J.E. Walsh, R.E Moritz, W.D. Hibler III, A.J. Semtner, R. Colony et A.S. Thorndike. Nous sommes également reconnaissants aux présidents des séances d'études ainsi qu'à Mme I. Peterson, à M. D. Hendsbee et au personnel de l'IOB, qui nous ont prêté leur concours avant, pendant et après la rencontre. Soulignons que celle-ci était financée (en partie) par le Groupe fédéral interministériel de recherche et de développement énergétiques et par la Société canadienne de météorologie et d'océanographie.

TABLE OF CONTENTS

Page

Preface.. iii
Contents... v

TOPIC I - ICE CLIMATOLOGY

Northern Hemisphere Sea Ice Variability: Observed and Simulated. 3
J.E. Walsh.

On the Sea Ice Budget of the Greenland Sea. 21
R.E. Moritz.

Spring and Summer Sea Ice Conditions in Eastern Canadian Waters 1950 to 1985 (abstract only). 59
J.P. Newell.

Sea Ice Conditions in the Labrador Sea-Grand Banks Area. 60
W.P. Zakrzewski.

Air-Sea Heat Flux and the Seasonal Distribution of Sea Ice over the North East Newfoundland Shelf. 88
G. Symonds.

A Buoyancy Flux-Driven Cyclonic Gyre in the Labrador Sea. 115
Y.H. Seung.

TOPIC II - ICE AND ICE-OCEAN MODELLING

Large-Scale Ice-Ocean Modeling. 165
W.D. Hibler, III.

The Modelling of Ice Motion Near Adams Island. (abstract only). 185
J.F. Sykes and J.D. Cushon.

On the Response of Sea Ice to Wind Stress - Studies with a Regional Sea Ice Model (abstract only). 186
V.R. Neralla and S. Venkatesh.

Ice Edge Meanders off Labrador in NOAA Imagery and Modelling Interpretation (abstract only). 187
M. Ikeda and I. Peterson.

Modeling Mesocale Phenomena Relevant to the Greenland Sea MIZ. (abstract only). 188
S. Hakkinen.

A Numerical Study of Sea Ice and Ocean Circulation in the Arctic. 189
A.J. Semtner.

Page

A Coupled Ice-Mixed Layer Model for the Greenland Sea. 225
M.N. Houssais.

A Coupled Ice-Ocean Model for Shallow Shelf Seas. (abstract only). 261
W.P. Budgell and D.K. Manak.

Ice Drift on a Complex Continental Shelf - the Bering and Chukchi Seas. (abstract only). 262
J.E. Overland and C.H. Pease.

Heat Budgets of Labrador Shelf Ice. (abstract only). 263
M. Ikeda.

TOPIC III - FORMATION, MOVEMENT AND DEFORMATION OF SEA ICE

Micromechanics Approach to Sea Ice Dynamics. 267
M. Ostoja-Starzewski, R. Jessup and S. Venkatesh.

Statistical Kinematics for the Sea Ice Discontinuum. 282
A.S. Thorndike.

Observations of the Transfer of Heat Between Water and Ice. (abstract only). 296
P.F. Hamblin and E.C. Carmack.

Simulation of Sea Ice Climatology at Three Arctic Locations. (abstract only). 297
R. Gabison.

Effects of the Annual Ice-Cover on Tidal Currents and Freshwater Content of Canadian Inland Waters. 298
S.J. Prinsenberg.

Field Observations of Flow Patterns Generated by an Ice Keel in Stratified Flow. 328
D.R. Topham, H.D. Pite, P.Johnston and D.L. Richards.

Solitary Wave Solutions for the Sea Ice Momentum Equations. (abstract only). 350
T.E. Keliher.

Wind Stress Over Rough Ice in a Marginal Ice Zone. (abstract only) 351
R.J. Anderson.

TOPIC IV - ICEBERGS

Page

Long-Range Prediction of Iceberg Severity in the Labrador Sea. 355
W.I. Wittman, L.H. Hester, W.S. Dehn and J.E. Walsh.

The Long Range Prediction of Iceberg Season Severity Using Empirical Orthogonal Functions. (abstract only). 386
L.W. Davidson.

An Evaluation of the International Ice Patrol Drift Model. 387
D.L. Murphy and I. Anderson.

Observation and Modelling of Iceberg Drift off Newfoundland. (abstract only). 410
S.D. Smith.

Analysis and Prediction of Labrador Shelf Iceberg Trajectories. (abstract only). 411
J.F. Middleton and C.J.R. Garrett.

On the Numerical Characterization of Iceberg Shape. (abstract only). 412
J.C. Lewis.

Iceberg Severity Revisited. 413
J.R. Marko, D.B. Fissel and J.R. Birch.

Iceberg Splitting and its Implications for Deterioration Modelling. 429
D. Diemand and J.H. Lever.

Deterioration of Icebergs. (abstract only). 441
M. El-Tahan and S. Venkatesh.

On the Deterioration of a Grounded Iceberg. 442
S. Venkatesh.

Temperature, Salinity and Density Profiles Around Icebergs in the Labrador Sea. 472
D.E. Pearson.

TOPIC V - REMOTE SENSING

Enhancement of NOAA AVHRR Digital Data for Sea Ice Analysis in an Operational Environment. 495
B.R. Ramsay and M.A.J. Zieger.

Motion of Ice in the Beaufort Sea from Satellite and Aircraft Images. 509
J.F.R. Gower, J.Y. Cherniawsky and G.A. Borstad.

Surface-Based Radar Classification and Detection of Ice. (abstract only). 523
E.O. Lewis and B.W. Currie.

Page

Interpolation of Nearshore Ice Motion. (abstract only). 524
R.F. McKenna, W.C. Lennox and J.F. Sykes.

Evaluation of Remote Sensing Products in the Radarsat Time Frame. (abstract only). 525
L. McNutt, S. Venkatesh and V.R. Neralla.

Determination of Sea Ice Concentration and Ice Edge Position in the Beaufort Sea Using Satellite Passive Microwave Data. 526
D.R.P. Williams.

A Climatological Analysis of Eastern Canadian Seaboard Ice Conditions Using Passive Microwave Satellite Data (1973-1985). 537
A.E. Walker.

Side-Looking Airborne Radar Detection and Identification of Icebergs. 546
N.C. Edwards Jr. and N.B. Thayer.

TOPIC VI - OPERATIONAL FORECASTING

The Iceberg Information Service of Environment Canada. 557
J.C. Falkingham.

Ice and Ice Management on the Grand Bank. 561
J.A.N. Ransom, J.R. Benoit and F.J. Dello Stritto.

Sea Ice Drift Measurements Using Satellite-Tracking Beacons. 583
D.M. Nazarenko and J.D. Miller.

Ice Monitoring and Forecasting for the Beaudril 'Kulluk'. 598
F.J. Eley.

Dome-Canmar's Operational Ice-Forecasting System for the Beaufort Sea. 615
J.W. Steen and J.D. Trobak.

Overview of Project to Measure Ice Forces at Adams Island. 651
R.M.W. Frederking, J.B. Maxwell and S. Prinsenberg.

TOPIC VII - FUTURE RESEARCH PROGRAMS

Radarsat Data Acquisition and Analysis Plans, 1986-1991, for Sea Ice Applications. (abstract only). 667
L. McNutt.

LIMEX - A Labrador Ice Margin Experiment. (abstract only). 668
J. Lever and P. Wadhams.

I

ICE CLIMATOLOGY

NORTHERN HEMISPHERE SEA ICE VARIABILITY:

OBSERVED AND SIMULATED

by

John E. Walsh[1]

ABSTRACT

Large-scale fluctuations of Northern Hemisphere sea ice are examined using 25 years of monthly gridded historical data and 30 years of simulated results obtained from a dynamic-thermodynamic sea ice model (Hibler, 1979). Correlations between the simulated and observed fluctuations in the various longitudinal sectors range from 0.4 to 0.9. Controlled experiments with the model show that the inclusion of dynamics is required for a realistic spatial distribution of simulated ice thicknesses in the Arctic. Interannually variable thermodynamic forcing is essential for the simulation of interannual fluctuations of areal ice coverage. Long-period fluctuations and trends are apparent in the simulated results and in the historical data, although some trends in the latter are attributable to changes in the data sources. The model results show large year-to-year differences in the pattern of net annual ice drift.

---

[1] Department of Atmospheric Sciences, University of Illinois, Urbana, IL 61801

1. INTRODUCTION

The development of numerical models for the simulation of large-scale sea ice fluctuations has evolved in response to several needs. First, global climate simulations require proper treatments of sea ice in order to obtain realistic vertical fluxes of sensible and latent heat at the ocean-atmosphere interface. These fluxes are large, variable, and highly sensitive to the presence or absence of sea ice. Second, quantities such as ice thickness, velocity, mass transport and vertical heat flux are not observed systematically over the large scale despite their importance to the high-latitude climate system. Ice modeling provides one of the more promising approaches to diagnostic information on these variables. Third, the utility of sea ice forecasts is broadened considerably if the prognostic quantities include ice strength and/or pressure, ice velocity, thickness and concentration. While forecasts of these quantities will likely require the use of ice models in some form, even real-time fields of these variables obtained from model simulations driven by antecedent data may be useful for operational purposes.

In view of the attractive potential of large-scale models for the applications listed above, it is imperative that model performance be evaluated in the context of available observational data. Systematic assessments of errors in model simulations will establish the priorities for further model development. This paper is an evaluation of the simulation of several decades of interannual sea ice fluctuations over the Northern Hemisphere. The use of this time frame permits assessments of systematic errors (biases) as well as the model sensitivities to the types of forcing fluctuations which occur interannually in the air-sea-ice system. The biases and the interannual sensitivities pose somewhat distinct challenges to model development, although both types of errors can limit the utility of model applications.

The vehicle to be used here is the two-level dynamic-thermodynamic model developed by Hibler (1979, 1980). The model formulation is summarized in Section 2. The corresponding data used for forcing and verification are described in Section 3. The comparisons of the simulated and observed fields in Section 4 will emphasize the seasonal biases in the simulated ice extent, correlations between simulated and observed departures from normal ice coverage, and the correspondence between simulated and observed trends of ice cover over a period of 15-25 years. Problems pertaining to deficiencies in the observational (verification) data will be noted. In keeping with the large-scale orientation of the model experiments, the assessment of model performance will not be limited to a specific region. It will be apparent, however, that the performance of the model is poorer in some regions (e.g., the North Atlantic) than in others. It will also be apparent that the more serious deficiencies in the simulated fields are consistent with the omission of various physical processes in the version of the model used here.

2. MODEL SUMMARY

Details of the model formulation are given by Hibler (1979, 1980), while more recent modifications pertaining to the model thermodynamics are described by Walsh et al. (1985). The essential features of the model are (1) a momentum balance based on geostrophically-derived air and water stresses, coriolis force, ocean tilt, internal ice stress, and inertial terms; (2) an ice rheology based on a viscous-plastic constitutive law and an ice strength parameter, P^*; (3) an ice thickness distribution characterized by the compactness A and the mean ice thickness h_{eff} averaged over an entire grid cell; and (4) a thermodynamic code in which vertical growth rates are estimated from heat budget computations at the top and bottom surfaces of the ice and from heat stored in a motionless oceanic boundary layer. The thermodynamic formulation utilizes a seven-level distribution of ice thicknesses equally spaced between 0 and $2h_{eff}$. The parameterizations of the various fluxes are based largely on Parkinson and Washington's (1979) formulation. Snow cover is treated explicitly with the aid of prescribed accumulation rates.

The domain of integration is a 38 x 31 cartesian grid covering the Arctic Basin and (except for Hudson Bay and the Baltic Sea) all the peripheral seas that experience seasonal ice cover. The resolution of the grid is 222 km. The use of this relatively coarse horizontal resolution was dictated by the availability of computer resources and the model's running time, which is approximately 8 minutes per simulated year on a Cray-1 supercomputer.

3. DATA

3.1. ATMOSPHERIC FORCING DATA

The model was run with a 1-day timestep using observed atmospheric forcing data from the period 1951-1980. Daily wind fields were computed geostrophically from the National Center for Atmospheric Research (NCAR) set of sea level pressure analyses, which are in the form of 5° x 5° latitude-longitude grids. Conversion to the cartesian coordinates of the ice model grid was accomplished by bilinear interpolation. A total of 10,950 daily pressure grids were required for the 30-year simulations.

Air temperatures were derived from the set of gridded monthly anomalies compiled by Hansen et al. (1983) at the NASA Goddard Institute for Space Studies. These anomalies were added to the climatological monthly mean air temperatures of Crutcher and Meserve (1970). Daily temperature fields were then computed by cubic spline interpolation from the monthly fields, which were assumed to correspond to the midpoints of the respective calendar months.

The relative humidities required for the latent heat and longwave radiative computations were prescribed to be 90% at all times and grid points. The unavailability of interannually varying snowfall data for the ice covered ocean required required the use of the climatological snow accumulation rates of Maykut and Untersteiner (1971). Finally, the geostrophic ocean currents used to compute the water stresses were derived from the dynamic topographies provided by S. Levitus of the Geophysical Fluid Dynamics Laboratory. These topographies are similar to those used by Parkinson and Washington (1979). Because the topographies are temporally invariant during the model simulations, a potentially large source of interannual sea ice variability is not included in the experiments.

3.2. SEA ICE DATA

The sea ice data used for model verification were monthly fields of ice concentration for the Northern Hemisphere. The data cover a 25-year period, 1953-1977, and were digitized by Walsh and Johnson (1979) on a grid of points separated by 111 km (60 n mi). The grid is shown in Figure 1. The data were obtained from several historical series of charts, including those of the U.S. Navy, the Canadian Atmospheric Environment Service, the British Meteorological Office and the Danish Meteorological Institute. The digitized ice concentration data were used to compute ice-covered areas in 20° longitudinal sectors. These sector coverages formed the basis of comparisons with the corresponding simulated fields of ice cover.

The major deficiencies of this sea ice dataset are (1) the use of estimated data in the early years (e.g., 1950's, 1960's) when the hemispheric data coverage was relatively poor, and (2) the temporal inhomogeneities introduced by the consolidation of data from several different sources. Consequences of these deficiencies will be illustrated in Section 5. Deficiencies in the observational data undoubtedly contribute to the discrepancies between the simulated and observed fields of ice coverage, especially on the interannual time scale.

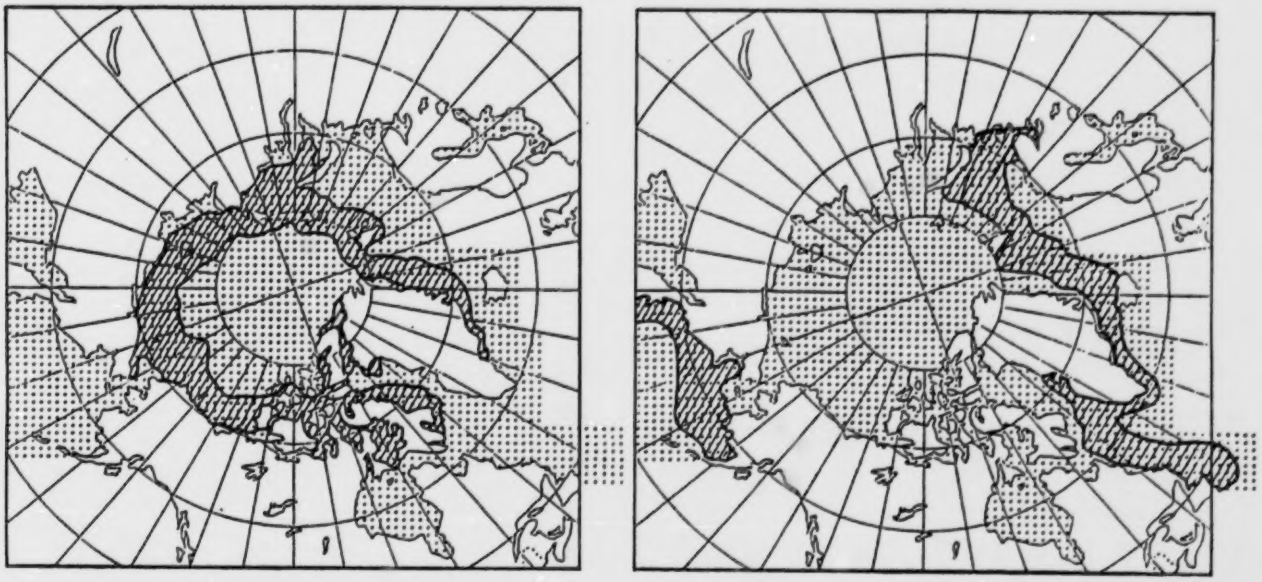

Ice extremes, 1953–1977

(a) August

(b) February

Figure 1. Composite maximum and minimum ice extent at the end of (a) August and (b) Febraury. Heavy lines are extreme positions of 50% ice concentration line based on the 25 August grids and the 25 February grids (1953-1977) of Walsh and Johnson (1979). Dots represent grid points used in digitization of monthly ice concentration data.

4. MODEL SIMULATIONS

Four simulations of the 30-year period, 1951-1980, will be described here. These simulations were designed not only to evaluate the model's performance relative to observations, but to determine the relative contributions of the model dynamics and thermodynamics to the simulated interannual fluctuations. The simulations will be denoted as follows:

DT: complete model simulation with interannually varying dynamic and thermodynamic forcing

DT_c: interannually varying dynamic forcing, climatological thermodynamic forcing

D_cT: climatological dynamic forcing, interannually varying thermodynamic forcing

T: no dynamics; interannually varying thermodynamic forcing

The thermodynamic fields in DT_c are the 30-year monthly means, the use of which preserves the seasonal cycle in the thermodynamic forcing. In D_cT the daily departures from the mean pressure (wind) field of an individual month were added to the 30-year mean for the appropriate calendar month. This strategy preserves the variance of the daily fields about the monthly means while eliminating the interannual variability of the monthly means. Deformation therefore occurs in response to the high-frequency variability of the dynamical forcing in D_cT. In simulation T, on the other hand, the dynamical forcing is omitted completely, thereby eliminating deformation as well as transport. Because T is characterized 100% concentration and uniform thickness (i.e., no leads) in each grid cell containing ice, T is clearly the least realistic of the four simulations.

5. RESULTS

As an illustration of the seasonal cycle of the simulated ice, Figure 2 shows the 30-year mean fields of ice thickness in simulations T and DT at the end of February and August. The thicknesses in T show a high degree of spatial symmetry about the central Arctic, where the mean annual temperatures are lowest. By contrast, the thicknesses in DT are highly assymmetric about the central Arctic. The mean drift pattern in DT results in a build-up of ice to thicknesses of 4-5 m north of Greenland and the Canadian Archipelago, while the thicknesses are generally 2 m or less in the Siberian and Alaskan portions of the Arctic Basin. Ice thicknesses in the latter regions are smaller in DT than in T because the

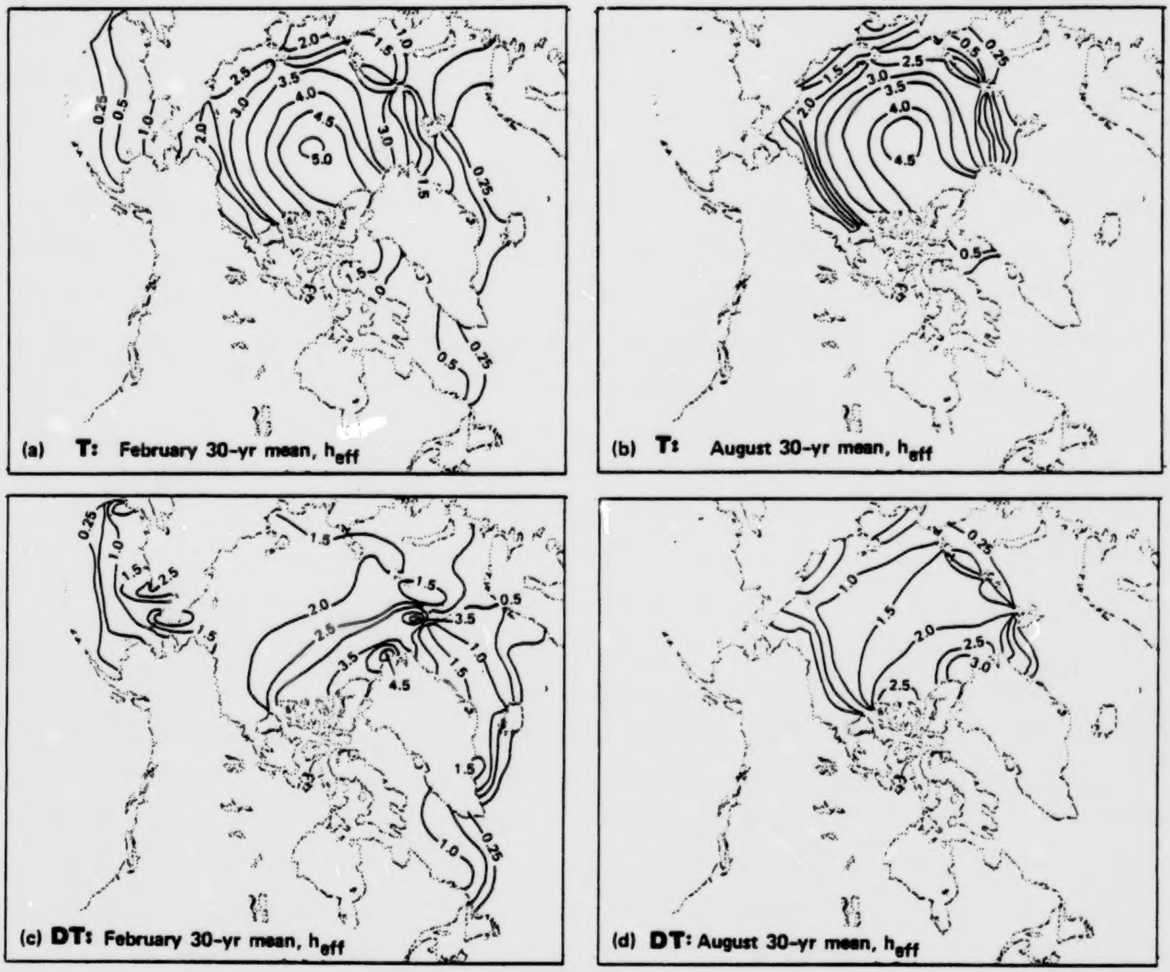
(a) T: February 30-yr mean, h_{eff}
(b) T: August 30-yr mean, h_{eff}
(c) DT: February 30-yr mean, h_{eff}
(d) DT: August 30-yr mean, h_{eff}
0.25
0.5
1.0
1.5
2.0
2.5
3.0
3.5
4.0
4.5
5.0

Figure 2. The 30-year mean contours of simulated ice thickness for the end of Feburary and August. (a) and (b) show thicknesses from simulation T, (c) and (d) show thicknesses from simulation DT.

absence of leads in T limits the solar absorption during the melt-induced summer retreat of the ice edge.

The spatial patterns of thickness in DT are much more consistent with LeSchack et al.'s (1971) observationally-derived thicknesses than are the corresponding patterns in T. However, several systematic biases in the thickness fields of DT are apparent from Figures 2c and 2d. First, in comparison with the data-derived plot in Figure 1a, the wintertime extent of the simulated ice is excessive in the western Bering Sea, in Davis Strait, and especially in the North Atlantic. The oversimulation in the North Atlantic has been shown by Hibler and Bryan (1984) to be attributable to the absence of oceanic coupling. Second, the summer melt is somewhat excessive, especially in the Siberian and Alaskan shelf areas and in the East Greenland Sea. The excessive summer melt, which contributes to the exaggerated seasonal cycle in DT, has been found to be due to the omission of internal heat storage (i.e., brine pockets) within the ice (Semtner, 1984). Finally, the annual mean thicknesses of ~2 m in much of the Arctic Basin are approximately 1 m less than the value of ~3 m thought to be typical of much of the Basin.

Despite the biases in the 30-year mean seasonal cycle, the interannual fluctuations of the simulated fields correspond generally with the observed fluctuations. Figure 3 shows the correlations between the simulated and observed anomalies of ice-covered area in 20° sectors during the 17-year period, 1961-1977. (As will be shown later in this section , the observational data for the years prior to 1961 were not sufficiently reliable for inclusion in the comparison.) The correlations between simulated and observed fluctuations are nearly all positive. The correlations are generally larger for DT than for the simulations in which the forcing is not fully variable. The 18-sector mean correlations are 0.68 for DT, 0.58 for D_cT, 0.57 for T, and 0.28 for DT_c. Thus the correlations are degraded more by the omission of interannually varying thermodynamics than by the omission of interannually varying dynamics. A comparison of correlations for D_cT and DT_c (Figure 3b) shows that the omission of dynamic variability has the stronger negative impact in the western Arctic (100°W-160°W), while the omission of thermodynamic variability has the stronger negative impact in the eastern Arctic (0°E-100°E) and in the North Atlantic (0°W-40°W). In the Siberian sectors (80°E-120°E), the correlations are $\lesssim 0.4$ in all four simulations, although the poor agreement may be partially attributable to errors in observational data for this region even in the 1960's. Support for this interpretation is provided by Figure 4, which shows time series of the departures from the 25-year monthly means derived for two sectors from the historical sea ice data of

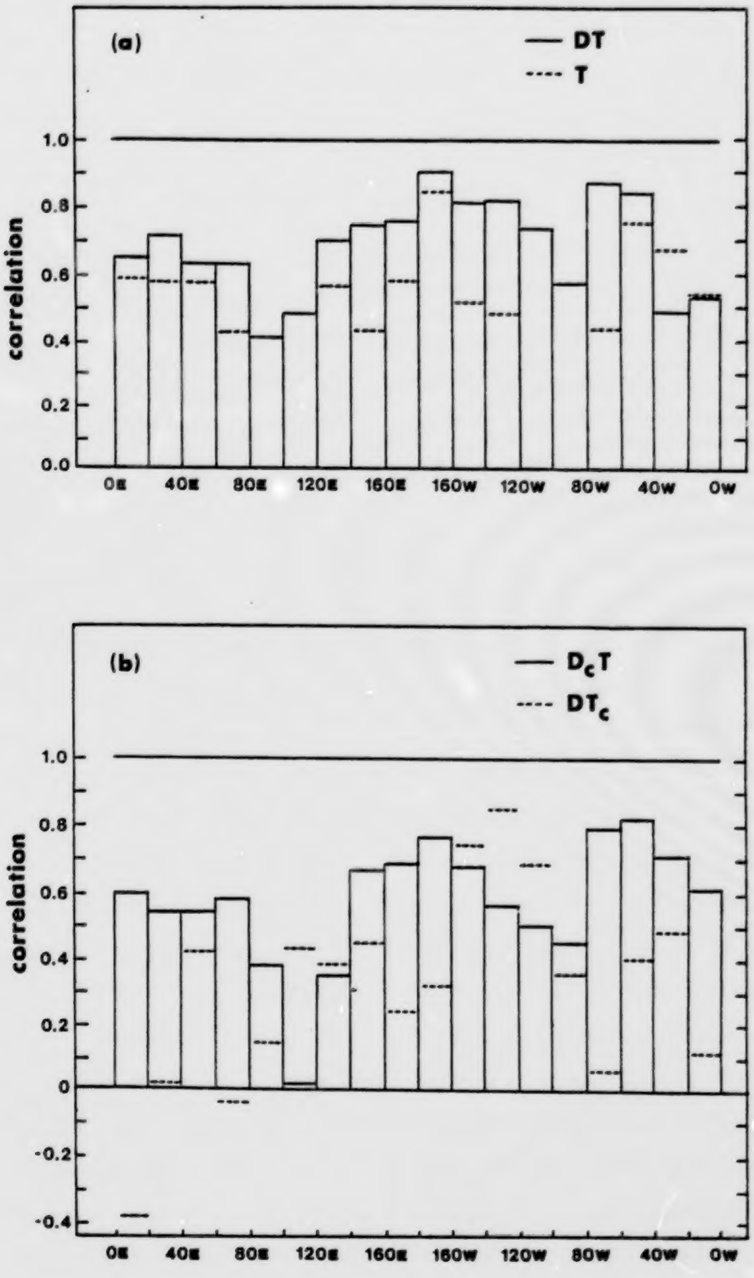

Figure 3. Correlations between anomalies of simulated and observed ice-covered area for the years 1961-1977. Results are shown for (a) simulations DT (solid) and T (dashed), and (b) simulations DT_c (solid) and D_cT (dashed).

Walsh and Johnson (1979). The anomalies for the Soviet sector (60°E-80°E) contain clusters of very similar annual patterns for the 1950's and early 1960's. Because this behavior clearly depicts changes in the data sources, the data are of little or no utility for the correlative applications attempted here. Indeed, the model results may correspond more closely to the actual interannual fluctuations than do the anomalies in Figure 4a.

The time series of anomalies for the eastern Canadian sector (40°W-60°W) is shown in Figure 4b. Some indication of a source-induced bias is present in the anomalies for the early and middle 1960's, when much of the data were obtained from the monthly charts of the British Meteorological Office. However, the generally heavier ice conditions of the 1970's, especially in 1972-74, are consistent with the large southward fluxes of icebergs recorded during those years (e.g., Wittmann et al., 1986). The broad temporal pattern of light ice conditions in the 1960's and heavy conditions in the early 1970's may therefore contain some validity.

As a further check on the compatibility of the simulated and observed fluctuations, linear trend lines were fitted to the time series of the monthly anomalies during 1961-1977 in each 20° sector. The trend lines are simply the slopes of the linear regression equations for the time series of anomalies in a sector. The statistical significance of each trend line was evaluated in terms of the ration β/σ, where β is the regression-derived slope and σ is the standard deviation of the slopes of a large number (~100) of randomly reordered series of the same anomalies (Brownlee, 1965). β/σ may thus be regarded as the number of chance-level standard deviations by which the actual slope exceeds zero. Figure 5a shows that the trends of the simulated anomalies are quite similar to those of the data-based anomalies during 1961-1977. For both simulated and observed anomalies, the 17-year trends are generally negative in the Eastern Hemisphere and positive in the Western Hemisphere. Exceptions are the Siberian longitudes (60°E-120°E) where, as shown above, the historical data are questionable, and the western Canadian longitudes (140°W-80°W) where the trends are indistinguishable from 0. Highly significant positive trends are indicated by both the model-derived and the data-based time series for the Bering Sea sectors (160°E-160°W), where Niebauer (1983) has also reported increases of ice cover, and the Davis Strait - West Greenland sector (40°W-60°W), for which the increase of simulated ice was noted earlier (Figure 4b).

Figure 5b shows that the agreement between the trends of simulated and observed ice cover is noticeably poorer when the comparison is based on data for a longer period, 1953-1977. The signs of the trends are opposite in six of the

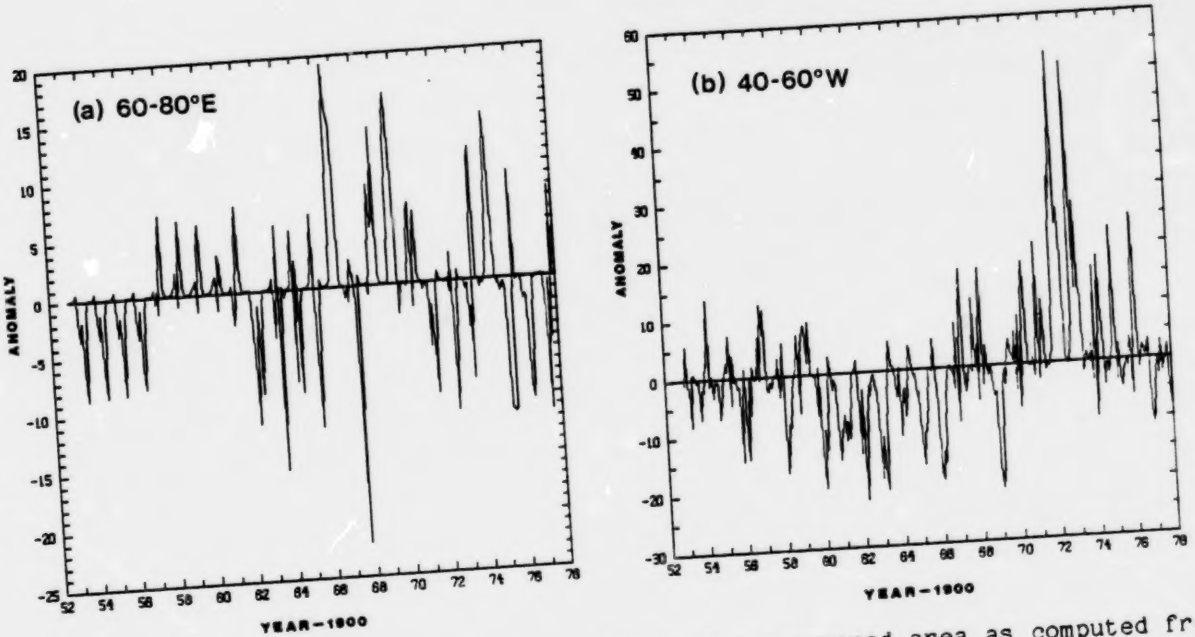

Figure 4. Time series of monthly anomalies of ice-covered area as computed from data of Walsh and Johnson (1979) for longitudinal sectors (a) 60°E-80°E and (b) 40°W-60°W. Anomalies are plotted as multiples of one grid-cell area (60 n mi x 60 n mi).

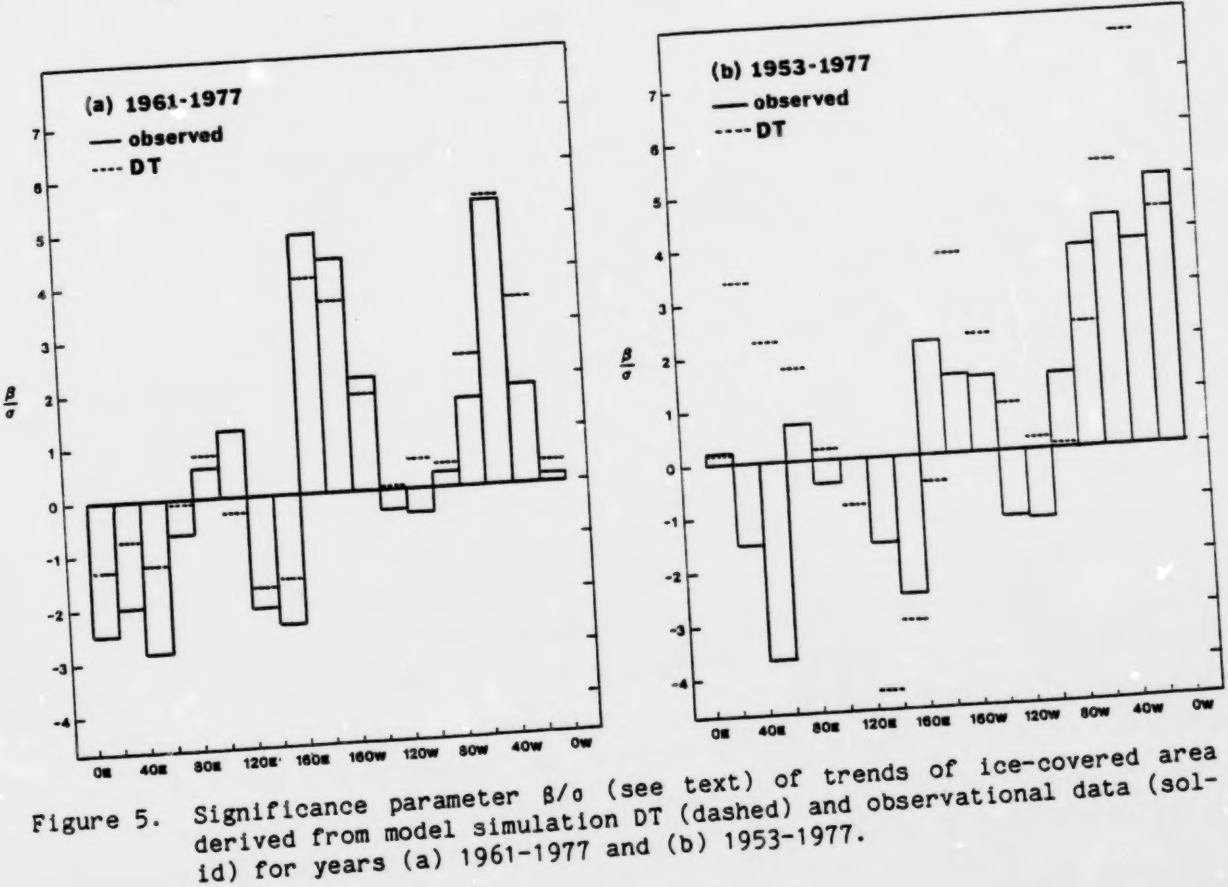

Figure 5. Significance parameter β/σ (see text) of trends of ice-covered area derived from model simulation DT (dashed) and observational data (solid) for years (a) 1961-1977 and (b) 1953-1977.

eighteen sectors, while the magnitudes of the significance parameters are dissimilar in most sectors. Since the model simulation is unlikely to have been less realistic in the earlier years than in the later years, one may attribute the degradation to the lower quality of the data derived from the earlier historical charts.

Figure 6 provides a comparison of the trends in the annual (accumulated 12-month) departures from the 25-year mean simulated thicknesses and ice-covered areas for the 1953-77 period. While the two variables show similar trends in the eastern longitudes, the increases of ice mass (thickness) are more significant than the corresponding areal increases in most western sectors. The differences between the trends in the North Atlantic sectors (20°E-40°W) are especially large. In simulation DT an increasingly vigorous pattern of ice drift in the Arctic Basin resulted in a thickness buildup north of Greenland with no corresponding increase of ice-covered area. The results in Figure 6 imply that trends or changes of regional ice mass and ice-covered area cannot always be assumed to be similar over the time periods considered here.

Figure 7 shows the 30-year mean seasonal drift vectors from simulation DT. The vectors have been scaled to correspond to net seasonal displacements. The advective removal of ice from the Asian coastal waters is apparent in winter, spring and autumn, while a similar removal from the Chukchi Sea and the Alaskan coastal waters is apparent in spring, summer and autumn. The North Pacific Gyre (Gordienko, 1958) dominates the drift pattern in the Arctic Basin during spring and autumn (and in the annual mean) but is noticeably distorted in summer and winter. This seasonality has received little attention in previous studies of arctic ice drift, although a similar seasonality is apparent in the monthly fields of sea level pressure.

The largest simulated ice velocities occur during winter in the Bering and East Greenland Seas (Figure 7). The outflow of ice from the Arctic Basin into the East Greenland waters is a prominent feature of the drift pattern of each season, although the interannual variability of this outflow is substantial. The simulated outflow varies by factors of 2-3 in successive years. As an illustration of the interannual variability of the simulated drift, Figure 8 shows the annual drift vectors for the individual years of 1973 and 1974. The well-developed gyre in the Arctic Basin during 1973 contrasts with the extremely weak drift during 1974. Large amounts of ice are evacuated during 1973 from the Asian coastal waters into the transpolar drift stream, which advects the ice vigorously towards the outflow region east of northern Greenland. The 1974 pattern is characterized by the virtual absence of transpolar drift and by little evacuation of

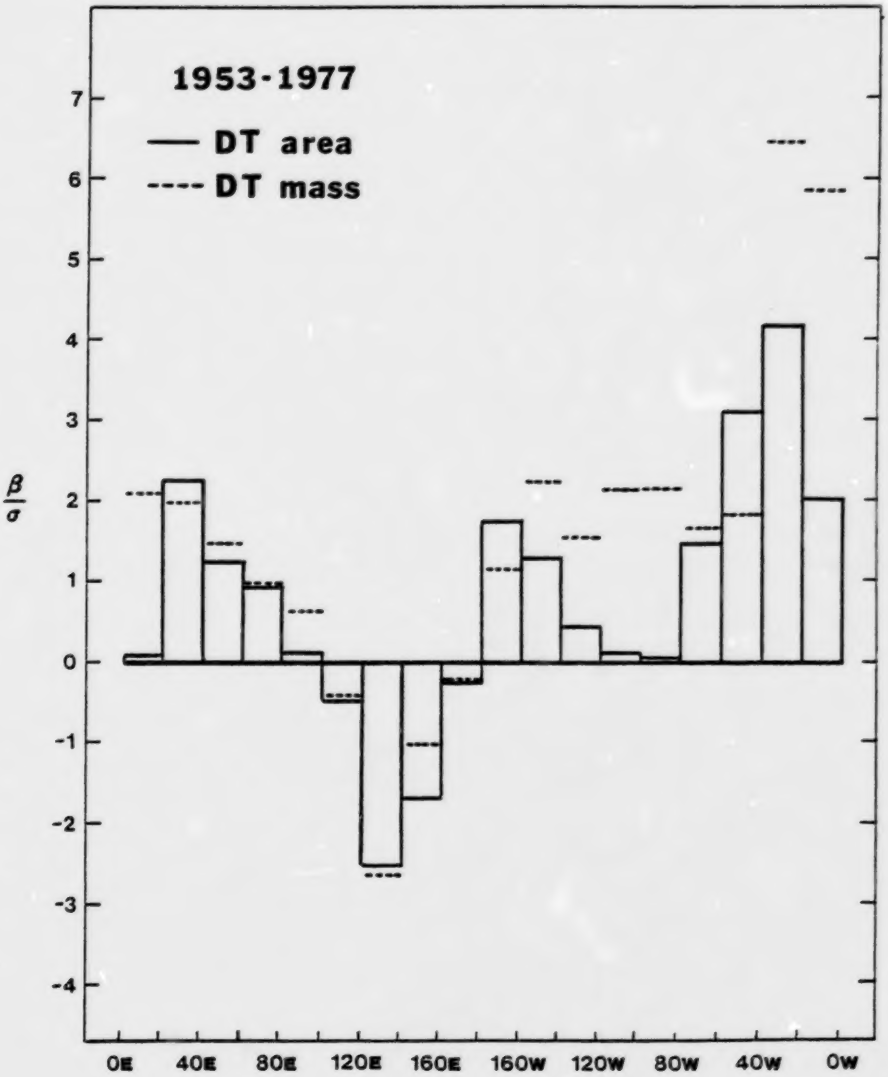

Figure 6. Significance parameter β/σ (see text) of trends of ice-covered area (solid) and ice mass (dashed) obtained from model simulation DT for the years 1953-1977.

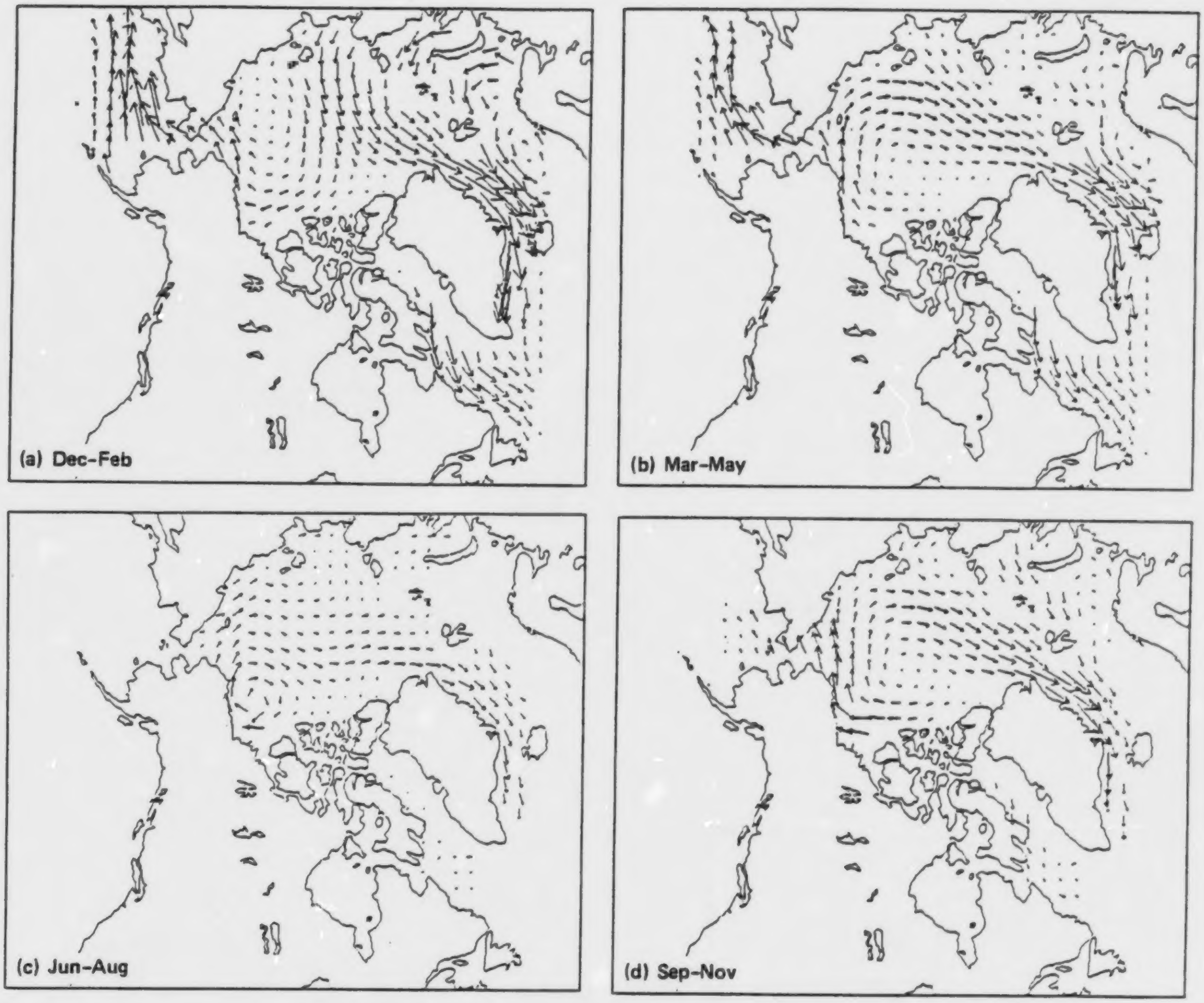

Figure 7. The 30-year mean seasonal drift vectors from model simulation DT. Vectors are scaled to correspond to net displacements during 3-month periods.

ice from the Chukchi, East Siberian and Laptev Seas. The simulated flux of ice mass through Fram Strait was nearly twice as large in 1973 as in 1974 (Walsh et al., 1985, Fig. 16). The contrasting patterns of drift in these two years are consistent with the 12-month sea level pressure fields, as 1974 was characterized by weak gradients in the sector bounded by 100°E, 160°W, 75°N and the pole.

In the Davis Strait and Labrador Sea regions of eastern Canada, strong outflow of ice is indicated by the model results for winter and spring (Figures 7a and 7b). As in the central Arctic however, the interannual variability of the simulated drift is substantial. During 1974, for example, the annual mean drift vectors in the Labrador Sea are nearly twice as large as in 1973 (Figure 8). These differences are consistent with the fluxes of icebergs across 48°N: 1386 in 1974 and 846 in 1973 (Wittmann et al., 1986). However, the weekly ice charts of the U.S. Navy/NOAA Joint Ice Center indicate that sea ice extent in the 40°W-60°W sector was generally greater in 1973 than in 1974 (see Figure 4b), especially in the early winter.

6. CONCLUSION

The results presented in the previous section illustrate the general correspondence between sea ice fluctuations obtained from model simulations and from historical datasets. Both sets of fluctuations, however, suffer from deficiencies. The historical data grids contain errors and omissions that are readily apparent in time series of computed anomalies, particularly in the 1950's and early 1960's. The quality of the historical data varies by region, although it is difficult to quantify this regional dependence by comparisons with simulated fields that also contain errors. The simulated fields are further complicated by substantial biases in both winter and summer. The bias toward excessive wintertime ice extent has already been eliminated in recent simulations by Hibler and Bryan (1984), whose use of a coupled ice-ocean model permits the inclusion of horizontal heat transport and convective mixing in the ocean. Similarly, recent preliminary experiments with Semtner's (1984) more complete thermodynamic formulation indicate that the excessive summer melt is reduced by the inclusion of internal heat storage.

Despite their shortcomings, the simulations described here permit several conclusions. First, the inclusion of dynamics is required for a realistic spatial distribution of ice thickness in the Arctic. Second, internally varying thermodynamic forcing is essential for the simulation of fluctuations of areal ice extent. Third, the pattern of ice drift shows large interannual variability,

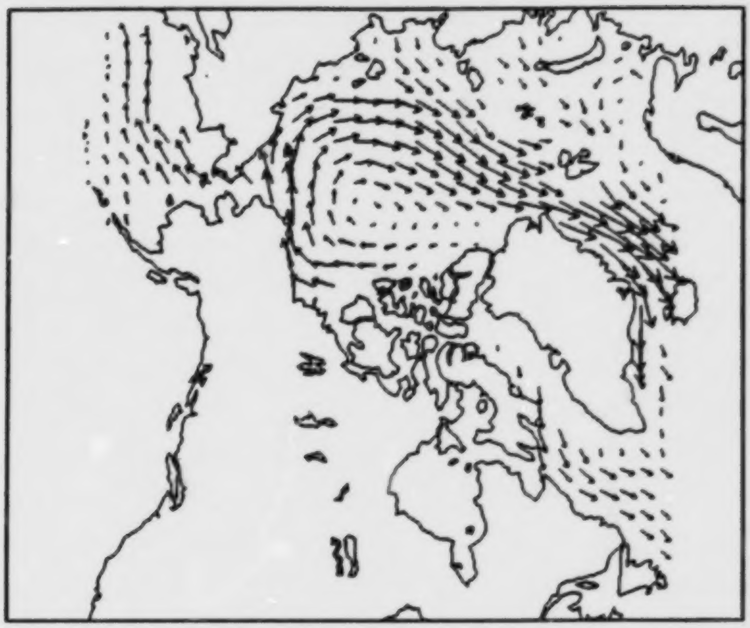

(a) 1973 DRIFT VECTORS

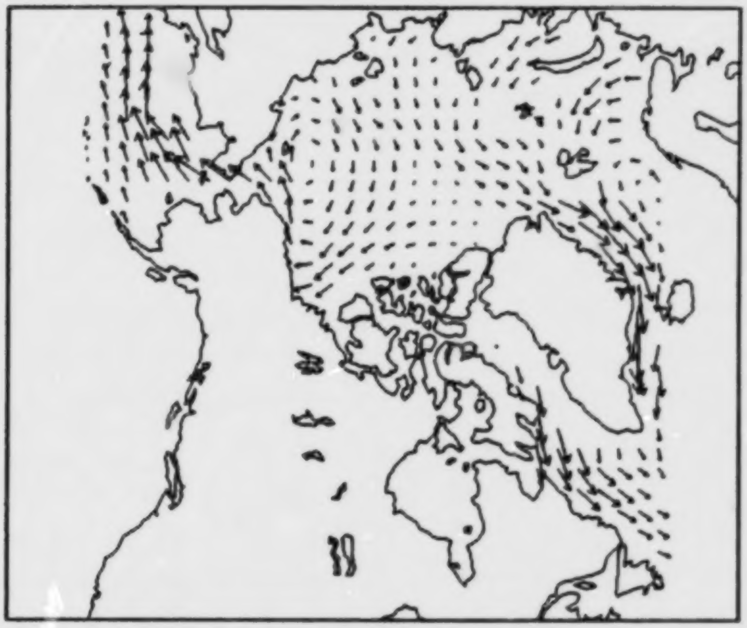

(b) 1974 DRIFT VECTORS

Figure 8. Annual mean drift vectors for 1973 and 1974 from model simulation DT. Vectors are scaled to correspond to 25% of the annual displacements in regions of year-round ice cover.

not only on a monthly basis but also on an annual (12-month) basis. This variability implies that the drift pattern for a single month or year cannot be assumed to be representative of the long-term mean pattern. It should be noted that the simulated drift vectors described here show no systematic bias with respect to the displacements of drifting Arctic buoys (Walsh et al., 1985).

Potential applications of the types of results obtained here include their use in evaluations of the vertical heat fluxes and other climatically relevant quantities. Analyses of the variability of such quantities may ultimately help to clarify the role of sea ice in short-term climatic fluctuations. Finally, the time series of simulated thicknesses and velocities provide quantitative information pertinent to the slow evolution of large-scale ice anomalies. It is possible that the physical basis of long-range (monthly to seasonal) forecasts of sea ice can be augmented by the analysis of ice thickness data and corresponding measures of the persistence of thickness anomalies.

ACKNOWLEDGEMENTS

This work was supported by the U.S. National Science Foundation, Division of Polar Programs, through Grants DPP-81201376 and DPP-8511443. Thanks are due Becky Ross for much of the computational work and Norene McGhiey for the typing of the manuscript.

REFERENCES

BROWNLEE, K.A. 1965. Statistical Theory and Methodology. Wiley, New York, 590 pp.

CRUTCHER, H.L. and MESERVE, J.M. 1970. Selected level heights, temperatures and dewpoints for the Northern Hemisphere. NAVAIR Report 50-1C-52, U.S. Naval Weather Service Command, Washington, DC.

GORDIENKO, P.A. 1958. Ice drift in the central part of the Arctic Ocean. Problems of the North, v. 1: pp. 1-30.

HANSEN, J., JOHNSON, D., LACIS, A., LEBEDEFF, S., LEE, P., RIND, D. and RUSSELL, G. 1983. Climatic effects of atmospheric carbon dioxide. Science, v. 220: pp. 873-875.

HIBLER, W.D., III. 1980. Modeling a variable thickness sea ice cover. Monthly Weather Review, v. 108: pp. 1943-1973.

HIBLER, W.D., III. 1979. A dynamic thermodynamic sea ice model. Journal of Physical Oceanography, v. 9: pp. 815-846.

HIBLER, W.D., III and BRYAN, K. 1984. Ocean circulation: Its effects on seasonal sea-ice simulations. Science, v. 224: pp. 489-492.

LESCHACK, L.A., HIBLER, W.D., III and MORSE, F.H. 1971. Automatic processing of arctic pack ice data obtained by means of submarine sonar and other remote sensing techniques. Propagation limitations in remote sensing. AGARD Conference Proceedings (J.B. Lomax, Ed.), No. 90, pp. 5-1 to 5-19 [NTIS AGARD-CP-90-71].

MAYKUT, G.A. and UNTERSTEINER, N. 1971. Some results from a time-dependent thermodynamic model of sea ice. Journal of Geophysical Research, v. 76: pp. 1550-1575.

NIEBAUER, H.J. 1983. Multiyear sea ice variability in the eastern Bering Sea: An update. Journal of Geophysical Research, v. 88: pp. 2733-2742.

PARKINSON, C.L. and WASHINGTON, W.M. 1979. A large-scale numerical model of sea ice. Journal of Geophysical Research, v. 84: pp. 311-337.

SEMTNER, A.J., JR. 1984. On modeling the seasonal thermodynamic cycle of sea ice in studies of climatic change. Climatic Change, v. 6: pp. 27-38.

WALSH, J.E., HIBLER, W.D., III and ROSS, B. 1985. Numerical simulation of northern hemisphere sea ice variability, 1951-1980. Journal of Geophysical Research, v. 90: pp. 4847-4865.

WALSH, J.E., and JOHNSON, C.M. 1979. An analysis of arctic sea ice fluctiations, 1953-1977. Journal of Physical Oceanography, v. 9: pp. 580-591.

WITTMANN, W.I., HESTER, L.H., DEHN, W.S. and WALSH, J.E. 1986. Long-range prediction of iceberg severity in the Labrador Sea. Proceedings, Canadian East Coast Workshop on Sea Ice, Bedford Institute of Oceanography, Dartmouth, N.S. (this volume).

ON THE SEA ICE BUDGET OF THE GREENLAND SEA

Richard E. Moritz

Polar Science Center/APL
University of Washington
Seattle, WA, 98105 USA

INTRODUCTION

Sea ice is an important element of the terrestrial climate system because its presence affects the fluxes of radiation, enthalpy, salt and momentum at the ocean's surface. Indirect evidence for this importance comes from the water mass inventory compiled by Sarmiento and Tottweiler (1984), which shows that 75% of the world ocean volume has properties corresponding to outcrops covering only 5% of the surface area, all at high latitudes. In particular, the ice covered seas east of Greenland have been identified as important source areas for north Atlantic deep water, although much remains to be learned about the rates and mechanisms by which this water mass is produced (Killworth, 1985; Aagaard, et al., 1985). Coupling between sea ice processes and the thermohaline circulation of the ocean suggests that the ice plays a role in climate feedback processes on time scales of tens to thousands of years.

Evidence for the influence of sea ice on atmospheric climate comes from GCM simulations of the response of surface air temperatures to an increase of atmospheric carbon dioxide. The CO_2 -induced changes in simulated meridional temperature gradient are sensitive to the temperature-albedo feedback arising from sea ice variations (Manabe and Stouffer, 1980; Washington and Meehl, 1984).

There is observational evidence that the area of ocean surface covered by sea ice varies on time scales of a few weeks to thousands of years (Walsh and Johnson, 1979; Bergthorsson, 1969; Ruddiman and McIntyre, 1973). Given the strong influence of ice on air-sea interaction processes, one expects these variations to influence climate variability in the ocean and the atmosphere. It has been noted (Lemke, et al, 1980; Walsh, 1983) that time autocorrelations of sea ice area anomalies (departures from monthly climatological normals) decay more slowly than correlations for atmospheric anomalies on the same spatial scale, suggesting that a portion of the atmospheric variability on time scales less than 6 months may be predictable as a forced response to sea ice anomalies.

A first step towards understanding the role of sea ice in the climate system is to estimate *ice budgets*. These budgets express variations of ice amount in terms of advective and thermodynamic processes driven by the atmosphere and ocean. Recent reviews on sea ice and climate conclude that available sea ice data sets are adequate to describe the large scale seasonal, annual and interannual changes in ice coverage occurring in the present climate (say the past 30 years), but that little is known quantitatively about the *processes* that produce these variations (Walsh, 1983; World Meteorological Organization, 1983).

The goals of the present research are to formulate climatological ice budget equations appropriate for diagnostic analysis using available data, and to estimate the ice area budget of the Greenland Sea region. Particular emphasis is placed on the climatological annual mean budget, and on the climatological annual cycle.

The present study emphasizes the observational aspect of sea ice science. In keeping with this emphasis, estimates of each term in a given ice budget equation are sought that depend primarily on measurements while remaining essentially independent of extraneous assumptions and hypotheses. Such estimates could serve as independent data against which to test the results of theoretical models. This ideal is compromised by several circumstances. First, some of the quantities that appear in the budget equations are not measured on the required time and space scales. For example, ice thickness is perhaps the most important state variable for which budget estimates are desired, but its measurement has been limited to occasional drill holes and submarine sonar transects which are insufficient for estimating climatological statistics. The second difficulty is that measurements refer to discrete points in space and time, whereas the averages and line integrals needed for diagnostic evaluation of the ice budget require variables at all points in some domain, so that an interpolation procedure is required. Finally, observations of the relevant state variables, including sea ice concentration and velocity, indicate that substantial departures from climatology occur aperiodically in space and time, and may persist for periods of a week or more so that many independent measurements are needed to reduce the sampling errors when estimating climatological statistics. All three of these problems force the investigator to adopt *modeling hypotheses* in order to estimate ice budgets from observations. For example, Thorndike and Colony (1983) base their optimal estimates of daily sea ice velocity fields on a homogeneous, isotropic, Gaussian model. Although such hypotheses may be tested for consistency with the data, there may be other, equally consistent models that produce different estimates of desired budget quantities. It is important, therefore, to consider the sensitivity of estimated budgets to the assumed model of the data.

In order to obtain budget estimates in this study, measurements made over the sea ice itself are used whenever possible. The analysis is also limited primarily to observations for which the probable measurement errors can be estimated with confidence. In each budget equation considered, we shall attempt to reduce to one (at most) the number of terms that cannot be estimated from measurements. The budget equation, together with the probable errors in its terms, then places a constraint on the value of this residual term.

The Greenland Sea has been chosen for study because it is the site of vigorous ocean-ice interaction, as evidenced by the formation of deep water and the current systems that play a major role in ice advection (Coachman and Aagaard, 1974; Pacquette, et al, 1985). The sea ice area there has large seasonal and interannual variability, and the largest trend of any arctic marginal sea during the period 1953-1977 (Walsh and Johnson, 1979).

STATE VARIABLES AND BUDGET EQUATIONS

Equations governing time changes in sea ice area are developed for an arbitrary region of the ocean's surface. The state variables chosen to describe the ice must satisfy several requirements:

1) The state variables should be physically relevant to climatic interactions among air, sea and ice.

2) The state variables should be related to the physical processes of ice advection, freezing, melting and deformation through equations expressing basic physical principles.

3) The quantities that appear in the equations should be measureable, or estimable from measurements in such a way that the probable errors of the computations can be specified.

Perhaps the most important sea ice state variables are ice thickness $h(\mathbf{x}, t)$ and the thickness distribution function $g(h, \mathbf{x}, t)$ (Thorndike, et al., 1975). The thermodynamic source terms that contribute to changes in ice thickness are related in a straightforward way to enthalpy and radiation fluxes in the atmosphere and ocean through the latent heat term in the energy balance equation. Unfortunately, available data are insufficient to permit an accurate diagnostic evaluation of the climatological thickness or thickness distribution budgets. Therefore, in this work we restrict the analysis to sea ice area, a state variable that is not without climatic relevance, due to its effects on regional albedo and air-sea energy flux. All of the techniques described below may be applied to ice thickness budgets when appropriate data become available.

The symbols $\mathbf{x}$ and (x, y) are used to denote horizontal Cartesian coordinates in a plane locally tangent to the sphere at some prechosen latitude and longitude. For dynamical computations, we shall take account of the sea surface slope, relative to surfaces of constant geopotential. Time is represented by the symbol t.

The presence of sea ice at a point is distinguished from that of any other material in the ocean by an indicator function

$$I(\mathbf{x}, t) \equiv \begin{cases} 1 \ \textit{sea ice at} \ (\mathbf{x}, t) \\ 0 \ \textit{no sea ice at} \ (\mathbf{x}, t) \end{cases} . \tag{2.1}$$

If, because of measurement limitations or physical interest, it is desirable to distinguish different ice types, based on their age or stage of development, or to consider only sea ice that exceeds some minimum thickness, the present formulation can be adapted simply by changing the definition (2.1).

Sea ice motion may be characterized mathematically with a Lagrangian position function $\mathbf{x}(t, \mathbf{X})$ and a velocity function

$$\mathbf{u}(\mathbf{x}, t) \equiv \lim_{\tau \to 0} \frac{\mathbf{x}(t+\tau, \mathbf{X}) - \mathbf{x}(t, \mathbf{X})}{\tau} \tag{2.2}$$

where $\mathbf{X} = \mathbf{x}(0, \mathbf{X})$ labels a point on a piece of sea ice according to its position at the initial time $t = 0$. $\mathbf{u}(\mathbf{x}, t)$ is assumed to be independent of $\mathbf{X}$, implying that the particular piece of ice that occupies $(\mathbf{x}, t)$ is identified uniquely by its initial coordinate $\mathbf{X}$. In nature, this condition may be violated, for instance, when adjacent pieces of ice break and pile up to form a pressure ridge. However, for practical purposes, the definition (2.2) is adequate when applied to the finite trajectories $\mathbf{x}(t, \mathbf{X})$ that are measured by tracking drifting camps and buoys. Thorndike (1986) has presented evidence, based on measurements of ice displacement, that the velocity defined by the limit in equation (2.2) exists, in the mean square sense. Notice that equation (2.2) leaves the ice velocity undefined at points where $I(\mathbf{x}, t) = 0$.

Large scale variations are described by ice state variables integrated over a given region. Consider the region R of area R, and whose boundary is Γ (Figure 1b). The total ice area inside Γ is

$$A\,(t) = \iint_{R} I\;dxdy\ . \tag{2.3}$$

Processes that change this regional state variable appear as terms in the ice area budget equation. In a time increment dt the area of sea ice that moves into R across a small segment dl of Γ is $[\,-\,\mathbf{u}I\cdot\mathbf{n}dl]dt$, where $\mathbf{n}$ is a unit vector normal to the element dl of Γ. The total area change by advection across Γ can therefore be written

$$dF_A\,(t) = \left[\,-\int_{\Gamma}\mathbf{u}I\cdot\mathbf{n}dl\right]dt\ . \tag{2.4}$$

$A\,(t)$ may suffer additional changes due to melting, freezing, and ice deformation occurring within R. The contributions from melting and freezing processes are denoted by the thermodynamic area source term $S_A\,(t)dt$. Similarly, the deformational changes are called $D_A\,(t)dt$. Using this notation, we can write the conservation principle for sea ice area in the form

$$\frac{dA\,(t)}{dt} = -\int_{\Gamma}\mathbf{u}I\cdot\mathbf{n}dl + S_A\,(t) + D_A\,(t)\ . \tag{2.5}$$

The thermodynamic source term represents only that part of the total melting and freezing in R that changes ice area into open water area, or *vice versa*. Equation (2.3) defines the state of the sea ice cover in the region of interest, while equation (2.5) expresses time changes in this state in terms of advective and thermodynamic processes driven by the atmosphere and ocean. These terms describe the instantanteous or synoptic average rates of change during a particular time interval.

Piecewise continuity in space ($\mathbf{x}$) of the functions $\mathbf{u}$ and I is sufficient to insure the existence of the integrals (2.3) and (2.4), irrespective of the existence of spatial derivatives. If the ice state is described by differentiable functions for velocity $\mathbf{u}$ and ice thickness distribution $g(h,\,\mathbf{x},\,t)$ (as it is in theoretical models used to simulate the ice climatology (e.g. Walsh, et al., 1985)) the results may be compared termwise to observational estimates of equation (2.5). This is so because (2.5) is an integral form of the conservation principle formulated for ice thickness distribution by Thorndike, et al. (1975). In order to achieve the equivalence, equation (3) in Thorndike, et al. (1975) is integrated over a thickness interval $(h_1,\,h_2\,)$, and a double limit taken $(h_1 \rightarrow 0)$, $(h_2 \rightarrow \infty)$ followed by integration with respect to $\mathbf{x}$ over the region R. Applying Gauss' theorem to the resulting flux terms yields

$$\frac{\partial A}{\partial t} = -\int_{\Gamma}\mathbf{u}C\cdot\mathbf{n}dl + \iint_{R}\lim_{h_1\to 0} f(h_1\,)g(h_1\,)d\mathbf{x} + \lim_{h_1\to 0}\,\lim_{h_2\to\infty}\iint_{R}\left\{\int_{h_1}^{h_2}\psi(h)\;dh\right]d\mathbf{x} \tag{2.6}$$

where C is the ice concentration, f is the thermodynamic growth rate due to vertical accretion and ablation, and ψ is the mechanical redistributor. Each term in equation (2.6) is equivalent to the corresponding term in (2.5), thus providing a recipe for post-processing simulation results from models that use $g(h)$ in order to compare with observational estimates. An additional term found in recent formulations accounts for ice area changes due to sidewall melting, and would appear in our $S_A\,(t)$ term.

In order to apply equation (2.5) to problems of climate, we consider in the next section time averages over an ensemble of years, and over the annual cycle that occurs in each year.

CLIMATIC AVERAGING

Climatic averaging may be described formally with the aid of a time partition

$$t = \tau + (n-1)P \tag{3.1}$$

where t is the time, τ is the day of the year: $0 \leq \tau \leq P$, $P = 365.25$ days is the annual period, and n is an index denoting the year number in a sequence of N years, beginning on some prechosen date.

Any function of time, such as the ice area $A(t)$, may be expressed in terms of the alternate variables τ and n: $A(t) = A(\tau + (n{-}1)P) = A(\tau,\,n)$. The ***time average*** , from τ_1 to τ_2, with $\tau_2 > \tau_1$, is defined as the integral

$$\bar{A}(n, \tau_1, \tau_2) \equiv \frac{1}{\tau_2-\tau_1} \int_{\tau_1}^{\tau_2} A(n, \tau) d\tau \tag{3.2}$$

computed with n fixed. The special choice $\tau_1 = 0$, $\tau_2 = P$, produces the *annual mean*, denoted by omitting the arguments on the left side of (3.2). Another average, called the *climatological mean* , is computed by summing over the N years with fixed τ

$$\langle A(\tau)\rangle \equiv \frac{1}{N} \sum_{n=1}^{N} A(n, \tau) \ . \tag{3.3}$$

Time changes and physical processes associated with the climatological annual mean (CAM), the climatological annual cycle (CAC), and the irregular fluctuations (IF), may be distinguished with the aid of subscripts as follows

$$A_o \equiv \langle\bar{A}\rangle \tag{3.4}$$

$$A_1(\tau) \equiv \langle A(\tau)\rangle - A_o \tag{3.5}$$

$$A_2(\tau, n) \equiv A(\tau, n) - A_1(\tau) - A_o \ . \tag{3.6}$$

These definitions imply the following

$$\begin{gathered} A(t) = A_o + A_1(\tau) + A_2(\tau, n) \\ \langle A_o\rangle = \overline{A_o} = A_o \\ \langle A_1(\tau)\rangle = A_1(\tau) \\ \overline{A_1} = 0 \\ \langle A_2\rangle = 0 \ . \end{gathered} \tag{3.7}$$

If the temporal variations of ice velocity $\mathbf{u}$ and the indicator function I are expressed as in (3.7) the CAM product of these functions becomes

$$\langle\overline{\mathbf{u}I}\rangle = \mathbf{u}_o I_o + \overline{\mathbf{u}_1 I_1} + \langle\overline{\mathbf{u}_2 I_2}\rangle \ , \tag{3.8}$$

making use of (3.7). The CAM ice area budget is therefore

$$\frac{\langle\overline{dA}\rangle}{dt} = - \int_\Gamma [\mathbf{u}_o I_o + \overline{\mathbf{u}_1 I_1} + \langle\overline{\mathbf{u}_2 I_2}\rangle]\cdot\mathbf{n}dl + S_o \ . \tag{3.9}$$

Here we have lumped together the deformational and thermodynamic source terms because our data set is inadequate to distinguish them. Unfortunately, theoretical models for the ice thickness redistributor are based only on integral constraints and plausible geometric arguments (Thorndike, et al., 1975; Rothrock, 1986). Hard evidence to support this theory has proven elusive because the relevant quantities $g(h, \mathbf{x}, t)$ and strain rate $\dot{e}_{ij}$ are difficult to observe. In fact, basic questions of definition continue to plague both entities. Still, one may safely assume that ridging processes are overwhelmingly irreversible: ice does not "unridge" by mechanical means. Therefore, one expects $D_A(t) < 0$, from which it follows that S_o places a lower bound on the thermodynamic source term $(S_A)_o$. The left side of (3.9) is equivalent to $[A(P, N) - A(0,1)] / NP$. If A is finite, this term vanishes as $N \rightarrow \infty$. Neglecting this term for large N yields

$$S_o = \int_\Gamma [\mathbf{u}_o I_o + \overline{\mathbf{u}_1 I_1} + \langle\overline{\mathbf{u}_2 I_2}\rangle]\cdot\mathbf{n}dl \ . \tag{3.10}$$

Equation (3.10) is the CAM ice area budget for a stationary climatic ensemble. Let us note some salient facts about this equation. First, it purports to describe the steady-state balance between advection and thermodynamic sources that maintains the CAM ice area in the region R. All quantities appearing in the equation are *statistics* rather than individual realizations. Moreover, the right side of the equation vanishes if these statistics are homogeneous in space, and the second term in the integrand vanishes for time homogeneous statistics (no annual cycle). These facts make it clear that the problem of computing climatological ice budgets depends on accurate estimates of spatial and temporal *inhomogeneities* in statistics of ice velocity and the indicator function.

The same averaging procedures are applied to the seasonal cycle of ice area $dA_1 / d\tau$,

$$\frac{dA_1}{d\tau} = -\int_{\Gamma} \left\{ [\mathbf{u}_1 I_1 - \overline{\mathbf{u}_1 I_1}] + [<\mathbf{u}_2 I_2> - <\overline{\mathbf{u}_2 I_2}>] \right\} \cdot \mathbf{n} dl \tag{3.11}$$

$$-\int_{\Gamma} [\mathbf{u}_o I_1 + \mathbf{u}_1 I_o] \cdot \mathbf{n} dl + (S_A(\tau))_1 \quad .$$

It may seem curious that the covariance $<\mathbf{u}_2 I_2>$ contributes to the ice flux across Γ. After all, when the indicator function I is zero, $\mathbf{u}$ is undefined by equation (2.2), and could be defined arbitrarily without affecting the advective transport term in equation (2.5). On reflection, one recognizes that while the definition of $\mathbf{u}|_{I=0}$ does not affect the total budget, it affects the partition of the flux into contributions from mean, periodic and aperiodic time variations. Moreover, different data processing procedures are appropriate for different definitions. In order to illustrate this problem, consider the definition $\mathbf{u}|_{I=0} \equiv 0$. In this case, the area flux across any element of Γ is $F = \mathbf{u}I \cdot \mathbf{n} dl = \mathbf{u} \cdot \mathbf{n} dl$. Setting aside for the moment the temporal and spatial inhomogeneities in statistics, suppose the ensemble average operator $<(\ )>$ applied to $\mathbf{u}$ corresponds to integration over the conditional probability distribution function

$$p_1\,(\mathbf{q}) d\mathbf{q} \equiv prob \left\{ \mathbf{u} \in [\mathbf{q}, \mathbf{q} + d\mathbf{q}|_{I=1} \right\} \tag{3.12}$$

and let

$$P \equiv prob \left\{ I = 1 \right\} \tag{3.13}$$

so that $1 - P$ is the probability that $I = 0$. The conditional expectation values for the flux F are

$$< F >|_{I=1} = \int_{-\infty}^{\infty} \mathbf{q} p_1\,(\mathbf{q}) d\mathbf{q} \cdot \mathbf{n} dl = <\mathbf{u}>|_{I=1} \cdot \mathbf{n} dl \tag{3.14}$$

and

$$< F >|_{I=0} = 0 \quad . \tag{3.15}$$

The (unconditional) expectation value for the flux is

$$< F > = <\mathbf{u}>|_{I=0}\, P + < F >|_{I=0}\, (1 - P) = < \mathbf{u} >|_{I=1} < I > \quad , \tag{3.16}$$

using (3.15) and the fact that $P = < I >$. Note that (3.16) contains no statistical moments of order greater than 1.

For inhomogeneous statistics, the distributions may be modified to read $p_1\,(\mathbf{q}, \mathbf{x}, \tau)$ and $P(\mathbf{x}, \tau)$, and the averages over p_1 and P identified with the ensemble average over N years. A result similar to (3.16) is again recovered

$$< F > = < \mathbf{u}(\mathbf{x}, \tau) >|_{I=0} < I(\mathbf{x},\tau) > \tag{3.17}$$

$$= \left[\mathbf{u}_o\,(\mathbf{x}) + \mathbf{u}_1\,(\mathbf{x},\tau)\right]\left[I_o\,(\mathbf{x}) + I_1\,(\mathbf{x},\tau)\right]$$

where (3.5) has been used and all averages of $\mathbf{u}$ are henceforth understood to be conditional on $I = 1$. Thererfore the CAM and CAC ice area budget equations do not contain the covariance term $< \mathbf{u}_2\, I_2 >$,

$$S_o = -\int_{\Gamma} (\mathbf{u}_o\, I_o + \overline{\mathbf{u}_1\, I_1}) \cdot \mathbf{n} dl \tag{3.18}$$

and

$$\frac{dA_1}{d\tau} = -\int_{\Gamma} \left\{ \mathbf{u}_1\, I_1 - \overline{\mathbf{u}_1\, I_1} + \mathbf{u}_o\, I_1 + \mathbf{u}_1\, I_o \right\} \cdot \mathbf{n} dl + S_1(\tau) \ , \tag{3.19}$$

provided that conditional ice velocity statistics are used. Ice velocity measurements analyzed in this study derive from time series of Lagrangian positions following drifting manned camps and data buoys, for which $I = 1$. Therefore statistics estimated from these measurements are conditional on $I = 1$. Care is needed, however, if one expresses the ice velocity as a function of atmospheric and oceanic variables, such as the geostrophic surface wind G and the geostrophic surface current c. Since these variables are well defined when $I = 0$, second moments such as $<c_2 I_2>$ and $<G_2 I_2>$ may contribute to budgets calculated this way.

ANALYSIS OF ICE CONCENTRATION

Measurements on the ice indicator function I are too sparse to provide reliable climatological statistics. Therefore, ice concentration data compiled by Walsh and Johnson (1979, hereafter WJ) are used in their stead. Ice concentration C is related to the indicator function by a relationship of the form

$$C(\mathbf{x}, t) = \iint_{\mathbf{R}} H(\mathbf{x} - \mathbf{s}) I(\mathbf{s}, t) d\mathbf{s} \tag{4.1}$$

where $H(\mathbf{x})$ is a weighting function. For example, the function

$$H(\mathbf{x}) = \begin{cases} 0 & |\mathbf{x}| > r \\ 1/\pi r^2 & |\mathbf{x}| < r \end{cases} \tag{4.2}$$

picks out the running average of I over a circular area of radius r centered on any desired point in R. Although the ice indicator function I is piecewise continuous, not differentiable, and varies on length scales of 1-10 km (Rothrock and Thorndike, 1985), its climatological statistics vary smoothly and it is assumed here that the space and time inhomogeneities of I_o and I_1 are identical to those of C_o and C_1. The WJ data set consists of 12 end-of-month values in each of the 25 years 1953-77, at grid points spaced 111 km apart in a rectangular array. The portion of this grid covering our study region is shown on Figure 1b. The concentrations, given in one-tenth intervals, were extracted from sea ice charts published by agencies of several nations. It is difficult to estimate the measurement error variance for ice concentration data deriving from sources such as these, because of differences, over time and between agencies, in the amount and quality of information on which the charts are based, and in analysis techniques, format and resolution applied to this information. Possible sources of error and bias are discussed by WJ. Improved estimates of the accuracy of ice concentration measurements ought to result from current and planned investigations of satellite passive microwave data (SSM/I Science Working Group, 1984). In the meantime, it is assumed here that the measurement errors in the WJ data set have mean zero and standard deviation 1/10. The ice chart data for the Greenland Sea region derive from analyses by agencies of several nations over a relatively long period, compared to other marginal seas in the Arctic. Moreover, an independent analysis of satellite imagery over the region agrees well with the WJ data set in the Greenland and Barents Sea during 1971-1980 (Vinje, 1984).

The ice area $A(t)$ within the contour Γ is estimated from the ice concentration measurements using a finite sum to approximate the integral in equation (2.3)

$$A(t) = \sum_{i=1}^{M} O_i \hat{I}_i(t) \tag{4.3}$$

where $\hat{I}_i(t)$ is the *measured* ice concentration at the *ith* point in the WJ array over R, and O_i is the ocean surface area represented by that point. The boundary segments Γ_1, Γ_2, Γ_3 (Figure 1b) pass through the grid points, bisecting the grid boxes to which the ice concenration applies. Therefore, on these contours O_i is assigned half the value given in the data set so that A includes no ice outside R. The time series of 300 end of month values $A(t)$ (Figure 1c) displays an obvious annually periodic component along with irregular fluctuations in a broad frequency band. The average ice area for the 25-year period is $A_o = 0.34 \times 10^6\ km^2$, equivalent to 53% of the total area $|R_1| = 0.64 \times 10^6\ km^2$. The variance of the signal $A(t)$ receives additive contributions from the annual cycle and the aperiodic departures, i.e. $var(A) = \overline{A_1^2} + \langle A_2^2 \rangle$. Applying this scheme to the time series yields

$$[0.097 \times 10^6\ km^2]^2 = [0.074 \times 10^6\ km^2]^2 + [0.063 \times 10^6\ km^2]^2 .$$

Thus typical departures from the annual cycle are comparable to the annual cycle itself. Figure 1d shows $A_1(\tau)$ with its maximum in late February and minimum in late August. The order of magnitude of the time derivative in equation (3.19) may be estimated as the range of A_1 divided by 6 months : $0.23 \times 10^6\ km^2 / 6\ mo = 0.4 \times 10^5\ km^2 / mo$.

Climatological variations in the spatial distribution of the ice cover are illustrated by Figure 1a and 2. The $I_o(\mathbf{x})$ field reflects the east-west juxtaposition at Fram Strait of the cold, low salinity East Greenland Current (EGC), setting southward over the Greenland shelf, and the warm, saline West Spitsbergen Current (WSC) that carries water of Atlantic origin into the Arctic Basin. The vertical heat flux from the latter stream pushes the ice edge northward,

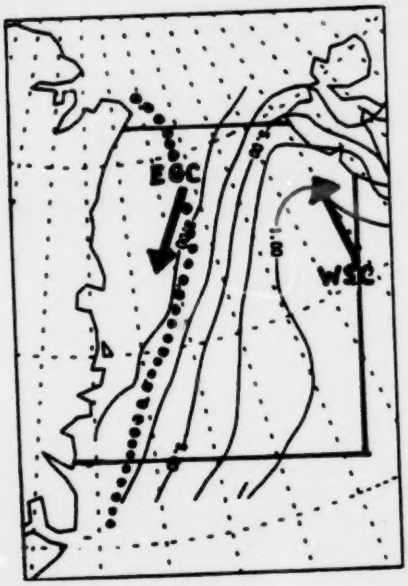

Figure 1a: CAM Ice Concentration contours (in tenths), Dominant Surface Currents, and 1000 m Isobath (dots).

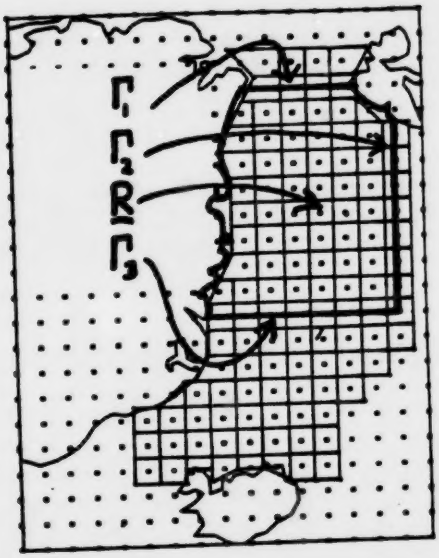

Figure 1b: Study area, boundary segments, WJ grid points, and grid boxes for averaging.

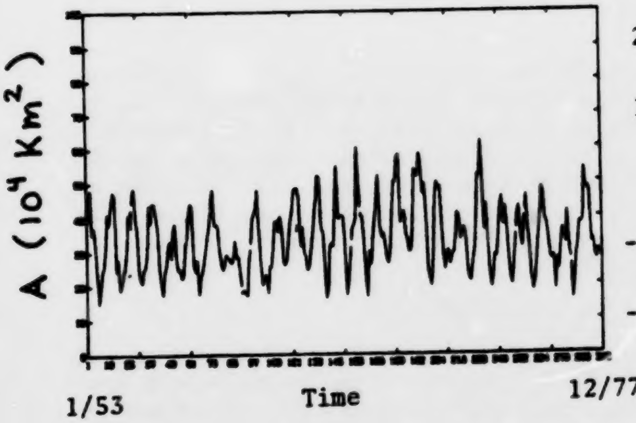

Figure 1c: Time series of ice area A(t) in the region R_1.

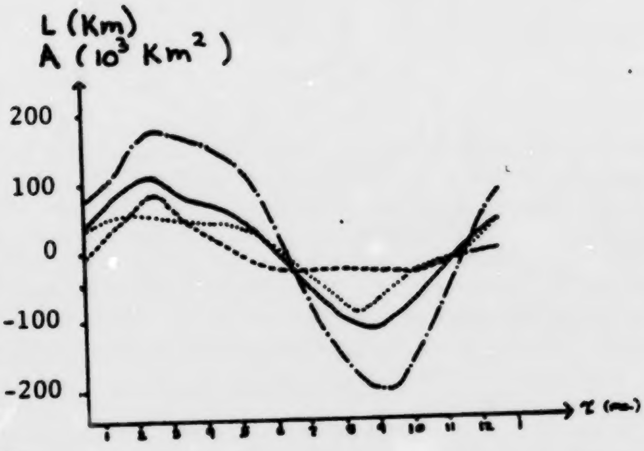

Figure 1d: Mean annual cycles of ice lengths on Γ_1 (dots), Γ_2 (dashes), and Γ_3 (dot-dash), and ice area A_1 (solid).

as evidenced by climatological ice concentration contours that describe an embayment poleward of 75° *N*. South of this embayment, the ice cover protrudes eastward in winter (Figure 2) over the 3000 meter depths of the Greenland Abyssal Plain. The Greenland shelf, delimited approximately by the 1000 m isobath that marks the steep continental slope, is more than 9/10ths ice covered through most of the year. A continual supply of polar ice is borne south by the EGC over this shelf. This polar water mass is nearly isothermal at the freezing point and therefore provides no significant oceanic heat source to melt the ice.

As we shall see presently, the EGC provides a dominant motive force for ice influx across Γ_1 and for ice efflux on Γ_3 . The prevailing surface winds act in the same sense. Likewise, winds and currents cooperate on Γ_3 to produce an influx. It is instructive to consider qualitatively the implications of a *uniform advective velocity*, importing ice on Γ_1 and Γ_2, and exporting it on Γ_3 , in light of spatial differences in the ice concentration on these three boundaries. The length of the ice cover on a boundary Γ_i , $i = 1, 2, 3$ is

$$L_i(t) = \int_{\Gamma_i} I(\mathrm{x}, t)dl \tag{4.4}$$

The CAM lengths are $(L_1)_o = 425\ km$, $(L_2)_o = 32\ km$ and $(L_3)_o = 353\ km$. With uniform velocities these figures imply a net ice influx due to the greater ice concentrations in Fram Strait compared to Γ_3, and a small contribution from the segment Γ_2. The CAC of these lengths is shown in Figure 1d. $(L_1)_1(\tau)$ is flat in the winter months, when the boundary is almost totally ice covered. The segment extending south from Spitsbergen is essentially ice free in summer, resulting in a flat $(L_2)_1$ curve as well. The most striking feature of Figure 1d is the large seasonal amplitude of $(L_3)_1$ suggesting that the CAC of L tends to produce a net ice outflow from $\mathbf{R}_1$ in winter, and net inflow in summer.

In order to estimate terms in equations (3.18) and (3.19) the ice concentration time series at each grid point was split into the three contributions $I = I_o + I_1 + I_2$. Standard deviations of I_1 and I_2 are mapped in Figure 3. Again the variations due to CAC and IF are of similar size. Spatially, both kinds of variability are at maximum near the climatological ice edge.

ANALYSIS OF ICE VELOCITY

Lagrangian position measurements, reported by manned camps and data buoys drifting through the Greenland Sea, are used exclusively in this research to estimate ice velocity statistics. The basic data comprise more than 3000 daily estimates of position and velocity during the years 1965 and 1976-1984. Figure 4 shows these positions and Table I lists the various data sources. Noteworthy features on Figure 4 include the gradual decrease in density of observations as one proceeds southward from Fram Strait, and the failure of trajectories initialized north of Fram Strait to visit both the inner shelf off Greenland, poleward of 75° *N* , and the abyssal plain over which the wintertime ice cover protrudes. The trajectories suggest that the ice in this latter region forms locally. From Figure 4 it is clear that sampling problems for ice velocity are most severe on Γ_2 (no data), and least severe at Fram Strait (Γ_1). The number of daily buoy observations in a set of boxes covering the region is presented in Figure 5.

Daily ice velocity is estimated from smoothed and interpolated time series of Lagrangian positions, according to the definition (2.2). For the bulk of our data, procedures described by Thorndike and Colony (1983) yield daily ice velocity estimates at each buoy position with an rms error of less than 0.5 cm/s. The largest velocity measurement errors (≈ ± 2 *cm/s*) apply to the ARLIS-II data. On time averaging, errors of this size become utterly insignificant compared to the sampling errors that influence the estimates of $\mathbf{u}_o$ and $\mathbf{u}_1$.

A subset of the buoy data, amounting to roughly 2/3 of the total, and confined to the period 1979-1984, includes estimates of the surface geostrophic wind G(x, *t*) for 1200 hours GMT at the buoy position. The daily G estimates are unbiased with an rms error smaller than 2 m/s. These data are referred to as "buoy winds", and aid in distinguishing contributions of air stress and ocean current advection to the total ice motion. A set of daily geostrophic wind estimates, called "grid winds", was compiled for the fixed WJ grid points shown on Figure 1b, by applying optimal interpolation procedures to the pressure data reported by the Arctic Basin Buoy Program 1979-1983. The grid winds are used, together with the ice concentration, to estimate the wind driven part of the ice flux across the three boundary segments.

Let us consider the first and second moments of all daily ice velocities and buoy winds in the region $\mathbf{R}_1$, and compare these with corresponding parameters for the central Arctic. Daily ice velocity in the latter region has been investigated by Thorndike (1986), who finds time averages between 0 and 3 *cm/s*, and vector standard deviations on

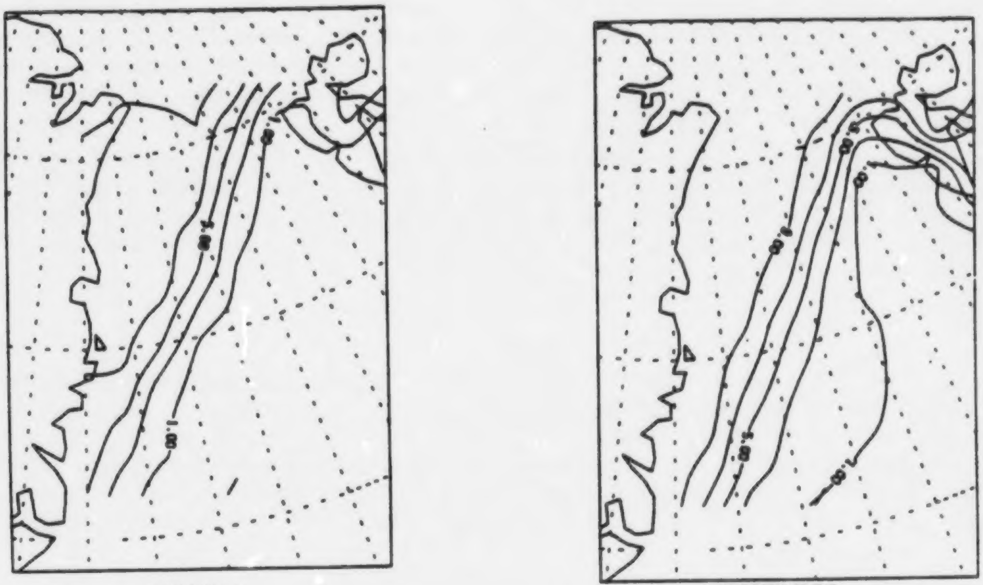

AUGUST NOVEMBER

FEBRUARY MAY

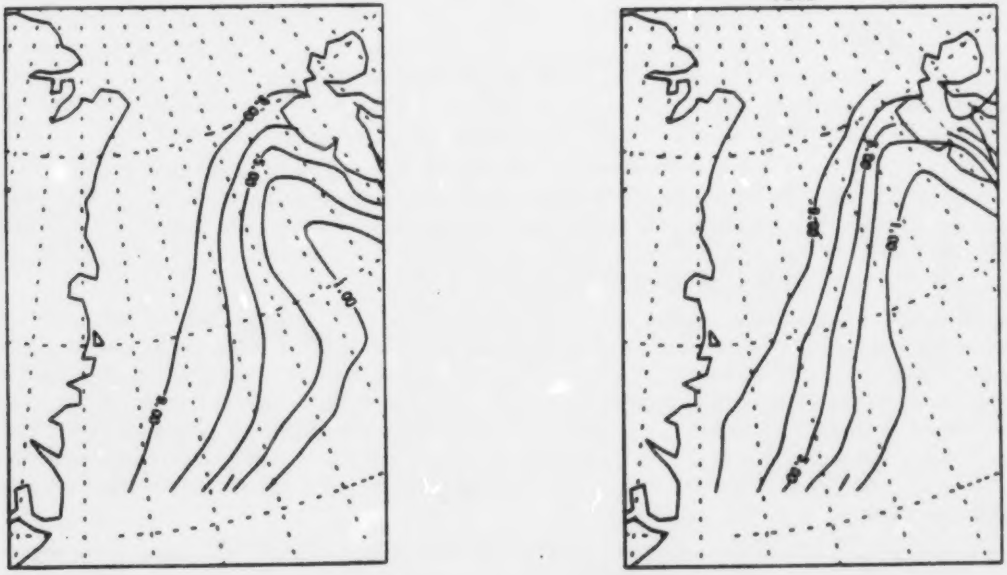

Figure 2: Monthly mean ice concentration fields $I(\underline{x},t)$ averaged over 1953-1977.

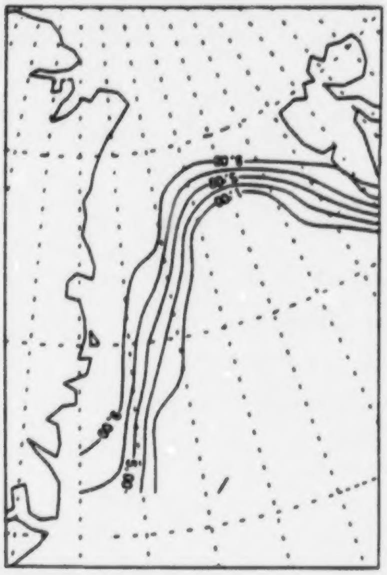

Figure 3a: February, 1960
Ice Concentration (tenths)

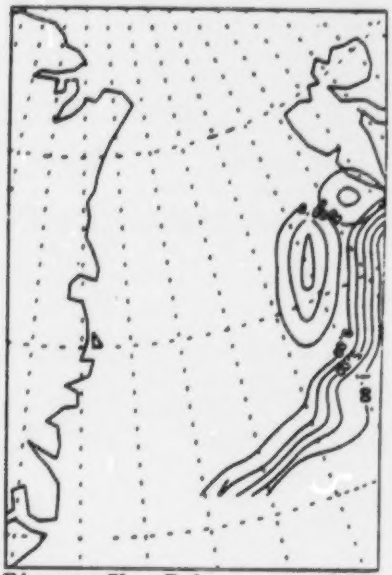

Figure 3b: February, 1972
Ice Concentration (tenths).

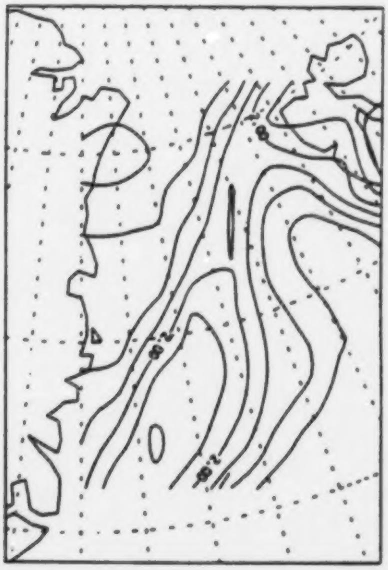

Figure 3c: Standard deviations of the MAC of ice concentration I_1 (tenths).

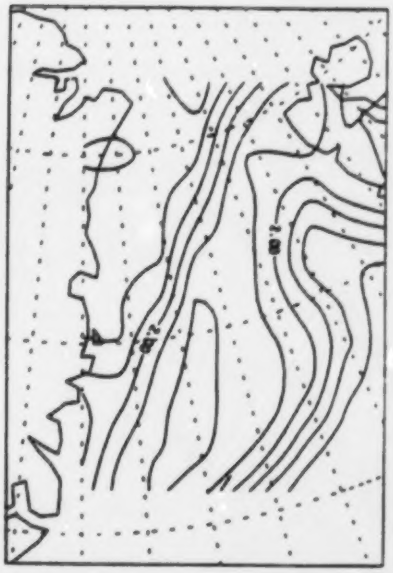

Figure 3d: Standard deviations of aperiodic ice concentration I_2 (tenths).

Table I. Drifting Buoys and Stations in the Data Set.

Data Source	Dates	No. of Buoys	Reference
Arctic Buoy Program	1979-83	17	Untersteiner and Thorndike (1982)
NORSEX	1979	5	Johannessen, et al. (1983)
ARLIS-II	1965	1	Tripp and Kusunoki (1967)
Bedford Institute	1983-84	15	Symonds and Petersen (1985)
Polar Research Lab	1981-83	5	Buck and Jaecks (1984)
Norsk Polarinstitutt	1976-79	12	Vinje (1982, 1986)

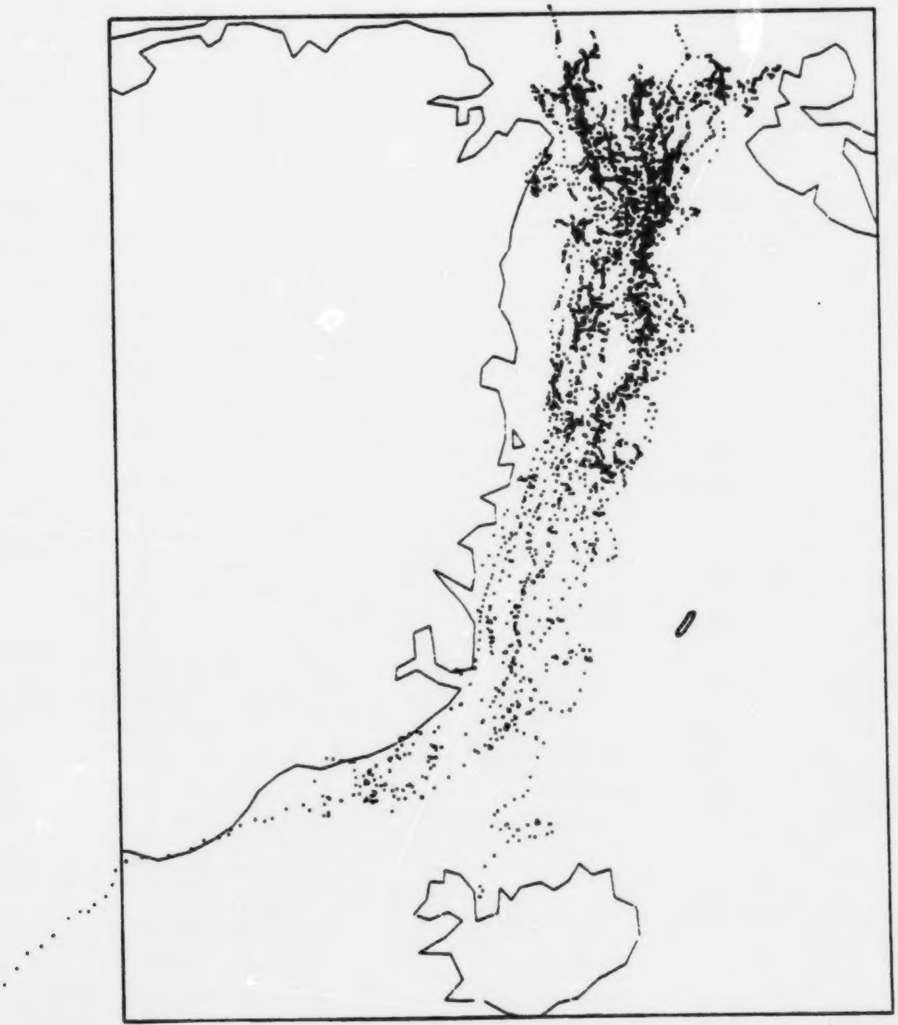

Figure 4: Daily positions of all buoys in the data set.

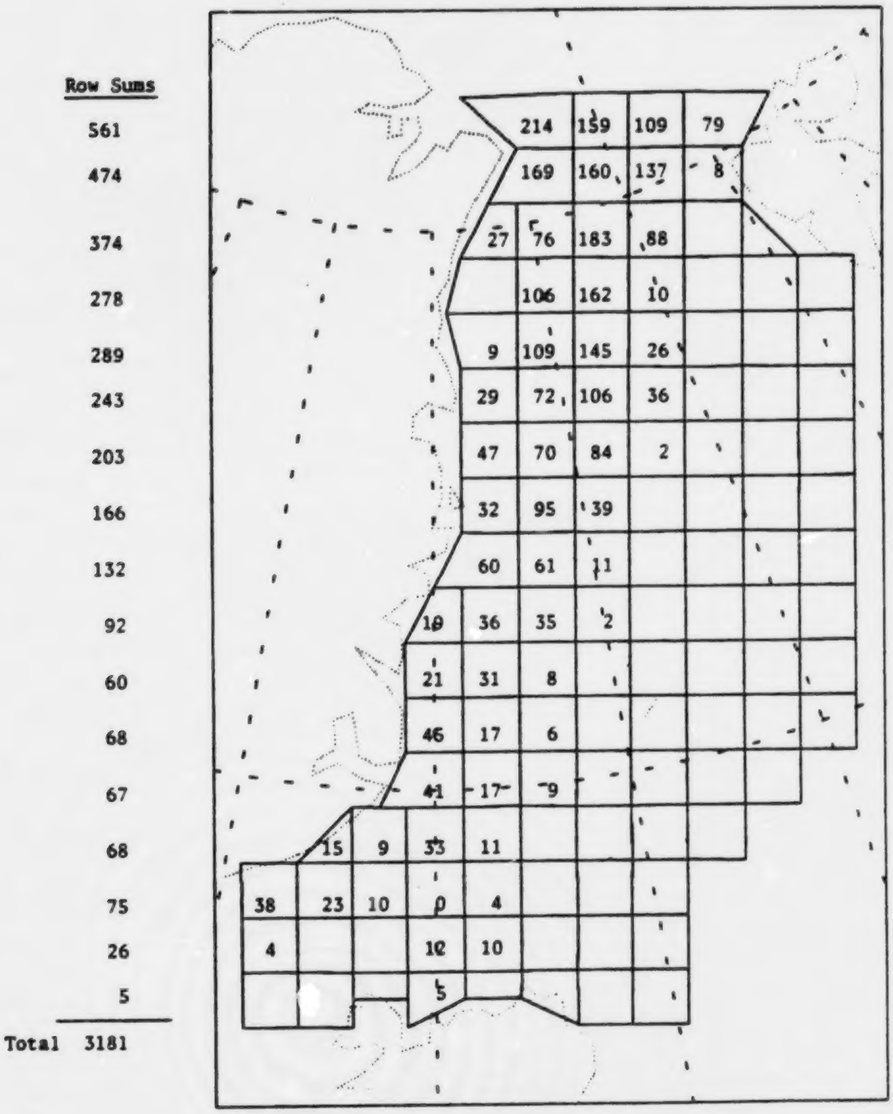

Number of daily buoy observations in 111 km squares.

Figure 5.

the order of $\sigma_u \equiv <\overline{u'^2 + v'^2}>^{1/2} \approx 8$ *cm/s* , where u' and v' are deviations of the velocity components from their respective mean values. The deviations from the mean conform approximately to a homogeneous, isotropic, Gaussian, stochastic process, with autocorrelation time and space scales of about 3 days and 900 km. Thorndike and Colony (1982, hereafter TC) studied daily ice motions as a response to local geostrophic wind velocity, using the linear equation

$$U(t) = AG(t) + c_o + \varepsilon(t) \tag{5.1}$$

wherein all quantities are complex numbers, the real and imaginary parts of which correspond to components in a 2D Cartesian system. The wind drift coefficient $A = |A|e^{-i\theta}$ and the constant c_o , representing non-wind driven motion, are estimated by requiring the residual ε to have zero mean and minimum variance when averaged over a large ensemble of measurements on U and G. Comparisons between equation (5.1) and the momentum equation for a Lagrangian piece of ice suggest that, for large enough wind speeds and small enough forces exerted by adjacent ice pieces, c_o may be interpreted as the time average surface geostrophic ocean current. In this interpretation, the residual $\varepsilon(t)$ accounts for time dependent ocean currents, effects of ice-ice forces, measurement errors, and approximations and uncertainties inherent in parameters that appear in the momentum balance, such as ice thickness, air and water drag coefficients, and so on. Based on this interpretation, TC concluded from drifting buoy data for 1979-1980 that the average ice motion U_o in the central arctic is about 50% wind driven and 50% current driven. For deviations from the time average, about 70% of the variance in U was accounted for by the linear term $AG(t)$ with a wind drift coefficient $|A| \approx 0.008$ and a turning angle $\theta \approx 10°$.

Table II summarizes the results of present computations for all buoy data in R_1, showing TC's central arctic values in parentheses for comparison. Here u and v are measured parallel and perpendicular to the x-axis shown on Figure 1b, which extends along 20° *W*. Principal axes are also employed, such that the component fluctuations u' and v' are uncorrelated with one another. The standard deviations of these principle components are called p and q, the former being the larger of the two. ϕ is the angle between the p-axis and the mean velocity vector $\mathbf{u}_o$ for the region R_1.

The means and standard deviations for ice velocity are much larger in R_1 than in the central Arctic, whereas the geostrophic wind statistics are similar in the two regions. The least squares analysis yields larger wind coefficients and smaller turning angles in R_1, but the differences between these and the arctic basin values are small. These results suggest that the geostrophic wind is related to ice motion in essentially the same way in both regions, except for a narrow region within about 25 km of the ice edge (Johannessen, et al., 1983). The larger mean and variance of the ice velocity imply a greater role for mean and time varying ocean currents in the Greenland Sea, since one does not expect inter-ice forces to increase the velocity variance. Direct measurements of the 150 meter currents over the shelf and slope east of Greenland on 79° *N lat.* are reported by by Aagaard, et al. (1985b) for a 400 day period in 1984-85. Their indicate southward flow, parallel to the isobaths, averaging about 8 cm/s. Unfortunately, their period of record is too short to yield climatological statistics for comparison with our estimates of c_o, and our buoy data are too intermittent in space and time to permit direct correlation between short term currents and $U - AG$ values. Standard deviations for 60 meter current velocity components over a 40-day period in summer, 1983 ranged from 7 to 9 cm/s over the basin east of the continental slope at 78.5° *N lat.* (Hunkins, 1984). These results are consistent with $U - AG$ in showing larger mean and variable currents in the EGC than in the central Arctic.

Seasonal changes in $|A|$ and θ have the same sign in the Greenland Sea as in the central Arctic: both parameters are larger in summer than in winter. As discussed by TC, this result is consistent with the facts that the atmospheric planetary boundary layer is stabler in winter than in summer, and that inter-ice forces are larger in the cold season.

The ratio p/q of the standard deviations of principle velocity components is about 1.7, suggesting anisotropic statistics, in contrast to the central basin. The smallness of the angle ϕ implies that the largest component fluctuations occur in a direction parallel to the mean flow. Returning to equation (5.1), we may ask how much of this anisotropy is associated with geostrophic winds and how much with ε, embodying mainly the effects of variable currents. As seen in Table II, the buoy winds in R_1 give a ratio $p/q \approx 1.4$ and a difference $p - q \approx 2 m/s$. The geostrophic winds statistics also show p nearly aligned with the direction of the mean, similar to the case for ice velocity. Note that the angle ϕ is poorly determined when p is small (winter), and when G_o is small (summer). With a multiplier $|A| \approx 0.01$ the difference $|A|(p - q)$ in wind driven ice motion components accounts for no more than a third (2 cm/s) of the total difference in ice velocity components, (6 cm/s). Therefore, most of the anisotropy is attributed to variable ocean currents and other effects embodied in ε.

Table II.

Statistics of daily buoy velocities and geostrophic winds in R_1

All Data

Variable	Winter (DJFM)	Summer (JAS)	All Year
$<\bar{u}>$	16.9 cm/s	10.2 cm/s	13.2 cm/s
$<\bar{v}>$	-3.2 cm/s	-1.8 cm/s	-1.9 cm/s
p/q	14.7/7.8 cm/s	15.6/10.5 cm/s	15.5/9.6 cm/s
ϕ	-7°	-10°	-9°
N	313	1020	2385

Data with buoy winds

Variable	Winter (JFM)	Summer (JAS)	All Year
$<\bar{u}>$	17.8 cm/s	10.2 cm/s	14.5 cm/s
$<\bar{v}>$	-3.3 cm/s	-2.0 cm/s	-2.3 cm/s
σ_u	15.6 cm/s (7.2)	18.9 cm/s (9.2)	19.0 cm/s
$<\overline{G^{(x)}}>$	3.0 m/s	0.0 m/s	2.2 m/s
$<\overline{G^{(y)}}>$	-3.1 m/s	0.0 m/s	-1.0 m/s
σ_G	9.4 m/s	6.1 m/s	7.4 m/s
p/q	7.2/5.5 m/s	5.0/3.5 m/s	6.2/4.2 m/s
$\|A\|$	0.0092 (0.0077)	0.0120 (0.0108)	0.0127
θ	1° (5°)	13° (18°)	1°
ρ^2	0.31 (0.65)	0.15 (0.76)	0.25
N	189	724	1629

Let us turn to the spatial inhomogeneities in ice motion statistics. The region $\mathbf{R}_1$ is partitioned into a number of boxes roughly 111 km on a side (Figure 1b). CAM ice velocity $\mathbf{u}_o\ (\mathbf{x}_i)$ and ocean current $\mathbf{c}_o\ (\ \mathbf{x}_i\ )$ are computed from all daily observations in each box, where $\mathbf{x}_i$ is the average of all the daily buoy positions contributing to the box statistics. Figure 6 shows the estimated CAM values and the variability, the latter depicted by an ellipse whose major axis is proportional to and aligned with p. Several spatial features may be discerned. The general shapes of the mean ice velocity and current velocity fields are similar. The ice speed is smallest (4–7 *cm/s*) in the row of boxes north of Fram Strait, increasing to 7–15 *cm/s* in the next row of boxes to the south. Further south even larger values $|\mathbf{u}_o| = 22$ *cm/s* occur, as in the row of boxes at Γ_3 . In most rows, the southward flow increases as one moves away from the coast, reaching a maximum over the continental slope, with smaller values on the shelf and over the Greenland Abyssal Plain. However, the decreased speed over the deep basin is poorly resolved because few buoys drifted there. Also evident is a tendency for the mean velocity vectors to parallel the isobaths, turning shoreward near 75° *N* where the shelf break does likewise. The sample mean values $\hat{\mathbf{u}}_o\ (\mathbf{x}_i)$ and their component standard deviations at the grid points $\mathbf{x}_i$ shown on Figure 6 are the input data for interpolation procedures used to estimate the *field* $\hat{\mathbf{u}}_o\ (\mathbf{x})$.

The component $\hat{\mathbf{u}}_o \cdot \mathbf{n}$ for each vector on Figure 6 is an estimate of the CAM field needed for equations (3.18) and (3.19). These estimates are subject to sampling variability, associated with fluctuations described by σ , the standard deviation of the given component. A measure of this sampling error is the standard error of the mean $SE_i = \sigma(\mathbf{x}_i\ )/\sqrt{NDF_i}$, where NDF_i is the number of degrees of freedom associated with the daily data in the ith box. Consecutive daily measurements of velocity by a Lagrangian drifter are not independent, a fact that can be demonstrated by computing the time autocorrelation for deviations from the mean. The autocorrelation is estimated as follows. Each daily buoy velocity measurement is expressed as a deviation from the sample mean for the box in which it finds itself on a given day. These deviations are transformed into components parallel and perpendicular to the box average $\hat{\mathbf{u}}_o\ (\mathbf{x}_i)$. Lagrangian time autocovariances are computed by forming the time-lagged products of these components, following each buoy trajectory. The sum of squares and sum of products at each lag are grouped together for all buoys and all boxes in $\mathbf{R}_1$, resulting in the estimates shown in Figure 7. Although these are Lagrangian estimates, the effects of spatial inhomogeneities in the mean have been reduced by this procedure. These plots suggest that fluctuations along the mean flow tend to persist on time scales of about 3 days, and those perpendicular to $\mathbf{u}_o$ for about 2 days. The integral time scale

$$T^* = \int_0^\infty r(\tau)d\tau \tag{5.2}$$

(in days), may be used to relate NDF_i to the number N_i of daily observations in the sample: $NDF_i = N_i\ /T^*$. The sampling variability is then treated as a measurement error $SE_i = \sigma(\mathbf{x}_i\ )\sqrt{T^*/N_i}$, on input to the optimal interpolation scheme, as in Colony and Thorndike (1984). T^* calculated from the data on Figure 7 is about 3 days for motion parallel to the mean and 2 days for motion normal to $\mathbf{u}_o$.

The methods employed here for estimating $\mathbf{u}_o\ (\mathbf{x})$ on the transects Γ_1 and Γ_3 are similar to those in Colony and Thorndike (1984), with modifications appropriate to the differences between velocity statistics in the Arctic Basin and the Greenland Sea. In each box (Fig. 5) we have a sample of N_i daily observations, from which are derived the average position $(x_i, y_i\ )$, the sample mean velocity components $\hat{u}_o\ (\mathbf{x}_i)$, $\hat{v}_o\ (\mathbf{x}_i)$, and their standard deviations $\sigma_u\ (\mathbf{x}_i)$, $\sigma_v\ (\mathbf{x}_i)$. Attention is restricted to the x-component u, which is parallel to $\mathbf{u} \cdot \mathbf{n}$ on the boundaries Γ_1 and Γ_3. If $\mathbf{x} = (x, y)$ denotes an interpolation point, then estimates $u_o\ (\mathbf{x})$ are needed for equations (3.18) and (3.19) on each of two lines extending through the center of a row of boxes (Figure 1b) and defined by $\mathbf{x} = \mathbf{a}$ constant. The input data for the estimation procedures are limited to averages from boxes in the given row and in the two nearest rows both above and below it. In other words, we choose a subset $\mathbf{x}_j$ of the data points such that $|x - x_j\ | \leq 222\ km$. This choice is motiviated by the desire to use indepedent data in estimating the fluxes on Γ_1 and Γ_3. The data are further restricted to boxes for which $N_j \geq 10$. From this reduced set of M box averages, we compute the *spatial average* $[\ u_o\ ] = \frac{1}{M}\sum_{j=1}^{M} \hat{u}_o\ (\mathbf{x}_j\ )$ and define a spatial deviation $\hat{u}'_o\ (\mathbf{x}_j\ ) = \hat{u}_o\ (\mathbf{x}_j\ ) - [\ u_o]$. The spatial standard deviation is given by $\sigma_s = \left\{ \frac{1}{M}\sum_{j=1}^{M} (\hat{u}'_o\ (\mathbf{x}_j\ ))^2 \right\}^{\frac{1}{2}}$. Following the procedures of optimal interpolation, we choose a linear estimator for the spatial deviation of the velocity component at point x

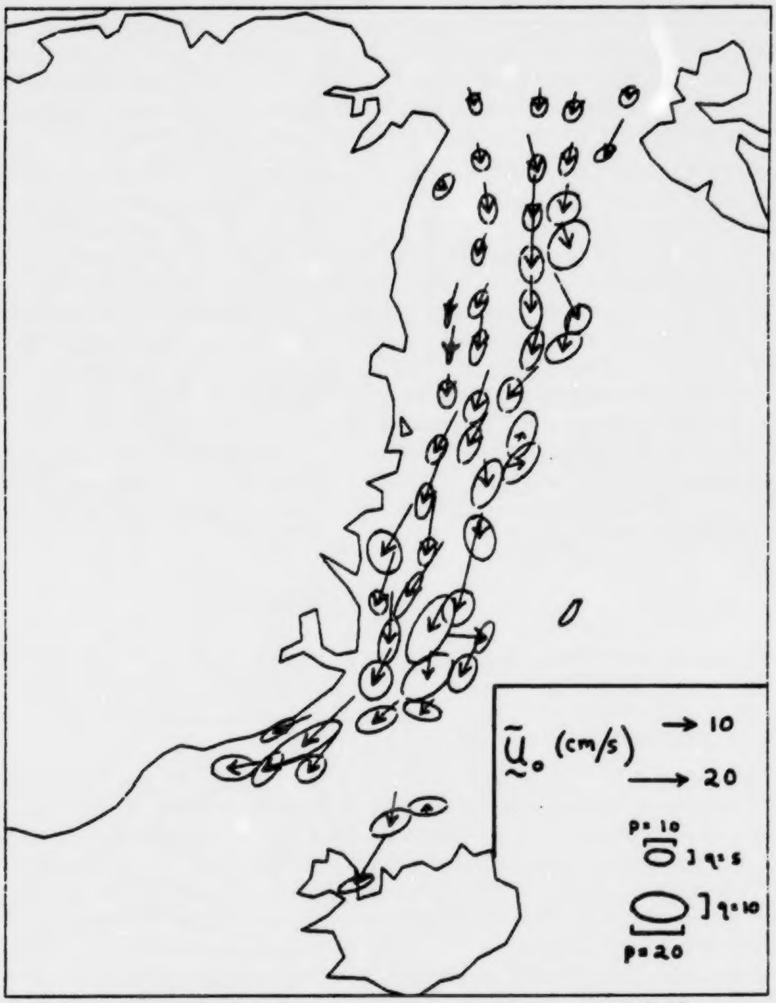

Figure 6a: Sample CAM sea ice velocity vectors and standard deviations p,q in principal coordinate format.

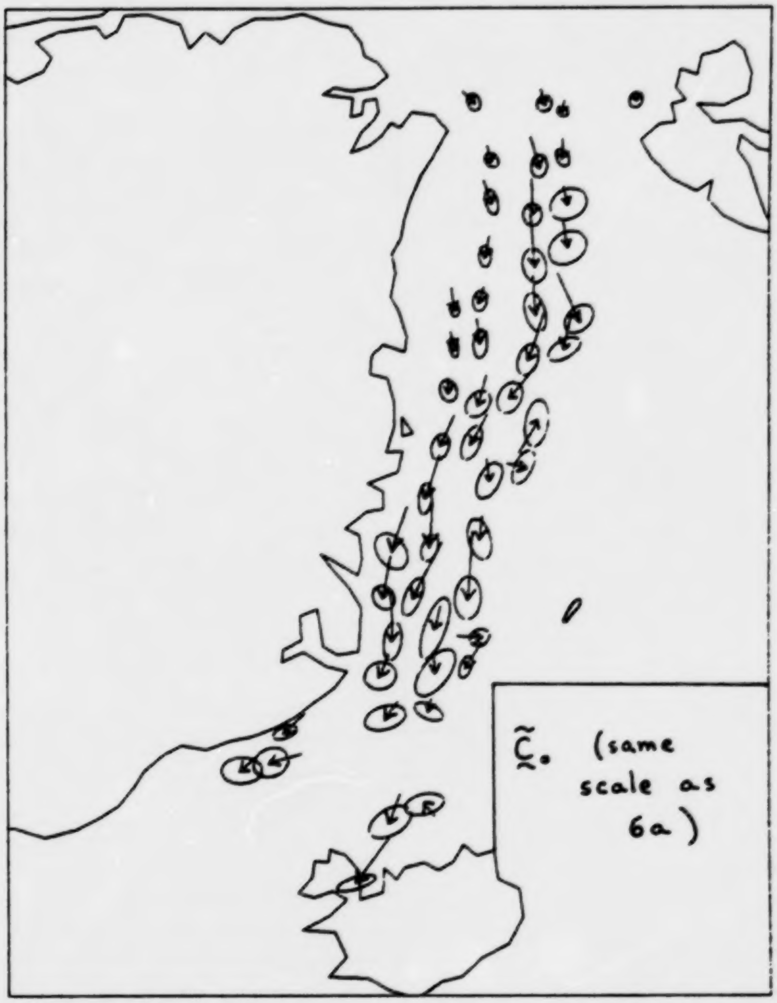

Figure 6b: Sample CAM residual current vectors and standard deviations p,q in principal coordinate format.

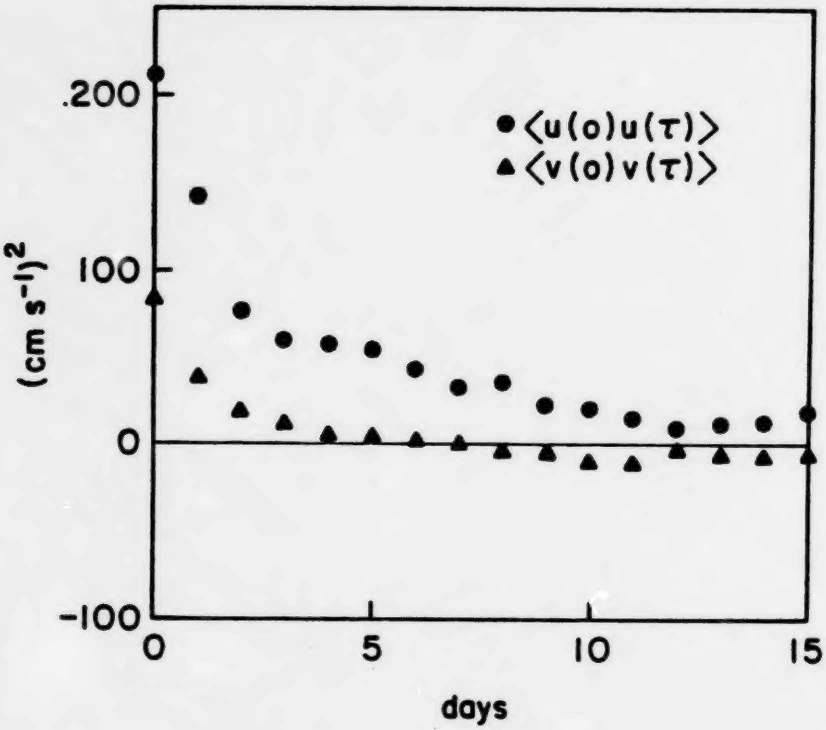

Figure 7: Time autocovariance estimates for sea ice velocity components parallel (u) and perpendicular (v) to the mean flow in $\underline{R}_1$.

$$\hat{u}'_o(\mathbf{x}) \equiv \sum_{j=1}^{M} \alpha_j(\mathbf{x})\tilde{u}'_o(\mathbf{x}_j) \tag{5.3}$$

so the estimate becomes $\hat{u}_o = \hat{u}'_o + [\, u_o \,]$. Two questions arise immediately: 1) How should the coefficients α_j, which weight the individual input data, be chosen? 2) How accurate is the estimate $\hat{u}_o$? Both questions are answered by introducing a statistical model for the *true* velocity component $u_o(\mathbf{x})$, distinguished from the observations and estimates by the absence of a superposed tilde or hat. The measurement error is $e(\mathbf{x}_j) \equiv \tilde{u}'_o(\mathbf{x}_j) - u'_o(\mathbf{x}_j)$. It is assumed that, on spatial averaging, these errors are unbiased, uncorrelated with the true velocity, and uncorrelated among different boxes, i.e.

$$\begin{gathered} [\, e \,] = 0 \\ [\, e u_o \,] = 0 \\ [\, e(\mathbf{x}_k) e(\mathbf{x}_j)] = \delta_{kj}\, \sigma(\mathbf{x}_j) \sqrt{T^{*} / N_j} \end{gathered} \tag{5.4}$$

The interpolation error is

$$\varepsilon(\mathbf{x}) \equiv \hat{u}'_o(\mathbf{x}) - u'_o(\mathbf{x}) \ . \tag{5.5}$$

Returning to equation (5.3), $u'_o(\mathbf{x})$ is subtracted from both sides, using the definitions above, to get

$$\varepsilon(\mathbf{x}) = \sum_{j=1}^{M} \alpha_j(\mathbf{x})(u'_o(\mathbf{x}_j) + e(\mathbf{x}_j)) - u'_o(\mathbf{x}) \ . \tag{5.6}$$

It follows that $[\varepsilon] = 0$ so the estimate is unbiased in this sense. The variance of ε is

$$[\varepsilon^2] = [(\alpha_j(u'_o(\mathbf{x}_j) + e(\mathbf{x}_j)) - u'_o)(\alpha_i(u'_o(\mathbf{x}_i) + e(\mathbf{x}_i))\,] \tag{5.7}$$

where summation is implied on repeated subscripts and the interpolation coordinate $\mathbf{x}$ is suppressed for brevity. A unique set of weighting coefficients α_j, that produces the minimum variance of ε, may be determined by the condition $\frac{\partial}{\partial \alpha_i}[\varepsilon^2] = 0$, from which it follows that

$$\alpha_j \Big[[u'_o(\mathbf{x}_j) u'_o(\mathbf{x}_i)] + [e(\mathbf{x}_j) e(\mathbf{x}_i)] \Big] = [u'_o(\mathbf{x}_i) u'_o(\mathbf{x}_j)] \tag{5.8}$$

Equation (5.8) is a system of M linear equations in the M unknowns α_j, which can be solved if the statistical functions $[\, u'_o(\mathbf{x}_1) u'_o(\mathbf{x}_2)]$ and $[e(\mathbf{x}_1) e(\mathbf{x}_2)]$ are known for all pairs of points $\mathbf{x}_1$, $\mathbf{x}_2$ in $\mathbf{R}_1$. Equation (5.4) provides the latter function. Correlations between mean velocity components at different points in space are assumed be homogeneous and isotropic as in Colony and Thorndike (1984, p. 10,626) depending on two parameters: the variance of u'_o, and a correlation length scale L. In the present research, we identify the variance with σ_s, the spatial variance. The length scale L is chosen, by trial and error, to reproduce in a smooth way, the features of the sample field (Figure 6) that can be discerned by eye and are associated with specific geographical features, including the transition from Arctic Basin to the Greenland Sea, the southward narrowing of the continental shelf, and the steep continental slope that is hugged by the core of the EGC (Paquette, et al, 1985). The assumptions of homogeneity and isotropy are not well-founded, but to abandon them is to claim that some particular anisotropic, inhomogeneous correlation structure agrees better with the data. The available data do little to reveal the structure of correlations between mean values at different points. In fact, the reader may notice an apparent inconsistency in the use of the averaging operator [()] on quantities that depend on $\mathbf{x}$, as in equation (5.7), whereas [()] was defined as an average over $\mathbf{x}$. This inconsistency arises because of our desire to define a smooth field with about the same mean and variance as the input data for the interpolation procedure, while at the same time achieving minimization of $[\varepsilon^2]$ as though the average applies to some ensemble at a fixed $\mathbf{x}$. We are unable to reconcile these different uses of [()], and therefore the ensemble remains an abstraction upon which no light is shed by the data. The optimal estimator (5.3), together with the assumed correlation structure are regrarded as empirical rules for generating smoothed estimates of the sample mean velocity field that are self consistent with the input data, (same space mean and standard deviation and same qualitative features) and such that values on Γ_1 are independent of those on Γ_3. The final difference between our procedure and that of Colony and Thorndike (1984) is our use of only one velocity component $\tilde{\mathbf{u}}_o \cdot \mathbf{n}$ as input and output. The chosen correlation function also specifies statistical relationships between the orthogonal component $\mathbf{u} \times \mathbf{n}$ and the desired variable $\mathbf{u} \cdot \mathbf{n}$. Rather than adopt a specific model for these relationships, we simply set all input values of $\tilde{\mathbf{u}}_o \times \mathbf{n}$ to zero.

The procedure described above is less than fully satisfactory, because we do not know whether the statistics of ε are overestimated or underestimated. Still, it does not follow that equation (5.7) is useless. These error estimates constitute our best guess. Moreover, spatial variations in $[\varepsilon^2]$, are determined by differences in the amount of independent data at nearby points, and inhomogeneities in the variance σ_u, as they ought to be. Finally, the estimation model presented above provides for continual improvement with the acquisition of new data, both from the standpoint of larger input samples, and the possibility for constructing ensembles and testing the assumptions on which the model is based.

On transects through rows of boxes south of Fram Strait, the buoy data do not sample ice covered areas over the central Greenland Sea Basin. The optimal interpolation scheme produces coefficients $\alpha = 0$ at points $\mathbf{x}$ more than a few correlation length scales removed from input data, and the estimates there would approach the average $[u_o]$. However, our own sparse data beyond the shelf break, and numerous studies of currents in the Greenland Sea, suggest that the current $\mathbf{c}_o \cdot \mathbf{n}$ decreases eastward from the base of the continental slope and vanishes in the middle of a mean gyre circulation centered roughly between the Greenland shelf break and the Mohn Ridge to the east (Paquette, et al., 1985, their Figure 1). Using their map of the gyre, we determine by eye one point on each of the rows of boxes (Figure 1b) at which to set $\mathbf{c}_o \cdot \mathbf{n} = 0$, and we assign as input there the wind driven value $\tilde{u}_o(\mathbf{x}_i) \equiv AG_o \cdot \mathbf{n}$ based on the grid winds.

The length scale $L = 222$ *km* produces a field (not shown) that reproduces well the qualitative features of the $\bar{u}_o$ field described previously. Table III presents a comparison between grid point values of the input $\tilde{u}_o(\mathbf{x}_j)$ and output $\hat{u}_o(\mathbf{x})$ on Γ_1 and Γ_3, for cases where the interpolation and data points nearly coincide. The fields agree to within 2 cm/s. Profiles of velocity across Γ_1 and Γ_3 are shown on Figure 8, along with the CAM ice concentration $I_o(\mathbf{x})$ and the flux implied by their product. Noteworthy features of the ice motion profiles are the greater speed on Γ_3, the similar shape of the two profiles, with single maxima, and the rapid decrease of velocity east of the shelf break on Γ_3.

There are no buoy measurements from which to estimate the CAM ice velocity on Γ_2 south of Spitsbergen (Figure 1b). Therefore, equation (5.1) is used with G_o estimated from the grid winds, with $\mathbf{c}_o \cdot \mathbf{n} \equiv -10$ *cm/s* assigned to the grid box adjacent to Spitsbergen, and with $\mathbf{c}_o \cdot \mathbf{n} \equiv 0$ elsewhere on Γ_2. The assumed structure of the mean current is based on information reported by Hanzlick (1983) in his study of the West Spitsbergen Current. He presents evidence that the core of the WSC is strongly constrained by the sloping isobaths, the flow weakening considerably only 40-50 km seaward of the shelf break. The CAM ice concentration is $I_o = 0.19$, in the grid point nearest Spitsbergen and does not exceed 0.03 on the remainder of Γ_2. Therefore, the errors introduced by negelcting any possible currents at these latter points are small. The wind driven motion accounts for about 2 cm/s of u_o on Γ_2.

A useful resolution of the climatological annual cycle would be provided by monthly values of $\mathbf{u}_1$ at points on each of the boundary segments, which would match the resolution provided by the WJ ice concentration data. Unfortunately, the samples become so small in this case that sampling errors overwhelm any possible seasonal differences in velocity statistics. The annual cycles of ice covered lengths on Γ (Figure 1d) suggest that a 3-month seasonal grouping might resolve the velocity variations adequately, because their product with $I_1(\tau)$ is all that is needed. Moreover, measurements of the West Spitsbergen Current (Hanzlick, 1983) suggest that the oceanic response to seasonal forcing is limited to periods greater than 1 month, and to the barotropic mode forced by the wind stress curl. Direct current measurements in the East Greenland Current are presently underway, but the accumulated data base is still to small to yield accurate estimates of the annual cycle.

The CAM and CAC of the geostrophic winds in R_1 are illustrated in Figure 9. The top figure shows the mean sea level pressure distribution, implying wind driven inflows on Γ_1 and Γ_2, with outflow on Γ_3. The mean maps for 3-month seasons DJF, MAM, JJA, SON (not shown) exhibit patterns similar to Figure 9a, with changes in the intensity of gradients. The strongest geostrophic winds occur in autumn and the weakest in summer. Monthly values of $\langle \overline{G(\tau)} \rangle \cdot \mathbf{n}$ are shown in Figure 9b. With a multiplier $|A| = 0.01$ these winds imply a seasonal variation of about ± 2.5 *cm/s* in wind driven ice motion.

In order to make at least a crude estimate of the total (wind plus current) seasonal variation of ice velocity, the buoy data are grouped into three-month seasons, and box-average sample statistics $\langle \bar{u} \rangle$ and σ_u computed as before. The optimal interpolation procedure is applied to these sample data along Γ_1 and Γ_3, and the resulting error variances inspected. It turns out that one grid point, on Γ_1, has sufficiently small errors to warrant a look at the seasonal cycle. This point, dubbed y_{max} and circled in Figure 1b, overlies the cross-stream maximum in u_o. The seasonal estimates are shown in Table IV, along with geostrophic wind data at the same point. The estimates suggest a seasonal cycle of ice velocity with an autumnal maximum of 18 cm/s and a spring minimum of 9 cm/s. Intermediate values occur in

Table III.

Comparison of sample and optimal CAM ice velocity components

Segment Γ_1: $x = 111$ km, $[u_o] = 8.7$ cm/s, $\sigma_s = 5.2$ cm/s

y	222 km	333 km	444 km
$\bar{u}_o$	7.8 cm/s	13.2 cm/s	7.8 cm/s
$\hat{u}_o$	7.2 cm/s	14.2 cm/s	7.7 cm/s
$\left[\bar{u}_o - \hat{u}_o\right]$	0.6 cm/s	-1.0 cm/s	0.1 cm/s
$\left[\varepsilon^2\right]^{\frac{1}{2}}$	0.2 cm/s	0.2 cm/s	0.3 cm/s

Segment Γ_3: $x = 999$ km, $\left[u_o\right] = 11.3$ cm/s, $\sigma_s = 9.4$ cm/s

y	0 km	111 km	222 km	444 km
$\bar{u}_o$	19.1 cm/s	23.0 cm/s	13.2 cm/s	3.1 cm/s
$\hat{u}_o$	20.2 cm/s	24.4 cm/s	10.8 cm/s	3.1 cm/s
$\left[\bar{u}_o - \hat{u}_o\right]$	-1.1 cm/s	-1.4 cm/s	2.4 cm/s	0 cm/s
$\left[\varepsilon^2\right]^{\frac{1}{2}}$	2.0 cm/s	0.7 cm/s	0.9 cm/s	0 cm/s

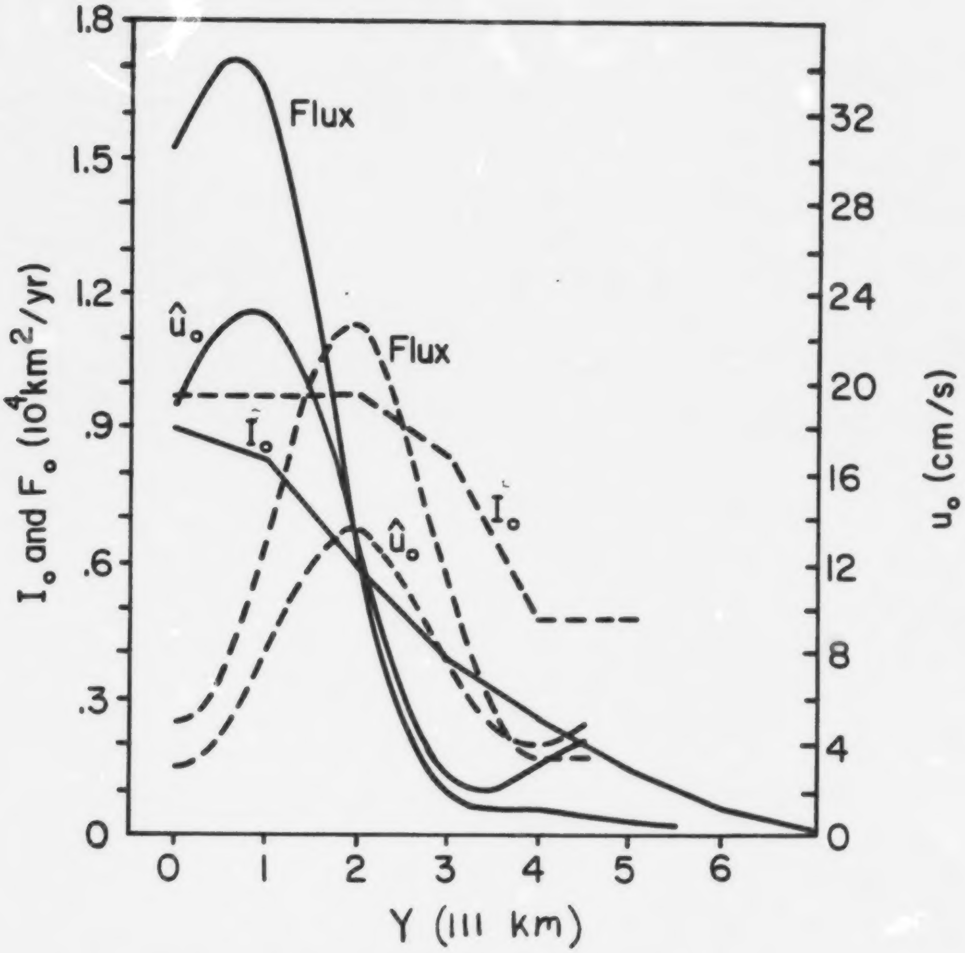

Figure 8: CAM ice concentration, optimal ice velocity estimates, and flux estimates on Γ_1 (dashed) and Γ_3 (solid). Fluxes are per 27.75 km cross section increments.

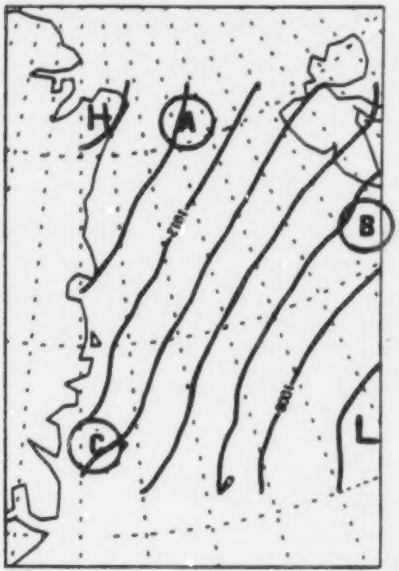

Figure 9a: CAM sea level pressure field p_o , 1979-83. (millibars)

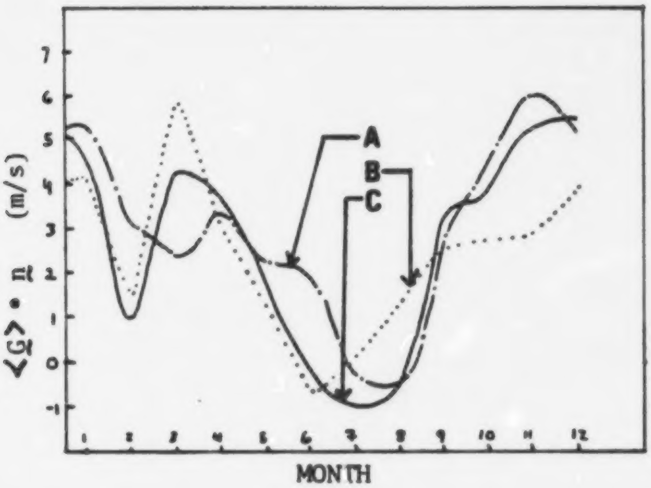

Figure 9b: Annual cycle of the component of the geostrophic wind normal to Γ at locations A, B, C on Figure 9a, averaged over 1979-83.

Table IV.
Seasonal ice and residual current velocity estimates
at (x,y) = (111,333) km

MONTHS →	SON	DJF	MAM	JJA
$\langle \hat{\bar{u}} \rangle$	18 cm/s	14 cm/s	9 cm/s	12 cm/s
$\left[\varepsilon^2\right]^{\frac{1}{2}}$	2 cm/s	2 cm/s	1 cm/s	1 cm/s
$\langle \bar{c} \rangle = \langle \hat{\bar{u}} \rangle - A \langle \overline{\mathrm{G}} \rangle \cdot \mathbf{n}$	12.2 cm/s	9.9 cm/s	6.8 cm/s	10.5 cm/s

$\langle \overline{\mathrm{G}} \rangle$ is estimated from the grid winds, 1979-83.

winter and summer. These seasonal differences are large compared to the estimated errors $[\varepsilon^2]^{\frac{1}{2}} \leq 2$ *cm/s*. Subtracting the wind driven motion $A<\overline{G}>$ for each season produces the seasonal mean currents shown in the table. Based on these data, a model is constructed for the monthly values of the component $\mathbf{c}_1(\tau) \cdot \mathbf{n} = c_1(\tau)$, at the point y_{max}, as follows:

$$c_1(\tau) = \Lambda \left(\cos\left(\frac{2\pi\tau}{12} + \Phi\right)\right) \tag{5.9}$$

where τ is measured in months, the phase angle Φ is chosen to give a maximum on 15 October, and the amplitude $\Lambda = 2.7$ *cm/s* is is chosen as the average of the SON and MAM deviations from $c_o(y_{max})$.

The ice budget requires $c_1(\tau, y)$ for all points y on Γ_1 and Γ_2. It is assumed that the *shape* of the cross-stream profile in the annual cycle of currents is identical with the shape of the CAM currents. Thus

$$c_1(\tau, y) = c_1(\tau, y_{max})S(y) \tag{5.10}$$

where $S(y) = c_o(y)/c_o(y_{max})$ is a shape function on Γ_1. On Γ_2 the same scheme is applied, with the additional assumption that the amplitude of the seasonal cycle $\Lambda = 5.4$ *cm/s* is larger than that on Γ_1, in proportion to the ratio of $c_o(y_{max})$ on the two segments. This assumption is motivated by the notion that the East Greenland Current is adjusted to seasonal forcing through the entire sector 70° *N* to 80° *N*.

Obviously the CAC of currents derived from the previous assumptions must be regarded as a rather crude estimate. The amplitude and phase of the cycle at y_{max} on Γ_1 are the only parameters supported by measurements. We therefore regard these estimates as provisional, intended to answer the question: could the annual cycle of currents make important contributions to the ice budget, when compared to other, more accurately known terms? The sensitivity of the calculations to Λ and Φ, on one or both boundaries, is considered below.

According to the model for the monthly currents the CAC of wind driven ice motion is of the same order of magnitude as c_1 at y_{max}, and dominates the annual cycle of ice motion wherever the CAM currents are small. It is worth pointing out that the annual cycles of the geostrophic wind (Figure 9) are not far out of phase with respect to the annual cycle of ice lengths (Figure 1d). By contrast, the October 15 current maximum puts c_1 nearly in quadrature with the MAC of ice concentration. In order to determine quantitatively the consequences for the ice budget of our estimates and assumptions, the data on ice concentration, ice velocity, wind and current are combined in the following section.

ANALYSIS OF THE ICE BUDGET

Estimates of u_o, G_o, c_1, G_1, I_o, I_1, and A_1, described in the preceeding sections, are combined here to evaluate the terms in equations (3.18) and (3.19). The annual cycle of the current c_1 on Γ_3 is not included in our calculations, because data are so sparse. Order of magnitude calculations based on seasonal variations in volume transport by the WSC (Hanzlick, 1983), and our own estimates of I_1, suggest that this term is negligibly small. The ice source/sink terms S_o and $S_1(\tau)$ are computed as residuals.

Table V presents the results for the climatological annual mean budget (equation 3.18). Ice advection on all three boundary segments is dominated by the CAM fields of ice velocity and ice concentration, much smaller contributions being made by $\overline{u_1 I_1}$. Figure 8 shows the profiles of u_o, I_o, and $u_o I_o \Delta l$ from which the estimates of these dominant terms derive. The ice covered length on Γ_1 is larger than that on Γ_3, but the larger CAM velocity across the latter segment more than compensates, producing a net efflux of ice area. Although the inflow on Γ_2 is less than 10% of the fluxes on the other segments, it is 30% of the *difference* between these two larger terms. The residual is $S_o = +0.20 \times 10^6$ km^2 yr^{-1}. This area source implies that ice equivalent to 30% of the area of R_1 is produced in a year, on average. As mentioned earlier, S_o is regarded as a lower bound on the thermodynamic source. Several previous investigators have studied aspects of the ice budget, such as the ice velocity field, the ice area flux through Fram Strait, and variations in the ice extent (cf. Koch, 1945; Vowinckel, 1962; Einarsson, 1972; Vinje, 1982; 1983; and references in these papers). Of these, only Einarsson treats the term S_A, finding a net source in the region between Denmark Strait and 76° *N*. He argues that the strong mean shear and large temporal variability of the EGC ought to open new leads in the ice during winter, leading to a strongly positive $<S(\tau)>$ at this season. Our results indicate that, on a climatological annual mean basis, these processes win out over the summer melting in R_1. Estimates of th
fluxes

Table V.

Estimates of terms inequation (3.18)

(units: 10^6 km^2/yr)

No.	Term	Γ_1	Γ_2	Γ_3
1	$-\int \mathbf{u}_o I_o \cdot \mathbf{n}\,dl$	+1.08	-1.40	+0.09
2	$-\int A\mathbf{G}_o I_o \cdot \mathbf{n}\,dl$	+0.35	-0.30	+0.03
3	$-\int A\overline{\mathbf{G}_1 I_1} \cdot \mathbf{n}\,dl$	+0.01	-0.02	+0.01
4	$-\int \overline{\mathbf{c}_1 I_1} \cdot \mathbf{n}\,dl$	-0.01	+0.04	0
5	$-\int \overline{\mathbf{u}_1 I_1} \cdot \mathbf{n}\,dl$	0	+0.02	+0.01
6	$-\int \left[\mathbf{u}_o I_o + \overline{\mathbf{u}_1 I_1}\right] \cdot \mathbf{n}\,dl$	+1.08	-1.38	+0.10

$$\int \mathbf{u}_o I_o \cdot \mathbf{n} dl$$

on transects between Γ_1 and Γ_2 are shown on Figure 10.

The CAM ice thickness distribution budget has been simulated by Walsh, et al. (1985) using a theoretical model forced by temporally constant ocean currents and oceanic heat flux, and a 30 year record of daily geostrophic winds and air temperature anomalies. Interestingly, their results include a strong *ice thickness sink* in $\mathbf{R}_1$, on the order of $-1.0\ m\ yr^{-1}$ (their Figure 14). This result is not necessarily inconsistent with our ice *area* source. Still, it would be most interesting to see simulated climatological statistics for the terms in equation (2.6) for comparison with the observational estimates.

Terms in equation (3.19), describing the annual cycle of ice area, are presented in Figures 11-13. The most important flux is $\mathbf{u}_o I_1$, corresponding to a temporally constant mean flow acting on the annual cycle of ice concentration. Both the mean flow, and the annual cycle of I_1 are larger on Γ_3 than on Γ_1 , yielding net efflux during January-April and net influx during August-October The fluxes due to $\mathbf{u}_1 I_o$ are large also, but tend to cancel when summed over the two boundaries, a consequence of the similarity of G_1 on the two segments, and of the identical phases Φ assumed for c_1 (τ). Contributions from products of monthly departures $\mathbf{u}_1 I_1$ are once again small compared to the other terms. Figure 14 summarizes the CAC ice budget, showing the rate of change of ice area $dA_1/d\tau$ and the estimated ice source $S_1(\tau)$. The vertical distance between these two curves on the figure is the total advective contribution to the budget for the given month. The amplitude of the annual cycle S_1 is four times as large as the annual mean source S_o. S_1 is approximately equal to $dA_1\ /d\tau$ during November-February, and again during May-August. In these months, seasonal changes in ice area are due primarily to melting and freezing in the region. By contrast, advection makes a substantial contribution during March-April, when the excess outflow across Γ_3 drains ice from $\mathbf{R}_1$, and during September-October, when the Fram Strait inflow acts to fill up the region. It is interesting to note that S_1 crosses zero around the first of October, in contrast to Einarsson's conjecture that ice area formed in new leads is balanced by deformational sinks (D_A in our notation) until early December.

DISCUSSION AND CONCLUSION

Basic state variables have been defined, and a conservation equation developed, governing the large scale ice area budget in an arbitrary region. Applying a formal scheme for time averaging, we obtain climatological budget equations that describe the annual mean and annual cycle of ice area. Using measurements on ice motion, geostrophic wind, and ice concentration, the terms in these equations are estimated for a region $\mathbf{R}_1$ in the Greenland Sea. It is found that the ice motion and ice area advection are driven predominantly by ocean currents (70%), with about 30% of the motion due to winds. The annual mean budget is dominated by the annual mean motion and annual mean ice concentration on the boundaries, with a much smaller contribution from correlations of monthly anomalies over the annual cycle. The larger annual mean velocities on the southern boundary produce a net efflux, which in steady state implies that $\mathbf{R}_1$ is a source region for ice area. The seasonal cycle of ice area is dominated by thermodynamic processes, except in March, April, September, and October, when advection makes a substantial contribution. Seasonal variations in the thermodynamic ice source are about four times larger than the annual mean source.

The work presented here must be regarded as "in progress", an appropriate status for inclusion in a workshop proceedings. Efforts are underway to refine and further interpret the budget results, and to compare them with simulations as a means of understanding and testing theoretical models.

A particular concern is to estimate the probable errors. Although the analysis is incomplete, a few preliminary results may serve to illustrate the uncertainty that affects these budgets.

Errors in the ice velocity statistics are dominated by time series sampling variability. Based on the interpolation error ε, we find that $\mathbf{u}_o$ is accurate to about 1-2 cm/s on Γ_1, and 2-4 cm/s at points on Γ_3. Independent errors of this size, advecting the ice concentration $I_o = 0.8$ in a 111 km grid square produce an error flux of approximately $\pm 0.1 \times 10^6\ km^2\ yr^{-1}$. This error applies to both the flux on a single boundary and, multiplied by $\sqrt{2}$, to the difference in flux and hence to S_o. This number is sufficiently close to the estimated source $S_o = 0.2 \times 10^6\ km^2\ yr^{-1}$ that one cannot rule out the possibility that $S_o = 0$, Available data indicate that a thermodynamic source (S_o positive) is *more probable*, than a thermodynamic sink. Fortunately, sampling problems such as this one are resolved with the accumulation of more ice data. A steady increase in ice motion data is expected from the ongoing Arctic Buoy

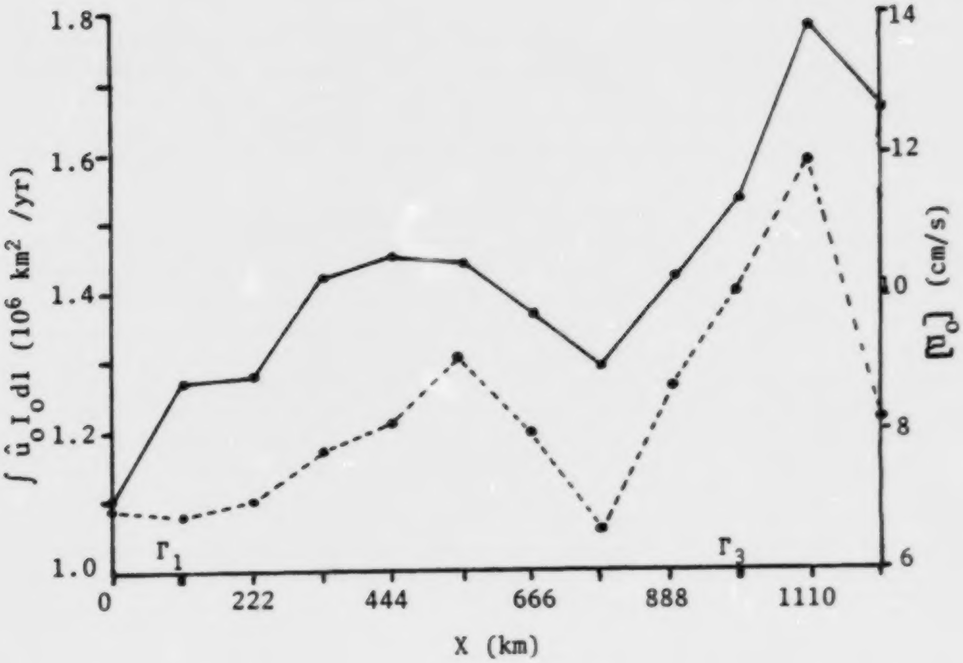

Figure 10: Fluxes (dashed line) due to CAM ice velocity and concentration on several transects, and spatial average velocity (solid line).

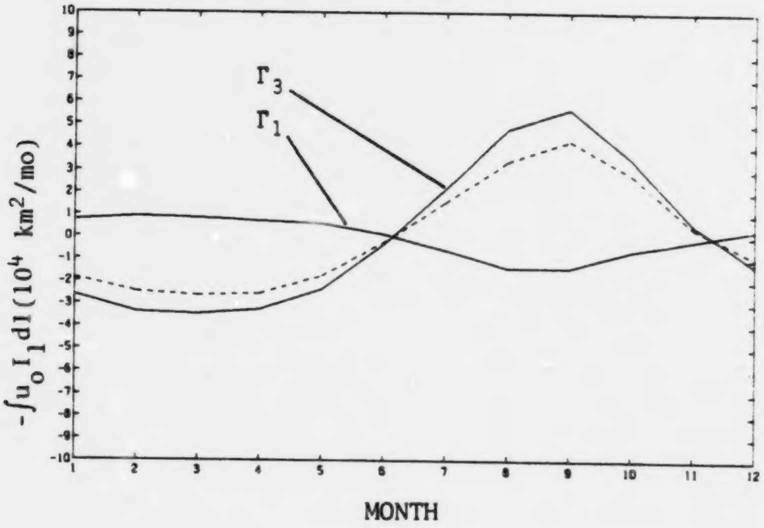

Figure 11: MAC of fluxes due to u_oI_1 . Dashed line is the sum of fluxes on Γ_1 and Γ_3 .

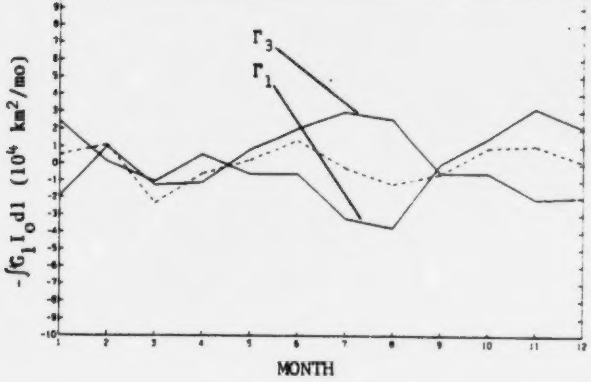

Figure 12a

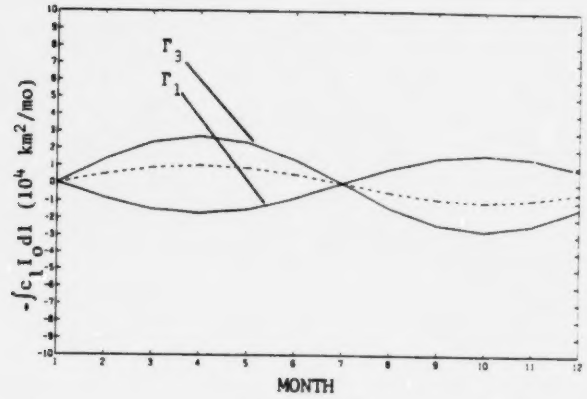

Figure 12b

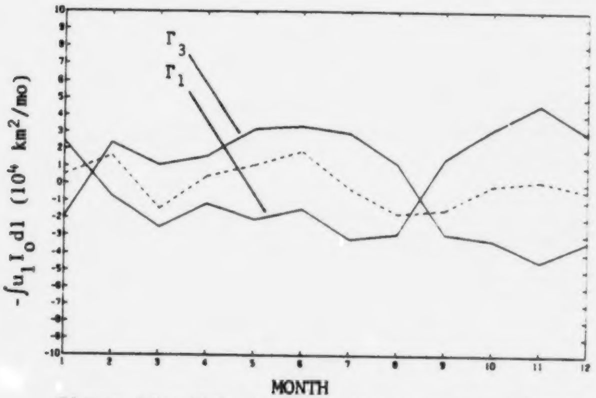

Figure 12c: MAC of fluxes due to $u_1 I_o$. Computed as the sum of values on Figs. 12a and 12b.

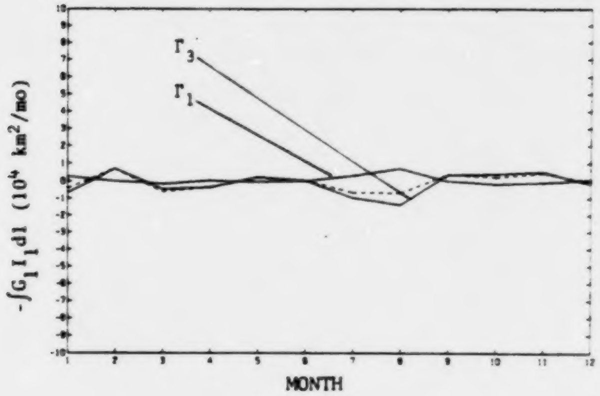

Figure 13a

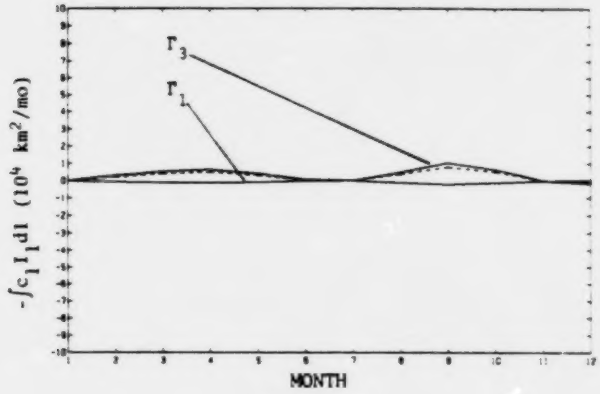

Figure 13b

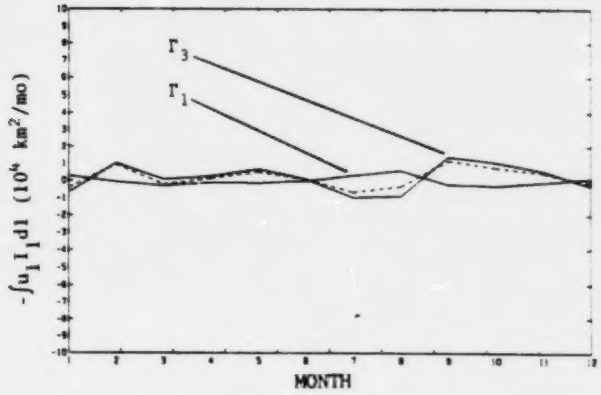

Figure 13c: MAC of fluxes due to $u_1 I_1$.
Computed as the sum of values on Figs. 13a and 13b.

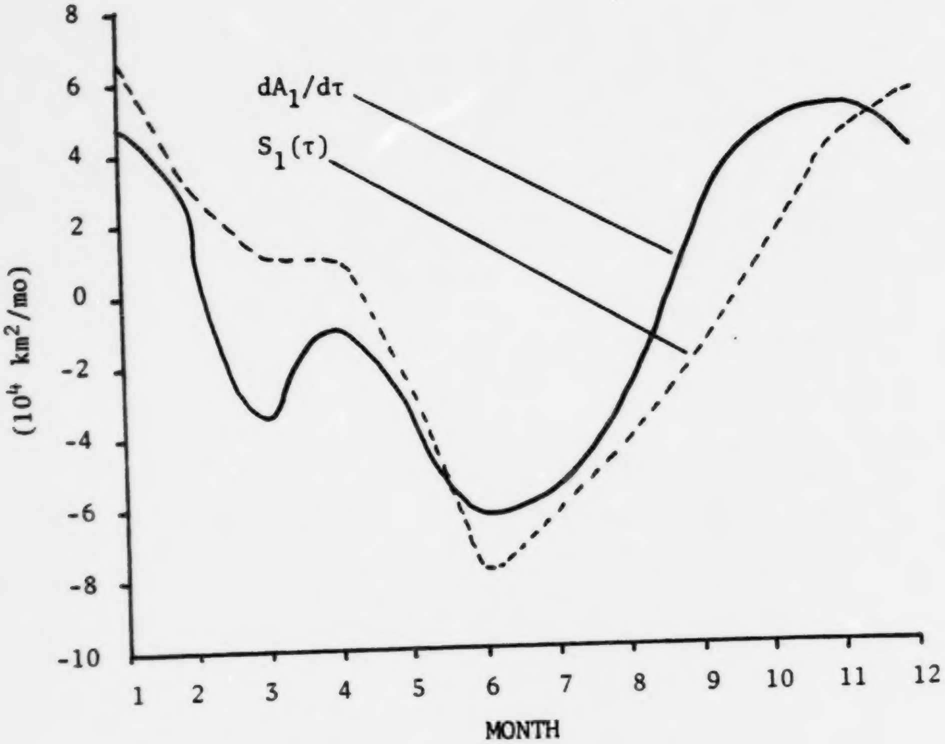

Figure 14: MAC of rate of climatological area change, and ice source.

Program, and other experiments. Perhaps even more important is the sea ice discplacement data from the synthetic aperature radar (SAR) instrument scheduled to fly on the ERS-1 satellite. With SAR data, one could monitor two transects such as Γ_1 and Γ_2 at time intervals of a week or so, resolving spatial variations on scales of 1 km or smaller. The primary limitation in sampling may then be imposed by the efficiency with which massive amounts of digital information can be processed. It is therefore encouraging to note recent work by Fily and Rothrock (1985), showing that velocity estimates can be derived automatically from SAR data using special correlation procedures.

The ice concentration data are sufficiently plentiful in time and space that sampling errors are small. The main source of uncertainty for this variable arises from the paucity of real observations used to construct the ice charts and, more recently, in uncertainties about the precision of mathematical relationships between microwave brightness temperatures and ice concentration. Recent work on this latter problem suggests that these uncertainties can be reduced to levels very useful for ice area budgets, using data from the new SSM/I multichannel passive microwave sensor (SSM/I Science Working Group, 1984). The simultaneous operation of the ERS-1 SAR and the SSM/I offer the prospect for improving the present estimates, and for extending the analysis to other regions.

REFERENCES

AAGAARD, K., J.H. SWIFT and E.C. CARMACK 1985. Thermohaline circulation in the Arctic Mediterranean Seas. *Journal of Geophysical Research*, v. 90, No. C3 : pp. 4833-4846.

AAGAARD, K., C. DARNALL, A. FOLDVIK and T. TORRESEN 1985b. Fram Strait Current Measurements 1984-1985. University of Washington School of Oceanography, Report No. M85-9, 85 pp.

BERGTHORSSON, P. 1969. An Estimate of Drift Ice and Temperature in Iceland in 1000 Years. *Jokull*, v. 19, pp. 94-101.

BUCK, B.M. and D.W. JAECKS 1984. Long term Statistical Measurements of Environmental Acoustics Parameters in the Arctic. Polar Research Lab Technical Report No. 53, Polar Research Laboratory, Inc., Carpinteria, CA.

COACHMAN, L.D. and K. AAGAARD 1974. Physical oceanography of arctic and subarctic seas, in *Marine Geology and Oceanography of the Arctic Seas*, Y. Herman, ed., pp. 1-72.

COLONY, R. and A.S. THORNDIKE 1984. An Estimate of the Mean Field of Arctic Sea Ice Motion. *Journal of Geophysical Research*, v. 89, No. C6: pp. 10,623-10,629.

EINARSSON, T. 1972. Sea Currents, Ice Drift, and Ice Composition in the East Greenland Current, in *Sea Ice*, Iceland National Research Council: pp. 23-32.

HANZLICK, D.J. 1983. The West Spitsbergen Current: Transport, Forcing and Variability. PhD. Dissertation, University of Washington Dept. of Oceanography.

HUNKINS, K. 1984. Ocean Currents and Temperatures in the Center of Fram Strait during MIZEX 83. MIZEX Bulletin No. IV, pp. 47-51.

JOHANNESSEN, O.M., J.A. JOHANNESSEN, J. MORISON, B.A. FARRELLY, and E.A.S. SVENDSEN 1983. Oceanographic Conditions in the Marginal Ice Zone North of Svalbard in Early Fall 1979 with an Emphasis on Mesoscale Processes. *Journal of Geophysical Research*, v. 88, No. C5: pp. 2755-2769.

KILLWORTH, P. 1985. Deep Water Formation. in: North Atlantic Deep Water Formation, U.S. National Aeronautics and Space Administration Conference Publication 2367: pp. 4-6.

KOCH, L. 1945: The East Greenland Ice. *Meddelellser om Gronland*, v. 130, No. 2.

LEMKE, P., E.W. TRINKL and K. HASSELMANN 1980. Stochastic Dynamic Analysis of Polar Sea Ice Variability. *Journal of Physical Oceanography*, v. 10 : pp. 2100-2120.

MANABE, S. and R.J. STOUFFER 1980. Sensitivity of a Global Climate Model to an Increase of CO_2 Concentration in the Atmosphere. *Journal of Geophysical Research*, v. 85, No. C10: pp. 5529-5554.

PAQUETTE, R.G., R.H. BOURKE, J.F. NEWTON, and W.F. PERDUE 1985. The East Greenland Polar Front in Autumn. *Journal of Geophysical Research*, v. 90, No. C3: pp. 4866-4882.

ROTHROCK, D.R. 1986. Ice Thickness Distribution-Measurement and Theory. in: *The Geophysics of Sea Ice*, N. Untersteiner, ed., Plenum Press (in press).

ROTHROCK, D.A. and A.S. THORNDIKE 1984. Measuring the Sea Ice Floe Size Distribution. *Journal of Geophysical Research*, v. 89, No. C4: pp. 6477-6486.

RUDDIMAN, W.F. and A. MCINTYRE 1973. Time transgressive deglacial retreat of polar waters from the North Atlantic. *Quaternary Research*, v. 3: pp. 117-130.

SARMIENTO, J.L. and J.R. TOTTWEILER 1984. A new model for the role of the ocean in determining atmospheric PCO_2. *Nature*, v. 308: pp. 621-623.

SSM/I SCIENCE WORKING GROUP 1984. Passive Microwave Remote Sensing for Sea Ice Research. Report, Applied Physics Laboratory, University of Washington. 55 pp.

SYMONDS, G. and I.K. PETERSON 1985. MIZEX: Ice Floe Trajectories through the Greenland Sea. Canadian Data Report on Hydrography and Ocean Sciences No. 33, Bedford Institute of Oceanography, Dartmouth, N.S., 68 pp.

THORNDIKE, A.S. 1986. Kinematics of Sea ice, in: *The Geophysics of Sea Ice*, N. Untersteiner, ed. Plenum Press (in press).

THORNDIKE, A.S., D.A. ROTHROCK, G.A. MAYKUT and R. COLONY 1975. The Thickness Distribution of Sea Ice. *Journal of Geophysical Research*, v. 80, No. 33: pp. 4501-4513.

THORNDIKE, A.S. and R. COLONY 1982. Sea Ice Motion in Response to Geostrophic Winds. *Journal of Geophysical Research*, v. 87, No. C7: pp. 5845-5852.

THORNDIKE, A.S. and R. COLONY 1983. Objective Analysis of Atmospheric Pressure and Sea Ice Motion over the Arctic Ocean. Conference on Port and Ocean Engineering under Arctic Conditions (POAC), Helsinki, Finland. 10 pp.

TRIPP, R.B. and K. KUSUNOKI 1967. Physical, chemical and current data from Arlis II: Eastern Arctic Ocean, Greenland Sea, and Denmark Strait area, February 1964-May 1965. University of Washington Dept. of Oceanography, Technical Report No. 185.

UNTERSTEINER, N. and A.S. THORNDIKE 1982: Arctic data buoy program. *Polar Record*, v. 21: pp. 127-135.

VINJE, T.E. 1982. The Drift Pattern of Sea Ice in the Arctic with Particular Reference to the Atlantic Approach, in: *The Arctic Ocean* L. Rey, ed., MacMillan Press Ltd., pp. 83-96.

VINJE, T.E. 1983. On the present state and the future fate of the Arctic sea ice cover. in: *Arctic Whaling*, H.K. Jacob, ed., University of Groningen, pp. 39-56.

VINJE, T.E. 1984. Frequency distribution of sea ice, ridges, and water openings in the Greenland and Barents Seas-A preliminary report on the 'Birds Eye' observations. Norsk Polarinstitutt Report No. 15, 27 pp.

VINJE, T.E. and O. FINNEKASA 1986. The Ice Transport Through Fram Strait. Norsk Polarinstitutt Skrifter.

VOWINCKEL, E. 1964. Ice Transport in the East Greenland Current and its Causes. *Arctic*, v. 17, No. 2: pp. 111-119.

WALSH, J.E. 1983. The Role of Sea Ice in Climatic Variability: Theories and Evidence. *Atmosphere-Ocean*, v. 21, No. 3: pp. 229-242.

WALSH, J.E. and C.M. JOHNSON 1979. An Analyis of Arctic Sea Ice Fluctuations, 1953-77. *Journal of Physical Oceanography*, v. 9: pp. 580-591.

WALSH, J.E., W.D. HIBLER III, and B. ROSS 1985. Numerical Simulation of Northern Hemisphere Sea Ice Variability, 1951-1980. *Journal of Geophysical Research*, v. 90, No. C3: pp. 4847-4865.

WASHINGTON, W.M. and G.A. MEEHL 1984. Seasonal Cycle Experiment on the Climate Sensitivity due to a Doubling of CO_2 with an Atmospheric General Circulation Model Coupled to a Simple Mixed-Layer Ocean Model. *Journal of Geophysical Research*, v. 89, No. D6: pp. 9475-9503.

WMO 1983. Report of the Meeting of Experts on Sea Ice and Climate Modelling. World Meteorological Organization, World Climate Research Programme, WCP-77, 35 pp.

SPRING AND SUMMER SEA ICE CONDITIONS IN EASTERN CANADIAN WATERS 1950 to 1985

by J.P. Newell
11 Gilham Crescent
Mount Pearl, Newfoundland, Canada A1N 3C6

Published sea ice charts from a variety of sources are used to investigate the retreat of sea ice in Eastern Canadian waters from the time of its maximum extent in March to the time of its minimum extent in early September. The dates of ice clearing at selected latitudes are presented for the years 1950 to 1985. The distribution of clearing dates at each latitude is described and the correlations between the clearing dates for different latitudes are presented.

Analysis of the data indicates that there is a weak negative correlation between Baffin Bay ice conditions and clearing dates south of Hudson Strait. This finding contradicts earlier research which indicated that both areas respond to atmospheric conditions in a similar fashion. A comparison of clearing dates with various atmospheric parameters indicates that the date of ice clearing is most strongly correlated with atmospheric conditions several months earlier. The significance of these findings for long range forecasting is reviewed.

SEA ICE CONDITIONS IN THE LABRADOR SEA - GRAND BANKS AREA

by

W.P. Zakrzewski*

Visiting Scientist
at Centre for Cold Ocean Resources Engineering
Memorial University of Newfoundland
St. John's, Newfoundland
A1B 3X5

* On leave from the Polish Academy of Science, Institute of Oceanology, in Sopot Poland.

ABSTRACT

Ice conditions of the Labrador Sea - Grand Banks area are presented. Ice age composition of pack is investigated.

Morphology of pack ice floes is described using all available characteristics (ice thickness, topography, floe size and shape). Ice drift offshore Labrador Sea is presented using the field data sets published by consultant firms.

Based on all the available published data spatial ice distribution offshore Labrador Sea and in Grand Banks is presented. Ice limit and its variations are described and explained. Ice regimes of areas under investigation seem to be governed mostly by global circulation while mesoscale effects are not so clearly visible.

State-of-the-art research on sea ice in the Labrador Sea - Grand Banks areas shows that careful field studies of ice conditions east of Canada are needed.

INTRODUCTION

The Labrador Sea - Grand Banks Areas belong to the Seasonal Sea Ice Zone (SSIZ). In general, the ice conditions of these areas have been scarcely studied when compared with the Arctic Basin. A short historical assessment of sea ice investigations conducted off the coast of Labrador and Newfoundland has been given by Smith (1931). He noted that the first systematic study of ice distribution in this region was inaugurated in the spring of 1913. Smith (1931) was the first to provide a systematic and extensive analysis of the ice conditions in the North West Atlantic Ocean. At present, ice conditions in the Newfoundland/Labrador region are monitored by Ice Forecasting Central (Ottawa) and the International Ice Patrol (IIP) as part of their routine ice service for shipping. Recently, the need for careful studies of sea ice distribution in the Labrador Sea - Newfoundland areas has become urgent due to the local interest of the oil industry. As a result, several exploration cruises have been recently organized, the results of which are discussed here.

ICE FORMS

ICE AGE COMPOSITION

Sea ice encountered in the Labrador offshore originates from various source areas. In general, the ice is formed in situ or is carried by winds and currents from the Davis Strait, Baffin Bay and Canadian Arctic Archipelago. Hence, Labrador sea ice is the conglomeration of floes of various origins and ages. Roughly speaking, it can be considered to be a stream of first-year (f.y.) pack ice in which multi-year (m.y.) ice floes are trapped. The majority of the pack ice off the coast of Labrador is f.y. ice as given by FENCO (1976, Table 4.1). They reported only 0.01% m.y. ice in the region, while NORDCO (1980) has given the percentage contribution of m.y. ice within pack ice off Groswater Bay to be equal to 0.5-8.0 %. This analysis was based on data given in the ice charts, 1969-1979. It should be noted that the percentage of m.y. ice varies with the season, being maximal in June. This is caused by summer melting of ice: f.y. deteriorates faster than m.y. ice because of its lesser thickness.

FIRST-YEAR ICE FLOE POPULATION

In describing the f.y. pack ice the following parameters were considered: 1) ice type and development; 2) size distribution of floe populations; 3) floe shape; 4) ice thickness, and, 5) ice topography.

Ice Type and Developmental Stages

Results of aerial photograph analysis published by FENCO (1976) are listed in Table 1. F.Y. ice is broken into three categories (white ice, grey ice and first year ice), all of which should be grouped together according to the WMO Sea Ice Nomenclature (1970). Hence, the total percentage contribution of f.y. ice to all ice encountered in the area of interest is 84.3%, while the remainder (15.7%) consists of brash ice, multi-year ice, and open water.

The stages of f.y. ice vary in abundance over the ice season. Grey-white ice, grey ice, and brash ice are common early in the season but decay rapidly, while the thicker white f.y. ice does not. As a result, the percentage contribution of the thicker white f.y. ice is very high at the end of the ice season (summer) while the other ice types are very scarce. This seasonal variation of the ice form composition is well known from the seas of the SSIZ (Zakrzewski, 1983) but is more obvious in areas where m.y. ice occurs (e.g. Canadian Arctic Archipelago, Melville Bay) as reported by Smirnov (1975).

Thickness of F.Y. Ice Floes

The thickness of f.y. pack ice in the Labrador Sea - Grand Bank Areas varies with time and location. In general, the level pack ice reaches its maximum thickness at the beginning of March (Grand Banks) or in the second half of March-beginning of April (offshore Labrador Sea), and thereafter thins rapidly due to melting. The spatial distribution of pack ice thicknesses is very simple. The mean absolute thickness of the level ice is approximately 1-1.5 m in the northern part of Labrador Sea, and about 0.3-0.9 m in the Grand Banks. Since the ice pack in the areas under consideration is driven by the Labrador Current, the ice stream flowing southwards exhibits a slight tendency to diminish in thickness from the coast to the middle of the sea. This southward diminution of ice thickness is very slight due to the continuous flow of thicker pack ice from the north.

FENCO (1975) has published the results of ice thickness measurements conducted in mid-April, 1975. Their results, based on 14 augered holes (FENCO, 1975, Table 1, p. 26) suggest that f.y. ice thickness ranges from 0.25 m to 3.81 m with a mean value equal to 2.35 m (excluding values larger than 3.5 m, mean ice thickness equal to 2.24 m is derived). A second data set, available from FENCO (1976), reports a mean ice thickness of 2.88 m for the 1975-76 season. However, the reported range of this parameter is surprisingly large (1.08 to 6.5 m). It is likely that the larger ice thickness values (3.7 m, 4.4 m, 4.8 m and even 6.5 m) represent data collected from m.y. floes rather than f.y. floes. Assuming a cut-off value for f.y. ice of

Table 1

PERCENT OF ICE TYPES FOR ALL RUNS

Multi year	.01%
First year	45.4 %
Grey White	21.5 %
Grey	17.4 %
Brash	4.9 %
Open	10.8 %

3.5 m and neglecting the above mentioned four measurements, one arrives at a mean ice thickness of 1.76 m.

One should be aware that the mean ice thickness of pack ice found in the FENCO (1975, 1976) reports is based on measurements obtained from the larger ice floes. However, pack ice is a conglomerate of different ice forms in various stages of development, with the larger floes typically being the thickest members. As a result, the mean thickness of all ice encountered in the Labrador Sea is probably much less than the values abstracted from the FENCO (1975, 1976) reports.

Size Distribution of F.Y. Ice Floes

Pack ice floes of various sizes have been reported from the Labrador Sea - Grand Bank areas where floes ranging from a few meters up to five kilometres in diameter have been encountered (Convay, 1972; FENCO, 1976; MacLaren Atlantic Limited, 1977). The most complete study of this region to date is that of FENCO (1976), who based their analysis on aerial photographs covering a large part of the Labrador Sea. F.y. ice floes larger than 300 m in diameter predominate (67.5%). Very small floes (10-50 m in diameter) are also commonly encountered (17.5% of all investigated ice floes) while the transition size categories (50-300 m) are rather less frequently encountered (only 15.01%). Floe size distributions of this sort reflect the general regularities of pack-ice fragmentation processes in the non-sheltered marine basins. The floe size distribution coincides fairly well with records of high winds blowing over the sea, which produce the concomitant waves responsible for ice fragmentation. If the broken ice floes do not refreeze to form a consolidated pack, the percentage contribution of floes of the small size category should gradually increase while that of the largest floes decreases as time passes. That is, the size floe distribution should reflect the air/sea conditions encountered during the ice season. Field data (FENCO, 1976, p. 107) confirm this conclusion.

The floe size distribution in the Labrador Sea is not particularly variable within any given location. From the data set provided by FENCO (1976, Vol. II), one can see that the variety of ice floe size-categories at any one location is not very large. This suggests that the Labrador Sea is either affected by stable dynamic factors which control ice fragmentation, or the stream of pack ice flowing with the Labrador Current is of a homogenous nature. If so, the permanent ice drift to the south and lack of possible source areas of ice inflow to the Labrador Sea (e.g. the central part of the Davis Strait is commonly ice free in the winter) probably result in the low variability of f.y. floe size noted by FENCO.

Topography of the F.Y. Ice Pack

Ridges and other forms of deformed ice have been frequently reported in the Labrador Sea. Some qualitative information on ridged and rafted ice in the northwestern part of the Atlantic Ocean is provided in the Oceanographic Atlas of the North Atlantic Ocean (1968), but this data set is not complete enough to define distribution characteristics. For this information, we must rely on the FENCO (1976) study. This study shows that, in general, ridge sails varied from 1.5 to 3.0 m high with a mean height of approximately 2 m. If we assume that the ice and seawater densities were 870 and 1025 kg/m^3, respectively, one can calculate that the total ridge thickness is approximately 13 m, given a ridge sail height of 2 m.

The ice blocks which form the ridges range from 0.2 to 2 m in max. dimension while the average ridge width was determined to be approximately 6 m. The length of ridge links was typically on the order of a few hundred meters, although some ridges extended continuously up to 1-3 km.

The spatial distribution of ridges was not uniform in the Labrador Sea. Two average values for ridge spacing were reported by FENCO (1976) to be 150 and 300 m. Given this spacing, the mean ridge density should be around 6.67 and 3.33 ridges per kilometer of track. Thus the ridge density in the Labrador Sea is similar to values reported in the Gulf of Bothnia at the end of winter (5-10 ridges/km according to Lepparanta, 1981). Air-borne photographic analyses have been reported by FENCO (1976) for f.y. pack ice (white ice) while the younger stages of f.y. ice (grey ice, grey-white and brash ice) were neglected.

The region of pack ice was divided into three categories based on surface roughness. These are: 1) smooth (no surface roughness present); 2) medium (less than 80% of the area showed surface roughness), and 3) rough (more than 80% of area coverage was rough). The results of the FENCO (1976) study indicate that 24.6% of the investigated area of f.y. pack ice was smooth, 42.3% was medium-rough and 33.1% was rough. Thus, medium and rough categories of ice roughness appear to predominate. It is interesting to estimate the areal percentage contribution of deformed ice in the total area of ice-covered waters. It was found (FENCO, 1976) that the medium-rough and rough ice were encountered in 19.17% and 15% of the entire study area, respectively, while open water and level ice was recorded on 10.76 and 55.03% of all ice covered waters. Such a large percentage contribution of deformed ice with respect to the total ice occurrence can only be explained by the breakup and deformation of the pack ice by wave action in the Labrador Sea and more northern areas (Melville Bay, Baffin Bay and Davis Strait).

The data on ridge orientation off Labrador presented by FENCO (1976, Fig. 4.8) indicates how strongly the waves and/or swell affect the pack ice there. Assuming a minor initial roughness of pack ice in the Davis Strait and the negligible rotation of the ice floes after ridge formation in the Labrador Sea, the majority of ridges in the region are oriented more or less parallel to the Labrador coastline. The swell effect on ridging of sea-ice seems to be especially strong since the prevailing winds in Labrador are offshore during the winter and spring. This observation does not wholly agree with FENCO's observation that ridge orientation is random in the Labrador Sea.

Multi-year Ice Floe Population

Little data is available on m.y. ice floes in the Labrador Sea - Grand Banks areas. The FENCO (1980) report is believed to be the most comprehensive study of m.y. floes; however, one should be aware that this study is based on a helicopter (aerial stereophotography) ice survey conducted in 1979 only, and the ice statistics for other years may differ from the data set presented by FENCO (1980).

Locations of the four areas investigated are given in FENCO (1982). In each area specific characteristics of m.y. ice floes are discussed, including: 1) the number of floes in a given location; 2) average density of floes; 3) average surface areas of floes, and, 4) floe thickness. Some additional information on the size and shape of the m.y. floes based on a second FENCO (1976) report are also provided.

The abundance of m.y. ice floes was found to be variable with time and location. In particular, the maximum abundance of m.y. floes were observed in the Saglek, Cape Kiglapait, and Kikkertavak Island areas in May and in Fish Cove Pt. area in March (Table 2). However, the areas of each analysed region were not uniform as given in Table 2. Therefore, for a given location the number of m.y. floes was related to the arbitrary chosen area of 325 sq. km which is equal to the mean area of all the sea surfaces analysed in all locations during the whole period of investigation. These numbers were calculated using the formula:

$$N = A \times D_f \tag{1}$$

where N is the number of floes in the area of A = 325 sq. km, and D_f is the observed density of m.y. floes. The results of this analysis are given in Table 2.

The density of m.y. ice floes probably reflects the spatial distribution of m.y. ice in the Labrador Sea. In the areas of Saglek and Kikkertavak Island, the floe density was highest in May, while in the vicinity of Cape Kiglapait and Fish Cove Pt. it was highest in June and March, respectively. However, the density of m.y. ice in the Cape Kiglapait area in May (0.159) was close to its maximum value

Table 2

NUMBER OF MULTI-YEAR FLOES OBSERVED PER KM^2 OF PHOTO COVERAGE OFFSHORE LABRADOR - 1979 (FENCO, 1980)

Photo Line Analysed	Month	Area Analysed on Photos (km^2)	No. of Multi-Year Floes Observed on Photos	No. of Multi-Year Floes per km^2	No. of Multi-Year Floes per the area of 325 sq.km
Saglek (097°M)	March	605	11	0.018	6
	April	254	92	0.362	118
	May	542	429	0.792	257
	June	96	13	0.137	45
Cape Kiglapait (107°M)	March	360	18	0.050	16
	April	399	35	0.088	29
	May	346	55	0.159	52
	June	82	14	0.170	55
Kikkertavak Island (081°M)	May	407	41	0.100	32
	June	90	3	0.033	11
Fish Cove Point (084°M)	March	558	33	0.059	19
	April	160	3	0.019	6
		TOTAL	TOTAL	AVERAGE	AVERAGE
		3,899	747	0.192	54

(0.170) in June, suggesting that in all areas of the Labrador Sea (exclusive of its southern extremity represented by the Fish Cove Pt. area) the density of m.y. ice floes reaches its maximum in May (with respect to the four months under consideration).

The surface area of m.y. ice floes varies with time and location (Fig. 1). However, the average area of m.y. ice floes surfaces are comparable at all locations from March to May. This is contrary to FENCO's (1980, p. 15) statement that the average area of m.y. floe surfaces are larger in the vicinity of Saglek and Cape Kiglapait than in the two other locations. The diminution of average surface areas of m.y. floes to the south is evident during the month of June alone; that is, large floes are absent in the area of Fish Cove Pt. and decrease in both average and maximal surface areas throughout the month of May. However, this tendency has not been noted for other months.

Data on m.y. ice thickness in the Labrador Sea in 1979 have been reported by FENCO (1980, Table IV.4.3.a) and are presented here in Table 3. Unfortunately, these data may not be accurate as they appear to have been affected by systematic error; that is, FENCO (1980) reports extreme ice thicknesses (average - 14.2 m; maximal > 30 m) based on photogrammetric analysis. This may be the result of erroneous ice density values applied to this data. FENCO applied a value of ice density equal to 1000 kg/m^3 rather than a more reasonable value of 900 kg/m^3. The calculation of ice thickness from density is based on the equation:

$$\frac{h_s}{h_k} = \frac{\rho_i}{\rho_w - \rho_i} \qquad (2)$$

where h_s = thickness of the above water portion; h_k is the thickness of the submerged portion of an ice floe; ρ_w is the water density, and ρ_i is the ice density. From this one can compute the total ice thickness of a floe is the height of floe if freeboard is defined using the formula:

$$h = h_s + h_k = h_s \left(1 + \frac{\rho_i}{\rho_w - \rho_i}\right) \qquad (3)$$

where h is the total thickness of an ice floe. The term $\rho_i/(\rho_w - \rho_i)$ in the right-hand side of Eq. (3) strongly affects the total ice thickness and even a small error of ice density will produce a large computational error. Thus, for water density ρ_w = 1025 kg/m^3 and ice density ρ_i = 1000 kg/m^3 (FENCO, 1980, p. IV.4) we have h = 20.5 m for a measured freeboard h_s = 0.5 m. In contrast, given a reasonable value of ice density ρ_i = 900 kg/m^3, the total ice thickness becomes 4.1 m for the same freeboard. If we define ρ_i = 900 kg/m^3, the corrected values of ice thicknesses of

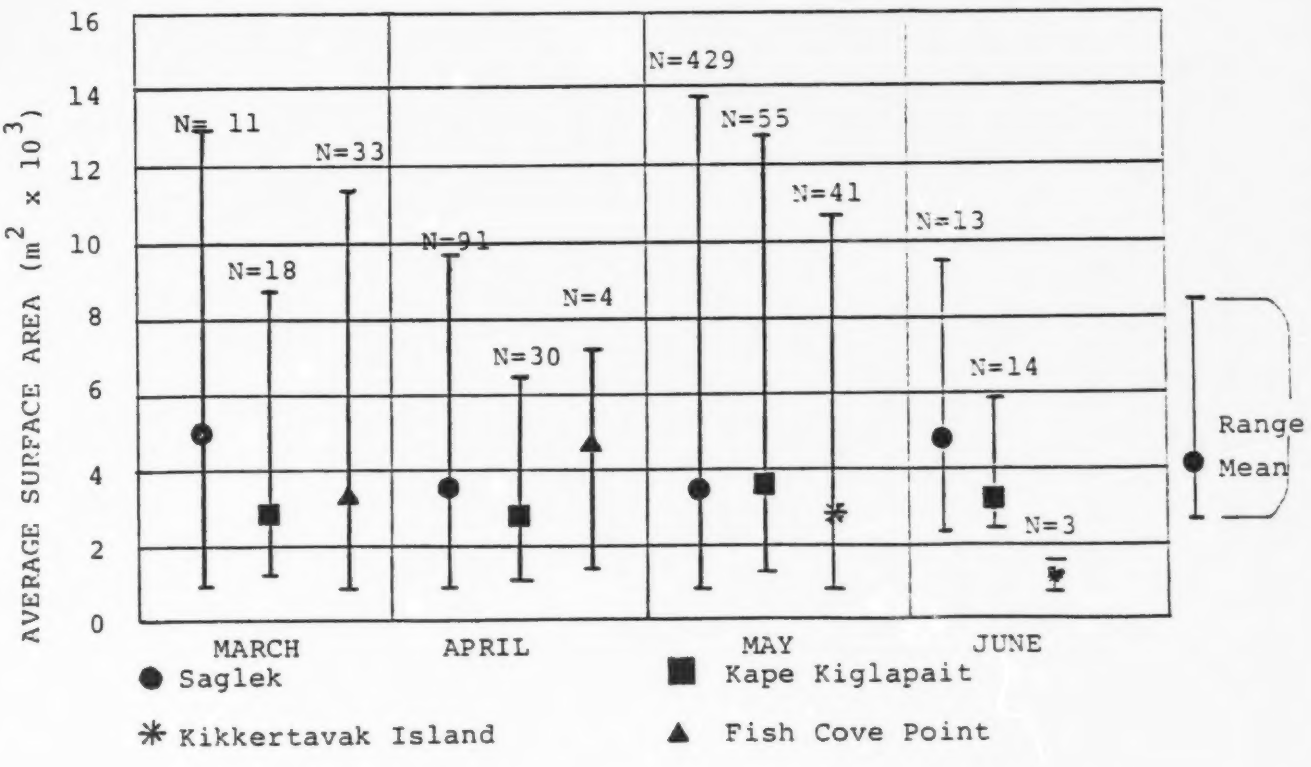

Figure 1 Surface areas of the m.y. ice floes offshore Labrador Sea in 1979 (FENCO, 1980)

Table 3

MULTI-YEAR ICE FLOE THICKNESS STATISTICS
FROM PHOTOGRAMMETRIC ANALYSIS
1979 by FENCO (1980)

values in brackets refer to corrected data

Line Sampled	Sample Population	Thickness Range			Average Thickness (m)
		Low (m)		High (m)	
Offshore Fish Cove Point 084° Magnetic	N = 8	9.5 (1.9	- -	26.2 5.24)	15.6 (3.12)
Offshore Kikkertavak Island 081° Magnetic	N = 10	4.3 (0.86	- -	19.8 3.96)	11.4 (2.28)
Offshore Cape Kiglapait 107° Magnetic	N - 44	5.1 (1.02	- -	32.2 6.44)	15.5 (3.10)
Offshore Saglek 097° Magnetic	N = 81	4.9 (0.98	- -	31.8 6.36)	13.9 (2.78)
Offshore Labrador (4-line Total)	N - 143	4.3 (0.86	- -	32.2 6.44)	14.2 (2.84)

the m.y. ice floes are given in brackets in Table 3. Thus, more reasonable thickness of m.y. ice lie in the range of 0.86 to 6.44 m, with a mean value of approximately 3 m. The maximal ice thicknesses were larger in the two northern locations when compared to their southern counterparts, yet there is no noticeable tendency towards thinner ice floes southwards when the mean values are considered.

The shape and dimensions of m.y. floes near Hopedale were investigated by FENCO (1976) during the winter of 1976. A summary of the study is presented in Table 4.

From Table 4, one observes that the majority of m.y. floes were rounded and/or oval in shape. This is probably due to long-lasting interactions between ice floes. The minimal ice thickness from the edge of the floes was reported. Diminution of ice thickness was especially significant in the submerged portions of the floes and seems to have been caused partly by pack ice interaction and partly by lateral melting of the ice floe. However, the reported thicknesses of ice provided new information on the m.y. floe population off the Labrador coast when compared with the values reported in the FENCO (1980) 1979 spring study. The mean thickness of m.y. ice in 1976 was approximately 6.7 m while the mean thickness in 1979 was equal to only 2.84 m (see Table 3). Let us assume that the accuracy of these two datasets is equivalent. If so, a likely reason for the reported difference in m.y. ice thickness between 1976 and 1979 is a change in origin of the m.y. pack ice. Areal dimensions of the floes are listed in Table 4. No floe was larger than 100 m in diameter during either study. This suggests that the fragmentation of m.y. pack ice on its way from the Arctic Basin and/or the waters of the Canadian Arctic Archipelago is intensive and strongly affects floe size. As a result, m.y. floes tend to be smaller than f.y. floes.

ICE DRIFT

Little data is presently available on ice drift in the Labrador Sea. However, the data set presented by FENCO (1976) seems to be the most adequate for our study. Three methods were used by FENCO to measure ice movement. However, only one (Satellite Navigation System (SNS)) is directly applicable to the movement of pack ice and will be described here.

The SNS has provided an interesting data set of f.y. and m.y. pack ice movement. The reported range of speed for the f.y. and m.y. ice is 0.05-0.55 m/s and 0.05-0.90 m/s, respectively. The most common ice drift is 0.15-0.20 m/s for both f.y. and m.y. ice. The direction of ice movement shows a large scatter especially in the f.y. pack ice data set. However, the drift of m.y. pack ice is

Table 4 Shape and dimensions and thickness of multi-year ice floes offshore Labrador Sea (FENCO 1976)

Date	Location		Thickness		Size	Shape	Topography
	Latitude	Longitude	Range (m)	Mean (m)	(m)		
19 March 1976	Not	Not clear	-	7.62	60 x 89	Rounded	N.A.*
16 April 1976	56-36N	59-25W	1.4 - 8.2	5.68	60 x 70	Oval	N.A.
20 April 1976	56-25N	57-52W	1.3 - 8.9	5.49	52.5 x 48	Oval	N.A.
21 April 1976	56-15N	59-38W	N.A.	6.5	Diameter = 50 m	Oval	N.A.
22 April 1976	56-08N	58-45W	4.67-11.02	N.A.	94 x 91.2	Hexagon	Very hummocked
23 April 1976	56-05N	59-00W	7.32-9.17	8.25	N.A.	N.A.	N.A.

* Not Available

rather more regular; almost 50% of all readings lie within a 36° arc (from 108 to 144° true). If a data set of 38 reading is statistically significant it can be projected that the drift of the thick m.y. ice floes is more affected by currents than that of the f.y. ice. This may be confirmed by the analysis of ice speed versus the wind speed ratio for pack ice. The most common values of this ratio are on the order of 0.02 to 0.04 for f.y. ice (41.4%) while m.y. pack ice does not exhibit a consistent ratio, with only 23.7% of all readings lying within this range where m.y. pack ice drift against the wind are rather common (42%).

The alongshore and offshore components of ice drift were also computed by FENCO (1976). Analyses of the percentage distribution by FENCO (1976) showed that ice drift is affected by along shore component of the Labrador Current.

SEASONAL CYCLE OF ICE OCCURRENCE

Occurrence of ice in the Labrador Sea follows an annual (seasonal) cycle. Ice accumulation takes place in late autumn-winter/early spring, while the melt and retreat of ice starts in spring and is so rapid that final ice decay occurs by late spring/early summer. The maximal ice extent is reported in March-April and the ice-free season extends from April-May to December-January (off the east coast of Newfoundland) and from July-August to November-December in the northern part of the Labrador Sea. Hence, the following scenario of ice ocurrence may be proposed:

SEASON	TENDENCY	ICE STAGE
Ice Season	Ice advance	Initial ice freezing Freeze-up Ice accumulation/ice growth Maximal ice extent
	Ice retreat	Melting of ice Break up Decay of ice
Ice free		Ice free

Of course, this ice occurrence scheme is not as ideal as presented. Ice drift significantly affects ice occurrence. Hence, pack ice originating from Baffin Bay or even the straits of the Canadian Arctic Archipelago can be encountered in the

Labrador Sea. This is why m.y. floes are found in the Labrador pack even though all f.y. ice melts at the end of the ice season.

Some studies have been conducted to track the development of ice in the Labrador Sea. Based on data from the period 1969-79, Crane (1978) monitored the extent of ice in the northern part of the Labrador Sea and Baffin Bay and found that two periods of ice advance and two ice retreats were distinguishable over a given ice season. The patterns of ice operating during the years of the early and late ice advance are similar off the coast of Labrador, while some differences are observable for the Foxe Channel, Foxe Basin and Hudson Straits (Crane, 1978; Figs. 4 and 5). In general, the Labrador Coast is the first area to become ice free when compared with areas located further to the north and east. In years of early ice retreat, the Labrador Coast is ice free by June 11, although a two week delay is observed in a small coastal zone off Cape Chidley. In years of late ice retreat, the ice decays along the coast southwards from the 59th parallel prior to June 11 while an extensive belt of pack ice spreads from Cape Chidley to 57°N latitude prior to August 6, leaving the area east of Cape Chidley ice free from August 20 onwards, due principally to the effect of the Labrador Current. The causes of these 'late' and 'early' ice retreat and advance have been determined from the analysis of meteorological observations (Barry and Keen, 1978). From this work it appears that years of late ice advance are marked by a predominantly eastern air flow, while air flows from the north and west mark years of early ice advance. Similarly, years of late ice retreat are associated with a more southerly airflow.

The spatial distribution of ice advance can be defined from freeze-up dates presented by Fraser (1975) for the period of 1959-1975. In general, the pack ice spreads seawards from the coasts; but in the Grand Banks region ice advances to the south. The isolines of ice advance in this region extend from the west to east and show the effect of the mixing of the Gulf Stream and Labrador Current.

The spatial pattern of ice retreat is also presented by Fraser (1975). Two general tendencies are observable. 1) Break-up occurs first offshore and migrates inwards towards the coast, and 2) break-up occurs first in the southern part of the Labrador Sea - Grand Banks areas, and last in the northern part of the Labrador Sea. Based on the dates of freeze-up and break-up, the length of the open water season at a given locality has been shown to increase towards the east and south (Fraser, 1975).

THE SPATIAL DISTRIBUTION OF SEA ICE

Sea-ice occurrences are characterized below according to their maximal extent, concentration and spatial arrangement.

THE ICE LIMIT AND ITS SEASONAL VARIATIONS

The ice limit is one of the most convenient characteristics for presentation of the spatial distribution of ice occurrence in the Labrador Sea, where several published data sets are available. Among others, Sowden and Geddes (1980) and an unclassified report entitled "Eastern-Western Arctic Sea Ice Analysis" prepared annually by the Naval Polar Oceanography Center, Suitland, MD, appear to be the best and most comprehensive. The ice limit varies from month to month within an ice season. According to Defant (1961), the mean extent of the ice is given in Fig. 2. Ice reaches its maximal limit in March-April.

The probability of encountering sea ice from March to August is given by Smirnov (1974) for the North Atlantic and reflects the ice extent. The Labrador Current effect is fairly well visible in this study. The course of the 0-isoline is significantly bent to the south along the coast of Labrador, while the whole central part of the Labrador Sea is ice free. More detailed charts of the probability of encountering ice in the northern part of the Labrador Sea and Davis Strait are given by Vladimirov (1964).

MULTI-ANNUAL VARIATIONS OF ICE EXTENT

Ice extent in the Labrador Sea - Grand Banks areas varies from year to year. To arbitrarily determine the severity of pack-ice conditions off Newfoundland, Miles (1974) used an index of ice extent previously proposed by Corcum (1971) and Groissmayer (1939) for the severity of an iceberg season. This index was formed by adding the latitude and longitude of the ice edge. Thus, as the index increases, the severity of ice conditions off Newfoundland decreases. Based on the data set from the period of 1921-1973 (exclusive of the years 1940-1942), Miles (1974) listed the annual indices of an ice season. The least severe ice conditions occurred in 1971 when the southern ice limit reached only 51°N. The most severe ice season occurred in 1921 when pack ice spread maximally to the south (42.5°N) and east (45°W). The years 1940-1942 were assumed by Miles (1974) to be of light ice based on the data provided in IIP bulletins. Hence, the 20's and 30's seem to have been very severe, while the 50's and 60's have been extrordinarily light. Such tendencies of the severity of the ice season are probably caused by multi-annual variations in atmospheric circulation. The ice extent off Newfoundland is strongly

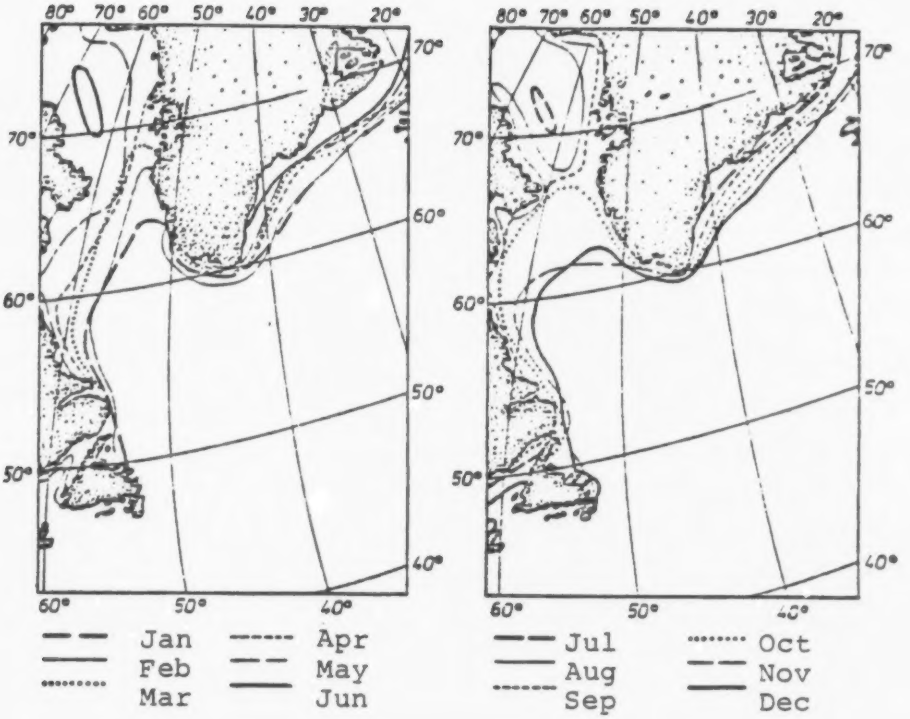

Figure 2 Seasonal variation of mean ice extent in the North West Atlantic Ocean (Defant, 1961)

affected by the wind regime of the North Atlantic region. As the strength of North-Northwesterly winds over the Labrador Sea corresponds to the intensity of the Icelandic Low, the average decadal ice index may be compared to the air pressure difference which exists between 50° N60°W and 60° N50°W during the months of December, January and February. The reduction of ice extent during this period corresponds pretty well to the weakening of the Icelandic Low (Miles, 1974). On the other hand, the reduction of strength of North-Northwesterly winds in the Labrador-Greenland region may produce a weakening of the Labrador Current which is primarily responsible for the southward drift of the pack ice.

Valuable information on the ice regime of the Labrador Sea has been provided by Sanderson (1975), who compared the variations of the ice covered regions of the Labrador Sea to those of the Greenland Sea, Barents Sea, and the Sea of Okhotsk (Fig. 3). Ice conditions in the Labrador Sea, Barents and Greenland Seas exhibit opposite tendencies in pack ice variability. During some years, in which heavy ice conditions occurred in the Barents and Greenland Seas in February, March and (sometimes) April, extremely light ice conditions were found in the Labrador Sea. Conversely, in years of heavy ice conditions in the Labrador Sea, light ice conditions were reported in the Barents and Greenland Seas. Sanderson (1975) noticed also that during the period 1966-1974 the maximal ice extent in the Sea of Okhotsk was reported one year later than in the Labrador Sea. These observations indicate that the ice regime of the Labrador Sea is (at least in part) governed by global atmospheric circulation.

ICE CONCENTRATION

Two tendencies are observed when the concentration of sea ice is analysed: 1) ice concentration decreases seawards from the coast, and 2) from north to south. Usually, ice concentration is minimal near the pack-ice edge. However, when the wind direction is from the open water, a compact ice edge is established.

Markham's (1980) atlas gives valuable quantitative data of ice concentration (Fig. 4). Basically, the heaviest ice conditions occur in February-March, with an obvious decrease in ice concentration to the south and east.

ICE ARRANGEMENT

Arrangement of pack ice can be studied using the ice charts published by several weather bureaus (e.g. MEDOC, IIP, Ice Central (Ottawa)). The pattern of pack ice distribution is related to wind regime and is most variable in the vicinity

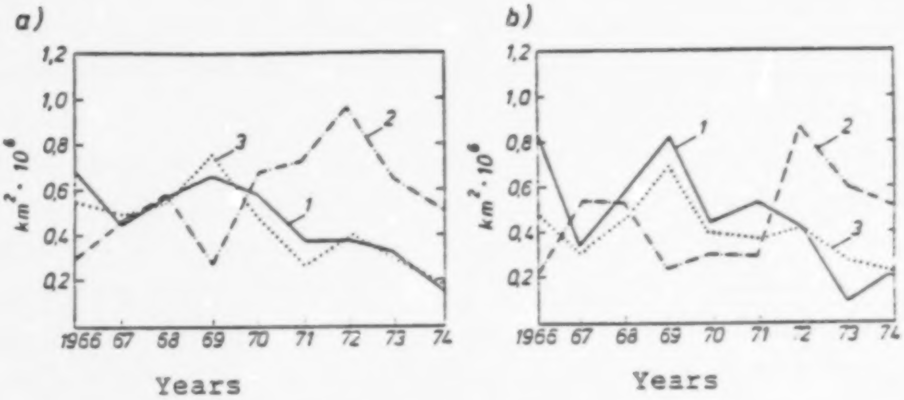

1 - Greenland Sea 2 - Labrador Sea 3 - Barents Sea

Figure 3 Variation of surface area of sea ice in the Labrador Sea, Greenland Sea and Barents Sea at the end of February (a) and at the end of March (b) (Sanderson, 1975)

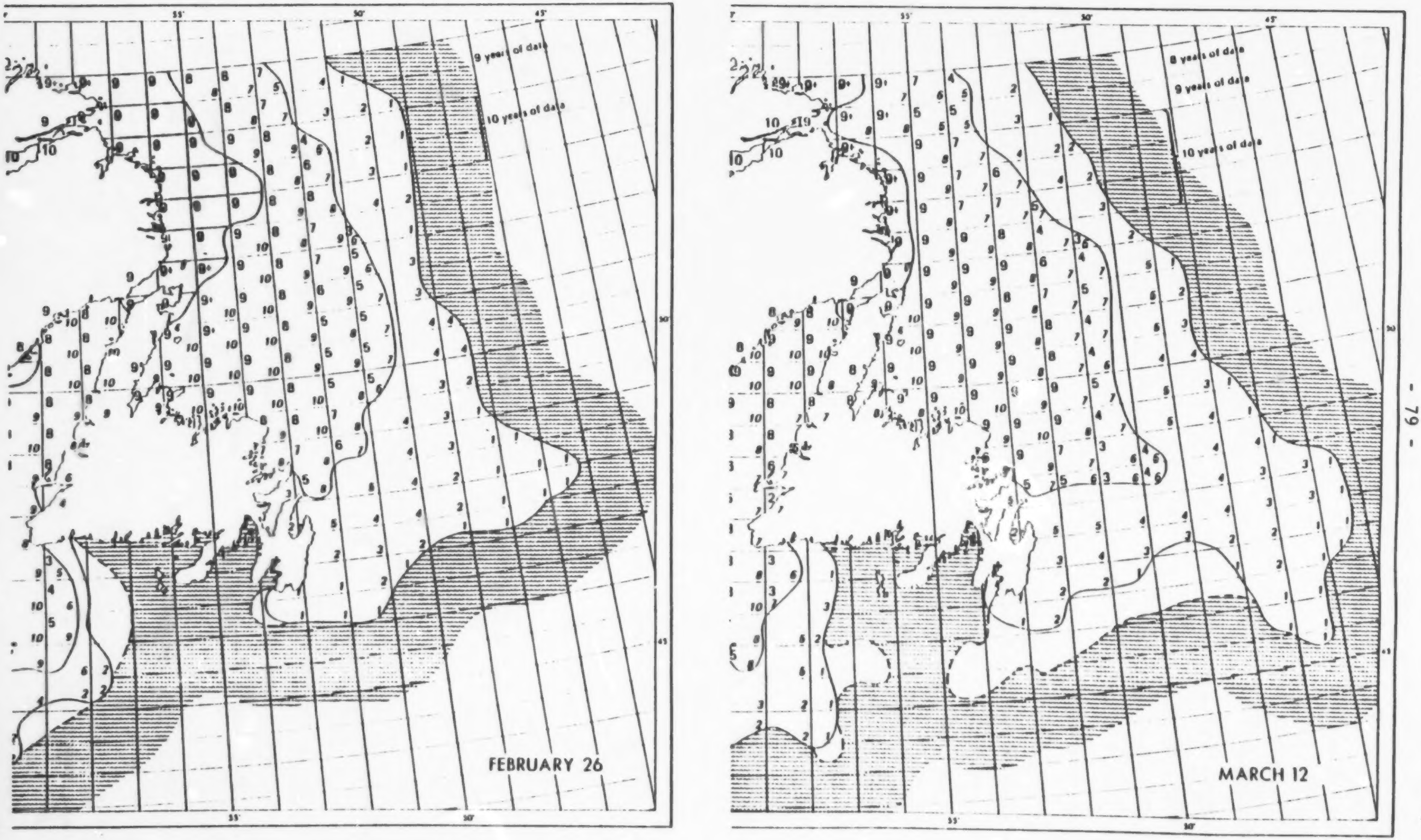

Figure 4 Mean ice concentration in the Labrador Sea - Grand Banks Area (Markham, 1980)

of the ice edge. Large ice belts and ice strips are common in this region. These ice features are of local origin. Local zones of ice divergence resulted by winds and wind-generated surface current can be also found, mainly betwen the parallels of 48-55° N. Several cases of polynyas have been found. Their dimensions are variable. Local openings of a few hundred meters in diameter are commonly reported even in heavy pack ice. Sometimes, large polynyas (on the order of tens of km. in diameter) can be encountered in the Labrador Sea far away from the ice edge. To date, it is rather difficult to precisely explain the origin of these openings which may be dynamically induced (produced by wind drift of pack ice, especially within vortex features) or thermodynamically induced (melting of ice due to contact with warmer water). A careful analysis of this phenomenon is required in the near future with the emphasis placed on determining the heat regime of such polynyas as well as investigating the dynamic factors which affect such mesoscale ice arrangement features. One can presume, based on Sanderson's (1971) study of ice edge variation affected by winds and formation of the 'Northern Bay' in the Greenland Sea, that mesoscale effects should also be visible in the Labrador Sea.

RESEARCH ON SEA ICE OFFSHORE LABRADOR SEA: STATE-OF-THE-ART, NEEDS AND PROSPECTS

Studies of sea ice in this region are not well developed. Almost all of the references used are reports on 'ice climatology' and/or raw data sources. There are very few quantitative papers presently available.

To analyse the problems faced in the Labrador Sea we shall divide the main fields of studies into the following topics:

1) ice climatology
2) physical properties of sea ice
3) ice drift
4) ice growth
5) ice deformation

ICE CLIMATOLOGY

The ice climatology of the Labrador Sea is advanced when compared to the state of research in the other categories. However, data is still scarce when compared to information available for the Arctic Ocean, Beaufort Sea and Bering Sea. The Markham (1980) Ice Atlas appears to be the most up-to-date and best presentation of sea ice in this sea. Other papers (e.g. Fraser, 1975) are also useful but lack precise comments.

A few data reports (e.g. FENCO, 1975; 1976; 1979; and 1980) provide a valuable input of raw data, and preliminary statistical analyses. However, the lack of a comprehensive summary of all data collected is evident.

ICE PROPERTIES

The physical properties of sea ice are very useful when known. Their application to several engineering problems (ice/structure, ice/ship, and ice/ice interaction) is well known and undisputed. Unfortunately, only a few reports present the physical or mechanical properties of sea ice in the Labrador Sea. These reports are given by FENCO (1975; 1976; 1979; and 1980).

Ice salinity, ice strength, elastic modulus were measured during spring and winter field ice surveys in the years of 1975 and 1976, respectively. Valuable notes on methodology applied for these measurements as well as data collection method are given by Fenco. However, it is difficult to compare computed and/or measured values of ice strength (unconfined compressive strength, flaking strength, confined compressive strength) to measurements collected from other seas (e.g. Beaufort, Bering or Greenland Seas) because of minor differences in the measurement technique. In any case, field work and measurements have been made and their results are applicable to several ice engineering problems.

It is worthwhile to review the papers which present the physical properties of ice samples taken from other waters surrounding Canada.

Numerous papers on the mechanical properties of ice are referenced by Frederking and Timco (NRC, Ottawa). Weeks and Anderson (1958) also provide a comprehensive review of the literature available at that time and present values of the strength of sea ice samples taken from the Hopedale area, Labrador. Other papers given by Weeks deal both with the methodology of measurements and the analysis of the mechanical properties of ice. Recently, Tucker, Gow and Weeks (1985) have provided an analysis of the physical properties of m.y. ice occurring in the Fram Strait. Here, we should note that the provided crystal texture analyses give good data for the ice occurring in the Greenland Sea as the pack ice drifts from the Arctic Basin through the Fram Strait to the North Atlantic Ocean. Work by Overgaard et al. (1983) has extended the knowledge of ice properties in the Greenland and Barents Seas. Weeks (1982) presented a report on the state-of-the-art of physical properties of the ice cover of the Greenland Sea. He emphasized the lack of several data. Labrador Sea ice seems to be rather unknown when compared to that of other Arctic marginal seas.

ICE DRIFT

Ice drift in the Labrador Sea is not well documented because of the lack of accurate and comprehensive data sets. However, it should be noted here that some data sets are available. The most comprehensive data set was gathered during the February 1977 Ship-In-The-Ice program (LeDrew et al., 1977). An integrated data set of wind, current and ice parameters were collected and are sufficient to study ice drift on the scale of 10-20 km. Valuable information on ice drift was collected during FENCO's ice experiments in the late seventies. However, these data sets are not integrated and they should not be put into the ice models. They are adequate for the limited use of monitoring the drift of the ship in the pack ice field or approximating the drift of selected parts of the pack ice field or approximating the drift of selected parts of the pack ice fields and/or separated floes.

Requirements for modelling the Labrador pack have been given by Denner and Keliher (1981). They used Udin and Ullerstig's numerical sea ice model for the Labrador Sea, obtaining reasonable results. However, they noted that theere was insufficient input data. The surface currents during the ice season are not known except by climatological estimates. Ice thickness had to be derived from satellite data. On the other hand, it is interesting that Denner and Keliher (1981) have received reasonable data running erroneous ice drift model given by Udin and Ullerstig (1976). Other papers on ice drift confirm the lack of integrated data sets. However, Foley and Keliher (1982) used the new, revised climatological current data set for simulating the ice drift in the Labrador Sea. The accuracy of this data set may be questioned because Keliher and Foley (1983) estimated the ocean currents in the Labrador Sea using well known Hibler's (1979) ice model.

Ikeda (1985) and Ikeda (in press) simulated ice drift in the Labrador Sea using a coupled ice-ocean model, based on wind-driven coastal flow. This model operates on arbitrary chosen input data.

Walsh et al. (1985) gave the simulated ice drift vectors for the seas of the northern hemisphere. Among others, they have calculated the 30 years (1951-1980) mean seasonal and annual drift vectors for the Labrador Sea using Hibler's (1979) model. In this simulation, the pattern of the ice drift is simple. Ice drifts alongside the Labrador Coast to the Grand Banks. Unfortunately, Walsh et al. (1985) did not mention what source of currents was used.

It is seen that the ice drift in the Labrador Sea is poorly understood, predominantly because of the lack of input data. Simulations of ice drift have been done, however, they were probably based mainly on the climatological ocean current data set and/or other arbitrarily chosen input data.

ICE GROWTH

Ice growth is not well documented in the Labrador Sea. Walsh et al. (1985) contains some information on simulated ice thickness in the Labrador Sea in February. This simulation has been made using Hibler's (1979) ice model. They obtained ice thickness data which were within the same range as the data given in the Oceanographic Atlas of North Atlantic Ocean (1968).

ICE DEFORMATION

Ice deformation in the Labrador Sea is almost not well known. Information on the ridged and rafted ice are sometimes given in the papers on ice climatology. The papers by Wadhams (1973; 1978) on ice/wave interaction deal with the attenuation of the swell by pack ice. Wadhams made a hypothesis that the waves are responsible for the break-up of the pack ice in the Labrador Sea. This model has been verified with field data (pers. comm.).

CONCLUSIONS

The need of launching a well-prepared field experiment to investigate ice/sea and ice/atmosphere interaction is obvious from the lack of existing data. Detailed information on a possible experiment is given by Wadhams and Lever (1986). The Labrador Ice Margin Experiment (LIMEX) was a possible experiment for studying the sea ice off the coast of the Labrador and should provide answers to several questions related to the ice regime of this sea. The main objectives of the experiment under consideration should be: 1) the application of existing remote sensing methods and tools for monitoring the ice; 2) investigation of the dynamics and thermodynamics of sea ice; 3) studying of the mesoscale effects of the oceanic and atmospheric circulation on the ice extent and ice edge behaviour; 4) development of accurate forecasting models/relationships to monitor and predict the ice advance and retreat in the Labrador Sea in long and short term forecasts; 5) study the physical characteristics of ice in the Labrador Sea.

REFERENCES

BARRY, R.G., CRANE, R.G., LOCKE, C.W., LOCKE, W.W., III, and MILLER, G.H. 1977. The coastal environment of Southern Baffin Island and northern Labrador - Ungava. Final Report to Imperial Oil Limited, Calgary, Alberta. APOA Project 138.

BARRY, R.G., and KEEN, R. 1978. In: Barry, R.G., Jacobs, J.D., et al.. Energy budget studies in relation to fast ice breakup processes in Davis Strait, climatological over-view. Institute of Arctic and Alpine Research, Occasional Paper No. 26, University of Colorado, Boulder, pp. 8-67.

CONVAY, G.W., GREENFIELD, W. 1972. Grand Banks Ice Reconnaissance. Project #20D-90(72), DJS-226-422.910. Amoco Canada Petroleum Company Ltd.

CORCUM, I.I. 1971. Performance of formula for predicting the iceberg count off Newfoundland, Journal of Applied Meteorology, Lancaster, Vol. 10, pp. 605-607.

CRANE, R.G. 1978. Seasonal variations of sea ice extent in the Davis Strait - Labrador Sea area and relationships with synoptic-scale atmospheric circulation. Arctic, Vol. 31, No. 4, pp. 434-447.

DEFANT, A. 1961. "Physical Oceanography", Pergamon Press, London.

DENNER, W.W. and KELIHER, T.E. 1981. Numerical modelling of Labrador pack ice dynamics. International Conference on Port & Ocean Engineering under Arctic Conditions (POAC), proceedings, Vol. 3: pp. 1330-1347.

DINSMORE, R.P. 1972. Ice and its drift into the North Atlantic Ocean. International Commission for the Northwest Atlantic Fisheries, Special Publication No. 8.

FENCO, 1975, Spring Field Ice Survey Offshore Labrador. Report Submitted to Eastcan Exploration Limited. Foundation of Canada Engineering Corporation Limited.

FENCO. 1976. 1976 Winter Field Ice Survey Offshore Labrador, Vol. I and II. Submitted to: Eastcan Exploration Limited. Fenco Consultants Ltd. and Innovative Ventures Ltd.

FENCO, 1979. Freeze-up Study Offshore Labrador.

FENCO, 1980. Multi-year ice floe population offshore Labrador 1979. Submitted to Total Eastcan Exploration Ltd. Fenco (Nfld.) Limited.

FOLEY, J.S. and KELIHER, T.E. 1982. Recent studies from the Labrador Sea-Ice Model. 16th Annual Congress, Canadian Meteorological and Oceanographic Society, proceedings, 26-28 May 1982. University of Ottawa.

FRASER, J.E. 1975. Some Sea Ice Cover Statistics for the Canadian East Coast, Imperial Oil Limited, Production Resources and Technical Service Lab., Calgary, Alberta.

GROISSMAYER, F.B. Schwere und leichte Eisjahre bei Newfundland und das Vorwetter, Annalen der Hydrographie und Maritimen Meteorologie. Berlin, V. 67: pp. 26-30

IKEDA, M. 1985. A Coupled Ice-Ocean Model of a Wind-Drive Coastal Flow. Journal of Geophysical Research, 90, C5: pp. 9119-9128.

IKEDA, M. (in press). A mixed layer beneath melting sea ice in the marginal Ice Zone Using a One-Dimensional Turbulent Closue Model.

JACOBS, J.D., and J.P. NEWELL, 1979. Recent Year to Year Variations in Seasonal Temperatures and Sea Ice Conditions in the Eastern Canadian Arctic, Arctic, V. 32, No. 4.: pp. 345-354.

JELLY, K.C. and N.B. MARSHALL, 1976. Incidence of the Ice in the Approaches to North America during decade 1956-1965. Marine Observer. No., 218.

KELIHER, T.E. and DENNER, W.W. 19891. Sea Ice Dynamics in the Labrador Sea. Fall Meeting of the American Geological Union, San Francisco, 7-11 December, 1981.

KELIHER, T.E. and FOLEY, J.S. 1983. Estimates of ocean currents using a Labrador Sea ice model. Annals of Glaciology, V. 5.

LEPPÃRANTA, M. 1981. Statistical Features of sea ice ridging in the Gulf of Bothnia. Winter Navigation Research Board, Research Report No. 32. Helsinki.

LEVER, J. and WADHAMS, P. 1986. LIMEX - A Labrador Ice Margin Experiment. Proceedings of Canadian East Coast Workshop on Sea Ice. January 7-9, 1986, Halifax.

MACLAREN ATLANTIC LIMITED. 1977. Report on ice and Meteorological Observations in the Davis Strait During April, May and June 1977. Report prepared for Imperial Oil.

MARKHAM, W.E. 1980. Ice Atlas Eastern Canadian Seaboard, Environment Canada, Atmospheric Environment Service, Toronto.

MILES, K. 1974. An Index for Pack-Ice Severity off Newfoundland and its Secular Variations. The Meteorological Magazine, V. 103, No. 1222.

NORDCO. 1980. Lake Melville/Offshore Labrador Year Round Navigation Study 1978-79. Special Report submitted to the Special Project Department of Industrial Development, Government of Newfoundland & Labrador.

OCEANOGRAPHIC ATLAS OF THE NORTH ATLANTIC OCEAN. 1968. Section 3: Ice, Naval Oceanographic Office, Washington, D.C., Publ. 700.

OCEANOGRAPHIC ATLAS OF THE POLAR SEAS. 1958. U.S. Navy Hydrographic Office, Washington, Hydrographic Office Publication No. 705 (reprinted 1968).

OVERGAARD, S. WADHAMS, P. and LEPPARANTE, M. 1983. Ice properties in the Greenland and Barents Seas during Summer. Journal of Glaciology. V. 29. No. 101. pp. 142-164.

PETRO-CANADA. 1982. Offshore Labrador Initial Environmental Assessment. Prepared for the Labrador Group of Companies.

SANDERSON, R.M. G.P. DAVIS. 1972. Ice Conditions Through the Northwest Passage. Marine Observer, V. XLII, No. 236.

SANDERSON, R.M. 1975. Changes in the Area of Arctic Sea Ice 1966 to 1974. The Meteorological Magazine, V. 104, No. 1240, November 1975.

SMIRNOV, V.I. 1974. "Conditions of ice navigation in the waters of the Canadian Arctic Archipelago", (in Russian). Published by Gidrometeoizdat, Leningrad.

SMITH, E.H. 1931. Arctic Ice, with special reference to its Distribution to the North Atlantic Ocean, The Marion Expedition to Davis Strait and Baffin Bay. U.S. Treasury Department. Coast Guard. Scientific Results, Part 3, U.S. Government Printing Office, Washington.

SOWDEN, W.J. and F.E. GEDDES. 1980. Weakly median and extreme ice edges for Eastern Canadian Seaboard and Hudson Bay. Environment Canada, Ice Climatology and Application Division, Ottawa, Ontario, Jan. 1980.

TUCKER, III, W.D. GOW, A.J. and WEEKS, W.F. 1985. Physical Properties of Sea Ice in the Greenland Sea. Proc. of POAC, 1985. V. 1: pp. 177-188.

TUNNEL, G.A. 1961. Incidence of ice in the approaches to North America during the decade 1946-1955. Marine Observer, London, 31, pp. 78-85.

VLADIMIROV, D.A. 1964. Iciness of the Davis Strait, Trudy GOI, No. 71, pp. 100-119.

WADHAMS, P. 1973. Attenuation of swell by sea ice. Journal of Geophysical Research., V. 78, No. 18.

WADHAMS, P. 1978. Wave decay in the marginal ice zone from a submarine, Deep Sea Research, V. 25.

WALSH, J.E. and W.D. HIBLER, III, 1984. A model simulation of 20 years of Northern Hemisphere Sea Ice Fluctuations. Annals of Glaciology, Vol. 5.

WALSH, J.E. W.D. HIBLER, III, and B. ROSS, 1985. Numerical Simulation of Northern Hemisphere Sea Ice Variability, 1951-1980, J. Geophys. Res., Vol. 90, No. C3, pp. 4847-4865.

WEEKS, W.F. and ANDERSON, D. 1958. An experimental study of strength of young sea ice. Transvection of American Geophysical Union, V. 39, No. 4.

WEEKS, F.W. and O.S. LEE. 1958. Observations on the Physical Properties of Sea Ice at Hopedale, Labrador. Arctic, V. 11, No. 3. pp. 134-155.

WORLD METEOROLOGICAL ORGANIZATION (WMO) Sea Ice Nomenclature, 1970, TP. 245. Geneva, Switzerland.

ZAKRZEWSKI, W. 1983. Ice in the seas. Maritime Publishers, Gdansk (in Polish), 313 pp.

Air-Sea Heat Flux and the Seasonal Distribution of Sea Ice Over The North East Newfoundland Shelf

G. SYMONDS

Department of Fisheries and Oceans
Atlantic Oceanographic Laboratory
Bedford Institute of Oceanography
Dartmouth, Nova Scotia, Canada, B2Y 4A2

ABSTRACT

Over the North East Newfoundland Shelf the main source of ice is advection from the north by winds and currents. Using historical ice charts it is shown that the advance of ice is limited by ice melt throughout the winter months when the ocean provides the only source of heat, part of which is lost to the atmosphere and part goes to melting ice. Following techniques developed by Maykut [1978, 1982] the vertical growth of sea ice south of 55°N is examined in terms of the net heat loss from the ocean (F_w) and the conductive heat flux (F_c) through the ice to the atmosphere. F_c is estimated by assuming a linear temperature gradient through the ice from the freezing point of sea water at the underside of the ice to the surface temperature calculated by solving the radiation balance at the ice surface using monthly climatological data. The flux F_w is estimated from monthly averaged temperature profiles from Station 27 off St. John's, Newfoundland in the south and from historical data from the Labrador Shelf in the north. The results suggest that in the north ice growth of approximately 1 cm/day might be sustained off Hopedale (55°N) for December through March while in the south off St. John's an estimated melt rate of 3-4 cm/day can be sustained throughout the winter months. The flux F_w reaches 250 Wm^{-2} at Station 27 in January and it is suggested that much of this heat is derived from summertime heating when the whole of the North East Newfoundland Shelf is ice free.

INTRODUCTION

In the seasonal ice zone navigation and offshore operations are affected annually by the advance and retreat of the ice cover. Year to year variability in the advance, retreat and maximum extent of ice cover reflect regional climatic fluctuations. In the northern hemisphere the average sea ice coverage varies from 14×10^6 km^2 in winter to 7×10^6 km^2 in summer with a longitudinal dependent standard deviation of 10^4-10^5 km^2 (Walsh and Johnson, 1979). The longitudinal dependence results from the distribution of land masses which confine much of the seasonal sea ice zone to the Bering Sea, Okhotsk Sea, Baffin-Hudson Bay, Labrador Sea and the East Greenland Sea. In each of these regions advection from the north by winds and currents provides a significant source of ice while the seasonal advance and retreat of the ice edge reflects the seasonal cycle in the atmospheric heat flux. The absolute position of the ice edge depends on the rate of advection and the local growth and decay rates. These rates depend on atmospheric and oceanic heat fluxes and on characteristics of the ice cover such as the thickness and floe size distribution. The purpose of this paper is to consider the importance of ice advection relative to local growth and decay of ice in the seasonal sea ice zone. Particular attention is given to the contribution from the oceanic heat flux in limiting the seasonal advance of sea ice.

In the central Arctic it has long been assumed that the oceanic heat flux reaching the underside of the ice is a constant 2 Wm^{-2}. This estimate is based on investigations of the heat budget of sea ice and the oceanic heat flux required to maintain the observed ice thickness in the Central Arctic (Untersteiner, 1964; Maykut and Untersteiner, 1971). Aagaard and Greisman (1975) estimated advective exchange of heat and mass across the major boundaries of the Arctic Ocean and estimate a net heat loss from the ocean of 11 Wm^{-2}. The larger oceanic heat loss is attributed to above average heat loss to the atmosphere in the southwestern Eurasian Basin. In both cases the source of the heat is attributed to heat loss from Atlantic water in the Arctic ocean reaching the ice through vertical diffusive and/or convective processes. Maykut [1982] suggests that summer absorption of shortwave radiation by the upper ocean through leads and thin ice could account for most of the required oceanic heat flux in the Central Arctic. This implies a significant seasonal cycle may exist in the oceanic heat flux.

In the seasonal sea ice zone during the ice free months the upper ocean absorbs heat which is readily available to melt ice during the winter season. In the Antarctic the seasonal sea ice zone covers an area approximately $17x10^6$ km^2. Assuming an average ice thickness of 1.25 m Gordon [1981] estimated the daily heat requirement to produce the observed melt during the period from mid-November to mid-January to be 64 Wm^{-2}. Furthermore he estimates 34 Wm^{-2} is attributed to atmosphere-ocean heat flux while the remaining 30 Wm^{-2} is derived from the ocean through Ekman pumping and vertical diffusive and/or convective heat flux. These estimates do not take into account the heat absorbed by the ocean through leads and thin ice but nevertheless suggest the oceanic heat flux in the Antarctic seasonal sea ice zone is an order of magnitude larger than the commonly used value for the Central Arctic.

Numerical simulations of the seasonal sea ice coverage in Antarctica have required oceanic heat fluxes significantly larger than 2 Wm^{-2} to produce agreement with the observed seasonal distribution. Parkinson and Washington [1979] specify an oceanic heat flux of 25 Wm^{-2} in Antarctica while Pollard et al. [1983] use 15 Wm^{-2}. In both cases the models were designed to be coupled with atmospheric general circulation models and have various limitations particularly in the treatment of the dynamics and thermodynamics of ice.

In the northern hemisphere numerical simulations by Hibler and Walsh [1982] using a constant oceanic heat flux of 2 Wm^{-2} produced excess ice in the North Atlantic in winter. The thermodynamic computations in this model assumed only two thicknesses; open water and a mean thickness averaged over an entire grid cell. In an attempt to include the fact that ice growth rates depend on thickness (Maykut, 1982), Walsh et al. [1985] replaced the average thickness with seven thicknesses for the thermodynamic calculations. Even with the more detailed distribution the model indicated an excess of ice in the Greenland Sea, Baffin Bay and Labrador Sea in winter. This excess is attributed by Walsh et al. (1985) to poorly modelled oceanic effects. In the Greenland Sea Hibler and Bryan [1984] improved the simulated ice coverage by coupling Hibler's [1979] dynamic thermodynamic ice model with a multi-level baroclinic ocean model. The improved agreement was attributed to a large annual oceanic heat flux with a maximum in the Norwegian Sea of order 100 Wm^{-2}. In the vicinity of the observed ice edge in the East Greenland Sea the simulated oceanic heat flux is in the range 20-70 Wm^{-2}.

In the Bering Sea Hendricks et al. (1985) computed the heat budget at the ice edge and estimated the total heat loss due to ice melt and atmospheric cooling per unit length of ice edge to be 4.0×10^{7} Wm^{-1}. The major source of heat was found to be an advective input due to a northerly flow of warm water beneath the ice. Assuming the ice melt and oceanic heat loss occurs within 100 km of the ice edge Hendricks et al. (1985) estimate the advective term to be 260 Wm^{-2} and vertical diffusion of heat from the deep ocean to be 80 Wm^{-2}.

While considerable uncertainty exists as to the magnitude of the oceanic heat flux it is apparent from the preceding discussion that this heat flux is an important component limiting the seasonal extent of sea ice. In this paper the seasonal distribution of sea ice in the southern Labrador Sea is examined in terms of a mean southerly advection and local growth and decay due to atmospheric and oceanic heat flux. Using the model described by Maykut [1978] the heat conducted through the ice to the atmosphere is estimated. The source of this heat may be latent heat of fusion through ice growth at the ice-water interface or from the water column through diffusive and/or convective processes. Changes in the heat content in the water column may provide a measure of the heat lost to the atmosphere or by melting ice. The heat content of the water column for each month over the Labrador and Newfoundland shelves has been estimated from historical data (Lazier, 1982) and from data obtained at a standard oceanographic station off St. John's, Newfoundland (Keeley, 1981).

The data are described in the next section followed by a discussion of the seasonal distribution of sea ice in the southern Labrador Sea. Estimates of the mean southward flux of ice due to winds and currents are given in section 3. In the fourth section a brief outline of the thermodynamic model is presented followed by results and comparisons with observed changes in water column heat content. Discussion and conclusions follow in the final two sections.

DATA SETS

The Atmospheric Environment Service of Environment Canada has been producing summary charts of weekly ice conditions since 1959. These charts are based on aerial and shipboard observations, shore based reports and prevailing wind and temperature conditions and more recently satellite imagery. The charts for the decade 1963-1974 have been digitized on a 40x30 nautical mile grid (Markham, 1980). Total ice concentration, concentration of various ice types, ice edge orientation and per cent of open water are among the elements digitized. These data were later extended to 1978 by Esso Resources Ltd. The combined data set is available through the Atmospheric Environment Service (AES). These data have been used to estimate average area covered by ice south of 55°N for each month. North of this latitude the data become sparse particularly during the early months of the ice season. Ice thickness information may be obtained through the classification of ice type based on colour, each type being assigned a thickness category according to the AES convention.

At Station 27 (shown in Figure 1) the seasonal cycle in water column heat content is based on a 32 year time series reported by Keeley, [1981]. Data compiled by Lazier [1982] covers the Labrador Shelf from 52°N to 64°N for the time period 1928 to 1979. Monthly mean temperatures over 200 m are used to estimate the heat content.

The winter radiation balance over the ice has been estimated using monthly averaged atmospheric data including incoming short and long wave radiation, air temperature, cloudiness, surface pressure, humidity and surface wind speed and direction. Since significant north-south gradients occur through the study region data from two coastal locations have been used; Hopedale in the north and St. John's in the south (see Figure 1).

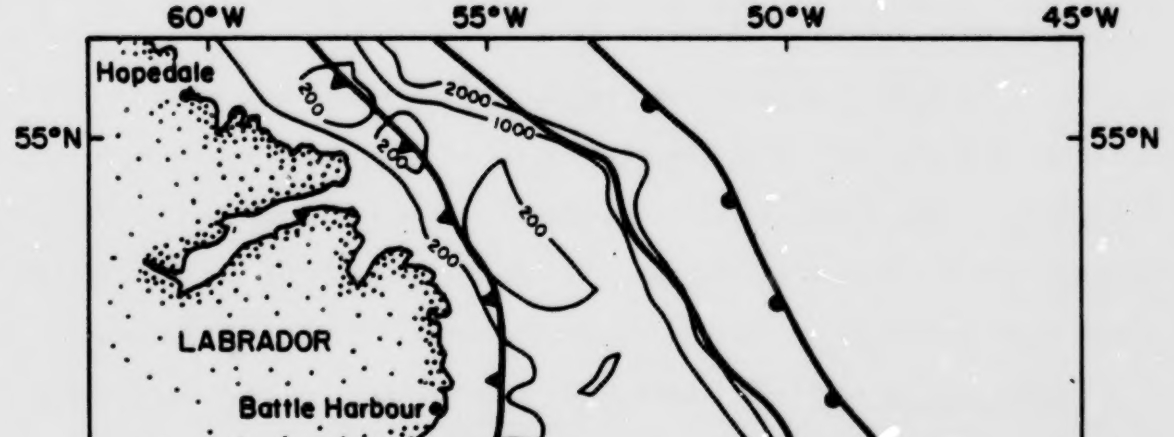

Fig. 1. Study region showing the mean (—), maximum (●) and minimum (▲) extent of ice for the period 1963-1978.

SEASONAL ICE DISTRIBUTION

The mean date of appearance of ice at latitude 52°N is January 1. Over the period 1963-1978 the earliest appearance was December 11 while the latest occurred on January 15. The mean date of disappearance of ice south of 52°N is June 4 while the earliest and latest dates of disappearance are May 7 and July 9 respectively. The mean, maximum and minimum extremes of ice for March are shown in Figure 1.

The mean advance of ice over the N.E. Newfoundland Shelf is illustrated in Figure 2 showing the mean extent of ice at the end of each month December to March inclusive. Also shown are the mean atmospheric pressure fields for the respective months. Obviously the longshore advance of the ice is at least partly in response to the wind. In the central Arctic Thorndike and Colony [1982] have shown that at time scales longer than a day 70% of the variance of ice drift is linearly related to the wind. They estimate that the ice moves at 0.8% of the speed and 8° to the right of the geostrophic wind. Monthly averaged geostrophic winds estimated by AES for a region offshore of Battle Harbour are shown in table 1 together with the associated ice drift according to Thorndike and Colony (1982).

Mean surface currents also contribute to the longshore motion of sea ice. The main feature of the circulation over the NE Newfoundland Shelf is the Labrador Current which is concentrated in an offshore branch which follows the 1000 m contour and an inshore branch along the 200 m isobath and separated from the offshore by a series of shallow banks. In the offshore branch mean current speeds are of the order of 0.30 m s^{-1} while in the inshore branch mean speeds are 0.15 m s^{-1}. Over the banks currents are small and erratic. During the summer of 1980 thirty one current meters were deployed on the Labrodor Shelf between 54°N and 59°N during the

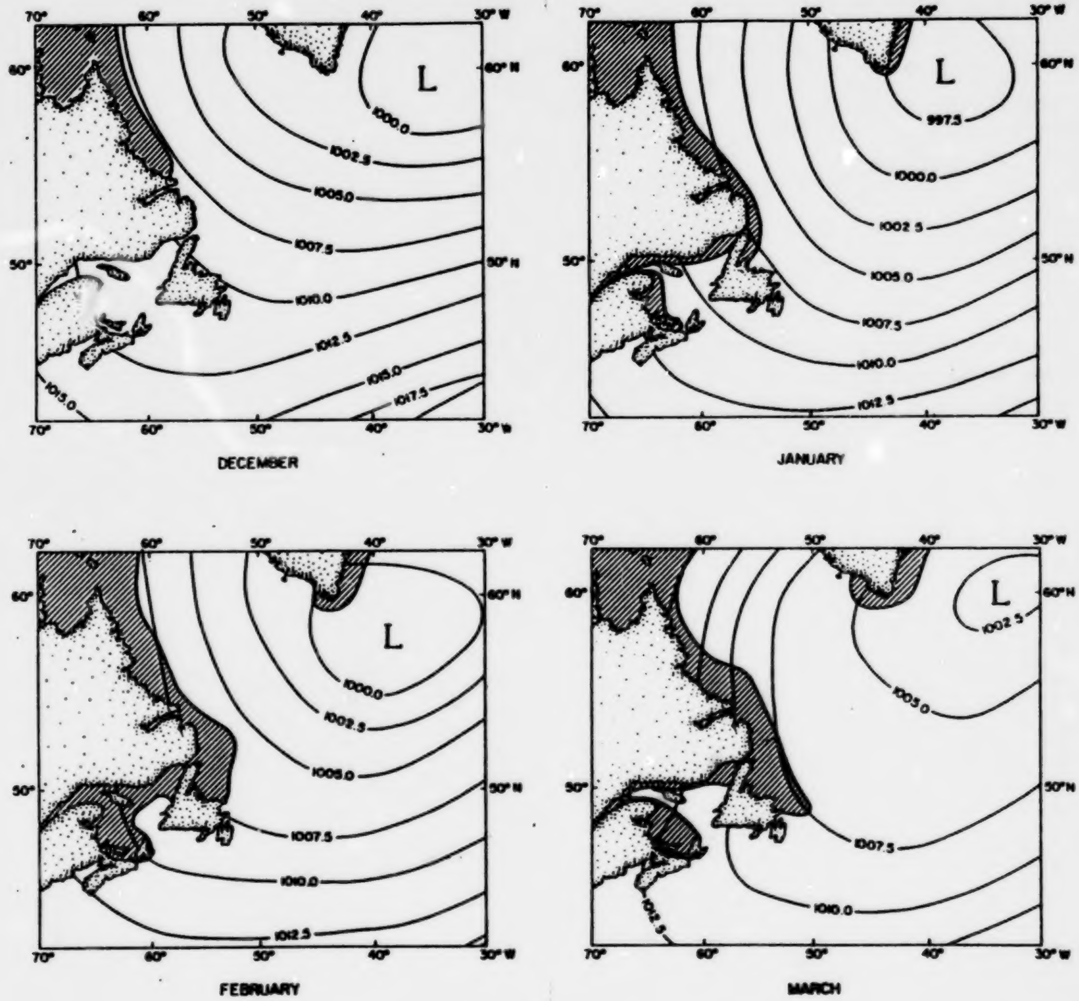

DECEMBER

JANUARY

FEBRUARY

MARCH

Fig. 2. Mean ice extent for each month December to March inclusive and the corresponding mean monthly surface atmospheric pressure fields.

	Dec	Jan	Feb	Mar	Apr	May	June
Geostrophic wind speed (m/s)	3.7	5.4	4.3	3.7	2.5	0.9	2.2
direction	134	151	139	166	206	126	69
Ice speed (m/s)	.03	.04	.03	.03	.02	.007	.02
direction	142	159	147	174	214	134	77

Table 1

Monthly mean geostrohpic wind and corresponding ice drift being .008 times the wind speed and 8° to the right of the wind direction given in degrees clockwise from north.

Offshore Labrador Biological Studies Program (Fissel and Lemon, 1982). Averaging over all meters within 70 m of the surface gives a SSE longshore current with a mean speed of 0.17 m s^{-1}. Allowing for the fact that local wind forcing contributes to the near surface currents we use 0.10 m s^{-1} as the component of longshore ice velocity due to surface currents. The combined wind and current component of longshore ice drift is then estimated to be in the range 0.1-0.2 m s^{-1}.

The mean longshore flux of ice is estimated as the mean monthly offshore extent of ice at latitude 54°N multiplied by the mean longshore velocity. The flux is expressed in terms of km^2 $month^{-1}$. The cumulative transport of ice across 54°N is shown in Figure 3 together with the observed monthly mean area south of 54°N covered by ice. The two curves shown in Figure 3 suggest that advection can account for much of the ice observed south of 54°N. However, through the winter months mean monthly air temperatures are 10°C to 15°C below freezing and during cold outbreaks -30°C or less are common. It is apparent then that local growth of ice is being limited since advection can account for most of the observed ice covered area. The ocean must provide the source of heat.

Heat loss from the ocean can occur as a heat flux through the ice to the atmosphere. The growth or melt of the overlying ice then depends on the relative magnitudes of the total heat loss from the ocean and the heat conducted through the ice to the atmosphere. The conductive flux depends on the thermal conductivity of the ice, the ice thickness and the temperature gradient through the ice. For thin ice we can assume a linear temperature gradient from the freezing point of sea water at the underside of the ice to the surface temperature of the ice. The latter is calculated by estimating the radiation balance at the atmosphere-ice boundary using the

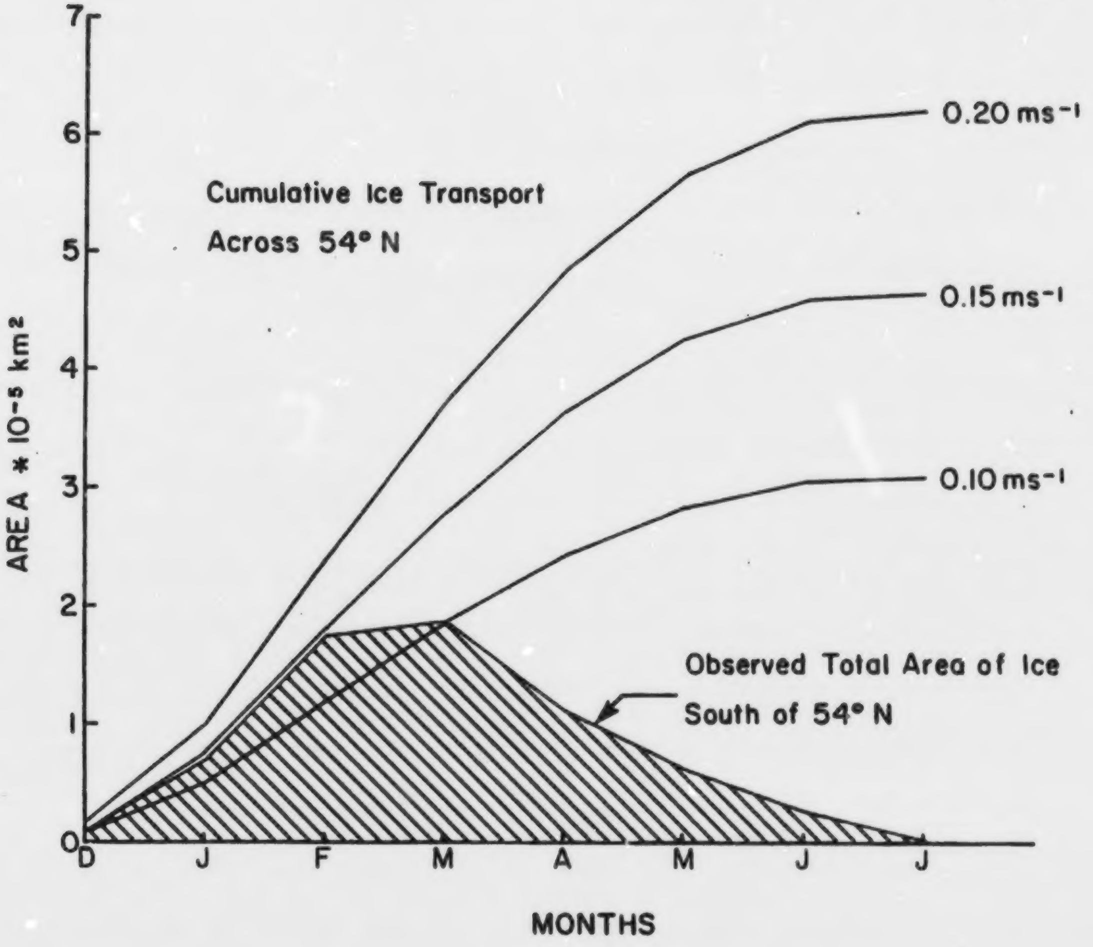

Fig. 3. Cumulative transport of ice across 54°N estimated using mean long-shore velocities of 0.10, 0.15 and 0.20 m s^{-1}. The shaded region is the observed monthly mean area south of 54°N covered by ice.

method described by Maykut (1982).

ESTIMATING REGIONAL ICE GROWTH RATES

Following Maykut, [1978, 1982] the growth rate at the bottom of the ice is given by

$$(\frac{dH}{dt})_H = \frac{1}{\rho_i L_f} (F_c(H) - F_w) \tag{1}$$

where $\rho_i = 900$ kg m^{-3} is the density of ice, $L_f = 0.3348 X 10^6$ Jkg^{-1} is the latent heat of fusion of ice, H is the ice thickness, $F_c(H)$ is the conductive heat flux through the ice and F_w is the oceanic heat flux. For thin ice (<1m) a linear temperature profile through the ice can be assumed (Maykut, 1982) in which case F_c is given by

$$F_c(H) = \gamma(T_f - T_o(H)) \tag{2}$$

where $\gamma = k_i k_s/(k_s H + k_i h)$ is the thermal conductance of the ice with a snow cover of thickness h, $k_i = 2.034$ W (m°K)$^{-1}$ and $k_s = .3097$ W (m°K)$^{-1}$ are the conductivities of ice and snow respectively, $T_f = 271.2$°K is the freezing point of sea water and T_o is the surface temperature of the ice.

The surface temperature of the ice is estimated following the method described by Maykut [1978, 1982]. The energy balance at the atmosphere-ice interface is given by

$$(1-\alpha)F_r - I_o + F_L - \varepsilon\sigma T_o^4 + F_s + F_e + F_c = 0 \tag{3}$$

where F_r is the incident shortwave radiation, F_L the incident longwave radiation, F_s the sensible heat flux, F_e the latent heat flux, I_o the shortwave radiation penetrating the ice and not contributing directly to heating at the surface, α is the albedo, ε the longwave emissivity and σ

the Stefan-Boltzmann constant. The formulation of the various terms in equation 3 is described in concise detail in Maykut [1982]. The lefthand side of equation 3 is expressed as a polynomial in T_o with input parameters being F_r, F_L, the air temperature T_a and the relative humidity. T_o is then obtained iteratively. If the solution yields $T_o > 273°K$ then T_o is set equal to 273°K and equation 3 equated to $-\rho_i L_f (dH/dt)_o$ giving the amount of surface melting. The net growth rate is then given by

$$f(H) = \left(\frac{dH}{dt}\right)_H + \left(\frac{dH}{dt}\right)_o \tag{4}$$

The incident shortwave radiation was estimated from Reed [1977]

$$F_r = F_o\ (1 - 0.62c + 0.0019\ A_n) \tag{5}$$

where c is the cloud cover in tenths, A_n is the noon solar altitude in degrees and F_o is the clear sky solar radiation.

The clear sky incident longwave radiation was estimated using the formula developed by Idso [1981] modified slightly by Andreas and Ackley [1982] for the Arctic and Antarctic

$$F_L = (1 + 0.275c)(0.601 + 5.95 \times 10^{-5}\ e_a \exp(1500/T_a))\sigma T_a^4 \tag{6}$$

where e_a is the vapour pressure of air and the first term in brackets is a cloudiness factor used by Parkinson and Washington (1979).

The monthly mean input data are shown in Table 2. Since strong north-south gradients are present through the study region climatological data from two coastal stations, Hopedale in the north and St. John's in the south have been selected. Using these data the surface temperature $T_o(H)$ and hence the conductive heat flux $F_c(H)$ are obtained for a range of ice thicknesses.

Hopedale	S	O	N	D	J	F	M	A	M	J
Incoming shortwave (Wm^{-2})	113.6	63.2	24.9	18.2	25.1	56.4	93.9	143.9	191.7	224.6
Incoming longwave (Wm^{-2})	253.6	230.2	213.7	180.5	167.4	165.6	184.1	205.8	230.5	249.6
Air temperature (°C)	7.7	2.4	03.3	-10.8	-15.9	-15.2	-10.6	-5.0	1.4	6.5
Relative humidity (%)	79	80	80	76	73	74	77	80	79	80
Labrador Shelf water temperature (°C)										
	.73	1.06	.76	.48	.02	-.44	-.60	-.55	-.19	-.26
St. John's										
Incoming shortwave (Wm^{-2})	138.4	83.0	40.6	29.7	35.9	63.9	104.1	151.2	195.2	221.8
Incoming longwave (Wm^{-2})	273.2	254.5	245.4	224.9	216.9	213.3	219.5	233.1	249.8	270.0
Air temperature (°C)	11.9	7.1	3.5	-1.3	-3.8	-4.2	-2.4	1.1	5.5	10.4
Relative humidity (%)	80	83	86	85	85	86	88	83	78	78
Station 27 water temperature (°C)										
	1.50	2.10	1.85	1.20	.43	-.29	-.78	-.82	-.66	-.16

Table 2

Monthly mean climatological input data

To account for variations in ice thickness the computed conductive flux is averaged over a prescribed thickness distribution shown in Figure 4. These distributions are based on fractional area covered by ice types categorized by AES (new, grey, grey-white, white and old ice) each with an assigned thickness range shown in the legend on Figure 4. The mean conductive flux ($F_c{}^i$) in the i^{th} thickness range is given by

$$F_c^i = \frac{1}{\Delta H_i} \int_{H_{i-1}}^{H_i} F_c(H)dH \tag{7}$$

The regionally averaged flux ($\bar{F}_c$) is then obtained by averaging over all the five thickness categories according to

$$\bar{F}_c = \sum_{i=1}^{5} \Delta G_i F_c{}^i \tag{8}$$

where ΔG_i is the fractional area covered by ice in the i^{th} thickness category. In the averaging procedure open water leads have been included in the thinnest ice category 0.01 - 0.05 m.

A measure of the oceanic heat flux F_w is obtained by estimating the changes in heat content in the water column given by $\rho_w C_p \ \Delta T/\Delta t$ where ΔT is the change in mean monthly temperature averaged over 200 m, $\rho_w = 1.028 \times 10^3$ kg m^{-3} is the density of sea water and $C_p = 3.98 \times 10^3$J kg^{-1}°K^{-1} is the specific heat of sea water.

MONTHLY FLUXES F_c AND F_w

The regionally averaged conductive fluxes computed for Hopedale and St. John's are shown in Figure 5. A positive flux is taken to be towards the ice-atmosphere boundary. Also shown in Figure 5 are the changes in

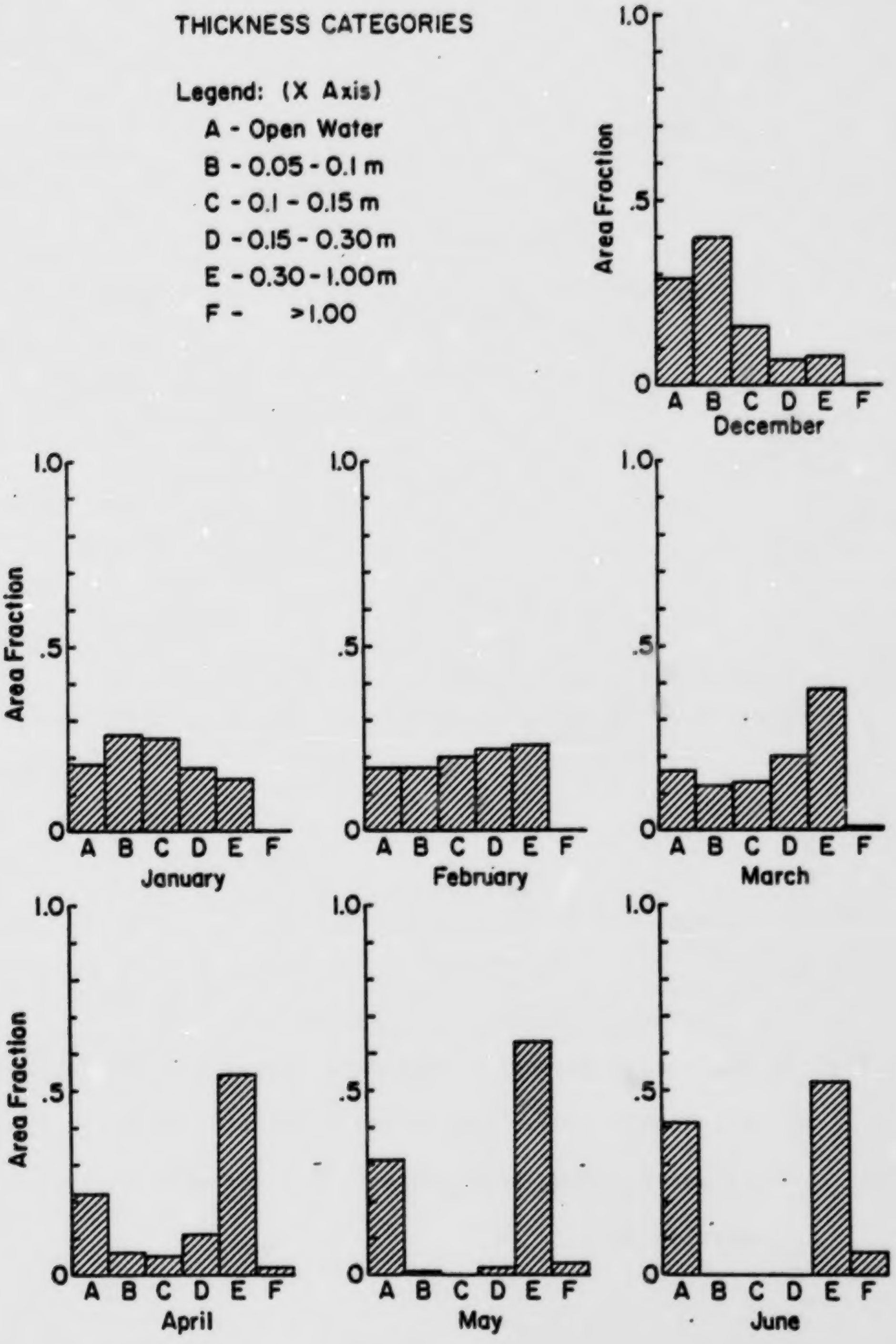

Fig. 4. Monthly averaged ice thickness distribution south of 55°N.

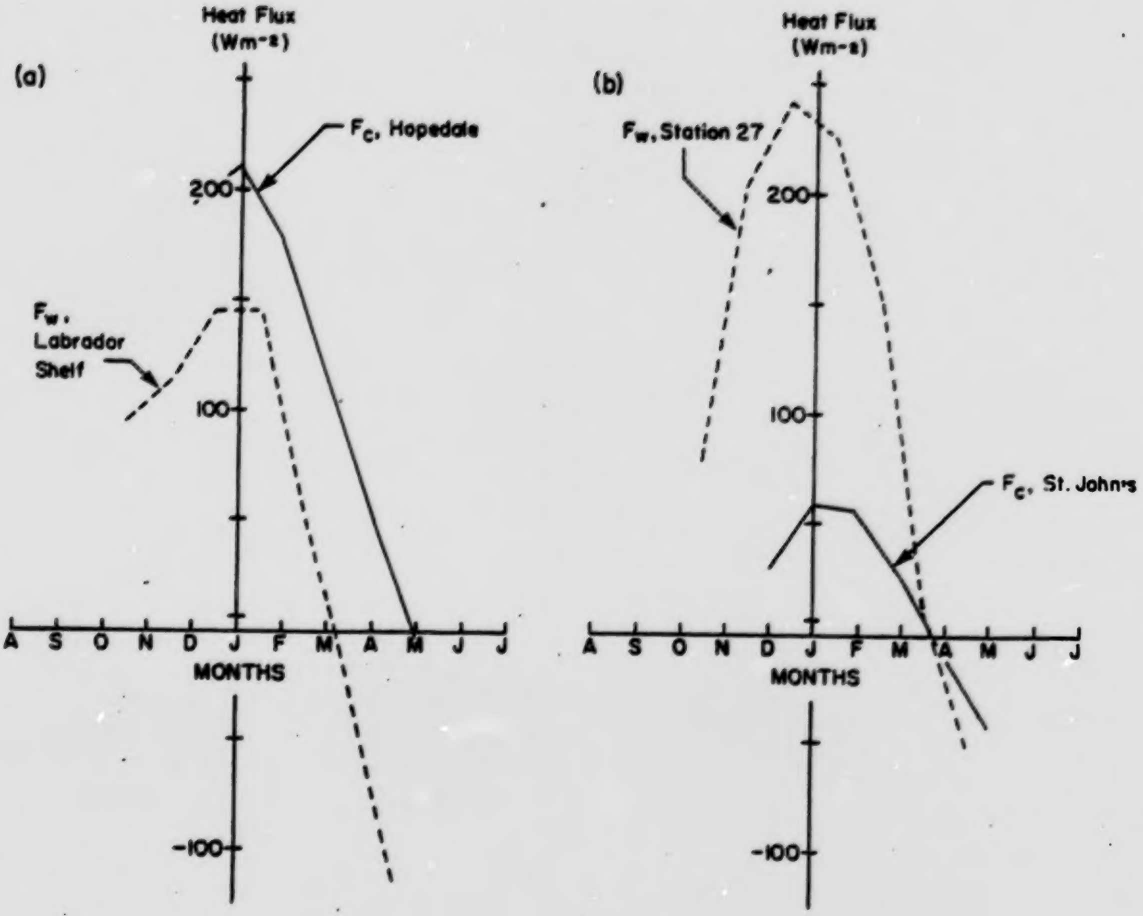

Fig. 5. Regionally averaged conductive fluxes (F_C) at Hopedale (5a) and St. John's (5b). The dashed lines are the monthly averaged change in water column heat content (F_W) for the Labrador Shelf and Station 27.

heat content in the water column over the Labrador Shelf (Lazier [1982]) and at Station 27 off St. John's, Newfoundland (Keeley [1979]). Cooling in the water column is represented as a positive flux of heat to the ice. In January at Station 27 the change in water column heat content is 250 Wm^{-2} and over the Labrador Shelf the heat loss is 150 Wm^{-2}. If these observed changes in water column heat content are due to atmospheric cooling and ice melt then the implied oceanic heat flux is similar in magnitude as the values found along the Bering Sea ice edge (Hendricks et al., 1985).

Local ice growth or melt is estimated from Figure 5 by comparing the change in water column heat content with the corresponding conductive heat flux through the ice in response to atmospheric cooling. At Hopedale, from December through April, $\overline{F}_c > F_w$. Ignoring horizontal advection Equation 1 implies that the additional heat ($\approx 50\ Wm^{-2}$) must be provided through bottom accretion of approximately 1 cm/day. On the other hand at St. John's, $\overline{F}_c < F_w$ from December through March resulting in bottom ablation of approximately 3 cm/day. Later in the spring the melt rate is accelerated with additional surface melt due to atmospheric heating.

To this point the conductive heat flux computed for the thickness distribution shown in Figure 4 has been considered. The dependence of this flux on ice thickness is demonstrated in Figures 6a and 6b which show the monthly conductive heat flux for selected ice thicknesses using the data from Hopedale and St. John's. If $F_w = 100\ Wm^{-2}$ during December through March equation 1 implies, off Hopedale for $H<0.4$ m, the ice will grow while for $H>0.4$ m the ice will melt. Off St. John's, for the same F_w ice of all thicknesses will melt. During spring the thicker ice begins melting from below while the thinner ice may still be growing.

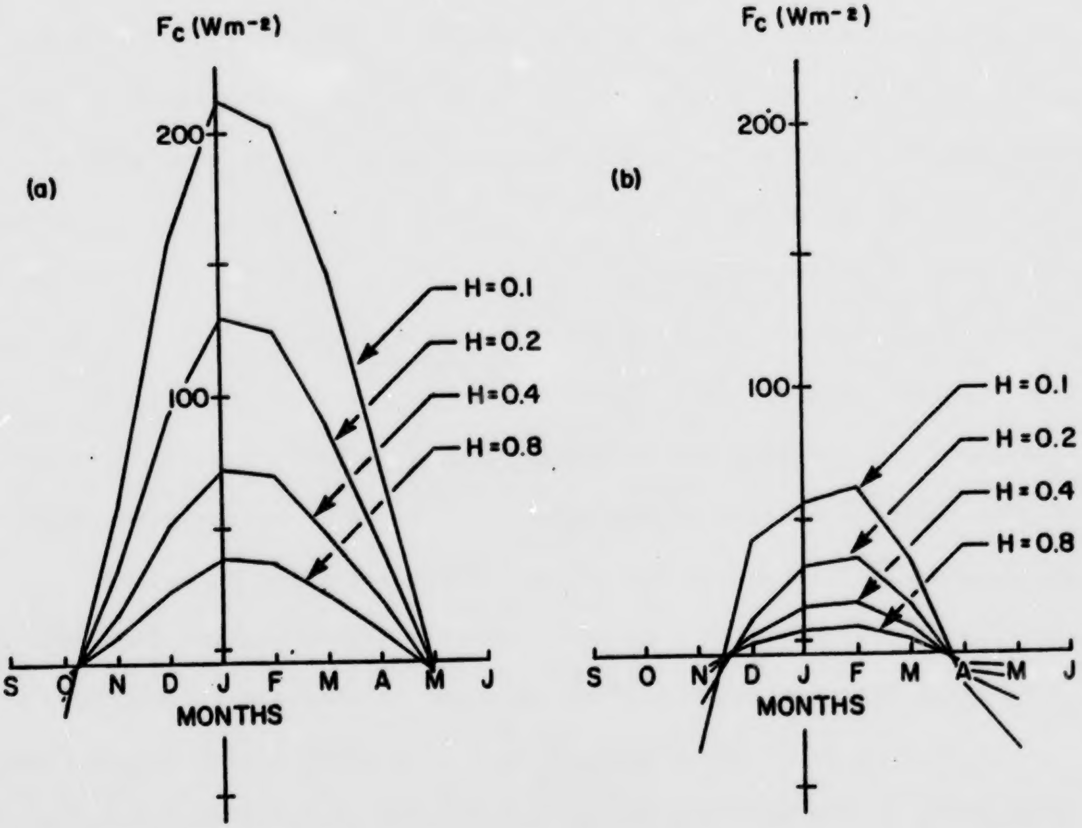

Fig. 6. Monthly mean conductive heat flux at Hopedale (6a) and St. John's (6b).

THE SEASONAL CYCLE IN WATER COLUMN HEAT CONTENT

The oceanic heat flux estimates shown in Figure 5 reflect the net change in water column heat content due to both horizontal and vertical exchange processes in the ocean. A more detailed heat budget as described by Hendricks et al. (1985) cannot be achieved with the data presented here however it is useful to consider some of the implications of the observed change in water column heat content.

Over the Labrador Shelf the decrease in water column heat content in January is approximately 150 Wm^{-2}. For this heat flux to be due solely to vertical turbulent diffusion implies a vertical heat flux through the water column given by $Q = \rho_w C_p K_z \overline{\partial T}/\partial z = 150\ Wm^{-2}$ where $\overline{\partial T}/\partial z$ is the mean temperature gradient through the water column and K_z is the vertical eddy diffusivity. The data reported by Lazier (1982) show a 2°C increase in temperature from the surface to 200 m through the winter months giving $K_z = 3.7 \times 10^{-3}\ m^2 s^{-1}$. Turbulence measurements in the upper ocean have resulted in a range of values for K_z from 10^{-2} to $10^{-6}\ m^2 s^{-1}$ with 10^{-4} to $10^{-5}\ m^2\ s^{-1}$ being most typical (Oakey [1985]). In the western Canadian Arctic Melling et al. (1984) estimate $K_z = 8 \times 10^{-5}\ m^2 s^{-1}$.

To account for larger scale mixing processes such as vertical convection Csanady [1976] suggests an effective eddy length scale in shallow seas could be the Ekman layer thickness and has parameterized the vertical eddy diffusivity as $K_z = u_*^2/200f$ where $u_*^2 = C_d q^2$ is the friction velocity, C_d the drag coefficient, q a typical current speed and f is the coriolis parameter. With $C_d = 10^{-3}$ and $q = 0.2\ ms^{-1}$ the preceding formula gives $K_z = 2 \times 10^{-3} m^2 s^{-1}$ the same order of magnitude as that estimated to maintain a vertical heat flux of 150 Wm^{-2} over the Labrador Shelf.

It is beyond the scope of this paper to examine in detail different formulations for vertical diffisuity but it is apparent from the preceding discussion that turbulent diffusion alone may not be able to account for the observed change in water column heat content.

Horizontal exchange processes have to be considered however the contribution from these processes to the seasonal change in water column heat content is difficult to estimate from the present data. Long term current measurements in the Labrador Current have revealed a seasonal variation in transport which, over the upper 200 m could have an amplitude of 10 cm s^{-1} (Lazier et al., 1986). Much of this transport is confined to the offshore (80%) and inshore (15%) branches of the Labrador Current while the remaining part of the Shelf contributes only 5% of the total transport so the effect of seasonal variations in transport are difficult to assess in terms of the seasonal heat budget of the Labrador Shelf. A seasonal signal in the longshore temperature gradient also occurs since only a limited amount of heat can be removed from the water column before ice begins to form. Hence cooling slows considerably in the north while a significant amount of heat is still being removed from the water column further south. This is reflected in Figure 5 where in spite of more intense atmospheric cooling the change in water column heat content over the Labrador Shelf is smaller than that observed at Station 27.

Seasonal changes in longshore transport and temperature gradient would contribute to seasonal changes in the water column heat content. The available data suggest both transport and longshore temperature gradient reach a seasonal minimum in late winter and a maximum in the fall leading by a few months the seasonal change in water column heat content shown in Figure 5.

Seasonal changes in the cross shelf temperature gradient could occur in phase with the variation shown in Figure 5 but the processes of cross shelf exchange are even more uncertain than longshore advection. Furthermore, near surface temperatures in the Labrador Sea are 2-3° warmer than the shelf water and so provide a heat source during the winter months. If cross shelf exchange is important then for net cooling to occur the added heat must be lost to longshore advection or to ice melt over and above the melt rates estimated in the previous section. Observations of the air-sea heat flux and corresponding ice growth rates throughout the winter months together with estimates of longshore and cross-shore temperature and salinity gradients are needed to resolve the relative importance of vertical and horizontal exchange processes limiting the seasonal advance of ice, similar to what has been done in the Bering Sea (Hendricks et al., 1985).

CONCLUSIONS

In the seasonal ice zone of the Western Labrador Sea south of 55°N the major source of sea ice is advection from the north by winds and currents. Estimates of the monthly mean radiation balance over an ice cover of variable thickness have been used to calculate the heat flux through the ice to the atmosphere. This flux reaches a maximum in January of 200 Wm^{-2} off Hopedale to 50 Wm^{-2} off St. John's. Simultaneous changes of heat content in the water column over the Labrador Shelf and off St. John's are 150 Wm^{-2} and 250 Wm^{-2} respectively. Off Hopedale the additional 50 Wm^{-2} lost to the atmosphere is attributed to ice growth of approximately 1 cm day^{-1} while off St. John's the excess heat loss from the water column results in a melt rate of 3-4 cm day^{-1}. While the contributions to changes in heat content by horizontal exchange processes cannot be estimated much of the heat lost from the water column must be derived from summer warming when the whole of the Western Labrador Sea is ice free. A detailed study of the seasonal heat budget is needed to clearly identify the sources and sinks of heat over the Labrador Shelf in particular as it affects the seasonal advance and retreat of sea ice.

ACKNOWLEDGEMENTS

My thanks go to I. Peterson who compiled the historical data sets and to R. Walker for preparing the figures. This work has been funded by the Office for Energy Research and Development.

REFERENCES

Aagaard, K. and P. Greisman, Toward new mass and heat budgets for the Arctic Ocean, J. Geophys. Res., 80, 3821-3827, 1975.

Andreas, E.L., and A.P. Makshtas, Energy exchange over Antarctic sea ice in the Spring, J. Geophys. Res., 90, 7199-7212, 1985.

Csanady, G.T., Mean circulation in shallow seas, J. Geophys. Res., 81, 5389-5399, 1976.

Fissel, D.B., and D.D. Lemon, Analysis of physical oceanographic data from the Labrador Shelf, summer 1980. Arctic Sciences Ltd., Sydney, B.C. 2 vol.

Gordon, A.L., Seasonality of Southern Ocean sea ice, J. Geophys. Res., 86, 4193-4197, 1981.

Hendricks, P.J., R.D. Muench and G.R. Stegen, A heat balance for the Bering Sea ice edge, J. Physical Oceanogr., 15, 1747-1758, 1985.

Hibler, W.D. III, A dynamic thermodynamic sea ice model, J. Physical Oceanogr., 9, 815-846, 1979.

Hibler, W.D. III, and J.E. Walsh, On modelling seasonal and interannual fluctuations of Arctic sea ice, J. Physical Oceanogr., 12, 1514-1523, 1982.

Idso, S.B., A set of equations for full spectrum and 8- to 14-μm and 10.5 to 12.5-μm thermal radiation from cloudless skies, Water Resources Res., 17, 295-304, 1981.

Keeley, J.R., Temperature, salinity and sigma-t at Station 27 (47°33'N, 52°35'W). An analysis of historical data. Marine Environmental Data Service, Tech. Rep. No. 8, 56 pp, 1981.

Lazier, J.R.N., Seasonal variability of temperature and salinity in the Labrador Current, J. Marine Res., 40 supplement, 341-356, 1982.

Lazier, J.R.N., D.G. Wright and K.R. Thompson, Seasonal Changes of velocity and transport in the Labrador Current, in preparation.

Markham, W.E., Ice Atlas Eastern Canadian Seaboard, Atmospheric Environment Service, Environment Canada, Toronto, 95 pp. 1980.

Maykut, G.A., Energy exchange over young sea ice in the Central Arctic, J. Geophys. Res., 83, 3646-3658, 1978.

Maykut, G.A., Large scale heat exchange and ice production in the Central Arctic, J. Geophys. Res., 87, 7971-7984, 1982.

Maykut, G.A., and N. Untersteiner, Some results from a time-dependent thermodynamic model of sea ice, J. Geophys. Res., 76, 1550-1575, 1971.

Melling, H., R.A. Lake, D.R. Topham and D.B. Fissel, Oceanic thermal structure in the western Canadian Arctic, Continental Shelf Res., 3, 233-258, 1984.

Oakey, N.S., Statistics of mixing parameters in the upper ocean during JASIN Phase 2, J. Physical Oceanogr., 15, 1662-1675, 1985.

Parkinson, C.L., and W.M. Washington, A large-scale numerical model of sea ice, J. Geophys. Res., 84, 311-337, 1979.

Pollard, D., M.L.Batteen and Y. Han, Development of a simple upper-ocean and sea-ice model, J. Physical Oceanogr., 13, 754-768, 1983.

Reed, R.K., On estimating insolation over the ocean, J. Physical Oceanogr., 7, 482-485, 1977.

Thorndike, A.S., and R. Colony, Sea ice motion in response to geotrophic winds, J. Geophys. Res., 87, 5845-5852, 1982.

Untersteiner, N., Calculations of temperature regime and heat budget of sea ice in the Central Arctic, J. Geophys. Res., 69, 4755-4766, 1964.

Walsh, J.E., and C.M. Johnson, Interannual atmospheric variability and associated fluctuations in Arctic sea ice extent, J. Geophys. Res., 84, 6915-6928, 1979.

Walsh, J.E., W.D. Hibler III and B. Ross, Numerical simulation of northern hemisphere sea ice variability, 1951-1980, J. Geophys. Res., 90, 4847-4865, 1985.

A BUOYANCY FLUX-DRIVEN CYCLONIC GYRE IN THE LABRADOR SEA

YOUNG-HO SEUNG

Department of Oceanography
Dalhousie University
Halifax, Nova Scotia
B3H 4J1 Canada

Abstract

The generation mechanism for a winter time cyclonic gyre in the western Labrador Sea, first observed by Clarke and Gascard (1983), is shown by using simple theoretical models. As suggested by them, this gyre is shown to be generated by the highly localized atmospheric cooling which occurs during outbreaks of cold, dry continental air. Motions are shown to be induced when the new density structure adjusts itself to geostrophic equilibrium. This density structure is shown to be determined not only by the atmospheric cooling but also by the eddy-mixing induced by baroclinic instability. This fact explains well the observed feature that the density maximum occurs farther offshore than might be expected from the atmospheric cooling alone.

Introduction

The winter time gyre in the Western Labrador Sea (Fig. 1) was first observed by Clarke and Gascard (1983, henceforth CG) when convection followed intense surface cooling. Hydrographic and current measurements suggest that the gyre as shown in CG's hydrographic section (Fig. 2), is somewhat elongated in longshore direction with its center at some 200 km from the ice-edge. CG (1983) conjectured that this gyre was possibly generated by the buoyancy flux associated with outbreaks of cold, dry Canadian Arctic Air Mass onto the Labrador Sea. The degree of air mass modification by moisture and heat exchange with the sea surface as it proceeds offshore must then determine the offshore scale of the gyre. In the longshore direction, the northern and southern limits of the gyre are determined by the presence of an ice-edge in the north (Fig. 1) and the atmospheric polar front in the south. This front is delineated by the average motion of cyclones which track north-northeast across the Labrador Sea from the eastern tip of Labrador (Bursey et al., 1977; see also Fig. 1). CG also remarked the fact that the minimum buoyancy occurs farther offshore than might be expected from atmospheric cooling alone (c.f. Fig. 2). They suggested that this may be due to mixing of fresh water from the shelf area.

Other effects which can take part in generating the gyre may be the wind stress curl and topography. A cyclonic gyre induced by these effects may accelerate the process of deep convection by removing the buoyancy stored in the upper layer during the warmer period. An example of the topographic effect is given by Hogg

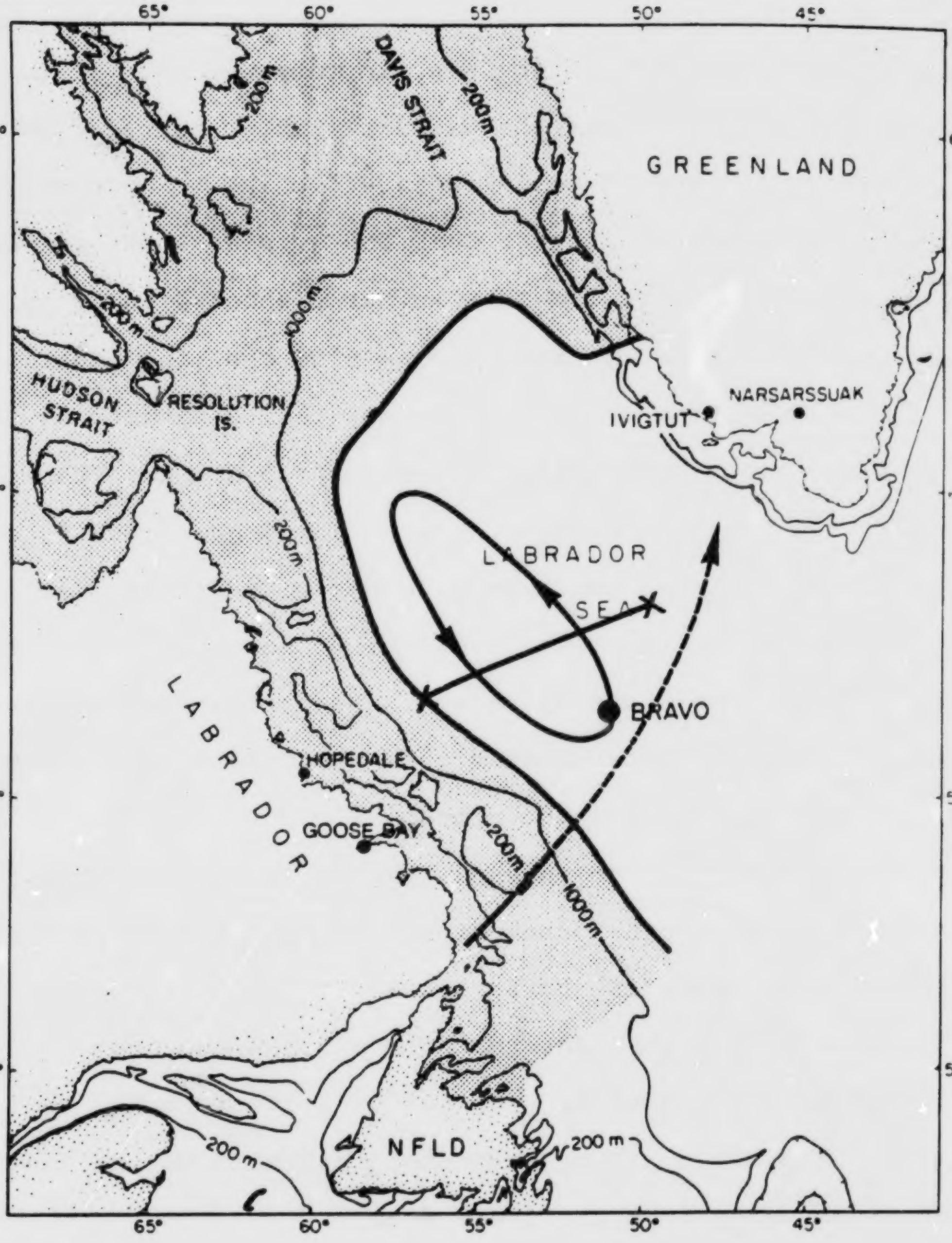

Figure 1. The Labrador Sea with: locations of meteorological stations (Hopedal, Goose Bay and Ocean Weather Ship Bravo); ice cover (shaded area); cyclone track (dotted arrow); CG's hydrographic sections occupied during March 1976 (solid line with crosses at both ends); presumed cyclonic gyre (solid arrows).

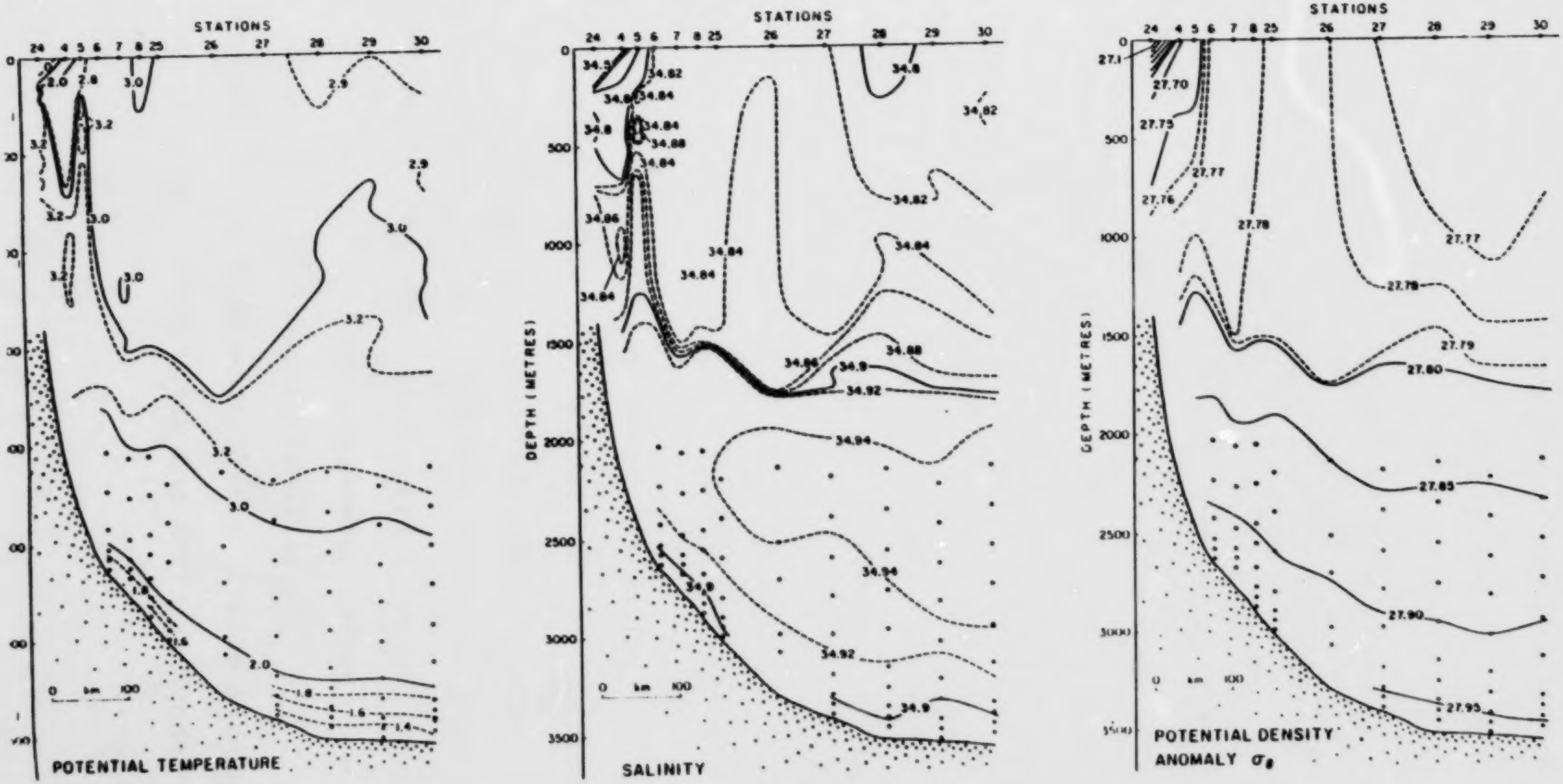

Figure 2. Outcrops from CG's hydrographic sections; after Clarke and Gascard (1983).

(1973) for the Medoc area. The effect of wind stress curl will be discussed later. In this area, however, there seems to be no evidence that a persistent gyre is driven by such effects.

In this paper, we show that simple theoretical models support these ideas. First, the scale of cooling will be modelled and then compared with the scale of gyre. Next, it will be shown that the highly localized cooling can generate a cyclonic gyre through the (dynamic) process of geostrophic adjustment. A brief consideration is made of the thermodynamic processes occurring when both realistic cooling and eddy-mixing are included. The latter effect is believed to result from baroclinic instability of the system under consideration. In reality, both the dynamic and thermodynamic processes interact with each other. A simplification is thus made by separating the two processes, the assumption being that this does not alter the fundamental physics.

2. Scale of Atmospheric Cooling

The scale of cooling can be estimated by considering a simple representation of air-sea exchange which modifies the cold, dry air mass. This modification occurs when the continental air mass is transported onto the sea by the offshore component of wind; the latter seems to be important in determining the coastal oceanographic conditions as well (Symonds, 1984). The observational evidence of air modification is provided by Bursey et al. (1977) showing a large temperature contrast between shore stations and Ocean Weather Ship Bravo (see Fig. 1 for location).

A simple model of Thermal Internal Boundary Layers (Venkatram, 1977) may explain the process of air modification. Fig. 3 schematizes this process. The air is initially stable with vertical potential temperature gradient γ (humidity is assumed vertically uniform as shown later) and well adjusted to the temperature (θ_L) and humidity (q_L) over the land. Due to the presumed insulating effect of ice, it begins to be modified only after crossing the ice-edge and gradually forms a mixed layer (θ_m, q_m) by gaining heat and water vapor from the sea ($F_{s\theta}$, F_{sq}). In the above, we therefore assume that ice packs are thick and compact enough to prevent significant air-sea heat exchange. The initial conditions for the boundary layer development are

$$\theta_m = \theta_L \tag{1}$$

$$q_m = q_L \tag{2}$$

$$h_m = 0 \tag{3}$$

at x=0, where h_m is the mixed layer depth and x measures offshore distance from the ice-edge. The offshore component of velocity (u_m) is assumed to be constant independent of changes in θ_m and q_m. Above the growing mixed layer, the initial state is retained. The undisturbed air above the inversion is entrained into the lower turbulent layer making an abrupt change of properties ($\Delta\theta$, Δq) across the inversion. This condition can be expressed as

$$\Delta\theta = \theta_L + \gamma h_m - \theta_m \tag{4}$$

$$\Delta q = q_L - q_m \tag{5}$$

Since the oceanic heat (water) capacity is much larger than that needed to modify the air above it, the oceanic conditions (θ_w,

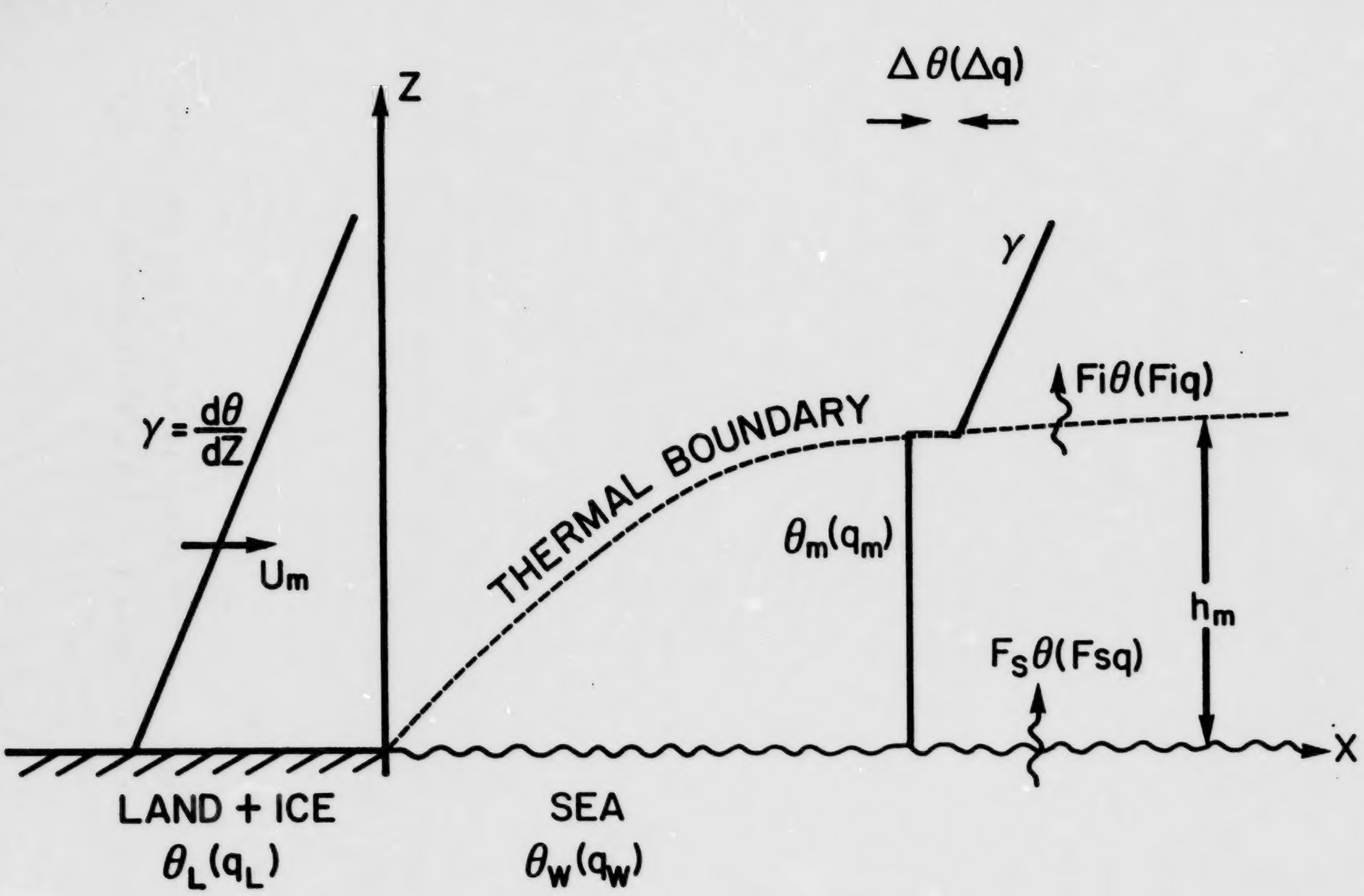

Figure 3. Schematization of Thermal Boundary Layer formation for air after crossing the ice-edge. See text for details.

q_w) can be assumed constant throughout the process. In this region, the sensible and latent heat flux are the most important terms in winter-time air-sea heat exchange (Smith and Dobson, 1984). Other effects, such as solar radiation, condensation and forced convection, are assumed negligible. Flux by longwave (black body) radiation from the sea surface is comparable (~300 w/m^2) to the total latent and sensible heat flux as seen later, but does not seem to play a significant role in the boundary layer development: optical depth of the (mixed) boundary layer is too small to absorb a significant part of longwave-radiated heat from the sea surface. Even when the air is well modified by convective mixing (increase of both temperature and humidity), most of the absorbed heat by water vapor will be lost through longwave radiation if the mixed layer is approximated as a black body.

With these assumptions, the offshore variation of temperature is given by the energy conservation law:

$$\bar{\rho}_a C_{pa}\, d\theta_m/dt = (F_{s\theta} - F_{i\theta})/h_m \qquad (6)$$

where $\bar{\rho}_a$ is the mean air density; C_{pa} is the heat capacity of air at constant pressure; t is time; and $F_{i\theta}$ is the heat flux across the inversion. Note that the small density variation is neglected in Eq. (6). Heat flux at the surface ($F_{s\theta}$) and inversion ($F_{i\theta}$) can be parameterized (or expressed) as

$$F_{s\theta} = \bar{\rho}_a C_{pa} C_h |u| (\theta_w - \theta_m) \qquad (7)$$

and

$$F_{i\theta} = -\bar{\rho}_a C_{pa} \Delta\theta\, dh_m/dt \qquad (8)$$

where C_h is the bulk transfer coefficient for sensible heat flux and $|u|$ is the wind speed. To close the system, we further assume that

$$F_{i\theta}/F_{S\theta} = -k \qquad (9)$$

where k is a fraction assumed constant (Betts, 1973). Tennekes (1973) takes k as 0.2 while Lilly (1968) and Deardorff et al. (1969) suggest a nearly zero k. Venkatram (1979) deduces numerically that k is smaller than 0.4 near the edge of boundary layer and roughly equal to 0.4 far from the edge. However, we will see later that the final results are relatively insensitive to the choice of k. Eq. (9) means that the heat flux due to entrainment ($F_{i\theta}$) is held at a small but constant fraction of that through the surface ($F_{s\theta}$) during the process. The justification of this assumption is given in earlier studies (Tennekes and Van Ulden, 1974; Mahrt and Lenschow, 1976).

Latent heat flux is accomplished by the transport of water vapour and the transfer process is the same as that of sensible heat except that the mixed (boundary) layer depth h_m is determined by the sensible heat flux alone. Conservation of water vapor leads to

$$\bar{\rho}_a \, L \, dq_m/dt = (F_{sq} - F_{iq})/h_m \qquad (10)$$

where L is the latent heat of vaporization and F_{iq} is the latent heat flux through the inversion. F_{sq} and F_{iq} can be parameterized (or expressed) by

$$F_{sq} = \bar{\rho}_a \, L \, C_e \, |u| \, (q_w - q_m) \qquad (11)$$

and

$$F_{iq} = - \bar{\rho}_a \, L \, \Delta q \, dh_m/dt \qquad (12)$$

where C_e denotes the bulk transfer coefficient for latent heat flux. Likewise, the boundary and initial conditions are

$$\Delta q = q_L - q_m \tag{13}$$

and

$$q_m = q_L \quad \text{at } x = 0 \tag{14}$$

Since the time scale of vertical mixing by convection is very small, the system will reach steady state quickly so the steady state solution is relevant. These solutions are given in Appendix A and are dependent on a parameter $\beta = C_h(k+1)^2/(2k+1)\sin\alpha$; where α is the counterclockwise angle the wind makes with the coastline, and C_e is assumed the same as C_h in calculation. Since C_h (taken as 1.3×10^{-3} henceforth) has a relatively small range of variation and the value of β is a relatively insensitive to the choice of k (taken as 0.3 henceforth), only the effect of α is considered.

Table 1 shows the statistics of long-term wind measurements in January, slightly modified from those given by Bursey et al. (1977). β are calculated only for offshore-blowing winds because the sea→air heat flux occurs mostly by offshore-blowing wind and no significant air-sea heat exchange is expected for onshore-blowing wind. For these β values, θ_m and q_m vary roughly in the way shown in Fig. 4. If the winter under consideration can be represented by the statistics shown in Table 1, the most probable heat flux, $\tilde{F}_{s\theta}(x)$, can be estimated as follows:

$$\tilde{F}_{s\theta}(x) = \int\int F_{s\theta}\ (\alpha, |u|, x)\ p(|u|, \alpha) Y(\alpha)\ d\alpha\ d|u| \tag{15}$$

where $P(|u|,\alpha)$ is the bivariate probability function of wind speed, $|u|$, and direction, α; $Y(\alpha)$ is a step function defined to be

$$Y(\alpha) = \begin{array}{ll} 1 & 0 < \alpha < \pi \\ 0 & \pi < \alpha < 2\pi \end{array}$$

If $p(|u|, \alpha)$ can be expressed as a multiplication of two

Table 1. Statistics slightly modified from those by Bursey et al. (1977) showing percentage frequency of wind direction and mean speed (m/sec) in January, averaged over 1963-1972. To obtain conditions more representative of the region under consideration, frequencies at Hopedale and OWS Bravo (see Fig. 1 for locations) are averaged whereas mean speeds are weighted-averaged. α_i is the counterclockwise angle made by wind with the coastline and β is a parameter determining the heat flux. See text for more explanations.

	Frequency (%)	Mean Speed (m/sec)		
Wind	$fr(\alpha_i)$	$\widetilde{\lvert u\rvert}(\alpha_i)$	$\alpha_i(°)$	$\beta(10^{-3})$
N	10.20	10.40	- 30	-
NE	6.85	11.46	- 75	-
E	6.85	12.20	-120	-
SE	4.05	10.49	-165	-
S	10.60	3.83	150	2.746
SW	20.70	7.35	105	1.422
W	18.85	10.49	60	1.586
NW	16.15	11.19	15	5.305
Calm	4.25	0.00	-	-

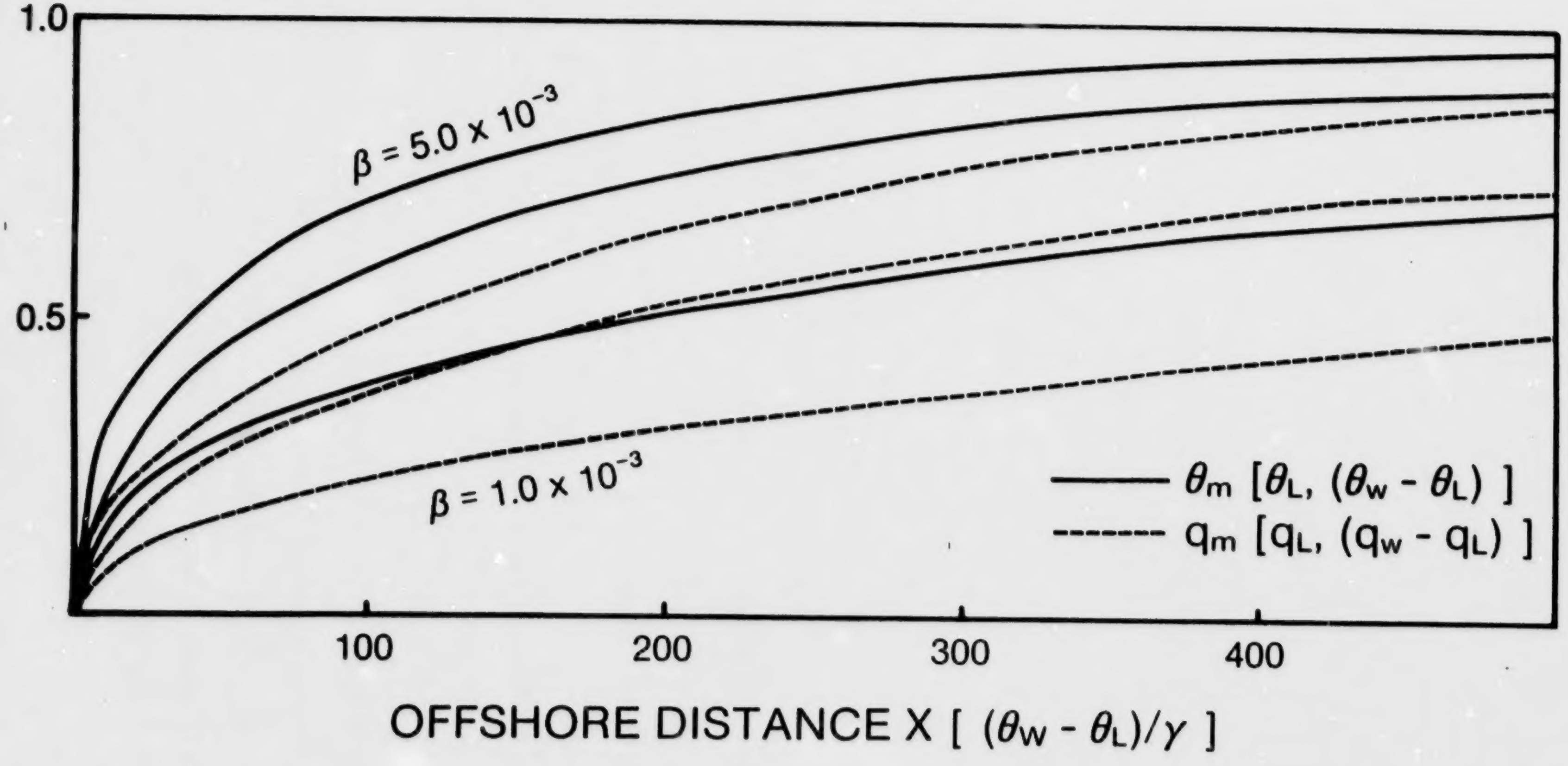

Figure 4. Changes of temperature (Θ_m) and humidity (q_m) with offshore distance (X) for $\beta = 1.0 \times 10^{-3}$, 3.0×10^{-3} and 5.0×10^{-3}; larger β corresponds to larger θ_m (or q_m). θ_m (or q_m) is non-dimensionalized by first subtracting θ_L (or q_L) and then dividing it by $(\theta_w - \theta_L)$ (or $q_w - q_L$). X is non-dimensionalized by dividing it by $(\theta_w - \theta_L)/\gamma$.

univariate probability functions i.e. $P(|u|,\ \alpha) = P_1(|u|)P_2(\alpha)$, the evaluation of $\tilde{F}_{s\theta}(x)$, by applying the data in Table 1 to Eq. (15), becomes straightforward: introducing Eq. (7) into Eq. (15), integrating with respect to $|u|$ and integrating again but numerically with respect to α, leads to

$$\tilde{F}_{s\theta}(x) = C_p\bar{\rho}_a C_h\ (\theta_w-\theta_L)\Sigma_i\ \widetilde{|u|}\ (\alpha_i)\ [1-\theta^{\star}{}_m(\alpha_i,x)]f_r(\alpha_i) \qquad (16)$$

for discrete values of offshore-blowing wind direction α_i. In Eq. (16) $\widetilde{|u|}(\alpha_i)$ is the mean wind speed of direction α_i; $f_r(\alpha_i)$ is the frequency of wind direction α_i; and $\theta_m{}^{\star}$ is the non-dimensionalized form of θ_m i.e. $\Theta_m{}^{\star} = (\theta_m-\theta_L)/(\theta_w-\theta_L)$. $\tilde{F}_{sq}(x)$, the most probable latent heat flux, is obtained by applying the same procedures.

Fig. 5 shows the results obtained. In determining the scale of cooling, the initial (upwind) vertical gradient of potential temperature, γ, and the temperature contrast between land and sea, $\theta_w-\theta_L$, are important. Here, we take θ_w as about 3° C, (c.f. Fig. 2). Radiosonde data obtained at Goose Bay (e.g. Fig. 6) indicate that the winter of 1976, the time of CG's observations, was relatively cold and dry. Data presented by Symonds (1984) clearly show that the winters of 1972 through 1976 were colder and had stronger offshore winds than other periods. Based on these radiosonde data, we take γ as 1° C/100 m and θ_L as -15°C. These values, when applied to Fig. 5, lead to the conclusion that 400 km from the ice-edge (about 500 km from the coast), the sensible and latent heat flux have diminished to by factors of three and two, respectively. If we take saturation conditions for q_w, the sensible + latent heat flux at this point becomes

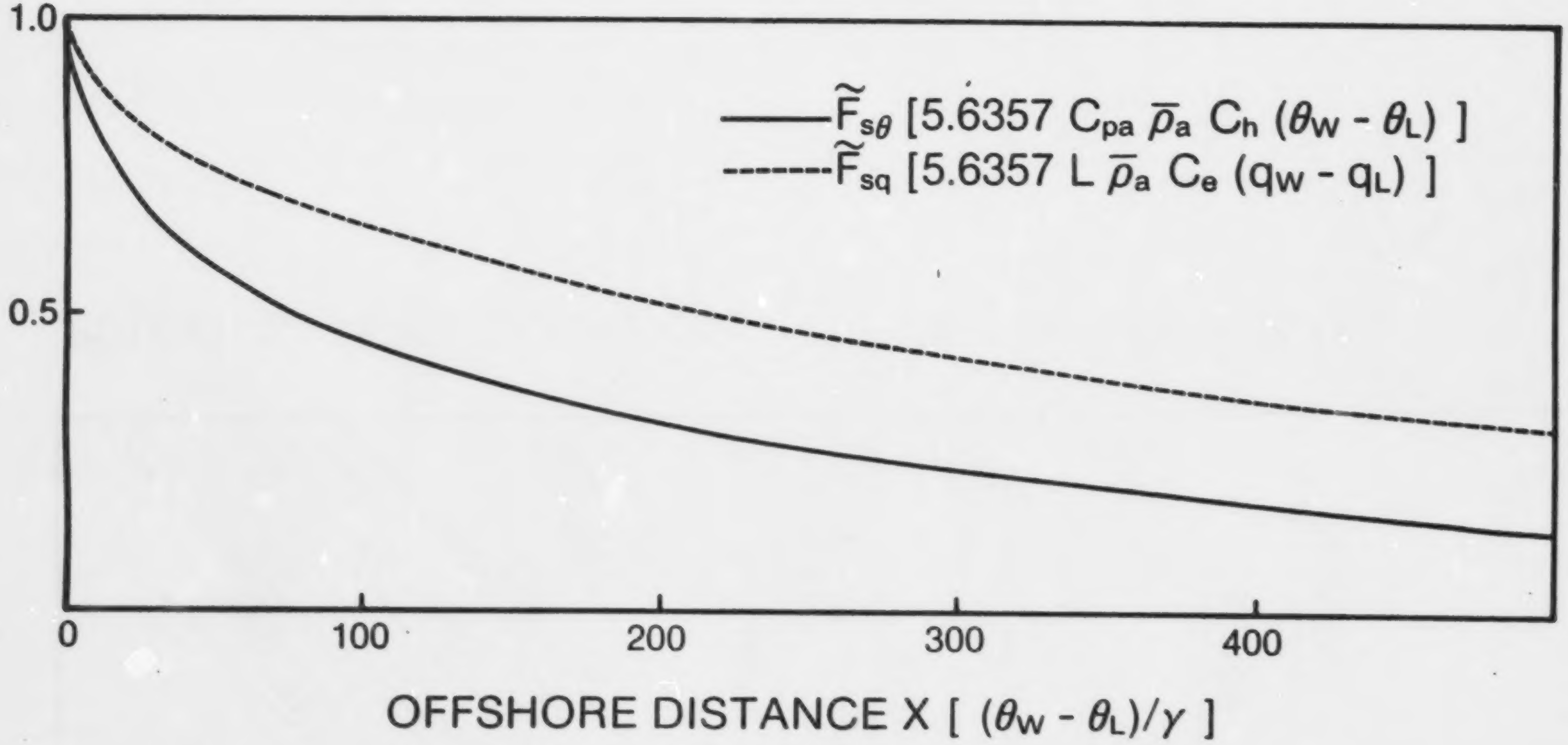

Figure 5. The most probable sensible ($\widetilde{F}_{s\theta}$) and latent ($\widetilde{F}_{sq}$) heat flux from the sea surface as a function of offshore distance X. Values in [ ] are non-dimensionalization factors; see text for detailed explanations.

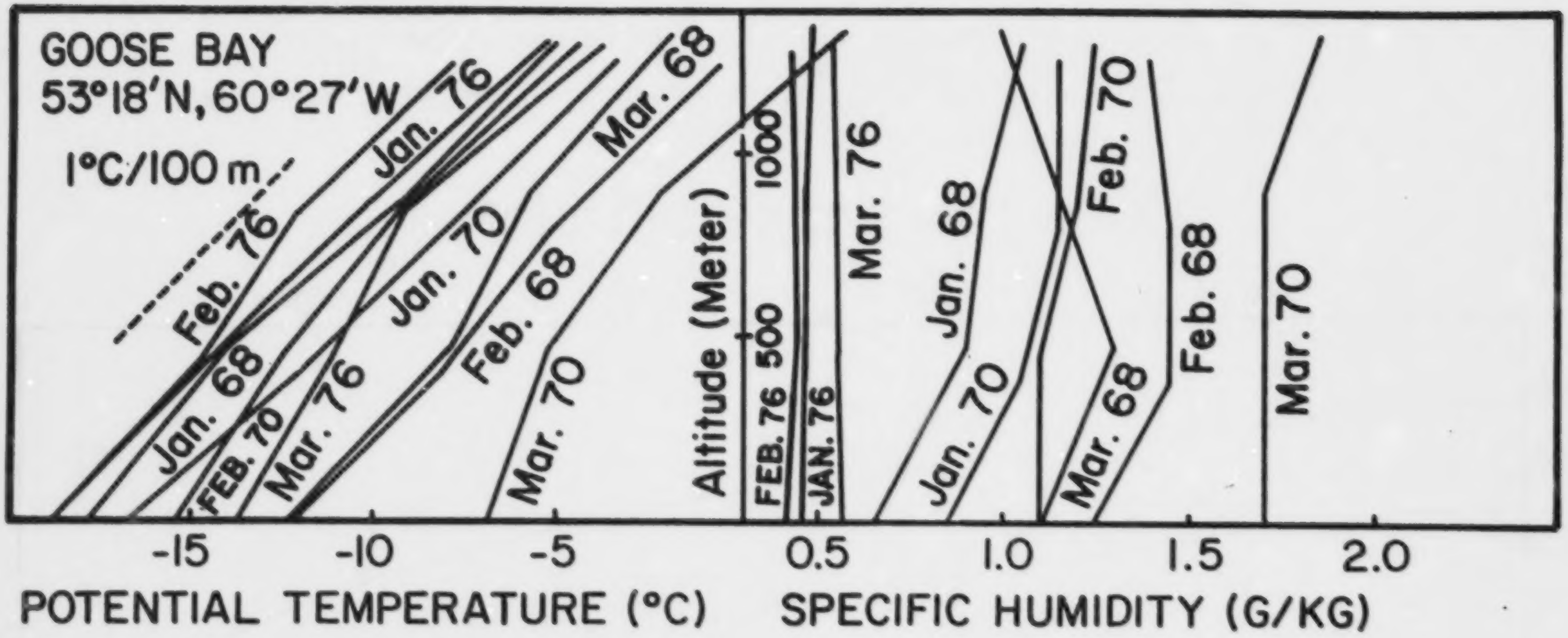

Figure 6. Vertical profiles of potential temperature and specific humidity at Goose Bay for January, February and March in 1968, 1970 and 1976. Dotted line represents the slope 1°C/100 m; data extracted from Monthly Bulletin of Canadian Radiosonde Data, Atmospheric Environment Service, Canada.

about 55 + 54 (w/m^2), diminished from about 183 + 107 (w/m^2) at the ice-edge. These values are somewhat less than the estimates made by Smith and Dobson (1984) for the OWS Bravo, about 500 km from the coast; their estimates are slightly smaller than 100 w/m^2 for both sensible and latent heat. Sensible and latent heat fluxes of 100 w/m^2, when they occur over a 1000 m thick water column for a period of one month, result in a temperature decrease of 13° C, a salinity increase of 3.5×10^{-3} ^{o}/oo (for initial salinity 35^o/oo), and a density increase of 0.016 kg/m^3 mostly due to the temperature change. Based on the results obtained, a reasonable estimate of the scale of cooling may be a few hundred kilometers, comparable to the cross-shore scale of the gyre observed by CG (1983; c.f. Fig. 2).

3. Cyclonic Gyre

In this section we are interested in the motions induced by the local buoyancy flux. Buoyancy flux here includes the effects of both sensible and latent heat flux. The effect of salinity change due to evaporation is not considered because, on the one hand, precipitation is of nearly the same order of magnitude as evaporation (Bursey et al., 1977) and, on the other hand, for a given evaporation the effect of salinity change is usually much smaller than that of latent heat flux. The motions induced by the buoyancy flux may, in turn, cause convergence (divergence) of buoyancy in the water column. It is therefore interesting to see whether or not the buoyancy change in the water column is entirely due to the cooling alone. Note that, under favourable conditions, the divergence of buoyancy can accelerate the process of deep convection and hence the formation of the cyclonic gyre.

The problem is approached as a Rossby adjustment process. As schematized in Fig. 7, a uniform cooling is imposed over a confined area (width $2L_c$) making the upper mixed layer denser. During the cooling period, the water masses are retained motionless. They are then permitted to adjust conserving the initial potential vorticity until finally they reach a state of geostrophic balance. We are only interested in this final state. Similar problems have been considered by Stommel and Veronis (1980) and Van Heijst (1985). As seen in Fig. 7, the ocean is assumed flat-bottomed with depth H, and initially two-layered with densities and depths ρ_1, H_1 and ρ_3, H_2 for the upper and lower layers, respectively. We first consider the two-dimensional case where a uniform cooling in the alongshore direction takes place from the ice-edge ($x=-L_c$) to $X=L_c$ farther offshore. The response will then be symmetric about the vertical plane parallel to $x=0$. We also assume that the surface elevation is negligible compared with the layer depths $h_i (i=1,2,3)$; i.e. the rigid lid assumption is made. In fact, the small surface elevation, which arises due to both shrinking of the water column and evaporation, can cause an important pressure change throughout the water column. However, the induced motion, which is mostly barotropic, has much larger scale than those considered here, so that the resulting barotropic motion is negligible: The upper layer (H_1) shrinks by an amount of $\Delta H = (\rho_2-\rho_1)H_1/\rho_2$ according to the mass conservation law, which leads to a pressure decrease of about $gH_1(\rho_2-\rho_1)$ in a barotropic sense throughout the

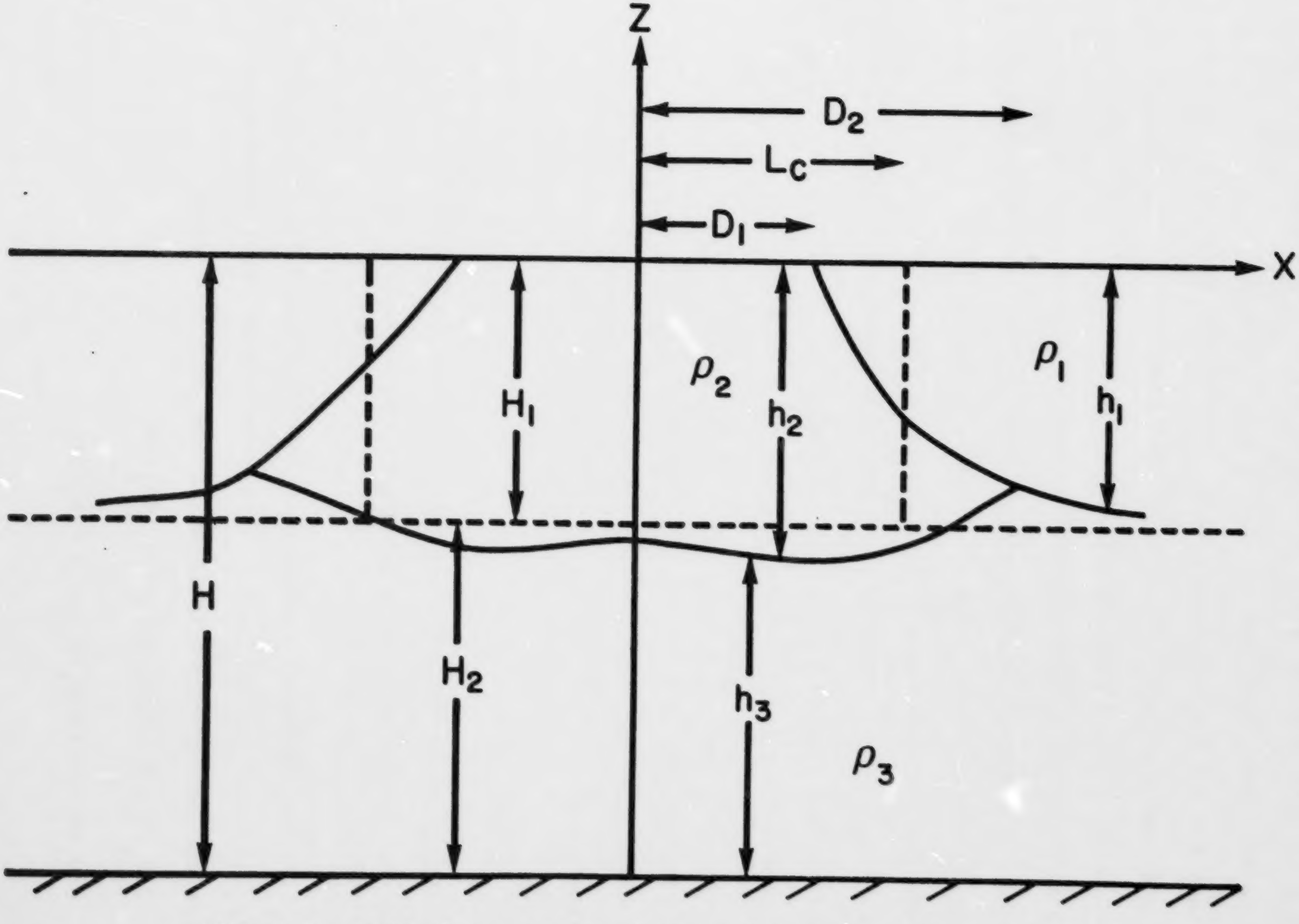

Figure 7. Definition sketch of the model ocean. Dotted lines represent the initial state. See text for more details.

water column. In the rigid lid assumption, the pressure increase due to the density change is $(\rho_2-\rho_1)gH_1$ at depth $z=-H_1$ which is the same as that in the former case. Since the barotropic motion has much larger scale (~ 1.7×10^3 km) than that of baroclinic one (~12 km), the former is negligible compared with the latter. The motions under consideration are thus primarily baroclinic.

When the system is released , layer 1 will override layer 2 extending toward the center of cooling whereas layer 2 will intrude between layer 1 and 3. The behaviour of layer 3 can not be imagined easily. However, in the final state, there should be 3 domains as follows:

Domain 1 ($0 \leqslant X \leqslant D_1$): $h_1 = 0,\ h_2 \neq 0,\ h_3 \neq 0$

Domain 2 ($D_1 \leqslant X \leqslant D_2$): $h_1 \neq 0,\ h_2 \neq 0,\ h_3 \neq 0$

Domain 3 ($D_2 \leqslant X$): $h_1 \neq 0,\ h_2 = 0,\ h_3 \neq 0$

for unknown Di's. In each domain, the total depth remains constant, i.e.

$$\sum_{i=1}^{3} h_i = H \qquad (17)$$

This situation is depicted in Fig. 7 for a hypothesized shape of layer 3. Solutions will be determined in each of the three domains.

For hydrostatic, inviscid, incompressible and Boussinesq ($\rho_j/\rho_i \simeq 1.0,\ i \neq j$) fluid, the geostrophic shear between the layers can be expressed in terms of the interface slopes:

$$f(V_2-V_1) = -[g(\rho_2-\rho_1)/\rho_2]\,(dh_1/dx) \qquad (18)$$

$$f(V_3-V_2) = [g(\rho_3-\rho_2)/\rho_3]\,(dh_3/dx) \qquad (19)$$

$$f(V_3-V_1) = -[g(\rho_3-\rho_1)/\rho_3] (dh_1/dx) \qquad (20)$$

In the above equations, Vi's denote the longshore (in right-hand cartesian coordinates) component of current in the ith layer; g is the gravity constants and f is the Coriolis parameter. Equations for conservation of potential vorticity in the three layers are

$$f/H_1 = [f + dV_1/dx]/h_1 \qquad (21)$$

$$f/H_1 = [f + dV_2/dx]/h_2 \qquad (22)$$

$$f/H_2 = [f + dV_3/dx]/h_3 \qquad (23)$$

At boundaries between the different domains, hi and Vi should be continuous, and the mass in each layer should also be conserved. Other conditions to be satisfied are symmetry of response about x=0, vanishing of disturbance as x → ∞ and the fact that the velocity at the edge, [Vi(Di), i=1,2], should be determined uniquely from Di. The last condition comes from the integrated form of the alongshore momentum equation

$$dV_i/dt = -fu_i \qquad i = 1,2 \qquad (24)$$

where u_i is the cross-shore component of current in ith layer. We can not determine u_i during the adjustment process, but the cross-shore excursions of some water particles can be determined. The water particle at the edge of ith (i=1,2) layer should have traveled a distance Di-L_c in X-direction.

Due to the non-linearity of the equations, solutions are obtained numerically for a paricular set of parameters. For the detailed solution procedure, refer to Appendix B.

The validity of the model is tested in two ways. First solutions are obtained for various ρ_2 including cases where it approaches either ρ_1 or ρ_2. Results are shown in Fig. 8. Second, the energy conversion ratio i.e. the loss of available potential energy to generated kinetic energy, is always three in all cases considered, consistent with previous works (Gill, 1982, Van Heijst, 1985). Looking at the curves in Fig. 8, one sees that as $\rho_2 \rightarrow \rho_1$, the interface between ρ_1 and ρ_3 becomes more horizontal, which is the case $\rho_2 = \rho_1$. Similarly, as $\rho_2 \rightarrow \rho_3$, the interface between ρ_1 and ρ_2 approaches the limiting curve for the case $\rho_2 = \rho_3$. In this case, the interface meets the surface at about 0.6 Rossby radii, R, from its initial position.

The same problems are considered for the axisymmetric case, details of which are presented in Appendix B. The results are quite similar to the 2-D case as shown for $\rho_1 = 1020$, $\rho_2 = 1025$ and $\rho_3 = 1030$ (kg/m^3) in Fig. 9. However, the energy conversion ratio varies by about 3% for the calculations performed: this may be a result of neglecting the cyclostrophic terms in the equations of motion.

Fig. 10 presents the results obtained by using the 2-D model and employing realistic parameters. Since the response to cooling is nearly independent of the magnitude of L_c, we present here a case $L_c = 2R$. If we take $H = 3000$ m, $g = 10$ m/sec^2 and $f = 10^{-4}$sec^{-1}, the maximum pycnocline elevation is about 20 m and the maximum velocity is about 60 cm/sec. This velocity is much larger than that observed by CG (1983); observations show that northward currents in layers 200-500 m depth are of order a few cm/sec, while the southward current near the ice-edge at 100 m

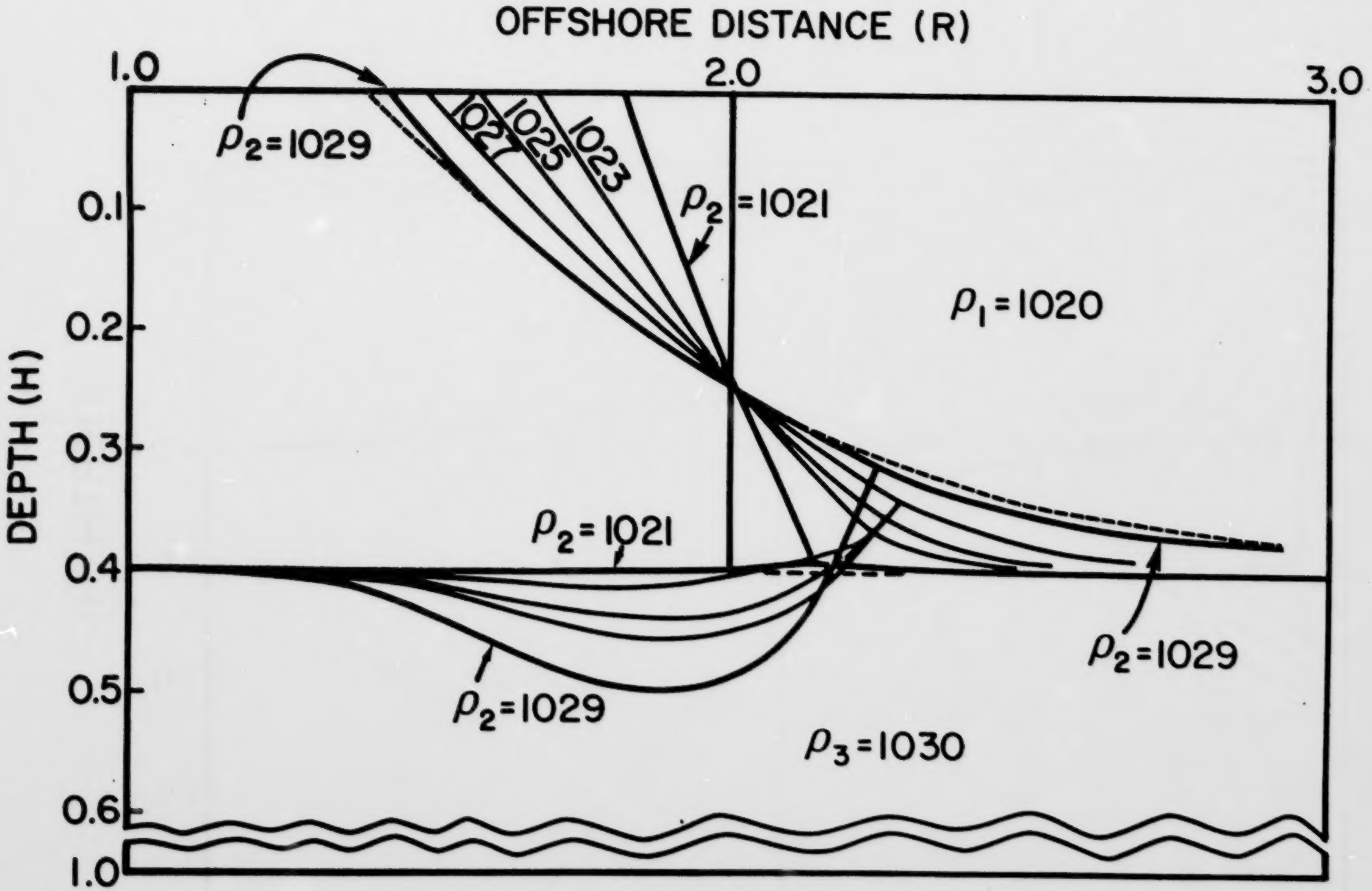

Figure 8. Configuration of interface shapes for various ρ_2 (in kg/m^3). Dotted lines show the extreme cases $\rho_2 = \rho_1$ and $\rho_2 = \rho_3$. Depth and offshore distance are non-dimensionalized by H, total depth, and R, Rossby radius, respectively. See text for more details.

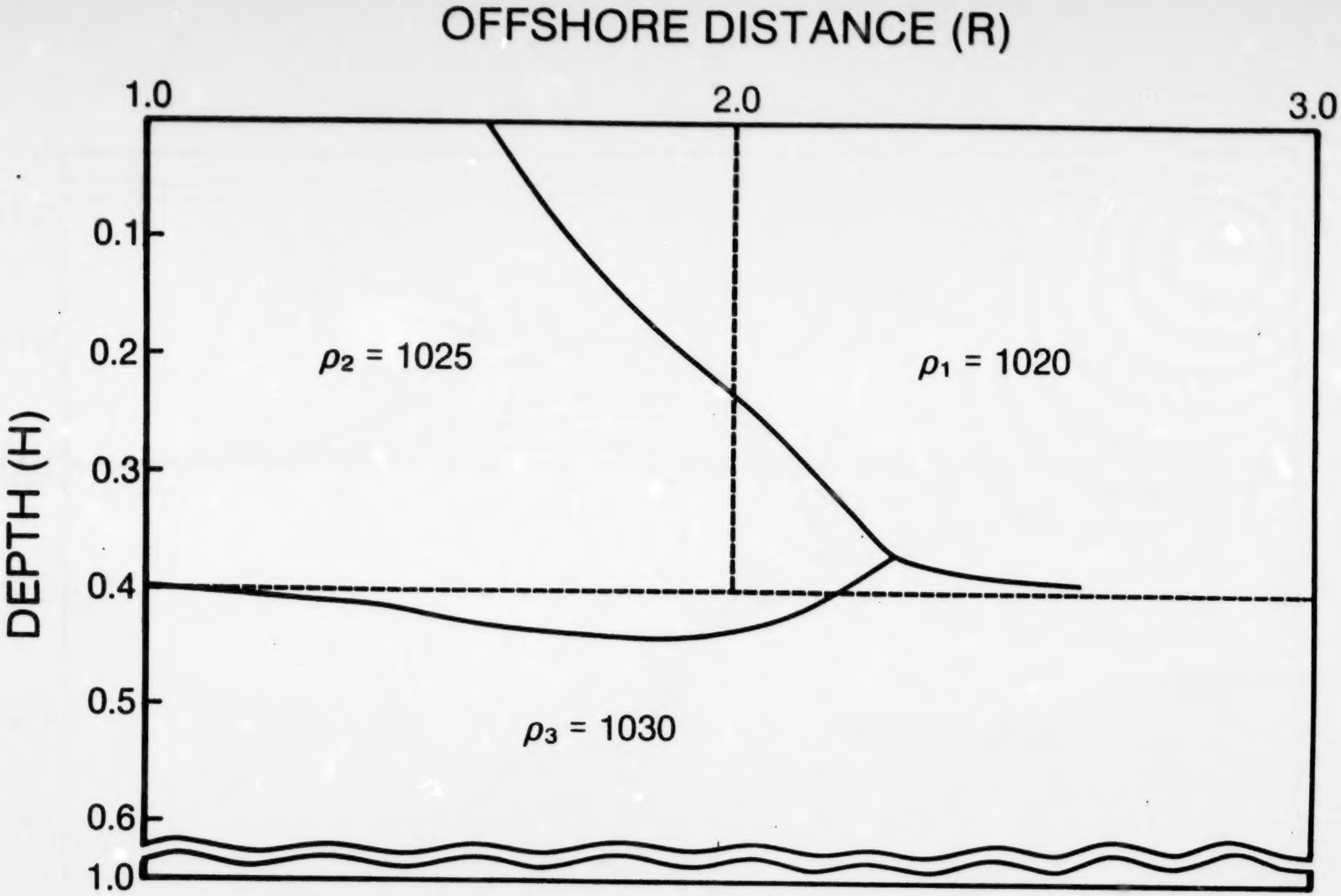

Figure 9. Solutions for the axisymmetric case. Dotted lines show the initial state. For more explanations, see Fig. 8.

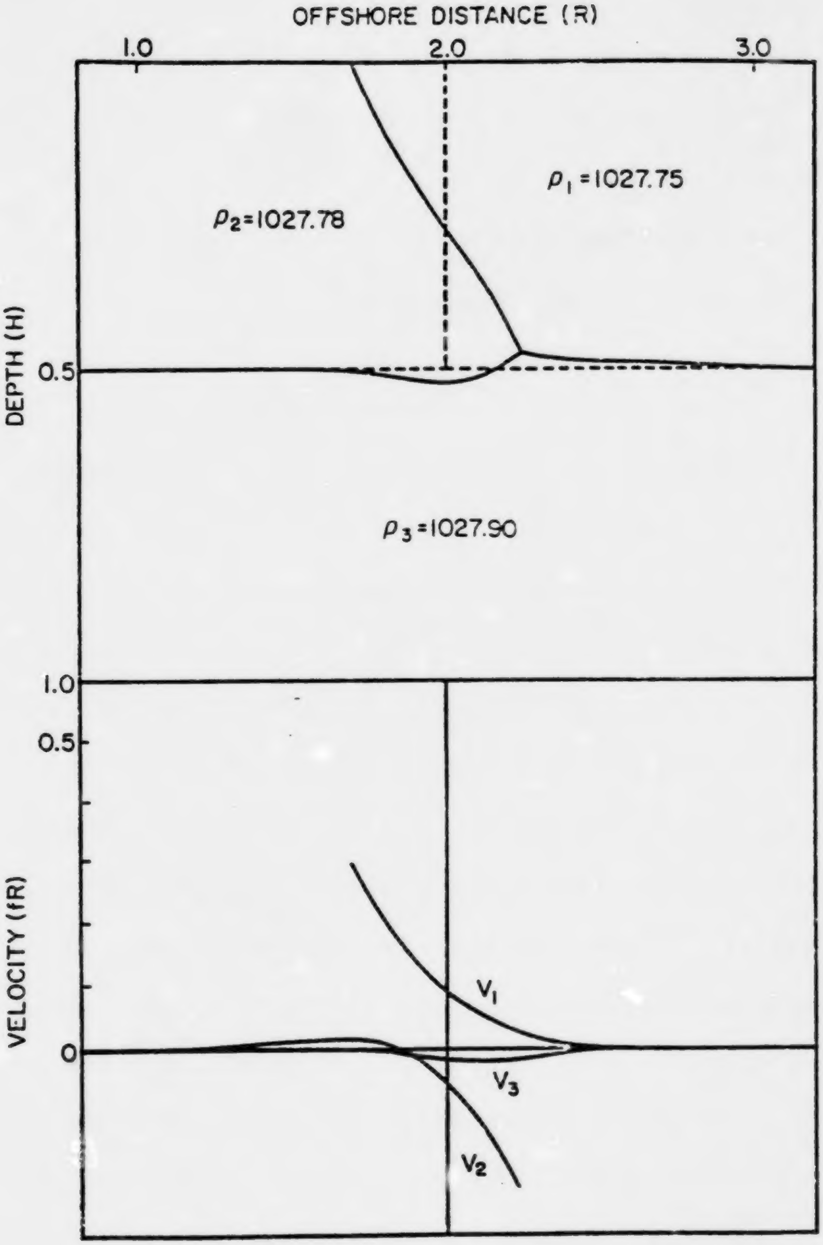

Figure 10. Solutions for realistic conditions. Velocity is non-dimensionalized by fR, multiplication of Coriolis parameter and Rossby radius. Dotted lines show the initial state. Densities are in kg/m^3. For more explanations, see Fig. 8.

depth is about 16 cm/sec. In reality, the density changes would occur over a distance $O(L_c)$ rather than distance $O(R)$. The latter is only a few hundreths of the former. The resulting current may then be weaker by the same factor. The small pycnocline elevation seems to indicate that the buoyancy change is due to the atmospheric cooling alone, an answer to the question casted early in this section.

4. Density structure

In the preceeding section, only the dynamic aspects were emphasized and questions arise about how the density structure observed by CG (Fig. 2) might have occurred. In particular, the fact that the density maximum occurs offshore rather than on the ice-edge where cooling is maximum requires explanation. The problem can be though of as a system which varies in time with a source and a sink of buoyancy. Here, the sink refers to the cooling and the source, the eddy-mixing of lighter waters outside into the region. This mixing is believed to be done by baroclinic eddies generated by instabilities at the boundary of the cooled region. This kind of feature is nearly always observed near the shelf break where the Labrador Current meets the offshore water (Allen, 1979; LeBlond, 1982). It may be especially intensified during the cooling season and extend all around the cooled region (Gascard and Clarke, 1983).

Consider an ocean initially having an upper mixed layer of depth and density h_o and ρ_o, respectively (Fig. 11). Below the mixed layer, the density is assumed to increase linearly with depth. A cooling of constant rate is imposed within an area such

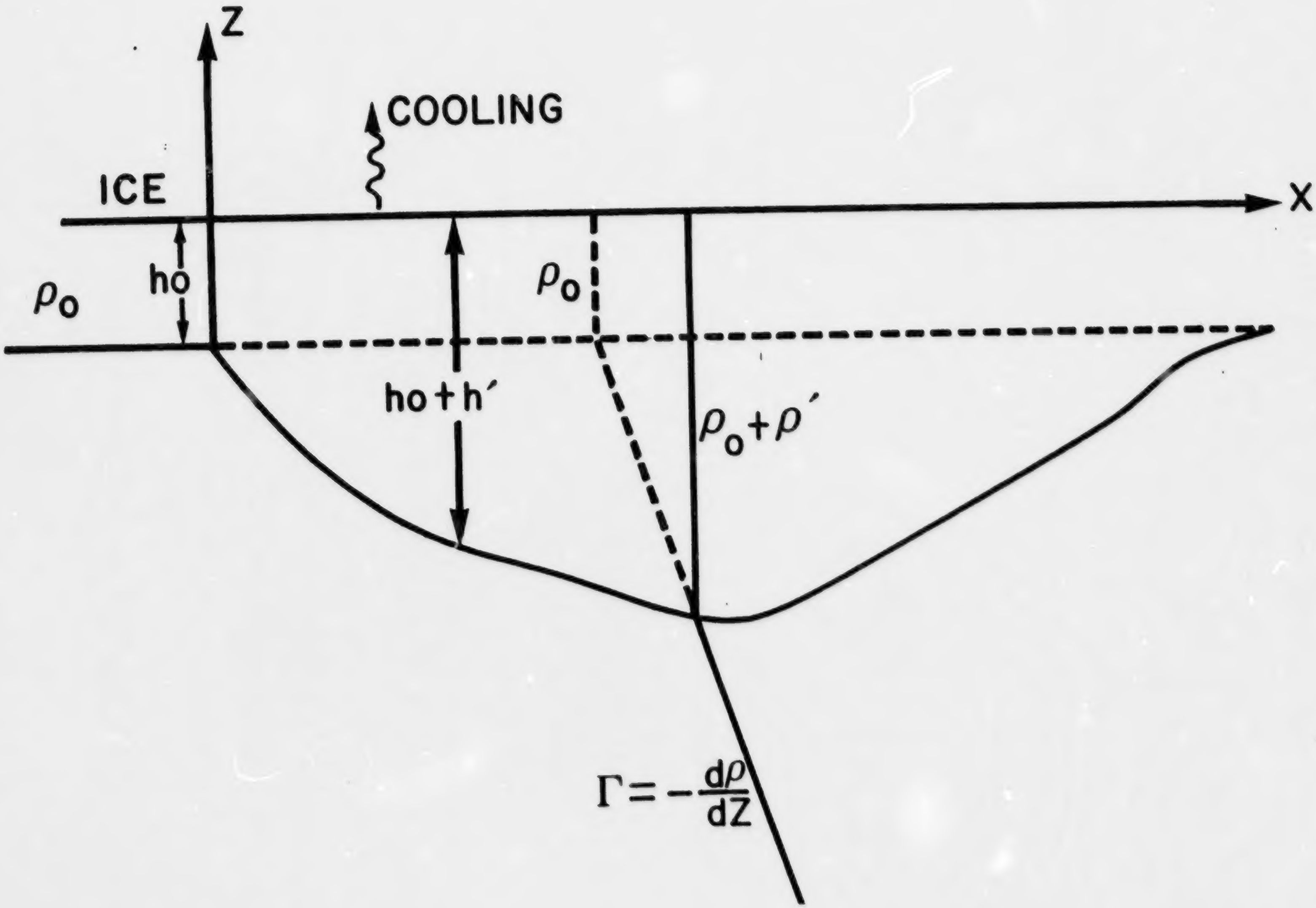

Figure 11. Schematization of mixed layer development by non-penetrative convection induced by cooling. Dotted lines show the undisturbed state. See text for more details.

that it decreases from Q_o at x=0 and vanishes at $x=2L_c$. This cooling then induces vertical convection. Since, in the ocean, the convection is believed to be non-penetrative (Anati, 1970; Gill and Turner, 1976; Killworth, 1979) or, if not, slightly penetrative (Farmer, 1975), the mixed (convecting) layer depth, $h_o + h'$, is where the mixed layer density, $\rho_o + \rho'$, equals the local density. At greater depths the density profile remains unchanged. At the bottom of the mixed layer, no density jump (and therefore no buoyancy exchange) is expected between upper and lower layers. This is different from convection in the atmosphere as considered in Section 2.

We emphasize here only the thermodynamic point and neglect the dynamic effects. As shown in the previous section, the possible dynamic effect may be the cross-shore movement of water particles as they come into geostrophic equilibrium. In this case, a vertical density gradient is generated within the otherwise mixed water column. However, this effect might be neglected on average because, the internal Rossby radius (~ 12 km) is small compared with the larger scale of the region under consideration (~ a few 100 km) and, the time scale of vertical convection (~ time scale for free fall of fluid parcel) may be much smaller than the time scale of geostrophic adjustment.

If the effects of baroclinic eddies are parameterized using an eddy diffusion coefficient K_e (Bryden, 1979), the governing equations are

$$h\partial\rho'/\partial t = \alpha Q_o (1-ax)/\rho_o C_p + \partial [K_e h\, \partial\rho'/\partial x]/\partial x \quad (25)$$

for density and

$$\partial\rho'/\partial t = \Gamma \partial h'/\partial t \qquad (26)$$

for non-penetrative convection. Here, $a = (2\,L_c)^{-1}$; α/ρ_o is the thermal expansion coefficient; Γ is the rate of density increase with depth (c.f. Fig. 9). Boundary and initial conditions are

$$\rho' \text{ (or } h') = 0 \quad \text{at } x = 0, 1/a \qquad (27)$$

$$\rho' \text{ (or } h') = 0 \quad \text{at } t = 0 \qquad (28)$$

Mathematical difficulties arise in solving Eqs. (25) through (28). However, the physical process governed by these equations can be understood by considering several simplified cases. First, the solution is obtained in the hypothetical case of no convection, i.e. $h=h_o$. This case corresponds to a situation where a density jump at the bottom of the initial mixed layer is large enough to prevent the growth of the mixed layer. In this case Eqs. (25), (27) and (28) lead to

$$\rho' = \alpha Q_o(\xi/3 - \xi^2/2 + \xi^3/6)/h_o\rho_o C_p K_e a^2$$
$$+ \sum_{k=1}^{\infty} C_k\, e^{-K_e\,(ak\pi)^2 t}\, \sin k\pi\xi \qquad (29)$$

where:

$$C_k = -2\alpha Q_o/a^2(k\pi)^3\, h_o\rho_o C_p K_e$$

and ξ denotes the non-dimensional distance i.e. $\xi = ax$. Eq. (29) indicates several facts: The time scale in which the steady state is attained is $\tau = (K_e\pi^2 a^2)^{-1}$. In steady state, the density maximum, ρ'_{max}, occurs at $\xi_{max} = 0.42$ with $\rho'_{max} = 0.064\alpha Q_o/h_o\rho_o C_p K_e a^2$. For typical parameter values shown in Table 2, ρ'max is about 0.69 kg/m^3. Fluxes, $-K_e \overset{h_o}{ha}\, \partial\rho'/\partial\xi$ (c.f. Eq. (25)), at both boundaries (ξ=0 and 1.0) increases with time, reaching final values of $F(0) = -\alpha Q_o/3a\rho_o C_p$ and $F(1.0) = \alpha Q_o/6a\rho_o C_p$, respectively at steady state. Using the values in

Table 2, we obtain $F(0) \simeq -0.83$ kg/m/sec and $F(1.0) \simeq 0.42$ kg/m/sec.

In the presence of convection, the steady state solutions of Eqs. (25) through (28) are given by

$$\rho' = \Gamma h' \tag{30}$$

$$h' = h_o [-1+[1+2\alpha Q_o (\xi/3 - \xi^2/2 + \xi^3/6)/K_e \rho_o C_p \Gamma h_o{}^2 a^2]^{1/2}] \tag{31}$$

In this case, ξ_{max}, $F(0)$ and $F(1.0)$ are all the same as in the absence of convection. However, ρ'_{max} is different. If we assume that convection is deep ($h' \gg h_o$), then Eqs. (30) and (31) give $\rho'_{max} \simeq 0.253 (2\Gamma\alpha Q_o/K_e \rho_o C_p a^2)^{1/2}$. If the values in Table 2 are used, then ρ'_{max} is about 0.12 kg/m^3 (so that the mixed layer density is (ρ_o + 0.12) kg/m^3) and h'_{max} is about 1200 m. In the case of no cooling but with vertical density gradient Γ still maintained, the mean density averaged over the same depth $h=h_o + h'_{max} = 1300$ m is about (ρ_o + 0.06)kg/m^3, which is about 0.06 kg/m^3 less than the value obtained above for the case of cooling. It can be said therefore that cooling leads to a density increase of up to 0.06 kg/m^3.

To test the estimate F(o), we present here a formulae which Pingree (1979) has used in estimation of cross-frontal mass transfer due to baroclinic eddies,

$$F_{b.e.} = \alpha_e (g'D)^{1/2} (D\Delta\rho_s/2) \tag{32}$$

Here $\Delta\rho_s$ is the surface density difference across the front and $(g'D)^{1/2}$, with $g' = g\Delta\rho_s/\rho_o$, is the maximum speed that could result from potential energy release. The coefficient α_e is a dimensionless multiplier which Pingree takes to be 0.0055, following Green (1970). To apply Eq. (29) across the ice-edge, we take $\Delta\rho_s/2$ as the average density difference across the ice-edge between the surface and depth D, in the same way as Garrett and Loder (1981). Using the values in Table 2 where D is taken the same as h_o without discussion, $F_{b.e.}$ becomes about 0.41 kg/m/sec which may be compared with $F(0) \simeq 0.83$ kg/m/sec found earlier. A box model used by Ikeda (in preparation) gives a somewhat smaller value ($\simeq 0.1$ kg/m/sec). However, this estimate represents the global influence of the entire Labrador Sea whereas we are concerned here with an area of more pronounced buoyancy contrast.

To estimate the time scale required to reach steady state, we assume that the total mass outflux by eddy-mixing at both boundaries is

$$-F(0) + F(1.0) = (1-e^{-t/\tau^\star}) \int_0^{1.0} (\alpha Q/\rho_o C_p a) d\xi \qquad (33)$$

where $\tau^\star$ is the time scale to be found and $Q = Q_o(1-\xi)$. This expression is in analogy with the total mass outflux for the case of no convection ($h=h_o$) which is obtained from Eq. (29) by differentiating ρ' at both boundaries $\xi=0$ and 1.0. This assumption is based on the fact that the diffusive flux seems to have the same pattern of variation in both cases: an initial increase with time resulting in the same values at steady state, as seen previously. Integrating Eq. (25) with respect to $\xi(\xi=ax)$ from $\xi=0$ to $\xi=1.0$, introducing Eq. (33), integrating again with respect to t from t=0 to t=∞, and using Eqs. (30) and (31) result in

$$\tau^\star = (12K_e a^2)^{-1}$$

Table 2. Typical parameter values used in numerical evaluation. Values are taken directly or inferred from references.

Symbol	Parameter	Value	Reference
α/ρ_o	thermal expansion coef.	10^{-4} K^{-1}	
C_p	heat capacity at constant pressure	$4x10^3 Jkg^{-1}K^{-1}$	
Q_o	maximum heat flux	$2x10^2$ wm^{-2}	Section 2
$2L_c(a^{-1})$	scale of cooling	$5x10^5$ m	
Γ	vertical density gradient	$10^{-4}kgm^{-3}m^{-1}$	Lazier (1973,1980, 1982)
$h_o(\simeq D)$	mixed layer depth	10^2 m	
$\Delta\rho_s$	density difference between shelf and offshore waters in winter	1.3 kgm^{-3}	CG (1983)
K_e	eddy-diffusion coef. on the shelf	$1.2x10^3m^{-2}sec^{-1}$	Garrett et al. (1985)

which is nearly the same as $\tau = (\pi^2 K_e a^2)^{-1}$ for the case of no convection (see Eq. (29)). Using the values shown in Table 2, we find τ^* to be about 6.7 months. It is difficult to judge in which state CG's density structure (Fig. 2) is, though it seems to be near to steady state. We only emphasize here that it is due to the influx of surrounding lighter waters by eddy-mixing that the position of maximum density moves offshore from the ice-edge, and finally stops near the center of cooled region.

4. Concluding Remarks

It should first be mentioned here that this work is largely based on the previous studies by CG (1983) and, therefore, it is not known if the results obtained here are valid for mild winter conditions. The major difference between colder and milder winters may be the condition of ice cover which is important in air-sea heat exchange.

In previous sections, we did not consider the effect of a longshore current in the gyre area. This is deemed acceptable because the existence of such a current would be expected to advect ice packs into the region, a situation that is not observed as seen later. Existence of any current which does not transport ice packs may alter the results obtained. Consider a uniform current of speed v entering the region of cooling $(y<0)$ through the line $y=0$. Since the water particle experiences a gradual change in its density while traveling, the water density is no longer independent of y. At time t from the start of cooling, the density field becomes such that the density increases linearly from $y=0$ to $y=-vt$ beyond which it is independent of t. For initial longshore advection $v=10$ cm/sec and time scale of cooling one month, the field of longshore density variation extends up to about 260 km south of the northern boundary of the region. This longshore density variation creates a cross-shore current. A detailed example is given by Nof (1983) for the case of Gulf Stream.

There may be some arguments about the possible role of wind stress in creating the cyclonic gyre (and hence aiding deep convection). Consider a typical wind stress $\tau^W \sim 0.1$ Pa (Thompson and Hazen, 1983); Coriolis parameter $f = 10^{-4}$ sec^{-1}; the lowest limit of atmospheric length scale La ~ 500 km; spin-up period $T^W \sim 3$ month. In reality, La is probably larger than 500 km and $T^W \sim 3$ month is based on the fact that atmospheric conditions are subject to seasonal changes. The pycnocline elevation, ζ, may then be estimated by

$$\zeta \sim \int_0^{T^W} (\text{curl } \tau^W/\rho_o f)\, dt \sim 4.8 \text{ m}$$

This is too small to contribute to the generation of any significant motion (localization of convection). Note that, in the open ocean, the large pycnocline elevation is achieved throughout a much longer spin-up time.

Another argument may be about any possible role of local ice melting. The melting of ice, even a small amount, can create a large buoyancy input in the ocean: a melting of 1 m thick ice is equivalent to 200 w/m^2 cooling rate for a period of 60 days in terms of buoyancy change. In previous sections, we assumed a distinct ice-edge and therefore no isolated ice packs (no local melting) in the cooled region. Recently obtained satellite images (Symonds, personal communication), on which ice pack trajectories are also marked, seem to support this assumption. However, there may be an effect of shelf water density change due to the underside-melting of ice cover. The problem of ice forming and melting is still in an early phase of research and further discussions can not be made.

Despite the arguments mentioned above, we conclude that CG's cyclonic gyre could be generated, in parallel with the formation of new Labrador Sea Water by highly localized cooling. Motions are induced when the new density structure adjusts itself to geostrophic equilibrium; apart from the cooling itself, this processes does not create any additional buoyancy change within the water column. As suggested by CG (1983), localized cooling can occur when the cold, dry arctic air mass over the North America moves offshore towards Greenland. The scale of cooling is dependent on how fast the air is modified over the sea through the sea → air heat transfer. Under typical conditions the scale is estimted to be a few hundered kilometres. Since the cooling is maximum over the ice-edge, the largest buoyancy removal is expected here. However, the density contrast across the ice-edge, and hence the vertical current shear, becomes so large that the structure is no longer stable. At this time, baroclinic eddies form and begin to play a stabilizing role. Under these two opposing effects, the density structure changes in such a way that the density maximum moves offshore and finds its final place near the center of the cooled region. CG's density structure (Fig.2) does not show much difference from the predicted steady state.

Future observations of a vertical section across the ice-edge may lead towards a better understanding of the effects of atmospheric cooling and associated dynamic/thermodynamic processes.

Acknowledgement

The author is indebted to Chris Garrett for his support and valuable suggestions. Allyn Clarke, Dan Wright and colleagues from the Bedford Institute of Oceanography also gave useful comments. The author would also like to thank Dave Brickman for reviewing an early version of the paper. This work was funded by the BIO through a DSS contract.

Appendix A

In appendices A and B, all calculations are done with non-dimensional variables which are represented by the same symbols as the corresponding dimensional variables used in Section 2 and 3; the equations appearing in these sections and used here (Appendices A and B) are assumed non-dimensionalized. This is only for the sake of convenience; where dimensional variables are needed, they will be differentiated from non-dimensional ones by using primes.

Changes in temperature and humidity are non-dimensionalized by using the temperature (or humidity) difference between land and sea i.e.

$$\theta_m = (\theta_m' - \theta_L)/(\theta_w - \theta_L)$$

$$\Delta\theta = \Delta\theta'/(\theta_w - \theta_L)$$

$$q_m = (q_m' - q_L)/(q_w - q_L)$$

$$\Delta q = \Delta q'/(q_w - q_L)$$

Distance variables are non-dimensionalized by using $(\theta_w - \theta_L)/\gamma$ i.e.

$$x = x'/(\theta_w - \theta_L)/\gamma$$

$$h_m = h_m'/(\theta_w - \theta_L)/\gamma$$

The steady state solution for $\Delta\theta$ can be obtained from Eqs. (4), (6), (8), and (9):

$$\Delta\theta = h_m k/(2k+1) \tag{A1}$$

Eqs. (4) and (A1) lead to

$$h_m = \theta_m (2k+1)/(k+1) \tag{A2}$$

Elimination of $F_{i\theta}$ between Eqs. (6) and (9) and introducing there Eqs. (7) and (A2) lead to the solution,

$$\theta_m = 1 - \mathrm{Exp}\,(-\theta_m - \beta x) \qquad \text{(A3)}$$

where $\beta = (k+1)^2\, C_h/(2k+1)\, \sin\alpha$; and α is the counterclockwise angle made by wind with the coastline.

Solutions for humidity can be obtained in the same way as for temperature. Introducing Eqs. (11), (12) into Eq. (10) and using Eq. (13) lead to the equation (steady state) for q_m which includes hm:

$$dq_m/dx = [C_e\,(1-q_m)/\sin\alpha - q_m dh_m/dx]/h_m \qquad \text{(A4)}$$

Assuming $C_e = C_h$, replacing next C_h by β and using Eq. (A2) lead to

$$dq_m/dx = \beta(1-q_m)/\theta_m(k+1) - (q_m/\theta_m)(d\theta_m/dx) \qquad \text{(A5)}$$

Using Eq. (A3), Eq. (A5) can be changed to

$$dq_m/d\theta_m = [\theta_m - q_m - (1-\theta_m)kq_m]/\theta_m(1-\theta_m)(1+k) \qquad \text{(A6)}$$

The first order solution of Eq. (A6) in k can be obtained by applying the initial condition (2):

$$q_m = 1 + [(1-\theta_m)/\theta_m]\; \ell n(1-\theta_m) \qquad \text{(A7)}$$

When Eq. (A3) is introduced back into Eq. (7) and, Eqs. (A3) and (A7), into Eq. (11), we can obtain the sensible and latent heat fluxes.

Appendix B

Variables are non-dimensionalized in such a way that the offshore distance x' and D_i' are divided by the Rossby radius $R = [(\rho_3-\rho_1)gH/\rho_3]^{1/2}/f$; depths h_i' and H_i', by H; and velocity V_i', by fR. The density differences are normalized by $\rho_3-\rho_1$ such that

$$\Delta_1 = (\rho_2-\rho_1)/(\rho_3-\rho_1)$$

and

$$\Delta_2 = (\rho_3-\rho_2)/(\rho_3-\rho_1)$$

As mentioned in Appendix A, we consider here only the non-dimensional variables; in the above and hereafter primes represent the dimensional variables; equations in section 3 used here are assumed non-dimensionalized.

In domain 1, Eqs. (19), (22), (23) and (17) give the solution,

$$h_2 = H_1 \, [1+c_1 e^{\alpha_1 x} + c_2 e^{-\alpha_1 x}] \text{ for } 0 \leqslant X \leqslant D_1 \qquad \text{(B1)}$$

where $\alpha_1 = [\Delta_2 H_1 H_2]^{-1/2}$ and, C_1 and C_2 are constants of integration to be determined later. Likewise, in domain 2, Eqs. (18), (19), (21) through (23) and Eq. (17) give the solution

$$h_1 = [H_1/(1+H_1)] \, [1 + C_3 e^{\beta_1 x} + C_4 e^{\beta_2 x} + C_5 e^{-\beta_1 x} + C_6 e^{-\beta_2 x}] \qquad \text{(B2)}$$

$$\begin{aligned} h_2 = {} & [H_1/(1+H_1)] \, [1 + (1-\beta^2{}_1 H_1 \Delta_1)(C_3 e^{\beta_1 x} + C_5 e^{-\beta_1 x}) \\ & + (1-H_1 \Delta_1 \beta_2{}^2)(C_4 e^{\beta_2 x} + C_6 e^{-\beta_2 x})] \end{aligned} \qquad \text{(B3)}$$

for $D_1 \leqslant X \leqslant D_2$

where

$$\beta_1, \ \beta_2 = [2\Delta_2+\Delta_1/H_2 \pm (4\Delta_2{}^2+\Delta_1{}^2/H_2{}^2-4\Delta_1\Delta_2 H_1/H_2)^{1/2}]^{1/2}/(2H_1\Delta_1\Delta_2)^{1/2}$$

and C_3 through C_6 are constants of integration to be determined. In domain 3, Eqs. (20), (21), (23) and Eq. (17) give the solution,

$$h_1 = H_1[1 + C_7 e^{\gamma_1 x} + C_8 e^{-\gamma_1 x}] \text{ for } D_2 \leq X \qquad \text{(B4)}$$

where $\gamma_1 = [H_1 H_2]^{-1/2}$ and C_7 and C_8 are constants of integration to be determined. The 10 unknown constants, C_1 through C_8, D_1 and D_2, can be determined by imposing the following 10 conditions:

1) symmetry of solution about x=0: $h_{ix}(0)=0$, i=2 or 3
2) vanishing disturbance as $x \to \infty$: $h_i(\infty)=0$, i=1 or 3
3) continuity of h at $x=D_1$: $h_i(D_1^-)=h_i(D_1^+)$, i=2 or 3
4) continuity of h at $x=D_2$: $h_i(D_2^-)=h_i(D_2^+)$, i=1 or 3
5) continuity of V at $x=D_1$: $h_{ix}(D_1^-)=h_{ix}(D_1^+)$, i=2 or 3
6) continuity of V at $x=D_2$: $-\Delta_1 h_{1x}(D_2^-)+\Delta_2 h_{3x}(D_2^-) = -h_{1x}(D_2^+)$
7) vanishing of h_1 at $x=D_1$: $h_1(D_1)=0$
8) vanishing of h_2 at $x=D_2$: $h_2(D_2) = 0$
9) mass conservation for water in layer 2: $\int_0^{D_2} h_2 dx = H_1 L_c$
10) mass conservation for water in layer 3: $\int_0^{\infty} (h_3 - H_2) dx = 0$

where the subscript x denotes differentiation with respect to x. In condition 6), the left hand side is the relative velocity between layers 3 and 1 obtained from Eqs. (18) and (19). In conditions 9) and 10), any arbitrarily chosen two of three layers can be considered instead of layers 2 and 3.

Velocities are obtained first by integrating the vorticity equations (21) through (23), then by using the geostrophic equations (18) through (20). For example, in domain 1, Eq. (22) leads to

$$V_2 = \int (h_2/H_1 - 1)\, dx + C_9 \qquad \text{(B5)}$$

ere h_2 is already obtained in the above (Eq. (B1)) and C_9 is a constant of integration to be determined. V_3 is then obtained by using Eq. (19) i.e.

$$V_3 = V_2 + \Delta_2 h_3 x \qquad \text{(B6)}$$

In determining velocities, three new constants of integration appear, one in each domain. These unknown constants can be determined by imposing the following conditions:

11) antisymmetry of velocity about x=0: $V_i(0)=0$, i=2 or 3

12) momentum balance for particles at the edge of layers:

$V_i\,(D_i)=-(D_i-L_c)$, i= 1 or 2

13) vanishing of disturbance as $x \to \infty$: $V_i(\infty)=0$, i=1 or 3

The condition 12) comes from Eq. (24) of section 3.

For axisymmetric case, we designate V and x as the azimuthal velocity and radial distance from the center, respectively. If we simply neglect the cyclostrophic term, the equations of motion become the same as before i.e. Eqs. (18) through (20) are valid. Potential vorticity equations are slightly modified:

$$V_{1x} + V_1/X + 1 = h_1/H_1 \qquad \text{(B7)}$$

$$V_{2x} + V_2/X + 1 = h_2/H_1 \qquad \text{(B8)}$$

$$V_{3x} + V_3/X + 1 = h_3/H_2 \qquad \text{(B9)}$$

Solution procedures are nearly the same as for the 2-D case except that solutions are given by modified Bessel functions i.e.

$$h_2 = H_1\,[1 + C_{10}\,I_o(\alpha_1 x) + C_{11}K_o(\alpha_1 x)] \quad \text{for } 0 \leqslant X \leqslant D_1 \qquad \text{(B10)}$$

$$h_1\ \textcircled{h_2} = [H_1/(1+H_1)][1+C_{12}I_o(\beta_1 x)+C_{13}I_o(\beta_2 x)+C_{14}K_o(\beta_1 x)+C_{15}K_o(\beta_2 x)]$$

$$\text{(B11)}$$

$$h_2 = [H_1/(1+H_1)]\,[1 + (1-\beta_1{}^2\Delta_1 H_1)\{C_{12}I_o(\beta_1 x)+C_{14}K_o(\beta_1 X)\}$$
$$+ (1-\Delta_1 H_1 \beta_2{}^2)\,\{C_{13}I_o(\beta_2 X) + C_{15}K_o(\beta_2 X)\}] \quad \text{for } D_1 \leqslant X \leqslant D_2$$

(B12)

$$h_1 = H_1 [1 + C_{16} I_0(\gamma_1 x) + C_{17} K_0(\gamma_1 x)] \quad \text{for } D_2 \leqslant X \qquad \text{(B13)}$$

where I_0 and K_0 are the modified Bessel functions of zeroth order of first and second kinds, respectively; C_{10} through C_{17} are constants of integration to be determined; α_1, β_1, β_2 and γ_1 are the same as for the 2-D case. To determine the unknown constants C_{10} through C_{17}, D_1 and D_2, the same conditions, 1) through 10), can be applied except that conditions 9) and 10) are so modified as to be appropriate to the coordinate system i.e. condition 9) to

$$2\pi \int_0^{D_2} Xh_2 \, dX = \pi \overset{L_c^2}{L2_g} H_1 \qquad 14)$$

and condition 10) to

$$2\pi \int_0^{\infty} X(h_3 - H_2) dx = 0 \qquad 15)$$

Velocities are determined in the same way as before (2-D case): first by integrating Eqs. (B7) through (B9), then by using Eqs. (18) through (20). For example, in domain 1, Eq. (B8) leads to

$$V_2 = (1/x) \int (h_2/H_1 - 1) \, Xdx + C_{18} \qquad \text{(B14)}$$

where C_{18} is a constant of integration to be determined. V_3 is then obtained using Eq. (19):

$$V_3 = V_2 + \Delta_2 h_{3x} \qquad \text{(B15)}$$

Three unknown constants, one in each domain, are determined by imposing conditions similar to 11) through 13): only the linear momentum in 12) is replaced by the angular momentum i.e. $V_i(D_i) =$

$f(L_c^2-D_i^2)/2D_i$ in place of $V_i(D_i) = -(D_i-L_c)$.

rences

llen, A.A., 1979: Current variability at the offshore edge of the Labrador Current. M.Sc. thesis, Dalhousie Univ., 164 pp.

Anati, D., 1970: On the mechanism of the deep mixed layer formation during Medoc '69. Cah. Oceanogr., 22, 427-443.

Betts, A.K.,1973: Non-precipitating Cumulus Convection and its Parameterization. Quart. J. Roy. Meteorol. Soc., 99, 178-196.

Bryden, H.L., 1979: Poleward heat flux and conversion of available potential energy in Drake Passage. J. Mar. Res., 37, 1-21.

Bursey, J.O., W.J.Saunder, A.D. Gates and G.L. Blackwood, 1977: The Climate of the Labrador Sea. Proc. Fourth Int. Conf. on Port and Ocean Engineering under Arctic Conditions. Memorial Univ. of Newfoundland, St. John's, 938-951.

Clarke, R.A. and J.C. Gascard, 1983: The Formation of Labrador Sea Water. Part I: Large-Scale Processes. J. Phys. Oceanogr., 13, 1764-1778.

Deardorff, J.W., G.E. Willis and D.K. Lilly, 1969: Laboratory investigation of non-steady penetrative convection. J. Fluid Mech., 35, 7-32.

Farmer, D.M., 1975: Penetrative convection in the absence of mean shear. Quart. J. Roy. Meteor. Soc., 101, 869-891.

Garrett, C.J.R. and J.W. Loder, 1981: Dynamical aspects of shallow sea fronts. Phil. Trans. R. Soc. Lond., A302, 563-581.

Garrett, C.J.R., J. Middleton, M. Hazen and F. Majaess, 1985: Tidal Currents and Eddy Statistics From Iceberg Trajectories off Labrador. Science, 227, 1333-1335.

Gascard, J.C. and R.A. Clarke, 1983: The formation of Labrador Sea Water. Part II: Mesoscale and smaller-scale processes. J. Phys. Oceanogr., 13, 1779-1797.

Gill, A.E., 1982: Atmosphere-Ocean Dynamics. Academic Press. p. 194.

Gill, A.E. and J.S. Turner, 1976: A comparison of seasonal thermocline models with observations. Deep-Sea Res, 23, 391-401.

Green, J.S.A., 1970: Transfer properties of the large-scale eddies and the general circulation of the atmosphere. Q.J.R. Meteor. Soc., 96, 157-185.

gg, N.G. 1973: The preconditioning phase of MEDOC 1969 - II. Topographic effects. Deep-Sea Res, 20, 449-459.

Ikeda, M., in preparation: Salt and Heat Balances in the Labrador Sea using a Box Model. Submitted to Atmos-Ocean.

Killworth, P.D., 1979: On "Chimney" Formation in the Ocean. J. Phys. Oceanogr., 9, 531-554.

Lazier, J.R. N., 1973: The renewal of Labrador Sea Water. Deep-Sea Res., 20, 341-353.

Lazier, J.R.N, 1980: Oceanographic conditions at O.W.S. Bravo 1964-1974. Atmos.- Oceans, 18, 227-238.

Lazier, J.R.N., 1982: Seasonal variability of temperature and salinity in the Labrador Current. J. Mar. Res., 40, supplement, 341-356.

LeBlond, P.H., 1982: Satellite Observations of Labrador Current Undulations. Atmos.-Oceans, 20, 129-142.

Lilly, D.K., 1968: Models of Cloud-topped mixed layers under a strong inversion. Quart. J. R. Meteorol. Soc., 94, 292-309.

Mahrt, L. and D.H. Lenshow, 1976: Growth Dynamics of the Convectively Mixed Layer. J. Atm. Sci., 33, 41-51.

Nof, D., 1983: On the response of ocean currents to atmospheric cooling. Tellus, 35A, 60-72.

Pingree, R.D., 1977: Baroclinic eddies bordering the Celtic Sea in later summer. J. Mar. biol. Ass. U.K., 59, 689-698.

Symonds, G., 1984: Sea ice as an indicator of climate change. BIO Review '84. Bedford Institute of Oceanography, 24-26.

Smith, S.D. and F.W. Dobson, 1984: The Heat Budget of Ocean Weather Station Bravo. Atmos.-Oceans, 22, 1-22.

Stommel, H. and G. Veronis, 1980: Barotropic Response to Cooling. J. Geophys. Res., 85, 6661-6666.

Tennekes, H., and A.D. Van Ulden, 1974: Short-Term Forecasts of Temperature and Mixing Height on Sunny Days. Proc. Symp. Atmospheric Diffusion and Air Pollution, Santa Barbara, Calif., pp. 35-40.

Tennekes, H., 1973: A model for the Dynamics of the Inversion above a Convective Boundary Layer. J. Atm. Sci., 30, 558-567.

Thompson, K.R. and M.G. Hazen, 1983: Interseasonal Changes of Wind Stress and Ekman Upwelling: North Atlantic, 1950-1980. Canadian Tech. Rep. Fish. Aquat. Sci., No. 1214.

Van Heijst, G.J.F., 1985: A Geostrophic Adjustment Model of a Tidal Mixing Front. J. Phys. Oceanogr., 15, 1182-1190.

Venkatram, A., 1977: A Model of Internal Boundary-Layer Development. Boundary-Layer Meteor., 11, 419-437.

II

ICE AND ICE-OCEAN MODELLING

LARGE-SCALE ICE-OCEAN MODELING

W.D. Hibler III[1]

ABSTRACT

Utilizing results from diagnostic ice-ocean models of the Arctic, Greenland and Norwegian Seas, physical characteristics and problems related to large-scale ice-ocean modeling are examined. In these models a 14-level baroclinic ocean model has been coupled to a two-thickness-level dynamic-thermodynamic sea ice model utilizing a nonlinear plastic ice interaction. Simulations of the ocean (for the Arctic Basin only) without the ice cover, and of the ice without the ocean model, are also done to examine certain physical problems.

To examine the magnitude of the bottom torque term in the Arctic Basin, steady state simulations with a fixed wind forcing and with and without baroclinic forcing were compared. The results show the vertically integrated flow to be about 30 times stronger when the bottom torque term is included. Comparison of surface currents and ice drift in the full coupled model shows the surface currents to account for about 50% of the ice drift. However, daily and monthly variation in ice drift were dominated more by wind variations than current variations (with the possible exception of the Barents Sea where the shallow depths yield large barotropic currents). With respect to ice edge variations, simulation results show that including modeled ocean circulation in seasonal sea ice simulations substantially improves the predicted ice margin location. Simulations with only vertical convection, and no lateral ocean movement, produce a less realistic ice edge. A closer look at temporal oceanic heat flux variations near the ice edge shows them to fluctuate substantially in winter, in coincidence with surges of sea ice freezing and melting.

In order to show the necessity for a nonlinear ice-ice interaction in ice-ocean simulations, seasonal simulations of an ice model using only free drift are compared to those using a plastic rheology. Results without ice interaction yield a totally unacceptable ice build-up, even after only a one-year integration.

---

[1] U.S. Army Cold Regions Research and Engineering Laboratory, Hanover, NH 03755.

I. INTRODUCTION

The presence of a dynamic ice cover causes the Arctic Ocean, together with the adjacent Greenland and Norwegian Seas, to differ substantially from more temperate oceans. In addition, because of the intense cooling with concomitant bottom water formation and complex feedbacks occurring at the ice margin, the Arctic Ocean has a climatic impact far exceeding its size, the importance of which has only recently begun to be appreciated by the climate community. In addition to the relevance to global circulation, the Arctic also provides a unique oceanographic laboratory for studying upper ocean dynamics.

The dynamic ice cover creates a more complicated surface boundary condition than exists in the open ocean. Complexities include ice interaction, wind and ocean drag modifications due both to ice floe distribution and salt fluxes, attendant eddies that seem to accompany the ice edge, and the boundary layers underneath the ice. On the large scale, a particular problem is the transport of ice into the Greenland Sea and the attendant fresh water fluxes there. Overall, the presence of an ice cover alters the surface boundary conditions of the ocean.

Because of the relative ease of measuring ice motion versus deeper currents, much of what we know about the Arctic ice cover comes from the ice drift patterns. It is therefore especially important to understand the coupling between the ice and the ocean and the differences between ice drift and ocean currents.

While not meant to be a comprehensive review, the present paper attempts to describe, with the help of numerical modeling experiments, the main physics of the large-scale ice-ocean circulation in the Arctic, Greenland and Norwegian Seas. Much (but not all) of this exposition is based on a manuscript submitted for publication by Hibler and Bryan (1986) describing a diagnostic ice-ocean simulation of the Arctic, Greenland and Norwegian Seas in which the ocean model's temperature and salinity were linearly damped towards climatology with a three-year time constant.

II. BAROTROPIC AND BAROCLINIC CURRENTS

Since the ocean currents play an important role in driving the ice drift it is important to understand the basic characteristics of the Arctic Ocean circulation in order to understand and predict ice drift. A particularly critical feature of the Arctic Ocean circulation is the rather complete geostrophic adjustment and the role played by the bottom torque term in the mean circulation. An essential difference between the Arctic and mid-latitude seas is the absence of any Beta effect leading to a western intensification of the currents. Instead, in the Arctic the barotropic flow is largely dictated by the bottom depth contours. If the currents were only barotropic, this fact would lead to extremely small surface currents. However, the geostrophic adjustment is rather complete so that a strong surface current can occur. This density adjustment also couples with the bottom topography to yield a bottom torque term on the integrated flow which is very significant.

It is important to understand the substantial magnitude of the bottom torque to understand the nature of the Arctic Ocean circulation. Properly simulating this term is also crucial in large-scale ice-ocean modeling.

The essential physics can be outlined as follows. Considering the ocean circulation in the absence of nonlinear momentum advection terms and viscous terms, the governing equations in cartesian coordinates, together with the Boussinesq approximation, are given by

$$\rho_o \frac{\partial u}{\partial t} = - \frac{\partial P}{\partial x} + \tau_x \delta(0) + \rho_o f v \qquad (1)$$

$$\rho_o \frac{\partial v}{\partial t} = - \frac{\partial P}{\partial y} + \tau_y \delta(0) - \rho_o f u \qquad (2)$$

with

$$\frac{\partial w}{\partial z} + \underset{\sim}{\nabla} \cdot \underset{\sim}{u} = 0 \qquad (3)$$

and

$$P = P_o + g \int_{-z}^{0} \rho \, dz = P_o + p' \ .$$

In the momentum equations the vertical and horizontal viscosity terms have been omitted as they are not essential to this argument. Considering a variable bottom depth of h, and a coordinate system with z being positive in a direction upward from the ocean bottom, the continuity equation may be integrated, yielding

$$\int_{-h}^{z} \frac{\partial w}{\partial z'} dz' = w(z) - w(-h) = - \int_{-h}^{z} \nabla \cdot \underset{\sim}{u} \, dz$$

$$= - \nabla \cdot \int_{-h}^{z} \underset{\sim}{u} \, dz + \nabla h \cdot \underset{\sim}{u} \ .$$

If we specify that the ocean currents at the bottom run parallel to the bottom slope, then $w(-h) = -\nabla h \cdot u$ and

$$w(z) = -\nabla \cdot \int_{-h}^{0} \underset{\sim}{u}\, dz \ .$$

Considering that the system has a rigid lid at $z = 0$ so that $w(0) = 0$, then

$$-\nabla \cdot \int_{-h}^{0} \underset{\sim}{u}\, dz = 0$$

and it is therefore possible to define a vertically integrated stream function for the system:

$$\frac{\partial \psi}{\partial x} = \int_{-h}^{0} v\, dz \qquad (4)$$

$$\frac{\partial \psi}{\partial y} = -\int_{-h}^{0} u\, dz \ . \qquad (5)$$

Vertically integrating the momentum equation, taking the curl and substituting in the definition of stream function for u and v we obtain

$$\frac{\partial}{\partial t}(\nabla^2 \psi) - \frac{\partial}{\partial x}\left\{\left(\frac{f}{h}\right)\frac{\partial \psi}{\partial y}\right\} + \frac{\partial}{\partial y}\left\{\left(\frac{f}{h}\right)\frac{\partial \psi}{\partial x}\right\}$$

$$= -\frac{\partial}{\partial y}\left\{\frac{1}{h}\int_{-h}^{0}\frac{\partial p'}{\partial x}\, dz\right\} + \frac{\partial}{\partial x}\left\{\frac{1}{h}\int_{-h}^{0}\frac{\partial p'}{\partial y}\, dz\right\}$$

$$+ \frac{\partial}{\partial y}\left(\frac{1}{h}\tau_x\right) - \frac{\partial}{\partial x}\left(\frac{1}{h}\tau_y\right) \ . \qquad (6)$$

The terms on the right-hand side involving the pressure are the bottom torque terms, and are clearly non-zero only when there is bottom topography (i.e. $h \neq$ constant).

As a demonstration of how large this term is, Figure 1 shows a numerical solution of Equation (6) for the Arctic Ocean (with a time-invariant surface wind and forcing taken from the 30-year averaged wind fields in Walsh et al. (1985), both with and without the density term included. In the numerical solution a rather large constant eddy viscosity of $A_m = 8 \cdot 10^9$ was also utilized. While this quantitatively affects the results it does not affect the main characteristics of the bottom torque term or the essential argument. As can be seen, without the baroclinic forcing (taken from Levitus, 1982) the flow essentially follows the contours of bottom topography with a greatly reduced flow. In the full baroclinic adjustment case, the flow is much more vigorous, perhaps 30 times as strong as in the barotrop-

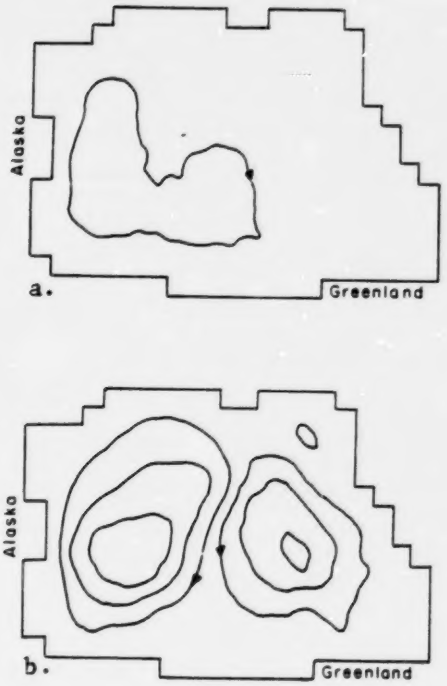

Figure 1. Contours of vertically integrated flow for the Arctic Ocean for (a) a barotropic model and (b) a baroclinic model with fixed density forcing. In the barotropic case the stream function contour interval was 0.2 Sverdrup. In the baroclinic case the interval is 1.0 Sverdrup. In both cases bottom topography was resolved using differing numbers of up to 14 vertical levels.

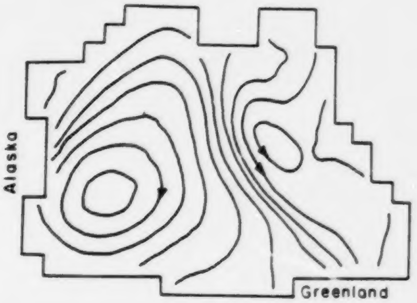

Figure 2. Contours of surface pressure from a baroclinic Arctic Basin simulation (whose integrated stream function was shown in Figure 1b). The contour interval is 0.10 dynamic meter.

ic case. This figure is a graphic illustration of the importance of properly simulating the baroclinic adjustment in ocean models, and also gives a good feeling for why the wind-driven component of the current fields is not critical in Arctic ice drift calculations over the deep ocean regions.

With respect to the surface currents from the simulation, Figure 2 shows the surface pressures from the simulations, which to a good approximation are streamlines for the surface currents. Basically the surface current structure yields a flow pattern resembling observations by Coachman and Aagaard (1974) with a pronounced surface gyre and a transpolar drift pattern.

A question of some interest with regard to such large-scale ice-ocean simulations is how rapidly the baroclinic currents change in response to wind forcing and how large the barotropic currents are. These characteristics were investigated by Hibler and Bryan (1986) in a diagnostic simulation of the Greenland/Norwegian Sea, some results from which are shown in Figures 3 and 4. (A somewhat more complete description of this model is given below in section IV.) Shown in Figure 3 are the daily rms fluctuations in surface ocean current speed versus the mean ocean speed averaged for a year on a transect across the Arctic Basin. As can be seen, in the central basin the mean current is substantially larger than the fluctuating current. However, in the very shallow regions the fluctuating barotropic currents can be very large, as for example in the Barents Sea.

While changing much more slowly than the barotropic currents, the baroclinic currents also undergo an evolution due to the average wind stress change, as shown in Figure 4. The final stabilized current field in Figure 4 is largely due to

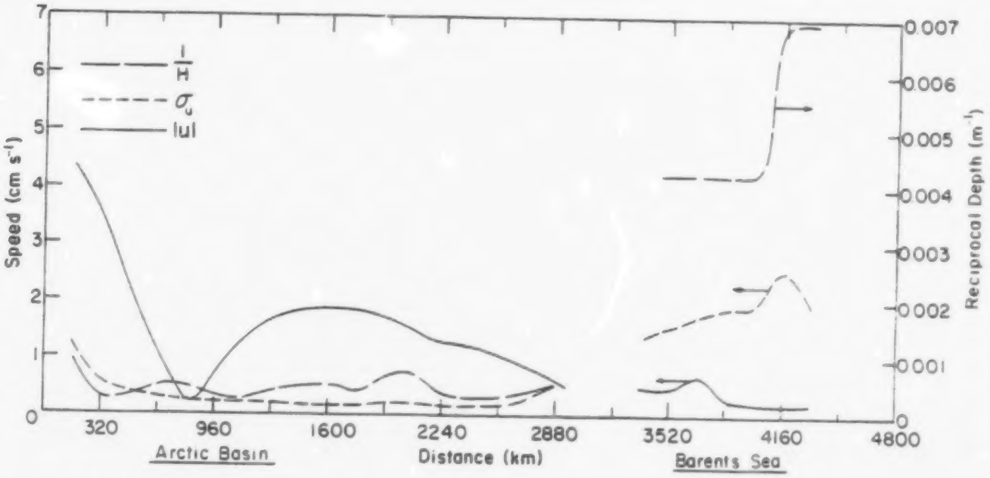

Figure 3. Annual averaged RMS value of the daily ocean current magnitude at the second level of a diagnostic ice-ocean model along a transect passing from the North Slope of Alaska, through the North Pole and on into the Barents Sea. Also shown are the mean annual current speed and inverse of the bottom topography.

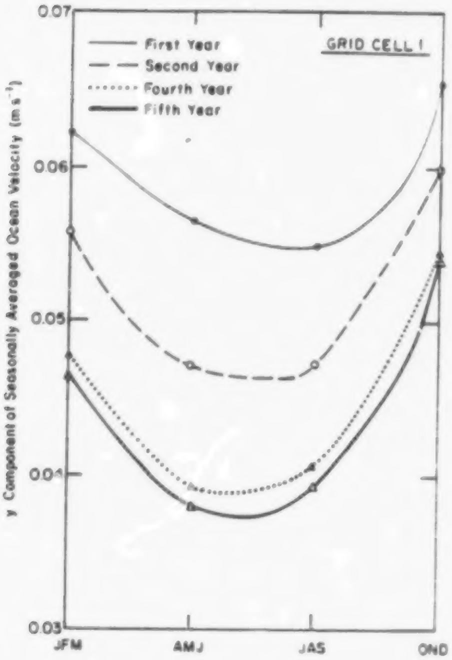

Figure 4. Seasonally averaged component of ocean surface current (current at the 2nd level) of a diagnostic ice-ocean model off the coast of Alaska during different times in the spin-up process.

diagnostic source terms in the Hibler-Bryan ice-ocean model which relax the model density field to observed mean climatology with a three-year relaxation time. However, the variation over the first few years gives an indication of the magnitude of changes that can occur from one year to the next if the wind forcing is variable. As a consequence, it is clear that significant amounts of interannual variability in the baroclinic currents can occur as the average wind stress forcing changes from year to year. Basically, in Figure 4 the seasonal change in the current magnitude is mainly a barotropic effect, while the year-to-year forcing is a baroclinic drift. This seasonal variation is substantially smaller in the central basin.

III. DIFFERENCES BETWEEN ICE DRIFT AND SURFACE CURRENTS

Results from the ice-ocean simulation mentioned above also give some insight into the essential differences between ice drift and ocean surface currents. It is notable, for example, that even near the coast where the current fluctuations are larger, the ice motion variations are much larger than the current variations. This characteristic is illustrated in Figure 5, which compares the mean seasonal *y* velocity component with the y component of surface ocean velocity (with, in this case, the same scale used for both plots) off the North Slope of Alaska. While there is some variation in the ocean currents, it is smaller than the ice motion.

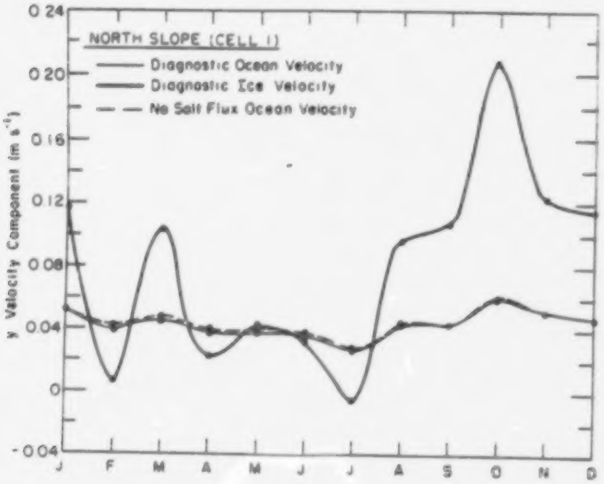

Figure 5. Time series of y velocity component of ice drift and ocean current velocities off the North Slope of Alaska. The ocean velocities are taken from the second level of the ocean model. Also shown (dashed line) is the velocity from a one-year sensitivity study where the salt fluxes due to ice melt and growth were set equal to zero.

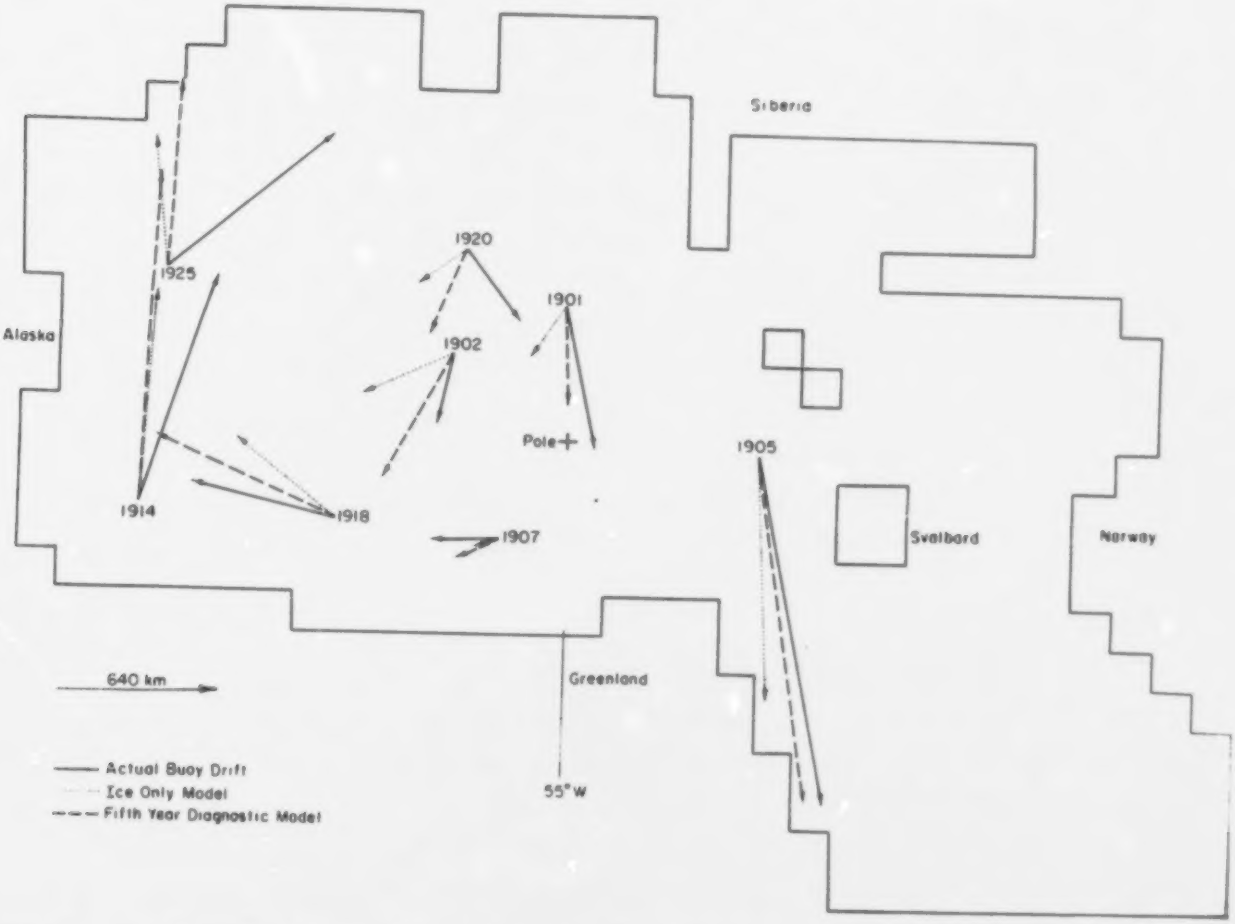

Figure 6. Long-term averages of (a) simulated and observed drift rates of ice buoys. Drift rates have been converted to distances by multiplication by time. The time intervals used were Feb-Nov for buoys 1901 and 1902, Mar-Sep for buoy 1905, May-Nov for buoy 1907, and Mar-Nov for the remaining buoys.

In order to give some idea of the long-term effects of ocean currents on ice drift, Figure 6 compares observed ice buoy (Thorndike and Colony, 1982) drift to simulated results, both with and without the ocean model included. Although of considerable magnitude, the ocean currents are smaller than the ice drift, and in buoy-drift comparisons they account for less than 50% of the net ice drift. Note also that inclusion of ocean currents tends to substantially modify the direction of the ice drift.

An important concept in ice-ocean coupling is the fact that the ice interaction can modify the wind stress transferred into the ocean. This effect is particularly pronounced on long time scales since large fluctuations in wind stress tend to aver-

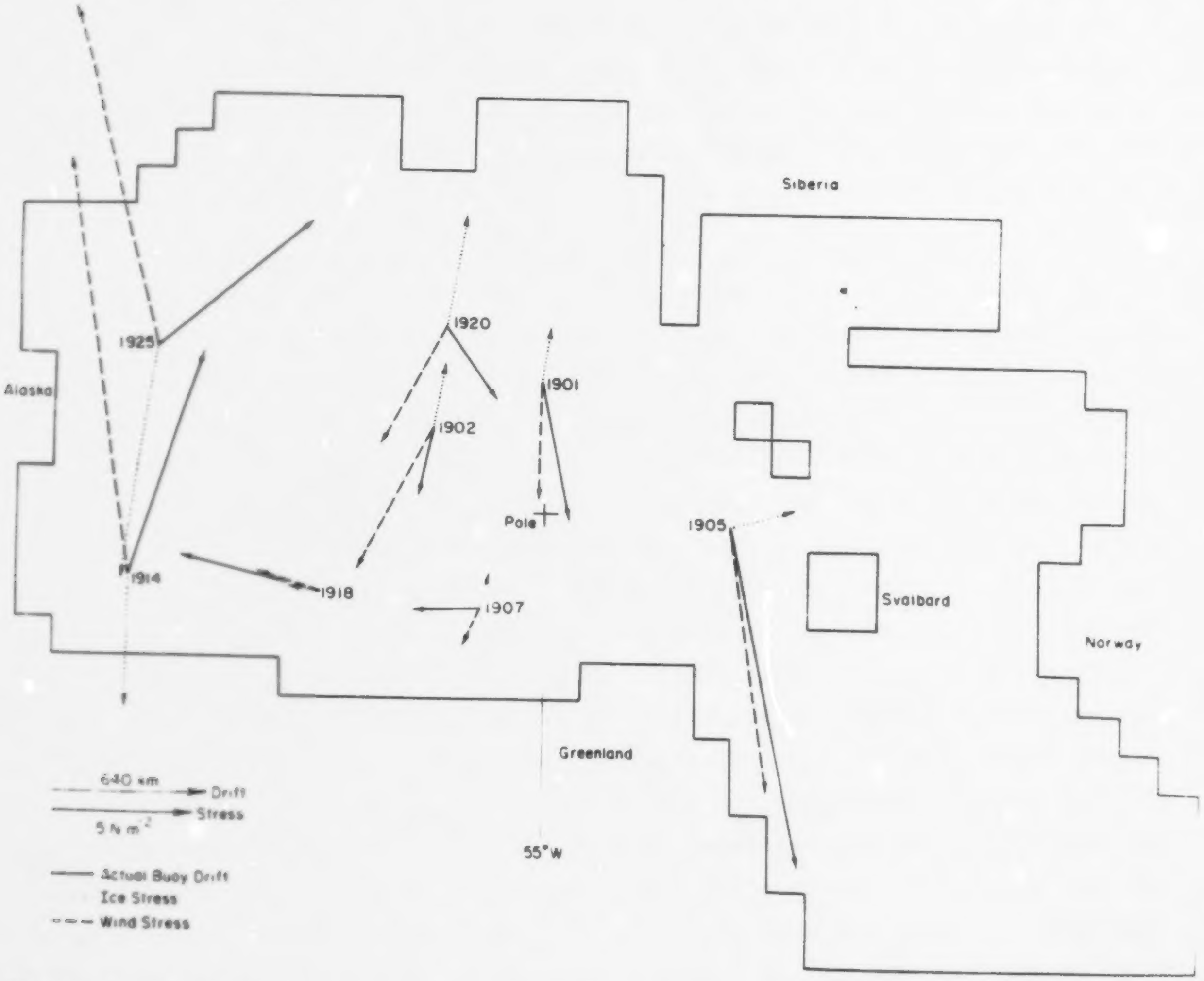

Figure 7. Wind stress and forces due to ice interaction at the locations of the ice buoys shown in Figure 6. The time intervals used for averaging were the same as used in Figure 6.

age out. As shown in Figure 7, the ice interaction at the buoy locations has a magnitude comparable to the mean wind stress. Also, while in most cases the ice stress opposes the wind stress, it can combine with the wind stress or be at right angles to the ice drift due to the configuration of the land boundary and the ice edge.

While these results tend to contradict the intuitive view that ice interaction does not play a significant role far from shore, they are quite reasonable if one considers the theory of a plastic rheology. In a one-dimensional constant strength plastic system (see, e.g., Hibler, 1985), the simulated ice drift will asymptotically approach the free drift value for large wind speeds but will be significantly different for small wind speeds. Thus, short-term fluctuations in ice drift will tend to follow the wind, while longer-term variations can be more strongly affected by ice interaction. This is one possible reason why the wind and ice drift have such a high coherence at high frequencies, and consequently such a high temporal correlation (Thorndike and Colony, 1982). In general these remarks highlight the need for more detailed sensitivity studies of this type of ice-ocean model, with verification based on more extensive data sets.

IV. THE ROLE OF OCEAN CIRCULATION IN ICE EDGE VARIATIONS

In order to examine the dominant effects of the full three-dimensional ocean circulation on the simulated ice margin and to examine ice-ocean coupling effects, Hibler and Bryan (1984) constructed a diagnostic ice-ocean model and used it to carry out a series of seasonal simulations of the Arctic, Greenland and Norwegian Seas. The term "diagnostic" refers to the fact that the ocean model contains a linear term which damps the ocean's temperature and salinity towards climatology. However, as discussed below, this damping is done in a relatively weak manner so that seasonal and month-to-month variation in the temperature and salinity due to ice-ocean coupling effects are prognostically simulated by the model.

This ice-ocean model was constructed by coupling the two-thickness-level thermodynamic sea ice model (Hibler, 1979) with a multi-level baroclinic ocean model (Bryan, 1969). The sea ice model supplies heat flux, salt flux, and momentum exchange boundary conditions for the top of the ocean. The ocean model, in turn, supplies current and heat exchange information to the ice model. Since the concern here was to examine the effect of ocean circulation on sea ice, observed oceanic temperature and salinity data (Levitus, 1982) were used to weakly force the ocean model so that its equilibrium time scale is similar to that of the ice model (3 to 5 years). This "diagnostic" method allows the ocean model to be forced to available climatological ocean data, while at the same time allowing considerable adjustment in the upper ocean due to the effects of ice/ocean interaction. In addition, the barotropic mode of the ocean is fully simulated so that temporally varying currents due to surface stress fluctuations are part of the model predictions. The basic idea here is to specify the ocean circulation over climatic time scales while modeling the shorter term fluctuations.

While, as discussed above, the modeled ocean circulation does affect the ice drift, probably the most noticeable effect is to greatly improve the winter ice mar-

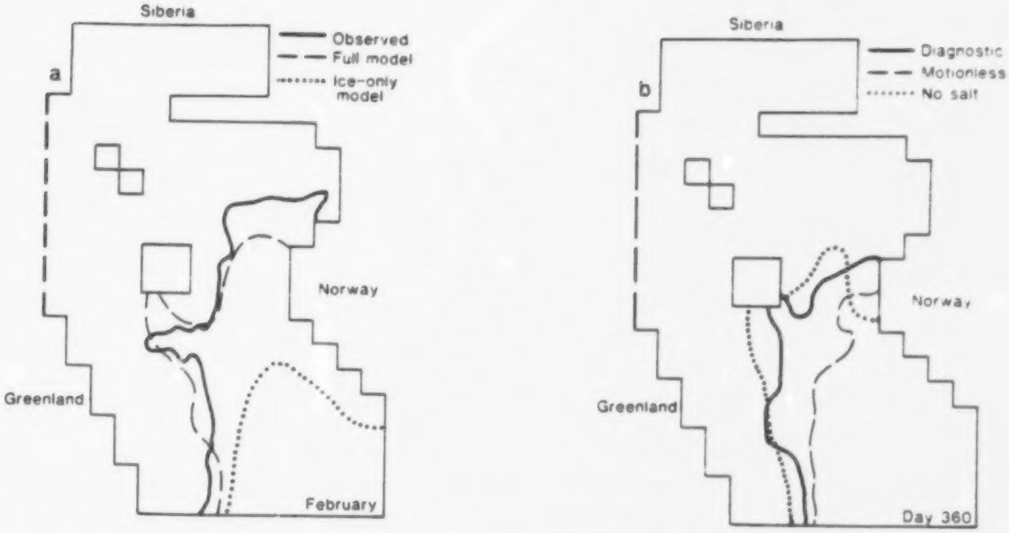

Figure 8. (a) February 50 percent concentration limits from the full coupled ice-ocean model and for the ice-only model, which includes a fixed-depth mixed layer. The observed limit is taken from Fleet Weather charts (Suitland, Maryland, U.S. Navy) for the end of February. (b) Simulated 0.05-m thickness contours for day 360 for the full model, a coupled model with a "motionless" ocean, and a coupled ice-ocean model with no salt fluxes due to ice freezing and melting. The "motionless" model and the no-salt simulations were run for only 1 year. The starting points for these simulations were the ice thickness and ocean fields at the end of the fourth year of the full diagnostic model simulation.

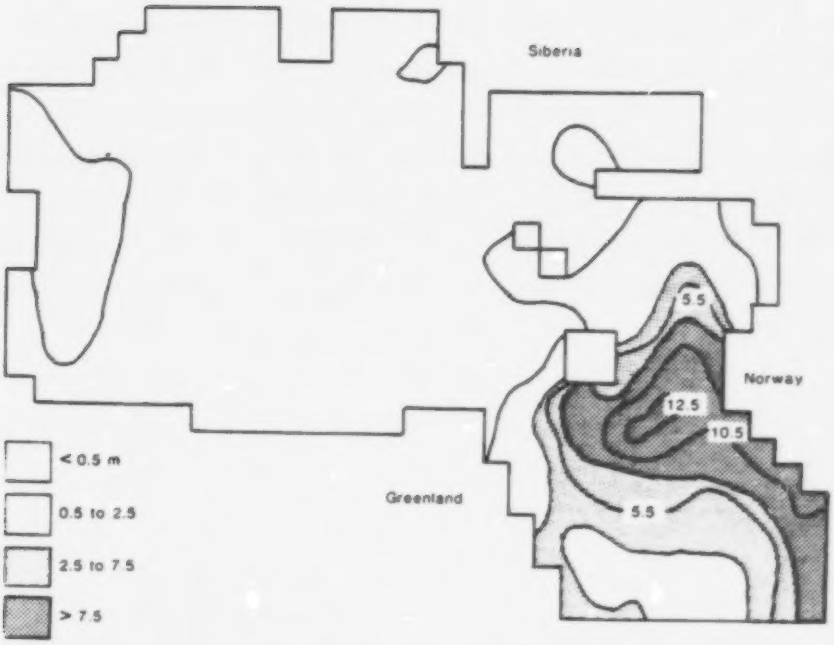

Figure 9. Average annual heat gained by the upper layer of the ocean from the deeper ocean and by lateral heat transport. The contours are in terms of the melting capacity of the heat (in meters of ice per year). A melt rate of 1 m of ice per year is equivalent to 9.57 W m^{-2}.

gin simulation (Fig. 8a). This improved ice margin is due to the large oceanic heat flux from the deeper ocean into the upper mixed layer in this region (Fig. 9). The heat flux occurs primarily in winter and analysis shows that much of the enhancement is due to deep convection, which brings up warm water and prevents ice formation in early winter. This convection explains the absence of ice in the full model simulation far from the ice margin.

Near the ice margin a similar physics applies, but the precise location of the ice edge becomes more sensitive to the surface salt balance and to lateral effects in the oceanic circulation. The sensitivity simulations shown in Figure 8b, for example, indicate that the freshwater flux from melting at the advancing ice edge tends to seal off the ice margin to upward oceanic heat flux and allows a farther advance than would otherwise occur. A sensitivity simulation without lateral motion in the ocean (Fig. 8b) also tends to produce a more excessive edge at the end of one year, since the lateral transport of heat to both the deep and upper layers is missing. This latter result demonstrates the difficulty of simulating the seasonal cycle of sea ice using only a one-dimensional mixed layer model.

As can be deduced from the above figures, the ice edge position in the East Greenland Sea is largely determined by a competition between ice advection from the north and heat advection from the south, which ultimately reaches then ice through vertical convection. Melting can cause cold fresh water to cap off the warm salty water, but a lot of melting is required to do this. If the ice production increases we expect the front to shift southward.

While this overall view is largely correct, analysis of the temporal variations of vertical salt and heat fluxes at the ice margin show the ice advance to be substantially complicated by the local ice dynamics and boundary layer processes occurring at the ice margin. Figure 10, for example, shows the time series of monthly averaged ice thickness, freshwater flux, ocean-to-ice heat flux, and atmospheric heat gain at a location just inside the ice edge several hundred kilometers south of Spitsbergen. In this region the ice advance has created a more stably stratified upper ocean than further away from the edge. Hence vertical convection is possible to a lesser degree than further east. What occurs here is a very close oscillatory balance between fluctuations of the oceanic heat flux and fresh water flux, with an increase in heat flux coinciding with an increase in melting. This increased melting then helps stratify the system so the heat flux decreases. Subsequent freezing or lateral advection can restore the unstable possibilities. It is particularly notable that even though there is a substantial mean ice thickness, the monthly mean ice growth is always negative in winter.

Based on such finely balanced results, even in such a coarse resolution model (160-km grid sizes), it seems quite plausible that details of ice edge processes can play a significant role in the advance of the ice margin on a larger scale. In particular, a closer examination of the fluxes, whose monthly means are shown in Figure 10, indicates that open water can be freezing while thicker ice is melting. Consequently the net salt flux, and hence convection, can hinge on the local ice deformation and advection. Specifically, under large wind-induced divergence the ice growth can dominate, which in turn will lead to more convective overturning and a reduced stratification. With less divergence and more ice advection, on the other hand, the feedback may favor ice melt, which could cause a rapidly advancing ice edge. Once formed, the concomitant stratification might be very difficult to remove, and hence the larger scale circulation could be altered.

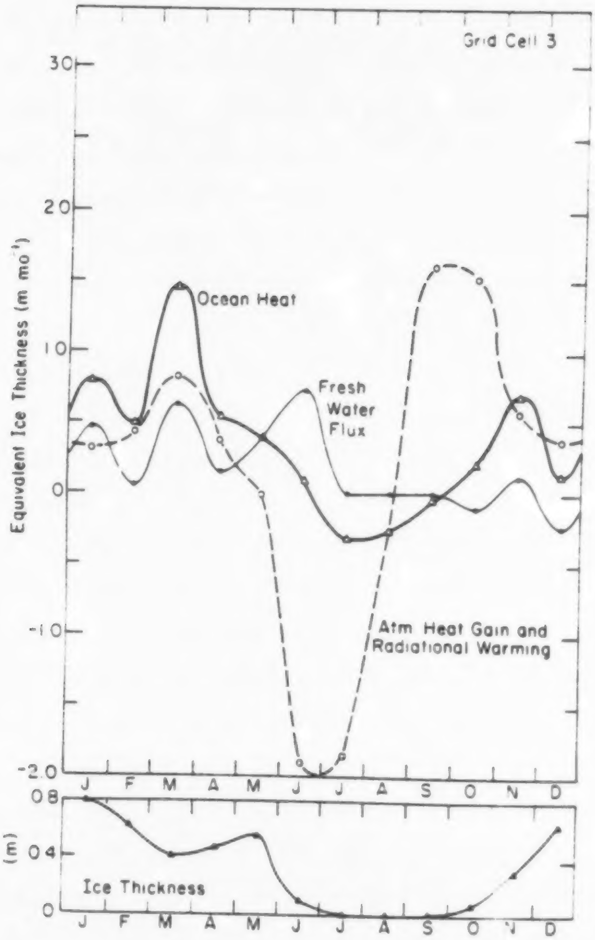

Figure 10. Time series of monthly averaged heat budget components near the East Greenland ice edge (for a diagnostic ice-ocean model) together with ice thickness and freshwater flux. The fluxes are in units of meters of ice per month. For comparison, 1 meter of ice per month is equivalent to 115 W m^{-2}.

It should be emphasized that these calculations have not included ocean eddy effects, which may play an important role in both the lateral and vertical heat exchanges. It is also quite possible for the ice melting and/or freezing to substantially modify the boundary layer drag characteristics and hence accelerate the ice divergence. In addition, the differing wind drag on ice and water can lead to a complex array of ice edge currents and fluctuation, which may in turn affect the ice edge advance and retreat. Clearly, modeling experiments with more complete vertical and horizontal parameterization of oceanic processes, together with remotely sensed and buoy-mounted oceanographic measurements, are needed to clarify the role of different processes in the ice edge advance and retreat.

V. THE ROLE OF NONLINEAR ICE INTERACTION IN SEASONAL ICE-OCEAN SIMULATIONS

As mentioned above, observationally we know that on short time scales ice drift tends to follow the wind. While not obvious, analysis of numerical and analytic ice models shows that this feature is characteristic of a plastic rheology. Because of the significant role played by the ice rheology in the ice-ocean simulations discussed above, the necessity of using a nonlinear rheology is discussed in more detail in this section. In addition, a simple rheology, usable with mean annual or mean monthly forcing, is briefly described in Section VI.

With a plastic rheology, the following characteristics and intuitive reasonable assumptions can be taken into account: discontinuous slippage near shore, rigid ice motion and/or lack of ice motion under considerable wind forcing, small or zero tensile strength (both for uniaxial divergence as well as two-dimensional dilation), and high compressive strengths. These first two points basically say that sea ice should offer very little resistance to being pulled apart, while at the same time offering considerable resistance to being pushed together. To obtain these characteristics one asserts that the stress state of the system is either zero (for dilation) or independent of the rate of strain (for compression). In one dimension this can be accomplished by taking a stress strain relation

$$\begin{aligned} \sigma &= \frac{\dot{\varepsilon}}{|\dot{\varepsilon}|} \quad \text{if } \dot{\varepsilon} < 0 \\ &= 0 \quad \text{if } \dot{\varepsilon} > 0 \;. \end{aligned} \tag{7}$$

In two dimensions, things become somewhat more complicated and one must introduce some type of yield curve in stress space, where the stresses lie on the yield curve when flow is occurring. The ratio, but not the magnitude, of the principal components of the strain rate tensor dictates where on the yield curve the stress lies. Considering sea ice to be a two-dimensional isotropic continuum, the most general constitutive law applicable to non-elastic deformation (sometimes called the Reiner-Rivlin relation) is

$$\sigma_{ij} = 2\eta\dot{\varepsilon}_{ij} + [(\zeta - \eta)(\sum_k \dot{\varepsilon}_{kk}) - P]\delta_{ij} \tag{8}$$

where σ_{ij} is the two-dimensional stress tensor, $\dot{\varepsilon}_{ij}$ is the two-dimensional strain rate tensor, and ζ, η and P are functions of the two invariants of the strain rate tensor.

Probably the best available smooth yield curve for sea ice is an ellipse as proposed by Hibler (1977). Applying the normal flow rule specifying that the ratio of the principal components is the same as a normal to the yield curve to an ellipse yields values of η, ζ and P in Equation (8) of

$$P = P^*/2 \tag{9}$$

$$\zeta = P^*/2\Delta \tag{10}$$

$$\eta = \zeta/e^2 \tag{11}$$

where

$$\Delta = [(\varepsilon_{xx}^2 + \varepsilon_{yy}^2)(1 + 1/e^2) + (4/e^2)\varepsilon_{xy}^2 + 2\varepsilon_{xx}\varepsilon_{yy}(1 - 1/e^2)]^{1/2} \tag{12}$$

and e = ratio of the major and minor axes of the ellipse. Note that a given stress can be produced by various combinations of strain rates, so that strain rate is not a unique function of stress.

Probably the most important ramification of a nonlinear ice interaction for large-scale ice-ocean simulation is that thickness build-up results are totally different with a plastic rheology as compared to free drift (where the ice is merely taken to follow the wind), with free drift yielding totally unacceptable ice build-up results for seasonal simulations. To demonstrate this fact a comparison series of coupled dynamic-thermodynamic simulations were carried out for the Arctic Basin using the two-level dynamic-thermodynamic model of Hibler (1979). The ice strength constant P* and grid are the same as used by Hibler and Bryan (1984). As can be seen from the velocity fields in Figure 11, the average annual ice velocity looks rather similar in both the simulations. However, the ice build-up in the full drift case is totally unacceptable. In particular, even after only one year the free drift simulation results in unrealistic build-ups of over 19 meters off the Canadian Archipelago, together with excessive ice convergence in the center of the Beaufort Gyre. The strong resistance to convergence in the plastic model, on the other hand, yields a relatively realistic build-up. Basically, the deformation field of the ice velocity is a much more sensitive test of a model's performance. This in turn infers that to optimally aid in model development, satellite remote sensing should either be capable of resolving ice deformation, or provide some type of measure of thickness or ridging. These results also illustrate the danger of just using the statistics of predicted ice drift (Thorndike and Colony, 1982) as a test of model

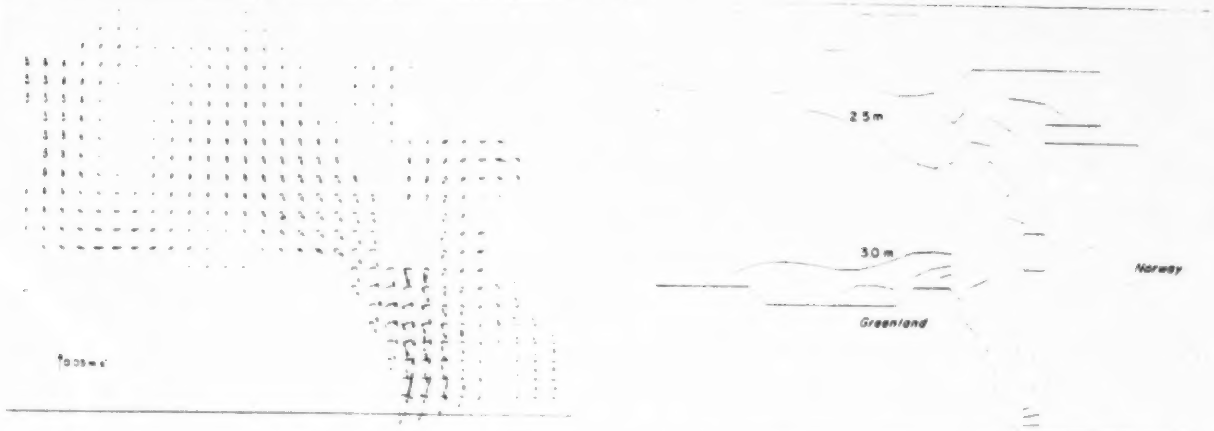

a. Full model.

d. Full model, first year.

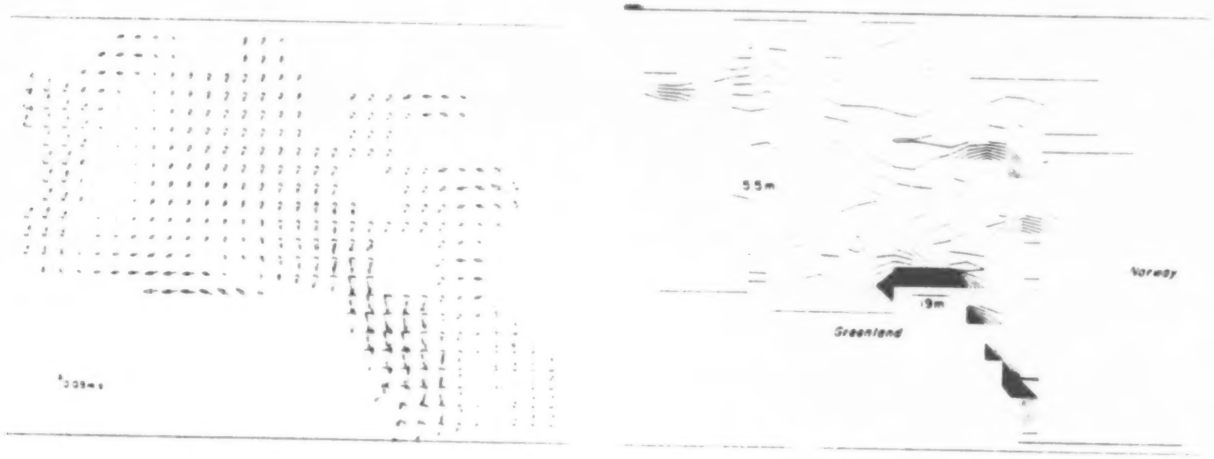

b. Free drift.

e. Free drift, first year.

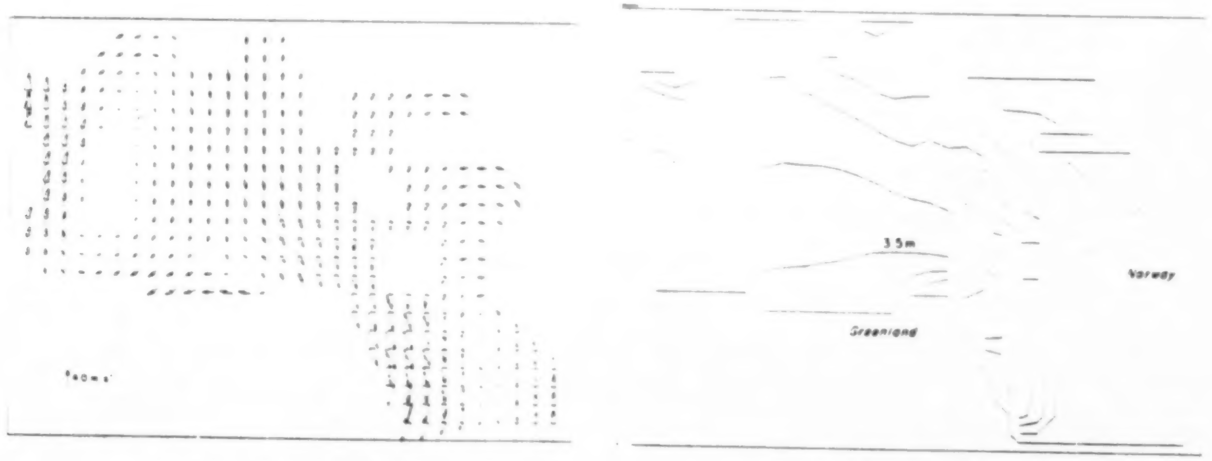

c. Annual average wind velocity.

f. Full model, fifth year.

Figure 11. Simulated annual averaged ice velocities (a,b) and ice thickness at the end of December (d,e,f) for a plastic model versus a free-drift model. Also shown is the average annual wind field (c).

performance. If a model yields good drift statistics but unrealistic ice build-up, for example, then its utility and physical basis are clearly limited.

As can be inferred from Figure 11, a plastic dynamic-thermodynamic sea ice model offers a consistent way to construct a weakly damped ice velocity field without excessive convergence. The computer time needed for this is not excessive. The year-long integration at one-day time steps for Figure 11, for example, required 6 minutes of Cyber 205 computer time, of which about 70% was used for solution of the momentum equation. Considering that the equilibrium time scale of the ice model is about 3 to 5 years, this means that the total computer time needed for equilibrium simulation of both polar covers is substantially less than the equilibrium computer time of an oceanic GCM.

VI. A POSSIBLE SIMPLER PARAMETERIZATION OF ICE DYNAMICS FOR USE IN CLIMATE ORIENTED OCEAN MODELS

In the above rheological treatment a full constitutive law including shear strength as well as compressive strength was utilized. Such a law is necessary in cases where one has daily time-varying forcing. However, in cases where one has mean monthly or mean annual forcing (as is used in many ocean models), a special case of the above rheology which may be useful is to consider a nonlinear bulk viscosity only. In this particular case the rheology becomes rather simple, specifically the stress tensor is given by

$$\sigma_{ij} = \zeta(\dot{\varepsilon}_{11} + \dot{\varepsilon}_{22})\delta_{ij} = \zeta\dot{\varepsilon}_1\delta_{ij} \qquad (13)$$

where

$$\dot{\varepsilon}_{ij} = \left(\frac{du_i}{dx_j} + \frac{du_j}{dx_i}\right)^{1/2} \qquad (14)$$

and δ_{ij} is the kronecker delta. To make this system have resistance to compression but not dilation take $\zeta = \zeta(\dot{\varepsilon}) > 0$ for $\dot{\varepsilon}_1 < 0$, and $\zeta = 0$ for $\dot{\varepsilon}_1 > 0$. In order to put a plastic limit on the system take ζ (when the ice is converging) to be given by ζ = minimum of $\{\zeta_{max}$ and $P^*/2\,|\varepsilon_1|\}$ where, in analogy to the simulation results of Hibler (1979) and Hibler and Walsh (1982), $\zeta_{max} = (2.5 \cdot 10^8$ seconds$)P$ and $P = 10^4 h\, e^{C(A-1)}$ Nt m^{-1} where h is the mean ice thickness in meters, C = 20, and A is the fraction of area covered by ice.

This rheology basically treats the ice as a cavitating fluid (strong resistance to compression, but no resistance to dilatation). In addition to being solved using the same numerical procedure employed by Hibler (1979) this system can also be

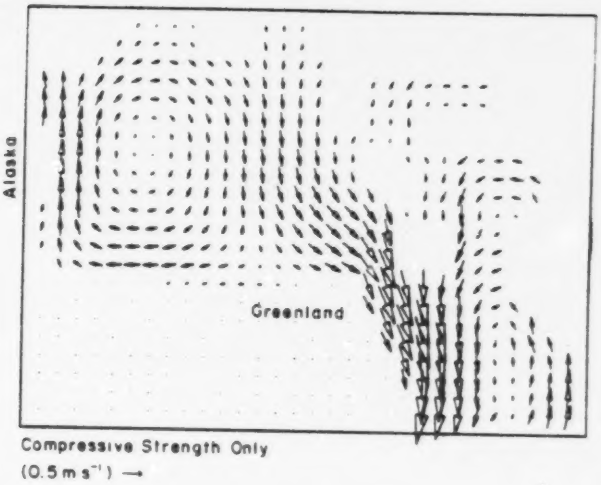

a.

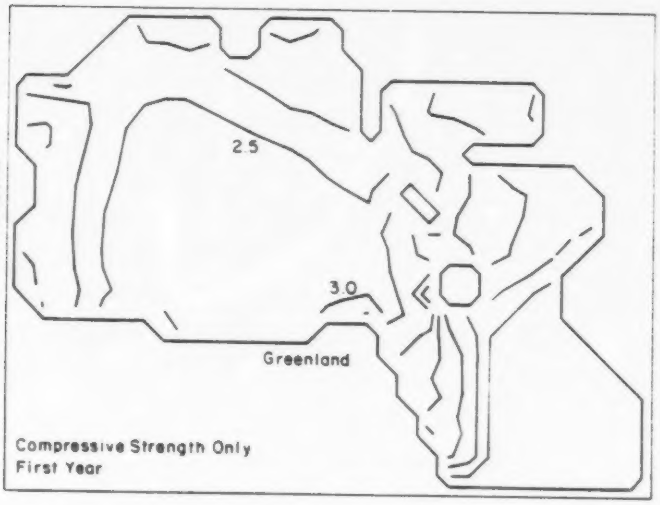

b.

Figure 12. Simulated annual averaged ice velocity (a) and ice thickness at the end of December (b) for a plastic model without shear strength (bulk viscosity only).

solved by direct integration, with very small time steps of the order of, say, one minute. Also, with constant forcing fields, one can make use of rather large distorted time steps if necessary when solving these equations.

Examination of the velocity field and ice build-up after one year with such a model (Fig. 12) shows the velocities to be a bit too large and the ice build-up to not be as realistic as in the full model. Also, the modification of the wind stress curl with such a model is very minimal. However, such a simple rheology does at least treat the main first order transport effects of ice dynamics. This particular rheology has also successfully been used by Semtner (1986) in a prognostic ice-ocean simulation using mean monthly atmospheric forcing.

VII. CONCLUDING REMARKS

The main goal of this paper has been to examine, using numerical modeling results, some of the main physical characteristics and problems occurring in large-scale ice-ocean model simulations. Most of the model results discussed have utilized multi-level baroclinic ocean models with typically 14 or more layers. In such models the treatment of vertical convection has been very minimal, so that an improved parameterization of the mixed layer dynamics is a high priority item for improvement, especially for forecast applications.

An aspect of the particular models discussed here has been the lack of a full prognostic simulation. A successful prognostic simulation has been carried out by Semtner (1986) using mean monthly forcing and the simpler rheology discussed in Section VI, together with specified transports across the southern boundary. However, simulations with a full rheology together with daily time-varying forcing have not yet been performed. Such efforts are currently in progress.

Although briefly alluded to here, eddy effects have not been discussed, and in fact very little theoretical or numerical work has been done on eddy effects with a full nonlinear ice cover. Such work is needed.

REFERENCES

BRYAN, K. 1969: A numerical method for the study of the circulation of the world oceans. J. Comput. Physics, v. 4: pp. 347-376.

HIBLER, W.D. III 1977: A viscous sea ice law as a stochastic average of plasticity. J. Geophys. Res., v. 82: pp. 3932-3938.

HIBLER, W.D. III 1979: A dynamic thermodynamic sea ice model. J. Phys. Oceanogr, v. 9: pp. 815-846.

HIBLER, W.D. III 1985: Modeling sea ice dynamics. In Advances in Geophysics, Vol. 28 (Issues in Atmospheric and Oceanic Modeling, Part A: Climate Dynamics), pp. 549-578.

HIBLER, W.D. III and WALSH, J.E. 1982: On modeling seasonal and internannual fluctuations of Arctic sea ice. J. Phys. Oceanogr., v. 12: pp. 1514-1523.

HIBLER, W.D. III and BRYAN, K. 1984: Ocean circulation: Its effect on seasonal sea ice simulations. Science, v. 224: pp. 489-492.

HIBLER, W.D. III and BRYAN, K. 1986: A diagnostic ice-ocean model. Submitted for publication to J. Phys. Oceanogr.

LEVITUS, S. 1982: Climatological atlas of the world ocean. NOAA Publ. 13, U.S. Dept. of Commerce, Washington, D.C., 173 pp.

SEMTNER, A.J. Jr. 1986: A numerical study of sea ice and ocean circulation in the Arctic. Submitted for publication (see also these proceedings).

THORNDIKE, A.S. and COLONY, R. 1982: Sea ice motion in response to geostrophic winds. J. Geophys. Res., v. 87: pp. 5845-5852.

WALSH, J.E., HIBLER, W.D. III and ROSS, B. 1985: Numerical simulation of Northern Hemisphere variability, 1951-1980. J. Geophys. Res., v. 90: pp. 4847-4865.

THE MODELLING OF ICE MOTION NEAR ADAMS ISLAND

by J.F. Sykes and J.D. Cushon
Department of Civil Engineering
University of Waterloo, Waterloo, Ontario, Canada N2L 3G1

The time averaged motion of shore-fast ice near Adams Island in Lancaster Sound is modelled through the solution of the momentum equation for the ice cover using the Galerkin finite element method. The data base for the study was developed by the National Research Council, Division of Building Research. One 18 day period was modelled using time averaged environmental inputs. In order to obtain a realistic velocity solution it was necessary to model shore boundaries with nonhomogeneous Dirichlet conditions: ice velocity components were prescribed such that the ice velocity vectors at shore boundaries were directed towards the ice cover, normal to the shoreline, thus simulating tidal jacking. The resulting solution agrees well with observations of ice velocity near the island.

A sensitivity analysis using the adjoint methodology was performed and showed which processes had the strongest influence on the ice velocity near the island. The velocity of the ice near the island is strongly influenced by the magnitude of the ice velocity values applied at the shore boundaries and less strongly by the surface shear stresses from wind and ocean currents. The ice strength, which represents the ability of the ice cover to resist deformation is also significant. The influence of coriolis acceleration and the areal mass of the ice are not significant.

The study clearly demonstrates the power of adjoint sensitivity techniques in which the sensitivity of a user selected performance measure to all of the system parameters can be determined in a single analysis. From a physical perspective, the work indicates that the mechanisms which may cause offshore ice motion should be studied.

ON THE RESPONSE OF SEA ICE TO WIND STRESS - STUDIES WITH A REGIONAL SEA ICE MODEL

by V.R. Neralla and S. Venkatesh
Atmospheric Environment Service
4905 Dufferin Street
Downsview, Ontario, Canada M3H 5T4

The Atmospheric Environment Service (AES) in cooperation with the oil industry developed a regional ice model for obtaining short range real time predictions of unconsolidated ice conditions for operational use. In this model, in addition to other usual stresses, internal ice stress is modelled using a viscous plastic rheology. Two categories of ice thickness - thin and thick - were originally used. With the availability of more detailed ice characterization data, it was deemed appropriate to use a better thickness categorization scheme. A multicategory ice thickness scheme is thus adapted in the AES regional ice model. This version also allows for a better specification of ice strength.

In this paper the performance of the model will be examined in terms of correlation between surface pressure gradients/surface winds and observed buoy motions in the Beaufort Sea. A detailed discussion of the results will be presented.

ICE EDGE MEANDERS OFF LABRADOR IN NOAA IMAGERY AND MODELLING INTERPRETATION

by M. Ikeda and I. Peterson
Department of Fisheries and Oceans
Bedford Institute of Ocenography
Atlantic Oceanographic Laboratory
P.O. Box 1006, Dartmouth
Nova Scotia, Canada B2Y 4A2

The ice edge off Labrador is observed to have meanders with various wavelengths between 30 and 300 km. The progression from the shorter scale meanders to longer scale ones occurs following a strong northwesterly wind event.

A linear stability model suggests that the shorter scale meanders are generated by baroclinic instability of the Labrador Current. The wind event induces downwelling and associated flow along the shelf break with an alongshore scale of ~ 200 km. This flow field initiates the longer scale meanders in the Labrador Current.

MODELING MESOSCALE PHENOMENA RELEVANT TO THE GREENLAND SEA MIZ

by S. Hakkinen
National Research Council-NASA Goddard Space
Flight Center, Code 671, Greenbelt, MD, U.S.A. 20771

The effects of externally driven flows, which can be of barotropic or baroclinic nature, or both, of the coupled ice-ocean dynamics are explored. The study utilizes a two-dimensional 2-layer ocean model coupled to an ice model. Of special interest is the interactions between the ice and the ocean in the presence of bottom topography. An example of this is the ice streamers in the East Greenland ice edge (the southern portion) which often show up in nearby topographic features. The oceanic and ice dynamics contributions to the development of these ice-ocean phenomena are investigated. The ice cover facilitates an effective way of coupling baroclinic and barotropic flow components of the ocean. The topography forces the barotropic flow to follow depth isobars to conserve potential vorticity, and it also excites topographic waves. Both of these factors are reflected in the ice movement.

A NUMERICAL STUDY OF SEA ICE AND OCEAN CIRCULATION IN THE ARCTIC [1]

Albert J. Semtner, Jr.

National Center for Atmospheric Research [2]
Boulder, Colorado 80307

February 1986

---

[1] A portion of this study is supported by the U.S. Department of Energy as part of its Carbon Dioxide Research Program.

[2] The National Center for Atmospheric Research is sponsored by the National Science Foundation.

ABSTRACT

A sea-ice model based on bulk-viscous dynamics and 3-layer thermodynamics is coupled to a multi-level primitive equation model of the Arctic Ocean and Greenland Sea. The combined model is forced by inflow through the Faeroe-Shetland Channel and Bering Strait and by observed monthly atmospheric forcing and river runoff. A long-term integration produces a realistic seasonal cycle of ice cover, whose extent is strongly influenced by ocean heat transport. The wintertime maximum is controlled by northward heat transport of 0.4 petawatts in the Greenland Sea and by southward transport of ice and water through the Fram Strait. The summertime mimimum extent of sea ice is influenced by subsurface flow through the Fram Strait of warm Atlantic water, which rises in winter and thins the ice lying over the Eurasian continental slope and along the Alaskan and Siberian coasts. The oceanic circulation in the Canadian Basin is anticyclonic at all depths, but changes to cyclonic in the Eurasian Basin below 200 meters. Offshore ice transport in the Barents Sea promotes oceanic convection on the continental shelf through enhanced brine rejection, whereas surface heat loss in the ice-free Greenland Sea produces intermediate water sources similar in T/S characteristics to observed water masses of the region. Two short additional integrations of the coupled model show that the Arctic sea ice is vulnerable to the environmental effects of atmospheric CO_2 increase, but relatively insensitive to the maximum proposed amount of Soviet river diversions.

1. INTRODUCTION

There is increasing interest today in Arctic Ocean processes from several different viewpoints. For one thing, oceanographers have recently discovered that the Arctic Ocean is a far more active participant in the global ocean circulation than previously thought. A large fraction of the bottom water in the Arctic, which directly affects the production of North Atlantic Deep Water, has its origin on the continental shelves of the Arctic Basin (Aagaard et al., 1985). The dense water is thought to be a result of brine rejection from sea ice, with subsequent drainage of dense water plumes down the continental slope. From a climatic point of view, the Arctic region is thought to be vulnerable to large climatic change from increased atmospheric CO_2 as a result of positive feedbacks related to high-latitude snow and sea ice (Manabe and Stouffer, 1980; Washington and Meehl, 1984). An additional environmental perturbation which is peculiar to the Northern Hemisphere exists in regard to planned Soviet river diversions, the effect of which has been argued either to decrease the extent of sea ice (Aagaard and Coachman, 1975) or to increase the ice extent (Antonov, 1976; Micklin, 1981).

For both oceanographic and climatic reasons, there is a need to construct and use numerical models of the sea ice and ocean circulation in the Arctic. A number of previous studies have dealt with some fraction of the complete system. For example, the ocean modelling studies of Semtner (1976b, 1984b) were done in an annual-mean context without an explicit component model for the sea ice. The climatic studies of Manabe and Stouffer (1980) and of Washington and Meehl (1984) ignored ocean circulation and the dynamics of sea ice. And the ice modelling studies of Hibler (1979), Parkinson and Washington (1979), Hibler and Walsh (1982), and Walsh et al. (1984, 1985) leave out interactive ocean circulation, although they do include some form of ice dynamics.

It is only recently that the first coupled ice-ocean model of the Arctic has been developed [Hibler and Bryan (1984), hereafter referred to as HB]. As shown in Fig. 1a, the inclusion of an oceanic component greatly improves the simulation of the wintertime ice edge in the Greenland and Barents Seas. However, some of the improvement may be due to the fact that the ocean model is diagnostically constrained on a three-year time scale to the observed temperature and salinity of the Arctic. This is evident from Fig 1b, which shows that even a motionless ocean (with only convection and diagnostic forcing) can favorably influence the location of the ice edge.

It is clearly desirable to remove the robust diagnostic constraint on the oceanic component of an ice-ocean model, in order to model oceanic phenomena having time scales longer than a few years in the intermediate and deep water and in order to predict future climatic states in which the oceanic variables may be substantially different from those at present. The purpose of this paper is to describe such a model and some results from it. The model is similar in many respects to that of HB. However, the ocean model is more fully prognostic in the sense that observed temperature and salinity are prescribed only at inflow boundaries such as the Faeroe-Shetland Channel and the Bering Strait. The coupled model also has higher resolution than that of HB. Moreover, to reduce the computer time

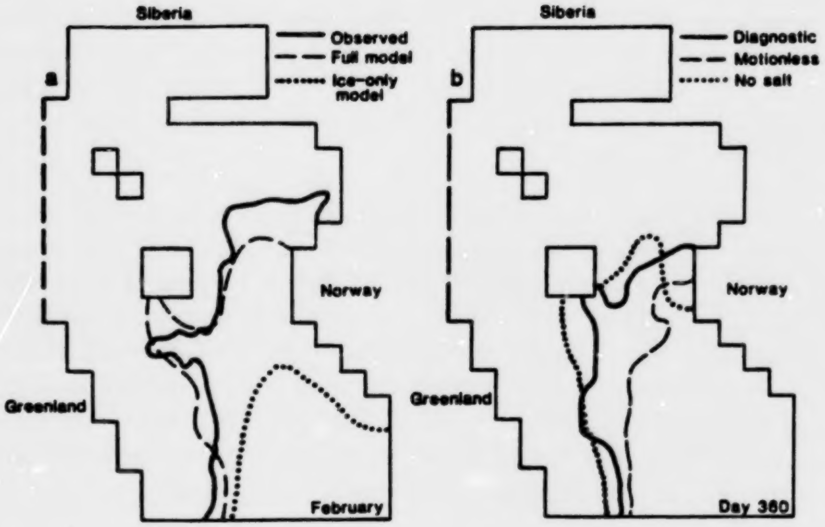

Figure 1. Results from the Hibler and Bryan (1984) model. The left panel shows February 1979 ice limits as observed and as simulated both with the HB coupled model and with only the ice model. The right panel shows the ice limits for three other integrations with a full diagnostic ocean, with a motionless ocean (having convection and diagnostic forcing), and with no salt processes.

required for the ice model and allow long-term integrations, a simplified sea-ice rheology suggested by Hibler (personal communication) is used.

Section 2 describes the dynamics and thermodynamics of the ice model used in the present study and goes on to describe the ocean model and its coupling to the sea-ice component. Section 3 gives a description of the simulated response of the ice-ocean model to the observed monthly forcing supplied by Walsh. Section 4 inquires into the importance of oceanic processes for the simulated ice extent and surface temperatures. Section 5 investigates briefly the effect of specified environmental changes on the ice-ocean system, and Section 6 summarizes the results of the investigation.

2. DEVELOPMENT OF THE SEA-ICE MODEL AND COUPLING TO THE OCEAN MODEL

The sea-ice model which is most commonly used today for both mesoscale and large-scale ice prediction is that of Hibler (1979). The model has been used to study the interannual variability of Arctic sea ice (Walsh et al., 1985) and to model the coupled ice-ocean system (HB, cited earlier). The model has shown considerable skill in representing ice processes, and it has pointed up the importance of both ice dynamics and ice compactness for the proper simulation of the observed ice cover. Accordingly, Hibler's (1979) model formulation is adopted for the present study, but the ice rheology is modified in a fashion (Hibler, personal communication) to allow a more efficient computation when the prescribed forcing varies only on monthly time scales.

The basic model formulation of Hibler has been implemented from scratch for the present study. The governing equations of Hibler (1979) have been followed, except for the modification in rheology, which is described in the Appendix to this paper. Basically, the model has prediction equations for ice thickness and compactness, involving advection, diffusion (for numerical reasons), and thermodynamic growth and decay. Prediction equations for the sea-ice velocity include momentum advection, Coriolis acceleration, sea-surface tilt, air stress, water stress, and internal ice resistance. Hibler's original formulation of internal ice resistance involves a pressure term, a shear viscosity, and a bulk viscosity. That formulation defines a plastic rheology in which stress is independent of strain rate, except when a viscous law applies for very small strain rates. In the present model only a bulk viscosity is used, whereby convergence is resisted in a plastic fashion but divergence is allowed to occur without resistance (which is similar to Hibler's fomulation). The numerical formulation of the present model is the same as that of Hibler (1979), except that an explicit timestepping scheme is used. The latter feature reduces the computer time requirement, since an iterative solution of an implicit timestepping scheme is no longer required. The reduction in computer time is at least threefold.

Hibler's (1979) model includes thermodynamics in the form of growth rates which are specified as a function of ice thickness and time of year. In the present study, a three-layer thermodynamic model of snow-covered sea ice is used. The model was developed by

Semtner (1976a), and it has been shown (Semtner, 1984a) to reproduce both the annual-mean ice thicknesses and the seasonal cycles of the more complicated thermodynamic model of Maykut and Untersteiner (1969, 1971).

The dynamic/thermodynamic ice model has been configured for the same grid orientation and grid spacing as in the ocean study of Semtner (1984b). The grid is shown in Fig. 2, and the grid spacing is 110 km. The model takes a thermodynamic timestep once every fifteen minutes. For reasons of numerical stability, the dynamic timestep is taken to be smaller by a factor of sixty, but has been found to allow the dynamical adjustment to stay in equilibrium with monthly varying forcing. The monthly forcing is computed using observed atmospheric forcing fields for the model grid which were supplied by Walsh. These fields are long-term monthly averages of those which were used in Walsh et al. (1985). Forcing terms are computed according to conventional methods, such as in Parkinson and Washington (1979). Time interpolation on a daily basis is carried out with a cubic spline method similar to that used by Maykut and Untersteiner (1971). To compensate for the use of time-averaged wind data, the drag coefficient for computing air-ice stress and air-water stress has been increased 20% over that of Hibler to 0.0018.

To test the dynamic/thermodynamic ice model prior to coupling to the ocean model, an idealized oceanic heat flux was specified. The flux was taken to vary linearly with latitude from 275 W/m^2 at 60 N to zero at 90 N. Figure 3 shows the predicted equilibrium September ice thickness both with and without the bulk-viscous dynamics. The inclusion of dynamics gives a more realistic simulation of the ice thickness, including a buildup of ice along the Canadian coastline and apparent transport of ice down the east coast of Greenland. Figure 4 (upper) shows that ice transport through the Fram Strait is as large as 0.1 Sverdrup; and Figure 4 (middle) indicates reasonable agreement of the seasonally averaged values of this transport with the results of Walsh et al. (1984). The motion field of the ice at the time of maximal export of ice through Fram Strain, as shown in Fig. 4 (lower), has speeds of approximately 20 cm/sec along the east coast of Greenland, several centimeters a second in the Transpolar Drift, and very small values in areas of convergence toward coastlines. The overall performance of the ice model appears consistent with the observed ice drift of Colony and Thorndike (1984).

The ocean model is essentially the multi-level primitive-equation model of Bryan (1969), but the model has been rewritten to vectorize on high-speed computers such as the Cray-1A. A general description of the finite-difference formulation is given in Semtner (1986a,b). The multi-level ocean model uses up to thirteen levels in the vertical in order to resolve the bathymetric variations shown in Fig. 5. The model is driven primarily by prescribed inflow through the Faeroe-Shetland Channel and to a lesser extent through the Bering Strait. These inflows, as well as the closure parameters for the model, are the same as in Semtner (1984b). The inflow is invariant in time, but the compensating outflow depends on the internally predicted fields. The river inflow around the margins of the Arctic Basin is specified on the basis of monthly values tabulated in Cattle (1985), and cubic splines are used to interpolate daily values.

The coupling between the ice model and the ocean model is relatively straightforward

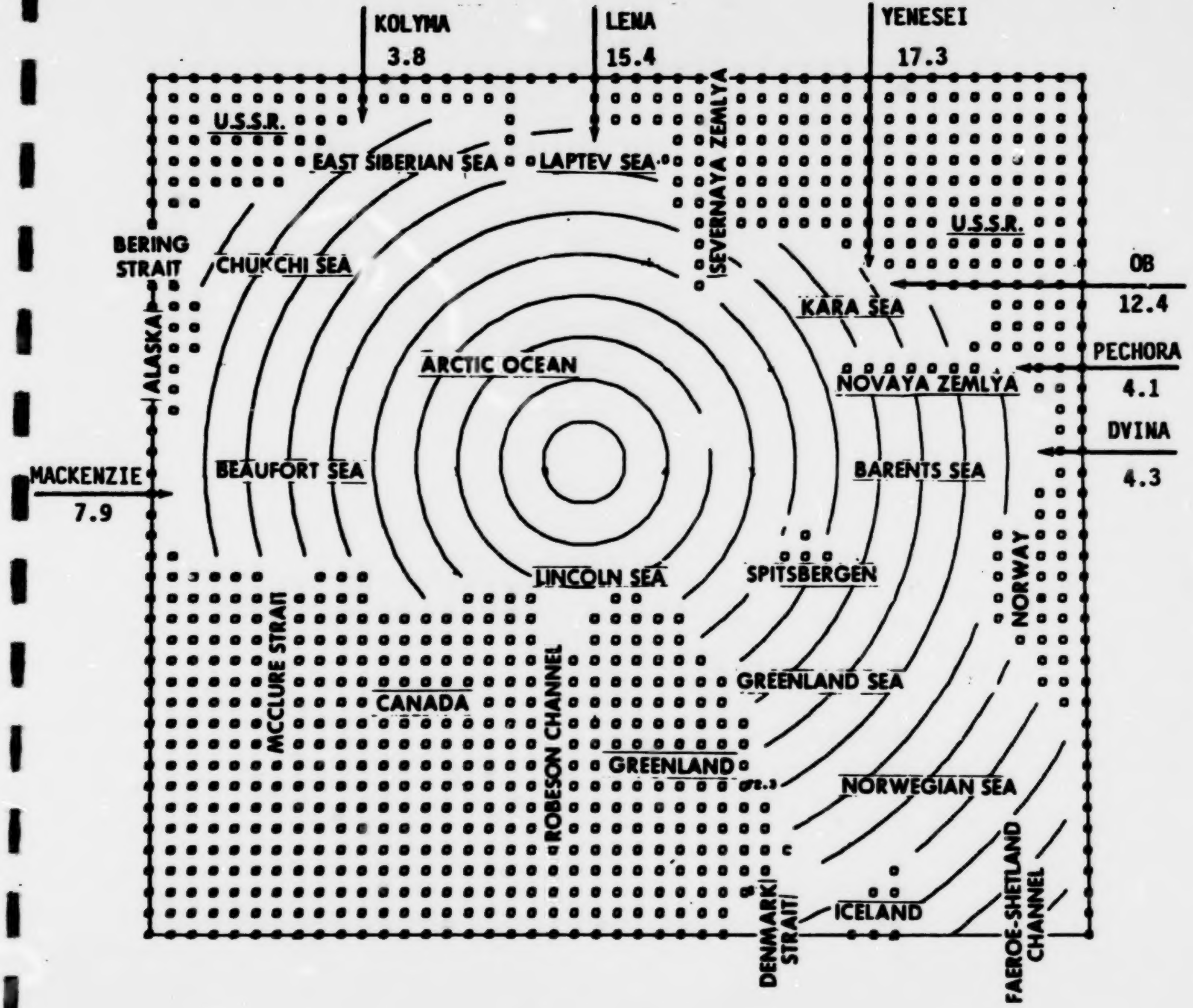

Figure 2. Arctic geography.

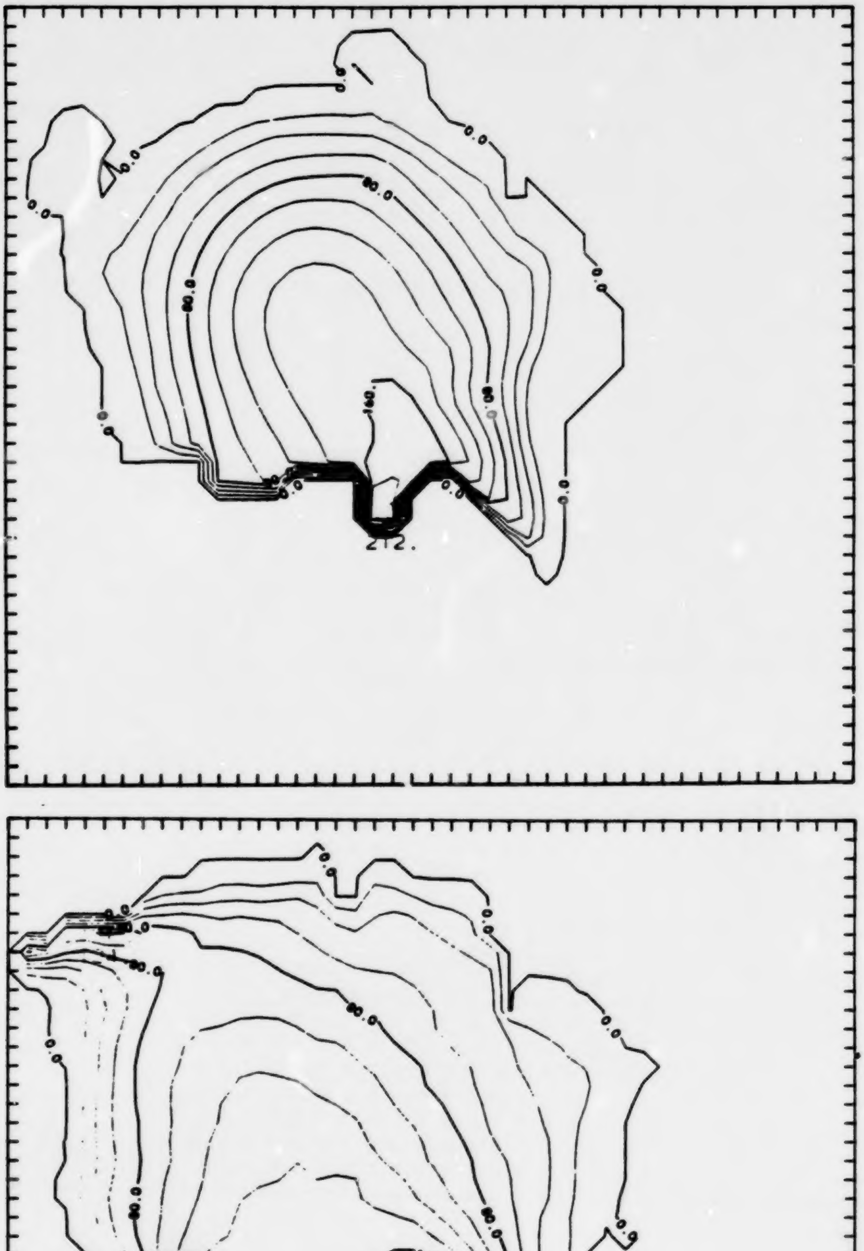

Figure 3. (upper) September 1 equilibrium ice thickness (cm) with no ice dynamics. Atmospheric forcing is from Walsh, and ocean heat flux is prescribed. (lower) September 1 ice thickness when bulk-viscous dynamics is included.

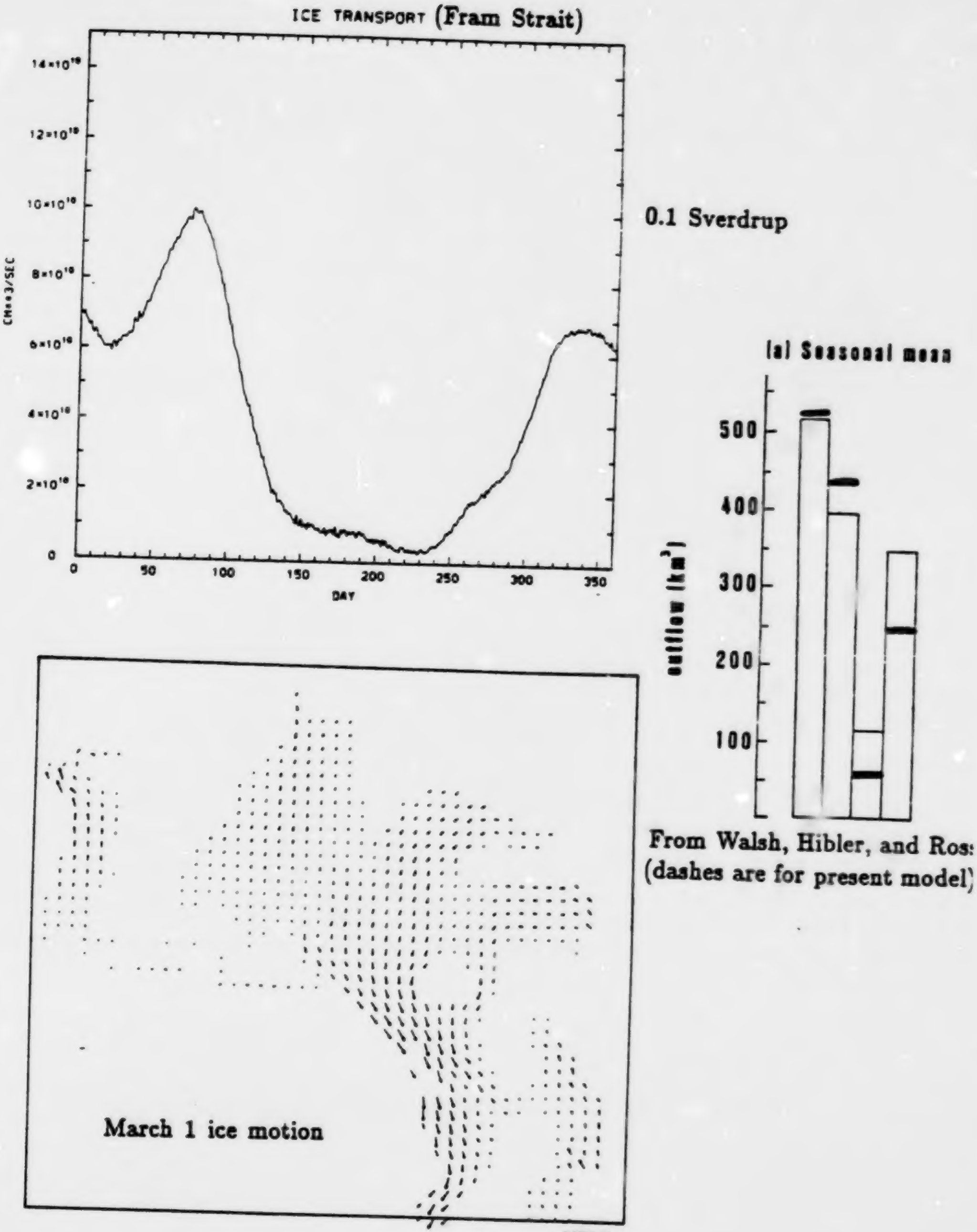

From Walsh, Hibler, and Ros
(dashes are for present model)

Figure 4. (upper) Simulated ice transport through the Fram Strait (middle) Comparison of seasonally averaged transports with the results of Walsh et al. (1984). Dashes are for the present model. (lower) March 1 simulated ice motion field (scale is 20 cm/sec).

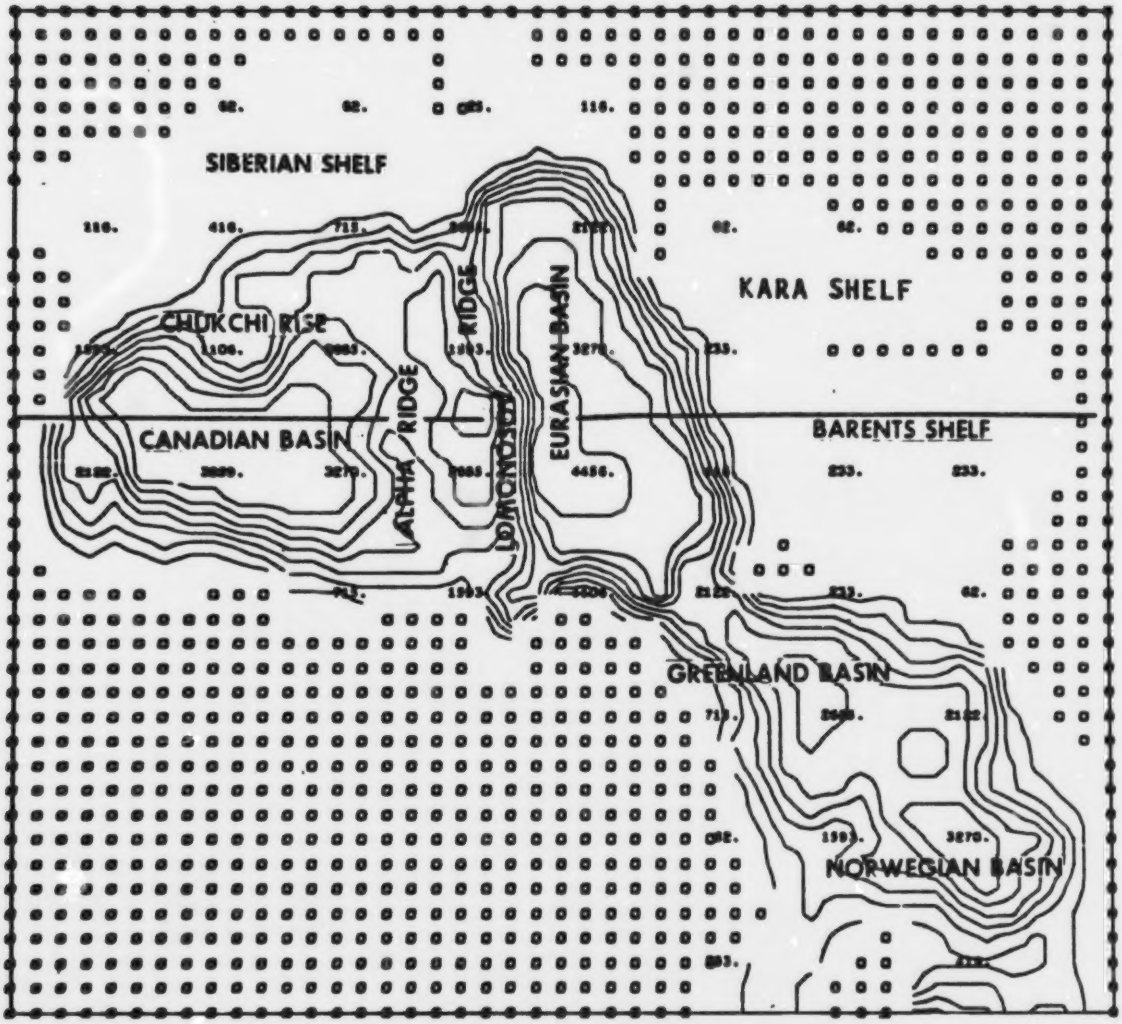

Figure 5. Arctic bathymetry (500 m contour interval).

⑤

in principle, but care had to be taken to preserve consistency and numerical stability in the coupling. Basically, the atmosphere is allowed to drive the ocean over the fraction of each grid cell that is ice-free. For the ice-covered part of the grid cell, the atmosphere interacts with the sea ice in terms of momentum transfer, surface heat budget, and precipitation. In the case of surface melting of snow or snow-free ice, the contribution of fresh water goes to freshening the upper layer of the ocean. At the base of the ice, momentum is exchanged with the upper ocean, ablation or accretion of ice occurs depending on the net balance of conductive flux within the ice and oceanic heat flux into the upper ocean, and the water is either freshened by melting or made saltier by brine rejection.

3. RESULTS OF THE COUPLED MODEL

The ice ocean model has been integrated for twenty years to obtain a quasi-equilibrium solution for the surface and intermediate depths. This section describes the predicted fields, starting with the ice and working downward into the ocean.

Figure 6 (upper) shows the predicted ice thickness on 1 January of year 20. The observed ice line from Vinje (1977) is also shown. There is very close agreement between predicted and modelled ice extent, the only discrepancy being an underprediction of the ice extent midway down the east coast of Greenland. This is probably related to the lack of an offshore oceanic current in the model which is analogous to the observed Jan Mayen current (cf. Fig. 9). The predicted ice thickness is maximal along the Canadian Arctic coast, in general agreement with observations, but the overall thicknesses are too small. Walsh et al.(1985) obtained a similar result using basically the same atmospheric forcing data. This may indicate slight errors in the net surface flux. Maykut and Untersteiner (1969, 1971) have shown that the equilibrium thermodynamic ice thickness is very sensitive to small changes in the components of the surface flux. In future experiments, some consideration will be given to a closer examination of the prescribed fluxes.

Figure 6 (lower) shows the predicted surface temperature (ice or open ocean) for January. Temperatures of approximately -30 C occur over the thick ice in the central Arctic Basin. Relatively warmer temperatures are found at the surface of thinner ice around the margins, where heat conduction through the ice presumably plays a role. A sharp change of approximately 10 C occurs at the ice edge (the -2 C line). In the ice-free portions of the Greenland and Norwegian Seas, the northward advection of heat along the Norwegian coast into the Barents Sea and also to the west of Spitsbergen are apparent.

Figure 7 (upper) shows streamlines of ice motion. Two distinct patterns are evident–a large relatively nondivergent clockwise circulation in the Central Arctic and a more linear flow away from the Eurasian coast, through the Fram Strait, and down the east coast of Greenland. The pattern of ice growth and decay, shown in Fig. 7 (lower), indicates that relatively small growth (less than 20 cm), which would be typical of the thermodynamic growth of thick ice, occurs in the clockwise circulation. However, the growth along the Eurasian coast is much larger, due to the offshore motion of the ice, which leaves open water and relatively thin ice behind. Note that a compensating melting occurs when

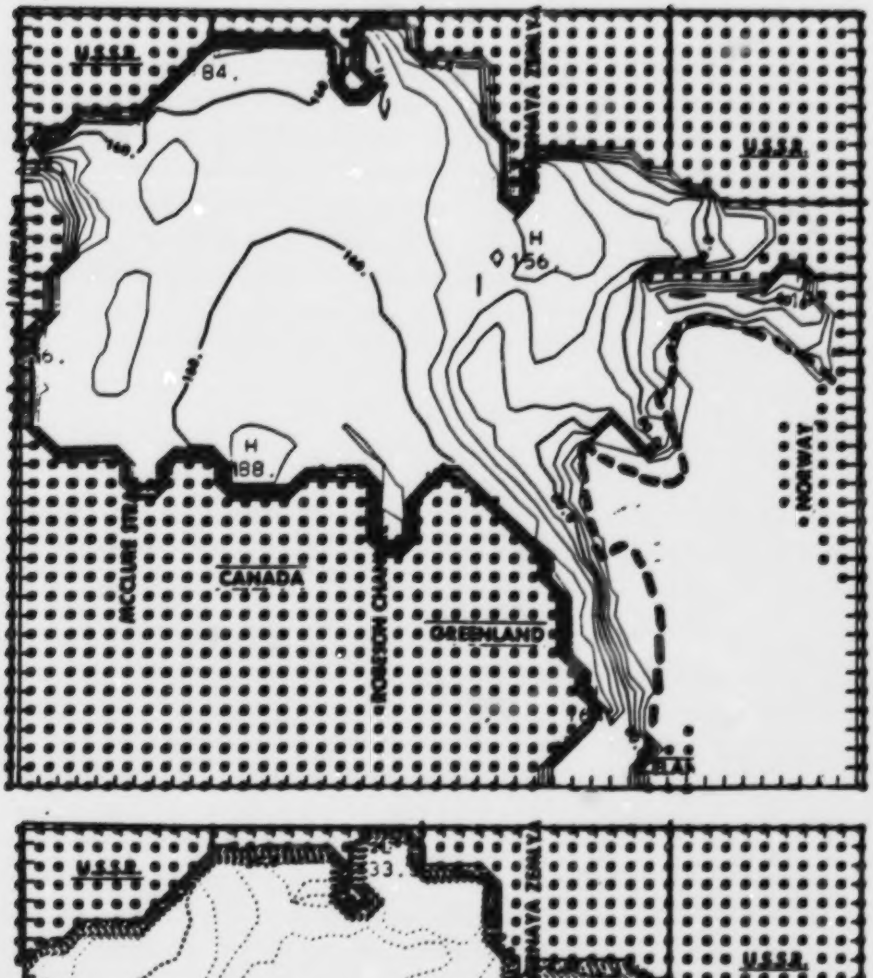

Figure 6. (upper) Simulated January ice thickness (20 cm contour interval) with observed ice line shown dashed. (lower) Simulated January surface temperature of ice and ocean (2 C contour interval).

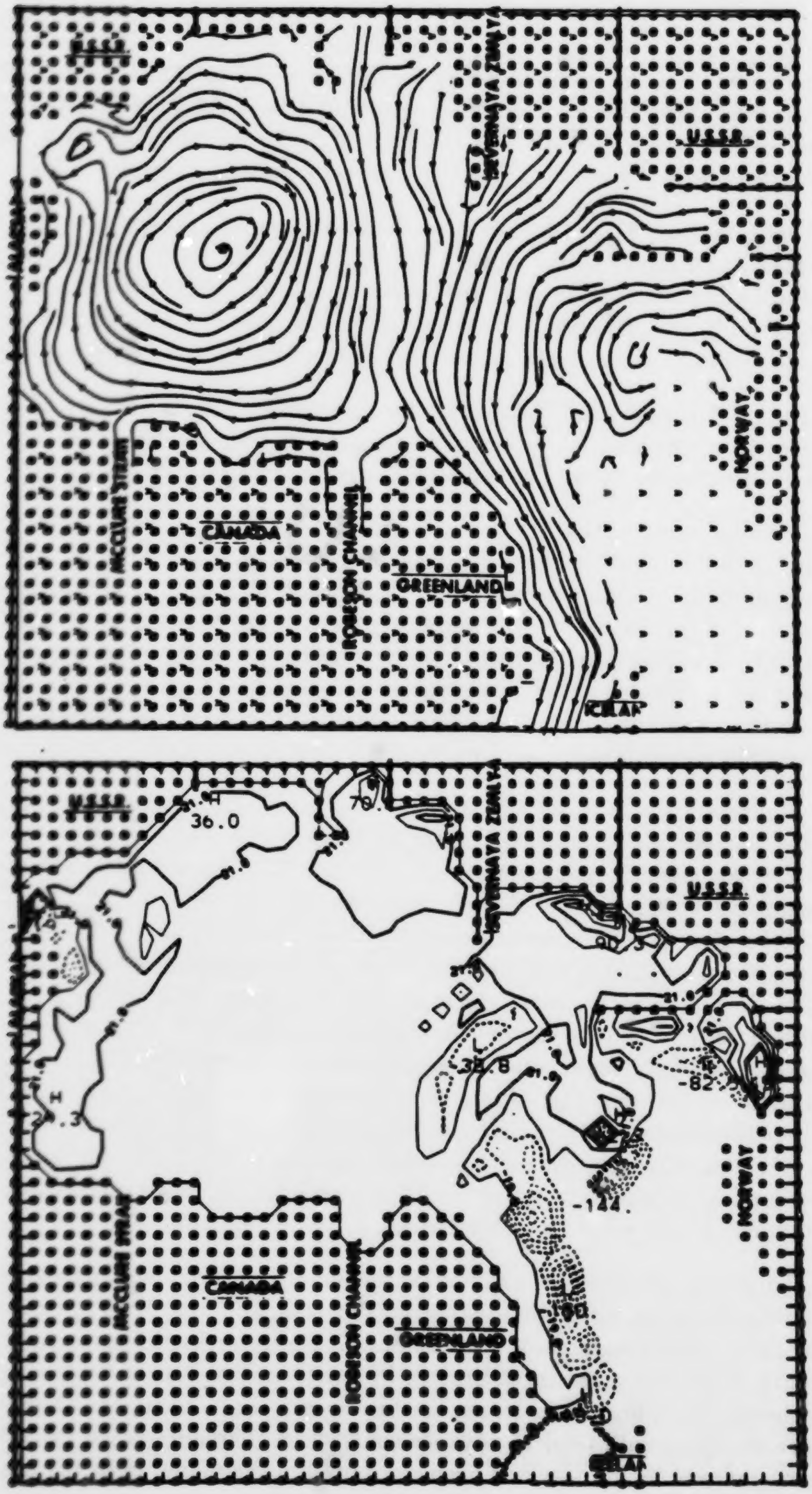

Figure 7. (upper) Streamlines of ice motion in January. (lower) Ice growth during January (20 cm contour interval).

the ice encounters the warm water of the Greenland Sea. Thus the ice drift through Fram Strait constitutes a mechanism for transporting low-salinity ice out of the Arctic Basin and leaving behind extruded salt and the heat of fusion released to the atmosphere. Viewed another way, it represents a poleward transport of heat and salt.

Figure 8 (lower) shows the simulated January surface salinity in the model. Even in winter, the surface salinity over much of the Arctic Basin is 32 parts per thousand or less, indicating stability relative to deeper values which are typically in excess of 34 parts per thousand. An exception is the southern Barents Sea as well as much of the eastern Greenland Sea. We shall examine these regions further in subsequent discussion.

Figure 8 (upper) indicates that the observed summertime surface salinity is not too different from the simulated January field, except near the Eurasian marginal seas, where intensified seasonal runoff freshens the near-shore water.

Turning now to the predicted oceanic fields, Fig. 9 shows the streamlines of the January velocity fields in the uppermost two levels of the model. The surface flow includes the ageostrophic Ekman component, which leads to a slight convergence of the clockwise circulation in the Central Arctic and to a cross-stream component of flow in the Transpolar Drift and East Greenland Current. The known major geostrophic current systems are more evident in the flow at 40 m, where there are clear representations of the Beaufort Gyre, the Transpolar Drift Stream, the East Greenland Current, the Norwegian Current, and a Barents Shelf circulation.

Figure 10 give a more quantitative picture of the oceanic circulation. A northward flowing current along the west coast of Norway with speeds of order 10 cm/sec splits into a weak west Spitsbergen component and a stronger Barent Sea current which is recognizable all the way to Novaya Zemlya. This is evidently why the ice edge shown in Fig. 6 (upper) has the configuration it does. East Greenland Current speeds cannot be determined from the figure, because many of the vectors are too long to be plotted, but speeds are typically 20 cm/sec or more near the coast. In the Central Arctic, most of the anticyclonic flow is at a few centimeters per second. The net transport of the vertically integrated velocity field, whose streamfunction is shown in Fig. 10 (lower), is about 6 Sverdrups in the Beaufort Gyre, 20 Sverdrups in the Greenland Gyre, and 7 Sverdrups in the shallow Barents Sea. The gyre circulations tend to follow closed lines of f/H (cf. Fig. 5), suggesting equivalent barotropic response. The relatively large transports of the Greenland and Barents gyres probably derive from the favorable forcing of the tangential component of the wind integrated around lines of constant f/H.

To give some idea of the annual variation of the three main gyres, Fig. 11 gives a plot of monthly transports of the circulations. Seasonal variations are enhanced by the rapid response of nearly barotropic circulations. It is interesting to note that the Greenland and Barents circulations are most intense by far from late fall to early spring and that they can thereby collaborate to transport heat northward during that time of year when the sea-ice margin would tend to advance southward. The northward transport of heat by the Greenland gyre in January has been computed in the model to be 0.4 petawatts, which is a

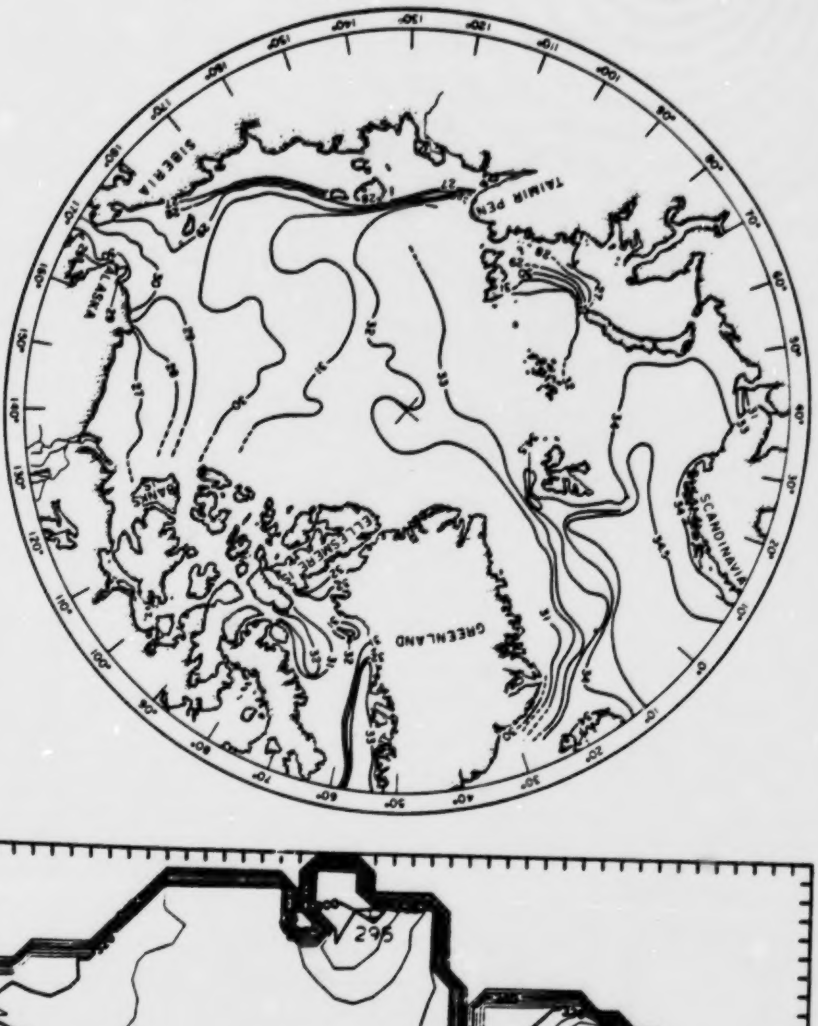

Figure 8. (upper) Observed summer surface salinity (from Coachman and Aagaard,1974). (lower) Simulated January surface salinity. Contours intervals are 1.0 and 0.5 ppt, respectively.

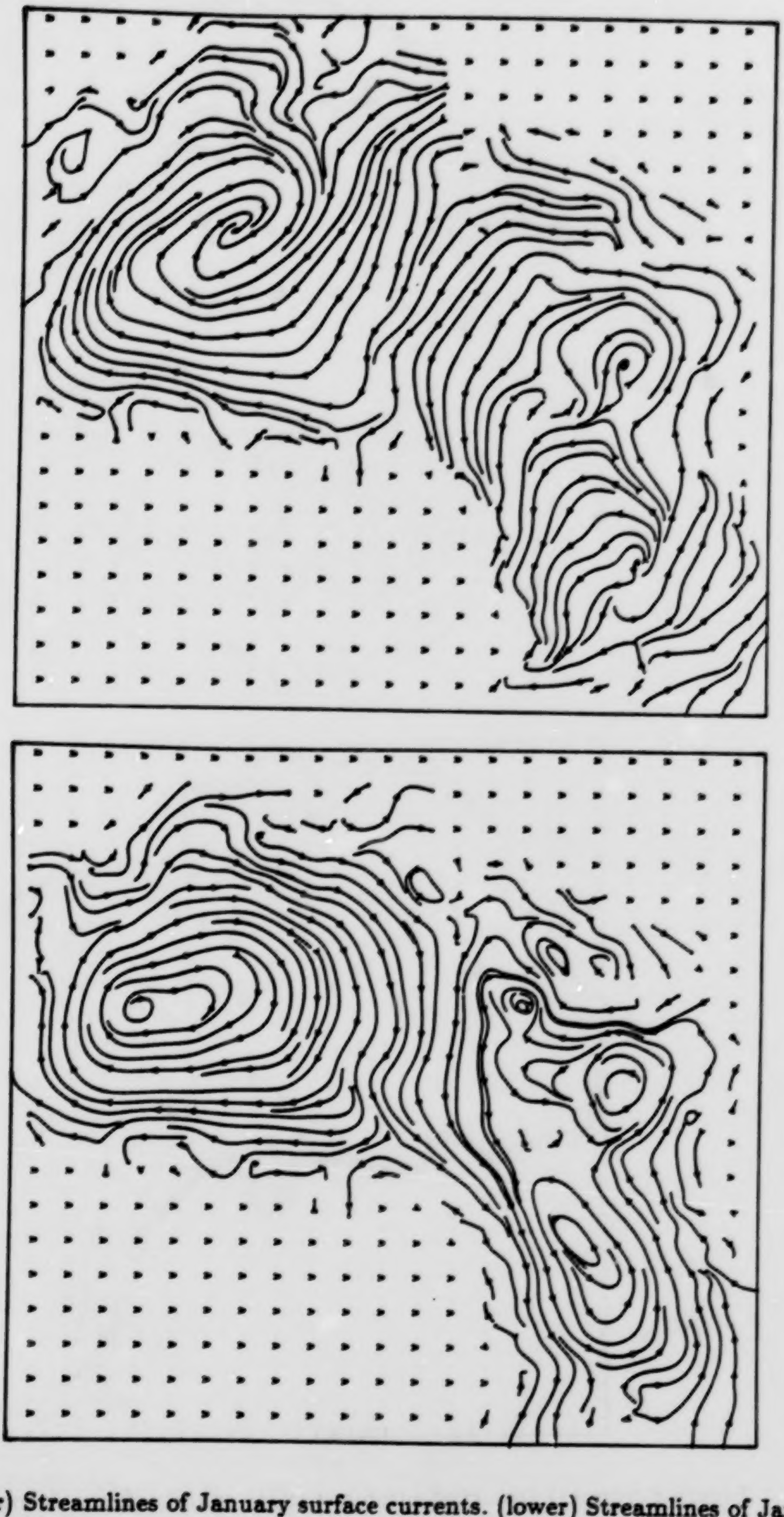

Figure 9. (upper) Streamlines of January surface currents. (lower) Streamlines of January currents at 40 m depth.

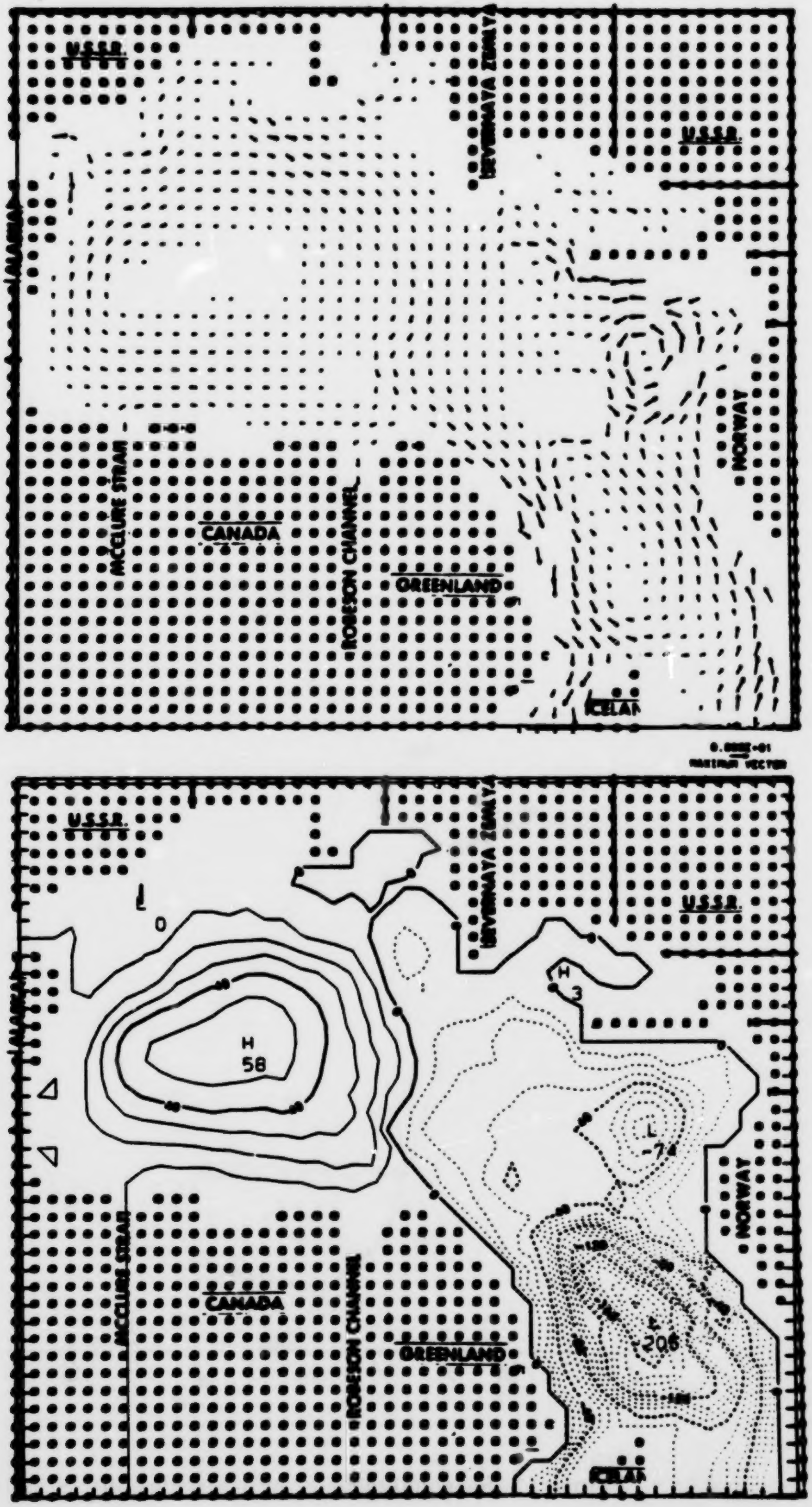

Figure 10. (upper) January velocity field at 40 m depth. (lower) Mass transport streamfunction for January (1.0 Sverdrup contour interval).

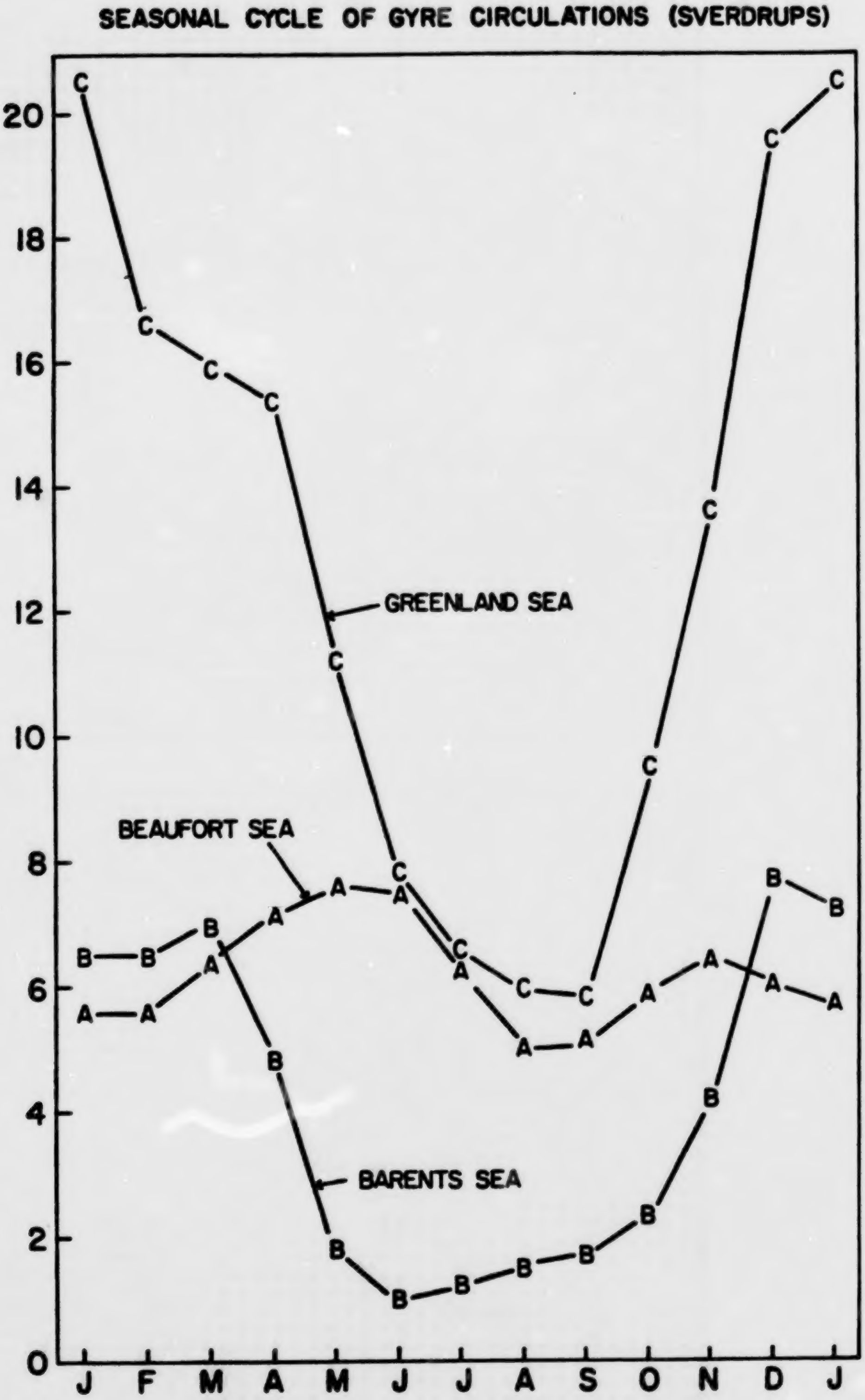

Figure 11. Seasonal cycle of gyre circulations (Sverdrups).

large value for heat transport even by mid-latitude standards. It is this mechanism which maintains ice-free conditions in much of the Greenland and Barents Seas throughout the winter.

An important feature of the observed Arctic Basin circulation is a layer of warm (i.e. above 0 C), highly saline water at several hundred meters depth, which is maintained by inflow through the Fram Strait. This layer is though to circulate cyclonically, in opposition to the surface flow (Coachman and Aagaard, 1974). Figure 12 (lower) shows that a layer occurs in the simulation which is above 0 C throughout the Arctic Basin, with the inflow northwest of Spitsbergen showing tabulated temperature and salinity of 1.2 C and 34.9 ppt, respectively. The adjacent layers above and below the layer at 565 m exhibit sub-zero temperatures over much of the Arctic Basin.

Figure 12 (upper) shows streamlines of the simulated Atlantic layer circulation. The circulation is cyclonic in the Eurasian Basin, but anticyclonic in the Canadian Basin. The latter situation disagrees with the circulation inferred from limited observations of the heat content of the Atlantic layer. The circulation in the Greenland Sea is cyclonic and facilitates the inflow of warm Atlantic water through Fram Strait. The circulations at 565 m are characteristic of those in the deeper levels as well.

An examination of the simulated temperatures and salinities below 1000 m indicates that wintertime deep convection occurs down to 1600 m at two sites in the Greeland Sea. One site in the East Greenland Sea produces 1.8 C water of 35.0 ppt salinity, while the other produces 1.5 C water of 34.95 ppt salinity in the Northern Greenland Sea. These values are plotted on Fig. 13 (adapted from Swift, 1984). They fall relatively close to the observed T,S characteristics of water masses labeled NEADW and NWADW which overflow the Faeroe-Shetland Channel and the Denmark Strait, respectively. Since the initial inflow conditions were substantially different, i.e. offscale in Fig. 13, the numerical model seems to do a fairly good job of producing intermediate water masses.

It should be noted that in the twenty year integration of the model, no source of abyssal water develops. This could be due to two things. On the one hand, deep convection of the central Greenland Sea may be inhibited by lateral heat diffusion and the lack of preconditioning by mesoscale disturbances. On the other hand, renewal processes due to plume dynamics such as might occur near the Barents Sea, where water of salinity 34.9 ppt exists below the ice at its margin, are not included in the model physics. In the future, some consideration should be given to the parameterization of these processes within the model for longer term integrations.

4. INFLUENCE OF THE OCEAN ON ICE AND CLIMATE

In many climatic studies, sea ice is included as a prognostic variable but the effects of ocean circulation are omitted. For example, the studies by Manabe and Stouffer (1980) and Washington and Meehl (1984) of the effect of increased atmospheric carbon dioxide on climate assumed that the ocean could be represented as a motionless mixed layer with only

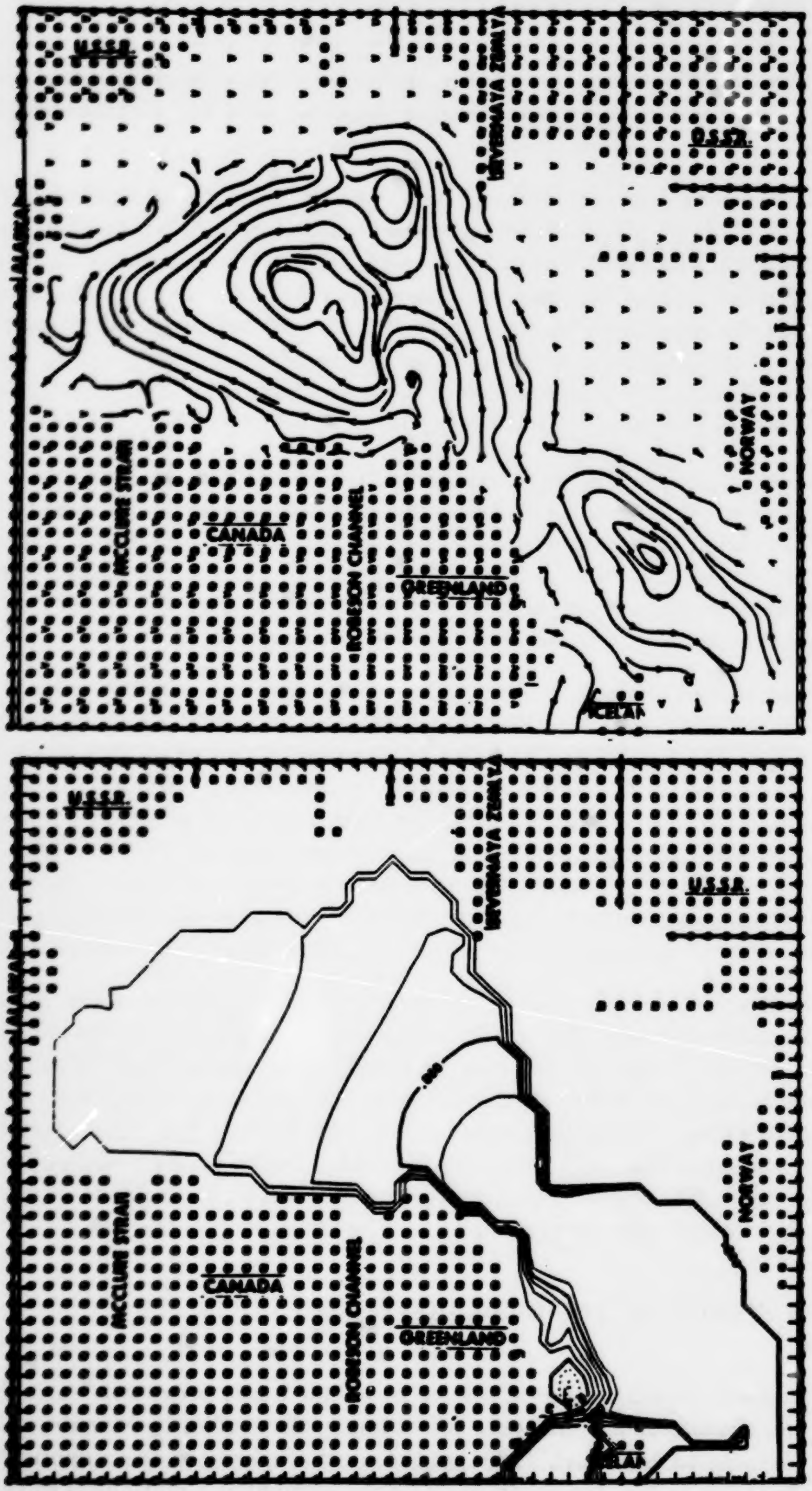

Figure 12. (upper) Simulated circulation in the Atlantic layer (565 m). (lower) Simulated temperature of the Atlantic layer (only temperatures below 1.0 C are shown, contour interval 0.2 C).

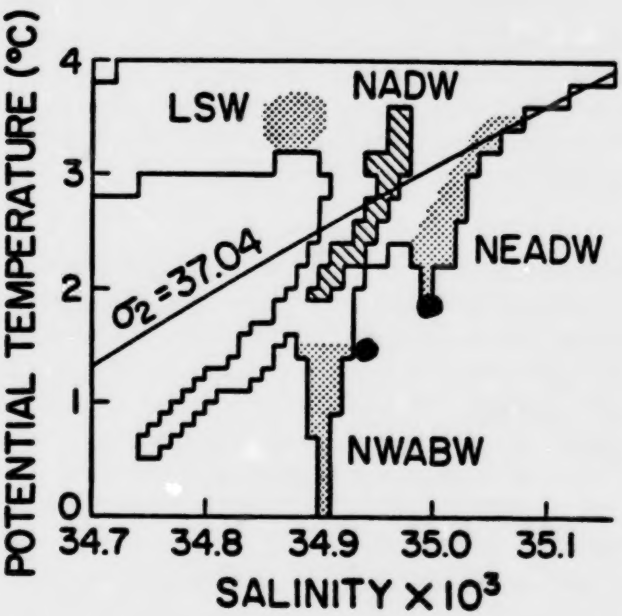

Figure 13. A temperature-salinity diagram of observed North Atlantic deep waters colder than 4 C. The masses indicated by NEADW and NWEAW are thought to originate from overflows out of the Greenland/Norwegian Sea. Adapted from Swift (1984). Also shown (by dots) are the T,S characteristics of the two intermediate water sources in the model after twenty years of integration.

a seasonal cycle of heat storage. The adequacy of this approach can be assessed within the context of the present ice-ocean model by running a case in which the ocean is replaced by a mixed layer of the same thickness as the upper layer of the full ocean model.

We have already seen that oceanic heat transport is important in maintaining the ice edge in the Greenland and Barents Seas. This result is similar to that obtained by Hibler and Bryan (1984), but the results are stronger in the sense that no interior diagnostic forcing was used in the ocean model. One might think that lesser oceanic effects on the ice edge would prevail in other seasons; however Fig. 14 indicates otherwise. The minimal ice extent in early September is indicated by Fig 14 (lower) to be unrealistically large when ocean circulation is omitted, in comparison with the observed edge or the modelled edge with active ocean circulation (Fig. 14, upper). Figure 15 shows that active ocean circulation also affects the compactness of sea ice at the time of mimimum ice extent. The isoline of 0.78 compactness in the case with active ocean circulation is nearly coincident with the 0.90 isoline in the mixed layer case. Similarly, the 0.90 isoline north of Greenland for active circulation coincides with the 0.96 isoline for the mixed-layer case. Such compactness differences of order 10% can have substantial effects on the net surface heat budget.

Insight into the mechanisms by which the minimum ice extent and compactness are affected by ocean circulation can be obtained by looking at the predicted ocean temperatures below the surface mixed layer in January (Fig. 16 upper). Water with temperatures above -1.6 C is predicted to exist near the Alaskan coast and and in the Kara and Laptev Seas. Water of temperature between -1.8 and -1.6 C is found along the coast in the Chukchi and East Siberian Seas. Such temperatures above freezing must be maintained by the oceanic circulation, whereby surface convergence in the Central Arctic (cf. Fig. 9, upper) is compensated by net upwelling around the margins. The result is a net heat flux which thins the existing ice cover during the winter, predisposing the ice to have an enlarged areal retreat in the summer season relative to the case of the mixed layer only.

The net heat flux underneath the ice cover for the month of January is shown in Fig. 16, lower. Heat fluxes vary by two orders of magnitude over the region. Along the ice margin in the vicinity of East Greenland, the Barents Sea, and the Bering Strait, heat fluxes which average 180 W/m^2 sustain melting and prevent the advance of the ice cover southward. (In the open water to the south, surface fluxes can be even greater—typically 250 W/m^2.) In the Central Arctic, heat fluxes are less than 10 W/m^2 over large areas, but there are smaller zones with fluxes of several tens of Watts per square meter. These smaller zones appear to be associated with upwelling of water from the Atlantic layer near the coast in the Kara, Laptev, and Chukchi Seas or in the vicinity of the continental slope of the southern Eurasian Basin. The latter region has been suggested to be an area of enhanced oceanic heat flux, relative to the rest of the ice-covered region (Aagaard and Greisman, 1975).

An additional effect on the sea ice other than that of oceanic heat flux is that of ocean currents, which influence ice not only through momentum exchange but also through the the tilting of the sea surface. Figure 17 indicates the net effect on ice motion due to the

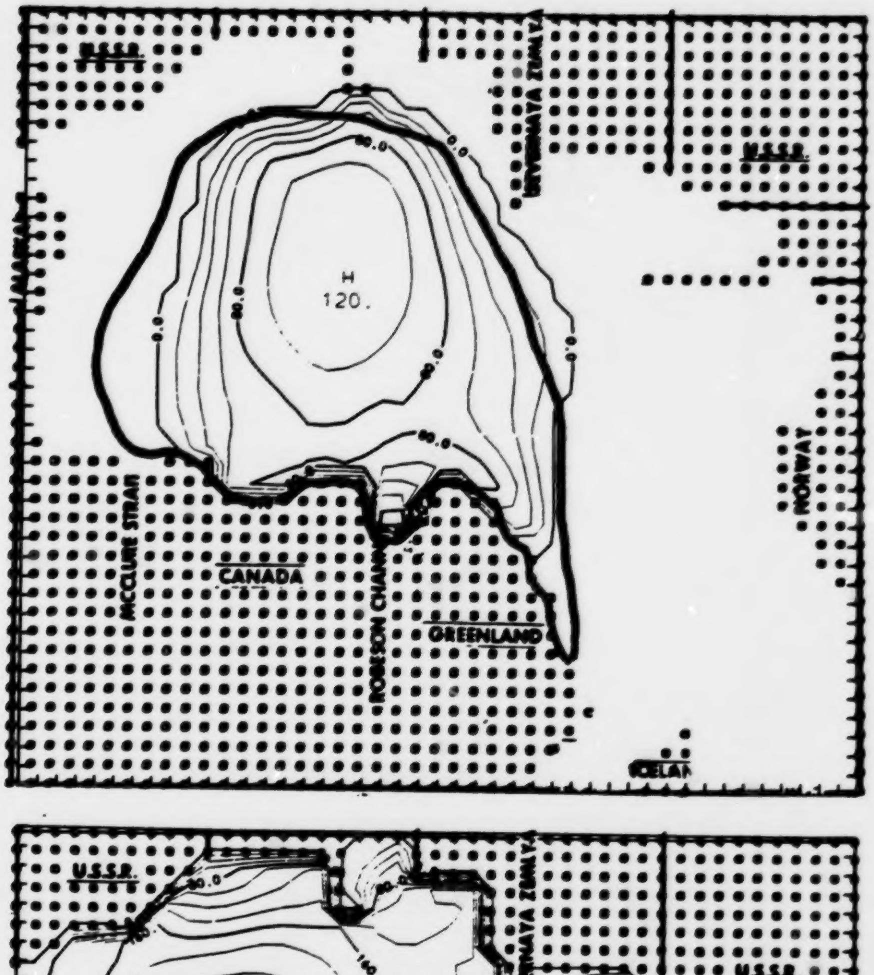

Figure 14. (upper) September ice thickness (cm) when ocean circulation is included. Heavy line is the observed summer minimum. (lower) September ice thickness (cm) when only an ocean mixed layer is used.

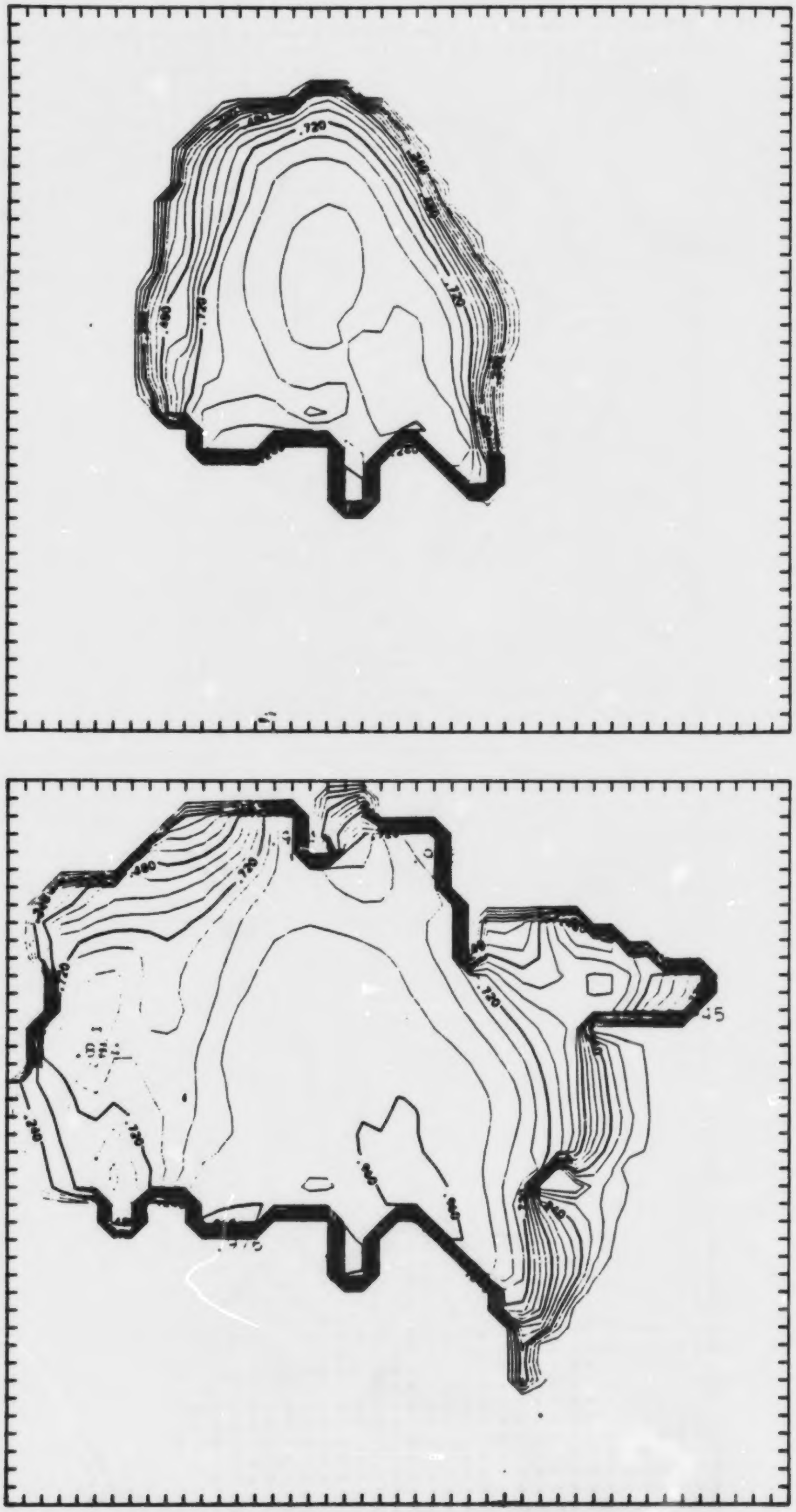

Figure 15. (upper) September ice compactness when ocean circulation is included. Contour interval is 6 %. (lower) September ice compactness when only an ocean mixed layer is used. Contour interval is 6 %.

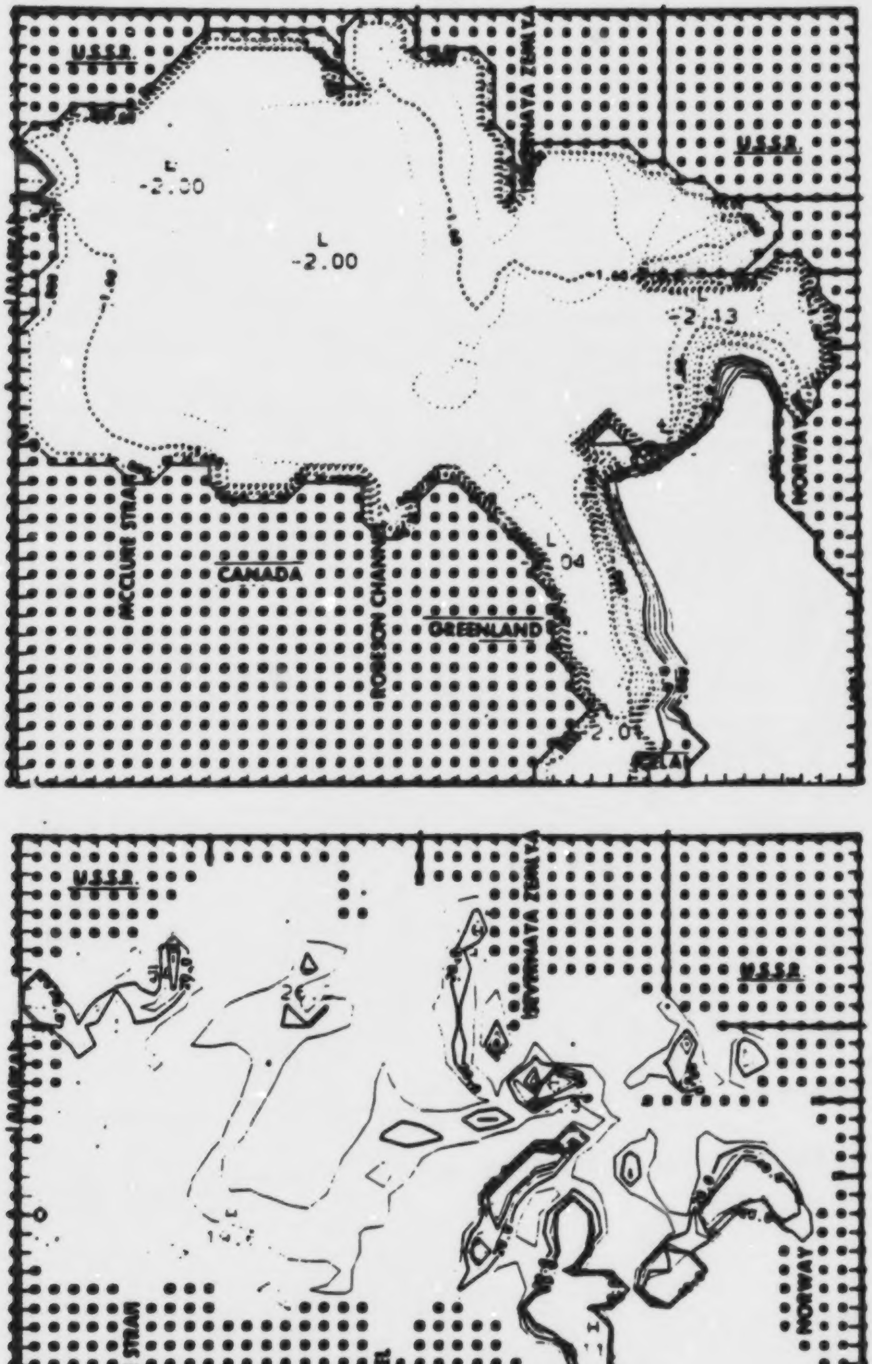

Figure 16. (upper) January ocean temperatures at 40 m. (lower) January oceanic heat flux to the sea-ice base (contour interval 10 W/m^2).

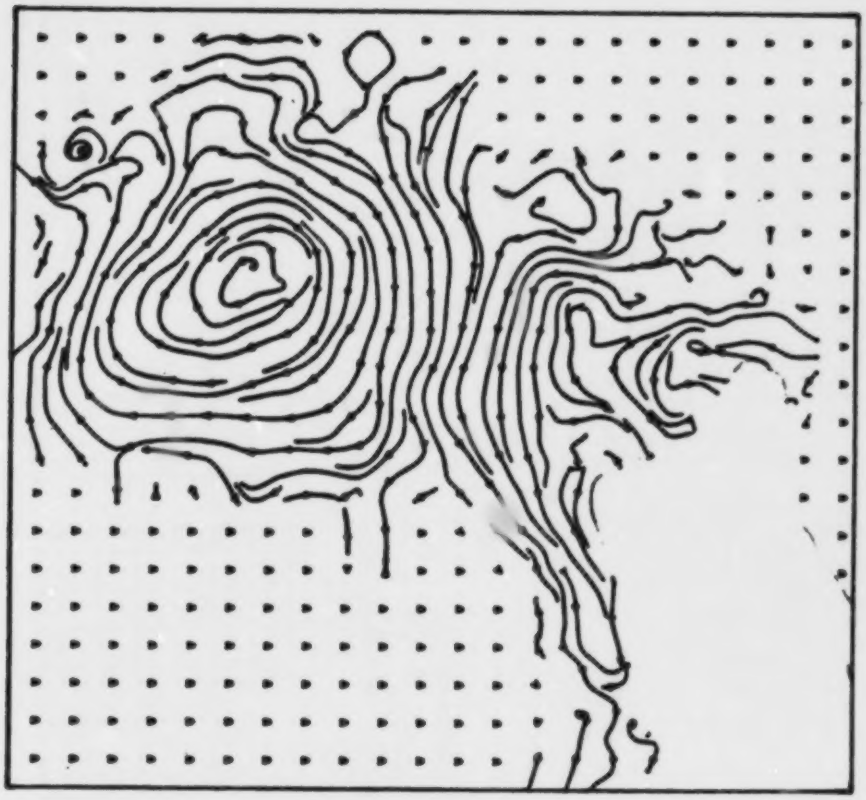

Figure 17. Streamlines of the difference in April ice motion due to active ocean circulation.

inclusion of ocean circulation. The pattern is very similar to that of the upper ocean (as it should be). In particular, the ocean facilitates the export of ice from the Eurasian coastline through the Fram Strait and down the East Greenland coast. In the Beaufort gyre, the net effect of ice ocean drag and surface tilt is to augment the ice drift with a relatively nondivergent anticyclonic component of circulation.

A final influence of ocean circulation is on the climate of the Arctic. Through the combined effects of heat transport, ice motion, surface elevation, and ice albedo feedback, the temperature and vapor pressure of the underlying surface are affected. Figure 18 shows the resulting changes in surface temperature for both January and September. Little change in temperature occurs in areas which remain ice covered, since heat conduction through sea ice is a relatively small component of the surface heat budget. However in areas which lose their ice cover, large differences result in surface temperature (and therefore in saturation vapor pressure as well). These changes can be expected to have a noticable effect not only on the regional climates near the temperature maxima, but also on the stationary wave patterns and precipitation zones of the entire polar region.

5. ARCTIC SENSITIVITY TO ENVIRONMENTAL CHANGE

The polar environment is commonly regarded to be fragile and vulnerable to anthropogenic changes. The Arctic Ocean in particular is thought to be vulnerable in two different ways. As a part of the global climate system which is especially sensitive to atmospheric temperature increase because of ice-albedo feedback, it may respond more dramatically to CO_2-induced climate change than other climatic components. Such has been suggested by the studies of Manabe and Stouffer (1980) and Washington and Meehl (1984), although the ocean was only considered to consist of a mixed layer. In addition, the Arctic Ocean may be sensitive to the effect of river diversions such as those proposed for the next several decades by the Soviet Union. A summary of previous research on the possible effects of such diversions is given in Cattle (1985). Depending on whether the erosion of vertical stability of the water column or a reduced horizontal transport of heat into the marginal seas is thought to dominate, one expects the extent of Arctic sea ice either to decrease or increase, respectively. The study of Semtner (1984b) is the only three-dimensional study that has been done to date; and within the limitations of not including the seasonal cycle of atmospheric forcing or an explicit formulation of ice processes, it suggests that little change will result from river diversions. Nevertheless, it appears that because of the environmental importance of the issues regarding both river diversions and carbon dioxide increase, some brief examination of the response of the present coupled ice-ocean model to environmental changes should be made.

Consider first the effect of massive Soviet river diversions. We rerun the experiment of Semtner (1984b) in which one-third of the flow is cut off from four major rivers (the Yenesei and Ob, which flow into the Kara Sea, and the Pechora and Dvina, which flow into the Barents Sea). A two-year continuation integration is carried out with the coupled model, at the end of which little change appears to be occuring in the water properties of the shallow Kara and Barents Seas. Figure 19 (lower) shows the seasonal cycle of ice extent

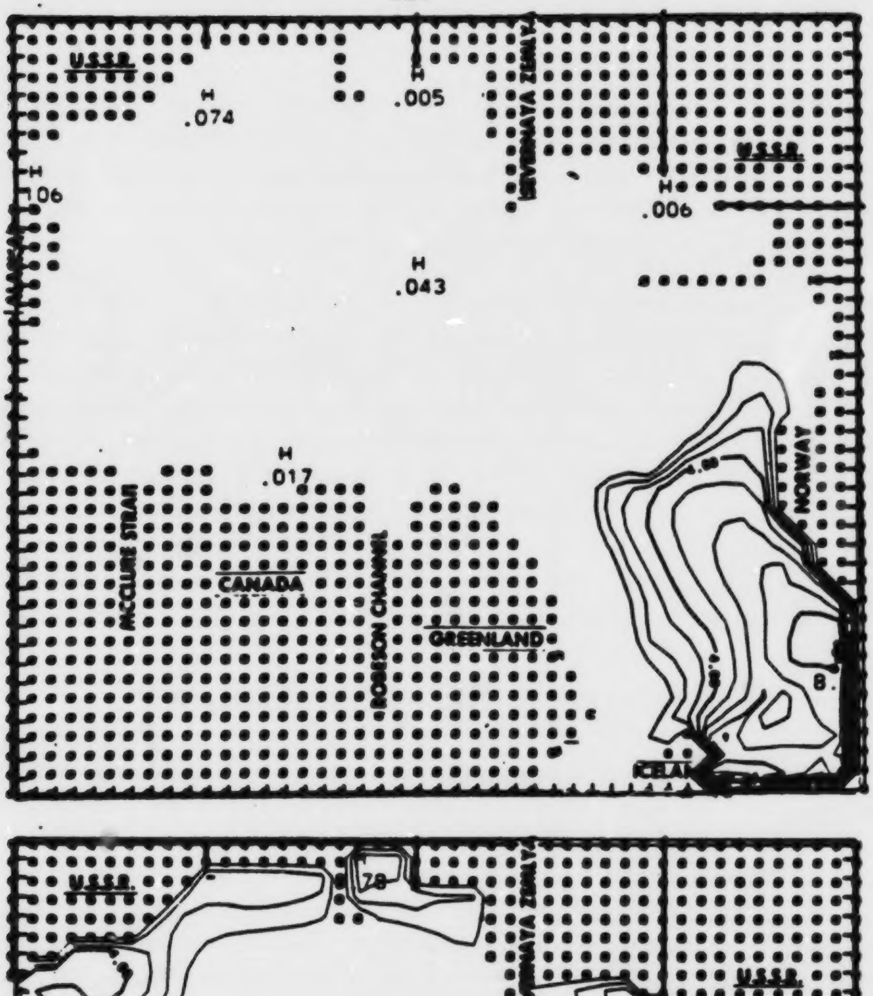

Figure 18. (upper) The difference in January ocean surface temperature due to active circulation. Contour interval is 1 C. (lower) The difference in September ocean surface temperature due to active circulation .

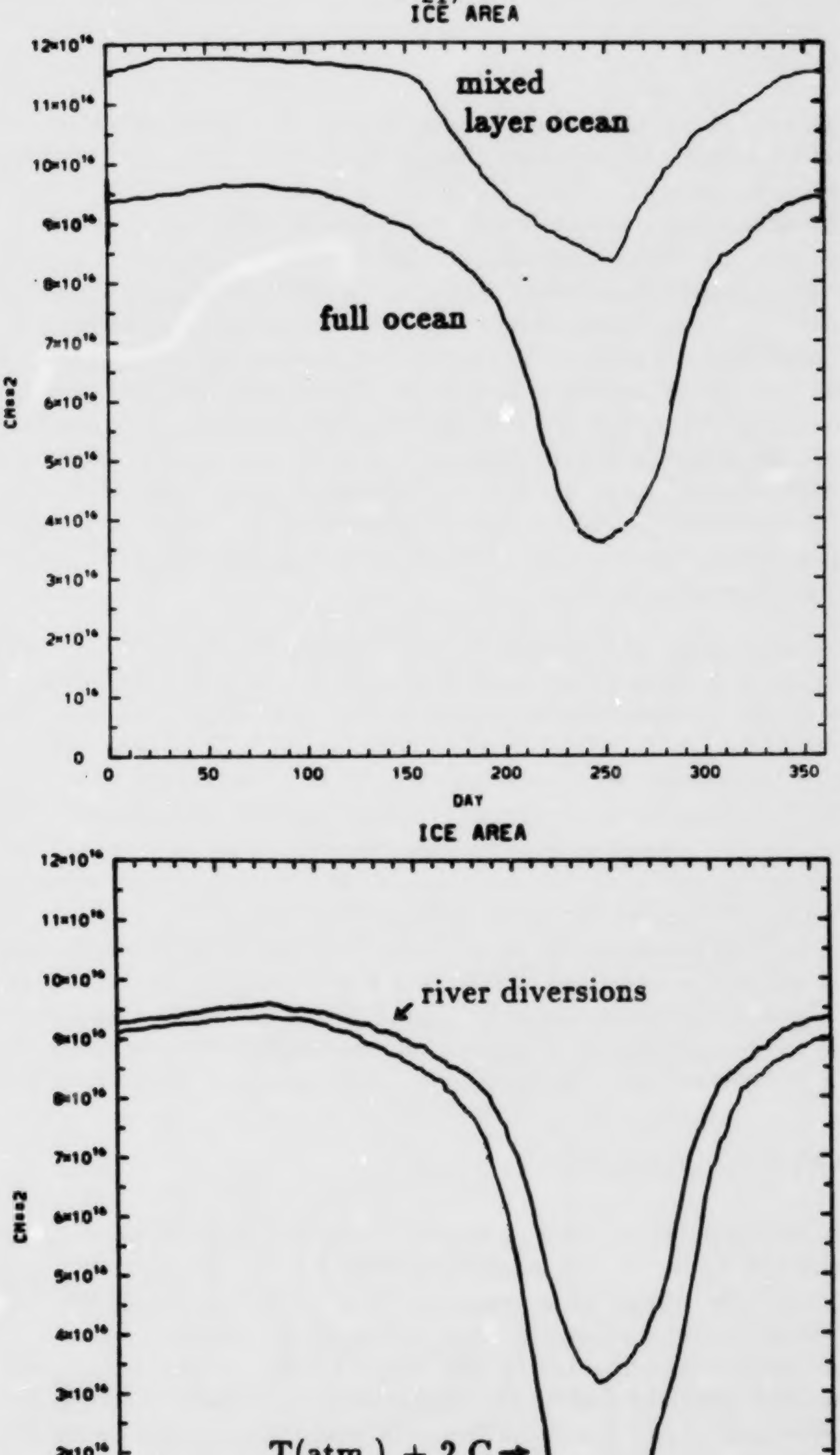

Figure 19. (upper) The annual cycles of ice area for the standard run and for the case of a mixed layer ocean. (lower) The annual cycles of ice area for the cases of maximal Soviet river diversions and of 2 C atmospheric temperature increase.

for the second year of the integration. For comparison, Fig. 19 (upper) shows the seasonal cycle of total ice area for the standard runs of the coupled model and of the model with only a mixed-layer ocean. The effect of the maximal amount of proposed river diversions is essentially negligible in comparison with the effects of excluding oceanic heat transport. This suggests that few effects other than local ones would result from large river diversion schemes. To get a better idea of the local effects, Fig. 20 (center panel) shows the predicted change in ice concentration (contour interval 5%). The main effect is a slight increase in ice concentration at the ice margin in the Barents Sea. Interestingly enough, this agrees with the results of the empirical study of Holt et al. (1984), who found a connection between reduced runoff from the rive Ob and subsequent increased ice concentration in the Barents Sea (cf Fig. 20, left panel). The model also gives an indication (cf Fig. 20, right panel) that somewhat thicker ice will result not only in the Barents Sea but also in the southern Kara Sea. Since the observational data base is inadequate to describe ice thickness variations, this latter prediction of the model cannot be checked against the data, but it provides a suggestion for future observations.

Next, an experiment of two years duration was carried out as a continuation of the standard run, but with the atmospheric temperature increased by 2 C throughout the year, as might occur from carbon dioxide doubling in the atmosphere. The result is a dramatic disappearance of the sea ice in late summer, as shown in Fig 19 (lower). This is consistent with other studies already mentioned above and also with the study of Parkinson and Kellogg (1979). It should be noted that since the modelled sea ice thickness of the standard run is somewhat low relative to observations, the result may be more representative of, say, a 4 C change, which is still not unreasonable to expect in polar regions from carbon dioxide doubling. One important aspect of the present simulation is that no catastrophic disappearance of ice throughout the year occurs. The possibility of such an occurrence has been mentioned (Ewing and Donn, 1956), and the present simulation with active ocean circulation suggests that this would not happen. In fact, as Fig. 21 shows, the wintertime extent of sea ice is only slightly reduced by increased atmospheric temperature, with the main areas of influence being in the Barents Sea and along the southeast coast of Greenland.

6. SUMMARY AND CONCLUSIONS

The oceanography and climate of the Arctic have been investigated using a coupled ice-ocean model of the Arctic Ocean and Greenland Sea. The ice component uses a 3-layer thermodynamic formulation due to Semtner (1976a) and a dynamic formulation similar to that of Hibler (1979) but with a simplified rheology suggested by him. The ocean model is similar to that of Semtner (1984b) and it is fully coupled to the ice model. The combined model is driven by Walsh's observed monthly atmospheric forcing, observed river runoff, and specified inflow through the Faeroe-Shetland Channel and Bering Strait. Model simulations have been carried out for a twenty year quasi-equilibrium and for two shorter runs which examine the effects of Soviet river diversions and of CO_2-induced atmospheric temperature increase.

The quasi-equilibrium solution gives a realistic representation of the seasonal cycle

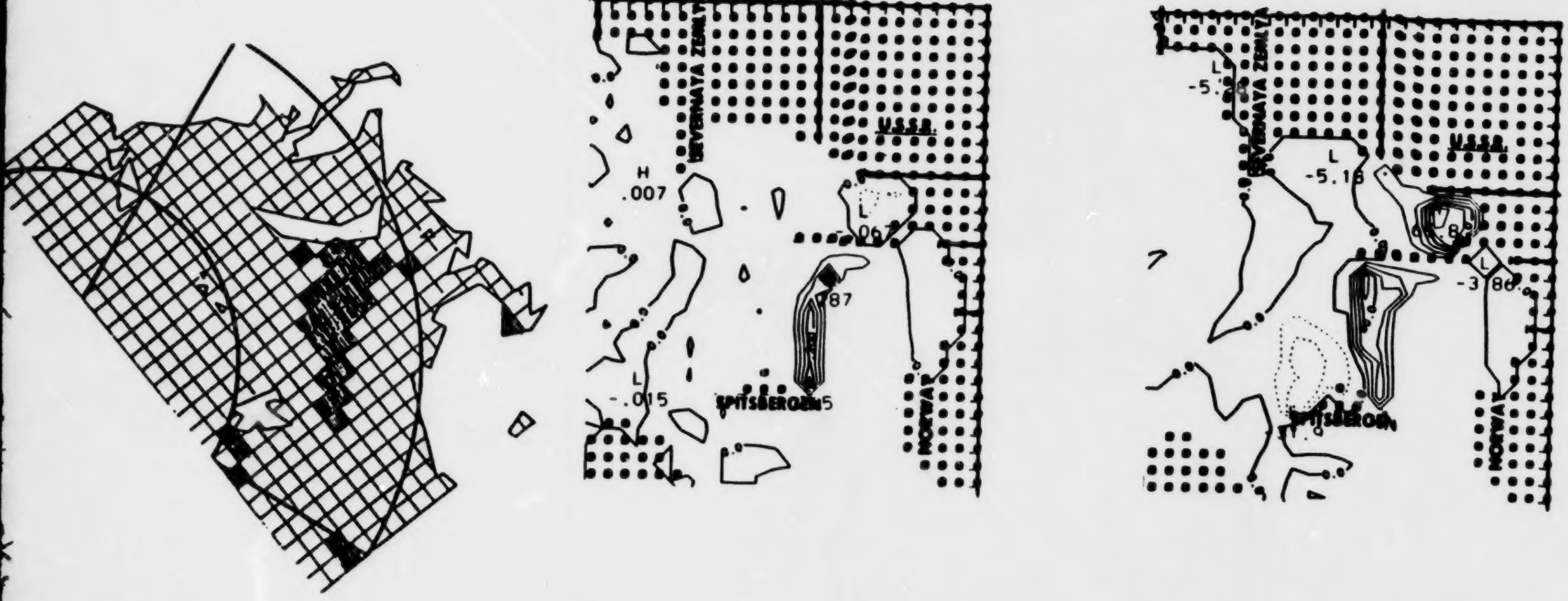

Figure 20. (left) Observed region of increased March ice concentration following a year of below normal flow into the Kara Sea from the Ob river. The anomaly persists into the summer. From Holt et al., 1984. (middle) The change in May ice concentration predicted by the model for the second year of specified river diversions. (right) The change in May ice thickness predicted by the model for the second year of specified river diversions.

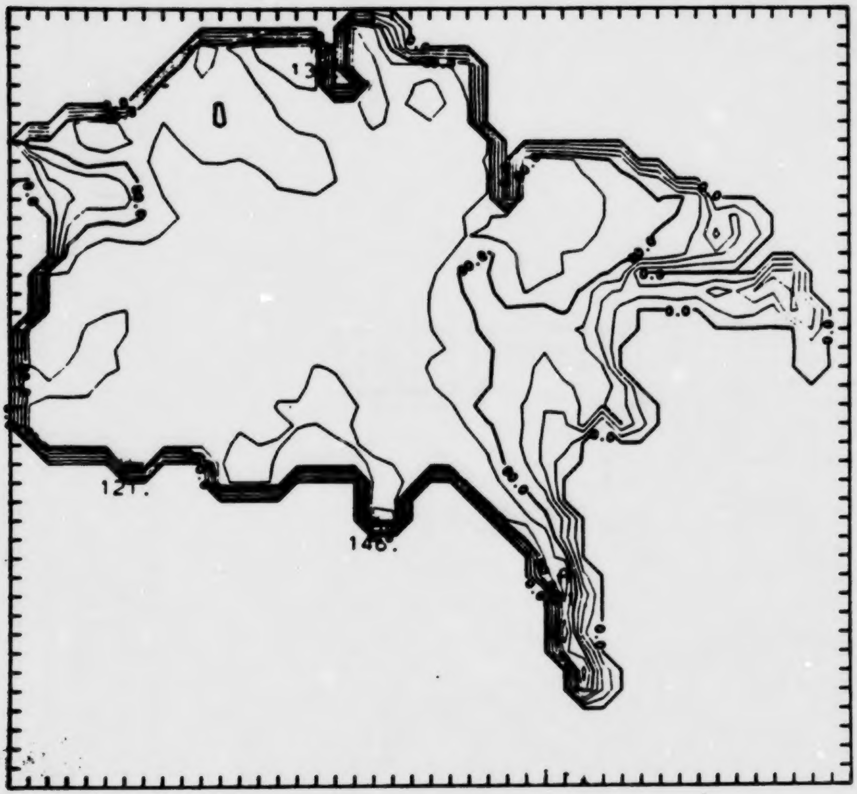

Figure 21. January ice thickness for the case of a 2 C atmospheric temperature increase throughout the year.

of sea ice and ocean circulation in the Arctic. This includes the representation of warm and cold currents in the Norwegian and Greenland Seas, the surface and intermediate layers in the Arctic Basin, and water mass transformations due to surface heat losses and ice growth and melt. Sea ice and ocean processes are found to influence each other very strongly. In particular, oceanic heat flux not only governs the wintertime extent of sea ice in the Greenland and Barents Seas but also governs the minimum summertime extent in the Arctic Basin, the latter being intimately related to the dynamics of the intermediate-depth Atlantic layer.

The simulated response of the Arctic Ocean to a very large quantity of Soviet river diversions shows very little change. In agreement with the observed correlation between river runoff and ice extent, the model predicts slightly more ice in the northern Barents Sea in spring. Also the ice is slightly thicker in the southern Kara Sea. In contrast, the effect of a specified atmospheric temperature increase of 2 C, such as might occur as a result of CO_2 increase, causes the entire ice pack to melt in late summer. The drastic change in surface properties at this time of year would probably have a significant effect on polar climate.

There are a number of further applications that can be done with the ice-ocean model. New parameterizations of mixing, including mixing along isopycnal surfaces can be tested. The distribution of transient tracers can be modelled and compared with observations. And the interannual variations of sea ice and ocean circulation can be modelled and compared with observations. Considering how important ocean heat transport is for the simulated ice extent, it seems highly likely that the inclusion of ocean circulation should improve the representation of interannual ice variations. The author expects to examine this particular area next before proceeding with the various model improvements.

Acknowledgements

The author wishes to thank William D Hibler, III for suggesting the simplified bulk-viscous ice rheology and John E. Walsh for supplying monthly average atmospheric forcing fields gridded for the coupled model. The author also wished to thank Warren Washington for making it possible to carry out this work at NCAR.

REFERENCES

Aagaard, K., and L.K. Coachman, 1975: Toward an ice-free Arctic Ocean. *EOS,* **56**, 484–486.

Aagaard, K., and P. Greisman, 1975: Toward new mass and heat budgets for the Arctic Ocean, *J. Geophys. Res.,* **80**, 3821-3827.

Aagaard, K., J.H. Swift, and E.C. Carmack, 1985: Thermohaline circulation in the Arctic mediterranean seas. *J. Geophys. Res.,* **90**, 4833–4846.

Antonov, V.S., 1976: The possible impact on the Arctic Ocean from the proposed transfer from the northern rivers of the USSR to the south. *Tr. Arkt. Antarkt. Nauchno-issled. Inst.,* **323**, 156–167. Translated in *Polar Geography,* **11**, 223–231.

Bryan, K., 1969: A numerical method for the study of the circulation of the world ocean. *J. Comput. Phys.,* **4**, 347–376.

Cattle, H., 1985: A survey of possible repurcussions of the Soviet river diversion programme on Arctic sea ice. *Polar Record,* bf 22, 485–498.

Coachman, L.K., and K. Aagaard, 1974: Physical oceanography of Arctic and Subarctic seas. In *Arctic Geology and Oceanography,* Springer-Verlag, New York, pp. 1–72.

Colony, R., and A.S. Thorndike, 1984: An estimate of the mean field of Arctic sea ice motion. *J. Geophys. Res.,* **89**, 10,623–10,629.

Ewing, M., and W. Donn, 1956: A theory of the ice ages. *Science,* **123**, 1061–1066.

Hibler, W.D. III, 1979: A dynamic thermodynamic sea ice model. *J. Phys. Oceanogr.,* **9**, 815–846.

Hibler, W.D. III, and K. Bryan, 1984: Ocean circulation: Its effects on seasonal sea-ice simulations. *Science,* **224**, 489–492.

Hibler, W.D. III, and J.E. Walsh, 1982: On modeling seasonal and interannual fluctuations of Arctic sea ice. *J. Phys. Oceangr.,* **12**, 1514–1523.

Holt, T., P.M. Kelly and B.S.G. Cherry, 1985: Cryospheric impacts of Soviet river diversion schemes. *J. Glaciology,* **5**, 61–68.

Manabe, S., and R.J. Stouffer, 1980: Sensitivity of a global climate model to an increase of CO_2 concentration in the atmosphere. *J. Geophys. Res.,* **85**, 5529–5554.

Maykut, G.A., and N. Untersteiner, 1969: *Numerical Prediction of the Thermodynamic Response of Arctic Sea Ice to Environmental Changes,* Rand Corp. Memo. RM-6093-PR, Santa Monica, Calif., 173 pp.

Maykut, G.A., and N. Untersteiner, 1971: Some results from a time-dependent thermodynamic model of sea ice. *J. Geophys. Res.,* **76**, 1550–1575.

Micklin, P.P., 1981: A preliminary systems analysis of impacts of proposed Soviet river diversions on Arctic sea ice. *EOS,* **62**, 489–493.

Parkinson, C.L., and W.W. Kellogg, 1979: Arctic sea ice decay simulated for a CO_2-induced temperature rise. *Climatic Change,* **2**, 149–162.

Parkinson, C.L., and W.M. Washington, 1979: A large-scale numerical model of sea ice. *J. Geophys. Res.,* **84**, 311–337.

Semtner, A.J. Jr., 1976a: A model for the thermodynamic growth of sea ice in numerical investigations of climate. *J. Phys. Oceanogr.,* **6**, 379–389.

Semtner, A.J. Jr., 1976b: Numerical simulation of the Arctic Ocean circulation. *J. Phys. Oceanogr.,* **6**, 409–425.

Semtner, A.J. Jr., 1984a: On modelling the seasonal cycle of sea ice in studies of climatic change. *Climatic Change,* **6**, 27-37.

Semtner, A.J. Jr., 1984b: The climatic response of the Arctic Ocean to Soviet river diversions. *Climatic Change,* **6**, 109–130.

Semtner, A.J., 1986a: History and methodology of modelling the circulation of the world ocean. *Proc. NATO Institute on Advanced Physical Oceanographic Numerical Modelling,* in press.

Semtner, A.J., 1986b: Finite-difference formulation of a world ocean model. *Proc. NATO Institute on Advanced Physical Oceanographic Numerical Modelling,* in press.

Swift, J.H., 1984: The circulation of the Denmark Strait and Iceland-Scotland overflow waters in the North Atlantic. *Deep-Sea Res.,* **31**,, 1339–1355.

Vinje, T.E., 1977: Sea-ice conditions in the European sector of the marginal seas of the Arctic, 1966–75. *Norsk Polarinstitut Arboke,* **1975**, 283–292

Walsh, J.E., W.D. Hibler III, and B. Ross, 1984: A model simulation of 20 years of northern hemisphere sea ice fluctuations. *Ann. Glaciol,* **5**, 170–176.

Walsh, J.E., W.D. Hibler III, and B. Ross, 1985: Numerical simulation of Northern Hemisphere sea ice variability, 1951–1980. *J. Geophys. Res,* **90**, 4847–4865.

Washington, W.M., and G.A. Meehl, 1984: Seasonal cycle experiment on the climate sensitivity due to a doubling of CO_2 with an atmospheric general circulation model coupled to a simple mixed-layer ocean model. *J. Geophys. Res.,* **89**, 9475–9503.

APPENDIX

The Bulk-Viscous Ice Rheology

Following the notation of Hibler (1979), the stress tensor is given by

$$\sigma_{ij} = \varsigma(\dot{\varepsilon}_{11} + \dot{\varepsilon}_{22})\delta_{ij} = \varsigma\dot{\varepsilon}_1\,\delta_{ij}\ ,$$

where

$$\dot{\varepsilon}_{ij} = \frac{1}{2}\left(\frac{\partial u_i}{\partial x_j} + \frac{\partial u_j}{\partial x_i}\right)$$

and δ_{ij} is the Kronecker delta. The bulk viscosity ς is taken to be zero for divergence ($\dot{\varepsilon}_1 \geq 0$); otherwise $\delta = P^*/(2|\dot{\varepsilon}_1|)$, where $P^* = h \times 10^4$(Newtons m^{-1}) for ice of thickness h. The bulk viscosity is not allowed to exceed $(2.5 \times 10^8\ \text{sec})P^*$.

A COUPLED ICE-MIXED LAYER MODEL FOR THE GREENLAND SEA

Marie Noëlle Houssais[1],[2]

ABSTRACT

A thermodynamic coupled ice-mixed layer model, designed to study the seasonal cycle of the ice-ocean interactions in the Greenland Sea is presented. The sea-ice model assumes a constant ice thickness and considers only the variations of ice compactness under the effect of the atmospheric and oceanic heat fluxes. The mixed-layer model predicts the rate of penetrative convection within the water column as a result of both the surface buoyancy flux and the mechanical energy input. The mixed layer is embedded in a three-dimensional primitive equations model which calculates the ocean velocity field and its contribution to the time evolution of the temperature-salinity distribution, and also, following Adamec et al. (1981), helps in describing the pycnocline characteristics at the mixed layer base. The model has been tested without advection or horizontal diffusion through a five-years simulation. The annual entrainment-retreat cycle of the mixed layer is well reproduced together with the advance-decay cycle of the ice cover. The horizontal distribution of the mixed layer depth is in agreement with our knowledge of the effect of an ice cover upon a mainly buoyancy driven oceanic convection. The main weakness of the model comes from the lack of oceanic advection, which is responsible for maintaining the horizontal temperature and salinity gradients and for supplying buoyancy in the upper levels of the ocean. In particular, the vertical salt distribution seems to be a key parameter for determining the efficiency of the oceanic overturning and of the related ice melting-freezing process.

I. INTRODUCTION

The mechanisms involved in the atmosphere-(ice-)ocean interactions in polar regions remain, at the present time, one of the major problems to be elucidated in order to improve our understanding of the polar and, hence, global climate. Various space and time scales are concerned in such interactions, although very little is actually known about their relative importance for the prediction of the climate variability.

As a first approach to these problems, the evolution of the atmosphere and ocean dynamics on a seasonal time scale has been paid much attention, as it is the most striking signature of climate variability that has been widely monitored by means of field experiments (such as, for the Arctic, AIDJEX 1975-76, summer MIZEX 83 and 84 and future winter MIZEX).

---

[1] Laboratoire d'Oceanographie Dynamique et Climatologie, 43-45 rue Cuvier 75 231 Paris Cedex05

[2] Presently at the U.S. Army Cold Regions Research and Engineering Laboratory, Hanover, NH 03755.

The study of the annual period in the energy spectrum of the atmosphere-ice-ocean system also turns out to be the prerequisite to the understanding of longer time scales, especially the complex multiyear variability. At these decadal periods, the likely influence of the seasonal signal has to be taken into account through adequate parameterizations of processes.

In this context of the seasonal variability of atmosphere-ice-ocean interactions, a special effort is required in the parameterization of mixing processes occurring in both the atmosphere and ocean boundary layers, in order to well reproduce the energy transfers between the three mediums. We thus present in this paper the numerical framework and the preliminary results of a numerical model for the behavior of the oceanic mixed layer under subarctic prescribed atmospheric conditions. The model has been run for the Greenland Sea, where the alternance of ice-covered and open-water areas provides the basis for a comparative study of the different forcing effects responsible for the mixed layer deepening/retreat: brine rejection and ice keel stirring under the ice, surface cooling and wind stress mixing in open water.

A number of coupled ice-oceanic mixed layer models have already been designed for climate purpose (Kim and Gates, 1980; Manabe and Stouffer,1980). Among these, the models of Lemke and Manley (1984) and Pollard et al. (1983) deal especially with the joint problem of a variable depth mixed layer under an active (as opposed to prescribed) sea ice cover. In their numerical experiments, advection together with horizontal diffusion is neglected in the equations of the mixed layer temperature and/or salinity. Although such a simplification may provide a good approximation of the seasonal cycle of the upper ocean in mid-ocean regions, this type of solution for the Greenland Sea cannot be expected to give an accurate description of the oceanic fields, since important horizontal transport of warm and salty, or cold and fresh, water occur respectively through the North Atlantic Drift and the East Greenland current. This is a reason why the model proposed here has been designed so that it can be easily embedded into an ocean circulation model which calculates the three-dimensional current pattern from which the advective effects in the mixed layer can be estimated. Such a kind of coupling is particularly interesting for the study of deep convection areas (as the Greenland Sea was first recognized by Nansen, 1906, and later by Mosby, 1959) where, in late winter, the mixed layer is expected to reach great depths. In such cases the hypothesis of a well-mixed velocity profile over the whole mixed layer depth does not hold any more as it does for the temperature and salinity profiles. In winter, the so-called Ekman layer depth should be of the order of 15 m, assuming an average value of 10^{-2} m^2s^{-1} for the vertical eddy viscosity coefficient, and includes only the very upper part of the mixed layer. A differential advection over the entire mixed layer thickness, as given by a multi-level circulation model, is then required.

Apart from this problem, both the models of Lemke et al. and Pollard et al. are submitted to a parameterization of the underlying pycnocline, assumed to have an exponential shape. The prediction of the pycnocline then requires a set of new variables (e-folding depth of the pycnocline, correlation coefficients with the mixed layer variables) which have to be calibrated by comparison with appropriate data sets. Because it is evident that calibration, especially of dissipation effects, remains one of the major problems of the mixed layer models, one can easily understand that such additional parameters are an extra source of trouble, especially when constraints of energy conservation depend upon the adjustment of the parameters. The description of the pycnocline given by a multi-level circulation model, in which one keeps track precisely of the mixed layer depth, is the alternative solution proposed here.

Finally, in most of the models mentioned above, the simple treatment of the ice cover is generally independent of the conditions prevailing in the underlying ocean, since there is no real reciprocal interaction between the ice and the ocean. Instead, sea ice acts on the ocean only as a buoyancy forcing, inferred from an estimation of the ice melting and freezing rates which are themselves deduced from observations or from a heat equation for the ice with some prescribed oceanic heat flux. More sophisticated and efficient models of sea ice (Hibler 1979, Parkinson and Washington 1979, Roed 1984) exist at the present time but, either the parameterization of the underlying mixed layer is quasi non-existent, or it is introduced as a fixed slab in which no entrainment or retreat is allowed at the pycnocline level. However, the heat transfer from the deeper layers to the upper layer of the ocean has been recognized in many studies as a crucial problem, as in Pollard et al. (1983) where the resulting heat transfer between the mixed layer and the deep ocean was found unrealistically large, probably causing large errors in a case where the atmospheric forcing (or ice forcing) would not have been prescribed.

The most complete ice-ocean model at the present time is the one developed by Hibler and Bryan (1986). By including a convective adjustment between the gravitationally unstable layers in their ocean model with a constant mixed layer depth, they have highlighted the importance of the local vertical overturning in the global heat and salt balance of the Greenland Sea. Even if the ice edge location in the Marginal Ice Zone seems to be mainly determined by the combined influence of ice advection from the North and oceanic heat advection from the South, vertical boundary layer processes appear also important at the ice edge in estimating the local melting-freezing balance and hence the subsequent underlying stratification. Since, once it has been established, the ocean stratification is difficult to destroy or rebuild, the consequent oceanic heat flux available at the bottom of the ice acts as a feedback mechanism on the time evolution of the ice distribution. Although our model, due to a very crude treatment of the ice, cannot take into account the detailed variations of the melting-freezing rates, in particular as a function of ice thickness that we have assumed uniform, it gives more insight into the vertical boundary layer dynamics by considering a totally prognostic mixed layer depth, with possible predicted entrainment of denser water, instead of adjusting the upper ocean stratification to a vertical structure prescribed by some model levels.

The prediction of a variable depth mixed layer in the Greenland Sea is particularly interesting to study the occurrence of deep convection events. For a long time, many mechanisms have been invoked to explain how surface or intermediate waters could eventually sink down to the bottom: neither interleafing of dense water flowing down along isopycnal surfaces (Metcalf, 1955), nor double diffusion processes (Carmack and Aagaard, 1973) seem to be really satisfactory. The vertical mixing process occurring under the effect of surface cooling and salt rejection in polar regions provides the most likely explanation, even if it is incomplete and has to be supported by observations. In fact most of the studies carried out on this subject, at least in the Weddell Sea (Killworth, 1979, Martinson et al., 1981), demonstrated that a preconditioning like the one induced by topographic effects or by the baroclinic instability of the large-scale field, is required to allow for effective overturning down to the bottom. However, while these studies are based on the assumption of a non-penetrative mixing, it is not clear whether this idea has to be given preference over a fully penetrative convection (as considered by Kraus and Turner, 1967) which offers the advantage of conserving potential energy as buoyancy is removed at the surface and denser water is entrained at the mixed layer base. The results obtained with these two types of mixed layer models by Solomon (1973) in the Arctic ocean do not give a definitive answer to this problem and we finally chose to use a Kraus-Turner type model for the present study.

II. MODEL DESCRIPTION

The description of the general numerical framework is divided into three parts. First the thermodynamic sea ice model is outlined, then the mixed layer entrainment model and finally the technique for embedding this mixed layer into a multilevel ocean circulation model are described. The preliminary results presented in section III have been obtained with this coupled ice ocean model for a simplified case with no advection or horizontal diffusion. Although, as said earlier, such an approximation is not well justified for the Greenland Sea due to the importance of the meridional transport (Aagaard 1970), these results reveal to what extent vertical processes, as compared to horizontal ones, drive the ice-ocean dynamics in areas of penetrative winter overturning.

THE SEA ICE MODEL

Because the main goal of this study was to highlight some aspects of the vertical dynamical processes in the Greenland Sea, we restricted our interest to the thermodynamic behavior of sea ice, and neglected to consider the two-dimensional momentum and continuity equations of sea ice, which would allow for prediction of the ice drift field and of the ice mass redistribution field. However, since, from a one-dimensional point of view, the sea-ice dynamics determines an important mechanism, which is the mechanical input of turbulent kinetic energy into the upper ocean, it has been taken into account in the mixed layer model through the introduction of a prescribed friction velocity at the ocean surface.

Our thermodynamic sea ice model is very similar to the one designed by Roed (1984), where the ice thickness time changes are considered negligible compared with ice compactness changes (the percentage of ice covered area). As mentioned by Roed, this very crude approximation is motivated by observations of typical Marginal Ice Zone conditions, as encountered in the Greenland Sea, where lateral melting or freezing seem to predominate over vertical melting of freezing, as a consequence of the motion and breakup of individual floes.

The vertical thermodynamic budget of an ice floe of unit area and constant thickness H_o allows the prediction of the ice compactness by compensating any imbalance in the vertical fluxes by an increase (or decrease) of the ice mass. When downward fluxes are considered negative, this budget can be written:

$$L_I\, H_o \frac{\partial A}{\partial t} = A\,(F_{AI} - F_{WI}) + (1-A)\,(F_{AW}(T_f) - F_{WA})\; H(\max(T_f,T_c) - T_m) \qquad (1)$$

where H is the Heaviside step function, L_I the volumetric latent heat of fusion for sea ice. F_{AI} and F_{AW} are atmospheric radiative and heat fluxes, reaching respectively the ice surface at temperature T_I or the open ocean surface as it just comes to the freezing point T_f. F_{WI} and F_{WA} are the oceanic heat fluxes respectively at the ice bottom and immediately below the open ocean surface, and T_c is a critical temperature for the underlying mixed layer, below which surface freezing can occur. The idea here is that ice formation does not necessarily require that the whole mixed layer be at the freezing point, but requires only that a very thin surface sublayer have its temperature T_s equal to the freezing point. This concept of a possible distinct surface sublayer has also been used by Killworth (1979) in his time dependent model, except that his cases B, C and D are considered here as one single case (ice case) while cases A and E are undistinguishable from each other in our no-ice case. In fact, unless the whole mixed layer temperature reaches the freezing point, the present ice model is always supplied by an oceanic heat flux F_{WI} coming from the warmer underlying mixed layer and transferred through the surface sublayer whatever its actual surface temperature is. This allows us to not predict the surface temperature as an explicit variable of the model.

Since F_{AW} is usually positive in the Arctic, the critical temperature T_c may be higher than T_f according to the following relation:

$$T_c = T_f + \frac{F_{AW}(T_f)}{k_w} \tag{2}$$

This relation follows from a simple parameterization of F_{WA} as:

$$F_{WA} = k_w\ (T_m - T_s)$$

where k_w is the ocean heat transfer coefficient, and from the statement that, just as surface freezing occurs (and before ice is formed) the heat fluxes at the ocean surface must balance each other so that $F_{WA} = F_{AW}$. Following the same argument, one can show that:

$$H(T_f,\ T_s) = H(\max(T_c, T_f), T_m) \quad \text{i.e.} \quad T_s \geq T_f + T_m \geq T_c \tag{3}$$

which expresses the freezing condition in (1).
The same kind of parameterization is also used for F_{WI}:

$$F_{WI} = k_w\ (T_m - T_f) \tag{4}$$

In relation (1), the first term on the right hand side is the contribution to the rate of change of the ice mass due to an imbalance in fluxes between the top and the bottom of the ice floes. The second term on the right hand side is the contribution due to an imbalance in fluxes at the atmosphere-ocean interface. Using (2), (3) and (4), (1) can be rewritten as:

$$L_I\, H_o \frac{\partial A}{\partial t} = A(F_{AI} - k_w\,(T_m - T_f)) \qquad \text{if} \quad T_m > \max\,(T_f, T_c)$$

$$L_I\, H_o \frac{\partial A}{\partial t} = A\, F_{AI} + (1-A)\, F_{AW} - k_w\,(T_m - T_f) \qquad \text{if } T_m \leq \max\,(T_f, T_c) \tag{5}$$

The surface fluxes F_{AW} and F_{AI} are expressed as the sum of the radiative, sensible and latent heat fluxes, using bulk aerodynamical formulas which involve the atmospheric and oceanic boundary layers or the ice conditions:

$$F_{A\binom{W}{I}} = (1-\alpha_{\binom{W}{I}})F_S - I_S + \varepsilon_{\binom{W}{I}} F_L - \varepsilon_{\binom{W}{I}} \sigma T^4_{\binom{m}{I}} + \rho_a Cp_a U_a C_s (T_{\binom{m}{I}} - T_a) + S_{\binom{W}{I}} E \tag{6}$$

where $\binom{W}{I}$ are subscript for water or ice.

F_S, F_L, I_S, E, U_a, T_a are prescribed climatological values respectively for the flux of short-wave solar radiation, of long-wave atmospheric radiation and of the penetrating solar radiation into the ocean, for the evaporation rate, for the wind speed and for the surface air temperature. S is the volumetric latent heat of evaporation (or sublimation), α the albedo, ε is the emissivity, C_s is a surface drag coefficient. The exact calculation of F_{AI} then requires to know the surface ice temperature T_I, which can be found by pointing out that, as long as $T_I < T_f$, no ice is melted at the floe surface and the fluxes must balance each other, so that:

$$F_I = k_I\,(T_f - T_I) = F_{AI}$$

where k_I is the ice heat transfer coefficient and F_I is the conductive flux through the ice floe. Then:

$$T_I = T_f - \frac{F_{AI}\,(T_I)}{k_I} \quad \text{when} \quad T_I < T_f \tag{7}$$

In all the calculations discussed above the ice thickness is kept constant and a realistic value for H_o has been chosen so that the ice concentration ever remains within the range [0,1]. The variations of the diagnostic variables, T_I and T_c depend only upon the time-space variations of the atmospheric fluxes F_{AI} and F_{AW}. The ice compactness, A, is the only prognostic variable calculated by the ice model.

THE ONE-DIMENSIONAL MIXED-LAYER MODEL

The mixed layer model predicts the bulk temperature and salinity, T_m and S_m, of the assumed fully turbulent well-mixed ocean surface layer. This is done by vertically integrating the one-dimensional conservation equations of heat and salt from the bottom of the mixed layer, $z = -h_m$, to the surface and neglecting the molecular diffusion across $z = -h_m$:

$$h_m \frac{\partial T_m}{\partial t} + (T_m - T(-h_m))\frac{\partial h_m}{\partial t} = -(\overline{w'T'})_o + \int_{-h_m}^{0} \gamma \; I_s \; \exp(\gamma z) dz \tag{8}$$

$$h_m \frac{\partial S_m}{\partial t} + (S_m - S(-h_m))\frac{\partial h_m}{\partial t} = -(\overline{w'S'})_o \tag{9}$$

where S is the salinity in $^o/oo$.

All the horizontal variations have been neglected here since the mixed layer model is only designed to take care of the vertical diffusion of properties from the ocean surface down to the pycnocline. The effects of the horizontal or vertical advection and of the horizontal diffusivity can be calculated in the stratified ocean circulation model which also entirely determines the three-dimensional distribution of velocities, temperature and salinity below the pycnocline.

Since we are equally interested in ice-free areas and ice-covered ones both the temperature and the salinity equations have to be solved. Indeed the salinity does maintain the vertical stability in the ice-covered upper ocean through the processes of brine rejections, during the freezing season, and fresh water supply, when ice melting occurs. As far as the temperature profile is concerned under sea ice, it is generally more uniform than the salinity profile, and usually drives smaller buoyancy forces in the opposite direction, as the very surface layer is always close to the freezing point. On the other hand, in open ocean, the mixed layer has to be defined on the basis of the actual temperature profile since, in septentrional regions, far from coastal runoff areas, surface cooling or heating are more efficient in driving entrainment or retreat than the surface salt fluxes.

The surface turbulent fluxes in (8) and (9) are expressed as functions of the atmospheric or ice forcings:

$$\begin{aligned} -\overline{w'T'}(o) &= -\frac{F_{AW}}{\rho_w c} && \text{if no ice} \\ &= \frac{k_w}{\rho_w c}(T_m - T_f) && \text{if ice.} \end{aligned} \tag{10}$$

$$\begin{aligned} -\overline{w'S'}(o) &= S_m(E-P) && \text{if no ice} \\ &= H_o \frac{\partial A}{\partial t}\frac{\rho_I}{\rho_w}(S_m - S_I) && \text{if ice} \end{aligned} \tag{11}$$

The second term on the right hand side of (8) accounts for the temperature increase due to the penetration of the solar radiation.

The system (8), (9) is not closed because the entrainment velocity $w_e = \partial h_m/\partial t$ has been introduced in the equations to represent the mixing exchanges between the mixed layer and the underlying deep ocean as:

$$- (\overline{w'T'})_{-h} = \frac{\partial h_m}{\partial t} (T_m - T(- h_m)) \qquad (12)$$

$$- (\overline{w'S'})_{-h} = \frac{\partial h_m}{\partial t} (S_m - S(- h_m)) \qquad (13)$$

The parameterization of w_e requires one more equation. The above so-called jump conditions highlight the necessity of a discontinuous T-S profile at the mixed layer base in order for the heat and salt entrainment fluxes in (8) and (9) to be non-zero. The pycnocline characteristics $T(-h_m)$ and $S(-h_m)$ are part of the discrete temperature and salinity profiles given by the stratified ocean circulation model but may subsequently be modified by the entrainment-retreat process. Both the pycnocline characteristics and the entrainment velocity are extra variables required by the mixed layer model to calculate the mixed layer characteristics T_m and S_m.

The above equations do not involve any assumption concerning a uniform velocity profile in the mixed layer. The problem in applying the above treatment to the momentum conservation equations arises for the fact that in polar regions, considerable surface cooling, combined with a very weak ambient stratification, helps in building a very deep winter mixed layer, as far as no ice is formed at the ocean surface. In such cases, the hypothesis of a deep well-mixed momentum layer on which wind-stress would act as a body force, even down to several hundred meters, is no longer reasonable, especially if one thinks of the Ekman depth or alternatively u^*/f as a realistic depth scale to characterize the combined effects of rotation and vertical diffusion. Even if there is still enough turbulence down to the mixed layer base to allow for mixing of temperature and salinity, the vertical variations of the mean velocity field, as a result of the boundary layer dynamics, seem to be found in the top few tens of meters of the water column, indicating that the rate of production of mean shearing motion by the wind is higher than the rate of its destruction by turbulent mixing. Such a non-uniform velocity profile is in contradiction with the bulk model assumption that no shear production of turbulence in the interior of the mixed layer occurs, except for the transition zone at the mixed layer base. In fact, Pollard et al. (1973) have shown that the shear production of turbulent kinetic energy should not be very important at time scales much larger than the inertial period, especially on the seasonal time scale.

The entrainment equation that predicts the entrainment velocity has been taken from Niiler and Kraus (1977) and is obtained from a parameterization of the different terms in the turbulent kinetic energy equation, vertically integrated from $z = -h_m$ to the surface:

$$w_e\,(\underset{(A)}{q^2} + \underset{(B)}{\Delta B\, h_m} - \underset{(C)}{s\left|\underline{\Delta u}\right|^2}) = \underset{(D)}{2mu_*^3} + \underset{(E)}{\frac{h_m}{2}\left((1+n)\,\overline{b'w'}(o) - (1-n)\left|\overline{b'w'}(o)\right|\right)}$$

$$+ \frac{g\alpha}{\rho_o c}\, I_S\, \left(h_m(1+\exp(-\gamma h_m)) - \frac{2}{\gamma}\,(1-\exp(-\gamma h_m))\right) \qquad (14)$$

where the effect of the downward momentum radiation by the internal waves through the mixed layer base has been neglected. ΔB and $\underline{\Delta u}$ are the buoyancy and the velocity jumps across the bottom of the mixed layer. The signification of all the terms in (14) is summarized in Niiler and Kraus (1977). The term (D), which is the mechanical energy input due to the wind or the ice stress is always a source term for the turbulent kinetic energy and is expressed as a function of the friction velocity $u_* = (\left|\underline{\tau}\right|/\rho)^{1/2}$ where $\left|\underline{\tau}\right|$ is the wind stress magnitude. The term (F) is related to the potential energy change due to the penetrating solar radiation I_S and is usually small. Since h_m is usually greater than γ^{-1}, the e-folding scale for I_S, especially in deep convection areas, this term is generally a sink term in the kinetic energy equation. The term (E) can be alternatively positive or negative, depending on the sign of $\overline{b'w'}(o)$, the surface buoyancy flux, given by:

$$\overline{b'w'}(o) = g(\alpha\overline{w'T'}(o) - \beta\overline{w'S'}(o)) \qquad (15)$$

where $\alpha = -1/\rho(\partial\rho/\partial T)$ and $\beta = 1/\rho(\partial\rho/\partial S)$ are the expansion coefficients of the density with respect to temperature and salinity. (E) represents the transfers between turbulent kinetic and potential energies and may therefore be associated with the generation of turbulence by convection. All the production terms on the right hand side of (14), namely mu_*^3 and $h_m\,\overline{b'w'}(o)$ when positive are subject to dissipation rates which are assumed depth dependent following Lemke and Manley (1984) and Kim and Gates (1980):

$n = e^{-h_m/h_c}$ where $h_c = 100$ m

$m = pe^{-h_m/h_w}$ where $p = 3$, $h_w = 20$ m

The use of such an exponential decay of the kinetic energy production as h_m increases, can have large consequences on the determination of the entrainment velocity, especially in a situation of a deep convective layer. Thus, especially in late winter in the Greenland Sea, when h_m becomes very large, the dissipation terms become so influent that (D) and (E) may be very small while (F) keeps an increasing positive value. The situation then occurs where there is no more entrainment but no retreat either: since the effect of the penetrating solar radiation is felt down to the mixed layer base, the mixed layer depth remains constant.

On the left hand side of (14), the term (C) can be neglected on a seasonal time scale (Pollard et al. 1973) since it represents the effect of the hydrodynamic instability of the mean velocity shear at the bottom of the mixed layer. This velocity shear is no more important when h_m increases beyond some limiting depth predicted by the inertial theory. The term (B), which represents the work against the stratification as denser water is lifted upward, is generally much larger than the term (A) which measures the flux of turbulent mechanical energy through the mixed layer base. In fact, again in case of a deep mixed layer (over 200 m deep) which is deepening further into a weakly stratified water mass, the buoyancy jump ΔB at the mixed layer base is often so small that (A) cannot then be neglected compared to (B). In fact, (A) prevents the entrainment velocity from getting too high by keeping the denominator in the w_e expression close to a finite value. It has been parameterized, using the relation given by Kim (1976), as $q^2 = 9 \max (10^{-4}\ m^2\ s^{-2}, u_*^2)$.

When entrainment occurs, that is when $w_e > 0$, equations (8), (9) and (14), together with (10) and (11), are used to predict new values of T_m, S_m and h_m. $T(-h_m)$ and $S(-h_m)$ are supposed to remain unchanged by the entrainment process. However, when production terms in (14) become smaller than the sink terms, part of the mixed layer turbulent kinetic energy is destroyed so that turbulence does not reach any more the base of the mixed layer. Then the entrainment process is stopped and (14) is no longer valid. However, a new value for h_m is diagnostically estimated by setting $w_e = 0$ in (14) and solving for h_m. (8) and (9) are then used to compute new values of T_m and S_m by substituting for w_e using dh_m/dt. As the mixed layer now retreats to a shallower depth, both heat and potential energy conservation requirements, which will be described in more details in the next section, allow also for changes of the temperature and salinity of the new pycnocline so that $T(-h_m)$ and $S(-h_m)$ have to be predicted by the model.

THE COUPLED MIXED LAYER-OCEAN CIRCULATION MODEL

All the physics of the sea-ice and of the mixed layer outlined above is subject to the knowledge of the conditions prevailing in the underlying deep ocean, within and below the pycnocline. This interior ocean is here described by a multi-level primitive equations model, which takes care of all the mechanisms involved in the determination of the three-dimensional ocean circulation and water mass distribution (advection, diffusion), except for the vertical diffusion terms in the temperature and salinity equations at the model levels belonging to the mixed layer, which are instead estimated using equations (8), (9) and (14). Also the effect of the advection on the mixed layer depth is taken into account by vertically integrating the continuity equation, so that:

$$\int_{-h_m}^{0} \nabla\cdot\underline{u}\; dz = \frac{\partial h_m}{\partial t} + \frac{1}{h_m}\int_{-h_m}^{0} \nabla_H\cdot(\underline{u}_H\cdot h_m)dz = 0 \qquad (16)$$

assuming that no mass transfer can occur across the mixed layer base in the advection process. The divergence term in (16) can be taken out of the sum in case the mixed layer assumption is also made for the vertical momentum profile. In (16), the subscript H refers to the horizontal currents and $\partial h_m/\partial t$ to the change in h_m due only to advection. The coupling between the general circulation model and the mixed layer model is achieved by a special treatment of the model level which contains the mixed layer base, that is the only level which T-S properties cannot be assumed to be vertically homogeneous throughout. This has been done following the embedding technique of Adamec et al. (1981) where the tendency terms dT_k/dt and dS_k/dt involved in the temperature and salinity equations of the k-level in the global circulation model, are distributed above (dT_1, dS_1) and below (dT_2, dS_2) the mixed layer base as (see Fig. 1):

$$\begin{aligned} \Delta Z_k dT_k &= \Delta Z_1 dT_1 + \Delta Z_2 dT_2 + \Delta T dh_m \\ \Delta Z_k dS_k &= \Delta Z_1 dS_1 + \Delta Z_2 dS_2 + \Delta S dh_m \end{aligned} \qquad (17)$$

where dh_m is the change of h_m over the time interval dt.

Assuming that dT_1 and dS_1 are respectively identical to the time changes dT_{k-1} and dS_{k-1} computed at the (k-1)-level immediately above the k-level, (17) can be solved to obtain the tendency term dT_2 and dS_2 immediately below the mixed layer (in the pycnocline). Although (17) does not give an exact estimation of the vertical distribution of the tendency terms, since it approximates $(uT)_k$ by $u_k T_k$ at the k-level, it has been slightly modified compared to Adamec et al. in order that heat

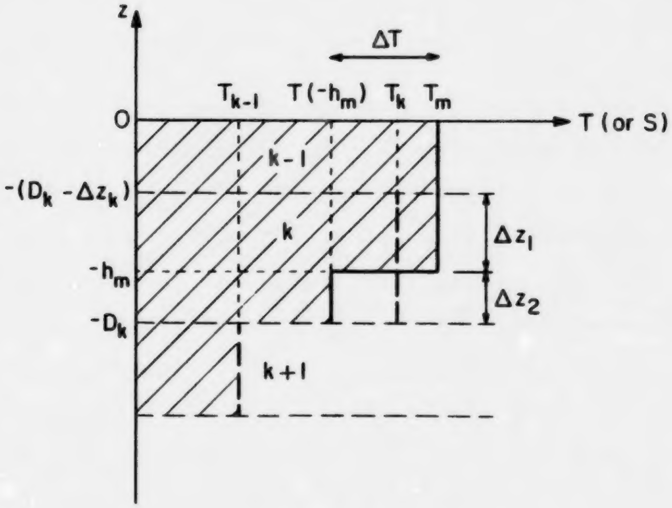

Figure 1. Schematic diagram of the mixed layer: its base, $z = -h_m$, is located within the k-level of the ocean circulation model. The vertical distribution of the salinity is assumed to follow the same step-like profile as the temperature.

and salt be conserved. Since the present paper is not so much concerned with horizontal advection and diffusion processes, no more details concerning the three-dimensional circulation model are given, neither details about the embedding technique which is extensively described in Adamec et al.

As the ocean circulation model provides at each time-step only the step-like structure of the vertical profile of temperature and salinity below the mixed layer, the problem of keeping track of the detailed structure of the pycnocline as the mixed layer retreats remains to be solved. In fact, in order to save computing memory, the model has only two extra T and S variables ($T(-h_m)$, $S(-h_m)$) to describe the pycnocline, which leads to a fictituous smoothing of the pycnocline shape and hence, to erroneous changes in the potential energy of the system. In order to satisfy both heat, salt and potential energy conservation requirements as the mixed layer retreats, a small change in T_m and S_m (in addition to the change due to the surface fluxes) is allowed so that the new mixed layer and pycnocline temperatures are given by (same expressions for salinity):

$$T'_m = T(-h_m) + \frac{(T_m - T(-h_m))\, h_m\, (D_k - h_m + D_m)}{D_k D_m}$$

$$T'(-h_m) = T(-h_m) + \frac{(T_m - T(-h_m))\, h_m\, (h_m - D_m)}{D_k (D_k - D_m)} \qquad (18)$$

where $D_k = \sum_{k=\ell} \Delta Z_\ell$,

$$D_m = \max\,(h'_m\ ,\ D_k - \Delta Z_k)\ ,$$

and h_m' is the new mixed layer depth. The whole coupling technique can be summarized as follows: first the ice model calculates the temperature and salinity surface fluxes and the ice distribution, then the multi-level model calculates the contribution of advection and horizontal diffusion in the temperature, salinity (and momentum) equations, together with the vertical diffusion effects except at the mixed layer levels. Also the integrated continuity equation (16) is solved for the advection effect on h_m. Then the coupling technique (17) is applied and finally the mixed layer equations (8), (9), (14) and eventually (18) are used to predict changes in the temperature and salinity profiles.

Nothing has been said about the surface momentum fluxes in case momentum equations are to be solved. While the wind stress acting over the open water can be estimated using the usual parameterization of the atmospheric boundary layer, the estimation of the ice keel stirring in case of an ice-covered ocean is more difficult. We will just mention that expressions for the ice-water drag as the one proposed by McPhee (1979) require to know the ice speed relative to the ocean, a quantity which is not available in our thermodynamic sea-ice model. A first attempt to overcome this problem was to assume a uniform stress over the basin. This would imply that, for a given wind speed, the stress exerted by the wind over the ice, when transferred to the ocean surface through the ice interaction, is identically equal to the wind-stress exerted over the adjacent open ocean. This is equivalent to assume that a larger drag coefficient characterizes the ice surface compared to the ocean surface (as it is usually recognized) and that the mechanical energy absorbed by the ice exactly compensates the resulting excess of wind stress transmitted to the ice (see for example Roed and O'Brien 1983).

III. RESULTS

The coupled ice-ocean model described above has been used to simulate the seasonal cycle of the ice-ocean interactions in the Greenland Sea. Since a special case with no advection and no horizontal diffusion has been considered, equation (16) has been ignored and only equation (5), with the help of (2), (6) and (7) for the ice, and equations (8), (9) and (14) with the help of (10), (11) and (17) for the ocean, have been solved. The domain (Fig. 2) extends from 70° to 80°N, which is about 1200 km long, and from 15°W to 10°E which is 500 to 1000 km wide, depending on

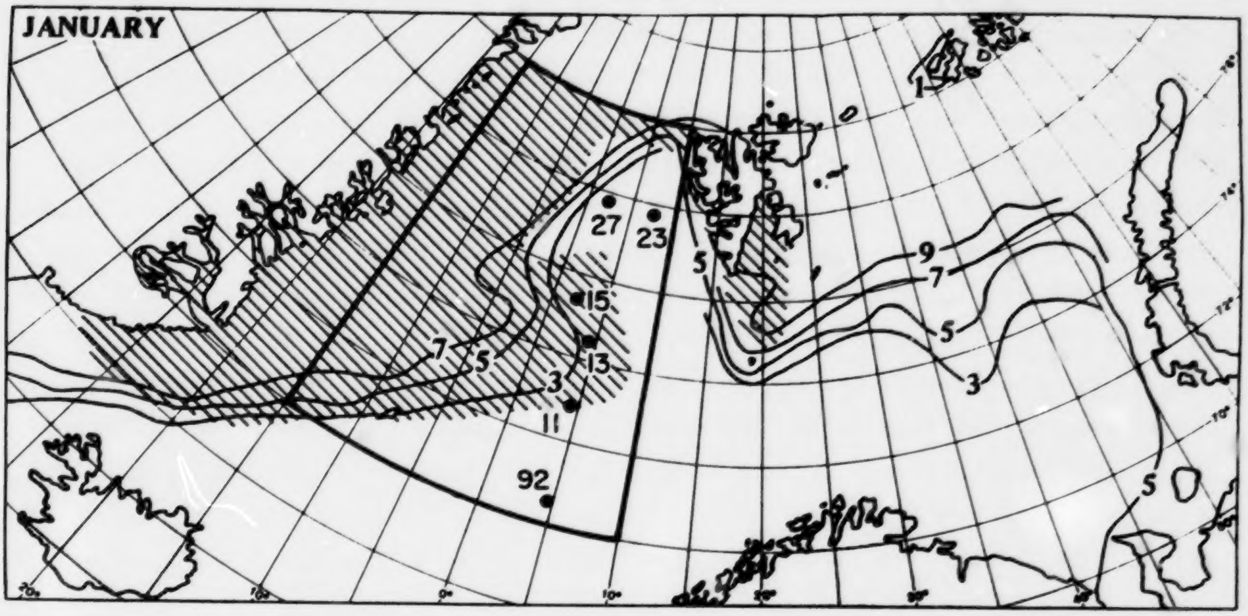

a. January.

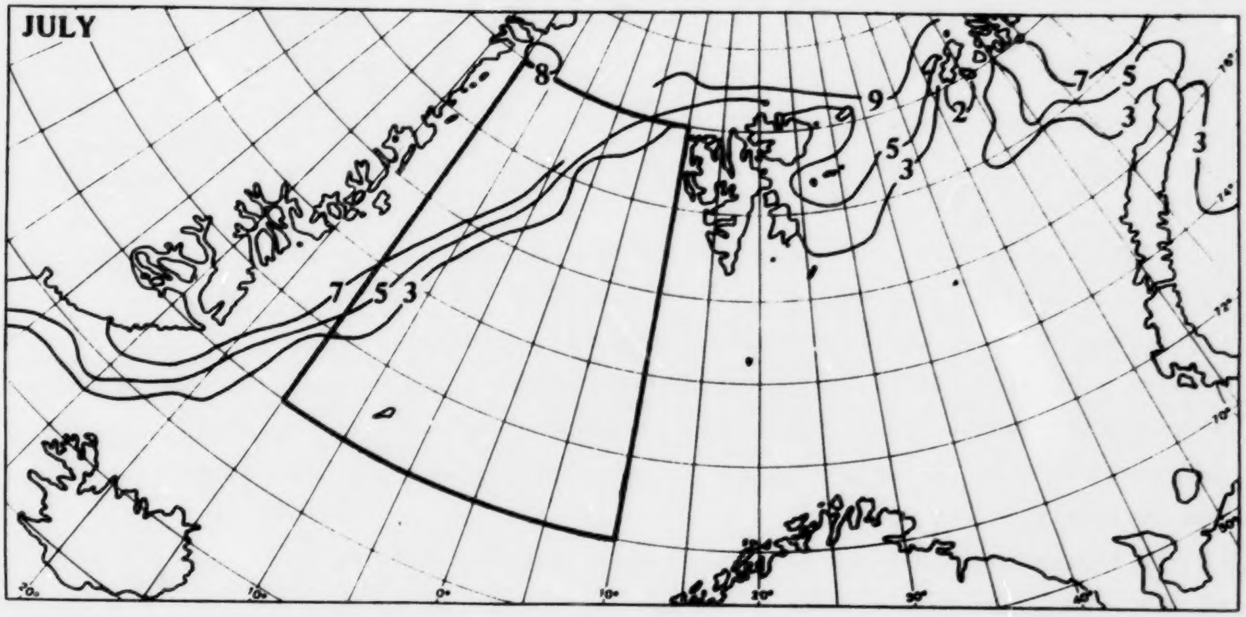

b. July.

Figure 2. Mean sea ice distribution in the Greenland Sea over the 1971-1980 period (from Torgny Vinje, 1981) for January and July. Superimposed as a heavy line frame are the limits of the investigated domain. Also shown on Figure 2a are some positions of stations carried out by CSS Hudson in February-April, 1982 and the related winter ice extent in 1982 (hatched area).

latitude, and includes the whole Greenland basin where winter deep convection is supposed to take place. The equations have been integrated explicitly using a leap-frog scheme with an Asselin filter applied at each time step to prevent any splitting of the solutions. The resolution of the grid, namely 15 km, has been chosen regarding to the necessity of solving in the future the whole set of ocean equations including the momentum equations, which would require a fine grid spacing in order to describe the mesoscale (10-100 km) phenomena, especially those observed at the ice edge (eddies, upwellings ...).

Since it is mainly the thermodynamics which is driving the system here, we have chosen a 12 h time step to run the model during 5 years. The atmospheric forcing is taken from climatological data from Vowinckel and Orvig (1970). Monthly mean values of F_S, F_L, E, P and U_a, T_a have been interpolated to daily values over an annual cycle that is repeated every year. The values of F_S, F_L, E and P are considered spatially uniform over the domain, while T_a (and hence the sensible heat fluxes) is allowed to vary horizontally according to the monthly maps of air temperature given by Vowinckel and Orvig. Also the ocean thermal radiation and the sensible heat fluxes are subject to the time space changes of the surface temperature $T_{\binom{m}{I}}$ predicted by the model. Finally, the friction velocity u_* was assumed constant in space and time regardless of the presence of sea ice, with a value of 8×10^{-3} m s^{-1} estimated from the mean wind stress values computed by Aagaard (1970) over the Greenland Sea.

The initial state is an ice-free ocean described by an early winter stratification based upon the analysis of all the Greenland Sea hydrographic data available at the present time at the French Bureau National des Donnees Oceanographiques in Brest (Houssais et al., 1986). Among others, the analysis has provided, at the standard hydrographic levels, horizontal maps of temperature and salinity which have been interpolated both in horizontal and in vertical, to adjust to the 50x80 grid points and 16 levels of the model.

Although the model has been run over a five-year period, the lack of advection starts to be really felt in the two last years of the run, when all the characteristic ocean features tend to become less pronounced as the missing oceanic currents cannot maintain the horizontal contrasts (temperature and salinity gradients) normally observed in this region. This is the reason why we first discuss here the results of the third year of simulation, which gives the best insight in the one-dimensional dynamics of the region, while some results obtained in the fifth year will be presented afterwards to illustrate the long-term evolution of the system when horizontal effects are neglected.

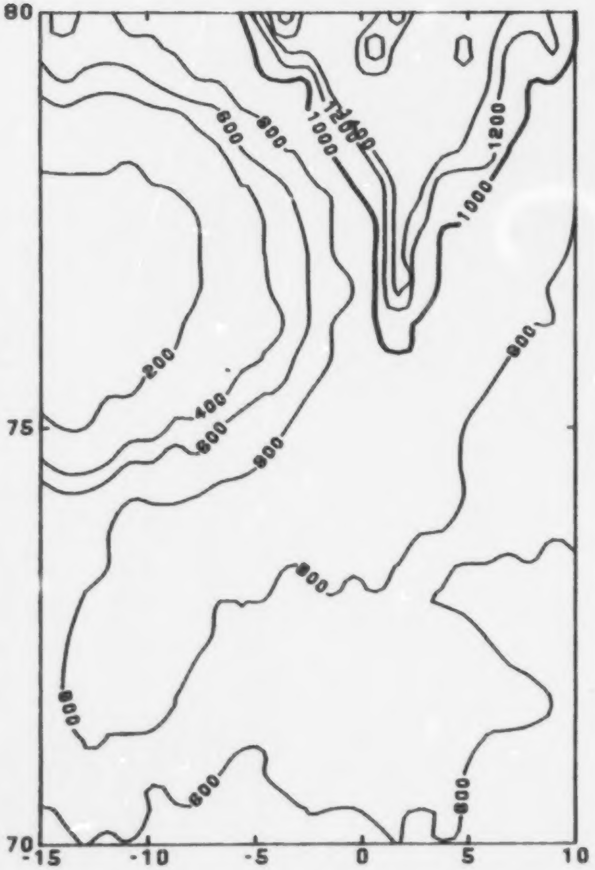

Figure 3. Winter mixed layer depth distribution (January 15).

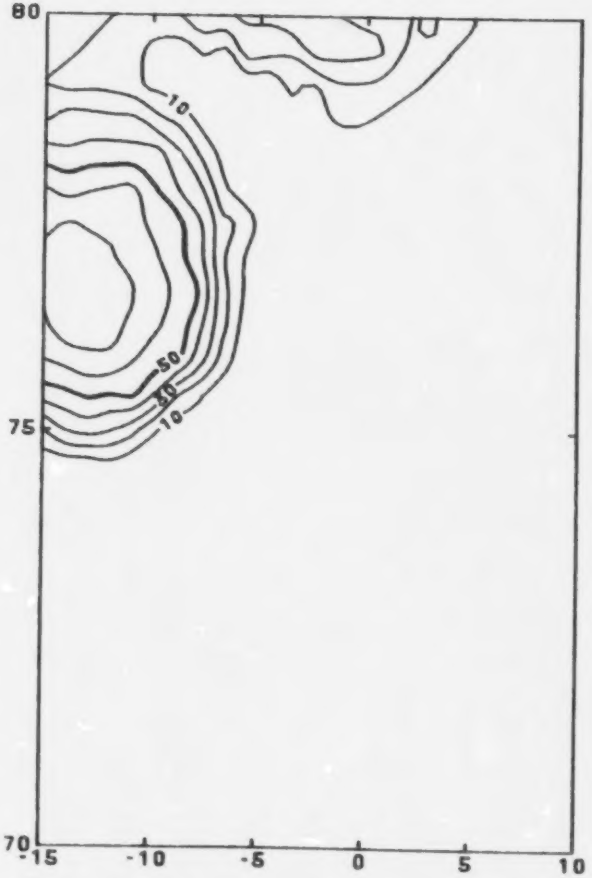

Figure 4. Winter sea-ice concentration distribution (January 15).

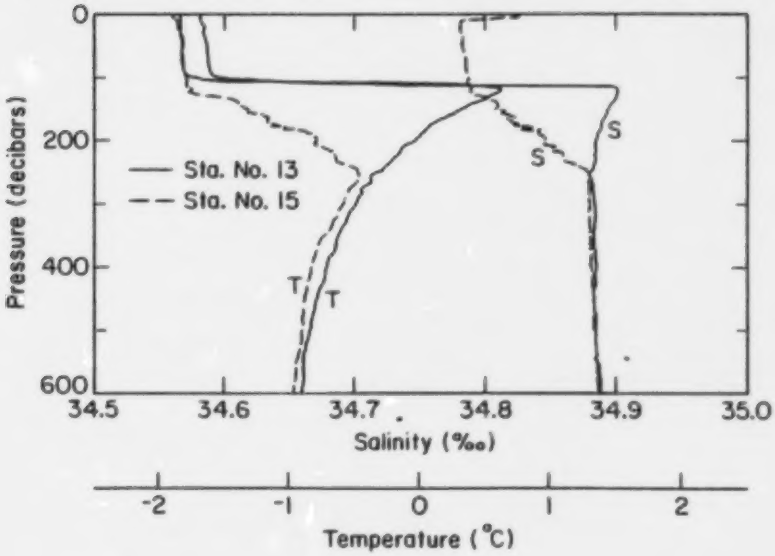

a. At stations located in the ice-covered area.

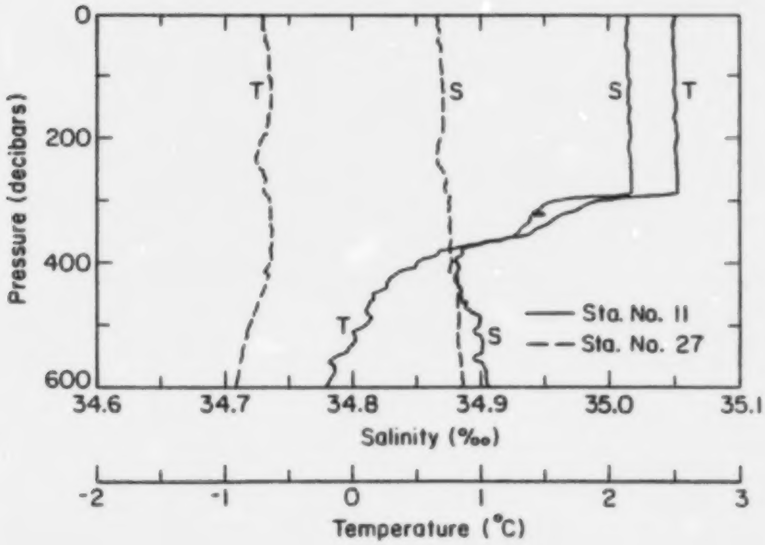

b. At stations located at the southern ice edge (st. 11) and in the ice-free area (st. 27).

Figure 5. Typical mixed layer temperature and salinity profiles obtained from the data collected during the CSS Hudson Cruise 82001 (14 February - 6 April 1982). After Clarke et al. (1984).

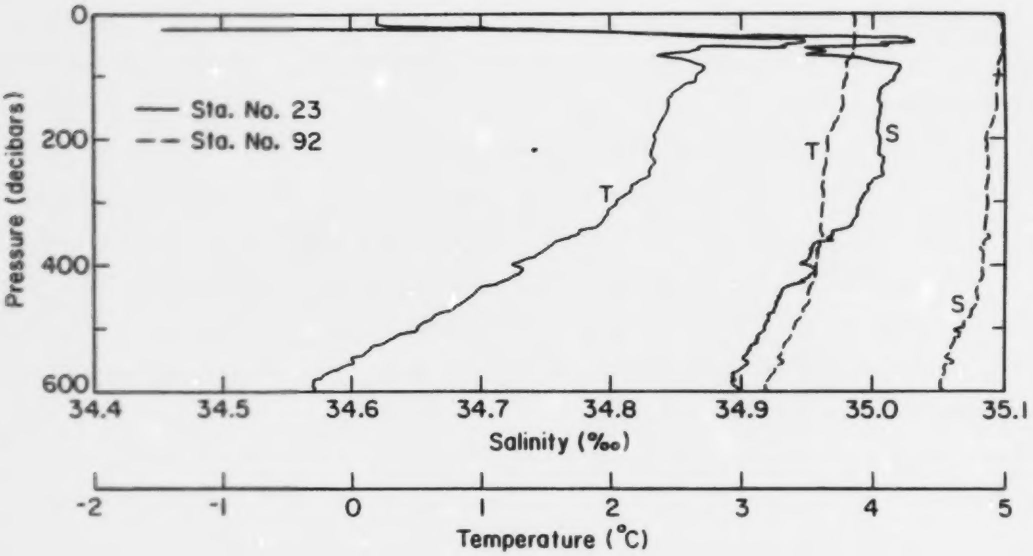

c. At stations located in the middle part of the Fram Strait (st. 23) and in the Norwegian Current (st. 92).

Figure 5 (cont'd). Typical mixed layer temperature and salinity profiles obtained from the data collected during the CSS Hudson Cruise 82001 (14 February - 6 April 1982). After Clarke et al. (1984).

In Figure 3 is shown the early winter (January 15) pycnocline topography (or the mixed layer depth distribution) and in Figure 4 the corresponding ice concentration. The mixed layer thickness reaches its minimum values in the northwestern part of the basin below the ice, with approximate depths of 150 m, while, on the opposite side of the basin, eastern values, corresponding to open water conditions, increase to at least 550 m. Obviously it is in the central part of the basin, extending South and East from the ice edge, along the Greenwich meridian, where the mixed layer exhibits the greatest depths with values reaching 1500 m in some places like the Fram Strait. These winter results can be compared with the hydrographic data collected by CSS Hudson between February 14 and April 6 1982 in the Norwegian Sea and more specifically, in the Greenland basin. Under the ice (Fig. 5a) as at stations 13 or 15, the vertical profiles are fairly homogeneous both in temperature and salinity over the upper 100-150 m, like in the model, and reveal a fresh and cold mixed layer overlying the warm and salty Atlantic water which is recirculating southward below the polar water. Further south, along the ice edge (st. 11), the mixed layer depth drops to 250-300 m which again compares very well with the model results. On the southern and eastern sides of the basin (st. 92), a deeper almost-mixed layer (500 m deep) is found, which is made of warm and salty Atlantic water, up to the surface, overlying the cold deep water. The same kind of profile is also encountered in some ice-free portions of the Fram Strait. Nevertheless, when the advection effects come to dominate as it is also the case in the Fram Strait, well-defined vertical T-S gradients are then encountered, as can be seen at some stations (st. 23) in the middle of the Fram Strait, where vertical processes are no more able to destroy the stratification established by the ambient water mass circulation. This kind of complex multi-layer T-S profile cannot be reproduced in our one-dimensional model and this is why the major discrepancy between the model and the observations is encountered in the northern central part of the basin where the mixed layer depths are clearly overestimated by the model. In fact, the available data do not really allow to verify the hypothesis of such a penetrative convection driven mixing process (at depths of 1500 m, the mechanical energy input into the ocean is no more an efficient mechanism for mixing due to the dissipation effects). None of

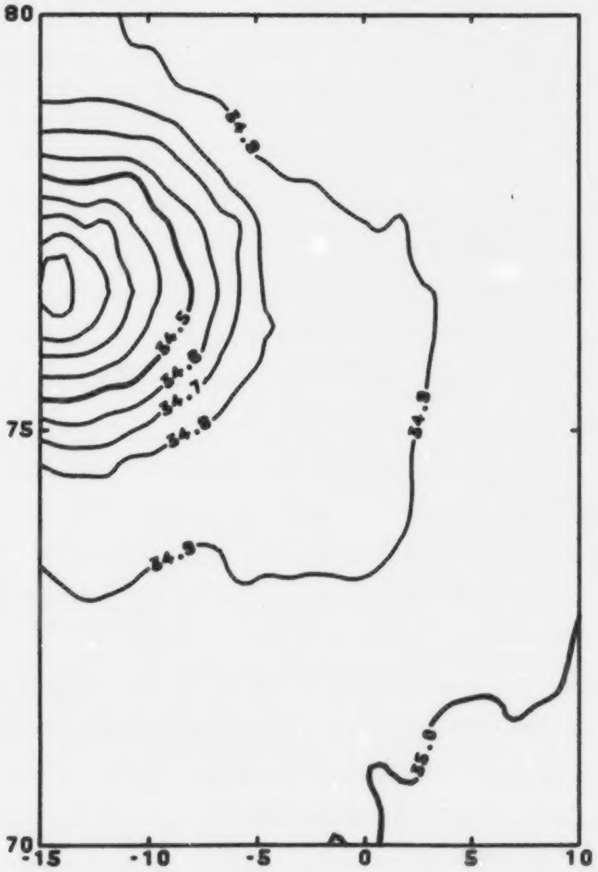

Figure 6. Winter mixed layer salinity distribution (January 15).

the collected profiles goes deeper than 600 m and most of them are rather uniform both in T and S over the upper 600 m (st. 27) but no real "straight line" well-mixed profile has been found.

These differences between model results and data are probably linked to differences revealed in the ice cover concentration (Fig. 4) and the horizontal mixed layer salinity distribution (Fig. 6). While in the 1982 winter, sea ice extended far east (Fig. 2), beyond the 0° meridian, and covered about 2/3 of the basin, including its central part, our model predicts a limited ice cover concentrated on the northwestern side of the basin, which promotes an intense surface cooling of waters located in the consequently larger ice-free areas. The underestimation by the model of the ice extent is clearly demonstrated by the comparison with the climatological maps of ice concentration constructed by Vinje for the period 1971-1980 (Fig. 2). The discrepancy is mainly seen in the ice edge which, in the model is fairly sharp and well defined while, from the observations, it appears smoother and causes ice to extend further east. On the other hand, the model ice concentrations are of the same order of magnitude as observed ones (even if the latter include ice of unknown and variable thickness), with maximum values of 80% in the west, decreasing toward the east. Also, the ice concentrations and the surface salinity are strongly negatively correlated. Nevertheless, the realistic values obtained for the highest ice concentration in the model do not seem to result in corresponding realistic values for the surface salinities below the ice, which are definitely too high compared with the mean values reported in the hydrographic atlas (Fig. 7). Why these salinities are too high is not clear. It is sure that the observed correlation between the low salinities and the high ice concentrations follows from the already existing T-S correlation characterizing the cold and fresh surface waters of the East Greenland current and not from the melting/freezing process which tends to produce the opposite effect in winter, when ice formation is responsible for salt rejection into the underlying water. Hence, low salinities observed below the ice in winter in the Greenland Sea are mainly the result of the fresh water advection from the Arctic basin that has not been considered in the model.

As a whole, the global horizontal distributions of both the sea-ice and the mixed layer depth are well correlated, resulting in a shallower mixed layer below the ice, in the East Greenland current, where the surface cooling is almost totally inhibited by the insulating ice cover, and in a deeper mixed layer over ice-free areas like in the West Spitzbergen current where intense surface cooling and, to a

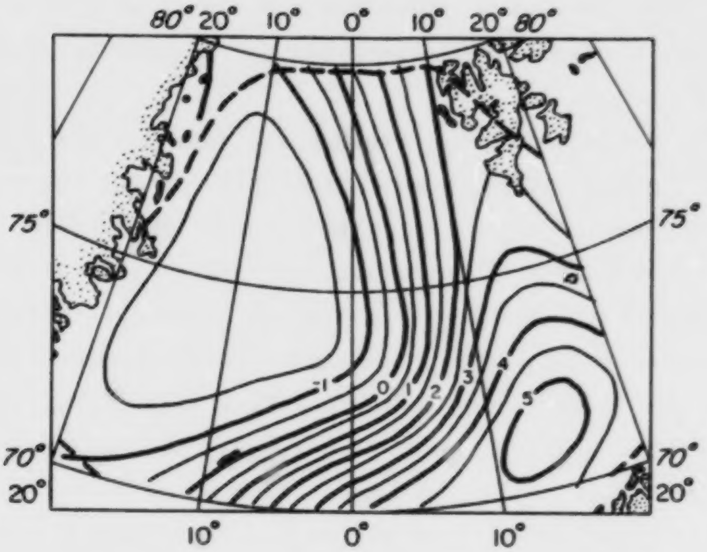

a. Temperature.

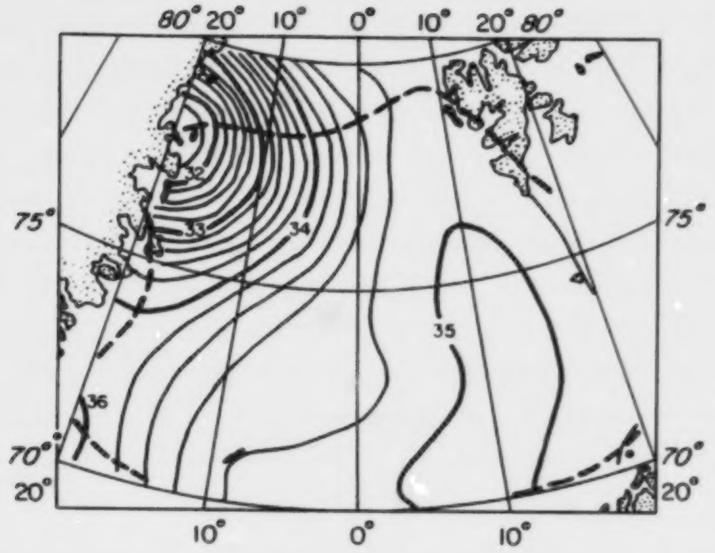

b. Salinity.

Figure 7. Mean winter temperature and salinity distribution at the level p = 20 dbar obtained from an objective analysis of the historical hydrographic data set of the French BNDO. The heavy dashed contour line is the 50% error limit provided by the analysis. After Houssais et al. (1986).

less extent, evaporation contribute also, and as a more prominent mechanism as the mixed layer gets deeper, to the entrainment of dense water.

In summer, the situation changes drastically as the mixed layer retreats to a new equilibrium depth under the effect of surface heating in open water or fresh water supply from the melting ice. The summer value of the mixed layer depth coincides approximately with the uppermost level of the ocean circulation model (20 m) so that the momentum boundary layer and the mixed layer are almost superimposed. The mean equilibrium summer depth of the mixed layer is similar to the Monin-Obukhov length but is in fact influenced by the e-folding scale of the mechanical energy dissipation, h_w. The pycnocline topography is rather uniform and gently sloping from the eastern side down to the western side of the basin (Fig. 8). This slope could be explained by the more efficient melting process, compared to surface heating, in providing buoyancy to the surface layer, the only other remaining process to maintain turbulence in the summer mixed layer being the mechanical energy input proportional to u_*^3 and assumed uniform over the domain. Whether or not this sloping of the pycnocline has been observed in the Greenland Sea is hard to say since it can be detected only on high resolution T-S profiles, but the order of magnitude seems to compare well with summer MIZEX 84 data (see for example Foster et al., 1985). The ice concentration in summer shows a much more diffuse ice edge, as can be expected in summer, but the ice extent is very small compared to Vinje's calculations (Fig. 9 and 2) with most of the ice confined to the northern boundary of the domain. The assumed constant and uniform 2-meters ice thickness seems to be an overestimation for the summer (and perhaps winter) ice characteristics in this area where most of the ice is rather less than 1-meter thick. Assuming a thick ice cover distributed over a limited area, instead of a thinner ice spreading out over a wider area, leads to drastic changes in the heat flux balance at the atmosphere-ice (or-ocean) interface, even if the initial ice volumes are identical. This difference could be responsible for the model tendency to produce too low ice concentrations all over the year.

There is no big difference in the surface salinity distribution between winter and summer so that the minimum salinity under the ice is now really overestimated, probably because of the underestimated melting rate. Indeed, the major problem here seems to have been caused by the too large initial salt content in the system. The initial climatological winter salinity distribution has been associated with a non-realistic ice-free ocean surface, leading to a considerable amount of brine rejections into the ocean during the first year of simulation, as the system was

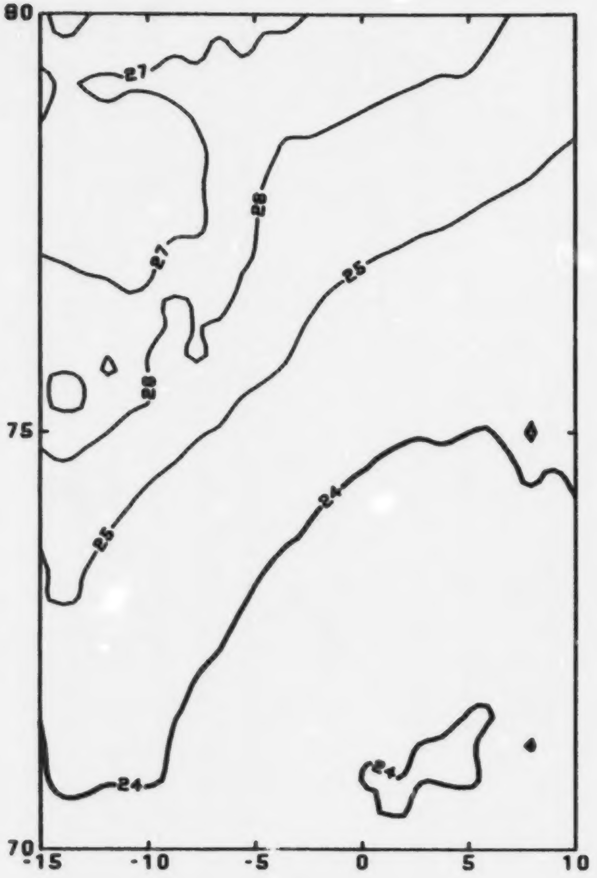

Figure 8. Summer mixed layer depth distribution (July 15).

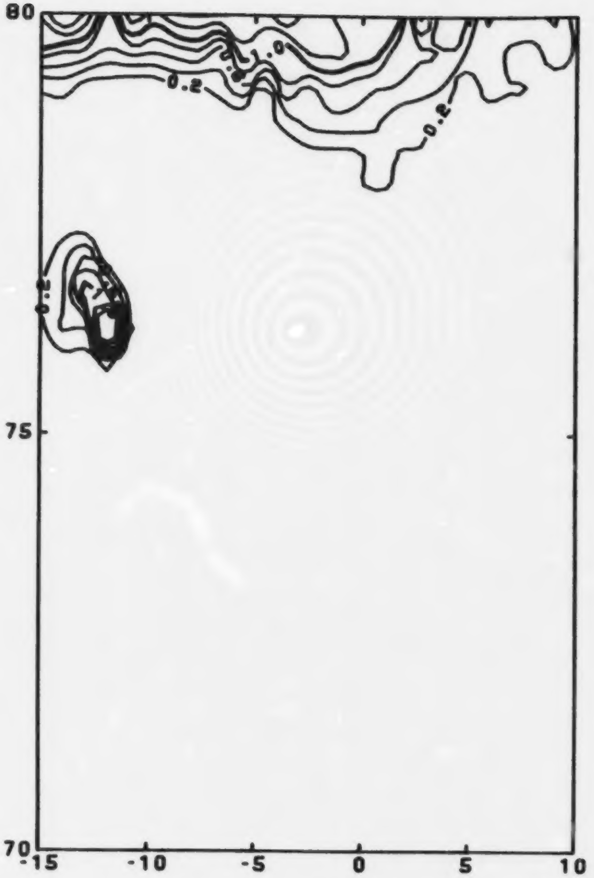

Figure 9. Summer sea-ice concentration distribution (July 15).

evolving towards a state of equilibrium through ice formation. This leads to drastic consequences in the subsequent evolution of ice-covered areas in the model since, as opposed to heat, the ocean has no way, in the absence of advection, to eliminate any extra amount of salt that could have been put into it. While surface sensible heat fluxes and thermal radiation allow the ocean to eventually lose extra heat, according to the predicted surface temperature, and adjust to an equilibrium temperature, the salt content, which only depends upon the evaporation/precipitation or melting/freezing rates, has no reason to evolve towards an equilibrium salinity, when no extra salt sources are considered, since there is no direct interrelation or feedback effect between the magnitude of the surface salt fluxes and the actual ocean salinity. The initialization and the time evolution of the salinity field in models of vertical convection was felt also by Martinson et al. (1981) to be a key parameter for the equilibrium cycle of the system. According to their results, depending upon the salinity of the upper mixed layer, the probability for the system to overturn in winter may change from zero to several overturns in a single winter. The salt content partially determines the stability of the water column and, hence, the amount of heat available for melting ice or delaying surface freezing, through overturning and mixing with the warmer deep layers. In fact, the vertical salinity distribution depends upon both the initial salt content and the fresh or salt water input which usually takes place in the upper layer. The salt sources of the mixed layer are either local, as the result of surface and entrainment processes considered here in the model, or have to be prescribed as external sources, for example, the river runoff. In the present model, no external fresh water input is considered, apart from precipitation. This, combined with a probably too high initial salt content put into the system, maintains an enhanced overturning, through the feedback effect of the ice-ocean interactions.

An interesting bit of information provided by the mixed layer models is the prediction of the ocean surface temperature which is considered as the test variable of these models. Figure 10 shows the winter and summer surface temperature distributions which, in fact, are the mixed layer temperature distributions. In winter, the wide patch of water with fairly homogeneous temperature which characterizes the center of the basin is found both in the model results and on the climatological maps (Fig. 7), with slightly lower temperature (≈ -1.5°C) obtained from the data analysis compared to the model temperature (≈ -0.9°C). The location of the NE-SW temperature gradient is exactly the same in the two cases but differs from the location of the ice edge. The maximum temperatures (2.5°C) are encountered in the

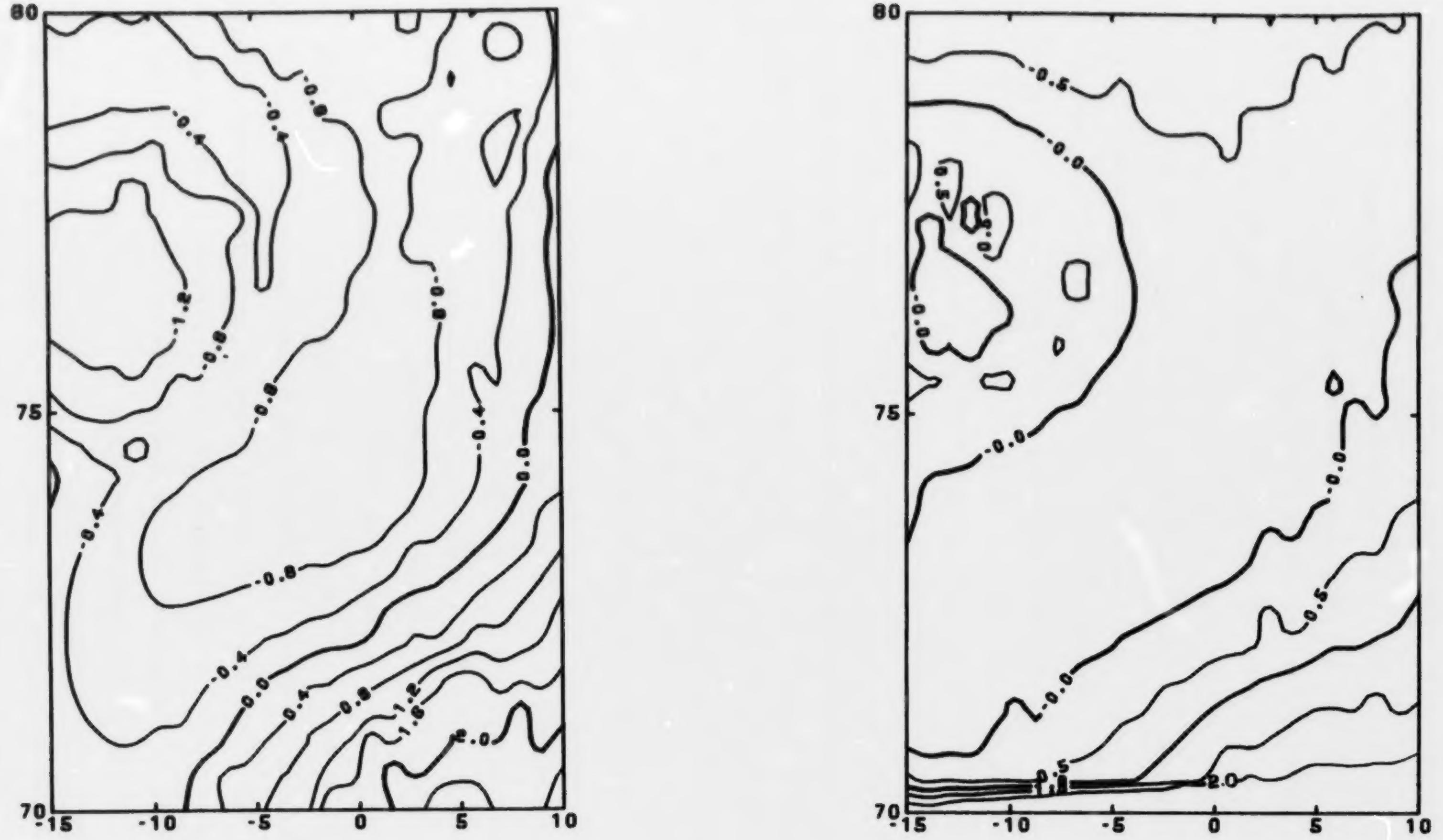

a. Winter.

b. Summer.

Figure 10. Winter and summer mixed layer temperature distributions.

Norwegian current in the southeastern part of the basin while the minimum ones are in the East Greenland Current, with values of the order of -1.5°C which illustrate the temperature difference which can exist, below the ice, between the surface freezing temperature and the vertically averaged mixed-layer temperature. On the other hand, as for the summer salinity, the model is not able to predict realistic values of the summer mixed-layer temperature, which appears everywhere too low and too spatially uniform.

Figure 11 shows the seasonal evolution of the mixed layer thickness at two locations which are representative of two different types of vertical water mass distribution: the East Greenland Current stratification and the Norwegian Current stratification. The maximum thicknesses occur in late winter (April) and the minimum in August. It is obvious that, below the ice (A), the ocean system has not yet achieved an equilibrium after two years, while in the open areas (B) the time evolution of the mixed layer depth exhibits an almost periodic behaviour. The problem encountered in case (A) is a consequence of the non-stationary ice distribution

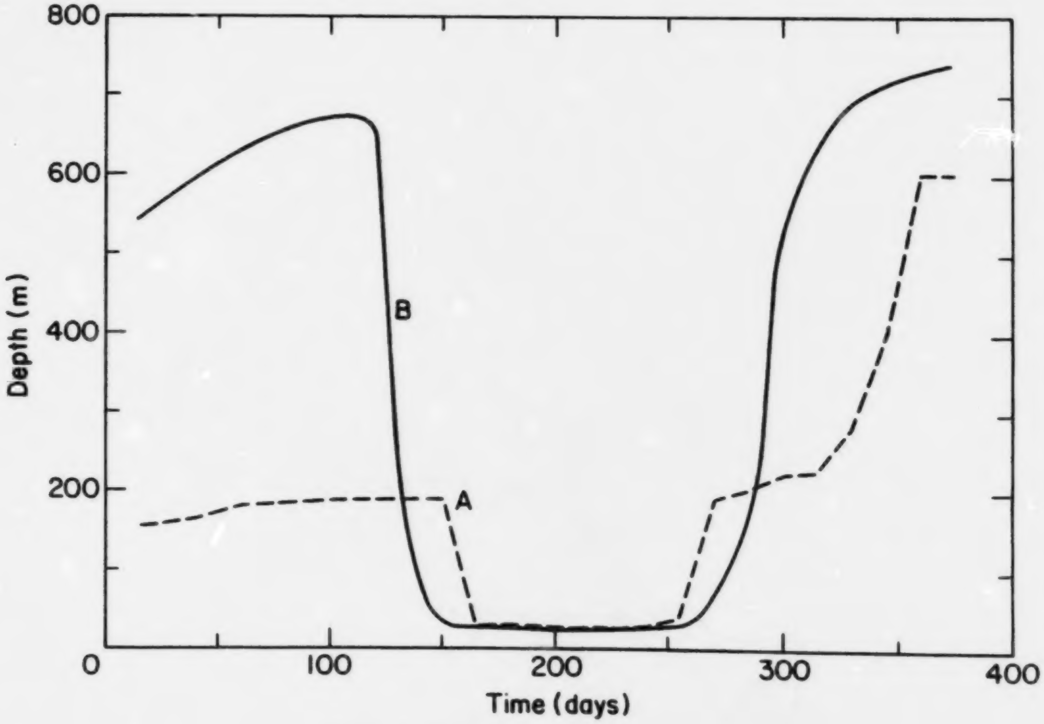

Figure 11. Seasonal evolution of the mixed layer depth (third year of simulation) at grid points located (a) in an ice-covered area (78°30'N, 12°30'W), (b) in open ocean (71°N, 7°30'E).

simulated by the model, as will be seen in the last section when the long term evolution of the model is examined. The abrupt retreat of the mixed layer in both cases (A) and (B) follows from the parameterization of the retreat process in which h_m has to be a diagnostic variable, and then is no longer really predicted, as soon as the entrainment process has been stopped. There is no observational evidence for this kind of behaviour, commonly found in the one-dimensional mixed layer models: in the MEDOC deep convection area, the retreat was found to occur primarily as a result of horizontal processes, like interleaving, which cannot be considered in the context of a vertical model. On the other hand, the very rapid deepening of the mixed layer in the early fall is the signature of a catastrophic overturning similar to the one obtained by Killworth (1979) in a model of the Weddell Sea, after the mixed layer has reached a depth of 180 to 300 m, depending on the observed ambient stratification.

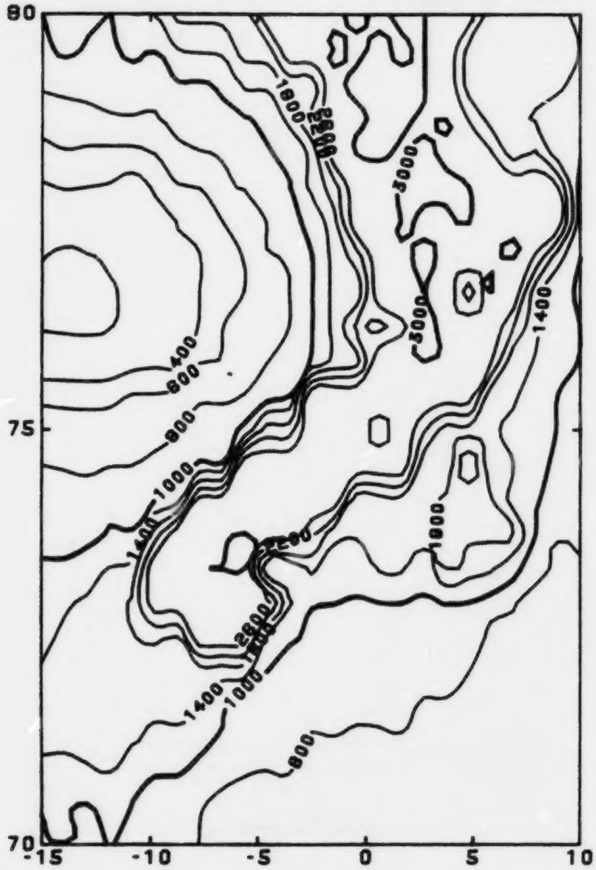

Figure 12. Late winter mixed layer depth distribution (April 15).

The late winter case is especially interesting in a region where deep convection and deep water formation are expected to take place at this time of the year. In fact, at many grid points in the interior basin, the entrainment process is responsible for mixing down to the bottom, as can be seen in Figure 12. This very active entrainment is the result of the efficient surface cooling acting on the ice-free homogeneous central part of the basin in which, in addition, no buoyancy is supplied by horizontal advection or diffusion. This behaviour has to be compared to the formation of "chimneys" in the Weddell Sea, as it has been observed by Gordon (1978), and then studied by Killworth (1979) as the signature of the efficient vertical mixing resulting in surface water overturning down to the bottom. His calculations revealed that, without considering any other mechaninisms than the surface buoyancy forcing and the consequent vertical mixing, catastrophic overturning down to the bottom should have occurred at most of the stations carried out in the Weddell gyre. However, the observations revealed that such deep convection events are rather local so that a preconditioning phase is required to explain the selection of some preferred sites among an entire area which is prone to overturning. The same kind of calculations carried out at a station in the Greenland Sea (74°N, 0°E) led to the same conclusion concerning overturning down to the bottom. There is no limiting process in the present model to prevent the entrainment velocity from being very high, a tendency which is enhanced by the small amount of work required to destroy the weak ambient stratification. In the real ocean the effect of the vertical heat and salt flux induced by the entrainment of denser water into the surface layer may be reduced by the horizontal circulation which, especially in the eastern ice-free portion of the Greenland Sea, supplies heat and salt at intermediate depths through the flow of Atlantic water. This northward flow is thought to have a stabilizing effect at the mixed layer base on the basis that buoyancy is mainly driven by the heat content in a region where both intense surface cooling and a warm mixed layer overlying the cold deep water are present. It is also likely that the mesoscale and large-scale dynamics may be involved in the renewal of the deep water (Gascard and Clarke 1983), through the baroclinic instability of the horizontal velocity field, especially near sharp horizontal density gradients. Finally, it is possible that the parameterizations used to estimate the surface fluxes, or the very smoothed density field used as the initial state, do not represent with enough accuracy the typical conditions encountered in the Greenland Sea, so that an accurate control of the bottom convection is not possible.

IV. CONCLUSION

The results described in the previous section illustrate the ability of our coupled ice-mixed layer model in simulating the seasonal cycle of the vertical mixing processes in areas like the Greenland Sea characterized by intense surface cooling and ice formation. In agreement with observations, the hypothesis of a surface layer equally mixed with regard to both heat and salt, has been made and has led us to the use of the vertically integrated conservation equations to calculate the mixed layer salinity and temperature. Buoyancy effects together with mechanical mixing have been considered in the entrainment equation with different dissipation rates according to the mixed layer depth and the subsequent prevailing source of turbulent kinetic energy. Two types of temperature and salinity profiles have been evidenced: one is found under the ice and is defined by a fresh cold mixed layer overlying the warmer and saltier Atlantic water, the other one is found in open ocean areas and includes a warm and salty mixed layer overlying the cold deep water. The entrainment velocity also depends greatly upon the density gradient at the mixed layer base which depends upon the temperature and salinity immediately below the mixed layer. Those are determined as explicit variables of the model through the coupling with an ocean circulation model, with the requirements of potential energy, heat and salt conservation. These conservative properties appear to be one of the most interesting features of the model. They allow for obtaining a fairly accurate representation of the vertical heat and salt exchanges between the mixed layer and the deep ocean which was recognized as a major problem in some previous studies (Pollard et al., 1983) where the pycnocline and the underlying deep ocean were poorly described. The potential energy conservation is applied to the whole vertical T-S profile, since a good estimation of the variations in the pycnocline shape (approximated here by a step-like profile) may become very important in the well-stratified regions encountered below the ice.

With no advection and horizontal diffusion, the model provides reliable results in winter for the mixed layer depth and its temperature and salinity. The large horizontal variations characterizing the mixed layer depth, with much shallower values encountered below the ice, seem to be consistent with the results of Lemke et al. (1984) which found that the surface mechanical wind- or ice-stress, assumed here uniform over the domain, accounts for only 1/3 of the mixing energy in winter. The remaining buoyancy driven turbulence is therefore responsible for the spatial differences in the mixed layer depths, and surface cooling is recognized as a more efficient driving mechanism, as compared to brine rejection below the ice, for ver-

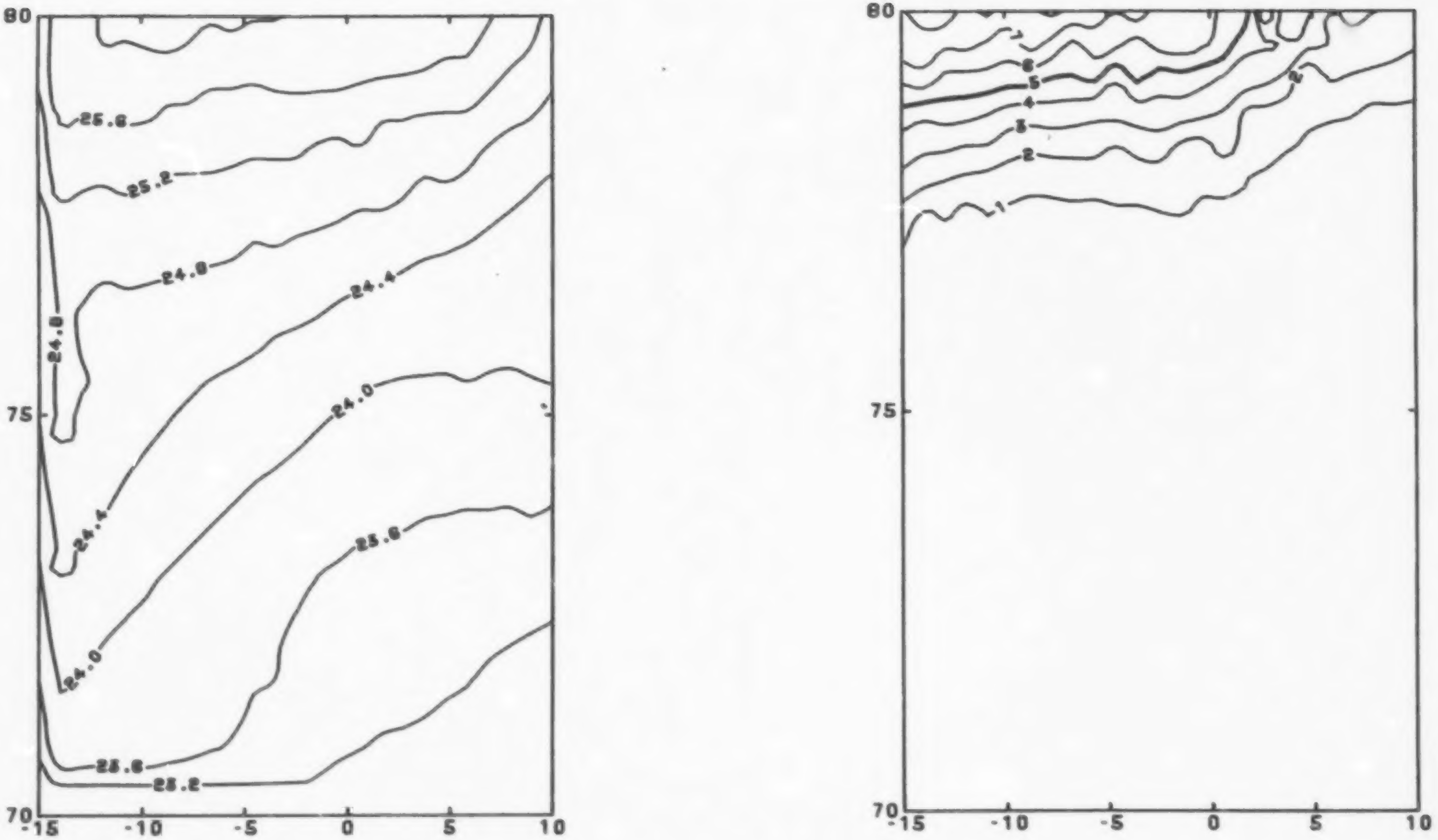

a. Mixed layer depth.

b. Sea ice concentration.

Figure 13. Summer mixed layer depth and sea ice concentration distribution after five years of integration.

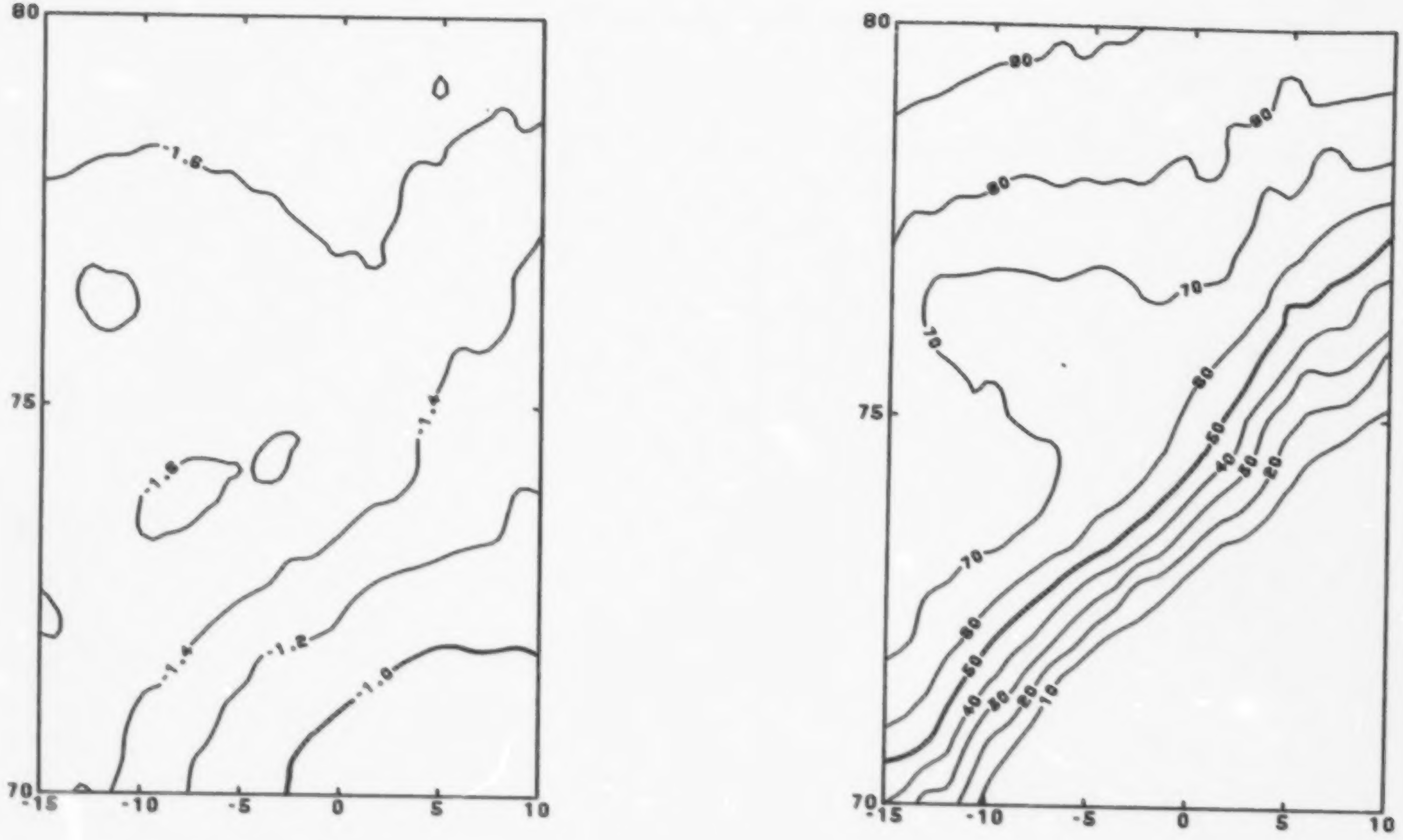

a. Mixed layer temperature.

b. Ice concentration.

Figure 14. Late winter mixed layer temperature and ice concentration distribution after five years of integration.

tical mixing. The summer retreat of the mixed layer is reproduced by the model bu perhaps occurs within a too short time. Also the summer ice does not extend far enough, a result which has also been obtained by Hibler and Bryan (1986). Although they found that the ocean has little effect on the ice decay phase, it is possible that the too active overturning allows the ice decay to occur earlier in the spring and then enhances the melting effects (see Fig. 15).

On the other hand, the bad summer temperature and salinity distributions given by the model lead us to discuss one of the main weaknesses of the model, which is th lack of advection. To evidence the long-term evolution of properties under the only effect of vertical mixing, we present here some results of the last summer (Fig. 13) and last winter (Fig. 14) of our 5-year run. The mixed layer depth is still well reproduced in summer (Fig. 8 and 13 compare well), and the ice concentrations are now higher, with maximum values of about 10% in the North, while the NE-SW ice edge orientation is now maintained. The temperature and salinity distributions are completely smooth both in summer and winter, so that no horizontal front-like feature is observed any more. This is a good illustration of the role of ocean currents in maintaining the global water mass distribution in the Greenland Sea. On a yearly basis the system is continuously losing heat through surface cooling with no possibility for it to gain any heat from outside. Then the temperature gets colder and colder until the whole basin becomes near the freezing point. As said earlier, the problem for the salinity is slightly different since the surface salt fluxes do not depend on the ocean surface salinity in the model. Below the ice, there is a strong discrepancy between observed and modeled salinity distributions which tends to prove that the presence of a fresh water surface layer on the western side of the basin is mainly the result of advection by the East Greenland current rather than due to a local melting process.

After 5 years, the ice distribution in winter is closer to the climatological values (Fig. 14 and 2) and the annual cycle presented on Figure 15 is almost periodic. The ice concentrations have then reached their equilibrium values, which are higher compared to the third year results, and consequently have induced a strong salt-driven overturning of the underlying water: the mixed layer, which is not presented here, is now deep all over the domain. The onset of the ice decay occurs consequently early in the spring before the mixed layer retreat (Fig. 11 and 15). The role of the oceanic and ice advections has been extensively discussed by Hibler and Bryan (1986): the main effect of the ice advection is to prevent a too deep convection below the ice by supplying large amounts of fresh water which tend

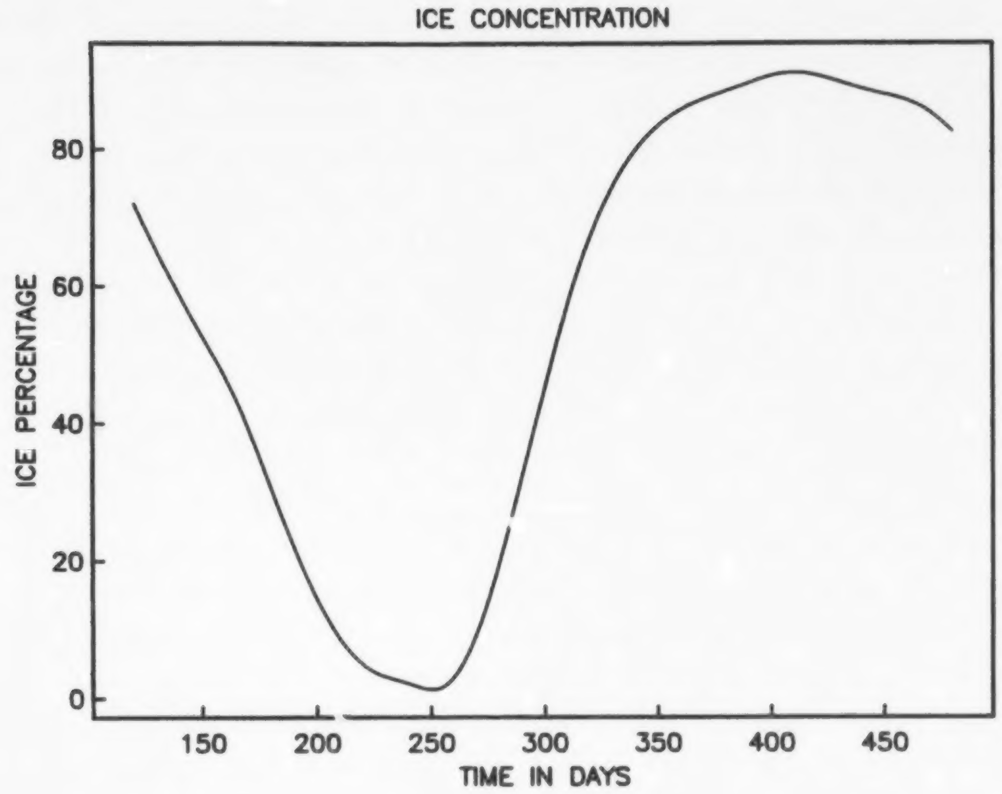

Figure 15. Seasonal evolution of the ice concentration at 78°30'N - 12°30'W.

to inhibit the convection. This would allow a thin ice cover to form along the ice edge and would give us better results for the ice extent. The influence of the lateral ocean advection in their model seems to result mainly in less advance of the ice edge throughout the whole winter season. This effect is mainly due to the heat supply since the lateral salt fluxes tend to induce an opposite effect, with more advance of the ice edge when salt is considered. Finally looking at Figure 14, it seems that the overall effect of neglecting the oceanic and ice advection is less drastic upon the ice distribution than upon the distribution of oceanic properties. It is important, at this state of the work, to think of including the advection terms in the conservation equations of the mixed layer. This improvement can be done by using the ocean circulation model to predict the three-dimensional ocean velocity field.

Acknowledgements

We would like to thank Jackie Castor for the rapid word-processing of this manuscript and Ed Perkins for the careful preparation of the figures.

This work was supported by the "Centre National de le Recherche Scientifique," through the P.N.E.D.C. ASP IOGA, and partly by the U.S. Army European Research Office, contract DAJA45-85-M-0383, via a reimbursable ONR grant through USACRREL. The computing support was provided by the "Conseil Scientifique du Centre de Calcul Vectoriel pour la Recherche."

REFERENCES

Aagaard, K. 1970. Wind-driven transports in the Greenland and Norwegian Seas. Deep Sea Research, V. 17, pp. 281-291.

Adamec, D., R.L. Elsberry, R.W. Garwood and R.L. Haney. 1981. An embedded mixed layer ocean circulation model. Dynamics of Atmospheres and Oceans, V. 6, pp. 69-96.

Carmack, E.C. and K. Aagaard. 1973. On the deep water of the Greenland Sea. Deep-Sea Research, V. 20, pp. 687-715.

Clarke, R.A., J.L. Reid and J.H. Swift. 1984. CSS Hudson cruise 82-001. 14 February - 6 April 1982. Vol. 2, CTD Data plots. Data rep. No 84-14. Scripps Institution of Oceanography, University of California, 172 pp.

Foster, T.D., B.S. McNamara, T.M. Bandurraga and E.G. Eckert. 1985. Physical oceanographic data. Marginal Ice Zone Experiment. R/V Polarqueen June-July 1984. Report, University of California, Santa Cruz.

Gascard, J.C. and R.A. Clarke. 1983. The formation of Labrador Sea water. Part II: mesoscale and smaller scale processes. Journal of Physical Oceanography, V. 13, pp. 1779-1797.

Gordon, A.L. 1978. Deep Antarctic convection west of Maud Rise. Journal of Physical Oceanograhy, V. 8, pp. 600-612.

Hibler, W.D. III. 1979. A dynamic thermodynamic sea ice model. Journal of Physical Oceanography, V. 9, pp. 815-846.

Hibler, W.D. III and K. Bryan. 1986. A diagnostic ice-ocean model. Submitted to Journal of Physical Oceanography.

Houssais, M.N., J. Raunet and J.C. Gascard. 1986. Hydrographic atlas of the Greenland Sea. To be published.

Killworth, P.D. 1979. On "chimney" formations in the ocean. Journal of Physical Oceanography, V. 9, pp. 531-554.

Kim, J.W. 1976. A generalized bulk model of the oceanic mixed layer. Journal of Physical Oceanography, V. 6, pp. 686-695.

Kim, J.W. and W.L. Gates. 1980. Simulation of the seasonal fluctuation of the upper ocean by a global circulation model with an embedded mixed layer. Rep. No. 11, Climatic Research Institute, Oregon State University, 60 pp.

Kraus, E.B. and J.S. Turner. 1967. A one-dimensional model of the seasonal thermocline, Part II. Tellus, Vol. 19, pp. 98-106.

Lemke, P. and T.O. Manley. 1984. The seasonal variation of the mixed layer and the pycnoline under polar sea ice. Journal of Geophysical Research, V. 89, pp. 6494-6504.

Manabe, S. and R.J. Stouffer. 1980. Sensitivity of a global climate model to an increase of CO_2 concentration in the atmosphere. Journal of Geophysical Research, V. 85, pp. 5529-5554.

Martinson, D.G., P.D. Killworth and A.L. Gordon. 1981. A convective model of the Weddell Polynya. Journal of Physical Oceanography, V. 11, pp. 466-488.

McPhee, M.G. 1979. The effect of the oceanic boundary layer on the mean drift of pack ice: application of a simple model. Journal of Physical Oceanography, V. 9, pp. 388-400.

Metcalf, W.G. 1955. On the formation of bottom water in the Norwegian Basin. Transactions of the American Geophysical Union, V. 36, pp. 595-600.

Mosby, M. 1959. Deep water in the Norwegian Sea. Geofysisk publicasjoner, V. 21, 62 pp.

Nansen, F. 1906. Northern waters: Captain Roald Amundsen's oceanographic observations in the Arctic Seas in 1901. Vid. Selskap Skrifter I. Mat.-Naturvidensk Kl., Dybwad, V. 1, No. 3, 145 pp.

Niiler, P.P. and E.B. Kraus. 1977. One dimensional models of the upper ocean. Modeling and Prediction of the upper layers of the ocean, Chapter 10, E.B. Kraus, ed., Pergamon Press, pp. 143-172.

Parkinson, C.L. and W.M. Washington. 1979. A large-scale numerical model of sea ice. Journal of Geophysical Research, V. 84, pp. 311-337.

Pollard, R.T., P.B. Rhines and R. Thompson. 1973. The deepening of the wind-mixed layer. Geophysical Fluid Dynamics, V. 3, pp. 381-404.

Pollard, D., M.L. Batteen, Y.J. Han. 1983. Development of a simple upper-ocean and sea-ice model. Journal of Physical Oceanography, V. 13, pp. 754-768.

Roed, L.P. 1984. A thermodynamic coupled ice-ocean model of the Marginal Ice Zone. Journal of Physical Oceanography, V. 14, pp. 1921-1929.

Roed, L.P. and J.J. O'Brien. 1983. A coupled ice-ocean model of upwelling in the Marginal Ice Zone. Journal of Geophysical Research, V. 88, pp. 2863-2872.

Solomon, H. 1973. Wintertime surface layer convection in the Arctic Ocean. Deep-Sea Research, V. 20, pp. 269-283.

Vowinckel, E. and S. Orvig. 1970. The climate of the North Polar Basin. World Survey of Climatology, V. 14: Climates of the Polar Regions, S. Orvig. ed., Elsevier: 370 pp.

A COUPLED ICE-OCEAN MODEL FOR SHALLOW SHELF SEAS

by W.P. Budgell[1] and D.K. Manak[2]

A dynamic ice-ocean model has been developed for describing ocean circulation and ice motion in homogeneous coastal seas. The circulation component of the joint model consists of a potential vorticity, potential enstrophy conserving finite difference approximation to the shallow water equations. The ice component of the model employs the same finite difference scheme to solve the ice momentum, mass and concentration equations. It is shown that, unlike existing ice models, the ice model developed in this study conserves mass.

Preliminary results from a numerical investigation of ice-ocean interaction in the Southern Beaufort Sea indicate that for low ice concentrations, sea ice distribution on the continental shelf is influenced by high wavenumber variability in the shelf circulation due to topographic steering and scattered shelf waves. At higher ice concentrations, internal ice stress causes small scale variability in both the ice and shelf circulation fields to be suppressed.

[1] Department of Fisheries and Oceans, Institute of Ocean Sciences, P.O. Box 6000, Sidney, British Columbia, Canada V8L 4B2

[2] Department of Physics, University of Victoria, Victoria, British Columbia, Canada V8W 2Y2

ICE DRIFT ON A COMPLEX CONTINENTAL SHELF
THE BERING AND CHUKCHI SEAS

by J.E. Overland and C.H. Pease
Pacific Marine Environmental Laboratory, NOAA
7600 Sand Point Way, N.E., Seattle, WA, U.S.A. 98115

The Bering and Chukchi Seas are two extensive (600 km), shallow (<100 m) and smooth (slopes of 10^{-4}) continental shelf regions connected by Bering Strait. Bering Strait, which is less than 60 m deep with a cross sectional area of $4.1 \times 10^6 m^2$, provides the only avenue of exchange for heat, ice, water and nutrients between the Pacific and Arctic Oceans. St. Lawrence Island to south of Bering Strait forms two additional Straits, Anadyr to the west and Shpanberg to the east. Norton and Kotzebue Sounds to the east are dynamically important appendages. The Bering and Chukchi Seas are seasonal ice zones, influenced by arctic, continental, and maritime air masses. In winter, arctic and continental weather elements predominate, with north to easterly winds, clear skies and large diurnal temperature range. Moist maritime air is associated with two storm tracks, one parallel to the Aleutian Island chain and one curving northward into the Bering and Chukchi Seas. Southward advance of the ice edge is controlled by wind driven advection and cooling of the ambient water column to the freezing point. Since southerly winds associated with northward propagating cyclones inhibit ice advance, the seasonal ice extent is primarily controlled by an externally determined variation in storm track position due to large-scale differences in the general circulation. Beyond a barotropic Rossby radius from coastlines (100 km), ice drift is determined by the local force balance in response to wind stress. Ice drift in the northern Bering-southern Chukchi Seas is influenced by a general northward flow of water driven by higher sea level in the Pacific. Approximately 75% of the ocean transport is through Anadyr Strait. This pattern is reversed or augmented by wind driven coastal currents resulting in ice drift through Bering Strait with speeds as much as 15% of the local wind speed. Little is known about the ice drift in the Gulf of Anadyr to the far west or the influence of ice strength in inhibiting coastal currents in the Chukchi Sea.

HEAT BUDGETS OF LABRADOR SHELF ICE

by M. Ikeda
Department of Fisheries and Oceans
Bedford Institute of Oceanography
Atlantic Oceanographic Laboratory
P.O. Box 1006, Dartmouth
Nova Scotia, Canada B2Y 4A2

A primary question of the Labrador Shelf ice is whether the ice is formed by local thermodynamics or advected from the north. Six different mechanisms are considered to be important: (1) cooling due to atmospheric forcing; (2) heat contained in the shelf water; (3) ice flow from the north; (4) colder water from the north; (5) shoreward surface Ekman flow from warmer Labrador Sea driven by northwesterly wind; and (6) shelf-offshore water exchange associated with mesoscale eddies.

Empirical formulae and various models are applied to estimate contribution from each mechanism; for example, the mechanisms (3), (4) and (5) are estimated using a cross-shelf ice-ocean coupled model driven by alongshore wind. Cooling due to atmospheric forcing is dominant for the completely open water case, while all mechanisms are comparable for the realistically ice--covered case.

III

FORMATION, MOVEMENT AND DEFORMATION OF SEA ICE

MICROMECHANICS APPROACH TO SEA ICE DYNAMICS

by

M. Ostoja-Starzewski[1], R. Jessup[2] and S. Venkatesh[2]

A new model is developed for the analysis of ice fields with discrete random microstructures. The analysis considers from the outset an ice field as an ensemble of interacting ice floes with random physical and geometrical properties. Using a graph representation of a field of pack ice in the material description, a basic micromechanical model is formulated in terms of random force and deformation fields on the graph. In this framework, a visco-elasto-plastic constitutive law is introduced for the inter- and intra-ice floe interactions. This model may then be used as a basis for the Monte Carlo-type simulations of the ice fields as well as for the study of their macroscopic mechanical behavior. Accordingly, the ranges of occurrence of macroscopically elastic and inelastic regions are analyzed and the particular constitutive laws for sea ice are obtained.

---

[1] School of Aeronautics and Astronautics, Purdue University, West Lafayette, IN 47907, U.S.A.

[2] Atmospheric Environment Service, 4905 Dufferin St., Downsview, Ontario, Canada M3H 5T4

INTRODUCTION

The majority of existing models of ice field mechanics have relied on a deterministic continuum hypothesis (see e.g. Pritchard, 1980). It is well known that fields of sea ice exhibit a variety of morphologies, whose very high spatial irregularity is indicative of the intrinsic randomness of their microstructures. Noting that the mechanical behavior of a deformable body is closely coupled with its microstructure, an approach taking into account the discreteness and stochasticity of an ice field is in order.

A research program addressing this problem has been in progress for the past two years (Ostoja-Starzewski, 1984b and 1985). In particular, two problem areas were under study: 1) derivation of the constitutive laws, and 2) fine scale computer simulations of ice field mechanics. Both these areas being closely related, we focus here on a micromechanical formulation that provides an Ansatz for the entire work.

FIELD OF SEA ICE AS A DISCRETE RANDOM MEDIUM

Deterministic continuum mechanics provides an excellent mathematical framework for a theoretical treatment of the bodies that do not display high irregularities in the field quantities (counterexample - turbulence). It also provides a convenient framework for a representation of the spatial and temporal behavior on the scales much larger than those of the observed irregularities. However, deterministic continuum mechanics does not easily admit random microstructural effects in the derivation of appropriate constitutive laws, and various methodologies were recently being explored to deal with that problem in the mechanics of engineering materials (see e.g. Axelrad, 1984). Ice fields belong in the category of those geophysical media whose microstructures display space inhomogeneous and anisotropic properties. In addition, the scale of observation and measurement may play an important role, as it has been observed that the morphology of an ice field can have fractal characteristics (Rothrock et al., 1980). This raises questions concerning the use of a continuum mechanical model with its inherent assumptions of differentiability of various field quantities.

It is clear now that a stochastic micromechanical model is needed to derive the governing equations, notably the constitutive laws, and to analyze their dependence on spatial and temporal scales and particular morphologies of ice fields.

In order to formulate the basic micromechanical model we restrict our attention to a class of fields of tightly packed ice floes in which one can distinguish a single characteristic scale - for example, the mean diameter of an ice floe. Accordingly, the probability distribution of this quantity is assumed to have finite first and second moments. Thus, by the microscale we understand the scale of individual ice floes in the field (order of meters to kilometers).

Similarly to the approach employed in the analysis of constitutive behavior of a saturated soil (Ostoja-Starzewski, 1984a), we introduce a graph representation G(V,E) of an ice field, see Fig. 1. Here V denotes the set of vertices - points at the centers of mass of all the ice floes in a given macro area, and E is the set of edges - lines connecting the vertices of the neighboring (i.e. interacting) ice floes. Now, if B_o denotes the body of the ice field at time t_o and B_t at time $t = t_o + \Delta t$ then

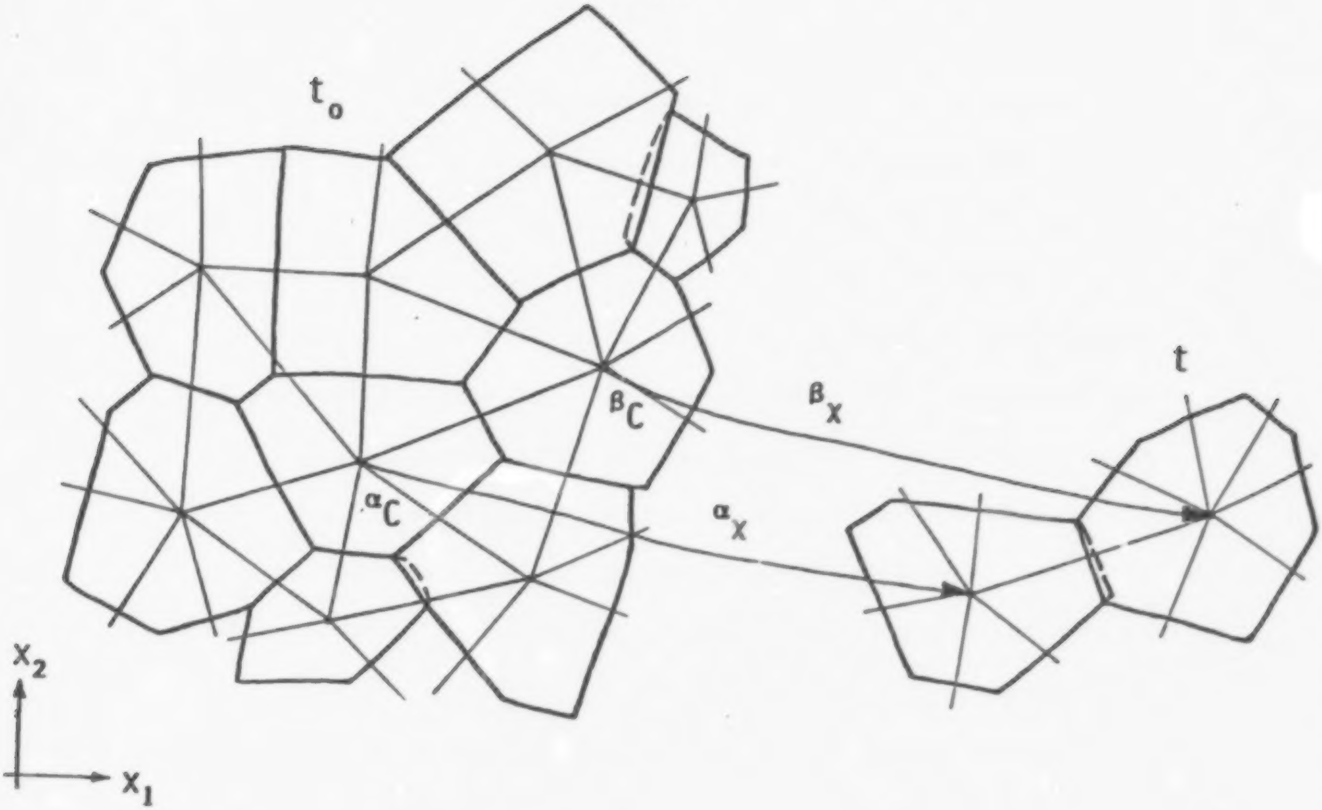

Figure 1. Graph representation of a group of ice floes within a field of pack ice. The thick lines show the contours of ice floes, the broken lines show the rafting effects, and the thin lines are the edges of the set E of G(V, E). $^{\alpha}C$, $^{\beta}C$, ... are the centers of mass of the floes α, β, ... in the field.

$$\chi : \mathcal{B}_o \to \mathcal{B}_t \qquad (1)$$

is the sought-for mapping giving the motion of the entire field. Considering that $\mathcal{B}_o = \bigcup_{\alpha} {}^{\alpha}\mathcal{B}$, where ${}^{\alpha}\mathcal{B}$ is a body of a single (distinguishable) ice floe α in the ensemble, the motion of $\mathcal{B}$, in our graph model, will be given by $\{{}^{\alpha}\chi({}^{\alpha}\underset{\sim}{X}, t);\ t\epsilon T;\ \alpha\epsilon V\}$, where ${}^{\alpha}\underset{\sim}{X}$ is the material coordinate of the center of mass of ice floe α.

Assuming the mapping χ of (2.1.1) is one-to-one, we can write the Eulerian description of motion

$${}^{\alpha}\underset{\sim}{X} = {}^{\alpha}\chi^{-1}(\underset{\sim}{x}, t) \qquad (2)$$

which gives the original positions of the microelements α. However we note that this would require no substantial overlap of ice floes in the Euclidean reference frame (x_1, x_2), i.e. no rafting ridging or crushing - an assumption too unrealistic and restrictive from the physical viewpoint. Obviously, crushing, rafting, ridging, etc. do occur. Hence we do not have a one-to-one mapping, and shall analyze the microscale mechanics in the material description primarily.

CONSTITUTIVE MODELLING AT THE MICROSCALE

It is clear that the microscale mechanics of the ice field exhibits a complicated behavior. We should model this with a ‘coarser description’ on the macroscale, the scale of most interest here. However, one needs to understand and describe the behavior on the microscale first before passage to the macroscale. Following are particular effects observed at the microscale:

a) ice floe mechanics,

b) ice-ice friction,

c) ice-water-ice (lubricated) friction,

d) buckling, cracking, crushing, rafting, ridging and lead formation,

e) random geometry of the field of pack ice.

We see on heuristic grounds that the phenomena a) through d) can be grouped in two loading cases:

normal loading: ice floe mechanics, crushing, rafting, ridging and lead formation;

tangential loading: ice floe mechanics, shear (ice-ice and ice-water-ice) and shear cracking.

We note that both loading cases may result in the inelastic deformations, although for a very tightly packed ice field all the stress components may fall within the elastic range. For the inelastic deformation phenomena the time factor is essential and any elastic-plastic constitutive law without viscosity is physically not too realistic - permanent deformations need finite time to develop. Accordingly we should introduce a rheological model for the nearest-neighbor interactions on the graph G(V,E) that would represent the variety of these microscale phenomena. A visco-elasto-plastic model of Fig. 2 appears to be the simplest and yet adequate micro-mechanical constitutive law for both the normal and the tangential loading cases. Its governing equations are:

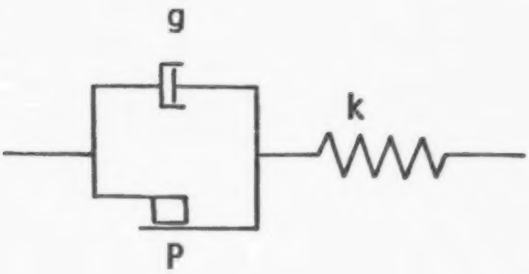

Figure 2. The visco-elasto-plastic model of normal and tangential interactions of two neighboring ice floes.

normal loading:

$$\begin{aligned} &\text{elastic range:} \quad {}^{\alpha\beta}\underset{\sim}{u}^{n} = {}^{\alpha\beta}\underset{\sim}{F}^{n}/k^{n} \\ &\text{inelastic range:} \quad {}^{\alpha\beta}\dot{\underset{\sim}{u}}^{n} = ({}^{\alpha\beta}\underset{\sim}{F}^{n} - {}^{\alpha\beta}\underset{\sim}{P}^{n})/g^{n} + {}^{\alpha\beta}\dot{\underset{\sim}{F}}^{n}/k^{n} \end{aligned} \tag{3}$$

tangential loading:

$$\begin{aligned} &\text{elastic range:} \quad {}^{\alpha\beta}\underset{\sim}{u}^{t} = {}^{\alpha\beta}\underset{\sim}{F}^{t}/k^{t} \\ &\text{inelastic range:} \quad {}^{\alpha\beta}\dot{\underset{\sim}{u}}^{t} = ({}^{\alpha\beta}\underset{\sim}{F}^{t} - {}^{\alpha\beta}\underset{\sim}{P}^{t})/g^{t} + {}^{\alpha\beta}\dot{\underset{\sim}{F}}^{t}/k^{t} \end{aligned} \tag{4}$$

In the above, the superscripts n and t indicate the normal and tangential quantities, respectively. Thus, with reference to Fig. 3, the total relative deformation ${}^{\alpha\beta}\underset{\sim}{u}$ of two interacting ice floes α and β is the vector sum of ${}^{\alpha\beta}\underset{\sim}{u}^{n}$ and ${}^{\alpha\beta}\underset{\sim}{u}^{t}$. Analogous decomposition holds for the total interaction force between α and β. Clearly, the elasticity and viscosity constants k^{n}, k^{t}, g^{n} and g^{t} in this model will be different in the normal than in the tangential loading case. The plasticity element, introduced here, will model: crushing, rafting and microscale ridging in compression, lead formation in tension, and permanent shearing and shear cracking in tangential loading.

It is important to note that all the constitutive coefficients in (3) and (4) - elasticities k^{n}, k^{t}, viscosities g^{n}, g^{t} and plasticity limits P^{n} and P^{t} - are random variables distributed on the set of edges E, that is random fields on E. The nondeterministic nature of the microscale constitutive laws is seen, in the present theory, as a much more important feature than the consideration of linearity vis-a-vis nonlinearity. The stochasticity of constitutive laws leads to an explanation of the mechanisms underlying the formation of various ice field morphologies to be discussed in more detail at a later stage. Also, we

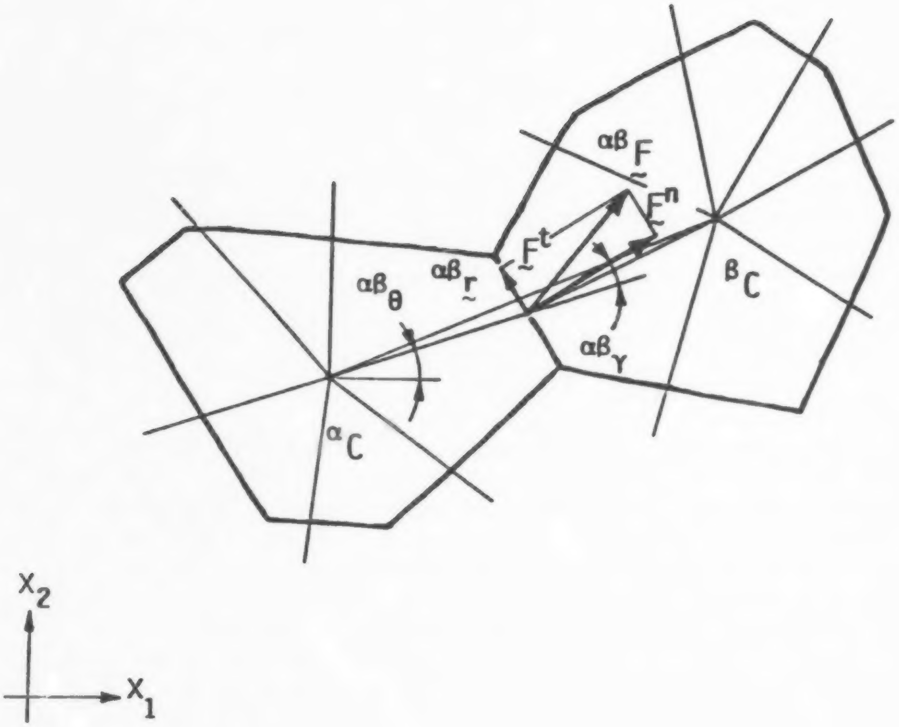

Figure 3. Geometry of two interacting ice floes.

would like to point out that in the discrete form of pairwise interactions the constitutive coefficients are scalars while in the continuum-type laws they are tensors. The former may prove advantageous when it comes to the assignment of physically measurable quantities to the constitutive coefficients.

The graph representation provides now a most realistic model of ice field mechanics which may be used as an Ansatz in the studies of micro- and macro-constitutive laws as well as in the fine-scale numerical simulations. In order to make a passage from the microscale discrete model discussed here to the macroscale continuum description needed in the macroscale geophysical analyses and numerical simulations, we need an intermediate stage - a microscale random continuum. In view of the failure of (2) to hold, the latter is introduced in the material description as a continuous medium most closely equivalent to the microscale model. The equivalence of energy and stress power associated with the volume ${}^{\alpha}V$ of a microelement α is used as a criterion for derivation of the continuum-type constitutive relations:

elastic range: $\underset{\approx}{E} = \underline{\underline{B}}\,\underset{\approx}{S}$

inelastic range: $\dot{\underset{\approx}{E}} = \underline{\underline{A}}(\underset{\approx}{S}-\underset{\approx}{R}) + \underline{\underline{B}}\,\dot{\underset{\approx}{S}}$

In the above $\underset{\approx}{E}$ is the Green's strain tensor, $\underset{\approx}{S}$ is the second Piola-Kirchhoff stress tensor, and an overdot indicates the time rate derivative. The constitutive tensors $\underline{\underline{A}}$, $\underline{\underline{B}}$ and $\underset{\approx}{R}$ can explicitly be derived for a particular ice floe α, and they are functions of the following quantities:

a) angles ${}^{\alpha\beta}\theta$, ${}^{\alpha\beta}\gamma$,

b) contact area ${}^{\alpha\beta}A$,

c) vector ${}^{\alpha\beta}\underset{\sim}{r}$,

d) ice floe thickness,

e) elastic and viscous coefficients k and g in (3) and (4),

f) yield limits P^n and P^t in $(3)_2$ and $(4)_2$.

In view of the randomness of the above quantities, the rheological coefficients $\underset{\approx}{A}$, $\underset{\approx}{B}$ and $\underset{\approx}{R}$ are also random in addition to being spatially inhomogeneous and anisotropic, i.e. random tensor fields characterized by the correlation distance equal to the mean floe diameter. Hence our designation: random continuum model.

PASSAGE FROM MICROSCALE TO MACROSCALE

In order to use the micromechanically derived local continuum-type constitutive law in the large "rough" scale analyses and simulations, one has to be able to assess the field statistics of:

- quantities a) through f) listed above,
- spatial distribution of elastic and plastic regions in the ice field domain.

In case of a large scale computer simulation (e.g. Hibler, 1979) of the Arctic Ocean, a part of it, or an Arctic Channel, such an assessment would have to be done preferably ahead of each time step calculation. In that respect two principal measuring techniques may be considered: Side Looking Airborne Radar System (SLAR) and Landsat. Their respective photograph characteristics would be as follows:

SLAR: adequate quality for the assessment of the ice field morphological statistics, independence of weather conditions, availability on an irregular basis.

Landsat: quality dependent on weather conditions, lower resolution, availability on a regular but "widely spaced" basis.

In order to study the effects of microscale randomness on the macroscopic response of an ice field, a computer program simulating the motion of a large rectangular array of square-shaped ice floes was developed (Ostoja-Starzewski, 1984b, 1985). With the geometrical randomness absent in this model, the heterogeneity of the ice field was reflected through the physical coefficients characterizing all the ice floes, and sampled from the uniform or Gaussian probability distributions. The program was used to study the elastic-plastic transitions and the finite motions of the ice field. In the first case, this Monte Carlo simulation revealed the existence of two principal ranges of mechanical behavior - macro-elastic and macro-inelastic - separated by the elastic-plastic transition regime. If an occurrence of a passage from the elastic to the plastic range at the microscale is taken as synonymous with the formation of a microridge (scale of 1 km in this simulation) then any spatially random ridge distribution in the ice field domain may be characterized by a fractal dimension. The simulations indicate that the elastic-plastic transition regime has a strongly non-integer fractal dimension and may be termed the strong correlation range. On the other hand, both, the macro-elastic and macro-inelastic ranges have near integer fractal dimensions, i.e. weak correlation range. A probabilistic analysis in terms of a random field on the graph G(V,E), similar to the one conducted for the soil model (Ostoja-Starzewski, 1984a), strongly corroborates these results.

The existence of two ranges of constitutive behavior due to the microscale material randomness - strong and weak correlations - necessitates different analytical procedures for the derivation of the macroscopic constitutive laws. In the case of weak correlations (macro-elastic or macro-inelastic behavior) a rather well known approach developed in the mechanics of multiphase media can be employed, with a restriction to infinitesimal motions. This procedure requires sufficient information on the ice field's random morphology in the given macro-area. Thus macro-elastic and macro-inelastic - including special cases of macro-plastic or macro-visco-elastic - constitutive formulas can be derived.

While the derivation of the constitutive formulas in the weak correlation case is based on the approximation of an actual random strain field by the average strain field (space-homogeneous distribution of elastic and inelastic regions in the ice field domain), this approximation is invalid for ice fields having morphologies characterized by the strongly non-integer fractal dimensions. In this case the physical quantities and hence the constitutive laws are strongly scale dependent. Derivation of a macroscopic relation governing the elastic-plastic transition is at present under study.

Finally, we comment on the computer simulations of finite motions of the sea ice. The graph model provides a natural framework for the introduction of microstructural randomness, and the computer runs show cooperative field effects with real-like irregularity features (e.g. ridging) as opposed to the smooth-type deformation fields of the deterministic simulations. Due to the limitation of computer memories and computational speeds, however, such simulations have generally to be limited to relatively small areas, e.g. an Arctic Channel or a region of the Arctic Ocean. Results on such fine time scale and spatial scale simulations will also be given in the future papers.

CONCLUSION

A micromechanics approach to modelling the sea ice dynamics has been presented. The study is restricted to fields of tightly packed ice which exhibit a single characteristic size at the microscale. The basic graph-type model allows the treatment of an ice field as an ensemble of interacting ice floes with random physical and geometrical properties. This model may be used for the derivation of the continuum-type constitutive laws, the analysis of their ranges of applicability and spatial scales dependence, and for the development of a Monte Carlo program for the simulation of fine scale motions of heterogeneous ice fields.

ACKNOWLEDGMENT

The authors are grateful to V.R. Neralla of the Atmospheric Environment Service for many discussions and comments on this research. This research was supported by the Department of Environment, Canada.

References

1. Axelrad, D.R., Foundations of the probabilistic mechanics of discrete media, Pergamon Press, Oxford, 1984.

2. Hibler, W.D., III, A dynamic thermodynamic sea ice model, J. Phys. Oceanogrpahy, 9, 815-846, 1979.

3. Ostoja-Starzewski, M., Quasi-static motion of a heterogeneous medium via dynamic random field, 21st Ann. Mtg. Soc. Eng. Sci., Blacksburg, Virginia, 1984a.

4. Ostoja-Starzewski, M., Micromechanics model of the stochastic evolution of the ice fields, Report to the Atmospheric Environment Service, Environment Canada, 1984b.

5. Ostoja-Starzewski, M., A stochastic micromechanics model of the ice fields, Report to the Atmospheric Environment Service, Environment Canada, 1985.

6. R.S. Pritchard (ed.), Sea ice processes and models, U. of Washington Press, Seattle and London, 1980.

7. Rothrock, D.A. and A.S. Thorndike, Geometric properties of the underside of sea ice, J. Geophys. Res., 85C, 3955-3963, 1980.

STATISTICAL KINEMATICS FOR THE SEA ICE DISCONTINUUM

by

A. S. Thorndike
Physics Department
University of Puget Sound
Tacoma, WA 98416

ABSTRACT

Ideas from the theory of turbulence can be used to describe the deformation of sea ice. A statistical description of the relative motion of pairs of ice particles is presented with an emphasis on how the statistics depend on the time interval over which the motion occurs and on the separation. The mean squared change in separation is shown to depend on the separation raised to a positive power between one and two. This is an empirical result based on observations from the Bering and Beaufort Seas.

STATISTICAL KINEMATICS FOR THE SEA ICE DISCONTINUUM

What are our reasons for having an interest in the motion of sea ice? Of first importance is the transport of ice from one part of the Arctic Ocean to another, and the transport out of the basin. These quantities figure into the heat, water, and salt balances of the ocean, and a geophysicist has no trouble justifying his interest in them. A second reason is a hunch, shared by others, I think, that there is a connection between the ice motion and the morphology of the ice pack. Better understanding of the way the ice moves may help to understand the large scale properties of the ice pack, such as its thickness distribution, its floe size distribution, the roughness of its surfaces, its strength, and so forth. In particular, there is a relationship between the way the ice moves and the ways in which leads are formed and closed. Because of this, the ice motion modulates the growth of new ice and may control the development of the mixed layer structure in the upper ocean.

The idea here is similar to strain hardening in other materials: as the material deforms, it changes its mechanical properties. For sea ice, one might claim that the material changes all its properties because of its motion.

The point I wish to emphasize is that we do not study the motion because it is somehow important in its own right. Rather our interest is an applied one. We entertain the hope that the ice motion may be a kind of proxy for more important processes. If this were known to be untrue, then we would stop analysing sea ice motion, except to determine the gross transports. As we go along in this study, we should keep the goals clearly in mind. We should make a stronger effort to tie our kinematic analyses to other geophysical processes.

Two approaches have been taken in studying the ice deformation. The first approach follows the classical analysis of the deformation of a continuum. It aims at determining kinematic quantities such as the divergence, the shear, and the vorticity of the ice. There are deep problems with this approach. They concern the definitions of the kinematic quantities, the absence of well defined time or space scales, the difficulties in estimation, and the unclear connection between these concepts and other processes of interest. The fundamental difficulty is that the ice motion does not vary continuously in space. This calls into question the notions of spatial derivatives, upon which the continuum analysis of motion is based. There may be some sense in which large scale average spatial gradients are well defined, but such a definition will surely involve specification of a length scale, and there is no natural scale. That the analysis is on shaky footing becomes apparent when trying to estimate quantities with limited data. There is no way to evaluate the uncertainties in the estimates unless one has a well defined quantity to estimate.

All of these objections would pale if there were any demonstrated successes of the above procedures. Suppose one could confirm a relationship between these kinematic quantities and any other independently measured quantity of interest. Then he could argue that, despite my objections above on matters of principle, the technique has an empirical justification. I would support that argument. But the fact is that such demonstrations have not been acheived. An example would be to predict the change in the thickness of ice in a region on the basis of the deformation record for some interval of time, and to compare this with the actual change in thickness.

The second approach to the study of ice motion has avoided the notions of spatial derivatives and the existence of natural space scales. As a precedent, one looks to L.F. Richardson, who asked in his classic paper

"Atmospheric diffusion on a distance neighbor graph": "Does the wind possess a velocity?" Here of course he was referring to the possibility that the time derivative, defined as a limit for small times, might not exist. After examining the evidence, Richardson could not answer his question, so he felt compelled to develop a theory of turbulence in which the concept of velocity does not appear. We are in a similar position. We need a theory of ice deformation in which spatial derivatives do not appear.

A natural idea might be to replace gradients like du/dx by differences like $u(x+L)-u(x)$. This involves the choice of a length scale, an action which is to be avoided because nature does not provide such a scale, and because, it that absence, we could never agree among ourselves.

There are three ideas behind this second brand of kinematics. The first is to examine the relative motions of pairs of points. The second is to examine how the relative motion depends on separation. The third is to worry only about the statistics of quantities. All three ideas are embedded in the definition of the function $B_p(L)$:

$$B_p(L) = \langle u(x+L,y)u(x,y)\rangle.$$

Note that B_p shows how the average product, or correlation, of velocities at two points, depends on the separation L between the points. There is no assumption of differentiability, no specification of a length scale. The estimation problems are somewhat ameliorated by the ensemble average which allows one to combine data from many different times and places.

Of course correlation functions like this are a staple to students of turbulence. Through the use of such functions one tries to characterize the statistical properties of the motion, and not describe the actual paths followed by the individual particles.

I will outline now some of the attempts I and others have made to apply these ideas to sea ice. For details and for actual data, one should refer to the original papers.

Consider two points separated by a distance l. Let $r(t)$ be the change in separation over a time t. Then $r(t) = t *(u(x+l)-u(x))$, and the square of $r(t)$ involves products of u at x and at $x+l$. Therefore when we examine the behavior of r squared, we could just as well speak of the correlation function B_p evaluated at $L=l$ and at $L=0$.

For molecular diffusion, the average square of r will be proportional to t, and independent of l

$$< r^2 > \sim t.$$

For a smooth flow, $< r^2 >$ will be proportional to t squared to l squared, at least for small l and t. The constant of proportionality will be the square of the typical velocity gradient.

For the isotropic, stationary, homogeneous, turbulent motion of an incompressible material, Batchelor (1960) states that $<r^2>$ increases like t squared and l to the power 2/3 for small time, and as t to the power one and l to the power 4/3 for large t. I cite these several situations, not because there is any a priori reason to expect sea ice to behave in one way or another, but to illustrate that a quantity like $< r^2 >$, or, equivalently, the correlation function B_p, can be used to discriminate different kinds of kinematic behavior.

The limiting behavior of $r(t,l)$ for small t and small l is of particular interest because it is the small l structure which is incompatible with the existence of space derivatives. To estimate the behavior at small distances requires abundant data from points close together. The first such data to be used for this purpose were the displacements measured at about 2 km intervals along a 800 km line. The displacements occurred over a three day time interval. The data were extracted from the SEASAT synthetic aparture radar mission by Hall and Rothrock. The plot of $< r^2 >$ versus l (Fig. 1) supports a power law dependence over a range of $2 < l < 500$ km. A power of 1.1 to 1.3 is indicated. The power is clearly not equal to 2.0 as it would be if the motion was spatially smooth. One hesitates to extrapolate on the basis of this single set of data to other regions or times. Other bits of evidence are accumulating which suggest that this result is characteristic for sea ice.

A second bit of evidence comes from the Bering Sea. Here a number of targets were tracked for a two week period. Length scales ranged from 5 to 50 km, and time scales from 1 hour to several days. The plots of $< r^2 >$ divided by t (Fig. 2) show this quantity to be proportional to t for small t and tending to become independent of t for t larger than about three days. This is identical to the t behavior for turbulent motion quoted above from Batchelor. The l dependence (holding t=3 days) follows a power law with power 1.8. This is not the 4/3 law which applies to the special turbulent motion Batchelor discusses, and of course there is no reason to expect it to be. Neither is it the same as the 1.1 to 1.3 power found from the SEASAT data in the Beaufort Sea. And neither is it 2.

The third source of data to consider comes from the array of drifting buoys which have been tracked over much of the Arctic Ocean since 1979. Here the data only resolve space scales ranging from 300 to 2000 km. I find it helpful to separate the motion of these buoys into a long term drift associated with the mean velocity field, and a short term, zero mean fluctuating motion. When the motion of pairs of points is considered, both the mean field and the fluctuating field can cause the buoys to separate. For the moment forget the mean field. The changes in

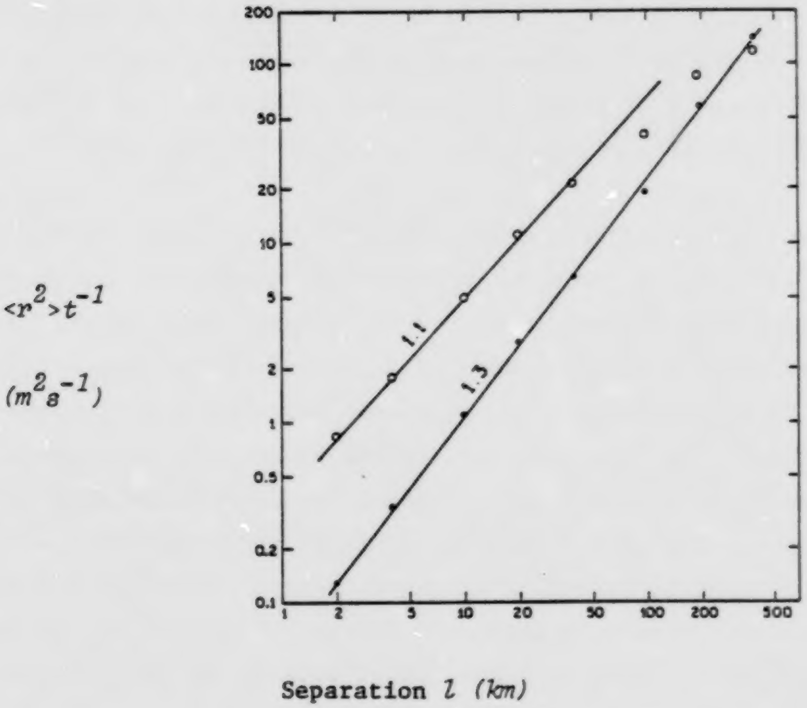

Figure 1.

$<r^2>t^{-1}$ versus l for $t = 3$ days. Beaufort Sea data of Hall and Rothrock, 1981, analyzed by Thorndike, 1986. The change in separation is resolved into components parallel to the separation (r_p), shown by the open circles and those normal to the separation (r_n), solid circles.

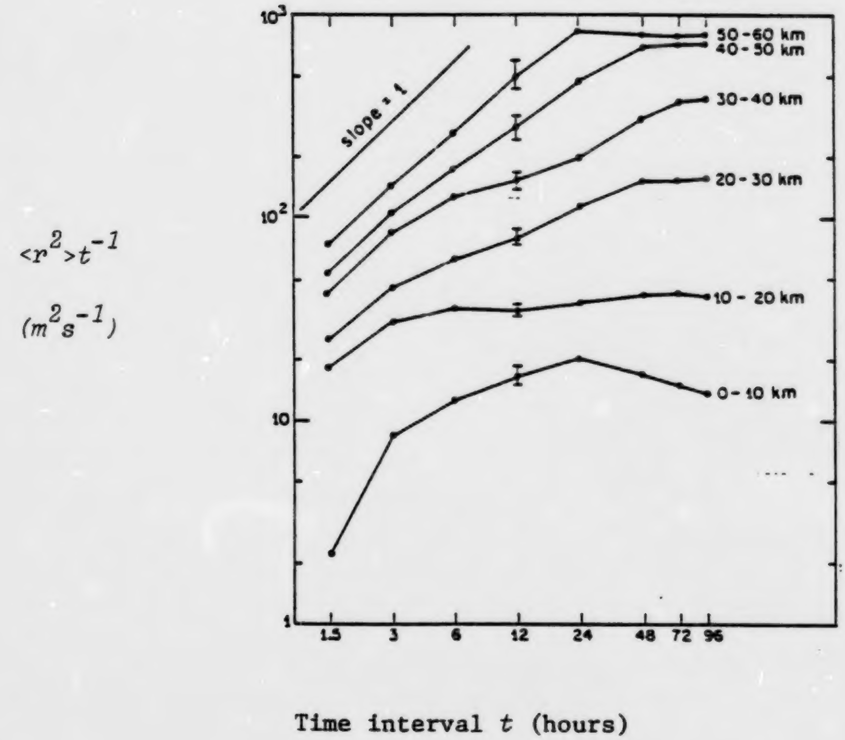

Figure 2.a.

$<r^2>t^{-1}$ versus t for the separations indicated. Bering Sea data.

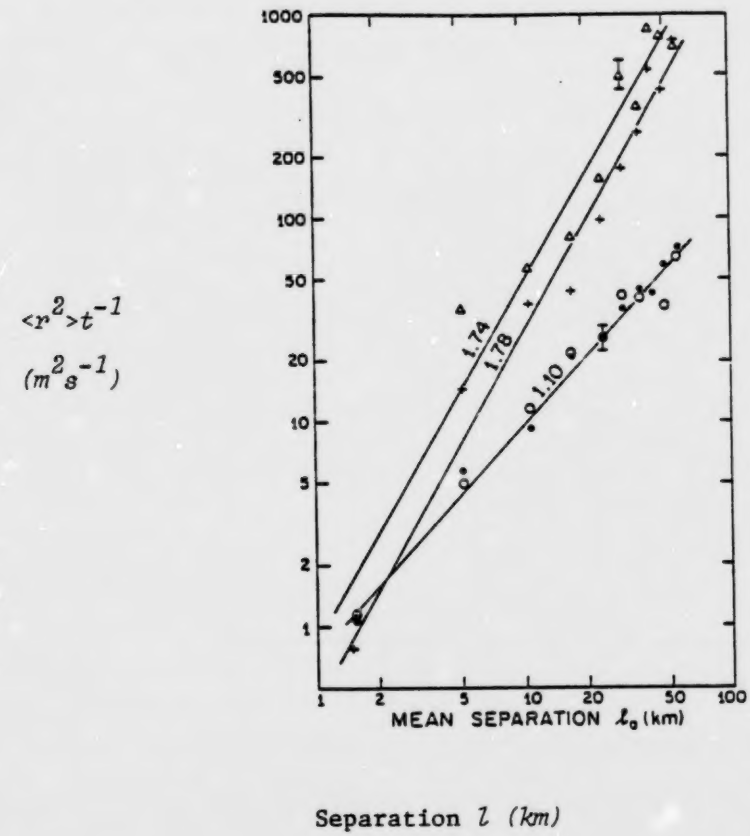

Figure 2.b.

$<r^2>t^{-1}$ versus l. The open circles depict $<r_n^2>t^{-1}$ and the closed circles $<r_p^2>t^{-1}$ for t = 1.5 hours. The triangles and plusses depict $<r_n^2>t^{-1}$ and $<r_p^2>t^{-1}$ for t = 72 hours.

squared separation due to the fluctuating motion increase as t to the power 1.5 and l to the power 1.0 for these scales (Fig. 3).

What does all of this mean? I interpret it as support for the second type of kinematics. That these statistics have systematic behavior as funtions of space and time, encourages me to think that we may be able to characterize the motion in a concise way. It remains to demonstrate that such a characterization has any value. I offer two arguments.

First, it is possible to deduce other statistical properties of the motion from these correlation functions. One example is that it is possible to make inferences about diffusion of sea ice from these functions. Imagine an oil spill contaminating a few square miles of the ice pack. What will be the long term behavior of the contaminated region? The rate at which the contaminated ice mixes with the surrounding ice can be estimated using the correlation functions. In Thorndike (1986), I compare the rate of spreading due to the long term mean flow and to the fluctuating motion. The fluctuations can cause a region with diameter 100 km to diffuse over a 200 km diameter during a period of ten years.

A second value in these statistics is that they can be used to test mechanisms of ice motion. For example in the paper just mentioned, I suggest that one way to think about the ice motion is as sequence of independent displacements along random cracks. Each event consists of picking a random line to be the crack, and picking a random displacement to occur between the ice on either side of the crack. Now repeat this a million times. The mechanism has, to me, a certain intuitive appeal since it captures both the discontinuous and the random natures of the actual motion (Fig. 4). But the point I want to stress here is that we can test such a mechanism by seeing what kind of statistics it would generate. In the present example, it turned out that the mechanism reproduced the dependence of $< r^2 >$ on t but not on l.

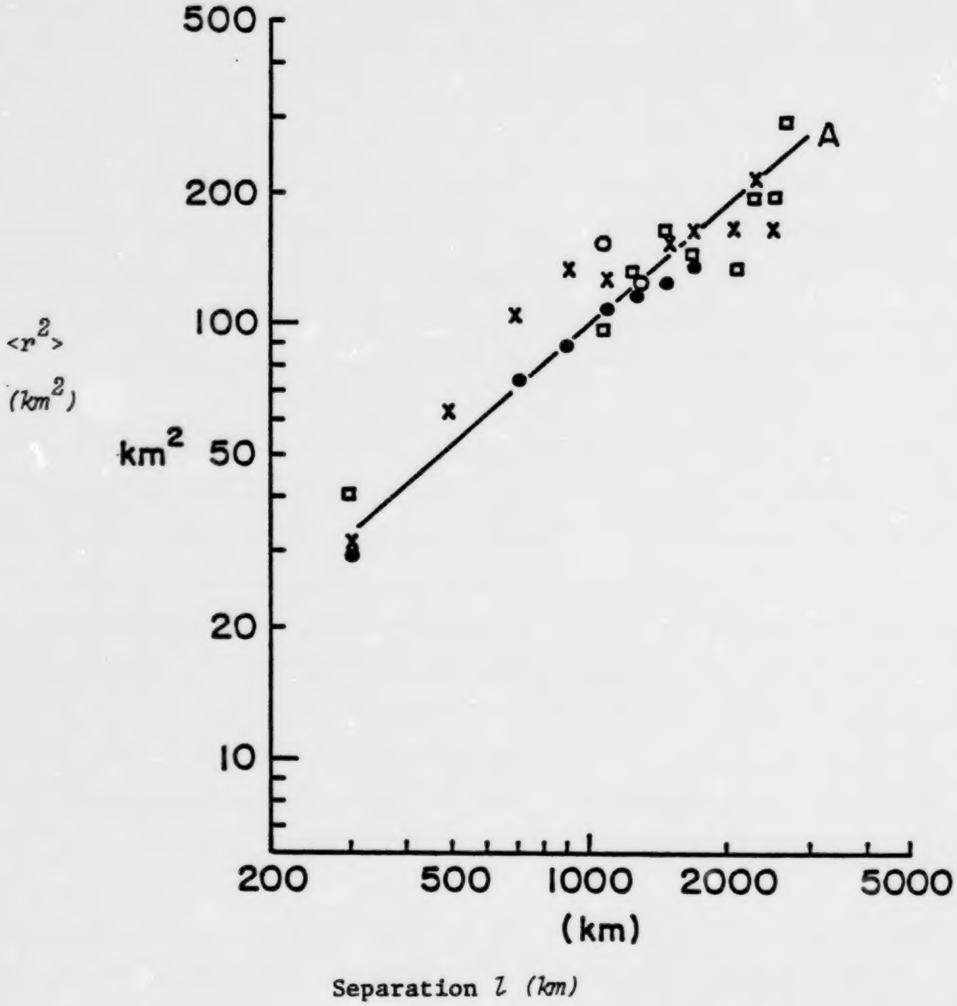

Figure 3.a

$<r^2>$ versus l, for t=1 day. Central Arctic data.

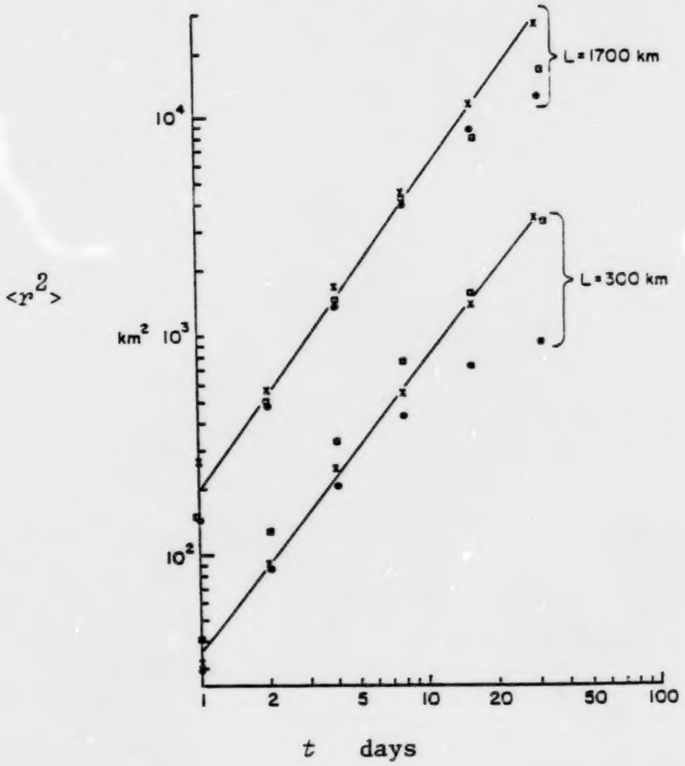

Figure 3.b

$<r^2>$ versus t, for l=300 km and l= 1700 km.

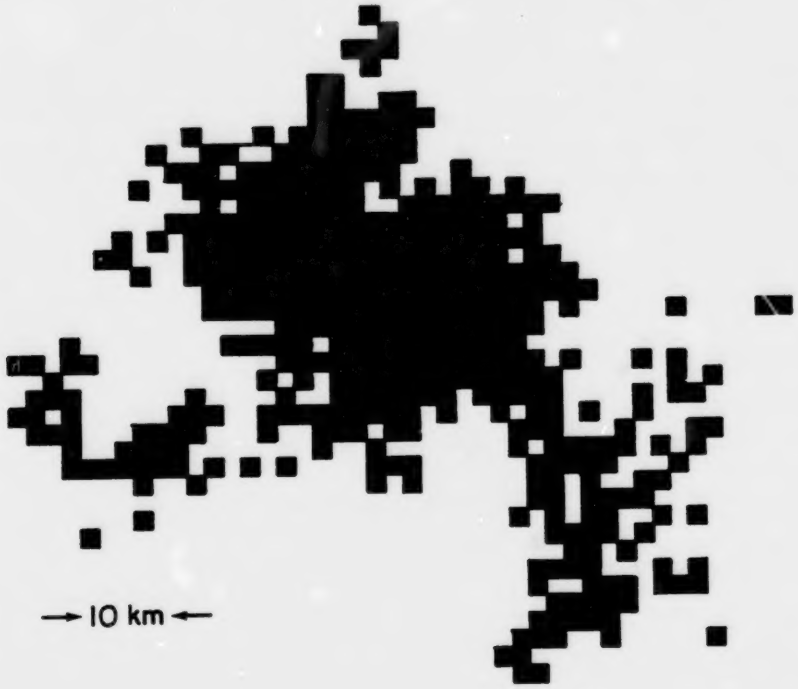

Figure 4.

The rearrangement of a 40 km square by 1000 horizontal and vertical cracks, corresponding to one year. The cell size is 2 km by 2 km, and the displacement associated with each crack is 2 km.

REFERENCES

BATCHELOR, G.K. 1952. Diffusion in a field of homogeneous turbulence,2, the relative motion of particles. Proceedings of the Cambridge Philosophical Society, 48, 345-362.

HALL, R.T. and ROTHROCK, D.A., 1981. Sea ice displacements from SEASAT synthetic aperture radar. Journal of Geophysical Research, 86, C11, 11078-11082.

MARTIN, S. and THORNDIKE, A.S. 1985. Dispersion of sea ice in the Bering Sea. Journal of Geophysical Research, 90, C4, 7223-7226.

RICHARDSON, L.F. 1926. Atmospheric diffusion shown on a distance neighbor graph. Proceedings of the Royal Society of London, A110, 709-737.

THORNDIKE, A.S. 1986. Diffusion of sea ice. Journal of Geophysical Research, to appear.

THORNDIKE, A.S. 1986. Sea ice kinematics, in Geophysics of Sea Ice, edited by N. Untersteiner, Plenum, New York, in press.

OBSERVATIONS OF THE TRANSFER OF HEAT BETWEEN WATER AND ICE

by P.F. Hamblin[1] and E.C. Carmack[2]

The flux of heat between sea water and ice is either ignored or set to a constant value in present sea ice models. A more accurate specification may be desirable especially in the vicinity of polynyas and ice margins.

Extensive observations of currents and temperatures under the ice in a number of lakes in the headwaters region of the Yukon River have permitted the determination of the sensible heat transfer coefficient between water and ice (Stanton Number) by four independent approaches. The method which relates observed ice and snow thickness and surface meteorology to under ice flow and water temperatures near an outflow polynya appears to be the most reliable. A mean value of the sensible heat transfer coefficient of 1.5×10^{-3} was inferred. This value is larger than that reported in laboratory studies but almost identical to the neutrally stable atmospheric boundary layer. Applications to polynya formation are discussed.

[1] National Water Research Institute, 867 Lakeshore Road, Burlington, Ontario
Canada L7R 4A6
[2] National Water Research Institute Branch, 4160 Marine Drive, West Vancouver,
British Columbia, Canada V7V 1N6

SIMULATION OF SEA ICE CLIMATOLOGY AT THREE ARCTIC LOCATIONS

by R. Gabison
Meteorological Services Research Branch
Atmospheric Environment Service
4905 Dufferin Street, Downsview, Ontario, Canada M3H 5T4

The formulation and application of a one-dimensional sea ice thermodynamic model is presented. The model sensitivity to changes in oceanic and atmospheric parameters is analysed and compared with previous studies. The model is applied to three locations in the Arctic; Cambridge Bay, Frobisher Bay and Alert Inlet, to study the model's ability to simulate the annual cycle of first year ice. The model results are compared with climatological data and discussed in terms of the main thermodynamic processes and the combined effect of oceanic tides and of sea ice deterioration by melting contributing to break-up. It is shown that the model is effective in simulating the climatology of first year ice at three Arctic locations. The study also suggests that improved model performance can be expected from additional research and application of a flexural forcing of the ice by waves and tides and deterioration of ice strength during melting.

EFFECTS OF THE ANNUAL ICE-COVER ON TIDAL CURRENTS AND FRESHWATER CONTENT OF CANADIAN INLAND WATERS

by

S.J. Prinsenberg

Department of Fisheries and Oceans
Bedford Institute of Oceanography
Dartmouth, Nova Scotia
B2Y 4A2

ABSTRACT

Admittance analysis on long current meter records from the Hudson Bay and Lancaster Sound is used to study the effect of the annual ice-cover on tidal currents. For each location, current speed and direction records from three depths were split up into monthly record sections on which admittance analysis was performed using the Halifax tide as a year-round open water reference signal.

In Hudson Bay the semidiurnal tidal current is reduced by ten percent and arrives twenty minutes earlier during maximum ice-cover conditions as compared to open water conditions. The weaker diurnal tidal current shows similar characteristics but its weaker signal does not produce as reliable (coherencies) and consistent results. Similarly, in the Lancaster Sound the semidiurnal tidal current decreases in amplitude and arrives earlier during the winter at the two larger depths but its amplitude increases in the surface mixed layer. This latter effect may be a local phenomena as severe ridging of the ice cover occurred at this location when the mooring was in place.

The salt rejection and freshwater content of the annual ice-cover are major contributors to the seasonal variation in the freshwater content of the water column. The freshwater content calculations show that much more ice-production per unit area is required than level ice observation indicate. Part of the discrepancy can be found in the ice accumulated in ice ridge formation which on the average account for 0.05 m of extra ice for each ridge occurring per kilometer. For Hudson Bay and the Lancaster Sound this means an extra 0.3 m of ice can be attributed to ice ridging increasing to as much as 1.0 m of ice for Foxe Basin where extreme rough ice conditions occur. Not only is it important to know the relationship

between ice-production per unit area and the observed level ice thickness for the freshwater budget of an area, but also the spacial and temporal distributions of the ice accretion and ablation as ice ridging usually occurs later and downstream from the place where the ice was actually formed.

INTRODUCTION

Large areas of Canadian northern waters have an annual ice-cover which advances in winter as far south as James Bay and the Gulf of St. Lawrence River and retreats in summer to the middle of the Canadian archipelago (Fig. 1). Maximum level ice thicknesses range from 1.0 m in southern James Bay to 2.0 m in Foxe Basin and Lancaster Sound (Markham 1981). During normal years landfast ice is found in sheltered inshore areas and north and west of Resolute Bay. A more mobile ice-cover with more than 9/10 ice concentration is found in other areas such as Baffin Bay and Hudson Bay.

As early as 1943, Zubov noted that the tide may be altered by an ice-cover as the range became smaller and high (or low) tide occurred later during the winter in two rivers draining into the White Sea. In the Canadian Arctic, Henry and Foreman (1977) observed marked changes in the Beaufort sea tide and an inspection of tidal records in other Canadian waters revealed that some areas are apparently unaffected while others, usually located farther inland, experience smaller tides and whose phases are altered during the annual period of an ice-cover (Godin and Barber 1980).

Salt rejection during the forming of the ice-cover and freshwater rejection during its decay affects the vertical stratification of the water column over large areas. The salt rejection over shallow continental shelves of the Arctic Ocean is thought to be responsible for the formation of the cold upper halocline of the entire Arctic Ocean (Aagaard et al. 1981). Melling and Lewis (1982) also detected this process in the Beaufort Sea shelf notwithstanding the large freshwater input of the MacKenzie River. The cold saline bottom water observed by Campbell (1964) in Foxe

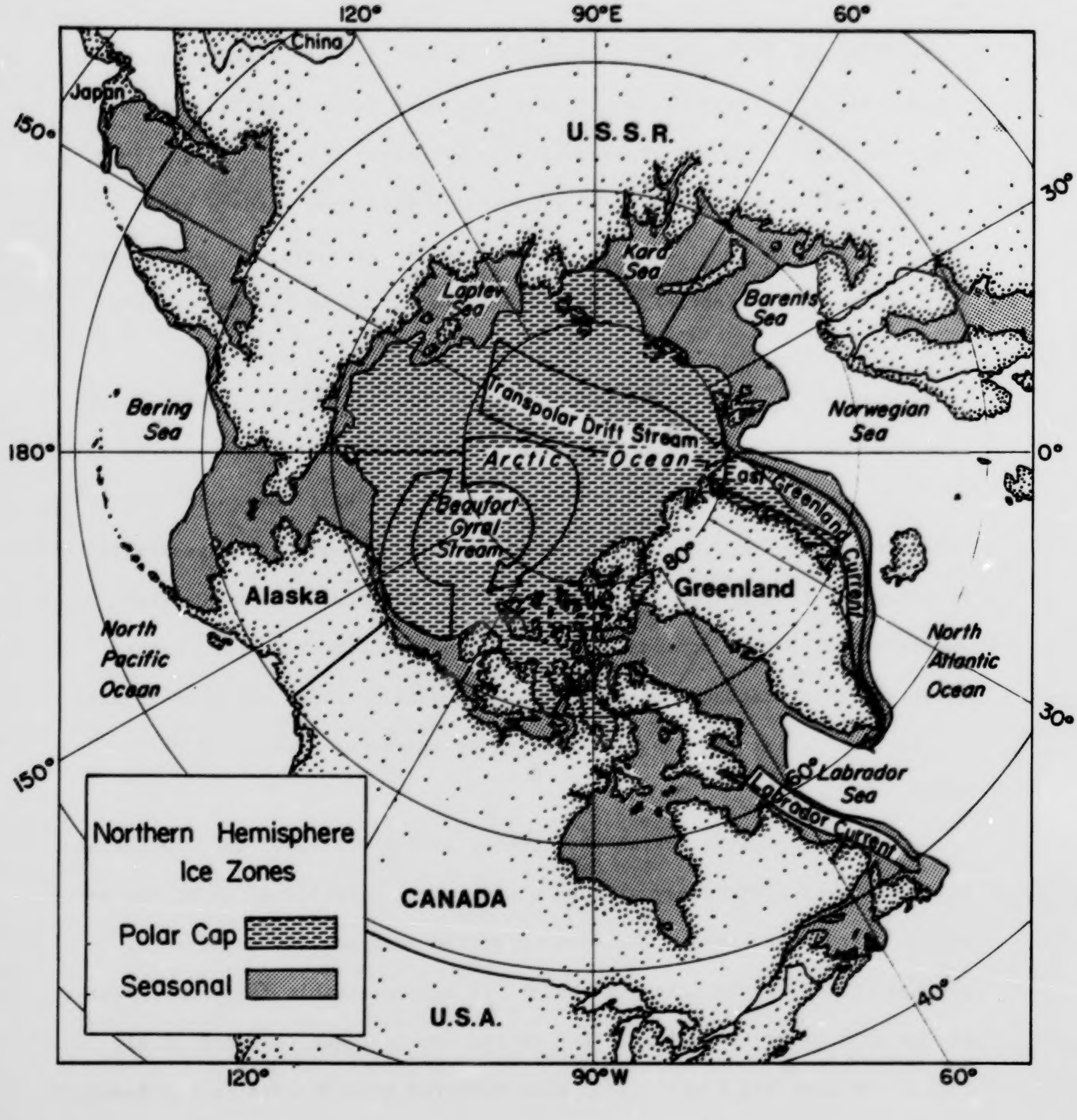

Figure 1. Maximum and minimum ice-cover extent in northern hemisphere.

Basin was similarly produced over the extensive shallow shelf located in the northern half of the basin. The large amounts of melt water, rejected during the ablation of the annual ice-cover, stabilizes the surface layer and suppresses mixing and upward transport of nutrients. The variation in the annual freshwater input supplied by both ice-melt and runoff of Hudson Bay and Foxe Basin to the Labrador Sea is thought to alter vertical stability of the water column and hence nutrient supply in the Labrador Sea as noticed in the yearly fish abundance downstream of the area of nutrient injection (Sutcliffe et al. 1982). It will be shown that the amount of salt and freshwater rejection from the ice-cover not only depends on the level ice thickness data as monitored at several locations in the Canadian Arctic but also on other ice-cover properties such as sublimation and size and frequency distributions of ice-ridges. The object of this paper is to show that the annual ice-cover in Lancaster Sound and Hudson Bay affects the tidal currents similarly as the tidal heights and that there exists a large difference between level ice thickness values and values of ice-production for unit area at several locations in the Canadian Arctic.

TIDAL HEIGHTS AND CURRENTS

Going north along the Labrador coast, the mixed but mainly semidiurnal tide becomes more and more semidiurnal and increases in amplitude to 3.0 m just north of the entrance to Hudson Strait (Dohler 1966). Northward through Davis Strait the semidiurnal tidal amplitude decreases into Baffin Bay to a location halfway along the coast of Baffin Island where an M_2 amphidromic point is located. From this point on, the tidal amplitude increases again as it moves into Smith Sound and into Lancaster Sound reaching amplitudes of 1.2 m and 0.7 m respectively (Fig. 2; Godin 1966).

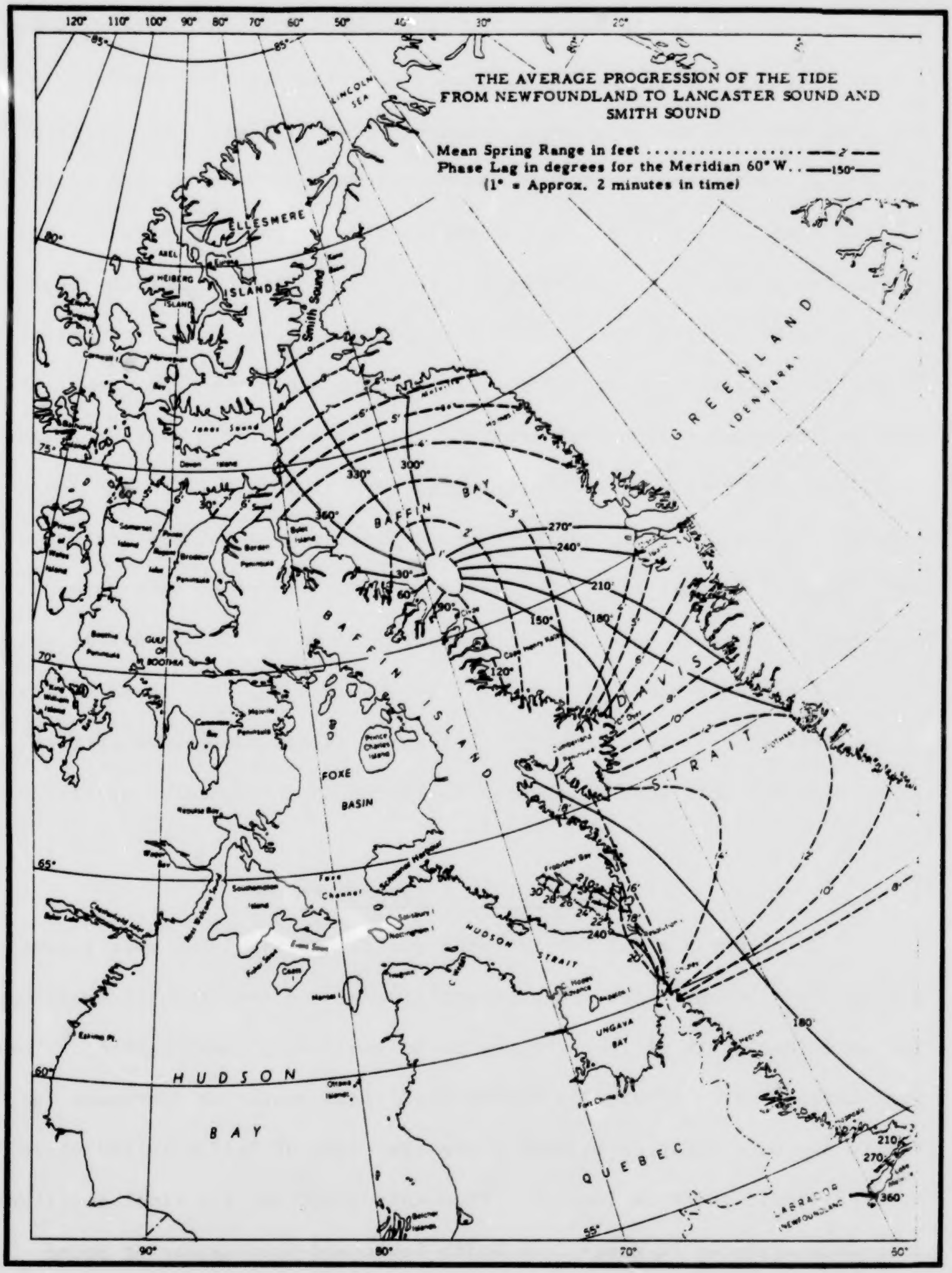

Figure 2. Tidal range (in feet) in Baffin Bay and Lancaster Sound (from Dohler, 1966).

The amphidromic point in Baffin Bay is closer to the Baffin Island coast than the Greenland coast because damping decreased the amplitude of the reflecting Kelvin wave propagating southward along the Baffin Island's coast relative to the incoming Kelvin wave propagating northward along the Greenland's coast. Similar motion of the amphidromic point towards the coast along with the reflecting Kelvin wave propagates is seen in coastal seas such as the Gulf of California (Hendershot 1981). Within Lancaster Sound the tide is semidiurnal, increases its amplitude from 0.6 m at the entrance to 0.7 m halfway up the Sound before decreasing again to 0.4 m some 1-1/2 hours later at Resolute Bay. Partial reflection of the tide occurs from the island arc located 50 km west of Resolute Bay. West of this area, the semidiurnal tide originating in the Atlantic Ocean decreases rapidly and makes an amphidromic point with the eastward propagating tide coming from the Arctic Ocean (Tait et al. 1980).

The tide in Hudson Strait, Foxe Basin and Hudson Bay is semidiurnal except for two locations; along the east coast of Hudson Bay and in northwestern Foxe Basin where the local semidiurnal tide is reduced and mixed but still mainly semidiurnal tides occur (Dohler 1966). The semidiurnal tide enters Hudson Strait with an amplitude of about 3 meters and reaches the entrance to Hudson Bay and Foxe Basin about 3 to 4 hours later. Within Hudson Bay the M_2 tide is a Kelvin wave and propagates anticlockwise around the Bay; part of which propagates into James Bay and part proceeds north along the east coast of Hudson Bay (Fig. 3). As the Kelvin wave propagates around Hudson Bay its offshore wave components interfere with each other, cancelling each other out at two locations (amphidromic points); one located in west-central Hudson Bay and one in east-central Hudson Bay (Freeman and Murty 1976). In between these amphidromic points, the

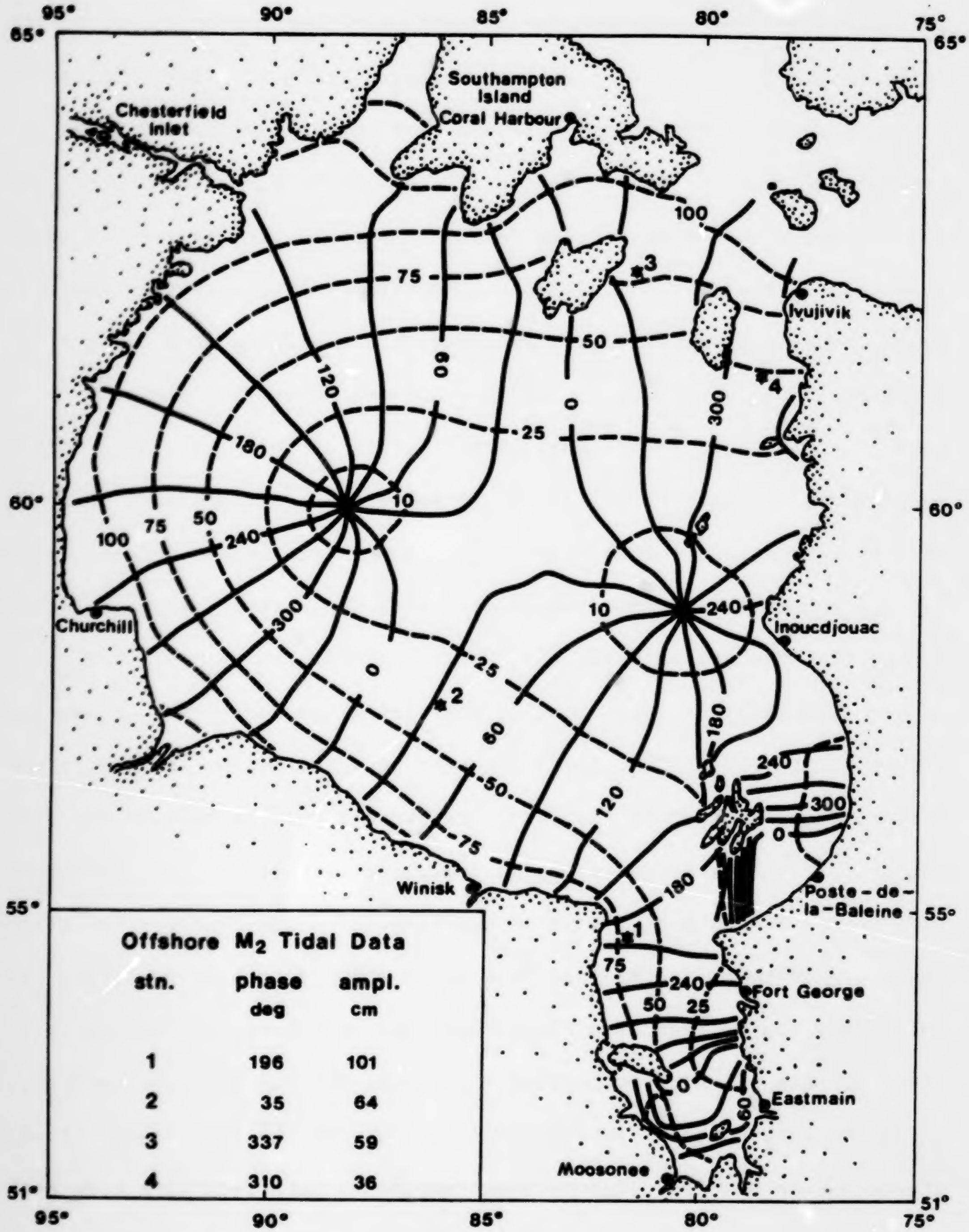

Offshore M_2 Tidal Data

stn.	phase deg	ampl. cm
1	196	101
2	35	64
3	337	59
4	310	36

Figure 3. M_2 tide with cophase lines in GMT+5 (degrees) and co-amplitude lines (cm) (modified from Freeman and Murty, 1976).

offshore tidal components that travel in opposite directions along the northern and southern shores reinforce each other and produce a small tide of 10 to 25 cm in the centre of Hudson Bay. The tidal wave propagates south around the Belcher Islands where reflection from the shallow bar to the south produces a standing wave pattern. Maximum M_2 tidal amplitude of 1.25 m occurs along the west coast of Hudson Bay decreases to 10 cm along the east coast of James Bay and the southeast coast of Hudson Bay.

Sensitivity analysis tested the model response for frictional variations (Freeman and Murty 1976). When the small linear friction coefficient was decreased by an order of magnitude, there was a negligible change in the location of the co-phase lines and the amphidromic points. However, an order of magnitude increase in the friction coefficient altered the location of the amphidromic points. High water arrived earlier while the amplitude was reduced; however, for sensible values of friction the model seemed to be relatively insensitive to the precise value chosen. Thus sensitivity analysis indicated that during the winter when there is a fairly stable ice-cover and frictional effects increases, the time of arrival of high water will advance along with a reduction in tidal amplitude.

To determine the annual changes in the magnitudes and phases of the tidal height and current due to the ice-cover, cross spectral analysis was carried out with the observed data and the data from the reference station located in an area which is ice-free year round. The parameter used is the amplitude and phase of the admittance which is the ratio of the cross spectrum and the power spectrum of the reference station for a given tidal frequency band (Godin and Barber 1980). If the observed data fluctuates relative to that at the reference station, the admittance should reflect these fluctuations. For tidal currents and heights, both the diurnal and semidiurnal frequency bands were used to follow the seasonal change in amplitude and phase for monthly record lengths. The reference station data used was that the predicted tide in Halifax, although other ice-free locations could have been used as long as the energy specta looked similar to the observed data spectra. Tidal height results showed that the semidiurnal tidal amplitude decreased during the winter continually anticlockwise around Hudson Bay relative to the summer tidal amplitudes and that high (or low) water arrived earlier (Godin and Barber 1980). At Resolute Bay located in western Lancaster Sound, no detectable change in amplitude or phase of the tide was found between the ice-free and ice-covered seasons.

Tidal current data from Hudson Bay and western Lancaster Sound showed that during the winter the current amplitude is reduced and the time of arrival of the maximum current (ebb or flood) is advanced. Three current meter records for a period of one year are available from a location 150 km northeast of Churchill (Hudson Bay) and another three records for an eight month period from a location 50 km southeast of Resolute Bay (Lancaster Sound) (Fig. 1). The admittance results of the Hudson Bay data from the three depths (25, 53 and 90 m) were averaged to obtain a mean change in amplitude and a mean phase advance relative to the maximum ebb or flood current. Results show that the amplitude of the semidiurnal tidal current decreases by 10% and that maximum flood (or ebb) occurs 20 minutes earlier during the winter relative to summer conditions (Fig. 4). The analysis of the diurnal currents show the same seasonal pattern; an amplitude reduction of 30% and phase advances of 30 minutes during the winter. However, this analysis is not as accurate because the diurnal currents are

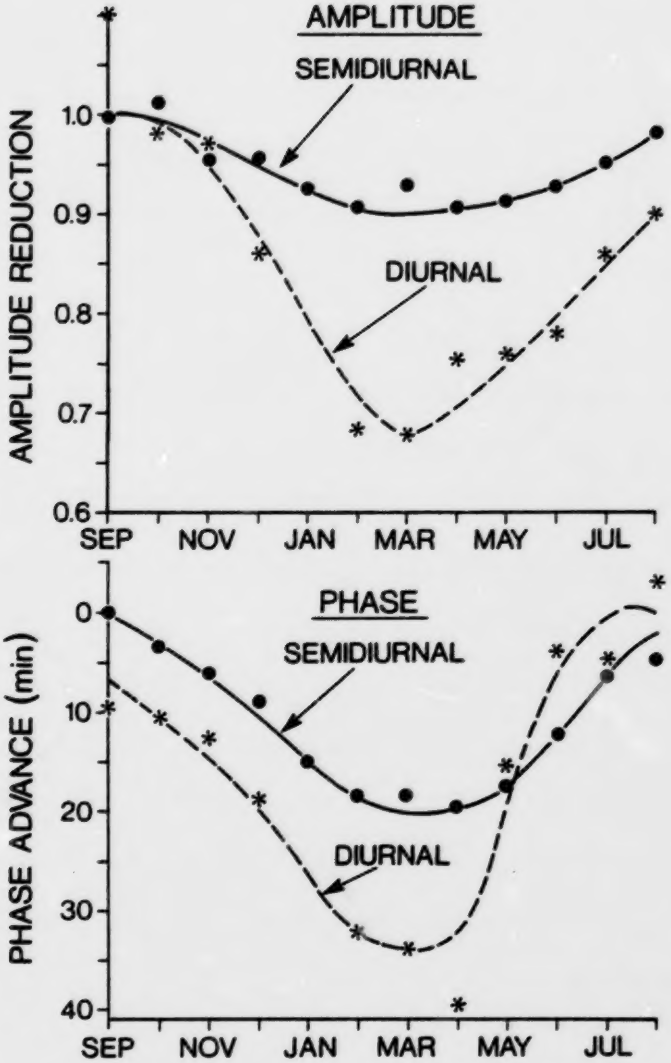

Figure 4. Seasonal variation in phase and amplitude of semidiurnal and diurnal tidal current observed 150 km northeast of Churchill.

weak and local generated diurnal tidal currents of comparable amplitudes are present.

The mooring southeast of Resolute Bay was recovered in April 1982 some 75 km east of its deployment location under extremely heavy ice rubble. The current meter data showed that a severe storm in late December broke up the newly formed annual ice-cover, taken the mooring eastward tangled up in ice keels which reached depths of 25 m or more. Ice conditions at the mooring site were thus not representative of the normal regional ice conditions throwing some suspicion on the representative aspect of these currents for western Lancaster Sound. The admittance analysis used only the eight-month sections of the current meter records before the mooring was moved. The analysis showed that the tidal currents at the largest two depths had similar seasonal variations as those in Hudson Bay. However, the surface data record (25 m) appeared to be strongly influenced by local ice conditions and its result was not included to obtain the mean seasonal response to the ice-cover shown in Figure 5. The amplitude of the semi-diurnal tidal current decreased on the average by 12% and showed a phase advance of 45 to 60 minutes for maximum ebb (or flood). Since the mooring location was only 10 km from the southern shore it is not known how representative these results are for the western Lancaster Sound in general since no detectable tidal height variations were observed some 50 km to the northwest in Resolute Bay.

DAMPED KELVIN WAVE

As shown above the co-oscillating tidal heights and currents in Hudson Bay and Lancaster Sound are damped and the arrival time of high

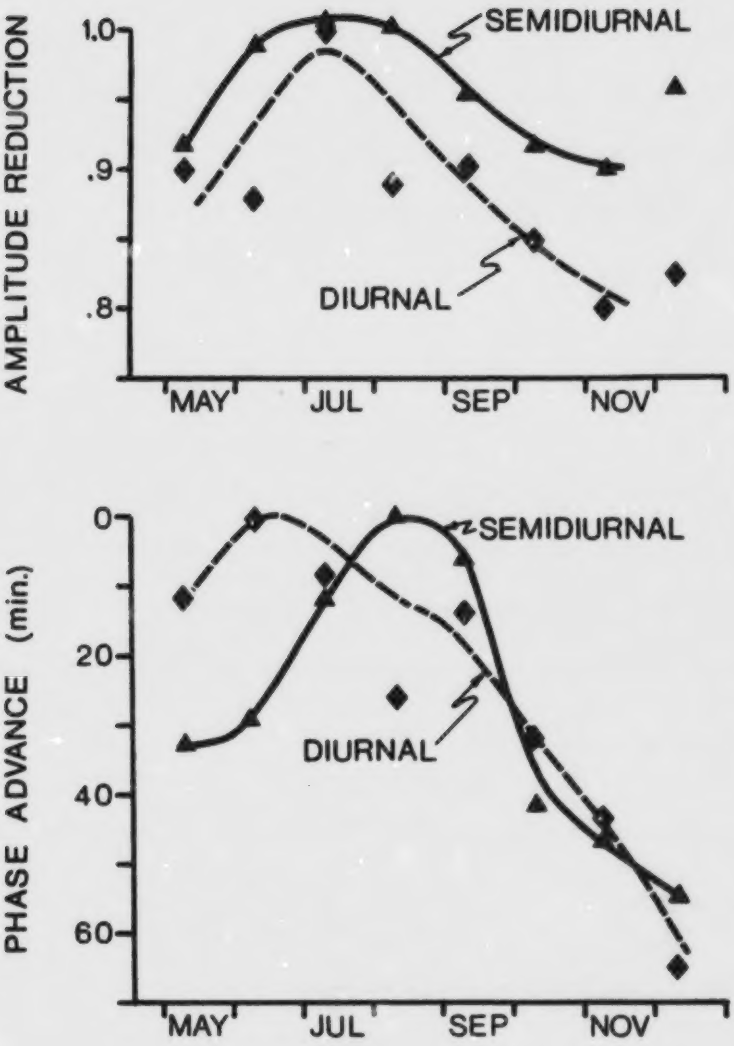

Figure 5. Seasonal variation in phase and amplitude of semidiurnal and diurnal tidal current observed in western Lancaster Sound.

water or maximum flood are advanced at most places when the annual ice-cover is present. In Hudson Bay, the effect also increases with distance travelled around the Bay. By assuming that the general Kelvin wave solutions for tidal height and velocity are still proportional to

$$\exp[kx + i\,(\ell y - \omega t)]$$

but that the wavelength ℓ in the direction of wave travel is now complex to represent damping by the ice-cover. With x the cross-stream axis and y the along-stream axis, the along-stream velocity v and tidal height η must satisfy the equations of motions and continuity

$$-\,fv = -g\eta_x$$

$$v_t = -g\eta_y - \delta v$$

$$hv_y = -\eta_t$$

where h is the constant depth value and δ the small coefficient of linear damping due to the bottom or the ice-cover. Substituting the tidal height and velocity into the equations and eliminating all variables except the tidal height amplitude η_0, the dispersion relationship is obtained

$$\left[\frac{\omega^2}{\ell^2} - gh + \frac{i\delta}{\ell}\left(\frac{\omega}{\ell}\right)\right]\eta_0 = 0$$

where the amplitudes of the tidal height and velocity are related by

$$v_0 = \frac{gk}{f}\,\eta_0$$

The dispersion equation has two roots

$$\frac{\omega}{\ell} = \frac{i\delta}{2\ell} \pm (gh)^{1/2}\left(1 - \frac{\delta^2}{4gh\ell^2}\right)^{1/2}$$

which reduces to $\pm(gh)^{1/2}$ for the non-frictional case, $\delta = 0$. When ℓ is defined as the sum of a real (ℓ_R) and imaginary (ℓ_I) parts and since the factor $(1 - \delta^2/4gh\ell^2)^{1/2}$ is real, the two roots can be rewritten as real and imaginary equations

$$\frac{\omega}{\ell_R} = \pm (gh)^{1/2} (1 - \delta^2/4gh\ell^2)^{1/2} = \pm (gh^*)^{1/2}$$

and

$$\ell_1 = \pm \frac{\delta}{2} / (gh^*)^{1/2}$$

where $(gh^*)^{1/2}$ is the modified phase velocity due to friction. These results show that for a progressive Kelvin wave, linear friction damps the amplitude of the wave in the direction it travels. Friction also decreases the phase velocity of the Kelvin wave which delays the arrival time of high water or maximum flood when friction increases due to the ice-cover.

The tidal model of Freeman and Murty (1976) used a linear damping coefficient of $0.125 \times 10^{-4}\ s^{-1}$ for Hudson Bay. With this value for δ the wave amplitude (or velocity) of a M_2 Kelvin wave decreases to 0.87 over a distance of ½ a wavelength which for an average depth of 100 m is a distance from the entrance to Hudson Bay to Churchill. When the ice-cover is present, the data indicates that it would further decrease by 10% which would require a 92% increase in the damping coefficient $(0.240 \times 10^{-4}\ s^{-1})$. This ignores the small damping (1.5%) that would occur in Hudson Strait and Labrador Sea. There the wave travels only a ¼ wavelength under the annual ice-cover and the friction coefficient is 5 times as small as it is inversely proportional to depth. Similarly, the phase velocity in Hudson Bay is 0.1% decreased for $\delta = 0.125 \times 10^{-4}\ s^{-1}$ relative to the non-frictional case. This causes only a 0.9 minute phase delay for each wavelength travelled and is thus a much smaller affect and in the wrong direction than the phase change observed in Hudson Bay during the winter.

The above simple theory can thus account for the observed decrease in tidal height and current due to the presence of the ice-cover but not for the observed phase variations. Another theory dealing with frictional boundary layers (Lamb 1932) is usually used to explain phase advance of a current in a boundary layer relative to those outside the boundary layer; but in this case the phase of the tidal height remains unaltered. This may happen under coastal landfast ice where offshore ice-free conditions occur such as the Labrador Sea; but not in Hudson Bay or Lancaster Sound. Here the ice-cover causes the extra damping of the wave's height and current as shown above but it also alters the location of the amphidromic points.

Non-frictional solutions of the reflecting Kelvin wave were first solved by Tailor (1921) and later presented in a simpler form by Defant (1961). The solution is made up of an incident and a reflecting Kelvin wave of equal amplitude with poincarée waves transferring the energy from the shore along which the incident wave enters to the shore along which the reflecting wave leaves. With friction, the tide is still made up of an incident Kelvin wave and a reduced reflecting Kelvin wave but their combined phase and amplitude pattern is altered. The pattern moves the west-central amphidromic point in Hudson Bay southward toward the shore along which the reflecting wave travels. Simply stated, one sees relatively more of the incident than the reflecting wave and thus the phase of their sum is advanced. Similar motion of amphidromic points are seen in James Bay and the Gulf of California where the amphidromic points actually occur inland due to the large damping in shallow coastal regions (Hendershott 1981). Thus, the observed phase advances in tidal height and current due to the ice-cover are achieved due to the change in the location of the amphidromic points nullifying the small phase delays caused by the decrease in phase velocity.

In western Lancaster Sound the Kelvin wave entering from Baffin Bay is partially reflected from the island arc 50 km west of Resolute Bay. When damping increases due to the presence of the ice-cover, the wave form becomes more progressive which advances the time of maximum flood current relative to time of high water, but also decreasing both the tidal height and current amplitudes. Only a decrease in tidal current is observed. So if the analysis is correct; then another explanation more along the line of Lamb's theory (1932) is required. The current observations were made very close to the southern shore so that the large observed phase advance of the current may in part be due to the increase of the frictional boundary layer when an ice-cover is present. This would advance and decrease the current but not the tidal height. Part of the observed changes may also be due to the changes in the internal wave generation pattern at the Barrow Sill as density structure varies between summer to winter.

However, the data shows that the effect of the ice-cover on tidal height and current in Canadian northern waters are dependent on the local wave form and reflection pattern so that no general statement on the ice effect should be expected but instead each area has to be studied on its own.

FRESHWATER CONTENT

The second topic to be discussed in this paper is the effect of the annual ice-cover on the vertical oceanic density structure. Although the freshwater exchange with the ice-cover does not alter the freshwater content of the water column over a period of a year, it does alter the vertical distribution of the freshwater content. During the ice growth period, freshwater is removed from the water column and the salt rejected is redistributed over an ever-increasing mixed layer depth. During the ice decay period, freshwater is added and just dilutes a shallow surface layer. The growth and decay of the ice-cover can be treated respectively as a large contribution by evaporation during the early winter and as a large contribution by precipitation during the early summer. It can then be compared to the normally occurring freshwater contributions of runoff, evaporation and precipitation.

Ice concentrations in Canadian Arctic waters are documented as bimonthly charts in the ice atlas of Markham (1981). The atlas also shows maps of maximum ice thicknesses based on 15 years of level ice data, but since this data was collected from inshore land fast ice and offshore ridging and rafting occurs, it is uncertain how representative these values are for the values of ice production for offshore areas. An accurate value of the ice-production per unit area is required to determine the amount of salt rejected to the water column and the degree and type of deep water formation.

In Hudson Bay the maximum ice thickness ranges from 1.0 m in southern James Bay to 1.75 m in northern Hudson Bay. It averages out to a thickness of 1.45 m for the total area which converts to a freshwater layer of 1.10 m spread over the total area of Hudson Bay when an average salinity content of 5 ppt was taken for the ice (Tucker et al. 1984). This freshwater layer compares to a 0.85 m layer of freshwater brought in annually by runoff which reduces to a 0.65 m layer if precipitation and evaporation are included (Prinsenberg 1980). This comparison shows that the stability of the water column downstream in Hudson Strait does not only depend upon runoff from Hudson Bay but also on the melt water of the annual ice-cover. When the relative freshwater inputs (in units of cm/week) are followed through the year (Fig. 6), the contribution of the ice-cover becomes even more significant because the melting of the ice-cover occurs over a much shorter period than the major input by runoff (Prinsenberg 1983). However, the circulation pattern in Hudson Bay indicates that most of the freshwater added by runoff enters and moves along the southern and eastern coasts covering only half of the total area of Hudson Bay. This increases the contribution of the runoff in this area relative to that of the annual ice-cover. In addition, the ice-cover contribution has to be corrected for sublimation but this only affects the freshwater removal rates during the ice growth period (Fig. 6). Using evaporation and precipitation values of Prinsenberg (1983), an additional 0.6 cm of ice per week is sublimated for the period of December through April (25 weeks). This adds an additional 0.15 m layer of ice (or 10%) to the maximum ice thickness values. Even with these adjustments, the ice-cover contribution to the surface layer stability is equal or larger than the runoff contribution so that the seasonal variability of both has to be monitored in order to determine seasonal variability of the water column stability and thus upward nutrient fluxes in Hudson Strait.

The changes in freshwater content from winter to summer at various locations in the Canadian Arctic show that more ice needs to be melted than level-ice thickness measurements indicate. In southern Hudson Bay the freshwater layer content changes by 3.6 m from winter to summer. When the freshwater contributions of runoff, evaporation and precipitation over the 25 weeks are spread over half of the surface area of Hudson Bay, 1.2 m of

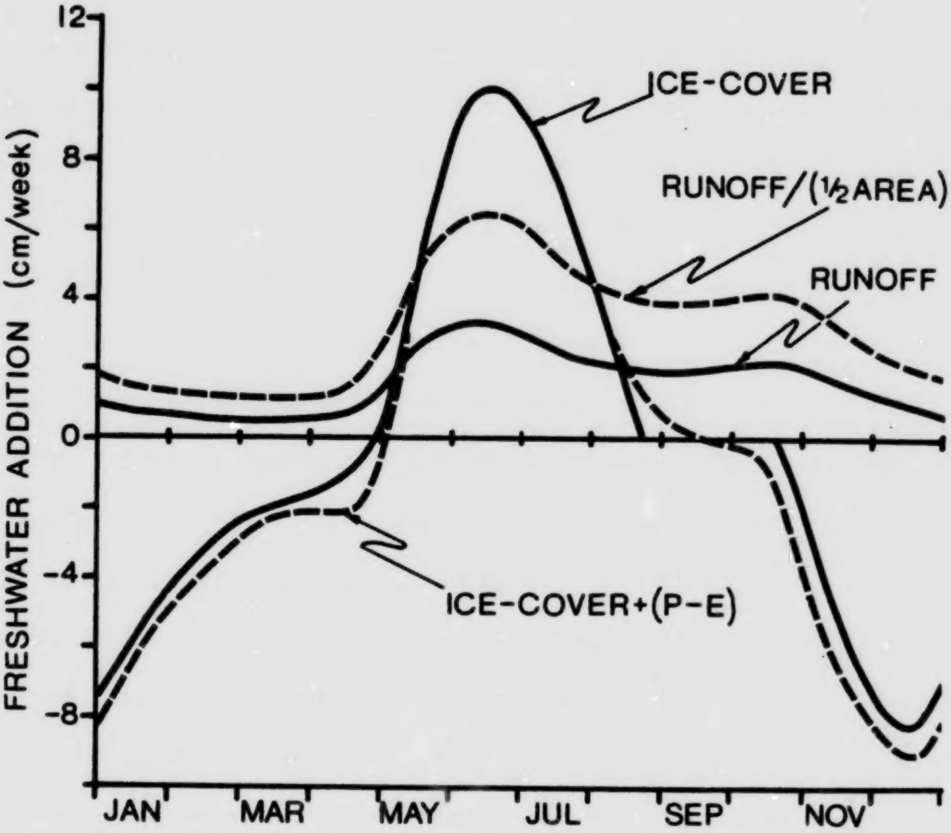

Figure 6. Monthly mean freshwater addition by ice-cover, Runoff (R) Precipitation (P) and Evaporation (E) for Hudson Bay (From Prinsenberg, 1983).

the 3.6 m freshwater layer is accounted for. Another 0.7 m of freshwater is added by advection entering Hudson Bay between winter and summer, leaving a layer of 1.7 m layer to be accounted for by the melting of the annual ice-cover. Since there is only 1.1 m of freshwater in the ice-cover, this suggests that 50% more ice is present and melts more than the 10% (1.6 m of ice) taken in the heat budget of Hudson Bay (Prinsenberg 1984). Similar calculations for Foxe Basin and Barrow Strait also indicates that more ice melt water is required to accommodate seasonal variations in the freshwater content (Table 1). Eventhough these calculations are at best crude estimates; the amount of additional ice required is large and consistent for several areas suggests that measurements of level ice thickness and offshore ice-production per unit area are different. It will be shown that part of the difference is due to the ice ridges and rubble fields of the ice-cover.

Data on size and frequency distribution of ice ridges in Canadian northern waters have become available due to research on proposed year-round shipping in the Canadian Arctic as a result of hydrocarbon development in the Beaufort Sea and Canadian Archipelago (Norcor 1978 and Arctic Pilot Project 1981). Ridge data from coastal areas of the Arctic Ocean treats both multiyear and first-year ice (Brooks 1983); whereas only first-year ice occurs in the areas here under consideration. Ridge size and frequency data for Hudson Bay and Hudson Strait presented by Markham (1986) indicates that these areas are not much different from Lancaster Sound. No data is available for Foxe Basin but here ridge frequency is expected to be high. For first-year ice, the keel depth of ridges range from 5 times their sail height for small ridges (<1 m) to 4.3 time their sail height for large ridges (>2 m) (Arctic Pilot Project 1981 and Markham 1986). This

TABLE 1

Freshwater Content (m/area) Variations Between Winter and Summer

	S. Hudson Bay	Foxe Basin	W. Lancaster Sound
Observed	3.6	2.8	3.9
R + P-E	1.2	.2	.9
Transport	.7	.6	(1.5)
Level Ice	1.1	1.2*	1.1*
Difference as Water	.6	.8	(.4)
Difference as Ice	.8	1.0	(.5)

* 25% of ice transported out

( ) uncertain values

along width an average width of 22 times the sail height can be used to calculate the extra ice volume V_E associated with the ridge of sail height a

$$V_E(m^3) = 5(-2a + 11a^2 - a^3)$$

for each ridge per km. This volume can also be regarded as an extra layer of ice spread over the total area (1 m x 1 km) (Fig. 7). For the usual size distribution (Fig. 7), an average thickness of 5 cm of extra ice for each ridge per km is obtained. This means that for southern Hudson Bay up to 0.5 m of extra ice is tied up in ice ridges decreasing to 0.2 m for northern Hudson Bay (Table 2). For Hudson Strait ridge frequencies are higher and thus up to 0.7 m of extra ice should be expected. No ridge frequency data is available for Foxe Basin but it must be larger than that observed in Hudson Strait so that up to 1.0 m of extra ice is expected there. Lancaster Sound only has 0.30 m of extra ice tied up in ridges even after assuming that the rubble fields along the coasts counted as one extra ridge per km.

This data compares favorable with the extra ice required from freshwater content considerations and thus suggests that part of the discrepancy in the amount of melt water derived from level-ice thickness data is contained in the extra ice associated with the ridging and rafting of the ice-cover. This makes the effect of the ice-cover on the stability of the water column even larger than it already is using level ice thickness data (Fig. 6) and thus much more attention should be put on research on the ice-cover characteristics of Canadian inland waters.

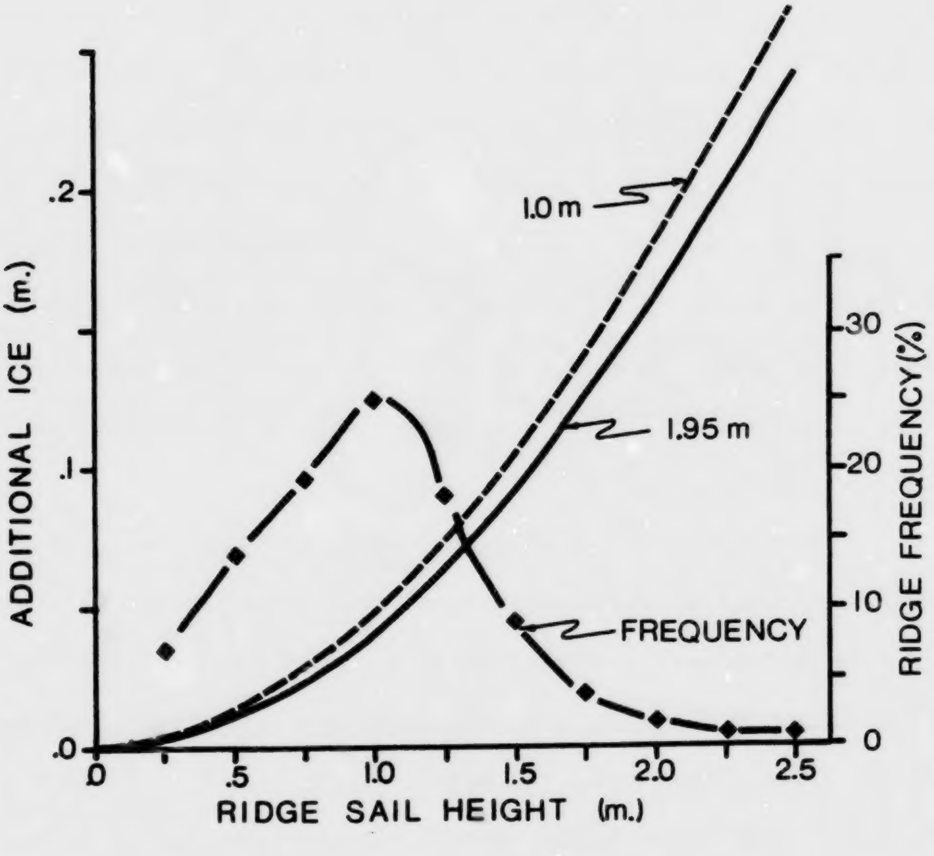

Figure 7. Ridge sail height frequency distribution for first year ice condition in Canadian Arctic and the additional ice thickness (m) associated in a single ridge per km of varying sail height in level ice-cover of 1.0 m and 1.95 m thick.

TABLE 2

Ice Accumulated in Ice Ridges

	Lancaster Sound	Hudson Bay		Hudson Strait	Foxe Basin
		North	South		
Ridge Freq. (#/km)	5+1	4	10	6-14	(10-20)
Extra Ice (m) by Ridges	.3	.2	.5	.3-.7	(.5-1.0)
Extra Ice (m) by Table 1	(.5)	--	.8	--	1.0

*Rubble field counted as 1 Ridge/km

( ) uncertain values

CONCLUSION

Data shows that the annual ice-cover affects currents and salinity structure of the ocean it floats on. The ice-cover not only decreases the current energy at the high-frequency end of the current spectra since wind generated currents area absent, but also the presence of the extra frictional boundary layer modifies tidal heights and currents. The ice-cover damps the tidal wave and advances the time of arrival of high water and flood current when locations of amphidromic points are shifted toward the shore along which the reflecting wave travels. For a progressive Kelvin wave (no reflection), the extra friction due to the ice-cover causes reduction of the tidal wave's amplitude and current and a small delay of the arrival time of high waters or flood current.

The large amount of freshwater exchanged between the annual ice-cover and the ocean influences the surface stability of the water column in coastal regions as much or more than the input by runoff. Using level sea-ice data to obtain the ice-cover freshwater contribution, the thickness of the ice has to be increased by as much as 50% to account for the extra ice tied up in the rafting and ridging of the offshore ice-cover. This increases the ice-cover contribution on the freshwater content even more. Thus the seasonal variation of both the runoff and ice-cover characteristics are required to determine the seasonal variability of the oceanic stratification and the upward flux of nutrients. More information is required on the ice ridge properties and motion of the ice-cover to understand the spacial as well as temporal exchange of freshwater between the annual ice-cover and the ocean.

REFERENCES

AAGAARD, K., L.K. COACHMAN, AND E. CARMACK. 1981. On the halocline of the Arctic Ocean. Deep-Sea Res. 28: 30-37.

ARCTIC PILOT PROJECT. 1981. Physical aspects of the route areas. Chapter 2, of Integrated route analysis, 522 p.

BROOKS, L.D. 1983. Statistical analysis of pressure ridge keel definitions and distributions, p. 69-78. In the proceedings of: The seventh international conference on port and ocean engineering under arctic conditions, Volume 1.

CAMPBELL, N.J. 1964. The origin of cold high-salinity water in Foxe Basin. J. Fish. Res. Board Can. 21: 45-55.

DEFANT, A. 1961. Physical oceanography Vol. II. Pergamon Press, Oxford, 598 p.

DOHLER, G.C. 1966. Tides in Canadian waters. Dept. Mines Tech. Surv. Can. Hydrogr. Serv., Mar. Sci. Branch, Rept. M54-966: 17 p.

GODIN, G. 1966. The tides in the Labrador Sea, Davis Strait and Baffin Bay. Manu. Rept. Serv. No. 2. Mar. Sci. Dir., Ottawa, 156 p.

GODIN, G. and F.G. BARBER. 1980. Variability of the tide at some sites in the Canadian Arctic. Arctic 33: 30-37.

HENDERSHOTT, M.C. 1981. Long waves and ocean tides, p. 292-341. In: B.A. Warren and C. Wunsch (Editors). Evolution of Physical Oceanography, MIT Press, Cambridge.

HENRY, R.F. and M.G.G. FOREMAN. 1977. Numerical model studies of semidiurnal tides in southern Beaufort Sea. Pacific Mar. Sci. Rept. No. 77-11. Inst. Ocean. Sci., Victoria, 71 p.

LAMB, H. 1932. Hydrodynamics 6th ed. Dover, New York, 738 p.

MARKHAM, W.E. 1981. Ice atlas of Canadian Arctic waterways. Envir. Can. Atmos. Env. Serv., Toronto, 198 p.

MARKHAM, W.E. 1986. The ice cover, In: I.P. Martini (Editor), Canadian Inland Seas, Elsevier, Amsterdam (in press).

MELLING, H. and E.L. LEWIS. 1982. Shelf drainage flow in the Beaufort Sea and their effect on the Arctic Ocean pycnocline. Deep-Sea Res. 29: 967-985.

NORCOR. 1978. A study of ice conditions along marine shipping routes in the Arctic archipelago. Norcor, engineering and Research Lim., 96 p.

PRINSENBERG, S.J. 1980. Man-made changes in the freshwater input rates of Hudson Bay and James Bays. Can. J. Fish. Aquat. Sci. 37: 1101-1110.

PRINSENBERG, S.J. 1983. Effects of the hydro-electric developments on the oceanographic surface parameters of Hudson Bay. Atmos.-Ocean 21: 418-430.

PRINSENBERG, S.J. 1984. Freshwater contents and heat budgets of James Bay and Hudson Bay. Cont. Shelf Res. 3: 191-200.

SUTCLIFFE, JR. W.H., R.H. LOUCKS, K.F. DRINKWATER and A.R. COOTE. 1982. Nutrient flux onto the Labrador Shelf from Hudson Strait and its biological consequences. Can. J. Fish. Aquat. Sci. 40: 1672-1701.

TAIT, B.J., D.A. ST. JACQUES and R.R. SOLVASON. 1980. Winter tidal surveys in Viscount Melville Sound. Lighthouse, special edition: Proceedings of the 19th Annual Canadian Hydrographic Conference, March 1980, p. 80-93.

TAYLOR, G.I. 1921. Tidal oscillations in gulfs and rectangular basins. Proceedings of the London Math. Soc. 20: 148-181.

TUCKER III, W.B., A.J. GOW and J.A. RICHTER. 1984. On small-scale horizontal variations of salinity in first-year sea ice. J. Geophys. Res. 89: 6505-6514.

ZUBOV, N.N. 1943. Arctic ice. Trans. U.S. Navy Electronics Laboratory: 491 p.

*FREEMAN, N.G. and T.S. MURTY. 1976. Numerical modelling of tides in Hudson Bay. Journal of Fisheries Research Board of Canada 33: 2345-2361.

(*Reference not in alphabetical order)

FIELD OBSERVATIONS OF FLOW PATTERNS GENERATED BY AN ICE KEEL IN STRATIFIED FLOW

by D.R. Topham, H.D. Pite, P. Johnston and D.L. Richards
Department of Fisheries and Oceans
Institute of Ocean Sciences
P.O. Box 6000, Sidney
British Columbia, Canada V8L 4B2

The results of a field experiment to investigate flow patterns generated by an isolated, approximately 2-dimensional ice keel in weakly stratified flow are presented. The main observation tool was an array of eight multiplexed depth sounder transducers which provided a flow visualization of local turbulence patterns generated by the keel. Lee waves, supression of separation by lee waves and internal hydraulic jumps are identified under a range of flow conditions.

Field observations of flow patterns generated by an ice keel in stratified flow

1.0 Introduction

The extensive ice cover over the Arctic Ocean plays a dominant role in the transfer of heat and momentum between the atmosphere and the underlying water column. In both these cases the mechanical mixing energy supplied by relative motion between the water and the ice cover is crucial to the transfer rates, Lemke and Manley (1984) for example estimate that during the 1975-76 AIDJEX experiment in the Beaufort Sea, mechanical mixing was responsible for maintaining the mixed layer during summer and accounted for about 30% of the winter deepening during ice growth.

The work presented here is part of the OERD sponsored 'Small Scale Ice/Ocean Interaction Project' (No. 67113) whose aim is to improve our understanding of the momentum exchange between the under ice surface and the water column. The area of immediate interest is the southern Beaufort Sea shown in Figure 1, where exploration for oil and natural gas has generated a need for better forecasts of ice motion.

The upper layer of the Arctic Ocean is commonly described in terms of a planetary boundary layer model and the work of McPhee and Smith (1976) showed that this was justified in an area of smooth multi-year ice with low to moderate relief. In such cases the momentum exchange is described by means of a drag coefficient defined at a standard reference height above the surface, and a quadratic variation with velocity at the reference height. In areas with significant ice ridging the downward protruding ice keels represent large perturbations of the boundary layer. The conventional representation of surface roughness by the roughness parameter z_o, requires that there be a large separation in scales between the roughness elements and the outerscale of the boundary layer. In the case of the atmosphere where the outerscale scale is of the order of 1000 m, surface features such as bushes, fences, low buildings, etc. satisfy this condition. For the Arctic Ocean however, with a typical mixed layer depth of about 30 m, almost any piece of

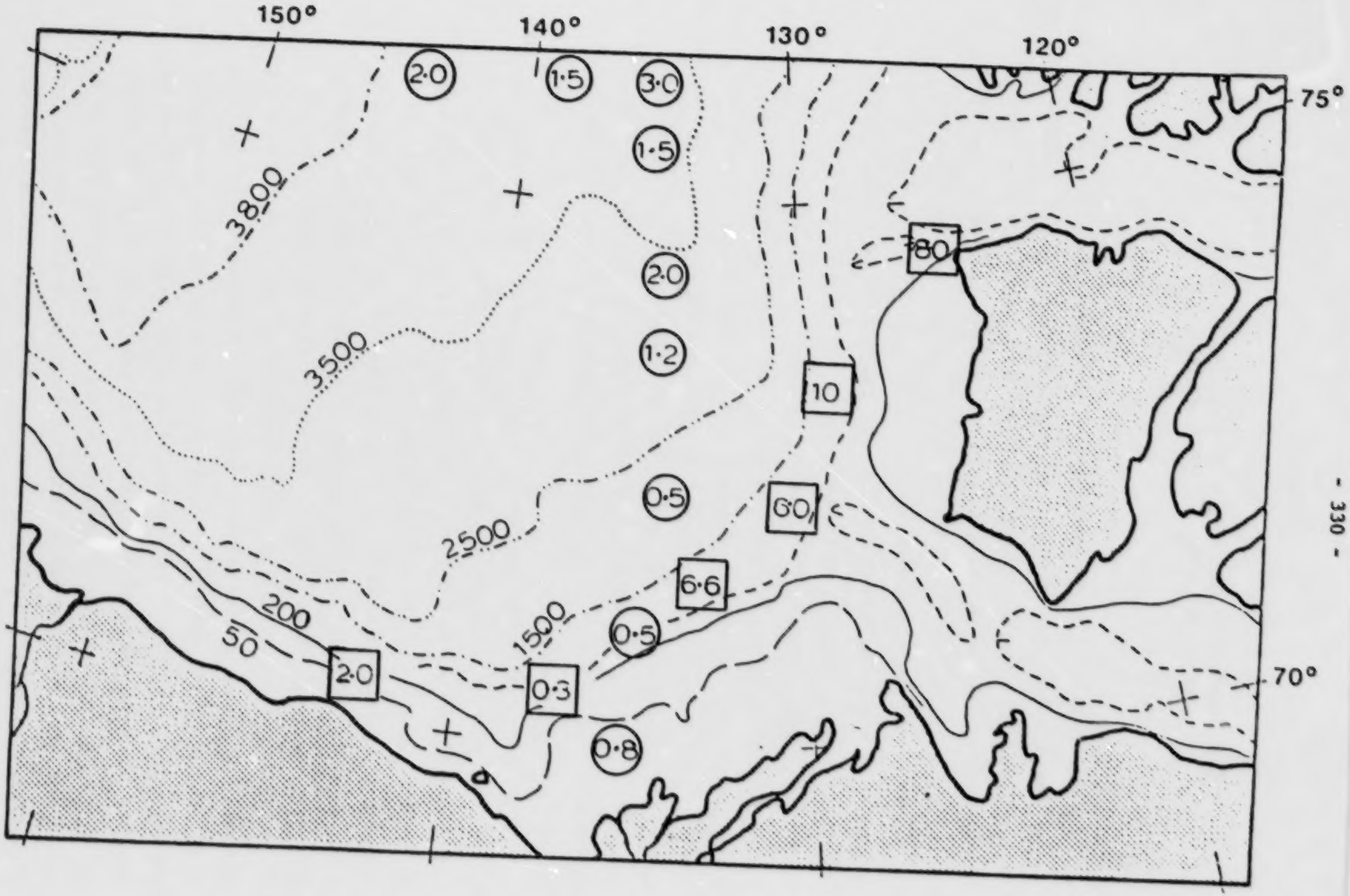

Figure 1. Beaufort Sea ice keel frequencies, keels per km., after Wadhams(1975).
Numbers in circles, April 1975; numbers in squares, September 1974.

ice remnant lying at the ice/water interface fails to satisfy the criterion of a wide separation of scales. This is particularly so with first year ridged ice where there has been little opportunity for melting to smooth features.

The combination of relatively steep sided ice keels with the underlying stratified water column takes us out of a conventional boundary layer regime into one of stratified flow over obstacles with the resulting emphasis on wave related phenomena. In the following section we combine ice keel statistics from the Beaufort Sea with stratified flow criteria to determine flow conditions likely to be associated with ice keels.

2.0 Ice keel flow regimes in the Beaufort Sea.

Wadhams (1975) presents statistics of sea ice ridging for the area of interest and discusses the statistical conversion from ridge height to keel depth. To convert the values of ridge height to keel depths Wadhams suggested ratios of 4 and 3 for shear zone and outer pack ice respectively have been used. These conversion factors yield a fairly uniform distribution of mean keel depths, the lower ridge heights in the shear zone being compensated for by the greater value of the conversion factor. The resulting overall average keel depth is about 5 m and centered about this value there is a general trend for keel depths to increase with keel frequency, i.e. intensely ridged areas have greater keel depths. Figure 1 shows areas covered by Wadham's data and indicates the expected keel frequencies over board areas.

The underlying water properties can be simplified for present purposes to a two layer system which we characterise by a mixed layer depth and a density step. Over the area shown there is a general tendency for the mixed layer to deepen from 30 to 40 m just beyond the continental shelf break to around 50 m under the main pack with density differences of the range 0.5 to 1 sigma t units. During early spring there is a thinning of the mixed layer at the shelf break itself associated with local upwelling resulting from brine drainage from the shelf. Conditions on the shelf itself can vary between highly stratified layers close inshore, to unstratified conditions under the flaw lead areas where convective mixing has penetrated to the ocean floor. In summer, ice melt water and Mackenzie River runoff tend to produce thin strongly stratified layers over the inner shelf regions.

Given these ice and oceanographic conditions we can now place the expected keel flows in the context of two-layer stratified flows in general. Baines (1984) has summarised such flows in some detail, and although the stratifications occurring beneath the ice are not strictly two-layer, they are close enough for the local flows to be classified according to a two-layer model. The simplest model is based in the hydrostatic approximation in which vertical accelerations are considered to be negligible; strictly this limits the solutions to small surface slopes, on 'long' obstacles, although the resulting flow classifications appear to be valid under more general conditions. The flow patterns may be classified in terms of two dimensionless parameters.

The Froude No. $F_o = \dfrac{U}{\sqrt{\frac{\Delta\rho}{\rho} gd}}$

and the obstacle height to layer depth ratio r

$$r = \frac{h}{d}$$

where h is maximum obstacle height, d the mixed layer depth, $\frac{\Delta\rho}{\rho}$ the relative change in density across the base of the mixed layer, and U the velocity of the upper layer.

The various flow regimes as determined by these two parameters are shown in Figure 2 where the illustrations depict flow under an ice keel. Only the region for Froude numbers less than unity are shown as this is the area of interest. Four regions are shown: in regime I the flow remains subcritical throughout and the interface is pulled up towards the keel. In regime II the flow changes locally from subcritical to supercritical across the crest of the keel and there is a return to subcritical conditions through a stationary

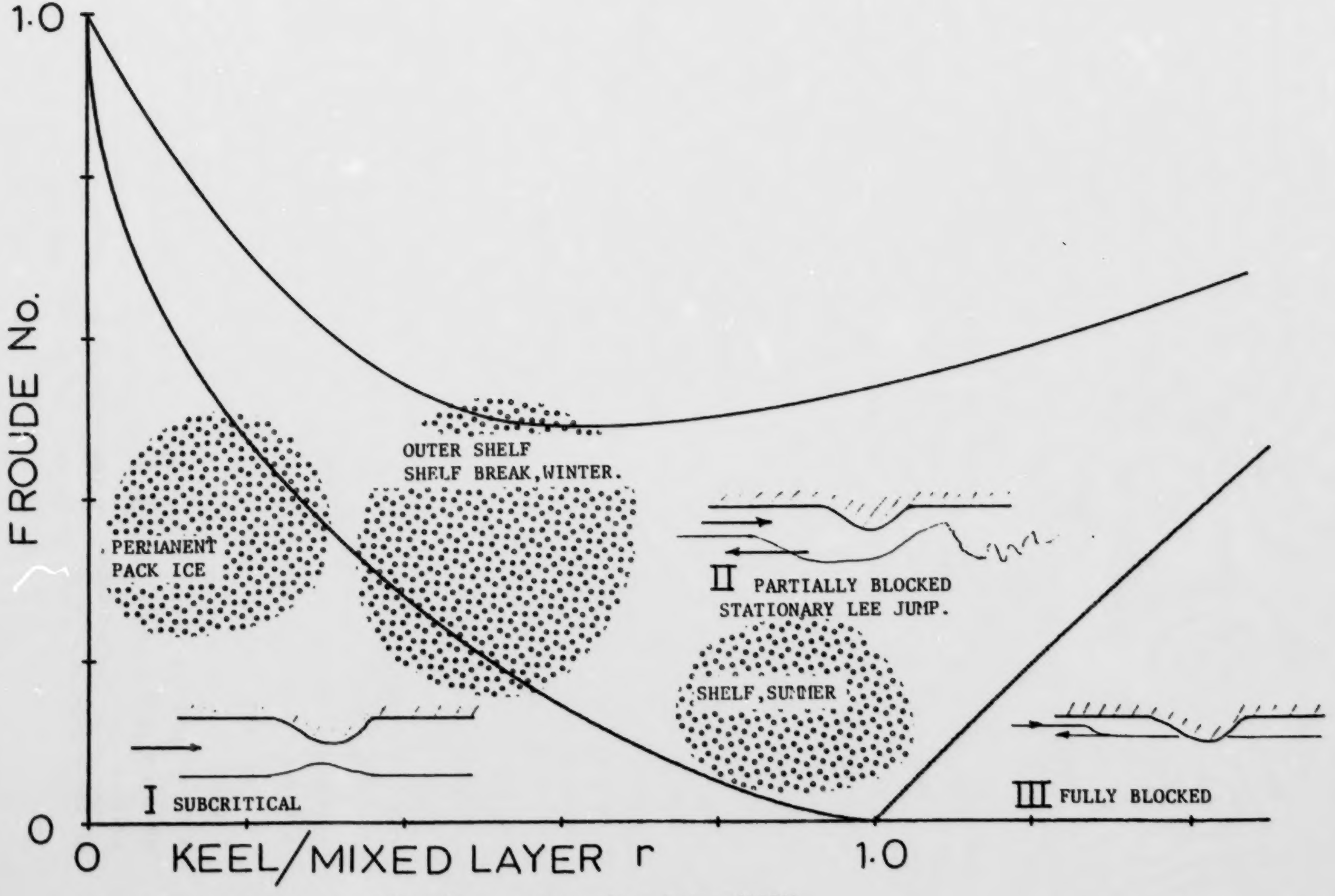

Figure 2. Two-layer stratified flow regimes, after Baines(1984).

internal hydraulic jump in the lee of the keel. Under these conditions there is an interaction between the width of the keel and the length of the standing internal wave which can control the boundary layer separation occurring for the typical keel slope angles of 20°-30°. Regime III is similar to regime II except that the downstream lee jump is unstable and is swept downstream. Regime IV is one of complete blocking where the approaching flow has insufficient kinetic energy to flow under the keel. For keels of finite length the blocked fluid tends to flow round the ends of the keel and the upper layer flow becomes distinctly three dimensional. Regimes II and III both involve starting flows in which a travelling upstream jump is generated which can propagate long distances.

If the aforementioned ice keel statistics and oceanographic conditions are combined with a typical current velocity, the expected Beaufort Sea ice keel flows can be defined. These are shown as hatched regions on Figure 2 for an assumed current speed of 20 cm/sec. It can be seen that the expected flows span the border between Regimes I and II, with summer conditions on the shelf approaching the fully blocked state of region IV. These flows encompass the hydrodynamically more interesting cases with unsteady long range upstream and downstream effects, control of boundary separation by lee waves, and strong internal hydraulic jumps.

The classifications of Figure 2 are for steady conditions and in situations where there is temporal forcing of the oncoming flow more complex interactions occur. An example is the release of large amplitude trapped lee waves as tidally driven flows over an obstacle start to decrease in magnitude. These lee waves advance as a travelling train of large amplitude internal waves accompanied by relatively intense local mixing. Several examples of such waves produced in fiords are described in Farmer and Freeland (1983).

For the unsteady effects to be important the transit time of a particle of fluid over the length of keel must be of the same order or greater than the period of the oncoming flow changes. Hence for the small physical scales of the ice keels, tidal flows and wind forced ice motions can be considered as quasi-steady. However, in the vicinity of the continental shelf break, tidal period internal waves interact with the topography to produce trains of higher frequency waves, typically of several metres amplitude with periods in the range 15 to 30 minutes. The large amplitude variations in mixed layer depth in an area where the mixed layer itself is relatively thin introduces the possibility of strongly dynamic interactions between the keel generated flows and these free running waves, with the consequent potential for still shorter wave length large amplitude trapped waves to be released as the Froude number and keel/mixed layer depth ratio are modulated by the free running internal waves.

The foregoing discussion has concentrated on the flow effects arising from the ice keel/stratified flow interactions as this is area where it is felt that the momentum exchange between the ice and the water is least well understood. In simple terms keels are usually regarded as having three components of flow resistance, skin friction, pressure or 'form' drag and wave related drag. The flow diagram of Figure 2 indicates that most of the flows lie in a region with strong control of separation and hence of form drag by lee waves, with the possibility of generating shortwave length, large amplitude highly dissipative free running waves within the under ice boundary layer. The influence of a particular keel may not be just local, but may be transmitted relatively long distances by wave related processes. These latter introduce modes of mixing into the boundary layer which not accounted for by conventional scaling arguments. As further evidence for the importance of the ice keels, the results of the recent Arctic Internal Wave Experiment (AWEX) carried out in the Beaufort Sea suggest that it is the ice keels which are primarily responsible for generating the background internal wave field over the whole Arctic Basin, Levine and Paulson, (1985).

It was therefore decided to concentrate the effort of this particular project on the aforementioned keel/flow phenomena as this was felt to be an area which was least well understood and embraced a number of relatively unexplored aspects unique to the ice/water interaction.

3.0 The single ice keel experiment

There have been at least two attempts in the past to investigate keel flows, both in the Beaufort Sea during the AIDJEX programme. These suffered from restrictions on their choice of site, being constrained to the vicinity of the AIDJEX camps and from unpredictability of the ensuing water motion relative to the ice, both regarding speed and direction. With this in mind it was decided to seek an isolated keel in fixed ice with well defined tidal flows such that the desired range of Froude numbers was reproduced on a regular basis. A survey of historical ice data suggested that the Barrow Strait area of the Northwest Passage had a high probability of furnishing suitable conditions. The experiment was accordingly planned for this area during April and May 1985.

Figure 3 shows the area of interest and in the event low-level flights pinpointed two possible keel sites designated site I and site II. A single Aanderaa current meter was deployed at 10 metres below the ice at each site and recovered after three days of recording at 2 minute intervals. Examination of these records and CTD profiles showed that both sites had substantial fractions of their flows normal to the keel, but a combination of weak stratification and fast currents put the Froude number range at site II too high for our purposes. Site I however, with a water depth of about 100 m, had a more suitable combination of conditions and was selected for the main experiment.

Having installed a small ice camp at the keel site the first task was to obtain a detailed map of the underice topography. This was done by Offshore Survey and Positioning Services Ltd. of Vancouver using a single beam Mesotech 971 sonar unit operating at 330 kHz with a 1.7° beam angle. The beam is automatically indexed through 360° in the vertical plane, with manual indexing in the horizontal. The acoustic head was mounted 40 metres below the ice surface on a rotationally rigid aluminum pole, and from this position an area about 80 m in diameter could be surveyed on both ice surface and seabed. Two reference reflectors at 40 m depth, set to form a 90° angle with

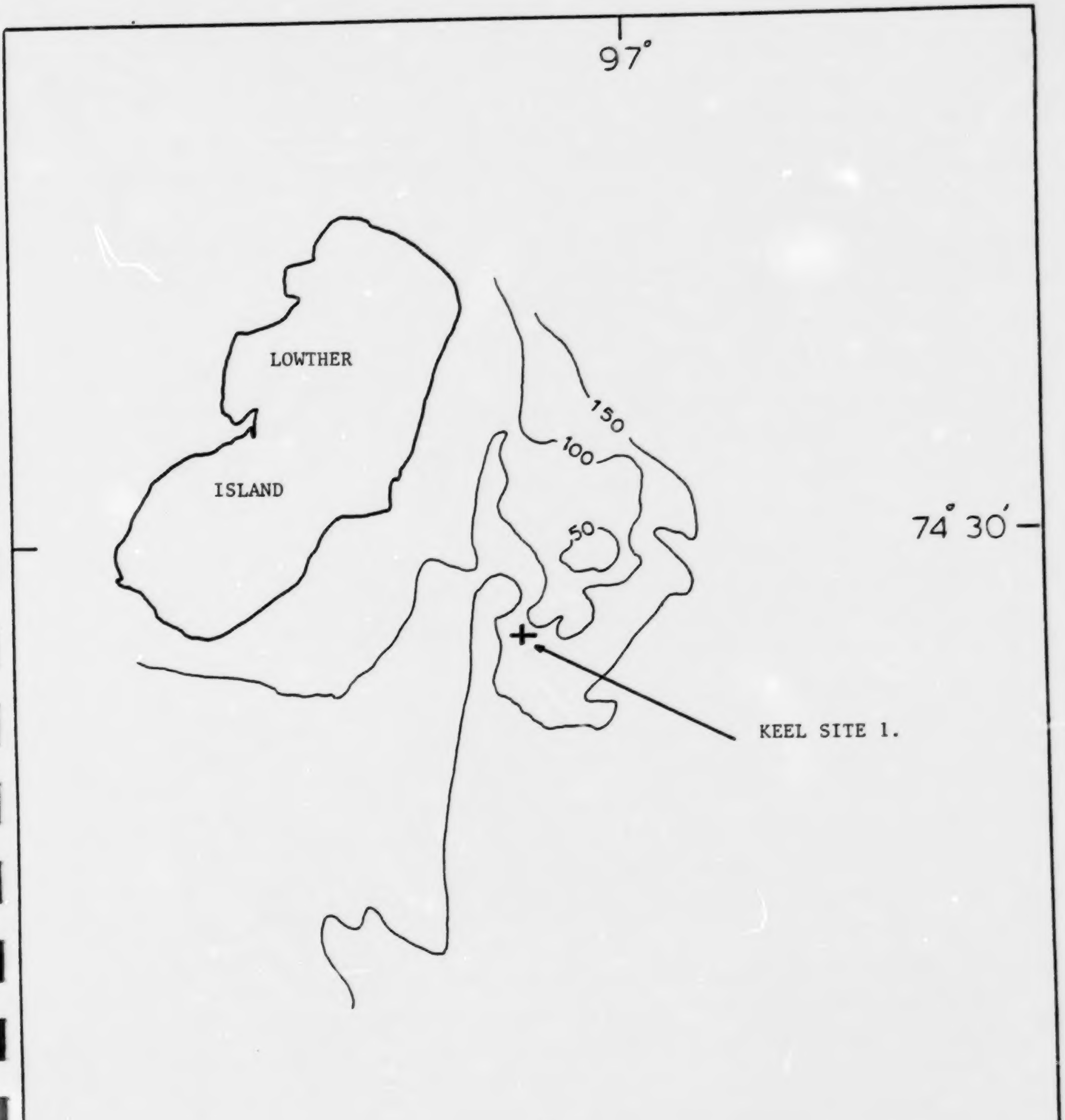

Figure 3. Test site in Barrow Strait.

the sonar head, provided a reference check at the beginning and end of each vertical sweep. Ten overlapping survey positions were laid out to cover approximately 240 m of keel length. The ten sets of data were combined after removing positioning errors to yield a smoothed data set of contours covering the entire length of keel. The keel survey technique and data processing details are available in the form of a contract report, Lyall (1985). The desired accuracy was to obtain vertical depths to within 50 cm and horizontal positions to within 1 metre.

Figure 4 shows a smoothed contour map of the merged data sets with 50 cm contour intervals. Most of the actual keel was covered by at least four overlapping survey positions and the smoothed contours are appropriate for overall hydrodynamic purposes. Visual examination of the keel structure with an underwater TV system revealed a typical first year formation with loosely packed slabs of ice about 50 cm in thickness, typical roughness scales being of the order of 1 m. These large scale elements were in fact resolved by the individual acoustic profiles but are submerged in the subsequent averaging. Figure 5 is a perspective view taken from beneath the ice. It can be seen that the keel is reasonably symmetrical in cross section and of uniform depth along its length.

3.1 Instrumentation

The instrumentation consisted of conventional recording current meters, acoustic depth sounders, and a profiling CTD. The layout was designed to give upstream and downstream velocity profiles combined with extensive acoustic visualisation of the flow patterns. The current meters were a combination of Aanderaa RCM4 units with modified rotor and direction vanes and Applied Microsystems vector averaging current meters. The Aanderaa rotor units were re-designed to remove azimuthal variations in speed calibration introduced by the rotor supports being held in a fixed orientation relative to the ice, Pite (1986).

Figure 6 shows the positions of the various instruments relative to the ice keel, where the layout is designed such that the

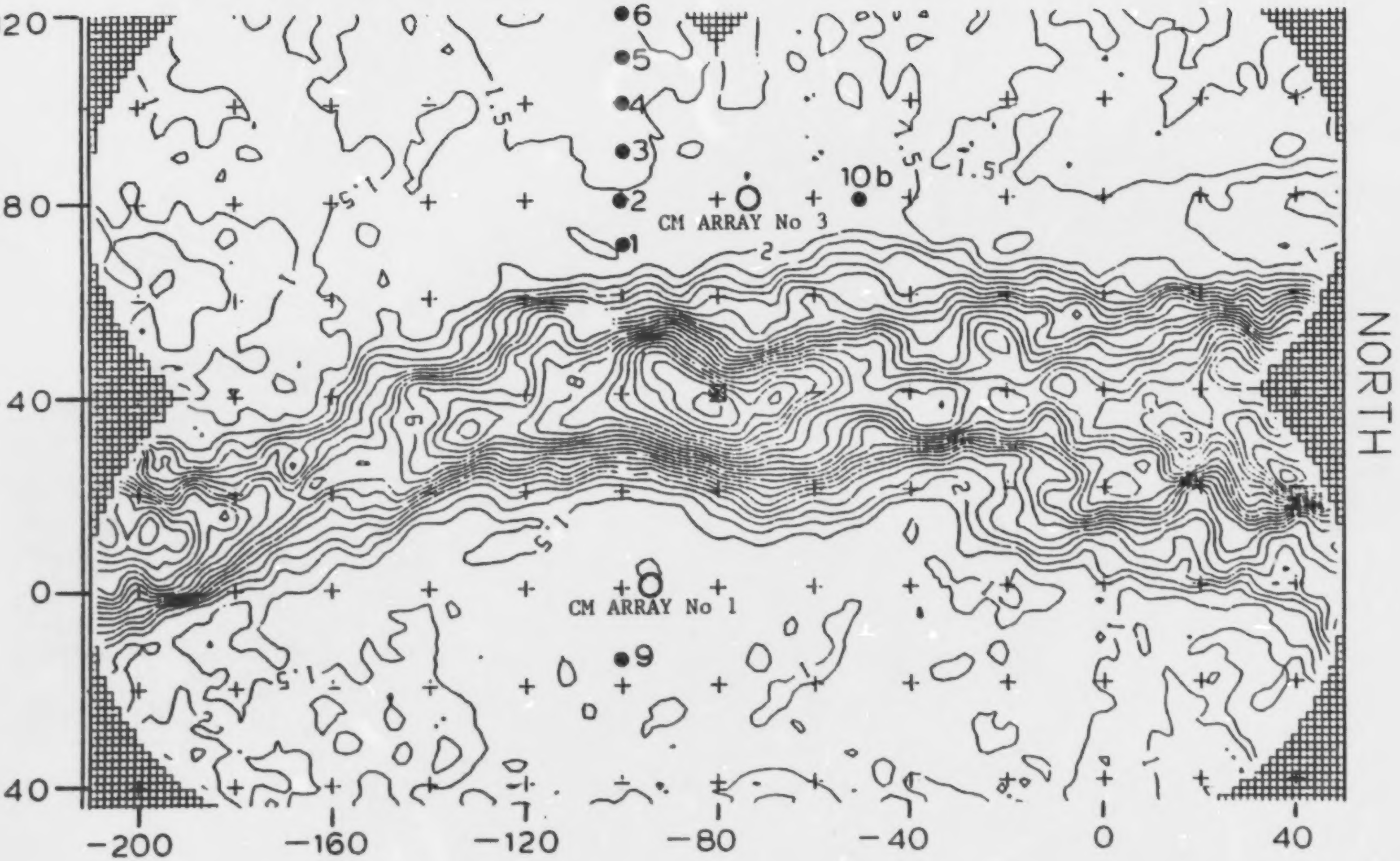

Figure 4. Contour map of the ice keel,showing near field instrumentation.

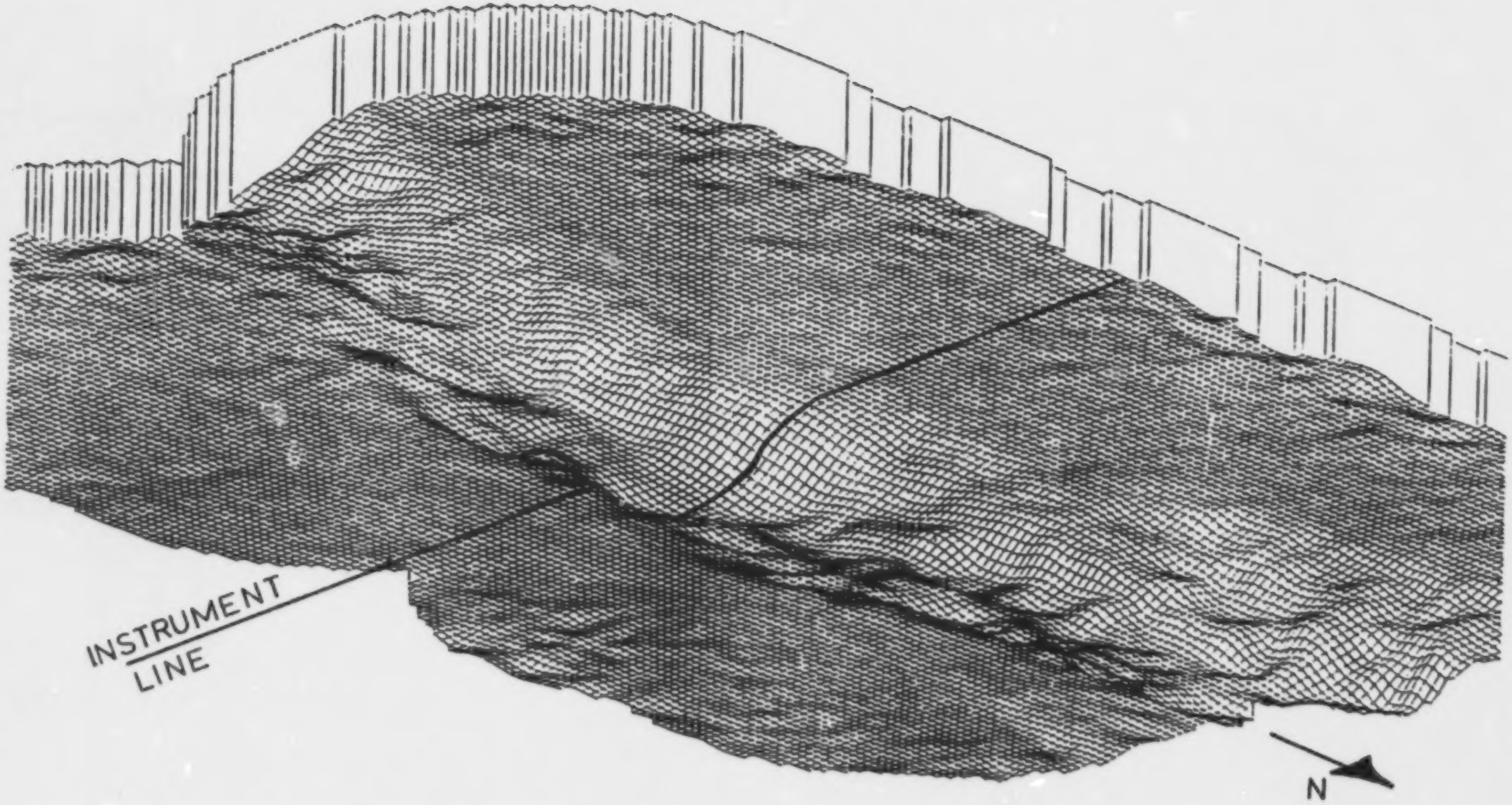

Figure 5, Perspective view of ice keel.

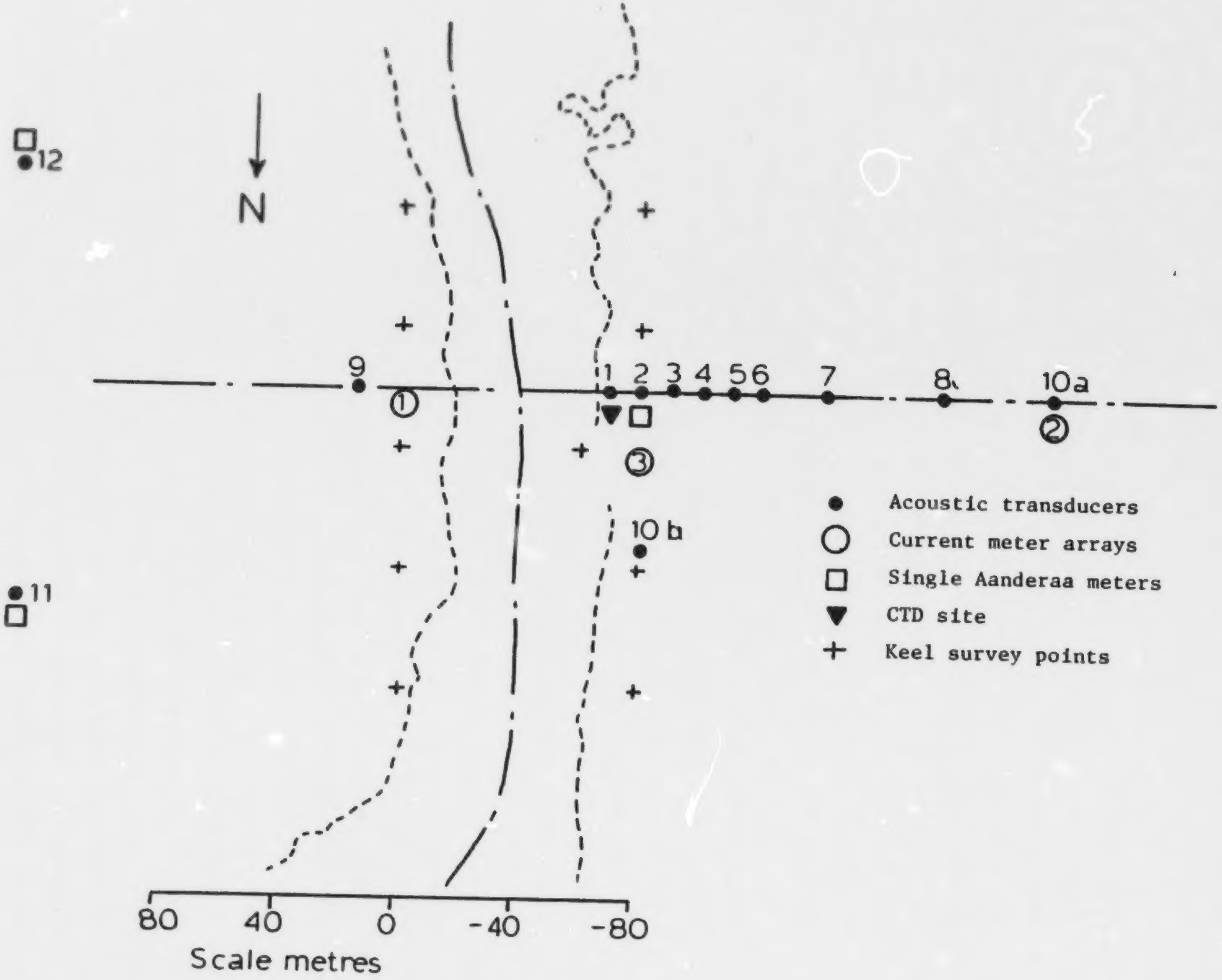

Figure 6. Instrument layout.

'downstream' side of the keel is to the west. The three current meter arrays each consist of 6 meters spaced approximately logarithmically in depth down to 32 m on rotationally rigid pole mountings to record flow speed and direction, water temperature and conductivity immediately upstream and downstream of the keel and farther downstream in the wake region. In addition to these, three single meters moored at 10 m depth on hydraulic hose formed a triangular array of about 160 m sides to provide information as to the direction of any significant free running internal waves intersecting the keel. The current meters recorded at 2 minute intervals for up to 12 days, the duration of the actual experiment.

The acoustic instrumentation consisted of twelve 200 KHz transducers mounted vertically through the ice, up to 8 of which could be multiplexed to a Furuno FCV 201 sounder/monitor unit. Their positions are numbered 1 through 12 on Figure 6 and the multiplexed group are shown relative to the keel contours on Figure 4. Stations 10A and 10B mark alternative sites of the same transducer which was re-positioned during the course of the experiment. This multiplexed data was recorded on standard half hour audio magnetic cassette tapes, with the capability for realtime display of two sequential channels in hardcopy form. An acoustic pulse length of 150 μsec was used throughout and with eight transducers multiplexed, each transducer fired at three second intervals. This repetition rate is fixed by the water depth and the time required for multiple reflections to decay. With the relatively low flow speeds at the experimental site, 10 to 20 cm/sec, this repetition rate is sufficient to resolve the flow features of interest. The remaining 4 transducers were powered by stand alone Furuno 606 sounders. In practice most of the acoustic data was taken with the multiplexed system alone because of mutual interference between separate sounder systems. Data was recorded with several configurations of multiplexed transducers covering a number of separate tidal cycles, including one complete 24 hour series. During some of the series, including the latter, CTD profiles were taken close to the keel at roughly half hour intervals. One series of vertical plankton tows was taken using a 505 μm mesh net to provide some information on the larger biological scatterers.

The data collected with these systems are sufficient to define the Froude number regime of the flow and to identify the resulting flow patterns. A total of 60 hours per channel of multiplexed acoustic data was recorded, selected portions of which will be subjected to digital processing to extract information on local particle motion and provide image enhancement.

4.0 Some selected results

At the time of writing some preliminary analysis has been performed and some rudimentary results will be discussed here. Figure 7 is a sample of the chart recorder plot from a single channel of multiplexed acoustic data. The transducer in question is no. 1, in the direct lee of the keel, the flow direction during this period being roughly normal to the keel. Superimposed on the acoustic chart is a series of density profiles taken with a Guildline Mark IV CTD.

Two types of acoustic signal can be discerned on the record, small intense signals of short duration which appear to track actual particle motions, and a more diffuse signal which mirrors the turbulent structures in the flow. The point scatterers are undoubtably biological in origin but it is not known at this stage whether the more diffuse volume scattering is from fine suspended matter or from the turbulent micro-structure itself. Concentrations of the diffuse scattering appear to coincide with regions of sharp density gradient, particularly the edges of such regions.

As time progresses there is a sudden deepening of the intensely reflecting surface layer from 6 m to close to 20 m followed by concentrated bands of turbulent scattering layers down to this level. Our interpretation is that a large amplitude leewave has moved across the transducer as the flow conditions change, the rapidly deepening sharp front occurring about one hour into the record marking the leading edge of a wave.

The spatial structure of this event can more easily be deduced

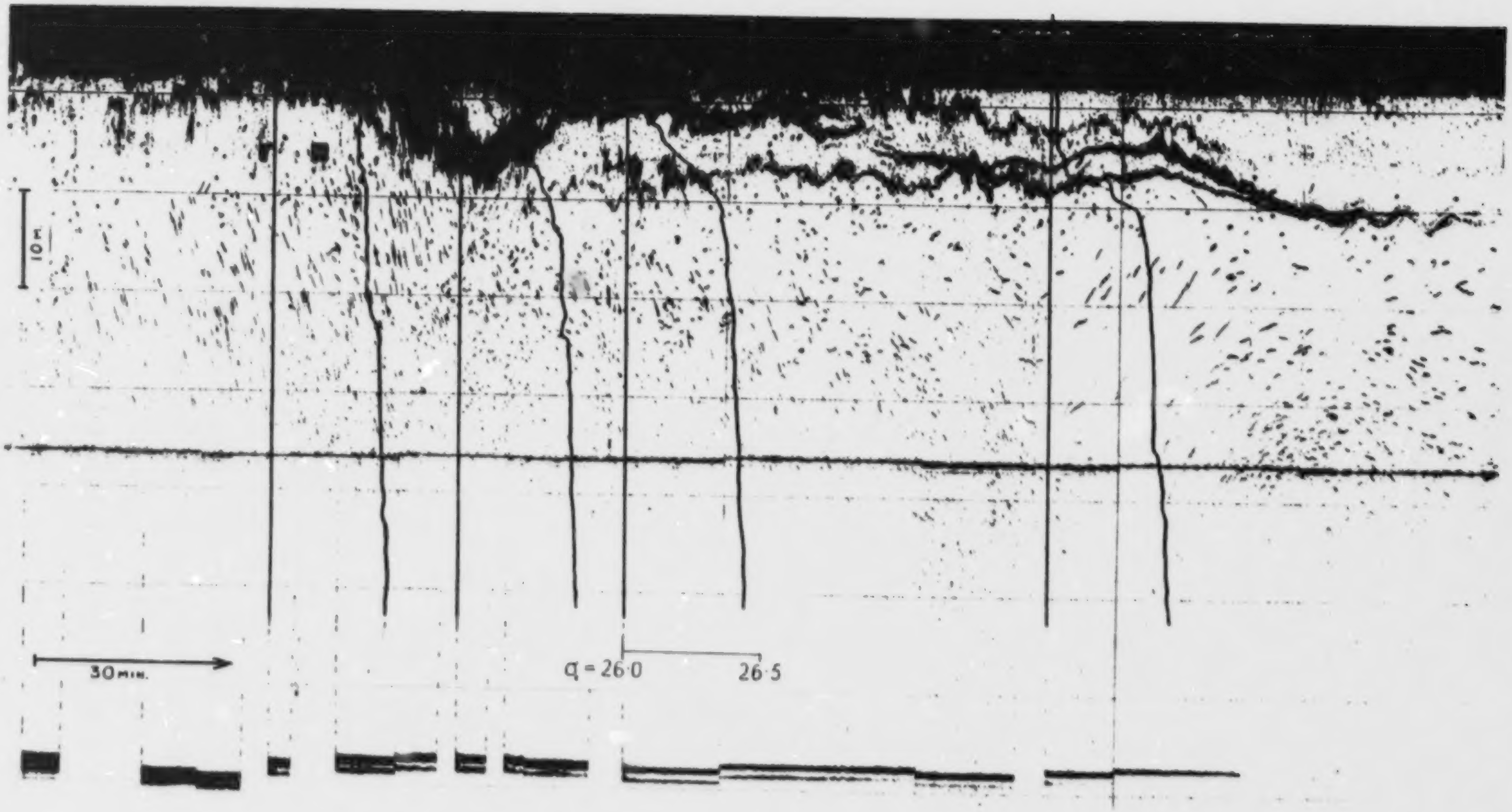

Figure 7. Sample of acoustic record with superimposed density profiles.

if short segments of all eight transducers are displayed in their positions relative to the keel. Figures 8a to 8d show a time series of such reconstructions at 8 minute intervals and on the left hand end of each a scale is displayed the upstream velocity distribution. The impression is of a large amplitude lee disturbance which advances forward as the oncoming flow slightly slackens. The mixed layer depth in the approaching flow is about 20 m with the flow itself confined to the mixed layer, with very little flow for some depth below this. The large scale velocity profiles are closely associated with the overall density structure and are suggestive of internal tides, possibly arising from the proximity of the Barrow Strait sill, an area known for its complex tidal interactions, Prinsenberg (1986).

Taking a typical mixed layer density difference of 0.2 parts in sigma t, a depth of 20 m, and a mean approach speed of 10 cm/sec, this yields an equivalent two-layer Froude number of 0.5, reducing to about 0.3 as the current slows over the time spanned by the illustrations. For a mean keel depth of 8 m this gives a keel to mixed layer depth ratio of 0.4, placing the operational point clearly in the region of partially blocked flow with lee jumps, Figure 2.

This single example has been selected for display because it illustrates the interplay of the various types of experimental information. With further refinement in processing considerably greater detail can be extracted from the acoustic records, for example, playback on a colour display reveals structure embedded within the black regions of the simple chart record. It is hoped to enhance these details by the application of suitable image processing techniques.

The field experiment described here is one aspect of the project as a whole and a complimentary laboratory investigation is planned for the coming year to look at unsteady wave-lee wave interactions using a newly constructed towing tank at I.O.S.

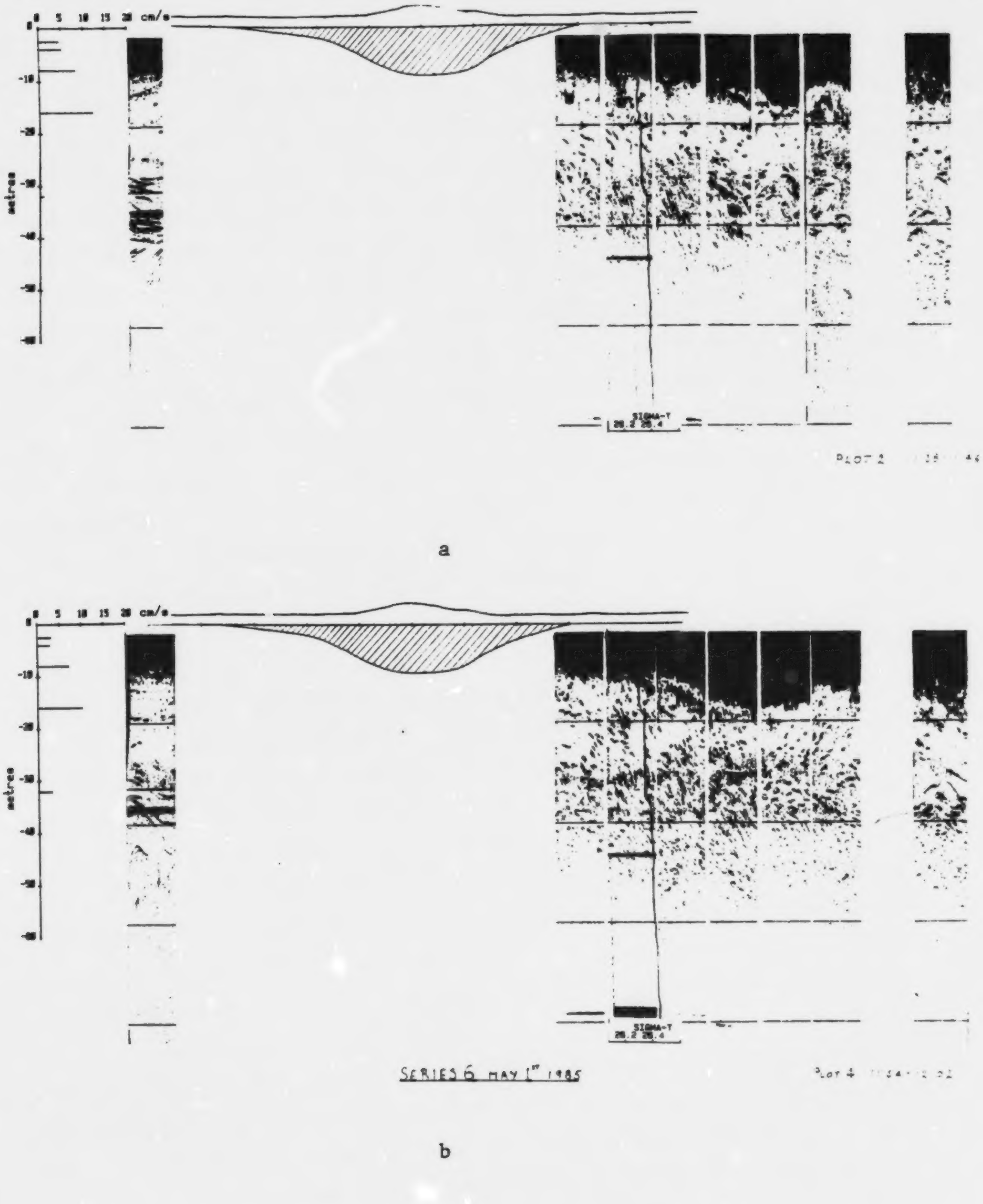

a

b

Figure 8. Reconstructed spatial diagrams showing upstream velocity profiles.

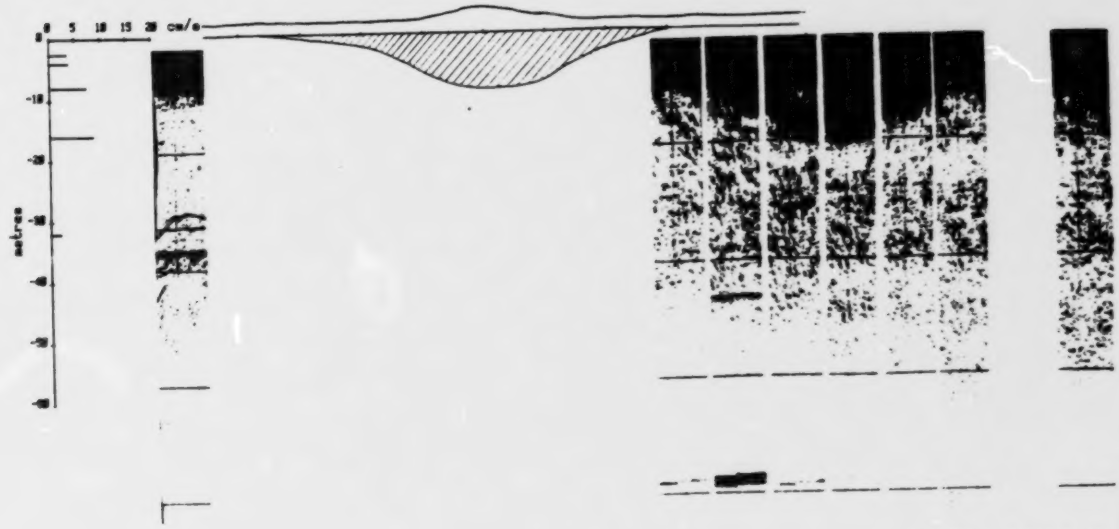

PLOT 5 12:02-12:10

c

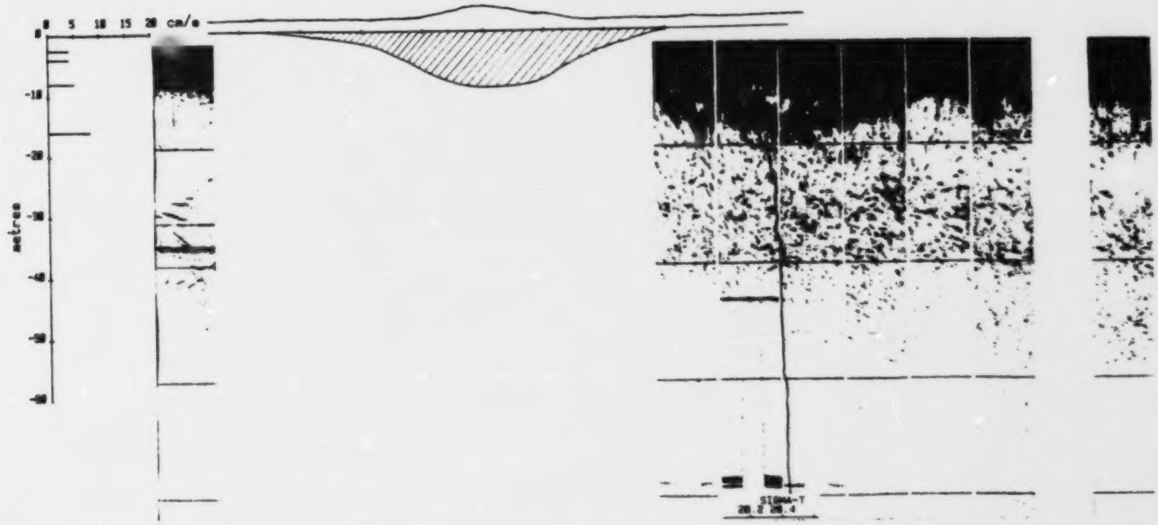

PLOT 6 12:10-12:18

SERIES 6 MAY 1ST 1985

d

Figure 8.(continued)

Acknowledgements

We would like to thank the Polar Continental Shelf Project and their staff at Resolute Bay for providing the logistic and operational support for this experiment. Also to the staff of the Marine Ecology Laboratory, Bedford Institute of Oceanography, and in particular, Dr. Glen Cota for taking underwater video footage of the ice keel and loaning us the plankton tow equipment.

References

Baines, P.G., 1984. A unified description of two-layer flow over topography, J. Fluid Mech., Vol. 146, pp 127-167.

Farmer, D.M., and H.J. Freeland, 1983. The physical oceanography of fjords, Progress in Oceanography., Vol. 12, No. 2, Pergamon Press.

Lemke, P., and T.O. Manley, 1984. The seasonal variation of the mixed layer and the pycnocline under polar sea ice., J. Geo. Res., Vol. 89, C4, pp 6494-6504.

Levine, M.D., and C.A. Paulson, 1985. Internal wave spectra in the Arctic Ocean, American Geophysical Union, Fall meeting, San Francisco, Paper 042C-10, 1645 H.

Lyall, R.C., 1985. Acoustic profiling of an Arctic ice keel. Contract Report DSS file no. 06SB.FP941-4-3252, Institute of Ocean Sciences, Sidney, B.C.

McPhee, M.G., and J.D. Smith, 1976. Measurements of the turbulent boundary layer under pack ice. J. Phys. Ocean, Vol. 6, pp 696-711.

Pite, H.D., 1986. The influence of support rods on the rotation speed of Savonius rotors. J. Atmos. and Ocean Technology (in press).

Wadhams, P., 1975. Sea ice morphology in the Beaufort Sea., Beaufort Sea Tech. Report No. 36, Dept. of Environment, Federal Gov't. of Canada.

SOLITARY WAVE SOLUTIONS FOR THE SEA ICE MOMENTUM EQUATIONS

by T.E. Keliher
Consolidated Technology Associates
P.O. Box 13731, Postal Station A
St. John's, Newfoundland, Canada A1B 4G3

The momentum equations for sea ice motion can contain several types of non-linearities. Here some solutions are obtained with the inclusion of the quadratically non-linear water stress (the linear case is also considered) and the non-linear advection term. For the one dimensional case a solitary wave solution can be found implicitly as a function of the variable $\theta = kx-\sigma t$, which assures constancy of the wave shape during propagation. The solution can be shown to go to zero at infinity as required by the definition of a solitary wave. The two dimensional solution is more difficult to obtain, but for the case of linear water stress an approximate solution can be found which closely resembles the one dimensional case. At present no solution for the case with the quadratic water stress has been found. It will probably be necessary to use a numerical solution to determine if these solitary waves are solitons.

WIND STRESS OVER ROUGH ICE IN A MARGINAL ICE ZONE

by R.J. Anderson
Department of Fisheries and Oceans
Bedford Institute of Oceanography
Atlantic Oceanographic Laboratory
P.O. Box 1006, Dartmouth
Nova Scotia, Canada B2Y 4A2

The principal objective of this study was to obtain values of wind stress and air drag coefficients for a variety of ice types and weather conditions characteristic of the MIZEX 84 area. The wind stress was directly measured using a three-axes Kaijo Denki sonic anemometer mounted on a 4 m mast placed on an ice floe and these values are compared with estimates of wind stress from the indirect dissipation method using shipboard sensors. Of particular interest is a 16-hour period during which 15 data runs were made with winds from the north, off the ice at 6-10 m/s and near-neutral atmospheric conditions. The mean drag coefficient referenced to 10 m was $10^3 C_D = 4.35 \pm 1.12$ which is higher than most values reported in the literature for marginal ice zones. The wide range of these values can be attributed to changing upwind ice conditions with time and this period will be discussed in detail.

IV

ICEBERGS

LONG-RANGE PREDICTION OF ICEBERG SEVERITY IN THE LABRADOR SEA

by

W.I. Wittmann[1], L.H. Hester[2], W.S. Dehn[3], and J.E. Walsh[4]

ABSTRACT

Statistical models for the long-range prediction of iceberg severity in the Labrador Sea are developed from observed data for the years 1947-1984. The predictors are the monthly fields of sea level pressure and 700 mb geopotential height over the northern hemisphere. The primary statistical tools are gridded correlation patterns, composite grids for mild and severe extremes of iceberg severity, and multiple regression. Statistical significance is established by repeated Monte Carlo simulations of the experimental procedure and by testing on independent data for the year 1985.

Statistically significant associations are found between the iceberg severity index and the atmospheric circulation fields of the antecedent October-March period. At lead times of 3-7 months, the median absolute errors in the long-range forecast of severity rank are approximately 4 ranks in a sample of 30 ranked years. The teleconnection patterns exhibited by the predictor fields are synoptically compatible with Eastern Canadian iceberg conditions in both mild and severe extremes.

1. Walter I., Sea Ice Consultants, Inc., 4710 Auth Pl. #175, Camp Springs, MD 20746

2. Larry H., Sea Ice Consultants, Inc., 4710 Auth Pl. #175, Camp Springs, MD 20746

3. William S., Sea Ice Consultants, Inc. 4710 Auth Pl. #175, Camp Springs, MD 20746

4. Dr. John E., U. of Ill. at Urbana-Champaign, Dept. of Atmospheric Sciences, 1101 West Springfield Ave., Urbana, IL 61801

I. INTRODUCTION

The annual variability of the iceberg count in the Labrador Sea region presents a multifaceted predictive problem within the framework of the geophysical sciences. The annual iceberg count (defined as the number moving south of 48°N latitude) has varied from 0 to more than 2000 over the past 30 years -- the number can vary by more than 1000 in successive years. The physical mechanisms responible for this high variability are complex and poorly understood, while little applied work has been done on the dynamics of the balance of forces affecting iceberg drift.

Calving rates of icebergs are most likely dependent on the thermal regime of the atmosphere, oceanic processes in the near-shore region, and the flow dynamics of ice sheets and glaciers.

Transport of icebergs from the source regions to the waters off Labrador and Newfoundland depends to a large extent on the large-scale atmospheric flow regime and the associated surface wind stresses. Additional complications are introduced by the oceanic currents, which can reinforce or offset wind-induced iceberg drift. Moreover, the temperature distribution in the upper ocean can directly limit the southward penetration of an iceberg by enhancing melt during transit. Even the distribution of sea ice may be relevant to the frequency of iceberg occurrence -- not only because sea ice serves as an integrator of atmospheric and oceanic forcing, but also because the presence (or absence) of sea ice may modify the oceanic environment encountered by drifting icebergs.

The Sea Ice Consultants, Inc. (SIC) approach to long-range prediction of iceberg severity is based primarily on a systematic use of surface and 700 mb atmospheric data. Several considerations dictate this reliance upon atmospheric parameters:

1. *Availability of Data:* Reliable, gridded atmospheric data are far more readily available than are either oceanographic or sea ice cover data. Unlike the oceanographic or sea ice parameters, 30 or more years of monthly atmospheric data are available for the region. This provides a sample large enough for the systematic application of statistical significance testing.

2. *High Correlation:* Atmospheric variability can be expected to correlate well with oceanic variability at the spatial and temporal scales considered here, as it does in the Bering Sea (Niebauer, 1983). Therefore, atmospheric fields should implicitly describe large portions of the thermal and current regimes.

3. *Scope of Project:* The funding and manpower constraints of the project mandate a highly focused effort toward development of a forecast system capable of straightforward implementation. Other potentially useful avenues of effort are noted in Section IV of this paper.

The statistical treatments of both predictand and predictor data sets are complicated by several factors. The distribution of the annual iceberg count, for instance, is non-linear and non-normal; while the atmospheric data fields are known to contain high levels of spatial and moderate levels of temporal correlation on the monthly time scale. These and other factors require that statistical procedures be carefully formulated with respect to sample selection, filtering, and regression analysis. Therefore, we have relied heavily on *Monte Carlo* testing procedures. These preserve the spatial and temporal dependences of the data in our determination of significance thresholds. Although such an emphasis on significance testing is computationally demanding, we feel that it is mandatory in this type of situation, where potentially useful signals may be masked by the large natural variability of the physical system under investigation. For this reason, the following sections contain unusually extensive documentation of the statistical significance tests in addition to examples of the levels of skill achievable by the approach formulated here.

We recognize that the iceberg counts contain considerable uncertainty. Both technology and use have changed the basis of the counts over the years. Nevertheless, we feel that the International Ice Patrol (IIP) Annual Reports, from which our count was taken, is probably the most accurate available. In particular, it is likely that the distinction between severe years and mild years is preserved.

II. THE SIC PROCEDURE

This Section describes the indexing of the predictand, the selection of the predictors, and the use of the selected predictors in a multiple regression framework.

A. INDEXING THE PREDICTAND

Figure 1 shows the number of icebergs reported by the IIP (i.e., the number crossing south of 48°N) for each year from 1947 through 1984. The period of the annual count is from 1 September through 31 August. Note the large year-to-year variability and the non-linear, non-normal nature of the distribution. For example, while the annual totals range from 0 to more than 2000, 22 of the 38 values are less than 160. Correlative statistics based on this distribution would be biased heavily toward (and dominated by) the few years with large totals. Therefore, we have used a rank index for the predictand. The index was derived from the totals given in Table 1. The 30 years, 1955 through 1984, were assumed to be a sample of adequate size for testing, while also having available the most accurate corresponding atmospheric and sea ice data sets. The most severe case (2204 icebergs in 1984) was arbitrarily assigned a rank of 1, while the mildest year (1966, count 0) was assigned a rank equal to the sample size -- i.e., 30. Table 1 lists both the iceberg count and the rank index for each year in the sample.

Because of the obviously non-linear distribution of the predictand, log-normal and power transformations were applied to the predictand. In preliminary tests, such transformations produced correlations generally similar to, but not significantly better than, those obtained with the rank index. The rank index has the advantage that errors in forecast rank can be readily interpreted within a categorical framework (e.g., terciles, quintiles, etc.).

B. SELECTING THE PREDICTORS

As noted in Section I, the SIC procedure is predicated on the assumption that atmospheric circulation data represents the most effective source of predictive information. This assumption is valid insofar as the dynamic and thermodynamic forcing of oceanic and sea ice fluctuations are atmospheric in origin. The essential element of atmospheric forcing is the large-scale circulation, which determines the surface thermal regime (via temperature advection) as well as the dynamic regimes of sea ice and the near-surface ocean layer. The dynamic role follows from the fact that wind stress is the primary motive force for sea ice and for

FIGURE 1: Annual IIP Iceberg Count (1947-1985)

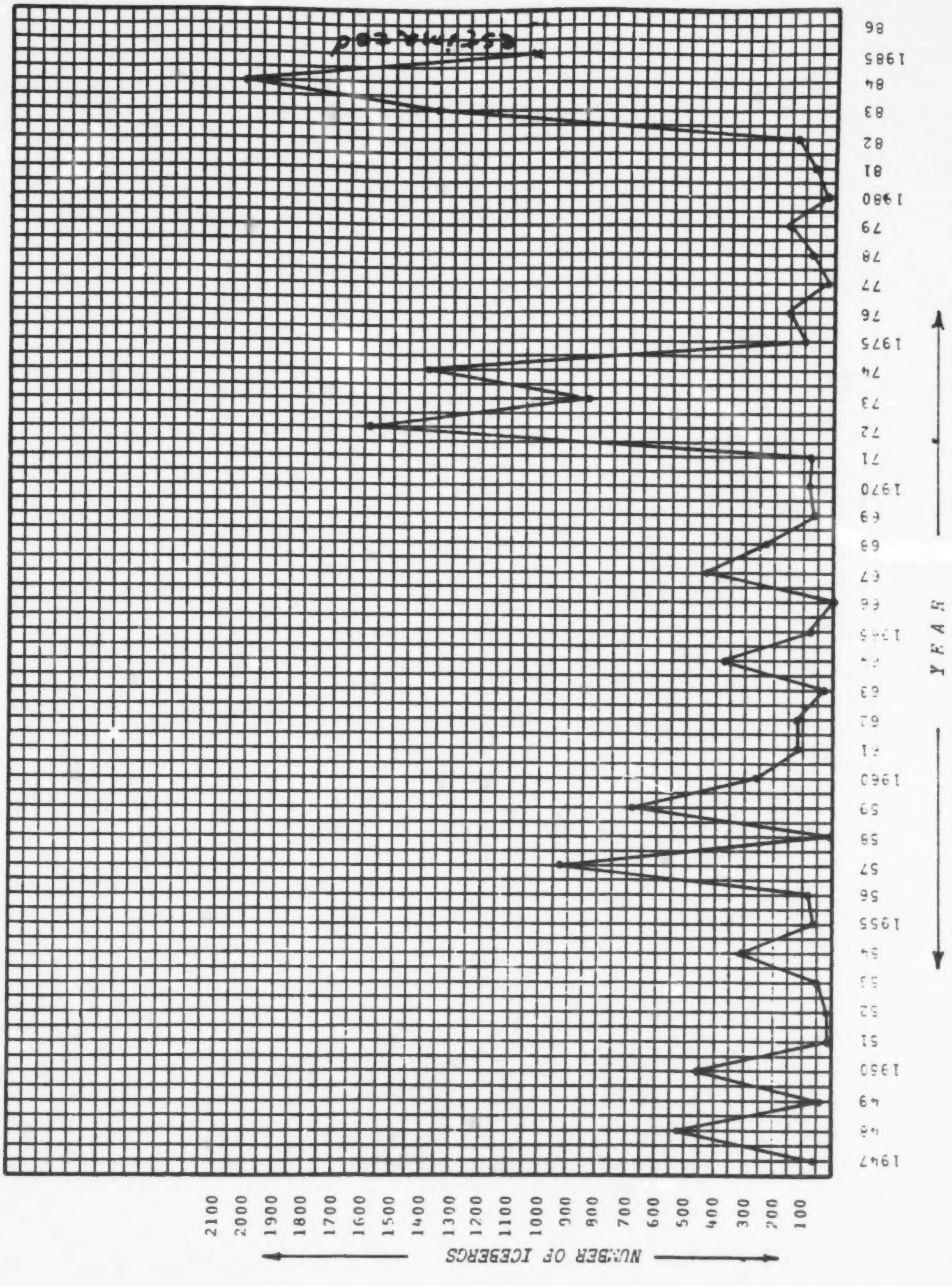

TABLE 1

Severity Index (Rank) of Iceberg Years

(1 = most severe)

Year	IIP Iceberg Count	SIC Index (Rank)
1984	2204	1
1972	1584	2
1974	1386	3
1983	1351	4
1957	931	5
1973	846	6
1959	689	7
1967	441	8
1964	369	9
1960	256	10
1968	226	11
1982	188	12
1979	152	13
1976	151	14
1962	121	15
1961	114	16
1975	100	17
1970	85	18
1956	80	19
1965	76	20
1978	75	21
1971	73	22
1981	63	23
1955	61	24
1969	53	25
1963	25	26
1980	24	27
1977	22	28
1958	1	29
1966	0	30

NOTE: The IIP has estimated the 1985 iceberg count to be 1031, which would make it fifth (of 31 cases).

IIP berg counts are from 1 September through 31 August annually.

surface currents in the ocean. These considerations dictate the use of sea level pressure data. We note that grids of sea level pressure (or of geopotential height, in upper air fields) permit the utilization of wind or circulation data. This stems from the fact that geostrophic winds are directly proportional to the gradients in these fields.

The requirement for lead times of several months or seasons in long-range forecasting introduces a reliance on large-scale atmospheric teleconnections as a forecast tool (Namias, 1972). Teleconnections to remote regions have recently been shown to represent predictive signals at lead/lag times of up to several seasons, e.g., the Southern Oscillation (Horel and Wallace, 1981). These teleconnections are most readily detectable in data for the upper air, where surface-induced perturbations of large-scale signals are minimal. For our purpose, we have used gridded data for the geopotential height of the 700 mb level, which is generally considered to be most representative of the vertically averaged tropospheric circulation.

The monthly gridded data used were obtained from the National Center for Atmospheric Research (NCAR) in a 5° latitude by 10° longitude format covering the area from 20°N to the North Pole. Thus, each grid contained a total of 540 data points. The NCAR grids extend through 1982. Grids for the years 1983 and 1984 were from the SIC data bank, which were originally obtained from the National Weather Service/NOAA monthly printouts.

Two basic techniques were applied. First, a *linear correlation* of each grid point with the iceberg index over the 30-year sample was computed. Second, a *composite difference* of the grid data between the mild and severe iceberg years was constructed. Both approaches were used for both sea level (MSLP) and 700 mb grids. All periods and lag times were considered -- i.e., the atmospheric data were averaged over all periods of 1-7, 9, 12, and 24 months ending each month from May of the preceding year through April of the current year. The data was staggered in this fashion to meet operational requirements. Forecasts issued after April are of little value to users.

Various filtering processes and/or tests were then applied. This strategy was necessary because of the spatial and temporal coherence of the data (i.e., the relatively high correlation between adjacent points) and because of the prohibitively large numbers of predictors (540 for each grid).

The statistical significance of the predictor field was of overriding concern in the development of the forecast system. Specifically, if field significance could not be demonstrated, then the existence of a predictive signal (and the validity of any derived forecast model) was considered highly uncertain. Therefore, each grid of point correlations or of composite differences was tested for field significance as follows:

1. The statistical significance of each grid point value in the field was determined. For the linear correlations, the significance test was based on the sample size and on the null hypothesis of zero correlation. In the case of composite difference fields, significance level was obtained from a two-tailed t-test and the null hypothesis of zero difference.

2. The areal fraction of the domain over which the point values were statistically significant were computed. The number of point values was converted to an areal fraction by the application of a latitudinal cosine weighting factor. The areal fractions were computed for an Arctic subset ($65^{o}N - 90^{o}N$) of the grid as well as for the entire grid.

3. The probability of achieving the areal fractions obtained in step 2 by chance was evaluated. This was performed with a series of from 100 to 500 Monte Carlo trials. The element of chance was introduced into the Monte Carlo trials by randomly reordering the predictand time series. Therefore, our methodology (as well as the spatial and temporal dependences of the predictor data) was preserved. Any desired significance level could then be determined by ordering the Monte Carlo results in order of decreasing areal fractions of point significance (e.g., in a trial of 100 runs, the 5th highest areal fraction corresponds to the 5% level of significance). Although they introduce substantial computational requirements, Monte Carlo tests represent the most rigorous estimates of significance because of their fidelity to the statistical forecasting procedure and to the distribution of the data, whether normal or otherwise. (Livezey and Chen, 1983).

Once a given field passed the Monte Carlo test, the individual point values were filtered to select the individual predictor points for inclusion in the multiple regression. This was accomplished as follows:

1. To insure spatial independence, a point was required to be a relative maximum or minimum (correlator or t-value) within its field.

2. The point was required to exceed the threshold values for significance in its own right.

3. When an otherwise successful point predictor occurred in two fields having overlapping periods, only the higher correlation and/or t-value was selected.

However, this rule could be superceeded by an operational requirement for greater forecast lead time. I.e., although a particular time combination would not yield the best possible prediction from a given point, it may have been the best predictor available at the time the forecast had to be issued. For example, a point may correlate at 0.74 for the 6-month period ending in April, while the 3-months ending in February for the same point correlates at 0.68. In this case, the additional lead time between February and April (when the data become available) more than offsets the difference in predictability implied by the lower correlation.

C. MULTIPLE REGRESSION

The procedure described in Paragraph B, generally extracted from 2 to 5 points. These were then used as the predictor points for the iceberg rank index in a multiple linear regression equation obtained by running the International and Mathematical Software Library (IMSL) subroutine RLMUL. The equation thus produced was used to generate hindcasts of the iceberg index for the 30 years in the sample, and to predict the next year's (1985) rank.

Since alternative strategies of statistical forecasting are available, we offer the following comments concerning our choice of method:

1. A popular alternative approach to statistical forecasting is the use of eigenvectors (empirical orthagonal functions) to represent the predictor fields (e.g., Davis, 1976). We chose not to use this approach for several reasons:

a. Because of the orthagonality constraint, each eigenvector in a computed set is required to be completely uncorrelated with all other eigenvectors in the set. But, the major anomaly patterns in the atmosphere generally exhibit some degree of correlation with each other. It follows that all eigenvectors, other than the first in a set, can represent statistical artifacts that are not amenable to physical interpretation (Buell, 1975).

b. The "black box" nature of the computations required for the inversion of the covariance matrix often makes it difficult to identify the reason for a poor forecast or a systematic bias. The SIC method permits direct estimates of the contribution by each predictor point, and an immediate assessment of the synoptic regime responsible for any given predictor value.

c. The requirement for ≈100K words of computer core storage for the inversion of the covariance matrix imposes a requirement for a mainframe computer.

2. The use of single-point correlations may be considered to be less comprehensive than a similar approach based on multiple-point combinations (sums and/or differences). However, our experience in this area has shown that the geometric increase in computing requirements entailed by multi-point combinations is not generally justified. Our procedure of extracting the extreme values from the correlation grids serves to retain, implicitly, the desired information (e.g., pressure gradient) about the multi-point combinations that is most relevant to the iceberg rank index.

III. RESULTS

A. THE 30-YEAR (1955-1984) CORRELATION SAMPLE

Following the procedure given in Section II, correlations between iceberg rank and MSLP (as well as 700 mb) were computed for various periods ending in each month from the preceding May through the current April. The locally significant areal fraction of each grid and its Arctic subset were computed. These fractions are given in Tables 2A and 2B. The Arctic subset was included for procedural consistency with experiments performed for the Alaskan North Slope. As will be discussed in Section IV, an expanded project might better use a subset of grid points centered on the Baffin Bay-Davis Strait area to determine a local signal in the correlation grids.

In Tables 2A and 2B, a general lack of skill is apparent in the early months (May - October of the previous year). Most entries for these months are at or near zero, but the values rise noticeably during winter. This tendency is generalized in Figure 2, which shows the average areal fraction of all periods for each month for the MSLP grid and its Arctic subset. Although only the MSLP plot is shown, a corresponding plot for 700 mb produces quite similar results.

The lag between the abrupt jump in predictability and the occurrence of maximum monthly iceberg totals (i.e., the lag between the December-February period in Figure 2 and the April-June period) indicates that the achievable range of predictability in the system is probably on the order of 4 to 6 months.

The most promising entries from Tables 2A and 2B were subjected to Monte Carlo testing. Figure 3 compares selected areal fractions with Monte Carlo thresholds for 10%, 5%, 2%, and 1% significance. One hundred trials were run for each case except for the 6-months ending in March MSLP, where 500 trials were run. While several of the tested fields clearly fail the Monte Carlo tests (e.g., 1-month 700 mb ending in May), other fields pass the test -- even at the 1% significance level (e.g. 6-month MSLP ending in March and 2-month 700 mb ending in January). The Monte Carlo trials led to the selection of two fields for predictive application:

1. 6-month MSLP ending in March
2. 2-month 700 mb ending in January

For purposes of illustration, the 6-month MSLP-March case is emphasized in the following discussion. In this case Figure 3 shows that the field exceeds the Monte Carlo threshold at 1% significance by a wide margin. The second case (2-month

TABLE 2A

Areal Fraction (percent) of MSLP Grids having Statistical Significance where N = 30

Prestige elite = entire grid (20-90N)

Italics = Arctic Subset (65-90N)

# Months in Period	Ending month of period											
	MAY	JUN	JUL	AUG	SEP	OCT	NOV	DEC	JAN	FEB	MAR	APR
1	3.7 *1.1*	0.3 *0.0*	0.2 *0.0*	0.3 *0.0*	0.0 *0.0*	5.8 *0.0*	0.0 *0.0*	1.5 *0.0*	17.8 *27.9*	0.5 *2.8*	0.8 *0.0*	0.5 *0.0*
2	0.5 *0.0*	1.9 *0.0*	0.0 *0.0*	0.0 *0.0*	0.0 *0.0*	2.6 *0.0*	3.6 *0.0*	2.4 *0.0*	12.1 *9.1*	14.3 *28.3*	2.4 *6.7*	1.3 *0.0*
3	0.9 *0.0*	0.7 *0.0*	1.2 *0.0*	0.0 *0.0*	0.0 *0.0*	0.9 *0.0*	2.4 *0.0*	5.2 *0.0*	12.2 *4.9*	14.4 *15.8*	13.6 *31.9*	3.1 *5.3*
4	0.8 *0.0*	0.6 *0.0*	1.0 *0.0*	1.3 *0.0*	0.0 *0.0*	1.1 *0.0*	1.1 *0.0*	3.1 *0.0*	13.1 *0.0*	15.9 *19.9*	14.6 *23.2*	13.3 *24.7*
5	1.4 *0.0*	0.4 *0.0*	0.3 *0.0*	1.0 *0.0*	1.0 *0.0*	0.0 *0.0*	1.0 *0.0*	2.6 *0.0*	10.9 *3.4*	17.6 *13.3*	14.2 *28.4*	15.7 *21.0*
6	2.0 *0.0*	1.6 *0.0*	0.4 *0.0*	0.3 *0.0*	0.5 *0.0*	1.0 *0.0*	0.5 *0.0*	1.3 *0.0*	9.6 *2.7*	15.1 *13.7*	19.0 *27.9*	14.9 *24.2*
7	3.5 *0.0*	1.9 *0.0*	0.8 *0.0*	0.0 *0.0*	0.3 *0.0*	0.4 *0.0*	1.0 *0.0*	1.1 *0.0*	7.0 *5.1*	15.4 *18.0*	15.5 *28.2*	17.2 *24.7*
9	2.4 *0.0*	2.4 *0.0*	3.3 *0.0*	0.9 *0.0*	0.2 *0.0*	0.2 *0.0*	0.9 *0.0*	0.8 *0.0*	9.0 *3.3*	11.5 *12.0*	15.9 *33.6*	16.6 *31.1*
12	1.9 *0.0*	2.3 *0.0*	2.8 *0.0*	1.8 *0.0*	1.0 *0.0*	1.7 *0.0*	0.5 *0.0*	0.2 *0.0*	4.8 *0.0*	9.0 *12.6*	9.8 *20.3*	15.0 *28.7*
24	1.5 *0.0*	1.5 *0.0*	1.2 *0.0*	1.2 *0.0*	1.2 *0.0*	0.6 *0.0*	1.4 *0.0*	0.9 *0.0*	0.9 *0.0*	1.4 *0.0*	2.1 *0.0*	1.0 *0.0*

TABLE 2B

Areal Fraction (percent) of 700 mb Grids having Statistical Significance where N = 30

Prestige Elite = entire grid (20-90N)

Italics = Arctic Subset (65-90N)

# Months in Period	Ending month of period											
	MAY	JUN	JUL	AUG	SEP	OCT	NOV	DEC	JAN	FEB	MAR	APR
1	2.8 *0.0*	0.5 *0.0*	0.4 *0.0*	1.4 *0.7*	0.1 *0.9*	5.7 *1.8*	0.0 *0.0*	1.4 *0.0*	14.7 *21.7*	0.0 *0.0*	2.6 *0.9*	0.2 *0.0*
2	1.0 *0.0*	1.2 *0.0*	0.5 *0.0*	0.7 *0.0*	0.2 *0.0*	1.5 *0.0*	2.1 *0.0*	0.9 *0.0*	8.5 *5.7*	13.7 *26.3*	3.5 *6.3*	3.1 *1.8*
3	1.0 *0.0*	1.6 *0.0*	1.4 *0.0*	0.0 *0.0*	0.6 *0.0*	1.1 *4.0*	2.8 *0.0*	2.7 *0.0*	11.0 *10.4*	11.3 *15.7*	15.8 *2.9*	6.1 *7.0*
4	0.4 *0.0*	0.8 *0.0*	1.1 *0.0*	0.8 *0.0*	0.0 *0.0*	0.7 *4.5*	1.8 *3.2*	2.5 *0.0*	10.0 *6.4*	12.8 *17.0*	13.0 *17.7*	14.2 *23.9*
5	0.4 *0.0*	0.4 *0.0*	0.7 *0.0*	0.8 *0.0*	0.7 *0.0*	0.0 *0.0*	1.0 *3.2*	3.0 *0.0*	10.8 *6.6*	13.5 *18.2*	13.7 *19.5*	12.3 *17.7*
6	1.7 *0.0*	0.7 *0.0*	0.2 *0.0*	0.5 *0.0*	0.5 *0.0*	0.0 *0.0*	0.0 *0.0*	1.8 *0.0*	10.5 *9.0*	11.8 *15.5*	14.9 *22.6*	13.2 *20.3*
7	1.5 *0.0*	0.9 *0.0*	0.3 *0.0*	0.0 *0.0*	0.5 *0.0*	0.0 *0.0*	0.0 *0.0*	1.1 *0.0*	8.0 *10.3*	12.8 *17.4*	15.3 *20.0*	15.2 *23.1*
9	0.5 *0.0*	0.5 *0.0*	0.5 *0.0*	0.5 *0.0*	0.2 *0.0*	0.0 *0.0*	0.0 *0.0*	1.1 *0.0*	7.7 *9.7*	8.4 *13.2*	15.0 *26.4*	15.5 *25.6*
12	0.5 *0.0*	0.5 *0.0*	0.2 *0.0*	0.0 *0.0*	0.0 *0.0*	1.1 *0.0*	0.8 *0.0*	0.0 *0.0*	3.3 *6.9*	8.1 *15.2*	10.5 *18.3*	13.5 *19.7*
24	0.3 *0.0*	0.0 *0.0*	0.0 *0.0*	0.0 *0.0*	0.0 *0.0*	0.0 *0.0*	0.0 *0.0*	0.3 *0.0*	0.3 *0.0*	0.0 *0.0*	3.6 *7.5*	2.7 *2.5*

FIGURE 2

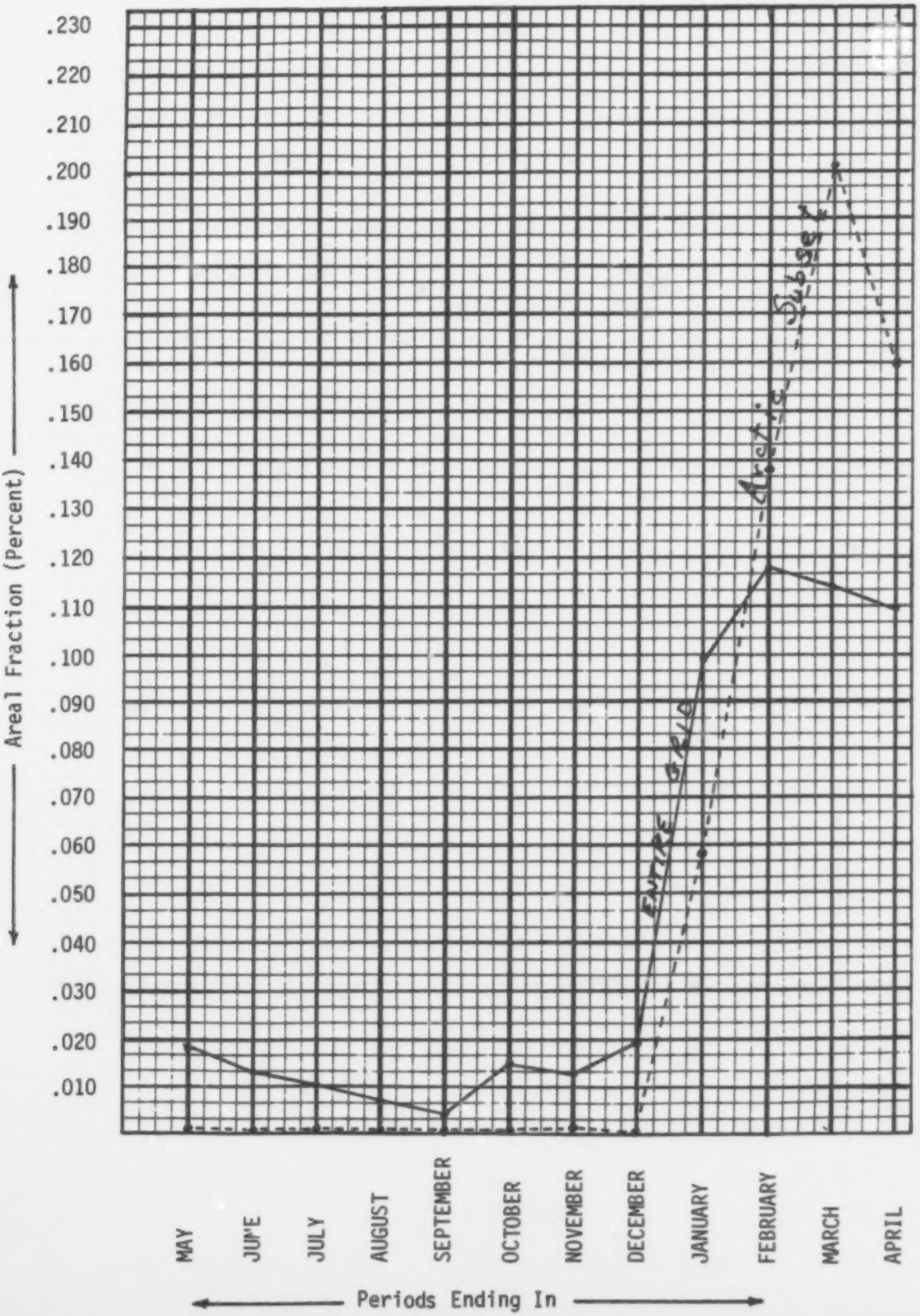
.230
.220
.210
.200
.190
.180
.170
.160
.150
.140
.130
.120
.110
.100
.090
.080
.070
.060
.050
.040
.030
.020
.010
Areal Fraction (Percent)
ENTIRE GRID
Arctic Subset
MAY
JUNE
JULY
AUGUST
SEPTEMBER
OCTOBER
NOVEMBER
DECEMBER
JANUARY
FEBRUARY
MARCH
APRIL
Periods Ending In

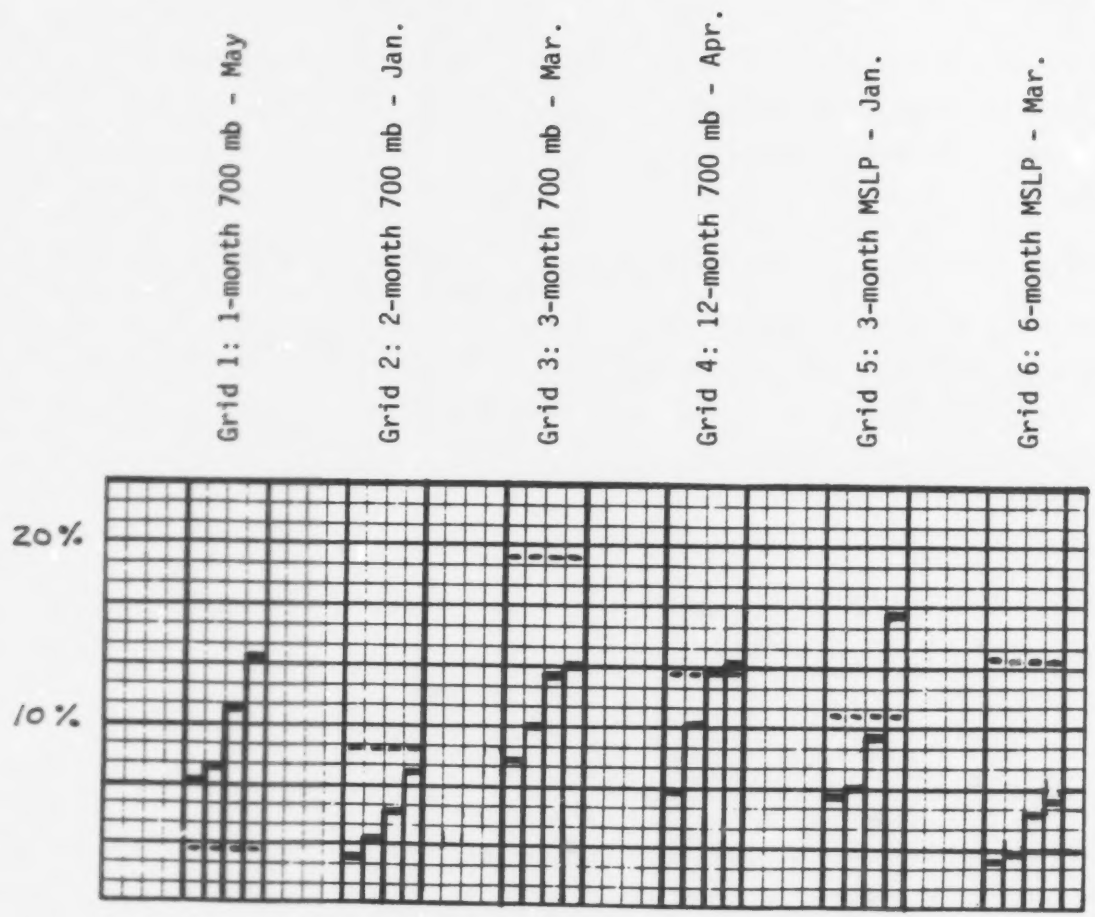

FIGURE 3: Monte Carlo Thresholds vs. Observed Areal Fractions

In Figure 3, the four bars for each grid represent the areal fraction thresholds obtained from the respective Monte Carlo run. For each grid, the thresholds are (from left to right): 10%, 5%, 2%, and 1% significance. For grids 1 through 5, 100 Monte Carlo trials were run in each case. For grid 6, 500 trials were run. The dashed line across all 4 bars represents the observed areal fraction for that grid. When the dash line lies above the end of a given bar, it exceeds the Monte Carlo threshold for that level of significance for that grid.

700 mb-January) narrowly exceeds the 1% threshold; but it provides two months additional forecast lead time, and is valuable for that reason.

Tables 3A and 3B are the correlation grids for the two selected predictor fields. (In the original computer runs, the order of the iceberg rank was reversed. Although this changes the sign of the correlation, the absolute value and the significance levels of the correlation are unaffected.)

Case 1. 6-Month MSLP-March Correlation Field

Table 3A is characterized by significant negative correlations (low MSLP in severe iceberg years) in the Canadian Arctic and the North Atlantic subarctic areas, and by significant positive correlations (high MSLP in severe iceberg years) in the subtropical and mid-latitude Atlantic. This north-south Atlantic anomaly gradient corresponds to the North Atlantic *seesaw* documented by van Loon and Rogers (1978) and by others.

Applying the criteria of Section II, we obtained the following points as predictors for use in the regression equation:

a.	65°N 40°W:	$r = -.67$	(low MSLP in severe iceberg year)
b.	40°N 60°W:	$r = +.65$	(high MSLP in severe iceberg year)
c.	45°N 20°E:	$r = +.70$	(high MSLP in severe iceberg year)

Table 4 gives the regression equation and compares the hindcast ranks with the observed ranks for the 30 years in the sample. The Table is summarized below:

Hindcast errors:	Mean absolute rank error	4.73 ranks
	Median absolute forecast rank error	4.50 ranks
	Correlation (fcst v. observed rank)	0.77

When the forecast domain is divided into terciles (Mild, Moderate, Severe), the following distribution is obtained:

0 category error:	22 cases
1 category error:	8 cases
2 category error:	0 cases

Case 2. 2-month 700 mb -January Correlation Field

In Table 3B, we find that the major North Atlantic features of the grid are quite similar to those of Case 1. That is, low heights over southern Greenland and high heights in the subtropical North Atlantic are associated with severe iceberg years. This field, however, produces an additional feature -- a region of sig -

TABLE 3A

6-months MSLP ending March: 30-year (1955-84) correlation grid results

3 (5)	20N	25N	30N	35N	40N	45N	50N	55N	60N	65N	70N	75N	80N	85N	90N
360W	.50	.52	.46	.47	.50	.54	.49	.29	-.03	-.32	-.47	-.55	-.55	-.55	-.48
350W	.39	.45	.50	.58	.63	.66	.55	.30	-.08	-.20	-.35	-.52	-.56	-.54	-.48
340W	.40	.34	.58	.68	.67	.75	.57	.24	.01	-.25	-.35	-.51	-.57	-.54	-.48
330W	.36	.33	.51	.61	.70	.65	.38	.08	-.06	-.23	-.34	-.47	-.56	-.53	-.48
320W	.34	.39	.40	.46	.67	.52	.11	-.07	-.17	-.24	-.35	-.46	-.55	-.53	-.48
310W	-.08	-.04	.48	.51	.34	.25	-.08	-.23	-.28	-.33	-.41	-.46	-.51	-.52	-.48
300W	.16	.27	.24	.40	.28	.05	-.24	-.33	-.35	-.40	-.46	-.46	-.49	-.51	-.48
290W	.32	.34	.34	.35	.37	.15	-.26	-.33	-.34	-.38	-.44	-.45	-.48	-.50	-.48
280W	.06	.20	.23	.29	.32	.19	-.28	-.31	-.31	-.34	-.43	-.45	-.48	-.49	-.48
270W	.13	.25	.14	.15	.31	.10	-.16	-.26	-.27	-.30	-.40	-.44	-.46	-.47	-.48
260W	.17	.35	.17	.16	.26	.53	.07	-.09	-.23	-.32	-.35	-.42	-.45	-.45	-.48
250W	-.02	.10	.12	.13	.20	.36	.17	-.06	-.23	-.38	-.38	-.40	-.42	-.43	-.48
240W	.19	.37	.35	.39	.44	.30	.19	.00	-.15	-.18	-.36	-.36	-.39	-.41	-.48
230W	.05	.20	.43	.25	.35	.06	.23	.12	-.19	.00	-.29	-.34	-.38	-.40	-.48
220W	.12	.14	.13	.25	-.15	.20	.00	.06	.19	-.21	-.24	-.34	-.37	-.38	-.48
210W	.19	.18	.07	.12	.09	.06	.20	.37	.28	-.13	-.14	-.32	-.36	-.38	-.48
200W	.15	.03	-.12	-.15	-.12	-.09	.12	.32	.31	.07	-.03	-.29	-.35	-.38	-.48
190W	.07	-.08	-.16	-.18	-.13	-.02	.16	.33	.37	.02	-.07	-.24	-.34	-.39	-.48
180W	.12	-.03	-.10	-.12	-.06	.03	.14	.28	.33	.12	-.05	-.19	-.34	-.40	-.48
170W	.09	.00	-.04	-.08	.05	.09	.19	.23	.36	.37	.15	-.16	-.34	-.41	-.48
160W	.23	.15	.04	.08	.13	.10	.20	.25	.26	.39	.27	-.15	-.35	-.43	-.48
150W	.27	.31	.25	.24	.21	.19	.23	.29	.29	.32	.36	-.16	-.38	-.45	-.48
140W	.20	.32	.29	.27	.22	.19	.16	.15	.12	.25	.31	-.19	-.41	-.48	-.48
130W	.15	.16	.10	.16	.17	.22	.13	-.06	-.10	.10	.15	-.27	-.44	-.50	-.48
120W	.19	.25	.13	.06	-.00	-.00	-.11	-.19	-.05	.05	-.04	-.37	-.48	-.52	-.48
110W	.26	.26	.30	-.20	-.19	-.17	-.22	-.24	-.19	-.22	-.29	-.43	-.51	-.54	-.48
100W	.05	-.12	-.26	-.15	-.29	-.25	-.21	-.21	-.21	-.28	-.36	-.42	-.51	-.56	-.48
90W	-.13	-.21	-.27	-.23	-.02	.15	.08	-.03	-.06	-.26	-.39	-.44	-.53	-.57	-.48
80W	.11	-.11	.09	.34	.45	.55	.46	.28	.03	-.26	-.43	-.48	-.55	-.56	-.48
70W	.15	.44	.50	.50	.59	.62	.51	.26	.01	-.33	-.47	-.45	-.55	-.59	-.48
60W	.34	.45	.56	.60	.65	.63	.49	.23	-.11	-.38	-.45	-.49	-.58	-.59	-.48
50W	.22	.35	.40	.56	.61	.55	.37	.02	-.34	-.48	-.50	-.49	-.55	-.57	-.48
40W	.21	.35	.44	.53	.58	.45	.30	-.12	-.56	-.67	-.59	-.48	-.53	-.55	-.48
30W	.15	.32	.43	.52	.52	.44	.32	.05	-.40	-.62	-.65	-.57	-.54	-.55	-.48
20W	.37	.43	.44	.52	.51	.45	.36	.17	-.29	-.64	-.65	-.62	-.55	-.55	-.48
10W	.46	.53	.48	.46	.46	.40	.43	.23	-.18	-.53	-.60	-.58	-.54	-.55	-.48
SIGNIFICANT AREAL FRACTIONS:					.190	.274									

TABLE 3B

2-months 700 mb ending January: 30-year (1955-84) correlation grid results

T (Z)	20N	25N	30N	35N	40N	45N	50N	55N	60N	65N	70N	75N	80N	85N	90N
350W	.04	.09	.24	.41	.51	.51	.43	.30	.12	.01	-.04	-.03	-.01	-.10	-.01
340W	.14	.13	.31	.40	.53	.47	.35	.23	.11	.04	.01	.00	.02	-.09	-.01
330W	.08	.05	.18	.35	.43	.30	.17	.08	.03	.01	-.00	.01	.04	-.07	-.01
320W	-.05	-.16	-.31	-.15	-.02	-.05	-.16	-.17	-.14	-.08	-.02	.01	.04	-.06	-.01
310W	-.14	-.33	-.43	-.37	-.26	-.34	-.39	-.35	-.28	-.16	-.05	.03	.04	-.06	-.01
300W	.13	.03	-.24	-.30	-.34	-.42	-.43	-.40	-.31	-.18	-.06	.02	.04	-.06	-.01
290W	.47	.27	-.06	-.26	-.35	-.33	-.31	-.30	-.22	-.14	-.06	-.01	.03	-.06	-.01
280W	[illegible]	.11	-.13	-.22	-.08	-.06	-.07	-.11	-.10	-.09	-.07	-.04	.00	-.07	-.01
270W	.16	.02	-.17	-.16	.08	.12	.12	.06	-.01	-.05	-.06	-.07	-.03	-.08	-.01
260W	-.11	-.18	-.07	.11	.28	.28	.29	.25	.11	.04	-.03	-.09	-.06	-.09	-.01
250W	-.12	-.05	-.03	.08	.38	.44	.45	.35	.15	.04	-.04	-.10	-.08	-.10	-.01
240W	-.03	.04	.15	.23	.40	.52	.50	.38	.13	-.03	-.09	-.14	-.10	-.12	-.01
230W	-.00	.13	.24	.33	.38	.43	.59	.29	.02	-.11	-.16	-.17	-.11	-.13	-.01
220W	.10	.20	.18	.20	.25	.25	.20	.01	-.16	-.19	-.22	-.20	-.12	-.13	-.01
210W	.15	.14	.17	.14	.13	.09	.01	-.09	-.16	-.18	-.23	-.19	-.11	-.14	-.01
200W	.18	.16	.17	.12	.03	.01	-.06	-.10	-.12	-.14	-.19	-.17	-.10	-.15	-.01
190W	.17	.16	.15	.09	.01	-.01	-.06	-.07	-.08	-.09	-.13	-.12	-.08	-.16	-.01
180W	.05	.16	.14	.07	.03	.01	-.02	-.02	-.02	-.02	-.04	-.05	-.05	-.16	-.01
170W	.08	.14	.12	.08	.02	.03	.02	.04	.04	.04	.04	-.01	-.05	-.17	-.01
160W	.20	.20	.13	.08	.00	.04	.05	.10	.12	.11	.09	.04	-.03	-.18	-.01
150W	.23	.32	.25	.19	.12	.13	.12	.15	.20	.16	.10	.03	-.05	-.19	-.01
140W	.30	.41	.41	.33	.24	.18	.14	.11	.15	.15	.09	.01	-.06	-.20	-.01
130W	.25	.25	.32	.26	.16	.08	.02	.01	.02	.02	-.02	-.07	-.10	-.20	-.01
120W	.29	.15	.29	.06	-.00	-.04	-.05	-.05	-.10	-.15	-.14	-.13	-.13	-.21	-.01
110W	.13	.17	.01	-.20	-.25	-.22	-.21	-.27	-.39	-.37	-.27	-.20	-.16	-.22	-.01
100W	.27	.17	.02	-.09	-.07	-.11	-.22	-.30	-.43	-.41	-.35	-.26	-.20	-.23	-.01
90W	.28	.45	.45	.40	.34	.18	-.10	-.29	-.37	-.39	-.37	-.30	-.24	-.24	-.01
80W	.32	.57	.62	.59	.50	.30	-.07	-.23	-.42	-.44	-.44	-.37	-.29	-.25	-.01
70W	.46	.60	.64	.68	.61	.41	.03	-.33	-.49	-.51	-.47	-.39	-.30	-.24	-.01
60W	.33	.59	.64	.67	.55	.32	-.09	-.46	-.60	-.58	-.51	-.41	-.31	-.24	-.01
50W	.16	.32	.47	.50	.44	.17	-.19	-.52	-.61	-.57	-.50	-.41	-.31	-.23	-.01
40W	.02	.12	.34	.45	.36	.12	-.17	-.46	-.54	-.51	-.45	-.38	-.28	-.22	-.01
30W	.05	.13	.31	.31	.29	.12	-.06	-.30	-.44	-.44	-.39	-.33	-.24	-.20	-.01
20W	.12	.14	.39	.33	.27	.16	.09	-.09	-.28	-.35	-.32	-.24	-.18	-.18	-.01
10W	.03	.12	.21	.30	.31	.28	.22	.03	-.10	-.24	-.22	-.17	-.12	-.16	-.01
0W	.09	.08	.21	.30	.30	.41	.38	.26	.07	-.05	-.12	-.09	-.06	-.13	-.01

TABLE 4

MULTIPLE REGRESSION OF 6-MONTH MSLP - MARCH FIELD vs. ICEBERG RANK (1955-1984)

Regression Statistics:

Coefficient of Determination (r^2)	0.59699
Coefficient of Multiple Correlation	0.77265
Standard Error of Estimate	5.90228
F-Ratio (Regression)	12.83829
Probability of Chance	0.00009
Number of Cases	30

Regression Coefficients:

Variable	Mean	S.D.	Coefficient
Iceberg Rank	15.5	8.80	
Constant			89.8174
40N 330W	17.25	1.67	- .9567
45N 340W	18.39	1.61	- 2.1266
49N 60W	14.43	2.10	- 1.2969

Hindcast:

YEAR	OBSERVED RANK	PREDICTED RANK	RANK ERROR	TERCILE ERROR
1955	24	30	6	0
56	19	28	9	1
57	5	8	3	0
58	29	26	3	0
59	7	7	0	0
1960	10	20	10	1
61	16	14	2	0
62	15	24	9	1
63	26	21	5	0
64	9	9	0	0
1965	20	19	1	0
66	30	25	5	0
67	8	11	3	1
68	11	17	6	0
69	25	27	2	0
1970	18	29	11	1
71	22	15	7	1
72	2	4	2	0
73	6	2	4	0
74	3	3	0	0
1975	17	10	7	1
76	14	1	13	1
77	28	22	6	0
78	21	13	8	1
79	13	12	1	0
1980	27	18	9	1
81	23	23	0	0
82	12	16	4	0
83	4	5	1	0
84	1	6	5	0

nificant positive values (high 700 mb heights associated with severe iceberg years) over northeastern Asia. The points selected from the 700 mb predictor field for the regression were:

a. 50°N 120°E: r = +.56 (high 700 mb in severe iceberg year)
b. 30°N 70°W : r = +.69 (high 700 mb in severe iceberg year)
c. 60°N 50°W : r = -.61 (low 700 mb in severe iceberg year)

Table 5 gives the regression equation and compares the hindcast ranks with the observed ranks for the 30 years in the sample. Actually, 5 points of interest were produced by the methodology. However, 2 sets of points were adjacent and of equal correlation. The process of multiple regression effectively eliminates (i.e., assigns very low coefficients to) such irrelevant points. These points were, therefore, not included as predictors for the final regression equation. Table 5 is summarized below:

Hindcast errors:	Mean absolute rank error	5.23 ranks
	Median absolute forecast rank error:	4.00 ranks
	Correlation (fcst v. observed rank)	0.74

Once more dividing the forecast domain into Mild, Moderate, and Severe tercile categories produces the following error record:

0 category error:	18 cases
1 category error:	12 cases
2 category error:	0 cases

The January prediction, as might be expected, does not perform quite as well as the March prediction. It does, however, compare favorably with the accuracy of long-range forecasts of weather elements , such as temperature and precipitation, which are forecast to be above or below normal 55-60% of the time with a lead time of only 30 days. The corresponding chance expectation is 50%.

B. THE COMPOSITE DIFFERENCE APPROACH

For the 6-month MSLP fields ending in March, composites were constructed of the anomaly field for the 5 most severe and the 5 mildest iceberg years. The composites were the means for 1957, 1972, 1974, 1983, 1984 and for 1958, 1963, 1966, 1977, 1980 respectively. These are shown as Figures 4A and 4B. The difference between the two mean grids is shown as Figure 4C.

The anomaly centers near southern Greenland and in the mid-latitude Atlantic are spatially coincident in Figures 4A and 4B. This implies that the same pattern

TABLE 5

MULTIPLE REGRESSION OF 2-MONTH 700 MB - JANUARY FIELD vs. ICEBERG RANK (1955-1984)

Regression Statistics:

Cofficient of Determination (r^2)	0.56531
Coefficient of Multiple Correlation	0.75187
Standard Error of Estimate	6.12989
F-Ratio (Regression)	11.27093
Probability of Chance	0.00016
Number of Cases	30

Regression Coefficients:

Variable	Mean	S.D.	Coefficient
Iceberg Rank	15.5	8.80	
Constant			264.74
50N 240W	83.92	2.01	- .9486
30N 70W	112.57	2.51	- 1.6917
60N 50W	74.74	5.35	.2705

Hindcast:

YEAR	OBSERVED RANK	PREDICTED RANK	RANK ERROR	TERCILE ERROR
1955	24	22	2	0
56	19	30	11	1
57	5	1	4	0
58	29	25	4	0
59	7	17	10	1
1960	10	19	9	1
61	16	23	7	1
62	15	8	7	1
63	26	24	2	0
64	9	10	1	0
1965	20	18	2	0
66	30	29	1	0
67	8	14	6	1
68	11	13	2	0
69	25	28	3	0
1970	18	27	9	1
71	22	11	11	1
72	2	3	1	0
73	6	5	1	0
74	3	2	2	0
1975	17	4	13	1
76	14	9	5	1
77	28	26	2	0
78	21	12	9	1
79	13	20	7	0
1980	27	16	11	1
81	23	21	2	0
82	12	15	3	0
83	4	7	3	0
84	1	6	5	0

FIGURE 4A

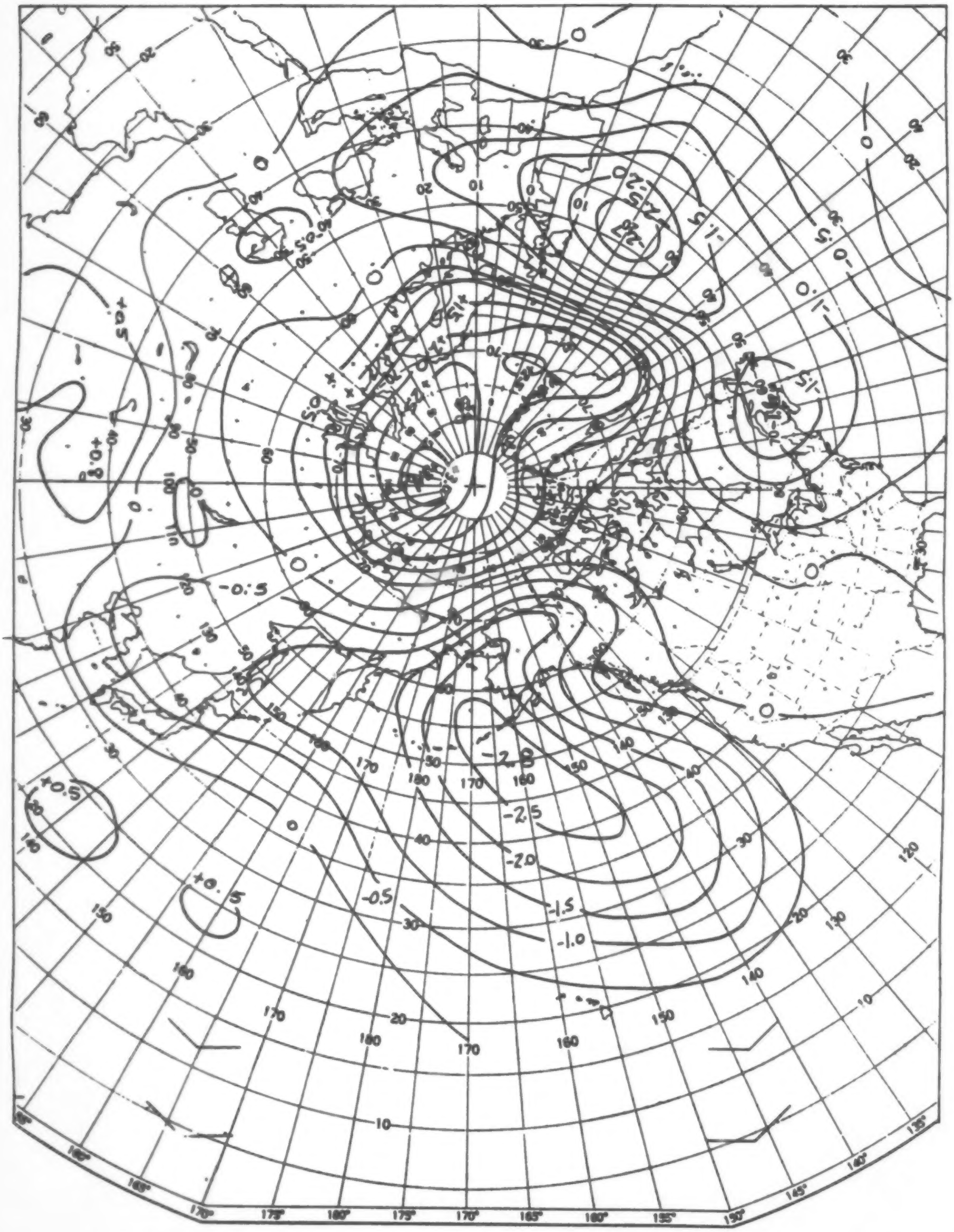

6-months ending in March MSLP anomaly field: Mean of the 5 mildest iceberg years (1958, 63, 66, 77, and 80). Isopleths are drawn for 0.5 mb departure from the 30-year mean (1951-80).

FIGURE 4B

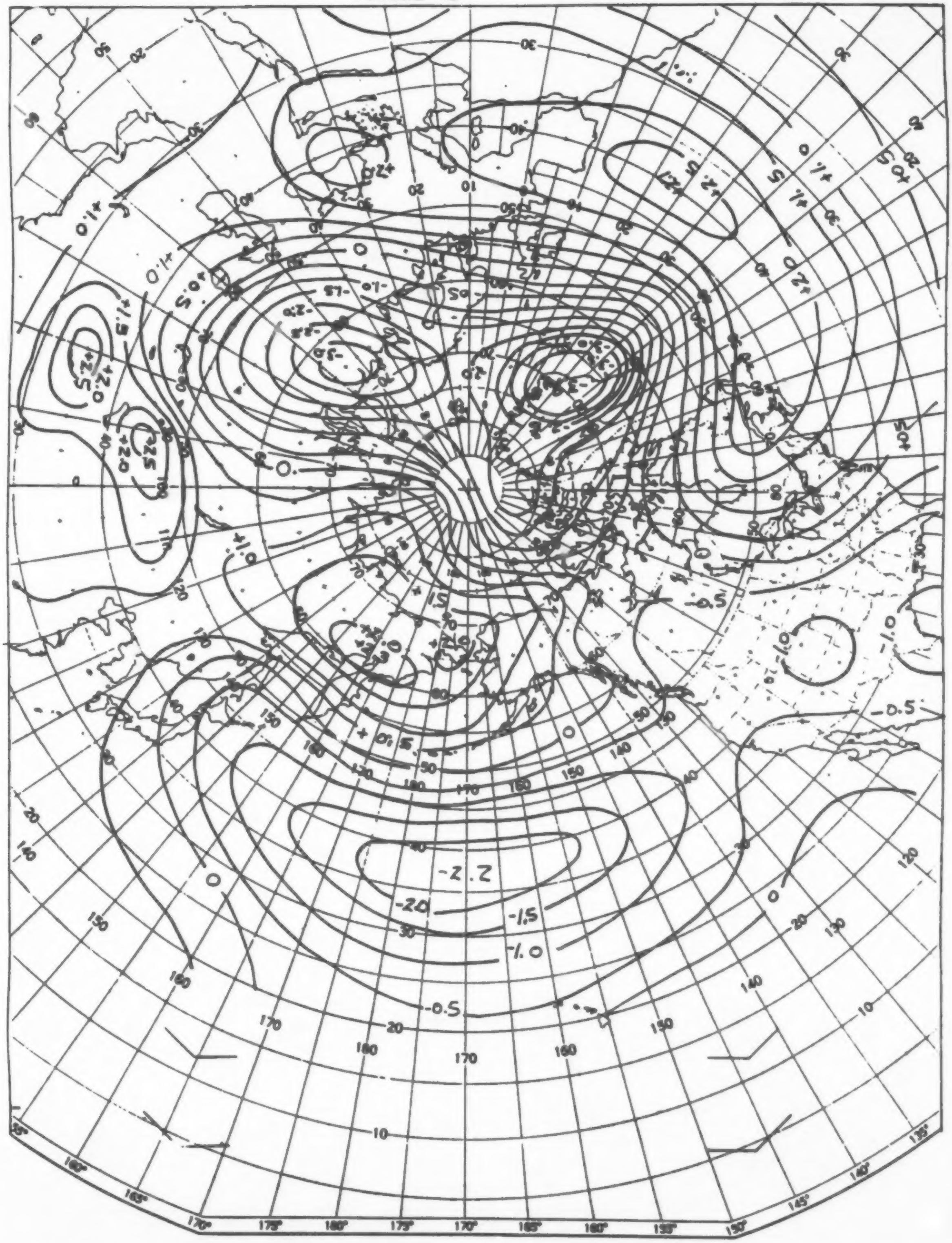

6-months ending in March MSLP anomaly field: Mean of the 5 most severe iceberg years (1957, 72, 74, 83, and 84). Isopleths are drawn for 0.5 mb departure from the 30-year mean (1951-80).

FIGURE 4C

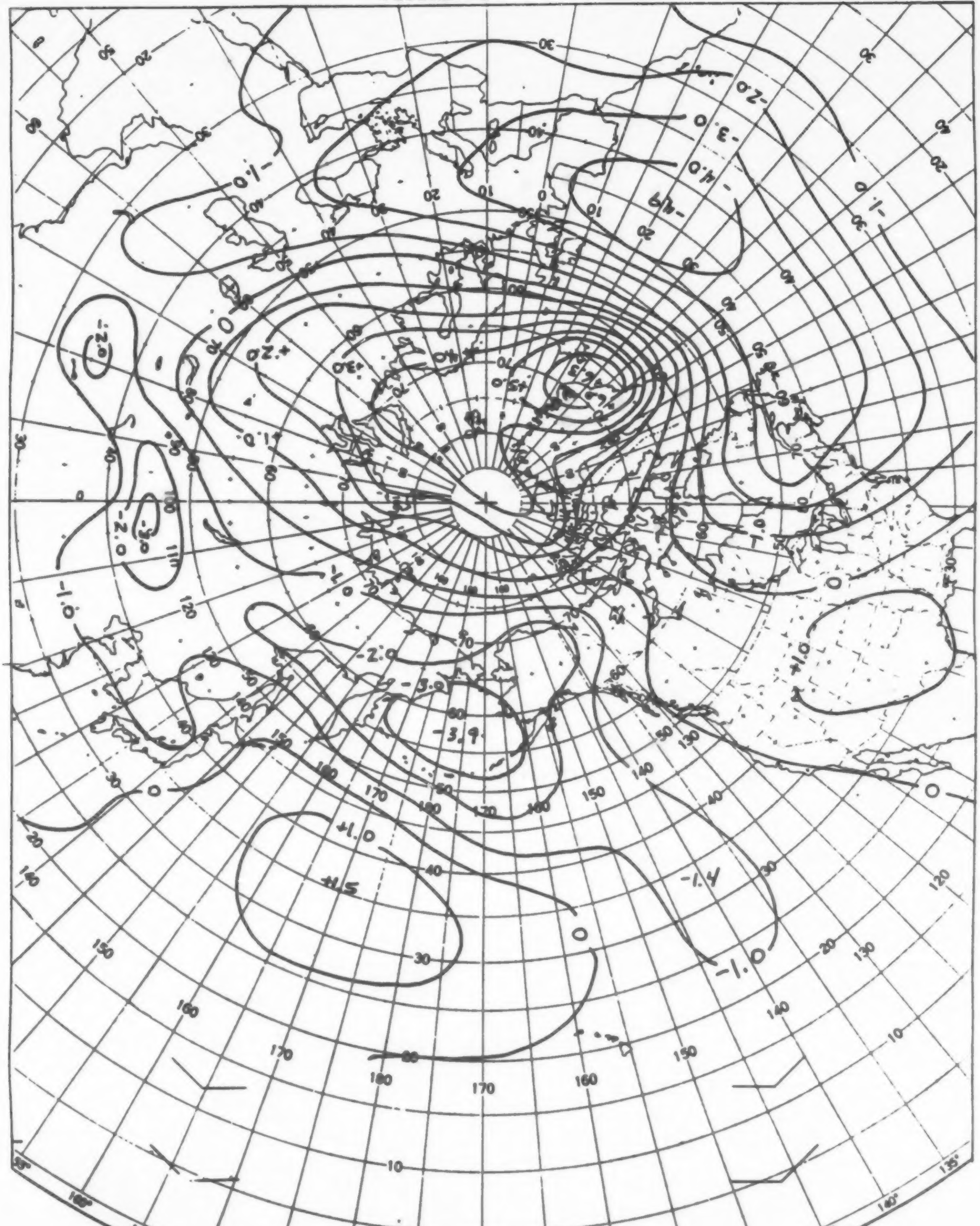

6-months ending in March MSLP: Difference between mild and severe iceberg years. The mean of the 5 most severe years (Figure 4B) has been subtracted from the mean of the 5 mildest years (Figure 4A). Isopleths have been drawn for each 1 mb difference.

of anomalies dominates both sets of extremes -- only the sign changes. The reciprocal nature of the two composites does not extend to the North Pacific, however, where the mid-latitude anomalies are negative in both cases. We note that the North Atlantic pattern is also extremely consistent with the correlation grid in Table 3A.

Over the iceberg source regions of Baffin Bay and the Labrador Sea, the geostrophic wind patterns implied by Figures 4A and 4B provide a physically plausible explanation for the extreme iceberg conditions in the respective composites. The anomalous airflow component is southward (with cold advection) during severe years and northward (with warm advection) during mild years. Statistical constraints on the system do not dictate the dramatic constrast between Figures 4A and 4B. Instead, the contrast argues for the existence of a physical control over both types of iceberg extremes.

Figures 5A and 5B show the actual mean MSLP for the same period as Figures 4A and 4B on an expanded scale centered over the area of interest. Here we see that the primary impact of the anomalies is upon the magnitude of, rather than the direction of, airflow. In both cases, the net airflow is southerly over the region. However, the airflow during mild years is much weaker in mild than in severe years. This situation will result in longer iceberg transit times and a greater likelihood of iceberg melt in the mild years. It will also permit intrusions of greater amounts of warmer ocean water by surface currents into the Labrador Sea.

C. THE 1985 FORECAST

Based on the IIP preliminary report of 1031 icebergs for the year ending 31 August, 1985, the severity rank for 1985 is 5th most severe (of 31 cases).

1. Forecast by 2-Month 700 MB Data Ending in January 1985

The following are the 700 mb heights* for the 2-month period ending in January 1985 for the three 700 mb predictor points selected from the "Case 2." correlation field:

a. 50°N 120°E: $P_a = 2831 \text{ m} = 83.1$
b. 30°N 70°W: $P_b = 3132 \text{ m} = 113.2$
c. 60°N 50°W: $P_c = 2702 \text{ m} = 70.2$

* For computational purposes, values are converted to decameters minus 200.

Insertion of these values in the regression equation from Table 5 yields:

FIGURE 5A

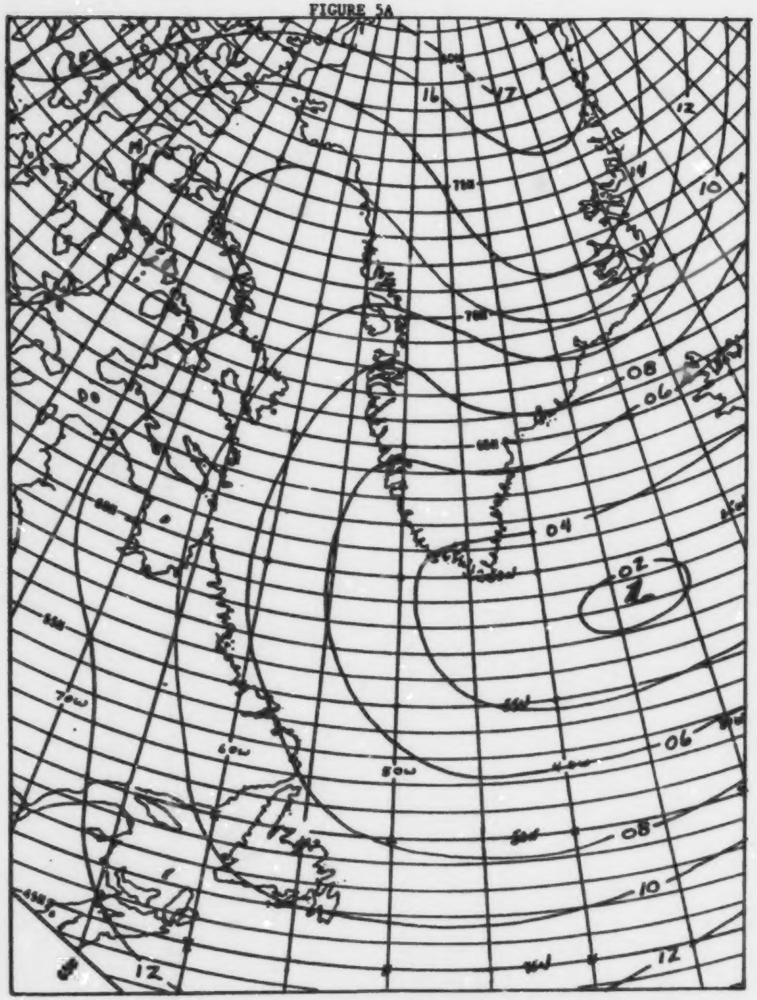

6-months ending in March: Mean MSLP for the five mildest iceberg years.
(1958, 63, 66, 77, 80)

FIGURE 5B

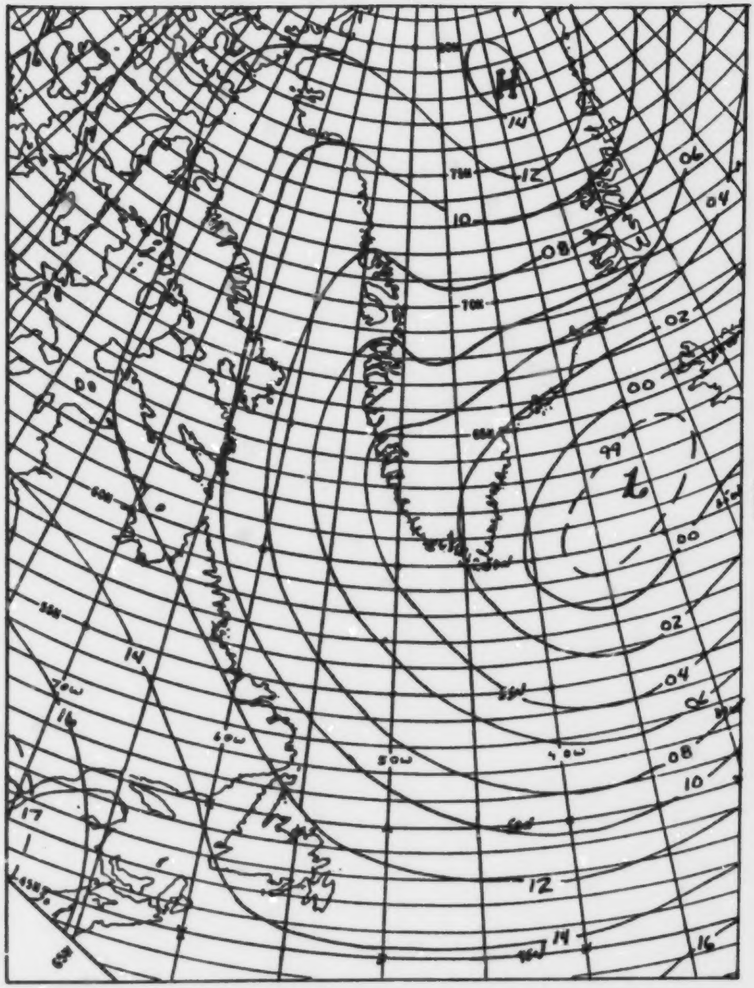

6-months ending in March: Mean MSLP for the five most severe iceberg years.
(1957, 72, 74, 83, 84)

$$Y = 264.74 - (.94)(P_a) - (1.69)(P_b) + (.27)(P_c)$$
$$= 264.74 - 78.11 - 191.31 + 18.95$$
$$= 14.27$$

which is the 11th most severe (of 31 cases). Therefore, the forecast is 6 ranks high, which is slightly less than 1 standard error of estimate (6.2) for the 30-year sample.

2. Forecast by 6-Month MSLP Ending in March, 1985

The following are the MSLP values* for the 6-month period ending in March, 1985 for the three MSLP predictor points selected from the "Case 1." correlation field:

a. $40^\circ N\ 30^\circ E$: $P_a = 1018.5$ mb = 18.5
b. $45^\circ N\ 20^\circ E$: $P_b = 1019.8$ mb = 19.8
c. $40^\circ N\ 60^\circ W$: $P_c = 1914.5$ mb = 14.5

* For computational purposes, 1000 mb is subtracted from each value.

From Table 4, the regression equation yields:

$$Y = 89.82 - (.95)(P_a) - (2.13)(P_b) - (1.3)(P_c)$$
$$= 89.82 - 17.56 - 42.17 - 18.85$$
$$= 11.19$$

which is the 9th most severe (of 31 cases). The forecast is in the correct tercile, but is 4 ranks high. This is within the median and mean errors, and well within the standard error of estimate (5.9 ranks) for the 30-year sample.

We note, for comparison, that chance expectation is a standard error of estimate of 9 ranks, with a standard deviation of 1 rank. This was determined by two separate 100-trial Monte Carlo runs made to test just that.

IV. CONCLUSIONS AND RECOMMENDATIONS

The results described in Section III show that the SIC methodology permits long-range forecasts of ice severity at lead times of 3 to 7 months. While the mean errors of the regression forecasts are approximately 5 ranks (out of 30), the ability of the equations to forecast the tercile of severity is amply demonstrated. On the basis of a variety of statistical measure of skill, the forecasting procedure used here is competitive with or superior to those used in other long-range forecasting applications. The SIC procedure has the additional advantages of statistical rigor and straightforward implementation. The latter permits the diagnosis of successes and failures directly in terms of regional atmospheric anomalies, rather than in terms of a series of statistically constrained large-scale patterns.

The results indicate that the accuracy of the forecasts increases slightly between January and March. The illustration of the forecast errors in Section III permits the individual user to weigh the relative advantages of an earlier forecast against the generally lower level of reliability.

The limited resources available for this study have not permitted a thorough exploration of all facets of the forecasting strategy. Several additional tasks have the potential to enhance the capabilities of SIC's iceberg forecasting system.

1. A high-latitude domain centered on the Davis Strait - Labrador Sea region should be used (rather than the 65°N - 90°N Arctic subset) in the determination of regional significance. Such an alternative domain would provide an optimal indication of the seasonality and duration fo the high-latitude signal. Conceivably, this domain could develop better predictors than those used in Section III.

2. Since geostrophic winds are directly proportional to pressure gradients, the use of MSLP (or 700 mb height) *gradients* deserves consideration. While crude measures of large-scale gradient information are implicit in the multilinear regression formulation, a systematic scan of north-south and east-west gradient correlations might well identify predictors which are more closely related to iceberg fluctuations than are pressure or height points. The framework of the predictive system would be little changed by use of gradients.

3. A greater reliance on the composite differences in the predictor selection process may enhance the regression-based forecasts of iceberg extremes.

There is an inevitable trade-off between the representativeness achieved by the use of the complete sample in the correlative approach and the extreme-year emphasis inherent in the composite difference grids.

4. Further experimentation with the formulation of the severity rank index is needed. The non-normality of the annual iceberg count is qualitatively similar to monthly precipitation data. This suggests that more systematic experiments with transformations (e.g., logarithmic, square root) of the iceberg totals may permit more effective and meaningful stratifications of the predictand data.

5. There is a need for more basic research into the physics of iceberg behavior in order to determine the appropriateness of our reliance on atmospheric circulation parameters. The dependence of iceberg break-up on temperatures and/or latitude, the force imbalances responsible for iceberg motion, the factors determining the interannual variability of the source region, and the most meaningful method of iceberg counting are all poorly understood factors relevant to iceberg prediction. A better scientific grasp of these factors will require a combination of year-round observation, modeling studies, and further statistical analysis.

6. A better knowledge of the "source region" is required for long-term forecasts. Some degree of initialization is essential for iceberg forecasts of any length, but is especially so for shorter term forecasts. We feel that the term "source region" should be subdivided into two terms:

Primary source region: the actual area where calving from glaciers takes place.

Secondary source region: the offshore oceanic waters (such as those in Baffin Bay) from which large numbers of icebergs transit into the target area of a forecast.

7. The 5-mild vs. 5-severe years approach suggests an analog system. Although not investigated thoroughly for lack of time and funds, we feel that a potentially useful approach would be the determination of an analog for the target year. Determination of the analog would be made by comparing the grid data from the year to be forecast with each historical year. The comparison would be quantified on the basis of root mean square error and on the standard deviation of the errors. The charts and area for this comparison would be similar to those in Figures 5A and 5B.

8. We feel that an investigation of the month-to-month distribution of iceberg occurrence would prove fruitful in any expanded project. A preliminary look at such data, for instance, reveals that it would be quite rare for a severe iceberg year to occur when there has not been a substantial influx of bergs by the end of February.

9. In other projects, we have observed that air temperature data from appropriate shore stations in the region can be correlated to the iceberg index with varying lag times and degrees of success. Clearly, this possibility should be systematically examined and expanded to include sea surface temperatures if feasible. These effects should be coordinated with the circulation pattern approach.

REFERENCES

Buell, E.C. 1975. The topography of empirical orthogonal functions. Preprints: Fourth Conference on Probability and Statistics in Atmospheric Sciences, Tallahassee, FL. Journal of the American Meteorological Society: pp. 188-193.

Davis, R.E. 1976. Predictability of sea surface temperatures and sea level pressure anomalies over the North Pacific Ocean. Journal of Physical Oceanography, 6: pp. 249-266.

Gilman, D.L. 1983. Predicting the weather for the long term. Weatherwise, 36: pp. 290-297.

Hovel, J.D. and Wallace, J.M. 1981. Planetary-scale atmospheric phenomena associated with the southern Oscillation. Monthly Weather Review, 109: pp. 813-829.

Livezey, R.E. and Chen, W.Y. 1983. Statistical field significance and its determination by Monte Carlo techniques. Monthly Weather Review, 111: pp. 46-59.

Namias, J. 1972. Long-Range weather forecasting. Patterns and Perspectives in Environmental Science, National Science Board: pp. 97-101.

Niebauer, H.J. 1983. Multiyear sea ice variability in the eastern Bering Sea: an update. Journal of Geophysical Resources, 55(C5): pp. 2733-2742.

van Loon, H. and Rogers, J.C. 1978. The seesaw in winter temperatures between Greenland and Northern Europe. Part I: General description. Monthly Weather Review, 106: pp. 296-310.

THE LONG RANGE PREDICTION OF ICEBERG SEASON SEVERITY USING EMPIRICAL ORTHOGONAL FUNCTIONS

by L.W. Davidson
Seaconsult Limited
Suite 301 Victoria Hall, 187 Gower Street
St. John's, Newfoundland, Canada A1C 1R2

Can long time series ($>$ 30 years) of monthly gridded fields of MSLP, 700 mb height, 700-1000 mb thickness and/or surface air temperature be successfully employed to predict the annual flux of icebergs across latitude 48°N? The method of empirical orthogonal function (EOF) analysis has been employed to characterize the dominant modes in anomalies of the atmospheric fields. Linear and multiple regressions have been performed between selected EOF coefficients and the annual iceberg flux to isolate apparent correlations at time lags of one to 12 months and for averaging intervals of one to 24 months. Iceberg flux forecast models developed on the basis of these correlations are described. The results of hindcast-mode applications for the years 1953 to 1982 and of a forecast-mode application for 1985 are presented and interpreted. Forecast quality is quantitatively assessed and is compared to the work of other investigators who employ "brute force" statistical methods.

An Evaluation of the International Ice Patrol Drift Model

By D. L. Murphy
and
LT I. Anderson, USCG
United States Coast Guard
International Ice Patrol
Avery Point
Groton, Connecticut 06340-6096

Abstract

The movement of four icebergs, three tracked by a surface vessel and one tracked by a satellite-tracked platform deployed onto the iceberg, is used to test the accuracy of International Ice Patrol (IIP) iceberg drift model. The drift data represent drift periods from 2.5 to 4.5 days duration and various dynamical regimes. Comparison is made between model solutions made using two sets of environmental inputs. The first consists of historical current data based on many years of hydrographic surveys and wind data derived from large scale atmospheric model. The second consists of on-scene measurements of wind and local currents. The current data were determined from the movement of freely-drifting satellite-tracked buoys deployed in the vicinity of icebergs.

The results show that if only historical current data and large-scale wind data are used to drive the model, the errors can be substantial even for drifts of short duration. In one case the observed error was 75 km after only 2.5 days of drift. In all four cases using on-scene measured data improved the model accuracy; in two of the cases the error was halved.

Introduction

Since 1979 the International Ice Patrol (IIP) has been using an iceberg drift model as an integral part of its iceberg tracking operations. During the season of maximum iceberg threat, typically March through August, IIP conducts aerial reconnaissance of its operations area (40^o - 52^oN, 39^o - 57^oW) on alternate weeks. During the week that the IIP Ice Reconnaissance Detachment (ICERECDET) is deployed to Gander, Newfoundland (IIP field operations base), daily flights are conducted on five consecutive days, each covering only a small portion of the IIP operations area. As a result of this reconnaissance schedule, IIP must often rely on the model predictions to set the limits of iceberg danger during periods when no ice reconnaissance is being conducted. In addition, the model drift predictions are used to help recognize icebergs that have been previously sighted, either by the ICERECDET or merchant vessels. Lacking this ability to recognize iceberg resights has the effect of inflating the numbers of icebergs south of 48°N, the traditional indicator of the severity of an iceberg season.

Despite the reliance that IIP places on the accuracy of the drift model results, relatively little testing of the model has been possible, primarily because adequate iceberg drift data, with accompanying environmental data, are expensive and often difficult to obtain. Moreover, only in the last few years has navigation in the operations area been accurate and reliable enough to permit the collection of good data.

Mountain (1980) tested the model using the tracks of two large tabular icebergs, a large pinnacle iceberg, and a freely-drifting satellite-tracked buoy. The drift durations were from 3 to 25 days. The results were quite variable, ranging from a small 9km error for the 3-day drift to a constant 90-150km drift in the 25-day case. Although he recognizes the limitations of this small data set, he suggests that the primary cause of the model error is due to inaccurate inputs, i.e., winds and currents.

This report describes the results of four case studies in which the performance of the IIP iceberg drift model was examined at four different locations (Figure 1) in the IIP operations area. The objectives were twofold: first, to test the accuracy of the drift predictions of the operational IIP iceberg drift model and, second, to investigate how the accuracy changes when on-scene measured wind and current data are used to drive the model.

Model Description

Mountain (1980) describes the details of the IIP operational drift model; thus, only a brief outline is presented here. The fundamental model balance is between iceberg acceleration, air and water drag, the Coriolis acceleration and a sea surface slope term. The resulting differential equations are solved using a fourth-order Runge-Rutta algorithm. The model is driven by a water current which combines a depth- and time-independent geostrophic flow with a depth- and time-dependent current driven by the local wind (time-dependent Ekman flow).

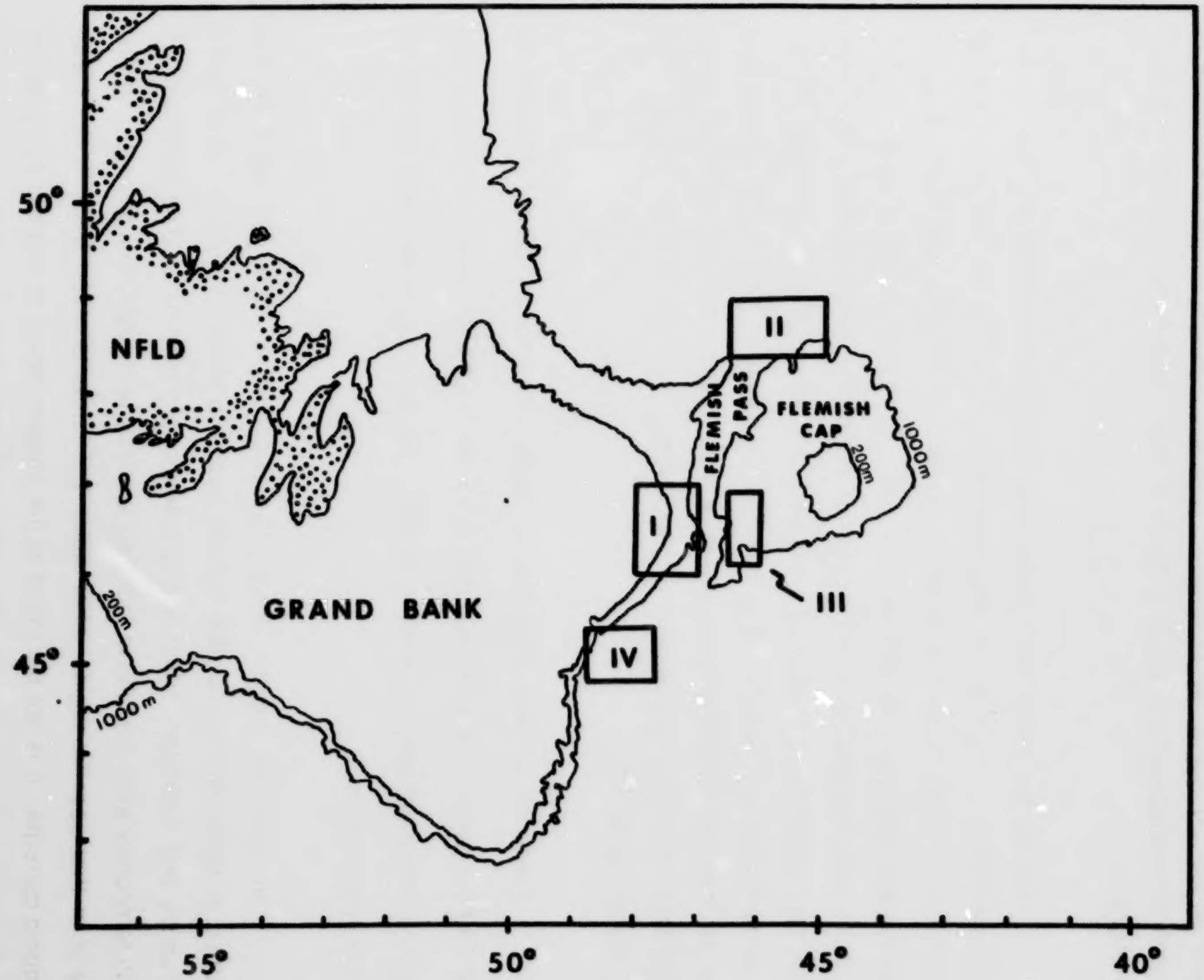

FIGURE 1. AREA OF STUDY.

When used operationally, the IIP drift model employs a mean geostrophic current field based on many years of hydrographic surveys. It is on a grid of 20 minutes of latitude by 20 minutes of longitude, except for the Labrador Current, which is defined on a more detailed grid of 10 minutes of longitude. Wind data, on a 1 degree of latitude by 2 degrees of longitude grid, are provided to the model every 12 hours from the surface-wind analysis of the U. S. Navy Fleet Numerical Oceanography Center (FNOC).

Finally, the model requires as input the mass and cross-sectional area of the drifting iceberg. Obviously, IIP reconnaissance operations do not permit precise measurement, of each detected iceberg. Often, IIP locates icebergs using the side-looking airborne radar (SLAR) with no visual confirmation. As a result, IIP can only classify icebergs into the broad categories of growler, small, medium, and large, and assume characteristic mass and cross-sectional areas for each category. When visual confirmation is available, it is possible to distinguish between tabular and non-tabular icebergs, resulting in somewhat different mass and cross-sectional areas. Regardless of the size and shape of the iceberg both the air and water drag coefficients are set to 1.5.

Presently, IIP estimates that the model drift error is 10 nm (~18.5km) for the first 24-hour period and an additional 5 nm (~9km) for each additional 24-hours of drift, up to a maximum error of 30 nm (~56km). The accuracy of this error estimate is evaluated in this report.

In 1983 IIP began using observed current data derived from the trajectories of freely-drifting satellite-tracked buoys to modify the mean geostrophic field (Summy and Anderson, 1983) during operational model runs. The modifications are both temporary and localized in that they are only applicable during the period that a buoy is in that specific region, after which the currents revert back to the mean geostrophic currents. It is not the intent of the present report to address this practice directly, but rather to compare the drift-model accuracy using two sets of input data: mean geostrophic data with FNOC wind and on-scene measured data. In doing so the importance of using on-scene data becomes clear.

Data Description

The data used in this study were collected from 1983 through 1985. All of the cases were drifts of short duration, with a maximum drift period of 4.5 days. In all four cases the drifting iceberg was close to at least one freely-drifting TIROS Oceanographic Drifter (TOD), from which local currents were determined. The TOD hull was a 3m spar and was fitted with a 2 x 10m window-shade drogue at the end of a tether. The drogue depths presented here refer to the depth of the center of the drogue. The TOD's were tracked by the NOAA/TIROS series satellites and the data provided to IIP by Service ARGOS, with a position accuracy of approximately 300m.

In three of the cases (II, III, and IV) a surface vessel was near the iceberg collecting local wind data. The data for each case are discussed separately. The numbers in parentheses after each date are Julian year dates, that is, dates numbered sequentially from 1 January.

CASE I

This case consists of a 2.5 day drift of a large tabular iceberg with a TIROS Arctic Drifter (TAD) aboard. The TAD, which is essentially a TOD with different packaging, had been deployed onto the iceberg on 27 March 1983 (86) by IIP, in cooperation with the Coast Guard Research and Development Center (R&DC).

The test period began at 1600Z on 12 May 1983 (132) when a TOD, drogued at 38m, was air-deployed from a C-130 at a location approximately 1km from the iceberg, which at the time was moving southward in the Labrador Current (Figure 2).

The test period ended on 15 May (135) shortly before the iceberg grounded for a 4-day period. The iceberg was last sighted with the TAD aboard on 21

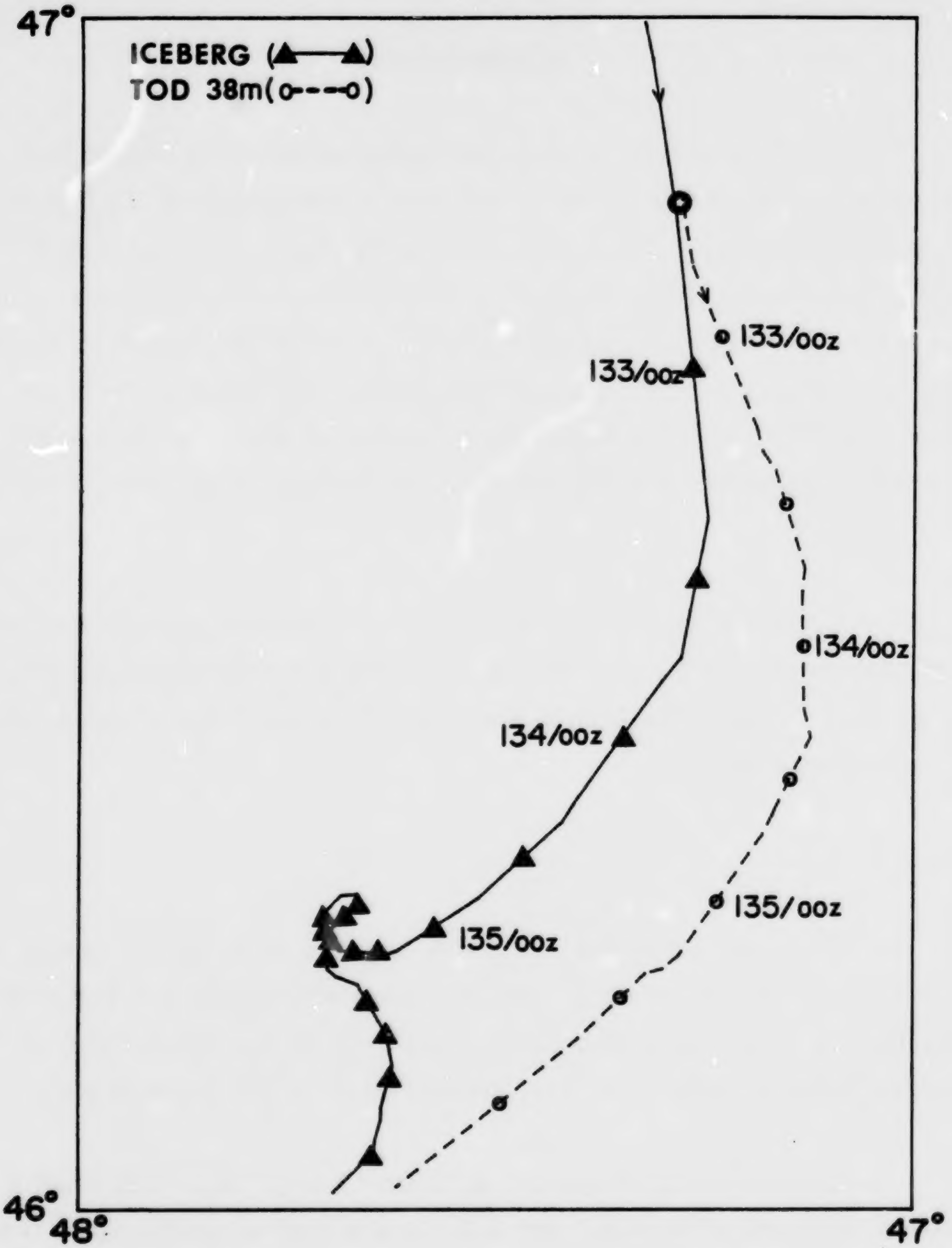

Figure 2. Iceberg and TOD trajectories for CASE I (1983).

May (147) by Mobil Oil Company, Canada (Anderson, 1983). On this date the iceberg was still classified as a large, with estimated dimensions of 150x110x30m. During the test period the maximum separation between the TAD (iceberg) and the TOD was less than 25km. No on-scene wind data were available.

CASE II

This case is a 4.5 day segment of an iceberg track obtained in 1984 by USCGC HORNBEAM. The test period began 17 July (199) at 1300Z when HORNBEAM deployed a TOD drogued at 38m approximately 500m from a medium (120x115x37m) pinnacle iceberg in the region north of Flemish Cap. Although the iceberg was rapidly deteriorating, it was in the medium size range (>60m) for most of the drift period. Only in the last 24-30 hours of drift was it at or slightly below the medium/small boarder. Hourly iceberg positions were recorded using radar ranges and bearings and the HORNBEAM's LORAN C position (Figure 3).

Hourly wind speed and direction were measured using the shipboard anemometer (Figure 4). The maximum separation between the iceberg and the TOD was less than 25km.

CASE III

The third case is a 3.5 day (27 - 30 April 1985) track of a medium (75x56x18m) drydock iceberg obtained from USCGC EVERGREEN south of Flemish Pass. Over the drift period the target iceberg was deteriorating but only on the last day of drift did it fall into the upper part of the small range. Again, hourly iceberg position (Figure 5) and wind data (Figure 6) were collected using shipboard radar and anemometer, respectively.

Two TOD's provided the current data. They were deployed, one drogued at 38m and the other at 58m, 300m from the iceberg on 27 April (117). Approximately halfway through the drift period both buoys were retrieved and redeployed close to the iceberg to minimize the separation between the iceberg and the TOD's. Upon redeployment the drogue at 38m was set to 8m. The maximum separation between

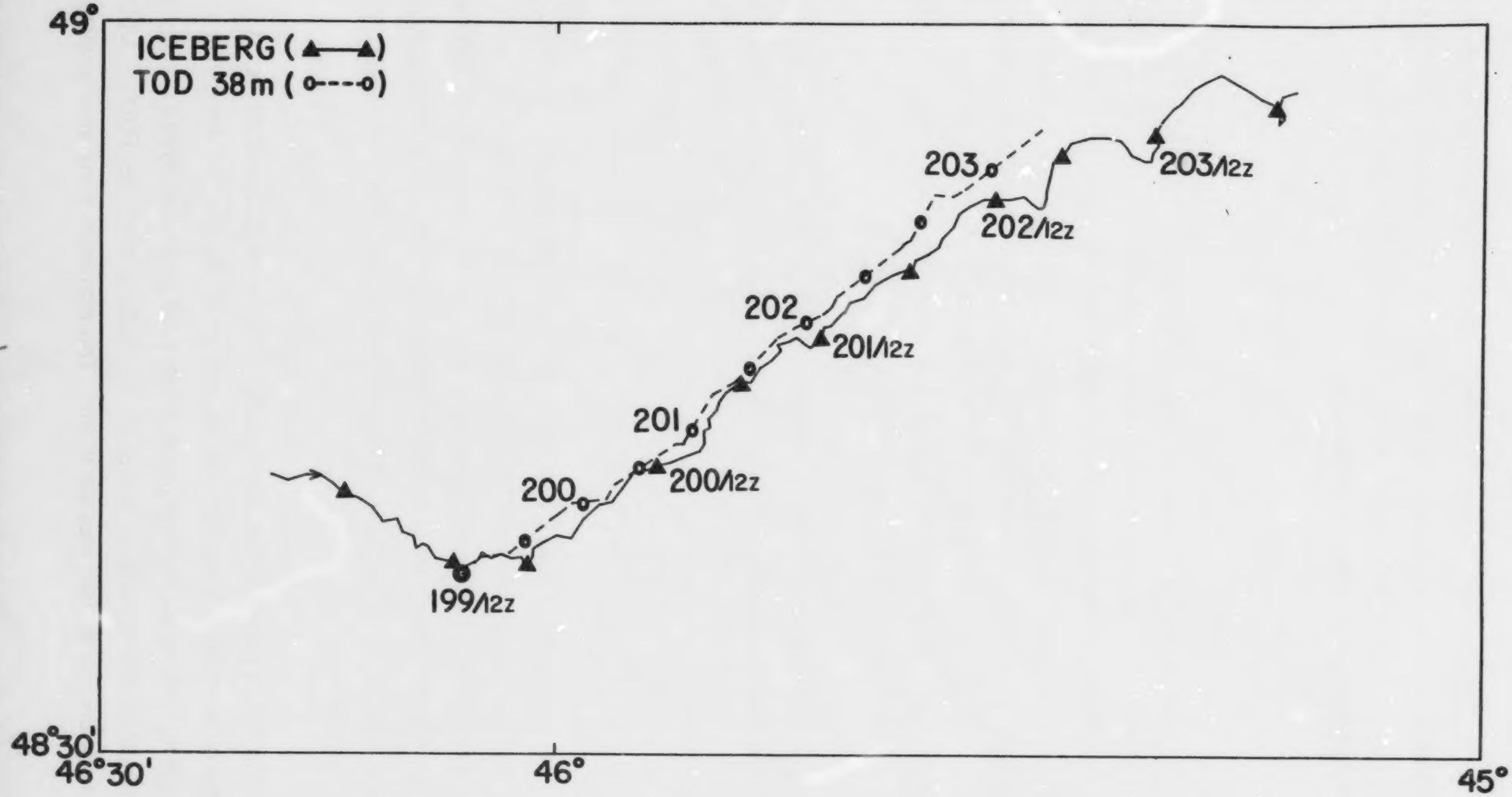

Figure 3. Iceberg and TOD trajectories for CASE II (1984).

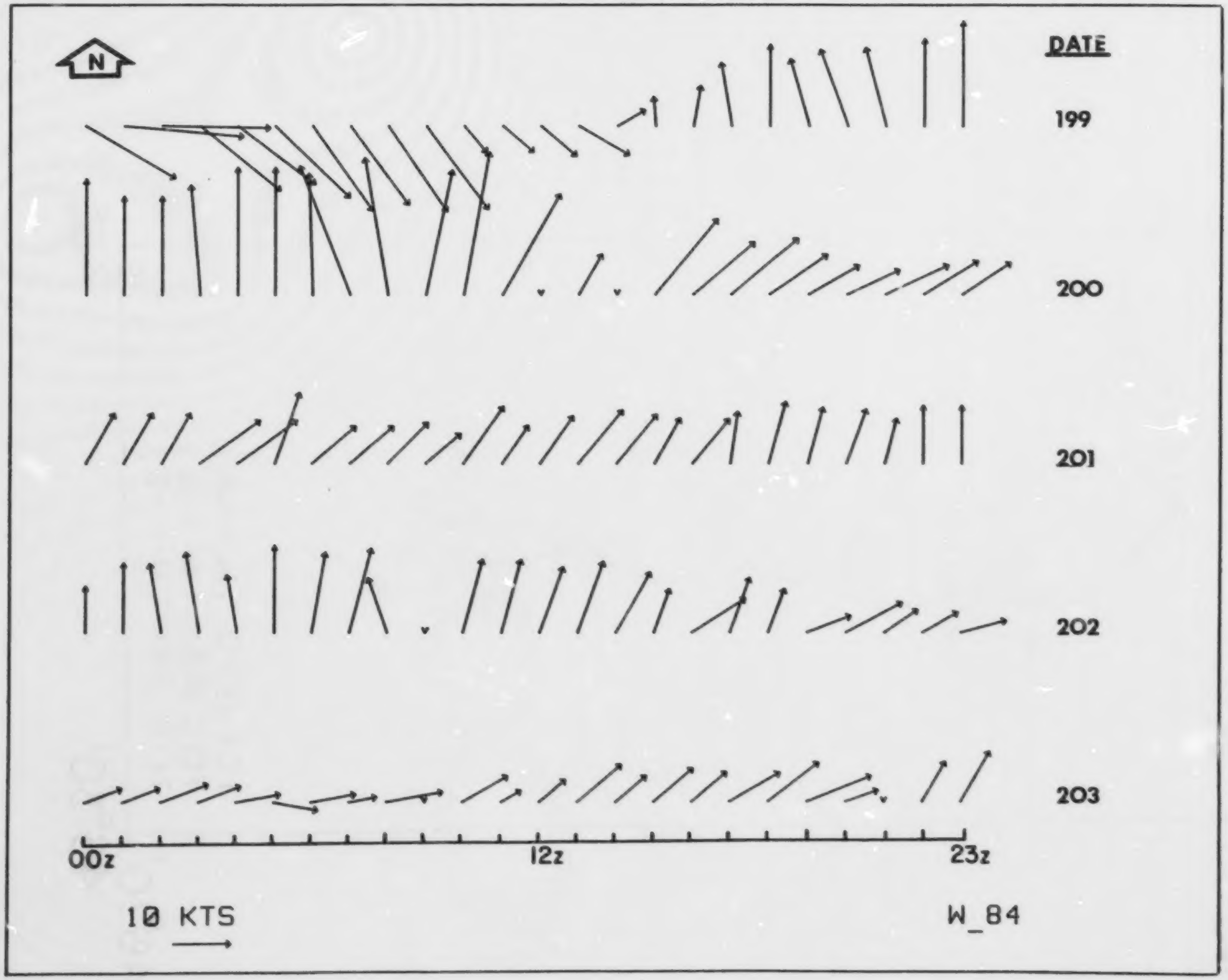

Figure 4. Hourly wind vectors for CASE II.

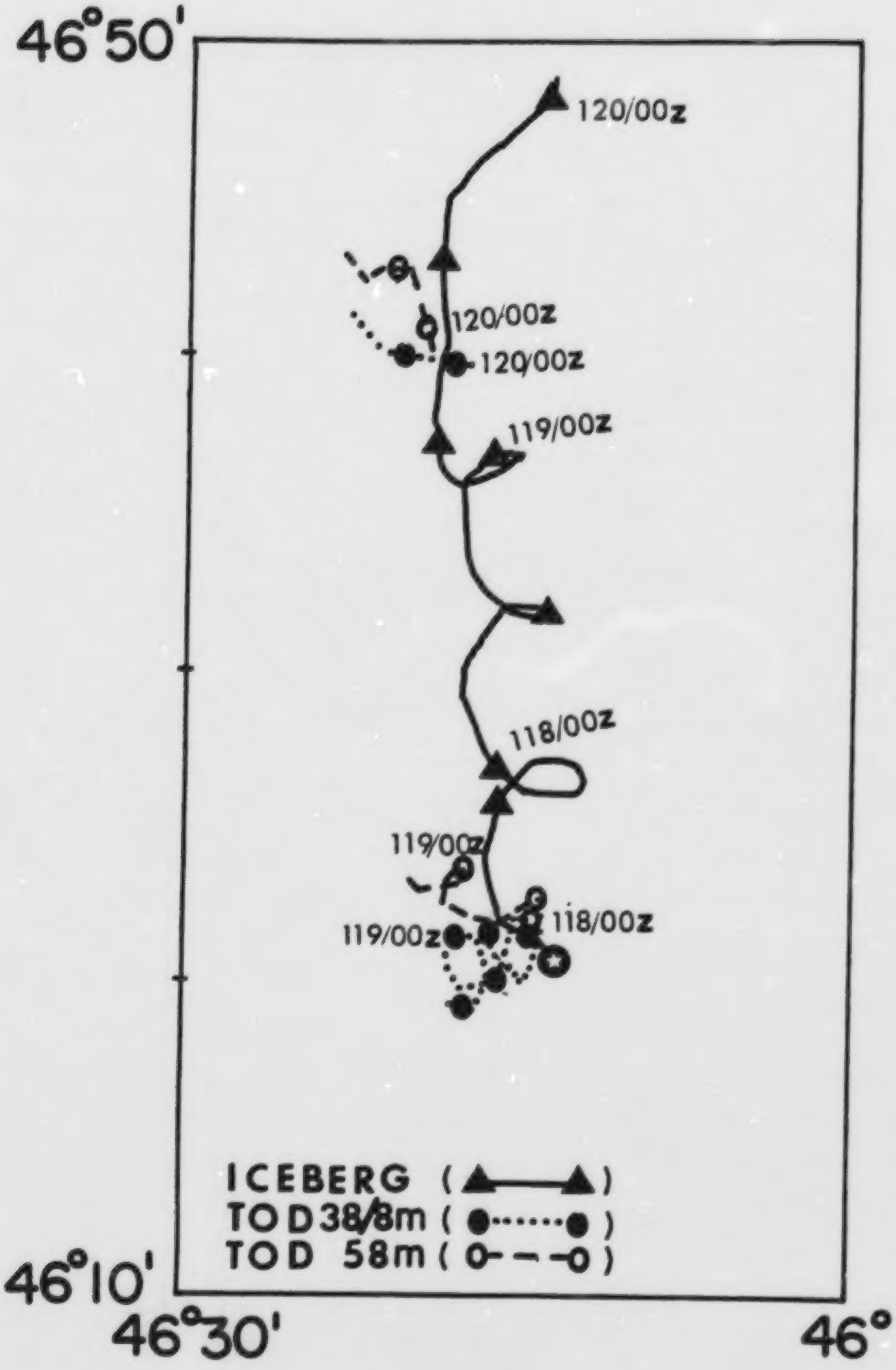

Figure 5. Iceberg and TOD trajectories for CASE III.

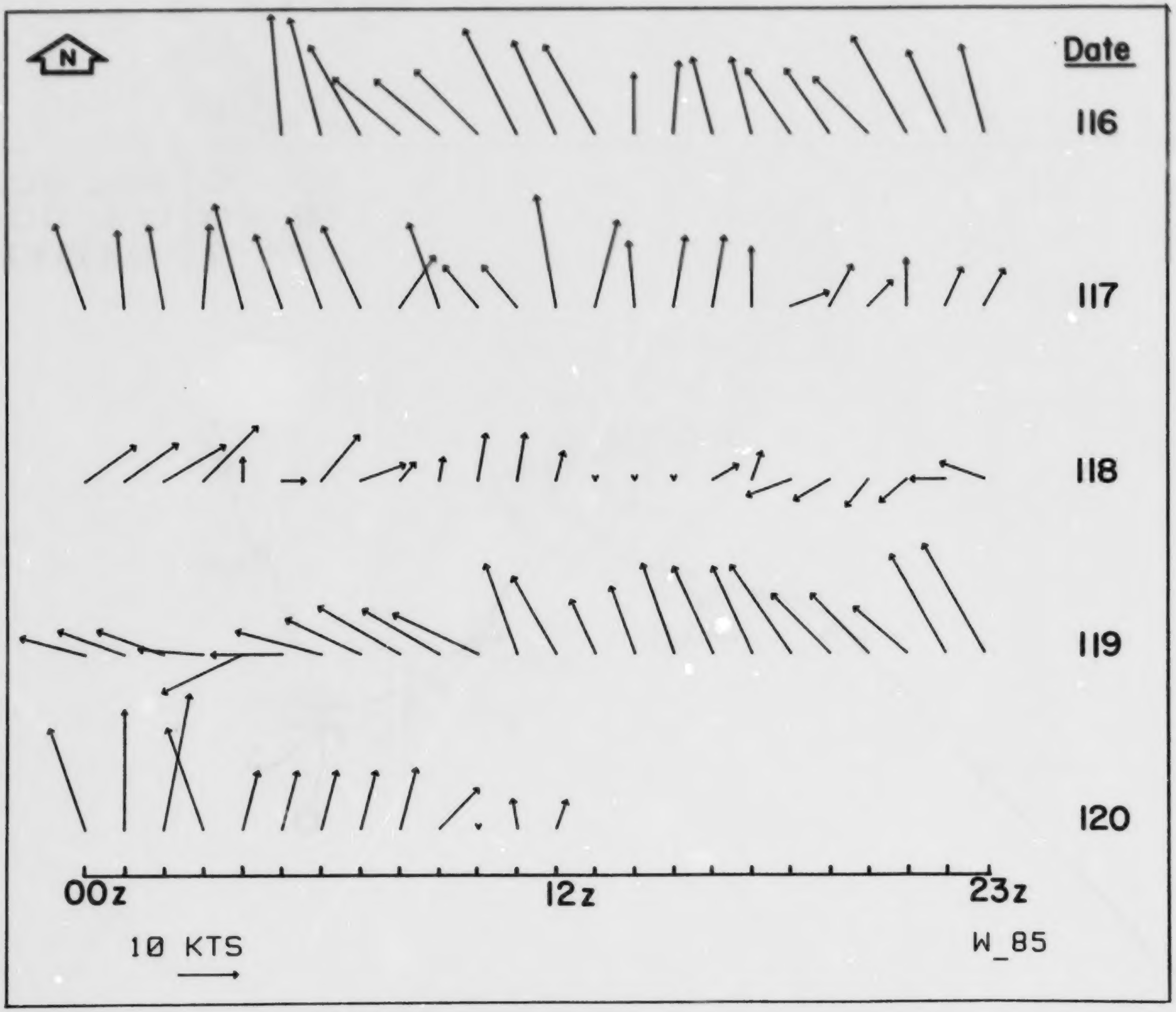

Figure 6. Hourly wind vectors for CASE III.

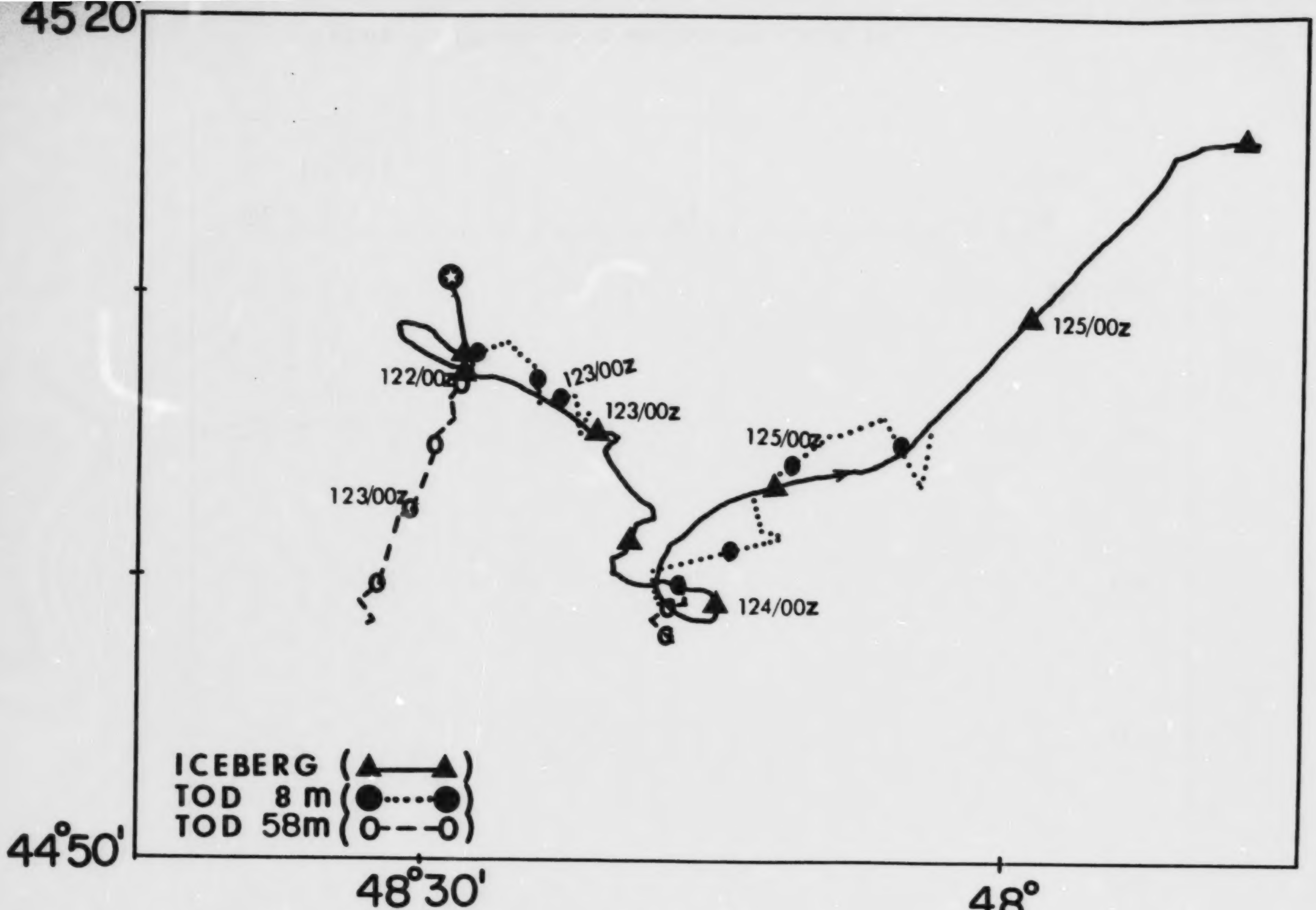

Figure 7. Iceberg and TOD trajectories for CASE IV.

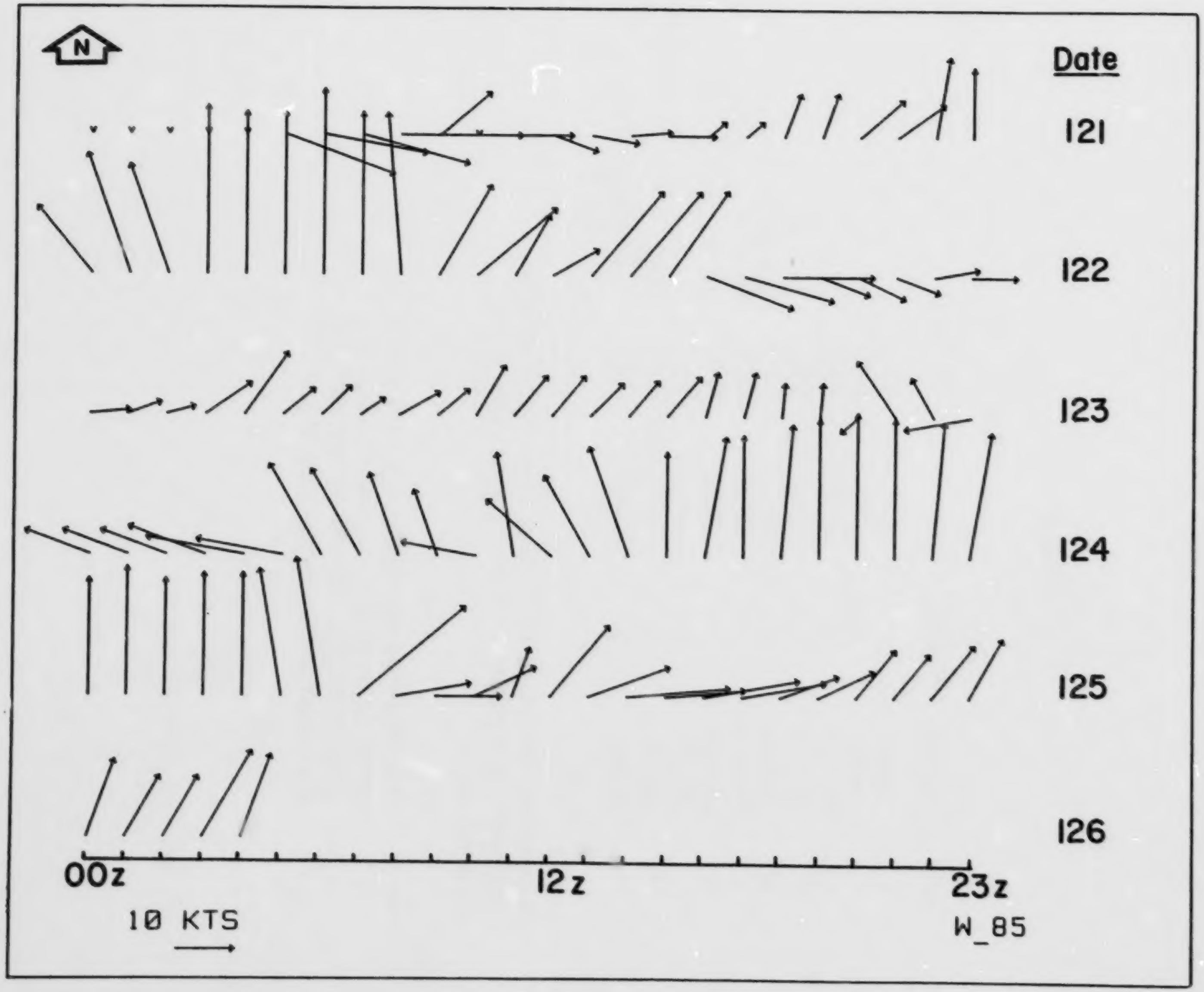

Figure 8. Hourly wind vectors for CASE IV

Table 1

			Inputs		
Case	Size	Run Number	Winds	Currents	
I	Large	1	SYS	SYS	
I	Large	2	SYS	OBS	(38m)
II	Medium	1	SYS	SYS	
II	Medium	2	OBS	OBS	(38m)
III	Medium	1	SYS	SYS	
III	Medium	2	OBS	OBS	(38m/8m)
III	Medium	3	OBS	OBS	(58m)
IV	Small	1	SYS	SYS	
IV	Small	2	OBS	OBS	(8m)
IV	Small	3	OBS	OBS	(58m)

Summary of the test runs. SYS=system, OBS=observed. The numbers in parentheses indicate the depth of the drogue center.

Note: The observed currents for this case were a combination of data from buoys drogued at different depths: 38m for the first half of the period and 8m for the second half.

the iceberg and the TOD's, which occurred during the first part of the drift period, was approximately 35 km.

CASE IV

A 4-day drift (1-5 May 1985) of a small (60x40x10m) drydock iceberg provides the data for Case IV. As in Case III, the area of study was south of Flemish Pass, and EVERGREEN tracked the target (Figure 7) and obtained the wind data (Figure 8). On the last day of the experiment there was a major calving event that left two small icebergs. At this time the parent (larger) iceberg had a maximum waterline length of 37m. Two TOD's, one drogued at 8m and the other at 58m, were deployed on 1 May (121); they were retrieved and redeployed at the iceberg on 4 May (124). The maximum separation between the iceberg and the TOD's was approximately 30 km.

Test Runs

Table 1 summarizes the runs made during the model tests. For each case the first run used the mean surface geostrophic current field from the IIP data base and wind data from FNOC. This set of inputs is referred to as system currents and system winds. The remaining runs for each case differed from the first run only in that available on-scene environmental data (observed) were used to drive the model.

The observed currents were obtained from the TOD trajectories by linearly interpolating to positions at 0000Z and 1200Z each day, and then calculating the 12-hour averaged current. When wind data were available, 12-hour averages were computed for use in the model. When no observed wind data were available, FNOC data were employed.

For each run the model computed a predicted iceberg position at 0000Z and 1200Z on each date. The range and bearing from the actual to the predicted iceberg position were computed for these times.

Results

Figures 9 thru 12 show the magnitude of the drift errors as a function of elapsed time for each of the four cases.

The system inputs in Case I (Figure 9) result in drift errors which increase rapidly and persistently until after approximately 2.5 days they exceed 40nm (~75km). The magnitude of this error is 52% of the total predicted drift. When observed currents drive the model, the errors are substantially reduced so that they are nearly consistent with the presently-used IIP error estimate. In Case I both the iceberg and the buoy were in the southward-flowing Labrador Current with typical current speeds of 0.4-0.5 m/s.

In Case II (Figure 10) the errors for the system/system run were less than 12nm (~22km) or 22% of the total predicted drift for the entire 104-hour drift period, well below the IIP error estimate. Using observed current and wind data improves the results to the point that after 104 hours the error is 2.5nm (~4.6 km). The drift test was conducted north of Flemish Cap with typical current speeds of 0.2 m/s, approximately half that observed in Case I.

The Case III system/system run (Figure 11) produced errors which increased persistently, exceeding the IIP error estimate after about 36 hours of drift. At the end of the drift period the error was over 30nm (~56km), which is 73% of the total predicted drift. In the early part of the drift period (<48hrs.) the use of the observed current and wind data produced no improvement in the results; indeed, at one point, the results were less accurate than the system/system case. This result is not surprising because the iceberg moved rapidly to the north while both buoys remained close to the deployment area. When the buoys were retrieved and redeployed at the iceberg (~60 hrs.), the model results computed using observed data improved somewhat.

Using the observed data to drive the model in Case IV (Figure 12) made an enormous improvement in the results. The system/system run produced errors

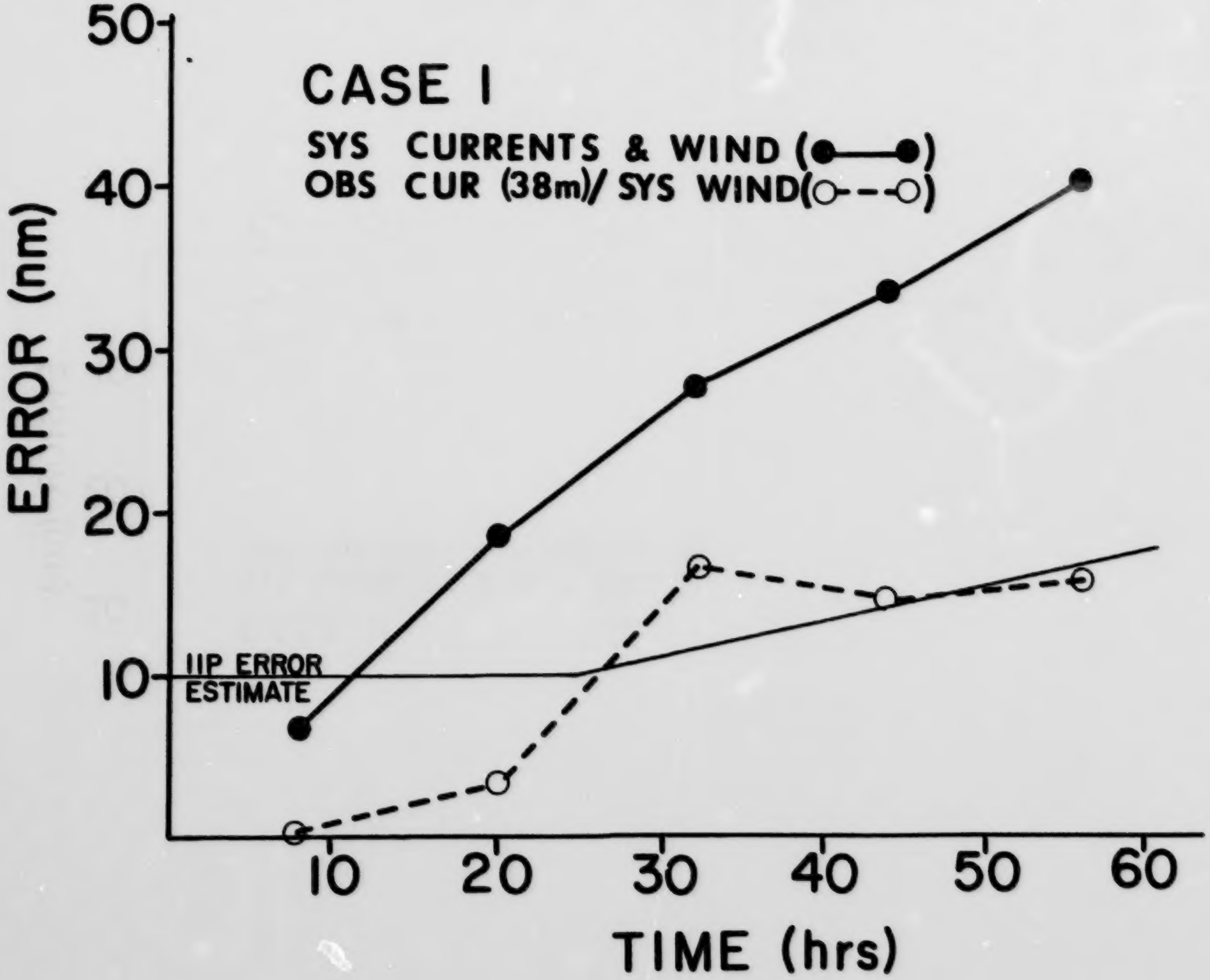

Figure 9. CASE I model errors.

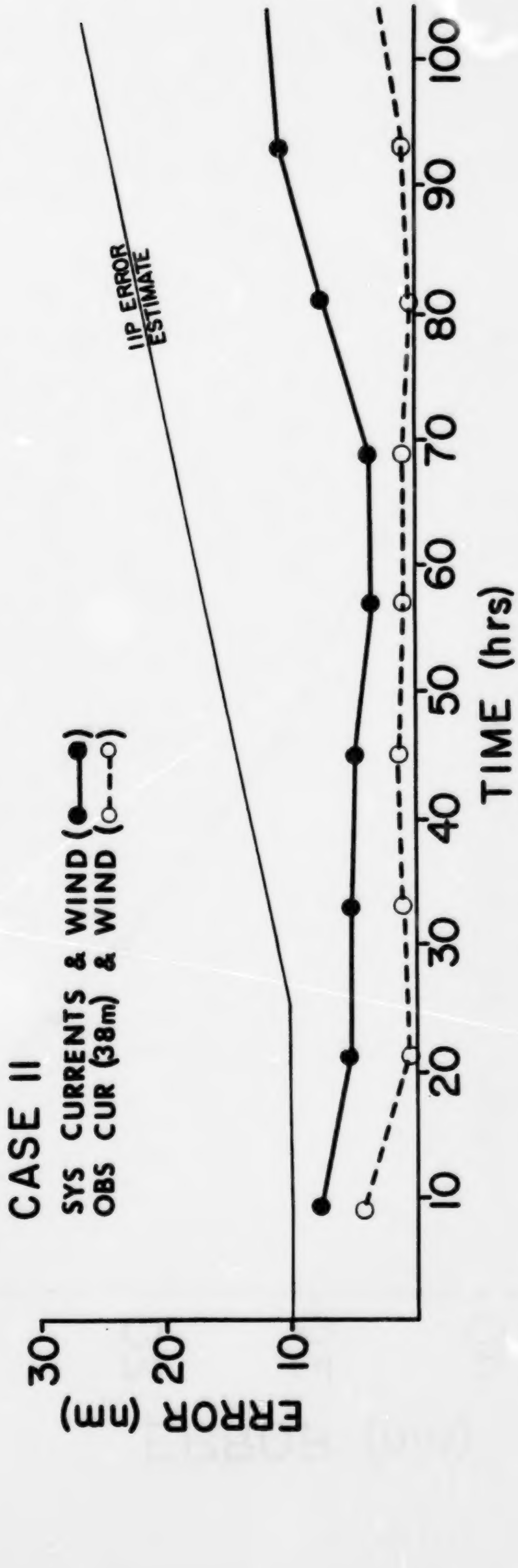

Figure 10. CASE II model errors.

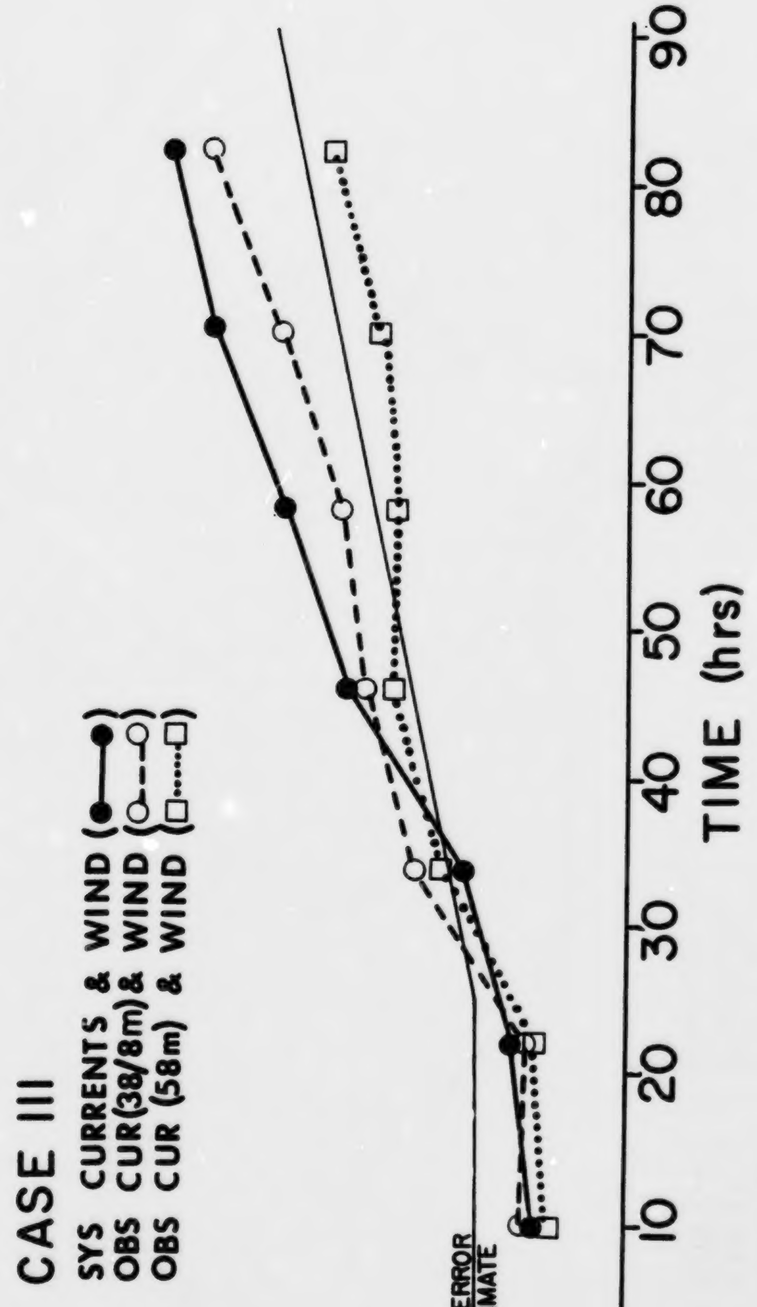

Figure 11. CASE III model errors.

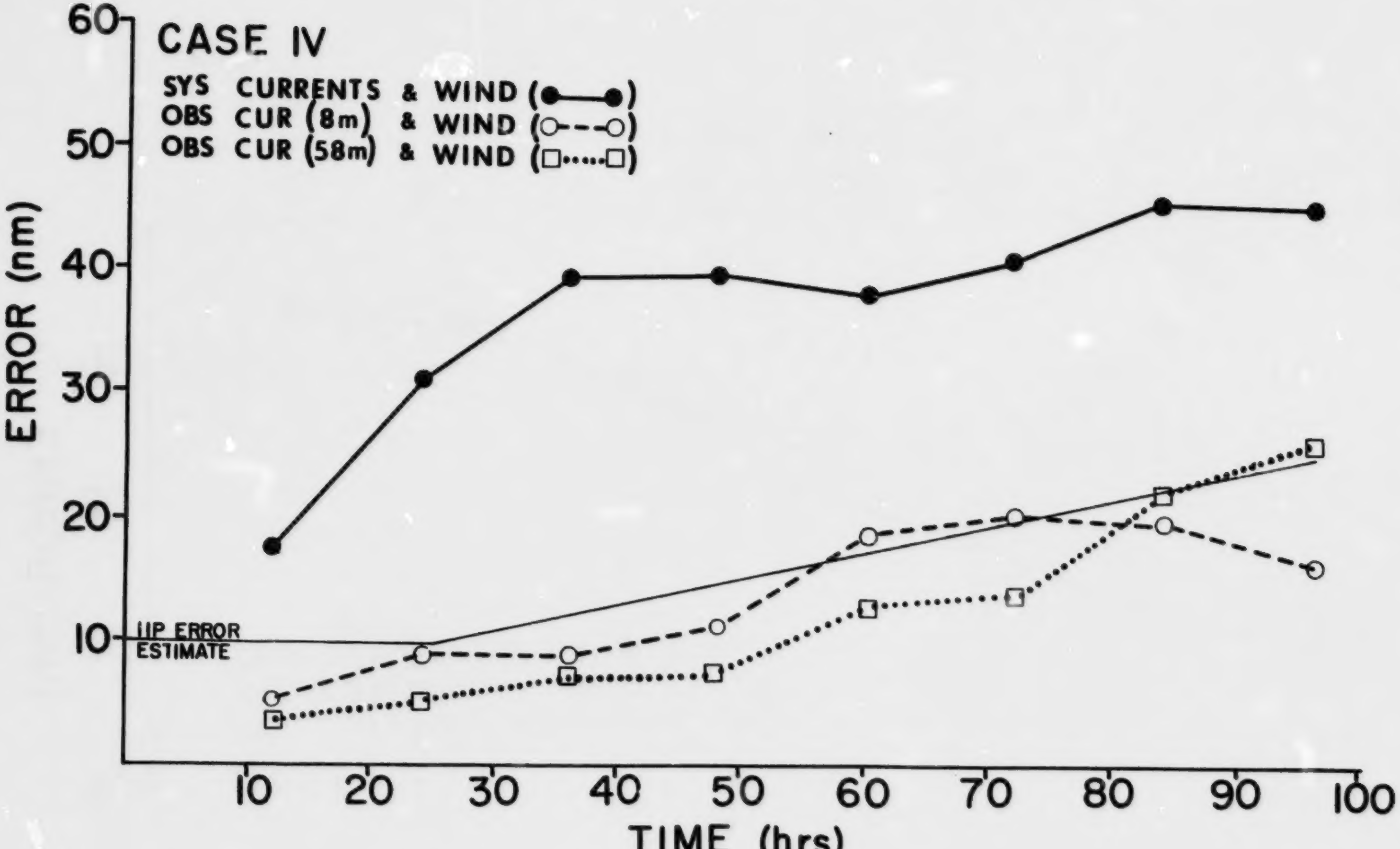

Figure 12. CASE IV model errors.

between 30-45nm (~56-83km) while, for the observed data, the errors were approximately half those values. For most of the drift period the currents measured at 58m provided more accurate model results than those measured 8m. At 84 hours this situation reversed and the 8m data produced better results. This is an expected result because as this small iceberg deteriorated, its motion should have been more consistent with the 8m currents than the 58m currents. However, the data are few and the difference between the results (8m vs. 58m) is small so there is no certainty that the reversal is meaningful.

Conclusions

No firm conclusions can be drawn from this small data set; but there is some consistency in the results that is worthy of note.

In all four cases, using on-scene measured data improved the model accuracy over the runs made using geostrophic currents and FNOC winds. The accuracy improvement was substantial in two cases: Case I and Case IV. Thus, the results of this study support the IIP practice of using TOD drift data to modify the geostrophic current. The more widespread the use of TOD's the more we can rely on the model results. No attempt was made to separate the improvements due to on-scene current data and on-scene wind data because of the small amount of data. However, Case I, for which there were no on-scene wind data, showed considerable improvement when on-scene current data were used in the model predictions.

In three of the four cases (Case II excepted) the observed drift error was larger than the IIP estimated error when the system winds and currents were used. For these three cases the drift errors were 52-73% of the total predicted drift; while for Case II the drift error was 22% of the total predicted drift. While it is tempting to suggest that the estimated position error be linked to the total length of the predicted drift (distance along the predicted path), no clear guidance can be given based on these results. The limited data show that if there is a TOD providing current information in the vicinity of a drifting iceberg the model will probably produce positions which are within the IIP error limits. If only geostrophic data are available the errors can be substantially larger, even for drifts of short duration. This issue is particularly important when an iceberg is setting the limits of iceberg threat.

The importance of collecting current data as close as possible to the tracked iceberg cannot be overemphasized. Early in Case III, when the TOD's and the iceberg separated rapidly, there was no improvement in the model errors when observed inputs were entered. Later in the drift period (after the buoys were redeployed) the model errors were smaller when the observed data were used.

Finally, the results of this study provide some guidance on the deployment of IIP operational TOD's. Although TOD drift data directly north of Flemish Cap are useful, the results of Case II showed that the model performed within the error estimates using the geostrophic currents. The TOD's deployed in the Labrador Current (Case I) and south of Flemish Pass (Cases III and IV), on the other hand, provided bigger payoffs.

References

Anderson, I., 1983. "Oceanographic Conditions on the Grand Banks During the 1983 International Ice Patrol Season". Appendix B of Report of the International Ice Patrol in the North Atlantic. Bulletin No. 69. CG-188-38. International Ice Patrol, Avery Point, Groton, CT 06340-6096, 73 pp.

Mountain, D.G., 1980. "On Predicting Iceberg Drift", Cold Regions Science and Technology, Vol 1 (3/4): 273-282.

Scobie, R.W. and R.H. Schultz, 1976. "Oceanography of the Grand Banks Region of Newfoundland March 1971 - December 1972. Report No. 373-70. U. S. Coast Guard, Washington, DC, 298 pp.

Summy, A.D. and I. Anderson, 1983. "Operational Use of TIROS Oceanographic Drifters by International Ice Patrol (1978-1982). Proc. 1983 Symposium on Buoy Technology. Marine Technology Society, Gulf Coast Section, Bldg. 2204, NSTL, MS 39529, p. 246-250.

OBSERVATION AND MODELLING OF ICEBERG DRIFT OFF NEWFOUNDLAND

by Stuart D. Smith
Department of Fisheries and Oceans
Bedford Institute of Oceanography
Atlantic Oceanographic Laboratory
P.O. Box 1006, Dartmouth
Nova Scotia, Canada B2Y 4A2

A dynamic model has been developed to calculate wind and water drag, Coriolis force, and pressure gradient forces on icebergs and by double integration of the acceleration to compute the drift track. Water drag is applied in 10 m segments to allow for variation of the current with depth. Air and water drag coefficients are adjusted for each iceberg to optimize the fit of the modelled track to the observed track.

Drift tracks of 10 icebergs in Newfoundland waters have been studied during 3 cruises of CSS Dawson. Radar ranges and bearings, along with LORAN C fixes of ship position, located the iceberg under study at 10 minute intervals for periods of 1 to 3 days. The mass and the cross-sectional areas in water in 10 m layers and in air were estimated from sonar profiles and photographs. Currents were measured continuously using a doppler acoustic profiler, and a bow mast was installed for minimal error from air flow distortion by the ship. Data are being compiled at 10 minute intervals and with currents averaged over 10 m depth intervals. Several modelled drift tracks are discussed.

ANALYSIS AND PREDICTION OF LABRADOR SHELF ICEBERG TRAJECTORIES

by J.F. Middleton and C.J.R. Garrett
Department of Oceanography
Dalhousie University
Halifax, Nova Scotia, Canada B3H 4J1

An analysis of 1,093 iceberg trajectories allows the influence of tides, wind and eddy motions on iceberg movement to be quantified. Principal results include a shelf diffusivity of about $10^3 m^2 sec^{-1}$, eddy length and time scales of 30 km and 40 hrs and downwind iceberg drift at 1.8% of the local wind speed. A stochastic model for the prediction of trajectories is developed and allows for the inherent predictability of shelf eddy motions, which in saddle regions may contribute 80% of the iceberg velocity variance. The implementation of the predictive model for the Hibernia region of the Grand Banks is outlined.

ON THE NUMERICAL CHARACTERIZATION OF ICEBERG SHAPE

by J. C. Lewis
Physics Department, Memorial University of Newfoundland
St. John's, Newfoundland, Canada A1B 3X7

A fundamental difficulty in the attack on problems related to icebergs, whether these are applied or fundamental, is the quantitative characterization of iceberg shape. This paper discusses areas in which this difficulty arises, and reviews several approaches to quantitative characterization of shape. It is argued that the roughness of an iceberg on specified length scales is of particular use for this purpose. A definition is given which quantifies the intuitive concept of roughness. This roughness measure can be defined and calculated at each point of the iceberg surface, and so can be applied to part or to all of the surface, and can be averaged over the any part of the surface, or part thereof, to give a global measure of the roughness of the part of the surface as a function of the length scale. Several examples are presented, and a computational method for determining the roughness from level contours is outlined.

ICEBERG SEVERITY REVISITED

by
J.R. Marko, D.B. Fissel and J.R. Birch

Paper presented at
Canadian East Coast Workshop
on Sea Ice
January 7-9, 1986
Dartmouth, N.S.

Arctic Sciences Ltd.
1986 Mills Road, R.R. 2
Sidney, B.C.
V8L 3S1

(604) 656-0177
Telex 049-7476

ASL File 41-094-M4
February 12, 1986

In making yet another attempt to examine the feasibility of iceberg severity prediction, our original intention was to utilize recent, high quality environmental data to evaluate the extent to which corresponding interannual severity variations are explicable in terms of the traditionally accepted sources of variability. A scheme representing the combined effects of three major sources of variability, as identified by the International Ice Patrol, has been sketched in Figure 1.

The depicted elements leading to an iceberg severity resultant include:

1) **iceberg sources:** the numbers and spatial distributions of icebergs in upstream source areas during the preceding winter;

2) **iceberg advection:** the rate at which icebergs move southward toward Labrador and into the Grand Banks region; and

3) **iceberg deterioration and loss:** the depletion of iceberg numbers by melting, break-up and long-term grounding.

It was believed that good data on both the iceberg source and the severity resultant elements were available, respectively, from the AES preseason SLAR surveys of upstream areas and from the annual IIP estimates of the number of icebergs passing south of 48°N.

Likewise, quantitative representation of the second advective element was expected to be derivable from the fields of sea-ice motion as deduced from NOAA satellite imagery. Use of these fields for iceberg advection required the further assumption of near-identity of iceberg and sea-ice motion in a mobile concentrated ice pack. Support for this assumption was found both in terms of comparisons of 1981 satellite-tracked iceberg drift with the movements and adjacent ice floes or determined from satellite imagery and by calculations (Canpolar Consultants, 1985) of the magnitudes of the iceberg driving forces relative to those needed to crush conventionally thick pack ice.

The fulfillment of these expectations was anticipated to lead to the deduction of those components of the remaining deterioration and loss element which would be essential to a functional severity prediction model.

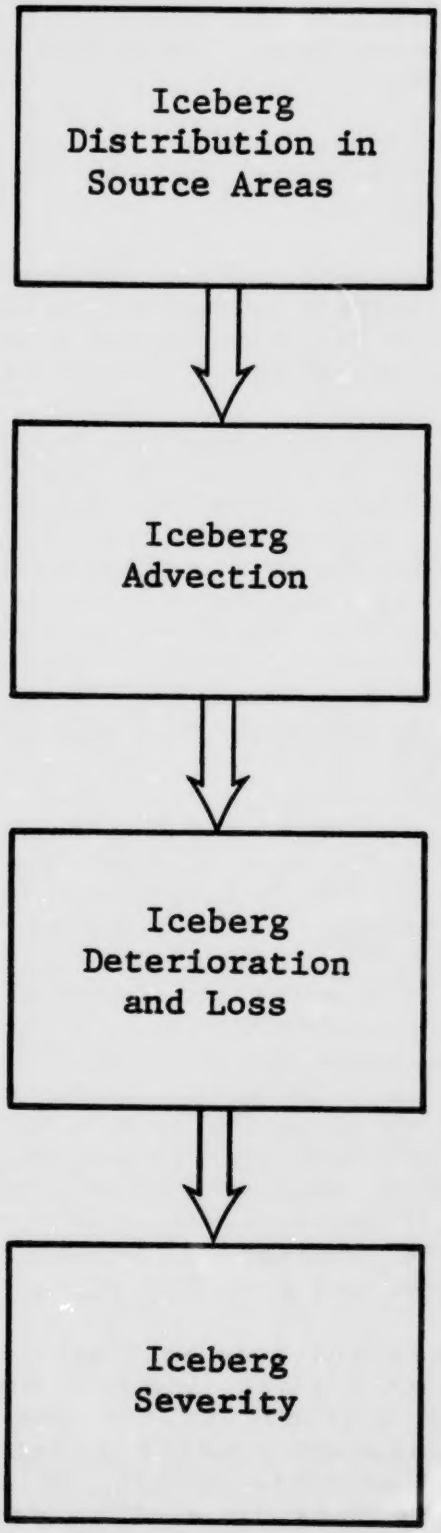
Iceberg Distribution in Source Areas
Iceberg Advection
Iceberg Deterioration and Loss
Iceberg Severity

Figure 1: Flow chart for an idealized physical model of iceberg severity.

Unfortunately, to date, this program has proved impossible to carry out due to:

1) the difficulties involved in achieving completeness of coverage and detail in even the most extensive AES preseason surveys; and

2) the numerous reported discrepancies between oil industry drillsite iceberg number estimates and the IIP seasonal counts which call into question the detailed accuracy of even the most recently reported severity values.

Instead, an alternative approach had to be taken which used other sets of physical environmental data of adequate quality and duration which could be expected to bear some relationship to the physical sources of severity variability. It was to be hoped that pairwise comparison of such data sets against the severity record could provide guidance in selecting the essential components of an effective severity prediction model.

After reviewing our options several data sets were constructed or pulled together from a wide variety of sources as indicated in Figure 2.

The first of the listed parameters, sea-ice extent, was of particular interest because of the expectation that sea-ice extent is related to the field of sea-ice motion and hence, by our above assumption, to the field of iceberg motion. Preliminary examination of the data indicated that the best correlations with the severity record were achieved with the January ice extents in Davis Strait (Figure 3). Abundant good data have been available for this period since 1972 when NOAA satellite coverage was initiated. Less precise and less reliable data from earlier years, dating back to 1953, were also obtained from Canadian, U.S., British and Danish aircraft and surface observations. The values used for this period were taken from Dr. John Walsh's difference between the multiplicative adjustment for a spurious 35% average difference between the extents reported for the pre- and post-1967 years.

Monthly air temperatures at coastal points were included because of the expected close (inverse) correlation between this parameter and the distance to the ice edge (and hence ice extent). The somewhat greater length of the historical temperature record held the promise of extending any sea-ice extent correlations back to earlier years. Again the best severity correlations were found with the January temperature at Frobisher Bay.

REVIEWED ENVIRONMENTAL DATA SETS

Sea-Ice Extent:	4/10 concentration Boundaries as deduced from: 1. AES Canada weekly and bimonthly ice charts 1970-1985 2. U.S. Naval Oceanographic Office Reports of the Arctic Ice Observing and Forecasting Program 1953-1971 3. U.S. Fleet Weather Facility Eastern Arctic Sea Ice Analyses 1972-1985 4. Danish Meteorological Institute Ice Conditions in the Greenland Waters 1960-1968 5. The summary of much of the above data on a 60 n.mi. x 60 n.mi. grid scale by Walsh (1979)
Air Temperature:	(AES) monthly means at St. John's 1942-1984 Goose Bay 1941-1984 Frobisher Bay 1946-1984 Cape Dyer 1959-1984
Wind Stress Anomaly:	(Thompson and Hazen, 1983) Along- and cross-shore deviations of mean December to February (1950-1980) geostrophic winds at 56°N, 58°W
Along- and Cross-Shore Windage:	Calculated from daily average winds at Ocean Weather Station Bravo for January-March 1945-1972
Monthly Mean Water Levels:	(Marine Environmental Data Service) for St. John's 1935-1983 Nain, Labrador 1963-1980 Frobisher Bay 1959-1983
Occurrences of Strong El Nino Events:	As listed by Rasmusson (1984) using the strength criteria of Rasmusson and Carpenter (1982)

Figure 2: Physical data sets reviewed for correspondences with severity.

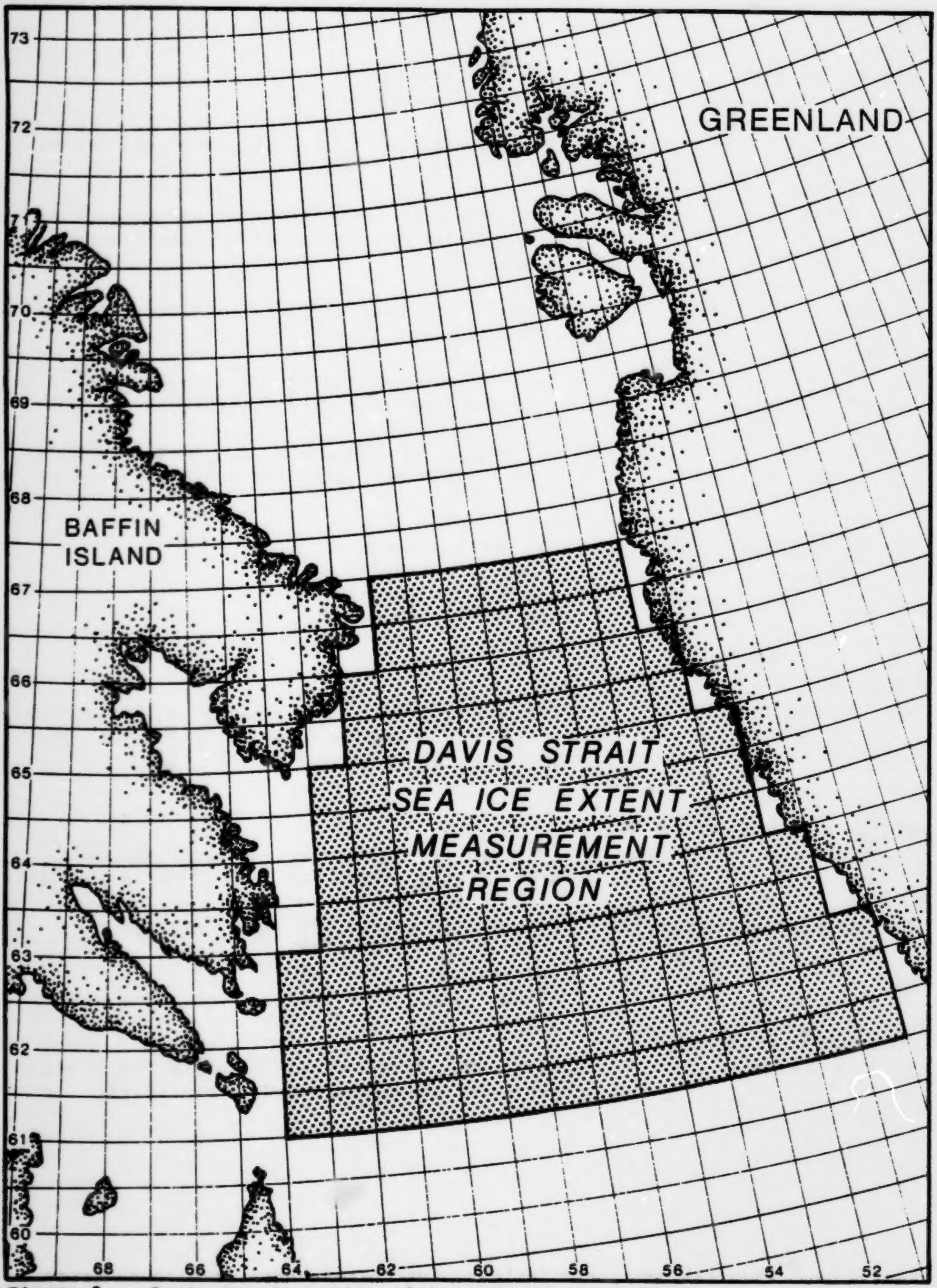

Figure 3: Davis Strait region of ice extent measurements.

Windage (measured at Station Bravo) and windstress anomaly (calculated from the geostrophic assumption and the atmospheric pressure distribution) were included because of the long-held assumption (Smith, 1931) that winds determined both the gross rate of southward iceberg movement and the probability of delay or loss to groundings on the Labrador shelf or to melting in the warm Gulfstream waters.

Water level data were included originally to reflect the presence of interannual differences in current speeds and current patterns and possibly in grounded iceberg refloatation rates. Initial examinations showed no discernible connection with iceberg severity and detailed comparisons with this parameter were not carried out.

Finally the inclusion of the ENSO (El-Nino Southern Oscillation) parameter in this approach was motivated by the observation, particularly in the era of modern data taking, that periods of high iceberg severity tend to follow the appearance of strong El-Nino occurrences as defined by Rasmusson (1984). The El-Nino phenomenon is associated with the tropical (Figure 4) or subtropical portions of two of three chains of alternating mean atmospheric pressure cyclones and anti-cyclones which girdle the earth. Long-term (Figure 5) changes in the relative levels of adjoining pressure features have been cited as the sources of pronounced climatic changes in many regions. The interplay between the so-called Azore anti-cyclone and the Icelandic cyclone has received the separate designation, the North Atlantic Oscillation (NAO). Its relationship to the ENSO event is complex and the subject of much current research. It was not the intention of this project to enter into this effort and our further exertions in this respect will be confined to noting that the Icelandic cyclone is likely to be a prominent factor in determining iceberg severity and then testing the historical accuracy of an empirical prediction rule which states that severe conditions always immediately follow a strong ENSO occurrence and that two immediately successive strong ENSO occurrence will, as well, induce severe conditions in a third year.

However, before making comparisons, some coarsening of the severity data was necessary to minimize the confusion which could be introduced if a significant component of the reported year-to-year variability was attributable to differences in observational effort and technology as opposed to real changes in the tested environmental parameters. Although, inevitably, we had to be somewhat arbitrary in handling this difficulty, we drew on the general assessment of the annual degrees of iceberg hazards

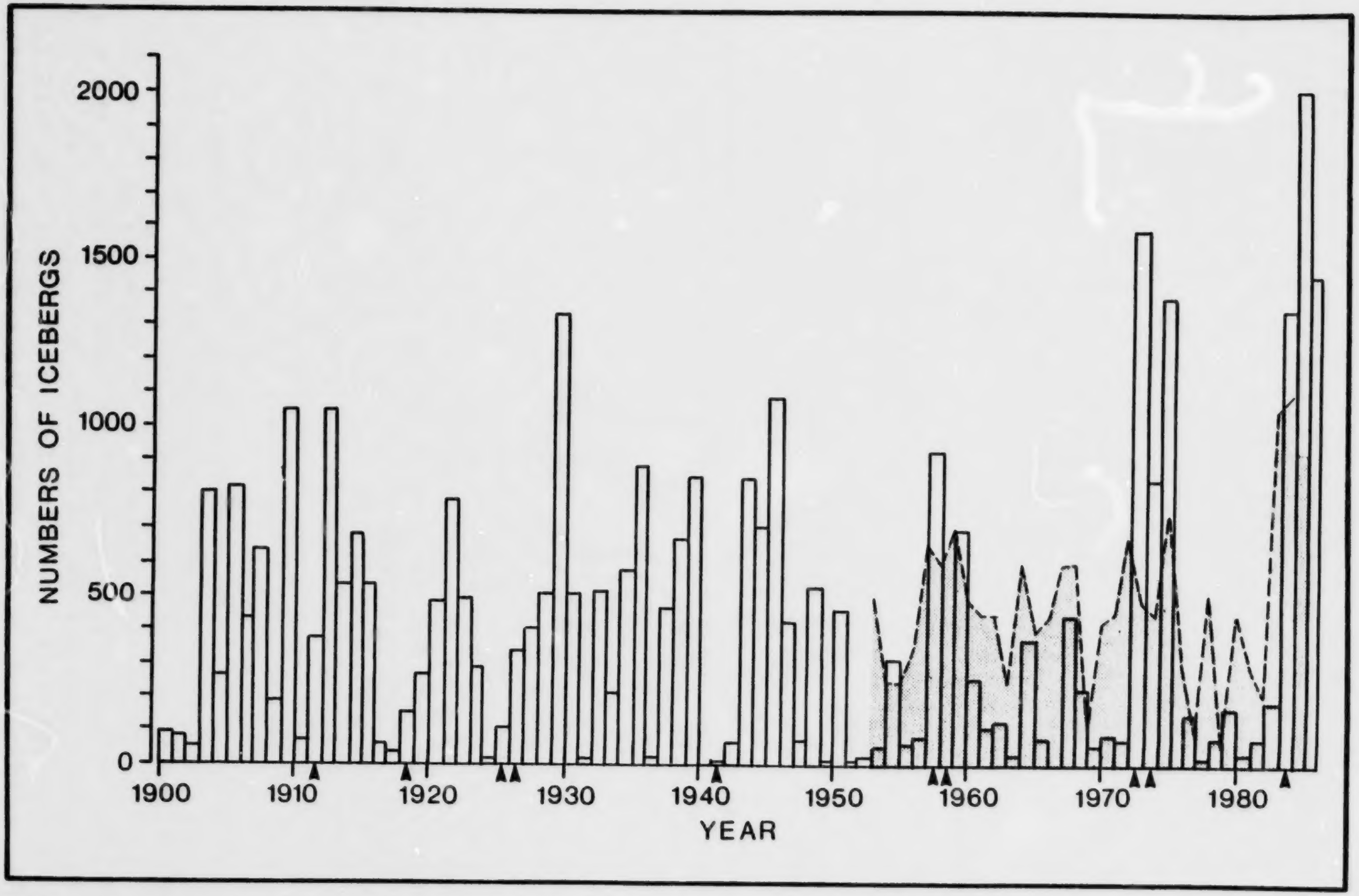

Figure 4: Historical annual counts of icebergs passing south of 48°N. Broken line and under-shaded curve denotes corresponding January ice extents in Davis Strait (in arbitrary units). Arrowhead marks along abscissa denote years which were immediately preceded by strong ENSO occurrences.

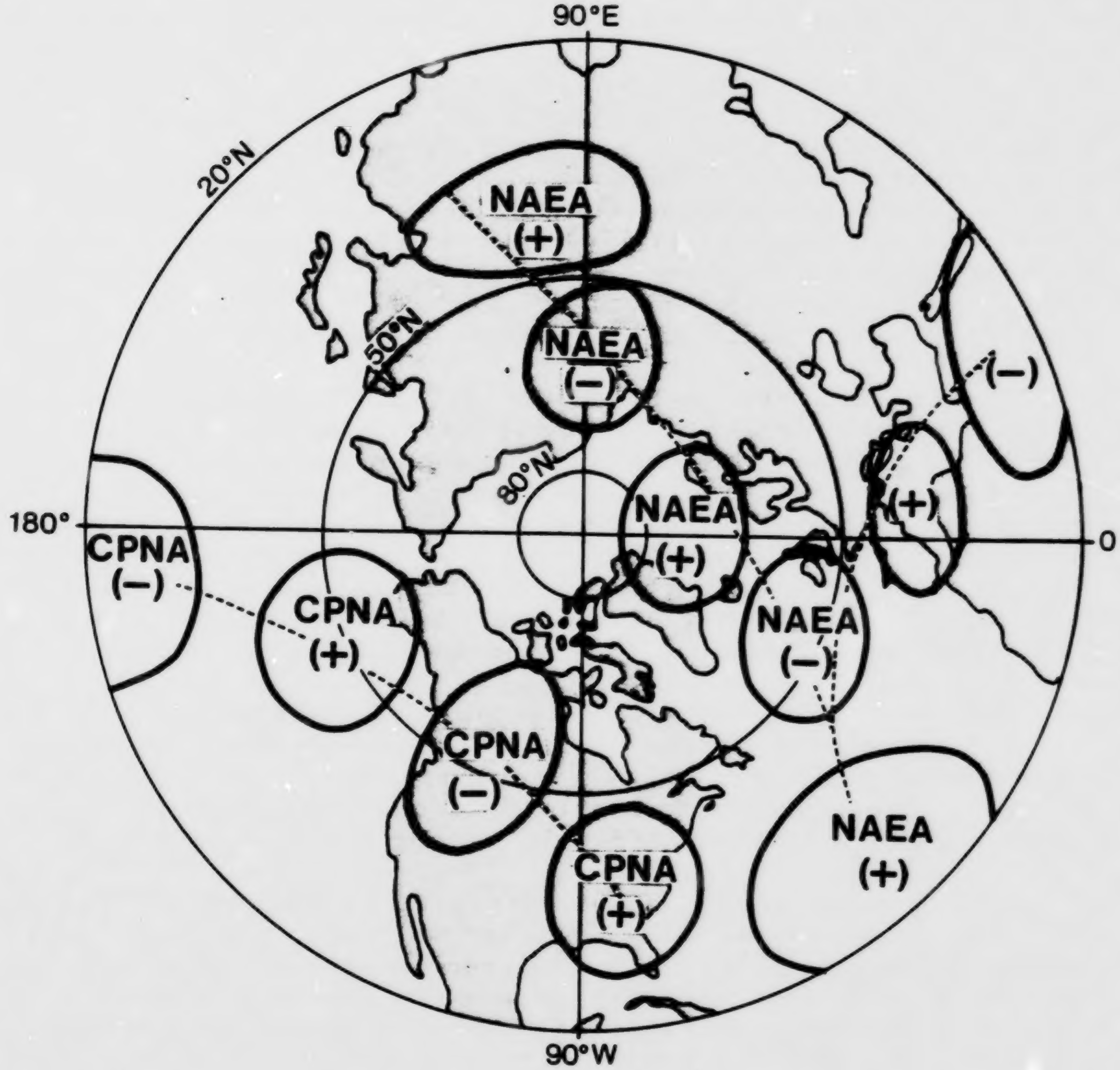

Figure 5: A schematic representation of two globe-girdling chains of mean atmospheric pressure cells having spatially alternating signs (+ or −) relative to the overall mean. The letter designations CPNA and NAEA denote, respectively, the Central Pacific East North American and the North Atlantic Eastern Asia chains (after Nobre et al., 1985).

offered by the IIP and other agencies and the corresponding reported severity numbers to conclude that, at least in the post 1941 period, reported iceberg numbers less than 200 and greater than 600 could be safely assumed to be indicative of low and high severities respectively. Counts in the remaining 200 to 600 iceberg range could be viewed either as a third, intermediate level of severity or as a 'gray zone' in which entries could correspond to seasons in which low or high severities were over- and underestimated, respectively. It might be significant to note here that no intermediate-level seasons have been recorded since the late 1960's. In any case, our treatment will assume the existence of a definable intermediate level while recognizing that 1-level prediction errors achieved in this 3-level severity scheme may be artifacts of measurement inadequacies.

Comparisons were carried out for all tested parameters, including the inherently binary (2-level) ENSO scheme. In the case of the other parameters, our method proceeded by dividing up the range of variability into three subranges, each to be associated with one of the high, low and intermediate severity categories. The boundaries of these subranges were chosen (Figure 6) so that in each case the corresponding probability distribution was identical to that of the historical severity record (60% low, 22% high, 18% intermediate).

The results of the 3-level comparisons are shown in Figure 7 in the form of time series plots of the observed and predicted annual severities for the years encompassed by each parameter data set. The broken line prediction values are only detectable in those years when they differed from the observed values.

Although the analysis and interpretation of these results has really just begun, it can be seen that the best correspondences with the historical record were achieved with the sea-ice extent and the ENSO parameters as indicated in the tabulation of the error statistics in Figure 8. Nevertheless, reasonably successful results were also achieved with the other tested parameters suggesting the likelihood of a common source of severity variability in interannual differences in the atmospheric pressure distributions. Moreover there appears to be some evidence that these differences may be related to long term periodicities in the temporal behavior of the global pressure distributions.

Interpretation of these results should recognize that:

1) The wind stress and windage indicators are not predictor quantities since they contain data from the months of

HIGH, INTERMEDIATE AND LOW PARAMETER BOUNDS

	HIGH	INTERMEDIATE	LOW
Sea-Ice Extent	>1.004	0.87< <1.004	<0.87
ENSO	preceded by strong event or within successive events one year of two	N.A.	high requirement not satisfied
Air Temperature	<-30.5°C	-25 to -30.5°C	>-25°C
Wind Stress Anomaly	>0.04 Pa	0.02-0.04 Pa	<0.02 Pa
Bravo Windage	$>27\times10^3$km	$20-27\times10^3$km	$<20\times10^3$km

Figure 6: The boundaries between the high, low and intermediate categories of each predictor assuming approximate equality between the corresponding probability distributions and that associated with iceberg severity.

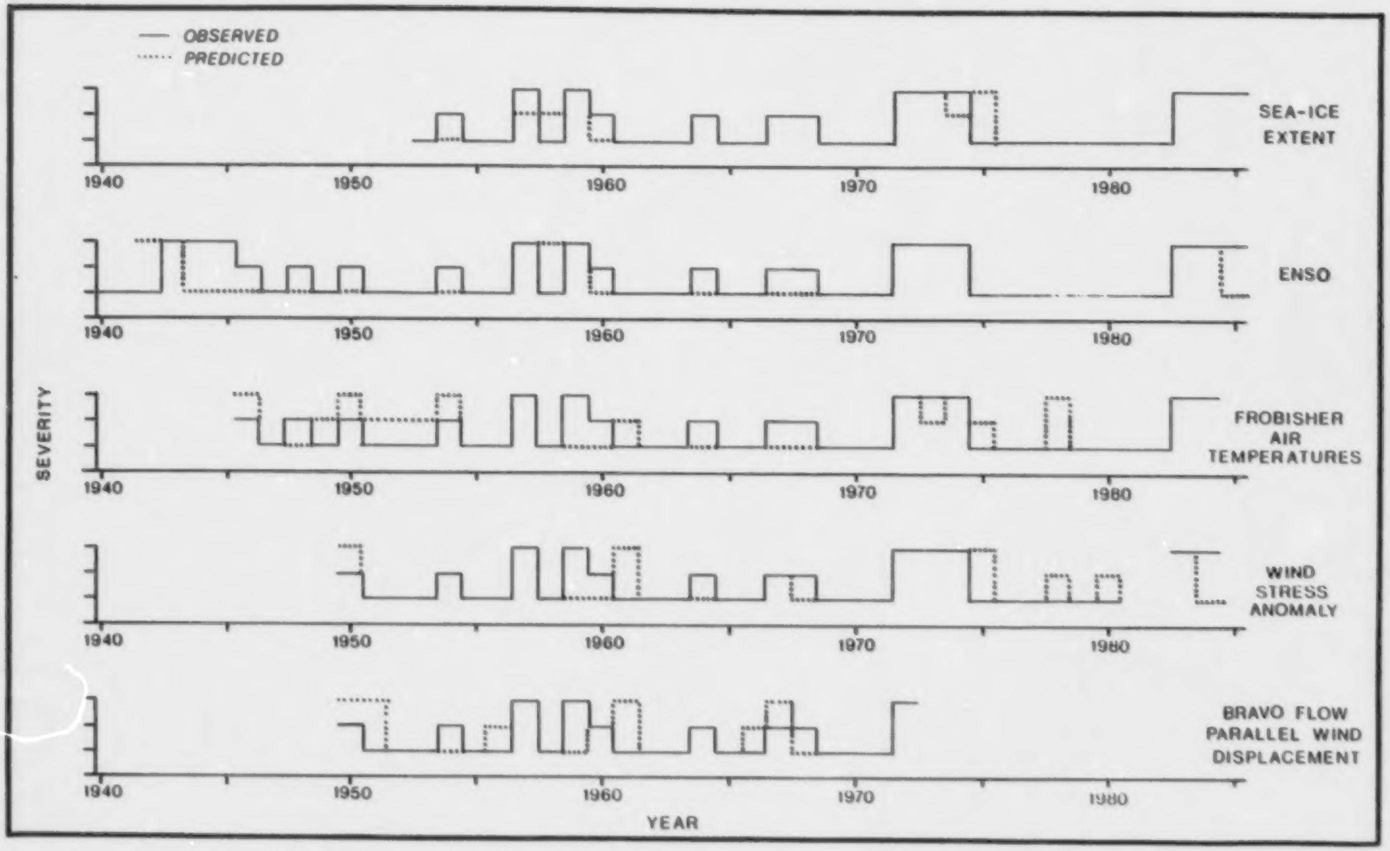

Figure 7: Predicted and observed severity levels for the tested indicators. The dotted prediction curves are visible only where they differ from the observed 3-level severity value.

PREDICTOR STATISTICS

PREDICTOR	MEAN ERROR	STANDARD DEVIATION	% CORRECT	% CORRECT OR ONE LEVEL ERROR	% TWO LEVEL ERROR
Sea-Ice Extent	-0.03	0.53	82	97	3
ENSO	-0.22	0.75	72	89	11
Air Temperature	-0.08	0.83	56	95	5
Wind Stress Anomaly	0.0	0.97	70	88	12
Bravo Windage	0.17	1.24	61	87	13

Figure 8: Predictor statistics in terms of mean and standard errors (in levels) and percentage distribution of error magnitudes.

February, March and April. The quality of the Bravo windage indicator was observed to decline as it was shifted to correspond to earlier November to January months.

2) The linked sea-ice extent and air temperature indicators, which are predictors, were exceptionally good at avoiding 2-level errors which are particularly unwelcome when they correspond to underprediction, i.e. high iceberg severity in a year of predicted low severity. In fact two of the three 1-level underestimation errors made by the sea-ice extent predictor disappear if category boundaries are selected without strict adherence to equality of the parameter and severity probability distributions. This change involves only a small shift in boundaries and yields zero errors in 29 of the 33 years tested.

The inherently conservative nature of the sea-ice extent predictor is evident if we look at a scatter plot of the annual low and high quality January ice extent data as a function of the actual reported severity numbers (Figure 9), and sketch in our high severity boundary at the 600 iceberg level. The only entries above the drawn 600 iceberg high-severity boundary level correspond to sea-ice extents greater than 1.0 in units of 61,000 $(nm)^2$). In other words, in the 33 year-long record, low ice extent (0.87 or lower) were never found to be followed by a high iceberg severity. Moreover, if, as indicated above, the restriction on identical severity and parameter distributions is dropped, a similar statement can be made with regard to those years in which intermediate severities were predicted. Taken together, these features of the sea-ice extent predictor appear to offer some measure of confidence to offshore industry planners.

Nevertheless, none of the studied predictors provided a fully reliable performance with respect to the historical record. Some of the differences could no doubt be attributable to corresponding errors in the compared data sets but certain discrepancies such as the prediction of high levels in 1975, a year of low severity, appear to have a real physical basis and were, moreover, not understandable in terms of comparisons with the corresponding cross-flow windage and windstress anomaly parameters which might be expected to be indicators of additional variability associated with abnormal rates of grounding or melting in warm offshore waters.

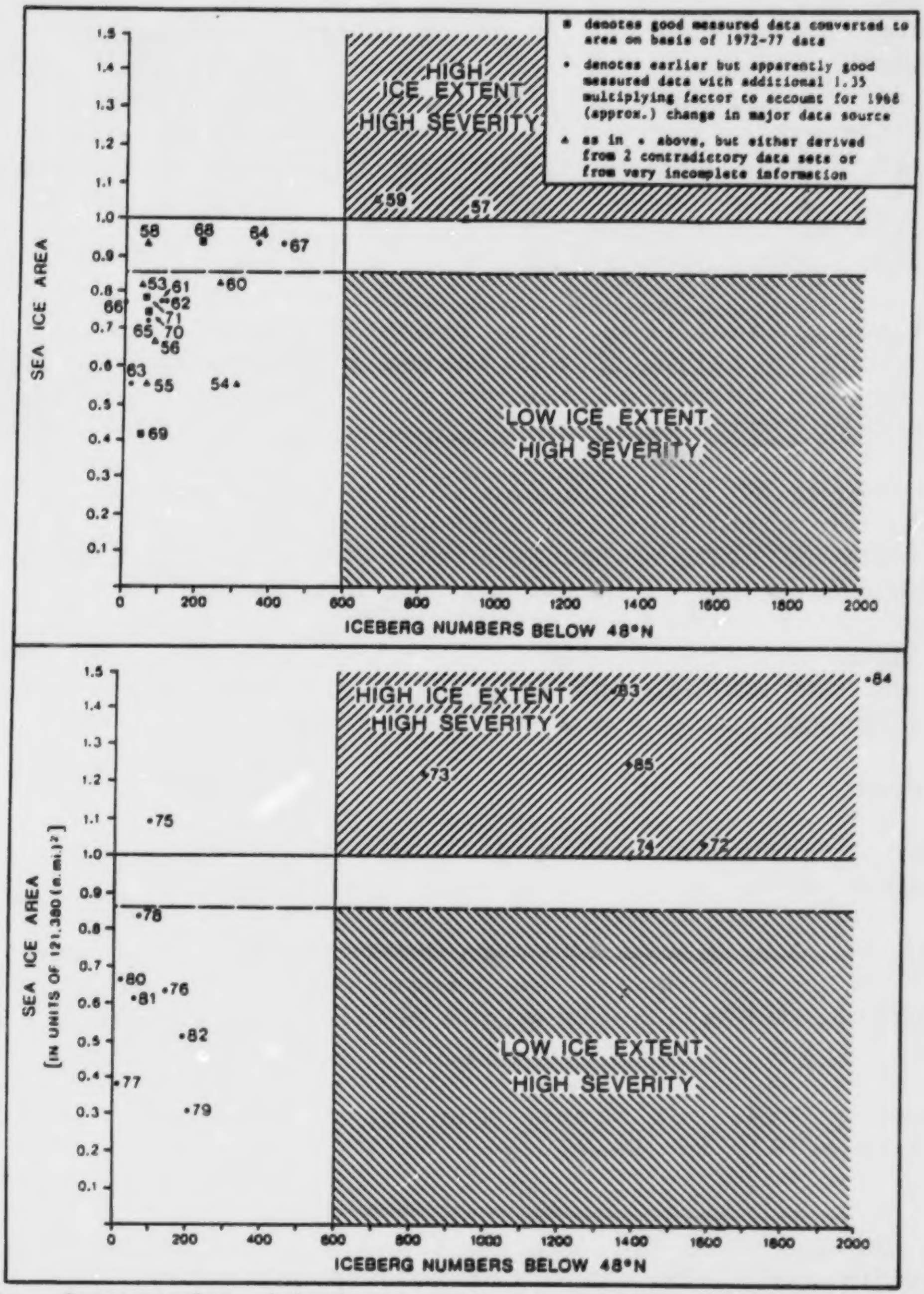

Figure 9: Scatter plot of both the early low quality and later higher quality data sets on the reported numbers of icebergs passing south of 48°N and the spatial extent of the January sea-ice cover in Davis Strait. The experimental data points corresponding to high severity, i.e. numbers greater than 600 and hence to the right of the drawn vertical boundary, all have normalized ice extents ≥ 1.0. The absence or presence of high severity entries for intermediate sea-ice extents depends on the precise specification of the high/intermediate extent boundary. No such ambiguity exists with respect to the data points associated with the low, <0.87, sea-ice extent regime. High iceberg severity was never observed to follow such conditions.

Further analyses and research efforts are needed to resolve such anomalies and to address more fundamental questions regarding the detailed origins of the apparent linkages amongst the sea-ice extent parameters, iceberg severity and the dynamical and thermodynamical processes of the atmosphere and ocean. Specific data are needed relevant to interannual variability in the source region iceberg distributions and, as well, in the sea ice/iceberg field of motion.

At the present time, it is probably best to continue to make predictions in terms of all tested predictors; resolving any conflicts in terms of the relative levels of performance indicated in Figure 8.

In terms of the upcoming 1986 season, present early data indicate no such conflict although we have not yet had the opportunity to examine the Frobisher Bay air temperature record. Nevertheless, since predicted (by the Navy-NOAA Joint Ice Center) ice boundaries correspond to ice extents of 0.75 (below the 0.87 lower limit of the intermediate category) and the late 1985 ENSO index was not strong, the expectation is that low severity will be experienced during the 1986 iceberg season.

References

Canpolar Consultants Ltd., 1985. Pack ice/iceberg drift. Draft report prepared for Seaconsult Ltd.

Norbre, P., A.D. Moura and C.A. Norbe, 1985. Planetary-scale circulation anomalies associated with droughts over northeast Brazil. Tropical Ocean-Atm. Newsletter, No. 30, pp. 11-13.

Rasmusson, 1984. El Nino: The ocean/atmosphere connection. Oceanics 27, pp. 5-12.

Smith, E.H., 1931. The Marion Expedition to Davis Strait and Baffin Bay, 1928. U.S. Coast Guard Bull. 19(3), pp. 1-221.

ICEBERG SPLITTING AND ITS IMPLICATIONS FOR DETERIORATION MODELLING

Deborah Diemand **James H. Lever**

Centre for Cold Ocean Resources Engineering
Memorial University of Newfoundland
St. John's, Newfoundland, A1B 3X5, Canada

ABSTRACT

Many iceberg deterioration models have been developed recently to supply a need by offshore operators to predict the numbers and sizes of icebergs likely to impinge on a specific area of interest such as a drilling site or wellhead. The more sophisticated models incorporate many environmental parameters such as wind direction and speed, currents, waves, air and water temperatures, etc., as well as factors intended to account for mass loss due to melting and calving. These factors are based on ablation rates as determined by laboratory studies, field observations and theoretical considerations and are reliable to a degree. They are predicated on the belief that mass loss in icebergs is a result of two mechanisms: melting and calving of small fragments. Observations on Makkovik Bank during the summer of 1985 make it clear that this is only partly true and that major calving events such as ram loss and iceberg splitting are quite common and should be accounted for in any deterioration model, as failure to do so will result in underestimation of of numbers and overesimation of sizes. Various mass loss mechanisms were documented and are discussed in terms of their implications for iceberg deterioration and model design.

1. INTRODUCTION

The population of icebergs on the Grand Banks of Newfoundland, or any other area south of Baffin Bay for that matter, is largely dependent on the deterioration rate experienced on the journey south from Baffin Bay. A number of models have been devised in an effort to predict iceberg drift and population density. Statistical correlations have been made between total iceberg counts and various environmental parameters in an effort to discover the best indicators of iceberg season severity. Complex operational deterioration models may also be applied to seasonal forecasts, but with high demands on input information. Either approach may be ineffectual if they are predicated on the notion that an individual iceberg will remain intact for the duration of its life, gradually diminishing through various ablation mechanisms. The observation this summer on DIGS '85 that icebergs may subdivide has important implications regarding deterioration modelling and iceberg season severity forecasting. This paper describes the observed iceberg splitting and briefly discusses a statistically based deterioration model under development at C-CORE.

2. ICEBERG DETERIORATION MECHANISMS

The reduction of icebergs is a result of mass loss due both to melting and to calving. In seawater at 0° and below, melting will be insignificant. It will increase with increasing temperature and become extremely rapid at temperatures common off the Canadian east coast in the summer. Of course, this rapid melting will only take place where this warm water is in contact with the ice. Since the Labrador Sea usually becomes stratified in the summer, this warm layer may only be in the order of 10 to 20 m deep so that large bergs, say 2 million tonnes or greater, will only be melting rapidly along a 10 m wide girdle, a relatively small proportion of the entire surface area, while smaller bergs in the order of half a million tonnes or less will be more strongly influenced, as a much larger proportion of the surface will be exposed to the warm sea. In addition, due to the greater surface/volume ratio of smaller bergs, all things being equal, the proportional ice loss due to melting will be much greater in these bergs than in the larger ones. It would appear that melting will play a relatively minor direct role in the reduction of very large ice masses, although contributing significantly in the indirect role of inducing calving.

Calving, on the other hand, continues throughout the year to some extent. Since the ice lost in small calving events usually originates on the vertical faces, it seems clear that this will be the major means of ice loss for large bergs, while being minor for smaller masses. However, there is another scantily documented form of calving, observed during DIGS '85 this past summer, resulting in enormous mass reduction. On two occasions a large tabular iceberg lost a large portion of its underwater mass through the calving of rams. Figure 1 shows this iceberg in the process of losing a ram. Both rams remained in the area for several days as small domed icebergs. On two other occasions, large icebergs split roughly in half by slumping in the middle and tipping such that the rams at either end heaved out of the water (see figure 2). It is thought that these two bergs were created by a splitting event themselves shortly before our arrival. If this is true, then this large mother berg produced six good-sized bergs in the course of about a week.

Both ram loss and large scale splitting are thought to be produced by the action of buoyancy forces. Buoyancy forces represent perhaps the most significant source of stresses in icebergs. All icebergs possess underwater rams of greater or lesser extent. Some can extend outward beneath the water surface for 50 m or more. Figure 3 shows an iceberg with a ram at the level of the water surface whose lateral extent was 70m or greater. Assuming that a large iceberg freshly calved from its parent glacier is of a tabular, blocky or near-tabular form, the development of these rams represents the first stage in its deterioration. After prolonged residence in the cold waters of Baffin Bay, little ablation will have taken place and no significant rolling. Any measurable amount of melting taking place will have done so at the water line, resulting in undercutting of the cliff faces and ice loss from them through small calving events. The underwater mass will be little affected and the berg will gradually take on an inverted T shape as indicated in figure 4, with often extensive rams extending outward from the sail. As the berg drifts south into the Labrador Sea and warmer surface waters, these rams will increase in extent as a percentage of the overall iceberg length..

The result of this is the establishment of regions of stress in the berg due to bending and shear forces. These stresses are caused by the upward buoyancy force acting on the rams. The maximum bending stress will occur along the centre line of the berg while maximum shear stress will occur along the vertical plane where the ram joins the central sail. The relative magnitudes will vary with underwater morphology and ice mechanical behaviour. Using elastic beam theory and simple iceberg geometry, estimates of shear and bending stresses due to buoyancy forces are possible. For example in the simply shaped iceberg shown in figure 4 with dimensions: length, l_W = 400m, thickness, H = 200m and breadth = 200m, maximum bending stresses will be about 0.34 MPa in a ram 25% of l_W (100m) while maximum shear stress will be about 0.24 MPa. In a ram 35% of l_W (140 m) maximum bending stress will be about 0.42 MPa with a maximum shear of about 0.33 MPa. A stress

Figure 1. Iceberg Freda. a) Immediately prior to ram separation. b) Recently separated ram partially hidden behind berg. c) Separated ram drifting off toward the right.

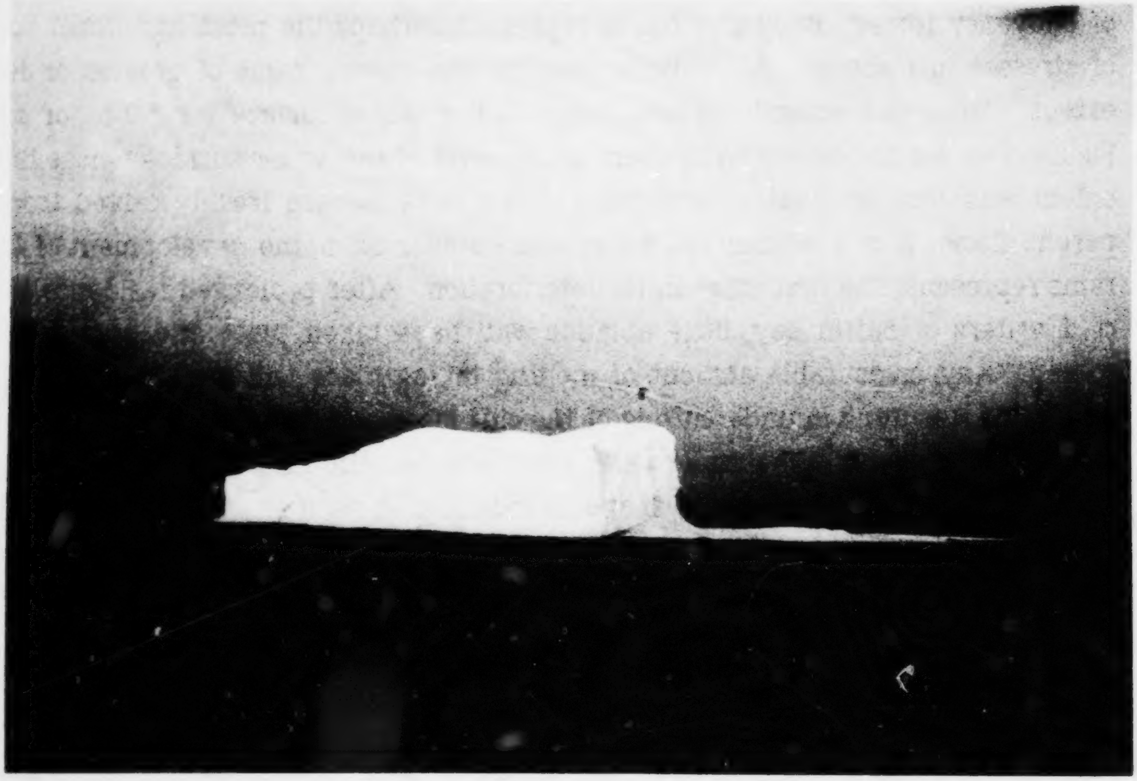

1a

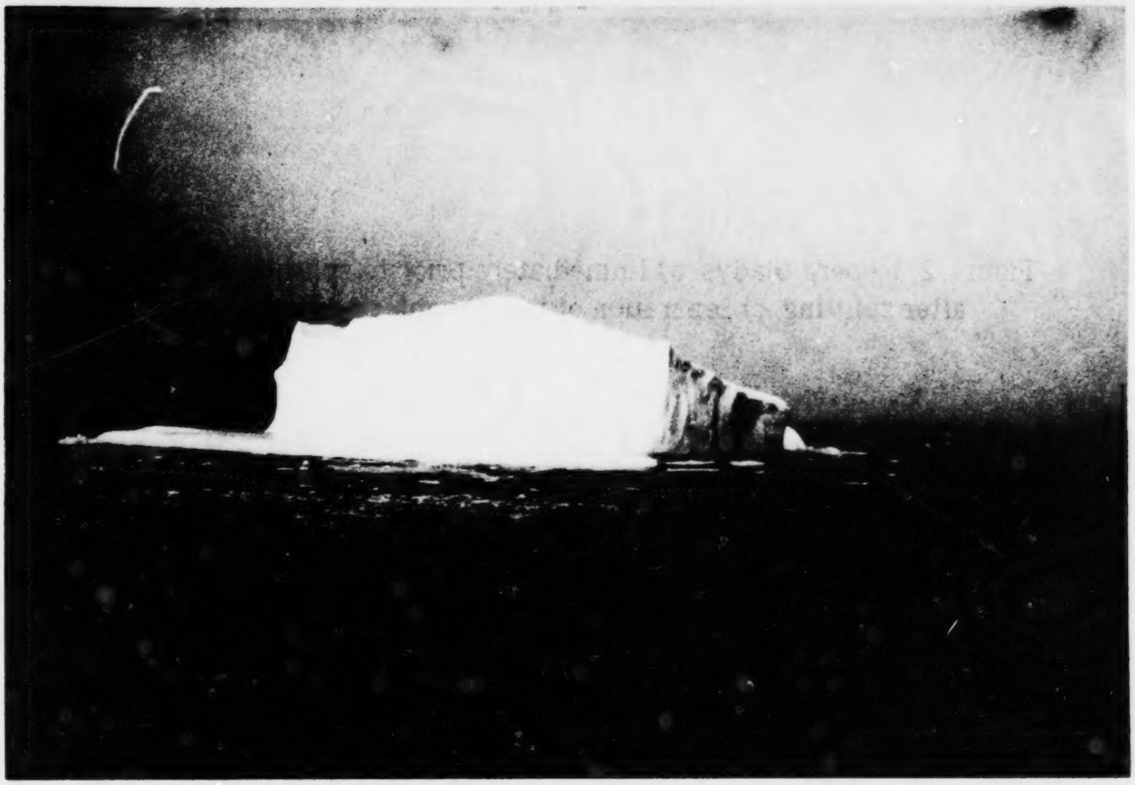

1b

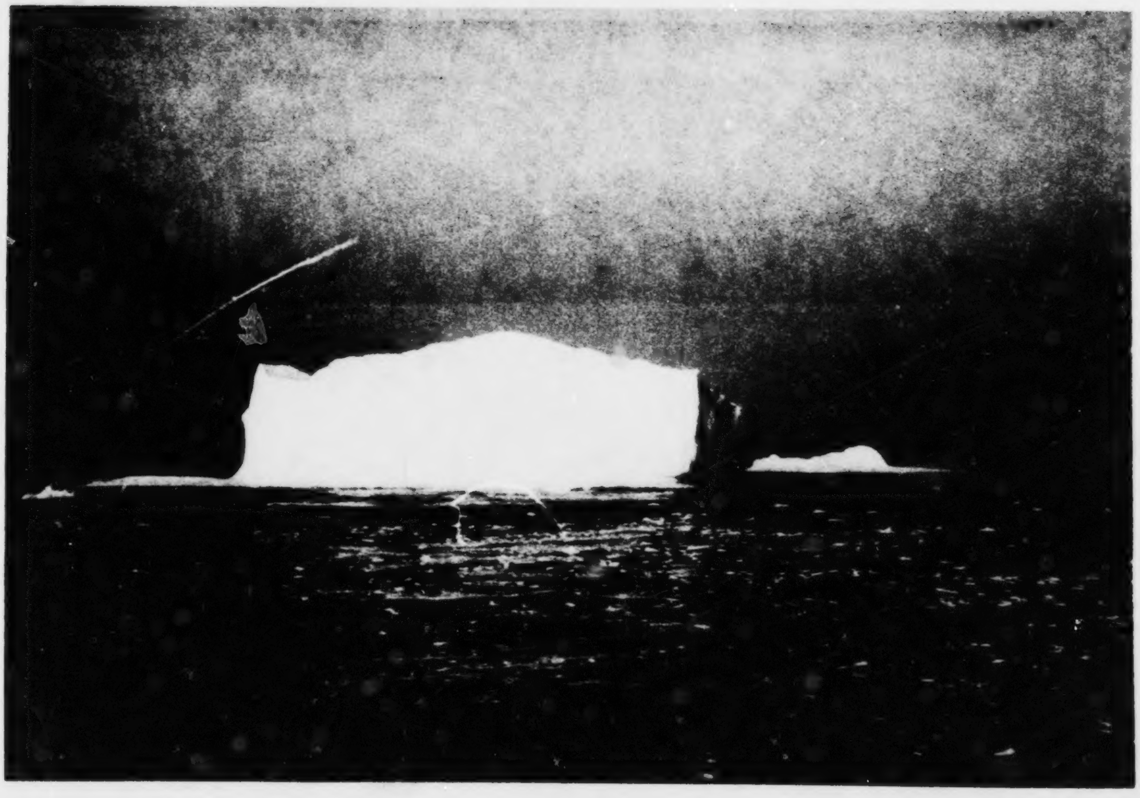

1c

Figure 2. Iceberg Gladys. a) Immediately prior to splitting. b) Immediately after splitting. c) Separation of two daughter bergs.

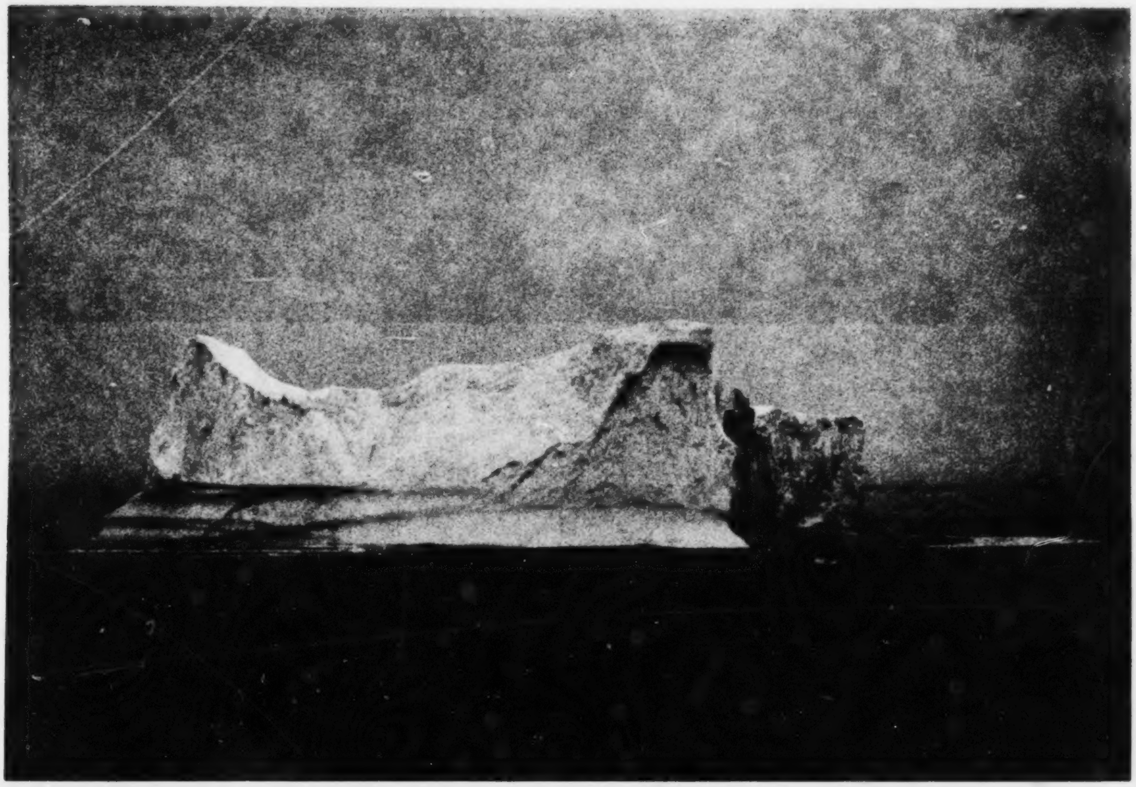

2a

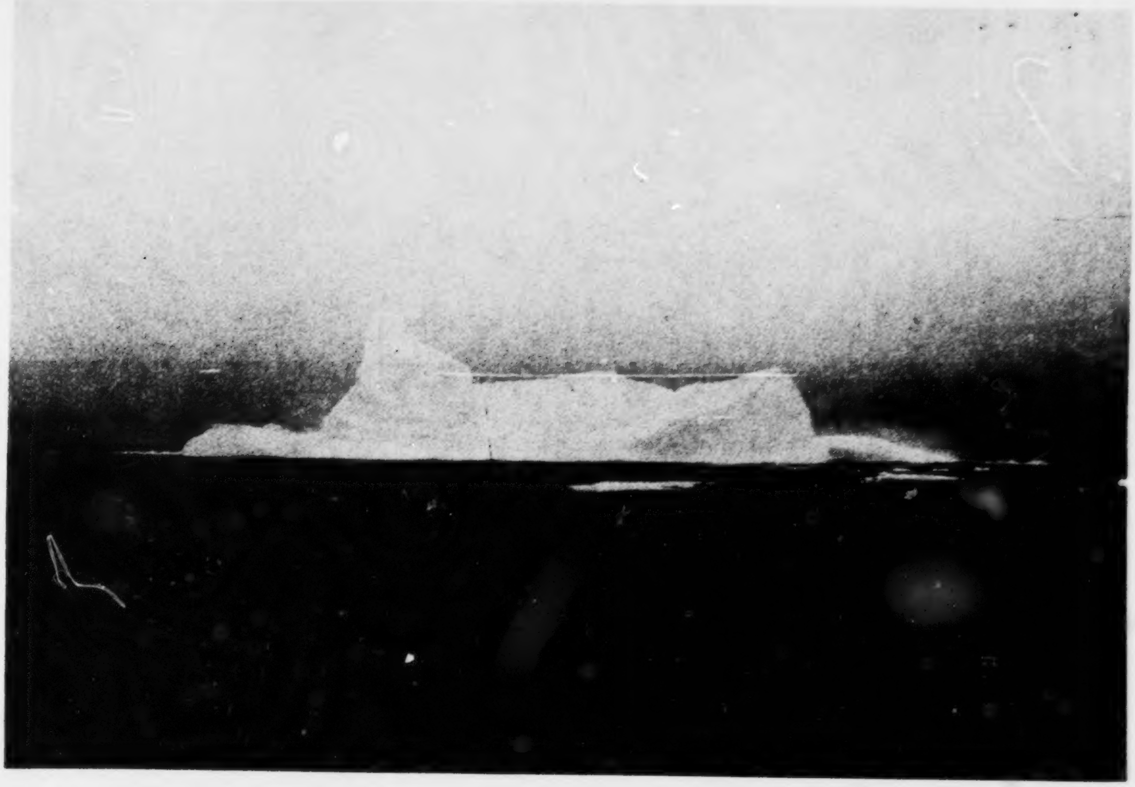

2b

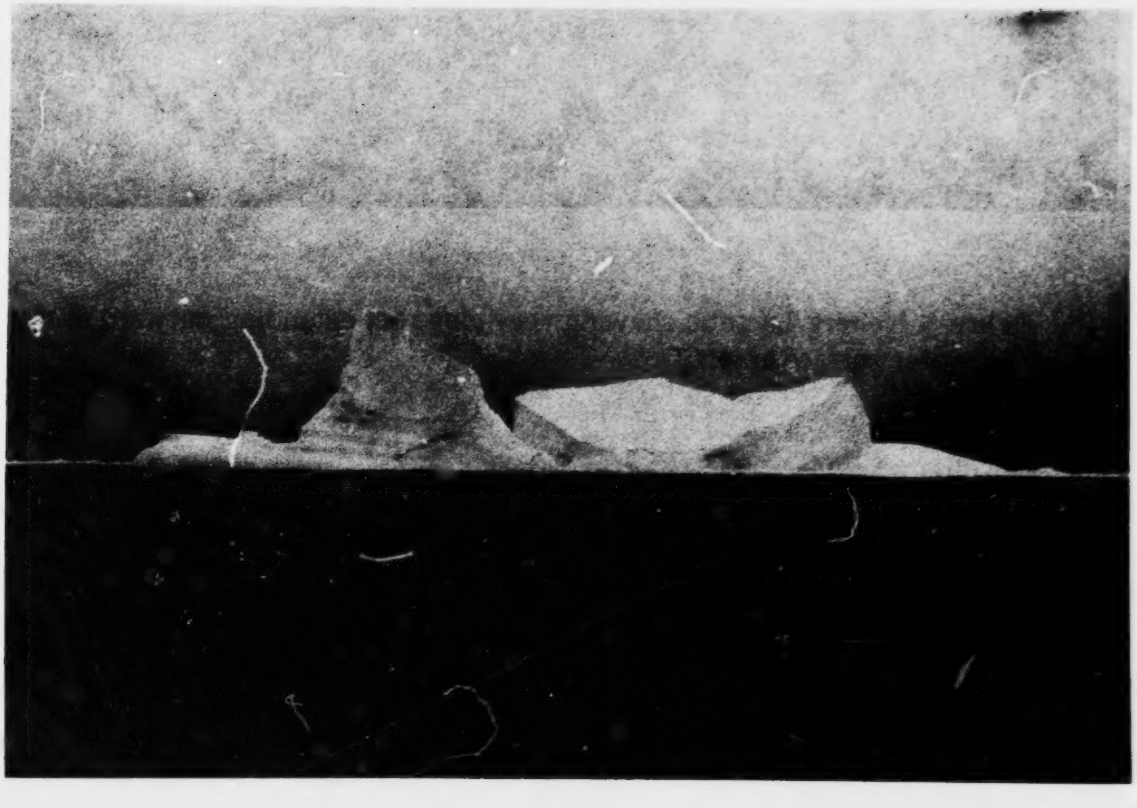

2c

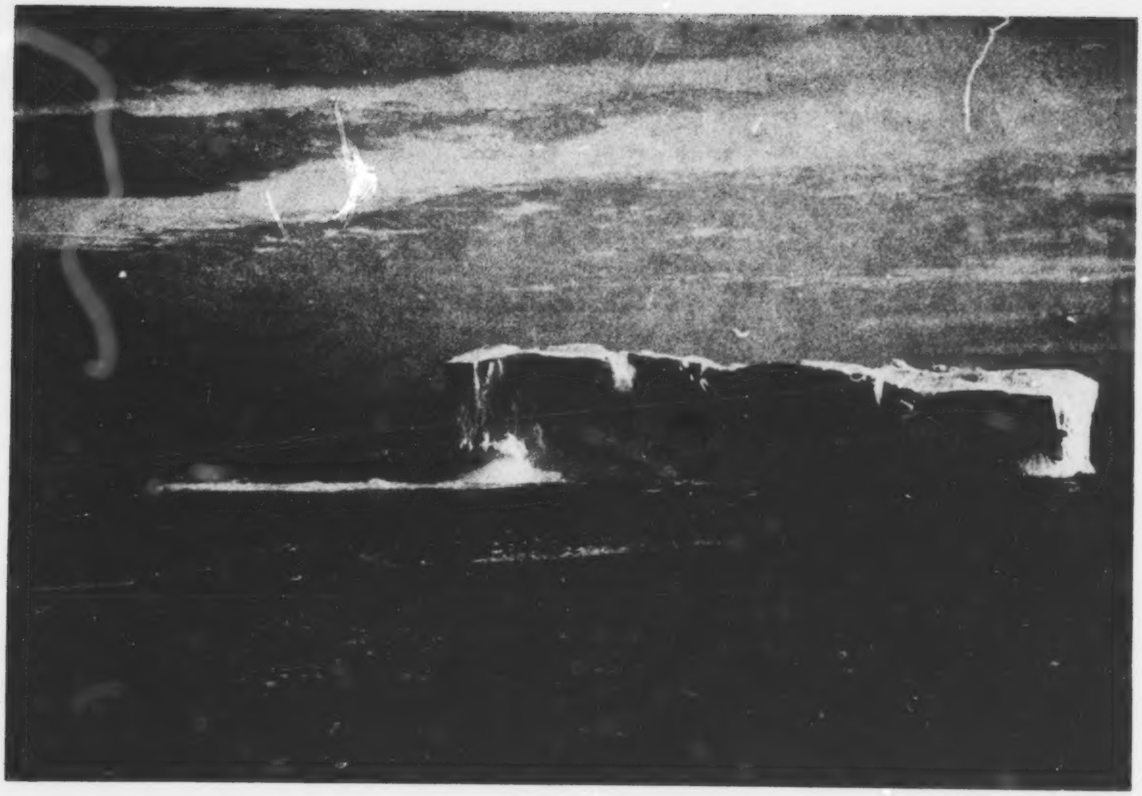

Figure 3. Iceberg Lucretia showing very long ram extending outward at the water surface at left.

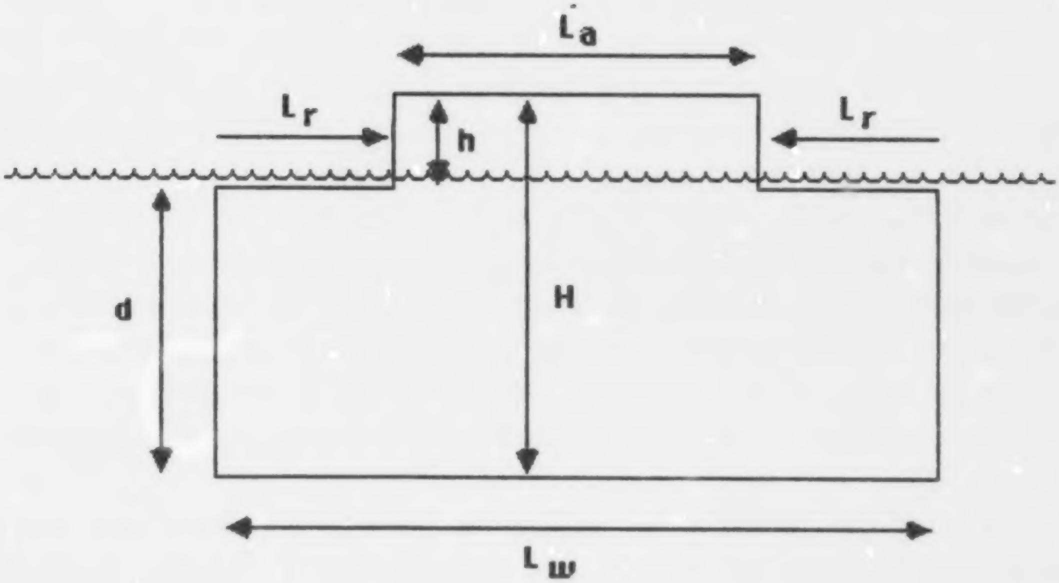

Figure 4. Schematic diagram of a partially ablated iceberg showing rams extending outward beneath the sea surface.

level of about 0.5 MPa may be sufficient to initiate tertiary creep. In addition, an ice mass of this size will almost certainly possess rehealed cracks, impurities or other areas of weakness which will facilitate crack formation/initiation. Evidence that little additional stress may be required for failure in many cases is provided by the above-mentioned major calving events in which two rams did break off and two large bergs failed virtually down the middle (Figures 1 and 2).

3. ICEBERG DETERIORATION MODELLING

These observations have important implications for the design of deterioration models, as the multiplication of icebergs is not accounted for in any of the existing models. In general, studies on the deterioration of icebergs have taken three forms: 1) laboratory model tests in which melting phenomena involved in the ablation process are studied. No estimates as to the significance of these phenomena in the overall reduction of the ice mass are given and the problem of calving is not addressed (*e.g.* Fuhs *et al.*, 1980; Josberger, 1982; Huppert, 1980). 2) large scale statistical studies on iceberg populations which focus on overall numbers or volumes of ice lost in the population in the process of iceberg drift from cold regions into warmer areas, but say nothing about the means of the loss (*e.g.* Morgan and Budd, 1978; Anderson, 1971). 3) theoretical studies of calving of icebergs and glaciers based on known mechanical and materials properties of ice in general (*e.g.* White *et al.*, 1980; Iken, 1977). These provide some useful input as they strive to discover, directly or indirectly, the mechanisms involved in the removal of masses of ice of various sizes, but cannot assess the relative importance of these mechanisms in iceberg reduction. Several operational models have been developed based on two or more of these model types (*e.g.* Anderson, 1983; Fenco, 1983), however, none have addressed the important issue of multiplication of icebergs due to large-scale splitting.

To investigate the influence of splitting on iceberg population and mass distributions, a statistical model must be used, since splitting is a ramdom event. A simple Monte Carlo simulation was developed at C-CORE whereby icebergs could be selected from an initial mass distribution and allowed to drift south from Davis Strait to the Grand Banks. Mass loss was assumed to be proportional to the product of a series of environmental factors reflecting average monthly fluctuations in sea surface temperature and the presence or absence of sea ice. Since wave erosion has been identified as the major melt mechanism (Anderson, 1983), mass loss was also assumed to be proportional to iceberg circumference. Using the available data on observed iceberg deterioration rates (Fenco, 1983), the constant of proportionality was calculated.

As each berg was allowed to drift south, splitting was randomly permitted with a varying probability of occurance depending on mass loss factors; the higher the mass loss for a given berg, the greater its chances of splitting. The rate of splitting could be changed from run to run to investigate its influence on population and mass distributions at various latitudes.

While the model is still in the early stages of development, it appears that iceberg splitting repopulates the smaller size categories which have become depleted through normal ablation. If no splitting is permitted, large icebergs (greater than say 5 million tonnes) will arrive on the Grand Banks having undergone very little percentage mass loss while the more numerous smaller bergs will have been eliminated. This would lead to an underestimation of the total population and an overestimation of the median iceberg size. On the other hand if a very high rate of splitting is permitted, all bergs will be reduced to such an extent that both total population and median size will be underestimated. An intermediate rate of splitting may best be estimated by starting with scarce observations, then fine tuning to match measured population and mass distributions.

The interplay between splitting and ablation leads to a potentially useful implication for seasonal iceberg forecasting: the number of bergs expected on the Grand Banks is most significantly influenced by the number of large icebergs entering the Labrador Current via Davis Strait. Each of these large bergs will likely account for many smaller ones through a combination of splitting and ablation, while smaller bergs in the initial distribution will not as easily complete the journey south due to these same effects. Thus, a knowledge of the numbers of very large icebergs present off northern Labrador or Davis Strait may be sufficient to predict with some degree of accuracy the numbers to be expected on the Grand Banks say six to eight months later.

References:

ANDERSON, C. (1971) The flow of icebergs along the Canadian east coast. Procedings of the Canadian Seminar on Icebergs, December 6-7, 1971, held at Maritime Command Headquarters, Halifax, Nova Scotia.

ANDERSON, I. (1983) Iceberg deterioration model, U.S. Coast Guard Bulletin No. 69. Report of the International Ice Patrol Service in the North Atlantic Ocean. Appendix C.

Fenco Newfoundland Ltd. (1983) Development of an Operational Iceberg Deterioration Model. Report to Canadian Atmospheric Environment Service.

FUHS, A.E., STOLFI, R., ERMAN, R. CLIFFORD, W., DENNER, W., WANG, P., BOURKE, R., & GRIFFIN, O. (1980) Experiments involving melting of a large ice block towed in sea water. *Cold Regions Science and Technology* 1:249 - 264.

HUPPERT, H.E. (1980) The physical processes involved in the melting of icebergs. *Annals of Glaciology* 1: 97 - 101.

IKEN, A. (1977) Movement of a large ice mass before breaking off. *Journal of Glaciology* 19: 595-60.

JOSBERGER, E.G. (1982) One peculiar ice-melt pattern explained, another peculiar pattern observed. Letter to the Editor In *Journal of Glaciology* Vol. 28, No. 99, pp. 391 - 393.

MORGAN, V.I. & BUDD, W.F. (1978) The distribution, movement and melt rates of Antarctic icebergs. In *First International Conference on Iceberg Utilization* (A. Husseiny, Ed.), Pergamon Press.

WHITE, F.M., SPAULDING, M.L., and GOMINHO, L. (1980) Theoretical Estimates of the Various Mechanisms Involved in Iceberg Deterioration in the Open Ocean Environment. U.S. Coast Guard Report No. CG-D-62-80. 126 pp.

DETERIORATION OF ICEBERGS

by M. El-Tahan[1] and S. Venkatesh[2]

The paper describes a series of theoretical and field studies to estimate the deterioration of Arctic icebergs. A model to estimate mass loss rate and life expectancy is described in detail. The deterioration mechanisms considered are solar radiation, buoyant convection, forced (water and air) convection, wave erosion and calving of the resulting overhanging slab. A quantitative assessment of deterioration mechanisms is presented. Verification of the predicted mass loss is presented using published data as well as the results of a field study designed specially for this purpose. Estimates of life expectancy and percentage of 'lost' icebergs are presented as a function of their mass, latitude and month of the year and are compared with IIP observations and the results of observations made on hundreds of icebergs on the Grand Banks.

The paper also presents the results of a study carried out to investigate the effect of iceberg deterioration on the prediction of the drift of iceberg ensembles. It was found that accounting for iceberg loss due to melting significantly improved the quality of iceberg ensemble drift predictions.

[1] Fenco Newfoundland Limited, P.O. Box 8246, St. John's, Newfoundland, Canada A1B 3N4
[2] Atmospheric Environment Service, 4905 Dufferin Street, Downsview, Ontario, Canada M3H 5T4

ON THE DETERIORATION OF A GROUNDED ICEBERG

S. Venkatesh
Atmospheric Environment Service
4905 Dufferin St.
Downsview, Ontario, Canada, M3H 5T4

ABSTRACT

This paper examines the deterioration of an iceberg grounded outside St. John's Harbour in Newfoundland, Canada, in terms of its initial velocity prior to grounding. Theoretical expressions for the lifting of the iceberg and hence its buoyancy loss during grounding are derived as a function of initial iceberg velocity and ocean bottom slope.

Wave erosion and calving, among others, are two of the most significant mechanisms for iceberg deterioration. With wave erosion occurring on the seaward side of the grounded iceberg, model simulations are compared with observational data from a field study conducted on the grounded iceberg between June 10 - 17, 1983. Model simulated time of refloatation of the iceberg agrees with observations, for initial iceberg velocity of 0.3 - 0.5 m/s. Model simulations of the deterioration of the iceberg beyond the point of refloatation are also compared with observations. Allowing for a ten percent error in the observed above-water volume of the iceberg on June 10, the model simulated mass losses are in good agreement with observations. Best results are obtained for the model initialized with data observed on June 14, 1983, the first day for which detailed observational data are available following refloatation of the iceberg.

INTRODUCTION

In a recent paper, Venkatesh et al. (1985) examined the deterioration of two icebergs that were grounded just outside the harbour at St. John's, Newfoundland. The field study, carried out over a two week period in June, 1983, was described and the observed deterioration compared with simulations from the iceberg deterioration model of EL-Tahan et al. (1984). For the first iceberg, which had an initial mass of about 1.6 million tonnes, the model simulated deterioration over a thirteen day period was in good agreement with observations. However, for the second iceberg, with an initial mass of about 0.8 million tonnes, there were some large differences between model simulated and observed deterioration. A significant portion of this difference occurred between June 10 and June 14 with the difference between observed and model-simulated mass being over 30% of the observed mass on June 14. The possible reasons for this difference, as noted by Venkatesh et al. (1985), included (i) the errors in estimates of mass loss due to deterioration introduced by the change in orientation of the iceberg between June 10 and June 14 and (ii) mass losses possibly caused by deterioration mechanisms not accounted for in the model (e.g. thermal cracking).

The objective of this paper is to examine the implications and impact of the orientation change on the deterioration of the iceberg. Formulations of the lifting of the iceberg during grounding are derived as a function of the initial velocity of the iceberg. Deterioration of the grounded iceberg in light of the lifting is examined. Model simulations of the time for refloatation of the iceberg are compared with observations. Deterioration of the iceberg beyond the point of refloatation is also examined.

DETERIORATION OF A FLOATING ICEBERG

The important mechanisms influencing the deterioration of an iceberg (see White et al. (1980)) include solar insolation, buoyant vertical convection, forced convection in air and water, wave erosion and calving of the resulting overhanging ice slabs. While the other terms are self-explanatory, buoyant vertical convection is the result of temperature and salinity differences between the iceberg melt water and the sea water. EL-Tahan et al. (1984) have shown that for a floating iceberg wave erosion and calving together account for more than 80% of the total mass loss. Iceberg waterline melt rate V_{mw} per °C of water temperature due to wave erosion is a function of the mean height H and period P of the waves and the roughness height R of the iceberg surface. It is given by the relationship

$$V_{mw} \times P/H = 0.000146\ (R/H)^{0.2}\ . \qquad (1)$$

Calving of the overhanging slab (overhang being caused by wave erosion) occurs when the overhang exceeds a critical length F_ℓ depending on the wave height and thickness of the overhanging slab. The failure length F_ℓ is given by

$$F_\ell = 0.33\ (37.5H + t^2)^{1/2} \qquad (2)$$

where all lengths are in meters.
These and other deterioration mechanisms are described in detail in EL-Tahan et al. (1984).

Application of the model to the deterioration of two icebergs grounded outside St. John's harbour in Newfoundland has been described in detail by Venkatesh et al. (1985). In that study the masses of the icebergs were computed from stereophotos of the above water portion of the icebergs and the density of the iceberg. In those calculations it was implicitly assumed that the iceberg velocity prior to grounding and hence the lifting of the iceberg during grounding was negligible. Thus the ratio of above water to under water mass of the iceberg was known, it being a direct function of the ice and sea water densities. The assumption also implies that, as the iceberg deteriorates, it will re-adjust to maintain the above-water to under-water mass ratio. If the iceberg is large, as was the case with one of the icebergs in the St. John's field study, the mass loss in short periods of time of the order of a few days will be a relatively small fraction of the total mass. This will require only a small re-adjustment in the floatation of the iceberg and depending on the ocean bottom slope and the forces moving the iceberg, it can remain grounded in the same area with no perceptible change in location. If, on the other hand, the initial grounding velocity was not negligible, computations of the total mass of the iceberg using only the above water mass and ice/sea water densities would have been in error.

THE PROCESS OF ICEBERG GROUNDING

For the smaller iceberg from the St. John's field study pairs of aerial stereophotos were taken on four different days and one photograph from each pair is shown in Figure 1. One notes from Figure 1 that the orientation of the iceberg changed between June 10 and June 14. This is apparent from the fact that the bay-like feature which was on the south east side of the iceberg on June 10 shifted to the south by June 14 and remained there for the rest of the observation period. This change must have been the result of the iceberg refloating (or almost coming to the point of refloating) sometime during that four day period. In order to calculate the deterioration of the grounded iceberg prior to refloating, we need to estimate the amount of lift of the iceberg during initial grounding.

A free floating iceberg drifting with a constant velocity is in a steady state with respect to the driving currents. When such an iceberg grounds in shallow water its kinetic energy E_k is converted to potential energy E_p with some loss due to bottom friction (E_b). In addition, as the iceberg decelerates, the relative velocity between the decelerating iceberg and the propelling current creates a force which tends to drag the iceberg further. (A similar force for the above water portion of the iceberg is negligible). If E_d is the work done by this force the energy balance of a grounding iceberg may be expressed by the relationship

$$E_k + E_d = E_p + E_b \quad (3)$$

The parameterization of each of the terms in Eq. (3) is discussed below.

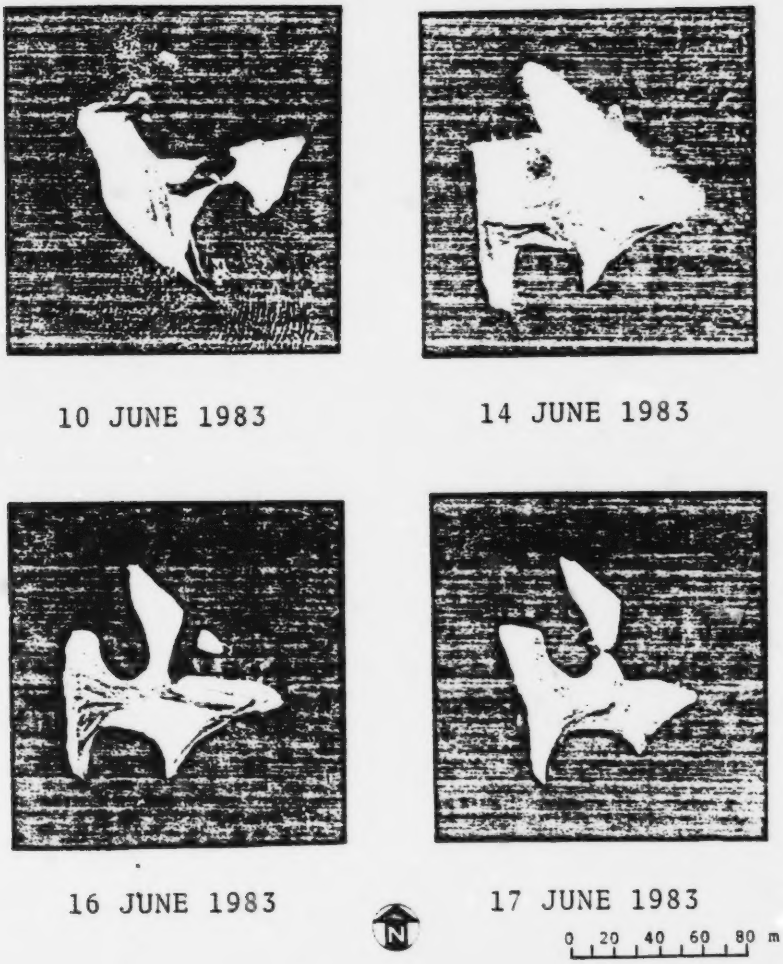

10 JUNE 1983

14 JUNE 1983

16 JUNE 1983

17 JUNE 1983

Figure 1. Aerial photo (from a stereo pair) of iceberg grounded outside St. John's harbour, Newfoundland (from Venkatesh et al., 1985). North is indicated in figure.

The net vertical force F_T acting on a floating iceberg is given by

$$F_T = F_b + F_g = 0 \tag{4}$$

where F_b and F_g are the buoyancy and gravitational forces respectively. Using the standard parameterizations of the two forces, Eq. (4) may be written as

$$F_T = V_u \rho_w g - V_t \rho_i g \tag{5}$$

where V_u and V_t are the under-water and total volume of the iceberg respectively, ρ_w and ρ_i the densities of sea water and glacier ice and g the acceleration due to gravity. Let A be the average cross-sectional area of the iceberg in the horizontal and S and L lengths such that $V_u = SA$ and $V_t = LA$. Then for a small displacement of the iceberg, the work done or the change in potential energy dE_p may be written as

$$dE_p = F_T dS = A\ g\ [\rho_w S - \rho_i L]\ dS. \tag{6}$$

Let ΔS be the net lift of the iceberg upon grounding. Then the change in potential energy of the grounded iceberg can be obtained by integrating Eq. (6). This gives

$$E_p = \int_S^{S+\Delta S} Ag\,[\rho_w S - \rho_i L]\,dS$$

$$= (AS\rho_w g - AL\rho_i g)\,\Delta S + \frac{1}{2} Ag\rho_w(\Delta S)^2 \,. \qquad (7)$$

With the coefficient of the ΔS term identically equal to zero Eq. (7) simplifies to

$$E_p = \frac{1}{2} Ag\rho_w\,(\Delta S)^2 \,. \qquad (8)$$

For small ΔS, A in Eq. (8) equals the horizontal cross sectional area of the iceberg at the water line and will henceforth represent that value.

The work E_d done by the drag force of the water current on the decelerating iceberg may be written as (see Chari, 1979)

$$E_d = \frac{C_d \rho_w A_p L_s V^2}{6} \qquad (9)$$

where C_d is the drag coefficient, A_p is the projected area of the submerged portion of the iceberg normal to the driving current, L_s is the length of scour on the ocean bottom and V is the initial steady state velocity of the iceberg. The scour length L_s is the distance over which the drag force is in effect.

The kinetic energy E_k of the free floating iceberg prior to grounding can be written as

$$E_k = 1/2MV^2 \tag{10}$$

where M is the mass of the iceberg. Assuming the ratio of the density of sea water to that of glacier ice to be 8/7 (ρ_w = 1.017 tonnes/m^3, ρ_i = 0.89 tonnes/m^3) the mass of the iceberg may also be written as

$$M = 7\rho_w(h-\Delta S)A \tag{11}$$

where h is a height such that hA equals the observed above water volume of the grounded iceberg. $(h-\Delta S)A$ then represents the above water volume of the free floating iceberg prior to grounding since ΔS is the amount of lift upon grounding.

The energy loss E_b due to bottom friction is a function of the shear characteristics, in particular the shear strength, of the ocean bottom. Chari et al. (1980) classify iceberg grounding into four categories ranging from horizontal ploughing where the ocean bottom is comprised of very weak sediment, to full uplift where the ocean bottom is highly consolidated or nearly rock. They also note that in the latter case there is essentially no energy loss due to bottom friction and iceberg grounding will result in a travel of the iceberg up the slope till the available energy is converted to potential energy.

The ocean bottom in the vicinity of the grounded iceberg in question in the St. John's field study is made up of solid bed rock (Newfoundland Design Associates Ltd., 1982). Hence during the grounding of the iceberg, energy loss E_b due to bottom friction can be assumed to have been negligible and set equal to zero.

Using the expressions derived above for the various terms, Eq. (3) may be written as

$$\frac{7}{2}\rho_w(h-\Delta S)AV^2 + \frac{C_d\rho_w A_p L_s V^2}{6} = \frac{1}{2}Ag\rho_w(\Delta S)^2 . \qquad (12)$$

Dividing Eq. (12) by A and re-arranging we get

$$g(\Delta S)^2 + 7V^2\Delta S - (7h + \frac{C_d A_p L_s}{3A})V^2 = 0 . \qquad (13)$$

With no bottom friction and full uplift of the iceberg, ΔS will equal m L_s where m is the slope of the ocean floor. With $L = \Delta S/m$ Eq. (13) becomes

$$g(\Delta S)^2 + (7V^2 - \frac{C_d A_p V^2}{3Am})\Delta S - 7hV^2 = 0 . \qquad (14)$$

From Eq. (14) ΔS can be determined if all the other parameters are known. For small ΔS the buoyancy loss B_ℓ due to iceberg lift is given by $\rho_w A\Delta S$.

DETERIORATION OF A GROUNDED ICEBERG

In the case of a freely floating iceberg subjected to deterioration, there is continuous change in the position of the iceberg with respect to the water surface. At any given time the ratio of under-water volume to total volume of the iceberg is equal to the ratio of density of glacier ice to density of sea water. Thus from a knowledge of the above water volume of the iceberg, the total volume can be computed. And mass loss over a given period of time can be calculated from changes in the above water mass of the iceberg.

However, when an iceberg is lifted up as a result of grounding there is no continuous adjustment as it deteriorates further. All the deterioration mechanisms described earlier are however still effective. In the grounded position the weight of the iceberg acting downwards is greater than the buoyancy force acting upwards. Deterioration proceeding in both the above-water and under-water portions of the iceberg, the iceberg will refloat when the net buoyancy loss due to lifting of the iceberg and deterioration under water becomes equal to the total loss in the weight of the iceberg. Comparison with observations of the time to refloat can be used as a measure of the effectiveness of the model in predicting the deterioration of a grounded iceberg. Once the iceberg becomes ungrounded, depending on the prevailing water currents and winds it can drift into deeper water or be grounded again in shallower waters. In the latter case unless the iceberg has sufficient time to reach a speed close to that of the prevailing water currents, the kinetic energy available for regrounding will be small and hence the lift of the iceberg upon regrounding will also be small. In general, if regrounding occurs very close to the location of initial grounding, regrounding forces would be small. For the iceberg in question in the St. John's field study, based on the fact that there was no significant change in the location, as opposed to orientation, of the iceberg between June 10 and 14, one may conclude that the iceberg refloated only momentarily before grounding again. Thus the velocity attained by the iceberg would have been small and one could assume that the force exerted during regrounding was negligible compared to that during the initial grounding.

For the grounded iceberg deterioration at the water line is caused by wave erosion. Above the water line the mechanisms at play include insolation, forced air convection and calving of the overhang caused by wave erosion. Below the water line the main deterioration mechanisms are forced water convection and buoyant convection.

As shown by earlier studies (EL-Tahan et al., 1984) wave erosion is the most important deterioration mechanism, accounting for over 65% of total mass loss. With the iceberg grounded fairly close to shore wave erosion will be mostly confined to that half of the iceberg facing the waves. Also erosion effects will not be fully realized near the edges of the iceberg. Hence we will assume that the effective length over which wave erosion takes place is 80% of one half the perimeter of the iceberg. The impact of these assumptions will be examined later in the paper.

OBSERVATIONAL DATA

Observational data collected in respect to the St. John's field study can be classified into iceberg related data, meteorological data and oceanographic data. Among iceberg related data, the above water iceberg dimensions were obtained from aerial stereophotos taken on several days. The iceberg parameters extracted from these photos included waterline perimeter, maximum length, width and height of the iceberg, above water volume of the iceberg and the horizontal cross-sectional area at the waterline. The last two were obtained by establishing a cross-sectional grid for each stereo pair, the grid being spaced to take into account major elevation changes on the iceberg. Further details of the iceberg dimension calculations are given in Venkatesh et al. (1985). Other iceberg related data included depth soundings near the iceberg (an indicator of iceberg draft) and side scan sonar profiles of the iceberg. The quality of the side scan data was such that only the general under water shape of the iceberg could be determined from them. The profiles for the iceberg in question indicated that the iceberg had nearly vertical sides. Thus the underwater surface area, required in the computation of forced water and buoyant convection mass losses, is taken as Ld where L is the iceberg perimeter at the waterline and d the depth of 0°C water temperature below which there is no melting of the ice. Iceberg parameters measured and required as input to the deterioration model are shown in Table 1.

The meteorological data consisted of wet and dry bulb air temperatures, barometric pressure, wind speed and direction, sky condition and visibility. Details on the measurement of these parameters are given in Venkatesh et al. (1985).

TABLE 1: Iceberg parameters estimated from stereophotos. Table also lists other parameters required as input by the deterioration model of EL-Tahan et.al. (1984). All dates are in June 1983.

Day/Time (GMT)	10/1424	14/1710	16/1244	17/1025
Maximum Length (m)	134	131	130	107
Maximum Height (m)	42	25	26	27
Maximum Width (m)	127	109	91	97
Waterline Perimeter (m)	460	571	533	525
Waterline Cross-Sectional Area (m^2)	9,068			
Above Water Surface Area $(m)^2$	11,500			
Under Water Surface Area* $(m)^2$	12,875			
Vertical Component of under water Surface Area* $(m)^2$	12,875			
Above Water Volume (1000 m^3)	116	65	46	38
Total Mass** (1000 tonnes)	826	463	328	271

*Above depth of 0°C water temperature.

**Computed from above water volume assuming that iceberg is floating.

Observations of oceanographic parameters relevant to iceberg deterioration consisted of sea surface temperature, sea temperature profiles, wave height and period and ocean currents. Again, further details on the measurement of the above parameters are given in Venkatesh et al. (1985). Ocean bottom characteristics in the vicinity of the iceberg have been discussed earlier in the paper. From hydrographic charts the ocean bottom slope at the location of the iceberg is estimated to be 30 m in 2.5 km or 1 in 83.3. The meteorological and oceanographic conditions required as input to the iceberg deterioration model are given in Table 2. And as discussed in Venkatesh et al. (1985) a mean water current of 0.1 m/sec was used in the computation of mass losses due to forced water convection.

The one piece of data that is not available but required to estimate iceberg lift upon grounding is the velocity of the iceberg prior to grounding. In the absence of this data we will need to determine the initial velocity or the range of velocities for which the model simulated time of iceberg refloatation agrees with that observed. The initial velocity or velocities thus determined will then need to be validated through other means.

The date of refloatation of the iceberg, which in this case is indicated by a significant change in its orientation, was determined from daily polaroid photos of the north, south, east and west faces of the iceberg. These photos were taken from the field study vessel located 230 m (1/8 n.m) from the iceberg. The time of refloatation of the iceberg could have been determined more accurately if the photographs had been taken at more frequent intervals. However, this was not the case as the original purpose of the St. John's field study was to study the daily deterioration of the iceberg as it remained grounded.

TABLE 2: Environmental conditions at the location of iceberg for the period June 10-17, 1983

DATE	WATER TEMP (°C)		AIR	6-HOURLY VALUES												
	SURFACE	VERTICAL AVERAGE	TEMP (°C)	WAVE PERIOD (sec)				WAVE HEIGHT (m)				WIND SPEED (m/s)			
June 10	7.0	3.5	15.0	7.0	6.5	6.8	6.3	0.9	0.8	0.8	0.9	4.0	6.0	6.0	5.0
11	5.0	3.3	7.0	7.0	8.0	6.0	6.0	1.0	0.9	1.2	1.4	4.0	4.0	4.0	4.0
12	5.6	3.0	13.5	7.0	6.5	7.0	7.0	1.2	1.3	1.2	1.2	6.0	5.0	5.0	5.0
13	5.5	2.8	7.0	7.0	7.0	6.0	6.0	1.0	1.1	1.3	1.5	2.5	4.0	5.0	5.0
14	5.4	4.0	3.5	6.0	6.0	6.0	6.5	1.7	1.5	1.3	1.4	5.0	5.0	5.0	5.0
15	5.5	3.6	4.0	5.5	6.0	6.0	6.0	1.4	1.4	1.4	1.3	4.0	4.0	4.0	2.5
16	5.9	4.0	5.0	6.5	7.0	6.0	6.0	1.0	1.5	2.0	2.4	8.0	7.5	7.5	5.0
17	5.8	3.2	8.0	7.0	7.0	8.0	8.0	1.6	1.6	1.8	1.5	4.0	2.5	5.0	5.0

RESULTS AND DISCUSSION

The first task is to compute the deterioration of the iceberg while it is grounded. The aerial stereophotos indicated that there was a significant change in the orientation of the iceberg between June 10 and June 14. Polaroid photos of the iceberg taken daily showed that this shift had occurred between June 11 and June 12. Thus in the absence of a precise knowledge of the velocity of the iceberg prior to grounding, we need to determine, using the various deterioration mechanisms and the formulations for the lifting of the iceberg upon grounding, the velocity or range of velocities of the iceberg for which refloatation will occur between June 11 and June 12. Assuming the iceberg to remain grounded, Table 3a gives the daily contributions of the various mechanisms to the deterioration of the iceberg over the period June 10 - 14, 1983. The numbers in this table, as noted earlier, are based on wave erosion, and hence calving, occurring over 80% of the half of the iceberg facing the waves. Also wave erosion is split equally above and below the water line. From Table 3a it is seen that wave erosion is the most significant deterioration mechanism followed by calving and then forced water convection. Table 3b gives on a daily basis the cumulative iceberg mass loss and the buoyancy loss due to deterioration. These values are derived from the various losses listed in Table 3a.

The lifting of the iceberg upon grounding can be computed from Eq. (14) for various iceberg velocities prior to grounding. In Eq. (14) A_p is obtained as the product of the length of the iceberg at waterline and the iceberg draft given by water depth. Here we have made use of the observation that the iceberg profile under water is nearly vertical. A, the cross-sectional area of the iceberg at the waterline is obtained from

Table 3a: Above-water and under-water volume losses of the grounded iceberg due to various deterioration mechanisms. All dates are in 1983. Wave erosion is effective over 80% of the seaward half of the iceberg.

	Loss Mechanism	June 10-11	June 11-12	June 12-13	June 13-14
Volume loss Above Waterline (m^3)	Insolation	205	190	177	390
	Forced air convection	647	231	511	204
	Wave erosion	7630	6544	7837	6902
	Calving	4160	4274	4019	3962
Volume loss Below Waterline (m^3)	Buoyant convection	546	466	381	319
	Forced water convection	2747	2408	2041	1756
	Wave erosion	7630	6544	7837	6902

Table 3b: Cumulative iceberg volume/mass loss and buoyancy loss to date due to various deterioration mechanisms. All dates are in 1983.

	June 10-11	June 10-12	June 10-13	June 10-14
Berg Volume Loss (m^3)	23565	44222	67025	87460
Berg Mass Loss (tonnes)	20973	39358	59652	77839
Buoyancy loss due to deterioration (tonnes)	11109	20687	31120	40250

stereophotos. Based on earlier studies (Fenco Newfoundland Ltd., 1982) the value for the drag coefficient C_d is taken as 1.0.

Table 3c gives the cumulative buoyancy losses due to lifting of the iceberg and under-water deterioration. The buoyancy loss B_ℓ due to lifting alone is also given in the table for various initial velocities of the iceberg. Figure 2 shows a plot of the cumulative buoyancy loss and total iceberg mass loss as a function of time and for various initial velocities of the iceberg. The iceberg will refloat when the cumulative buoyancy loss becomes less than the iceberg mass loss (from Table 3b). Thus for the iceberg to refloat during the 24 hour period between June 11 - 12 as suggested by observations, its velocity prior to grounding must have been 0.4 - 0.5 m/s. With no observational data available on the drift velocities of the iceberg prior to grounding, we can only discuss the appropriateness of the above-determined velocities.

An analysis of the drift speeds of 68 icebergs in the Newfoundland/ Labrador Sea areas and the water currents associated with these icebergs was carried out by EL-Tahan et al. (1983). It was found that the icebergs generally travel in the range of 0.1 - 0.5 m/s with the velocities going outside this range about ten percent of the time. Also, correlating iceberg drift speed with water current velocities, they found that drift speeds of icebergs were about 1.5 times the water current velocity at 15 m depth and about twice that at 50 m depth. Similar correlation studies by Soulis (1976) yielded a factor of 2.5 between iceberg drift speed and water current at 13 m depth. In the St. John's field study, on June 8 current speeds of 0.045 - 0.1 m/s were measured at 15 metres and 0.09 - 0.25 m/s at a depth of 40 m. The corresponding values on June 12 were 0.08 - 0.14 m/s and 0.12 - 0.25 m/s respectively. Thus given that the

Table 3c: Cumulative buoyancy loss to date due to deterioration and lifting of the iceberg as a function of the iceberg velocity prior to grounding.

V (m/s)	ΔS (m)	B (tonnes)	Cumulative Buoyancy loss (tonnes) (Due to (Deterioration below water line + Berg lift))				Refloat date in June
			June 10-11	June 10-12	June 10-13	June 10-14	
0.60	2.354	21709	32818	42396	52829	61969	12-13
0.50	1.885	17384	28493	38071	48504	57634	11-12
0.40	1.436	13242	24351	33929	44362	53492	11-12
0.30	1.025	9452	20561	30139	40572	50702	10-11

Table 4: Same as Table 3c except wave erosion is effective over 100% of the seaward half of the iceberg.

V (m/s)	ΔS (m)	B (tonnes)	Cumulative Buoyancy Loss (tonnes)				Refloat Date
			June 10-11	June 10-12	June 10-13	June 10-14	
0.60	2.354	21709	34757	45999	58425	69309	11-12
0.50	1.885	17384	30432	41674	54100	64984	11-12
0.40	1.436	13242	26290	37532	49958	60842	11-12
0.30	1.025	9452	22500	33742	46168	57052	10-11

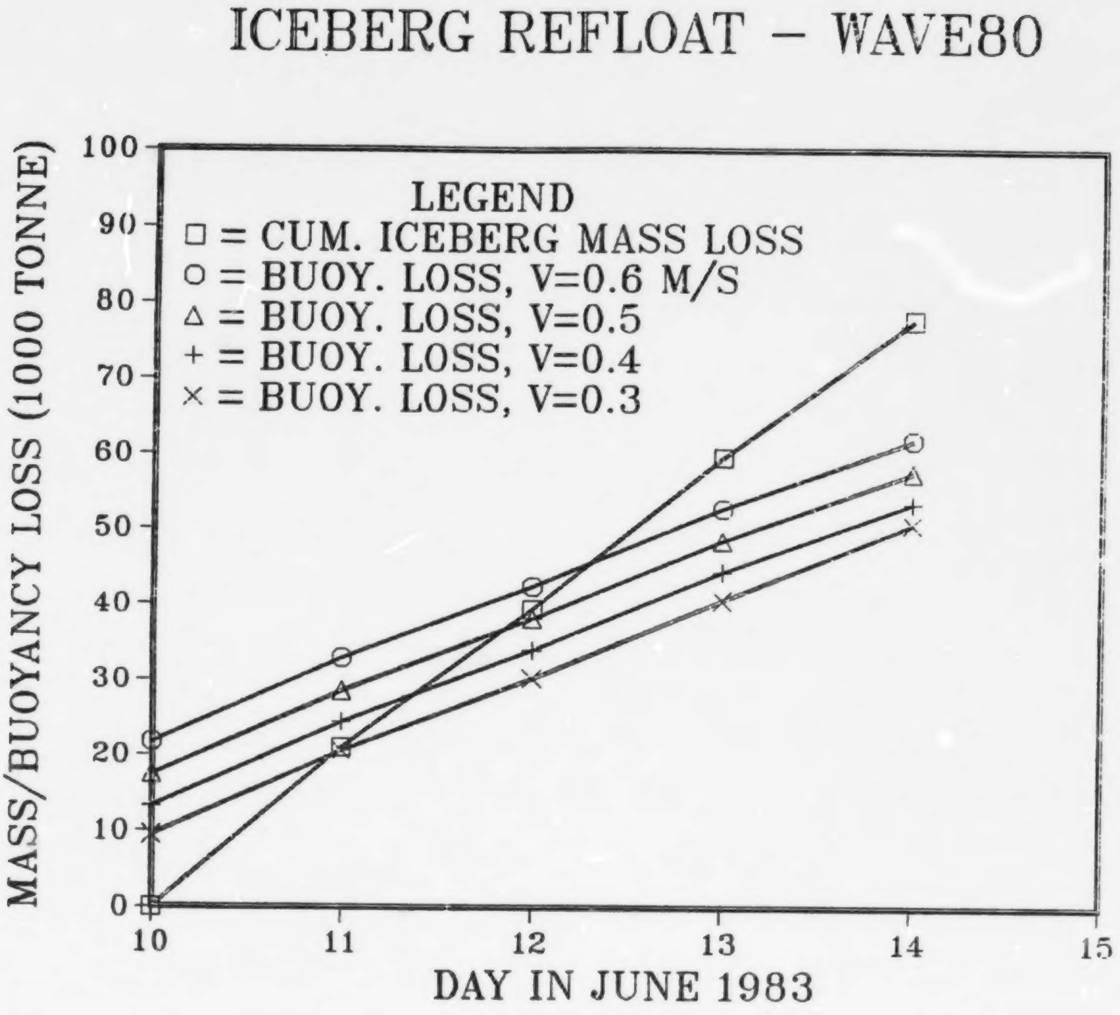

Figure 2. Cumulative mass and buoyancy losses of iceberg versus time. Buoyancy losses are given for various pre-grounding velocities of the iceberg. Wave erosion is effective over 80% of waterline perimeter on the seaward half of iceberg.

15 m currents are less than those at 40 m, one will get vastly different iceberg drift velocities if the above mentioned correlations for the two depths are used, thereby casting some doubt on the validity of these correlations. In spite of this remark if one uses a factor of 2 on the 40 m current, then iceberg drift speed of up to 0.5 m/s (corresponding to a current speed of 0.25 m/s) prior to grounding would have been possible. Thus one may conclude that the derived range of 0.4 - 0.5 m/s (see Table 3c) for the velocity of the iceberg prior to grounding is quite feasible. One may also note from tables 3b and 3c that even for a velocity of 0.3 m/s the refloating of the iceberg occurs very close to the end of the 24 hour period between June 10 - 11. Thus effectively the iceberg will refloat during the June 11 - 12 period for initial velocities in the range 0.3 - 0.5 m/s.

Table 4 and Figure 3 show the results assuming that wave erosion and calving occur over 100 percent of that half of the iceberg facing the waves. Under these conditions the iceberg will refloat during the June 11 - 12 period for pre-grounding velocities in the range of 0.4 - 0.6 m/s. For a velocity of 0.6 m/s refloatation occurs fairly late in the 24 hour period (Fig. 3). Thus in this case also refloatation of the iceberg occurs during the June 11 - 12 period for the expected range of initial velocities of the iceberg.

Having determined the time of refloatation of the iceberg, the next task is to compute its subsequent deterioration. As discussed earlier, the forces involved in re-groundings are negligible and the iceberg can be treated as a floating one in respect to its response to further deterioration. For the purpose of determining this deterioration the iceberg characteristics will be initialized to the beginning of the day on June 12,

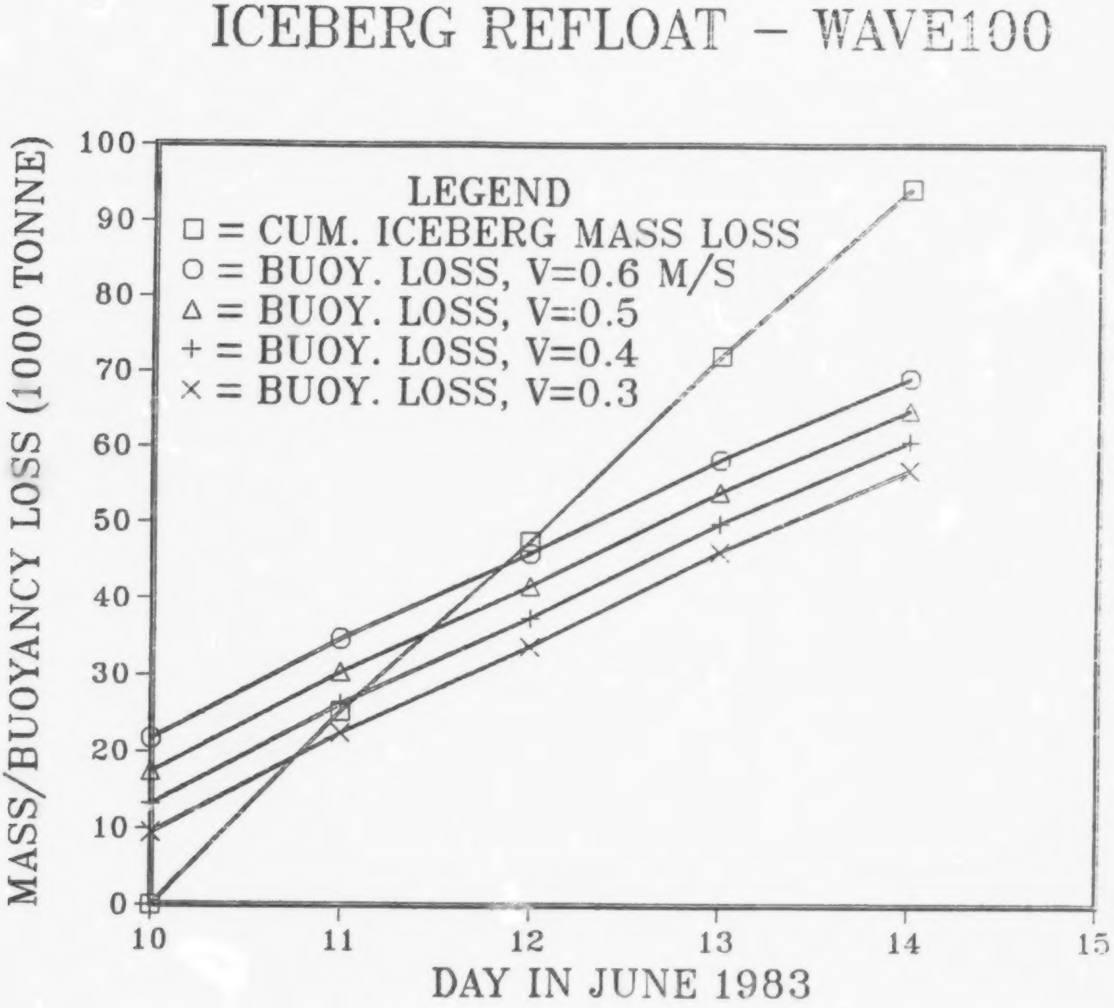

Figure 3. Same as Figure 2 but wave erosion is effective over 100% of waterline perimeter on the seaward half of iceberg.

1983. The above water volume on June 10 was known from the stereophotos (116000 m^3). The above-water volume loss for the period June 10 - 12 can be determined from Table 3a (23880 m^3). The difference is then the above water volume of the iceberg on June 12 (92120 m^3). Length and area parameters required as model input and observed on June 10 are multiplied respectively by the factors $(92.12/116)^{1/3}$ and $(92.12/116)^{2/3}$ to obtain their values corresponding to June 12. The perimeter of the iceberg at the waterline obtained in this manner is likely to be an underestimate since the observed value on June 14 was 571 m, much higher than that for June 10. It is obvious that when the iceberg refloated there was a considerable change in its orientation which resulted in a significant increase in the waterline perimeter. In the absence of a precise knowledge of the waterline perimeter after refloatation on June 12, we will use the value observed on June 14. Use of this value will lead to a lower estimate of deterioration since the waterline perimeter on June 12 was most likely higher than that on June 14. Figure 4 shows a comparison of observed and predicted iceberg mass on various dates. The predictions were obtained using the model of EL-Tahan et al. (1984). The curve marked "predicted (12 - 17)-1" is obtained with the waterline perimeter computed from the observed value on June 10 as described above. The curve marked "predicted (12 - 17)-2" is obtained using the waterline perimeter observed on June 14. Also shown in the figure is the simulation for the period June 14 - 17 obtained by initializing the model with observed data from June 14 and which agrees very well with observations.

One notes from figure 4 that the slope of the "observed" iceberg mass curve is much greater during the period June 12 - 14 than it is during the period June 14 - 17. This difference accounts for much of the

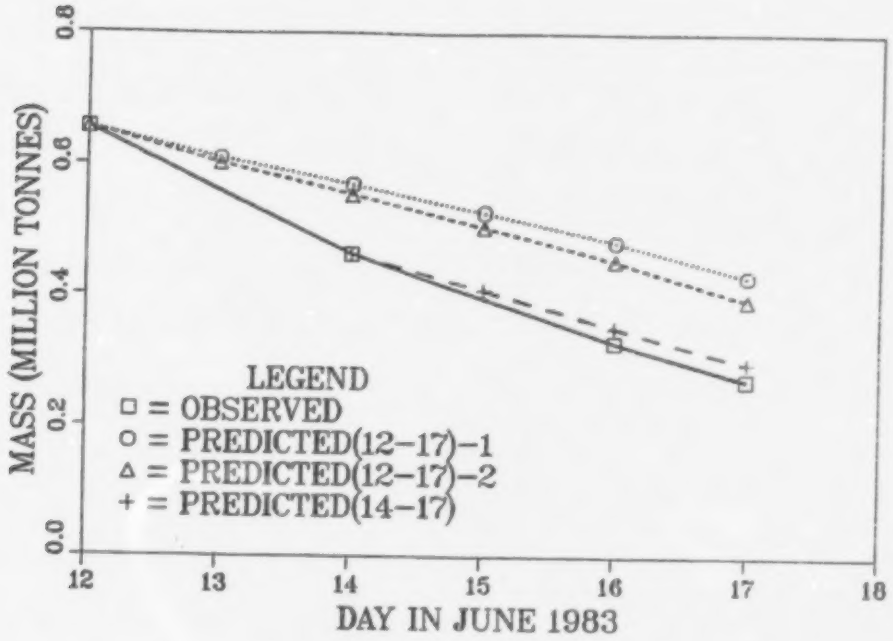

Figure 4. Observed and predicted mass reduction of iceberg following its refloatation. See text for explanation of the different curves.

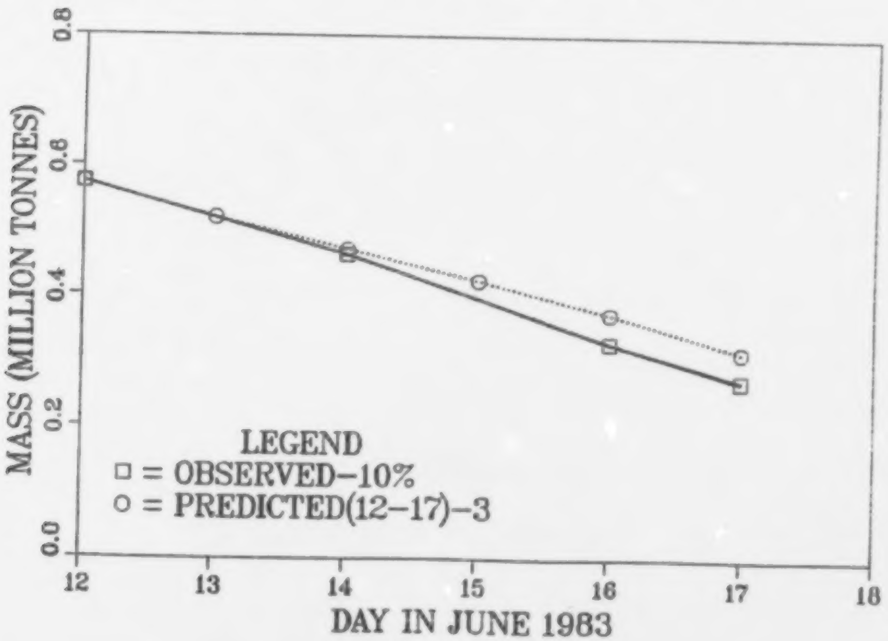

Figure 5. Observed and predicted mass reduction of iceberg following its refloatation. A ten percent overestimate is allowed for in the observed iceberg mass on June 10, 1983.

differences between the observed and model simulated iceberg mass as a function of time. With the total mass of the iceberg on June 12, when it refloats, being calculated from its above-water volume, any error in the latter is magnified eightfold. The above-water volume on June 12 is itself derived from the observed above-water volume on June 10 and above-water volume loss during the period June 10 - 12. It would be instructive to look at the results based on a 10% over-estimate in the observed above-water volume of the iceberg on June 10. All other parameters are the same as those for the curve marked "predicted (12 - 17) -2" in Figure 4. Thus the above-water volume on June 10 is 104400 m^3 and the iceberg mass on June 12, after allowing for deterioration losses is 573000 tonnes. Figure 5 shows the results of this analysis and it is clear that the results are much improved. It is also worth noting that model simulated iceberg mass on dates other than June 12 is within about 15% of the observed value.

SUMMARY AND CONCLUSIONS

In this paper the deterioration of a grounded iceberg has been described. The deterioration occurs in two stages. The first stage consists of the deterioration of the grounded iceberg up to the point of refloating. In the second stage, deterioration beyond the point of refloating is considered. In respect to the first stage expressions have been derived for the buoyancy loss of the iceberg as a result of lifting upon grounding, the amount of lift being a function of the iceberg velocity prior to grounding. A knowledge of this buoyancy loss is important in establishing the amount of mass that the iceberg has to lose before it can refloat.

The model simulations have been compared with data obtained from a 1983 field study conducted on an iceberg grounded outside St. John's harbour in Newfoundland. With no data on the pre-grounding velocity of the iceberg being available, the model derived date of refloatation of the iceberg has been compared with observed data (from daily polaroid photos of the iceberg) for a range of velocities. Other studies on correlations of iceberg velocities with water currents at different depths have been used to substantiate the iceberg velocities used. The model derived date of refloatation has been found to agree with the observed date for pre-grounding ice velocities in the range of 0.3 - 0.5 m/s. Model performance can be better evaluated with the availability of data on iceberg velocity prior to grounding as also data defining more precisely the time of refloatation of the iceberg.

In respect to the second stage, the deterioration of the iceberg has been based on the model developed by EL-Tahan et al. (1984). The model was initialized for the time of refloatation with data observed on June 10 adjusted to account for deterioration during the period in which the iceberg remained grounded.

Model results were improved with the use of iceberg perimeter at the waterline as observed on June 14. The basis for the use of this data was the apparently significant increase in the perimeter of the iceberg at the waterline at the time of refloatation. Best agreement was obtained when results from the model initialized with data on June 14 were compared with deterioration during the period June 14 - 17.

An error analysis performed indicated the need for accurate estimation of iceberg mass, particularly when it is calculated from only the above-water portion.

ACKNOWLEDGEMENTS

The author wishes to thank Mr R. Jessup, his colleague and Dr. T.R. Chari, Associate Dean of Engineering, Memorial University of Newfoundland for many useful discussions during the course of this work. The review of the original manuscript by Mrs. M. EL-Tahan and Mr. H. EL-Tahan of Fenco Newfoundland Limited is gratefully acknowledged.

REFERENCES

Chari, T.R. (1979). Geotechnical aspects of iceberg scours on ocean floors. Canadian Geotechnical Journal, Vol. 16, NO. 2, p 379-390.

Chari, T.R., Peters, G.R. and Muthukrishnaiah, K. (1980). Environmental factors affecting iceberg scour estimates. Cold Regions Science and Technology, Vol. 1, p 223-230.

EL-Tahan, M.S., EL-Tahan, H.W. and Venkatesh, S. (1983). Forecast of iceberg ensemble drift. Proceedings of the 15th Annual Offshore Technology Conference, Houston, Texas, U.S.A. May 2-5, 1983. p 151-158.

EL-Tahan, M., Venkatesh, S. and EL-Tahan, H. (1984). Validation and quantitative assessment of the deterioration mechanisms of Arctic icebergs. Proceedings of the Third International Offshore Mechanics and Arctic Engineering Symposium, New Orleans, U.S.A., Vol. III, p 18-25.

Fenco Newfoundland Limited (1982). Factors controlling iceberg drift and design of an iceberg drift prediction system. Contract report prepared for Atmospheric Environment Service, Environment Canada, Downsview, Ontario, Canada, M3H 5T4.

Newfoundland Design Associates Limited (1982). St. John's sewage disposal study, Volume II, physical environment of Freshwater Bay. Contract report prepared for the Department of Municipal Affairs, Government of Newfoundland and Labrador.

Soulis, E.D. Unpublished. Modelling of iceberg drift using wind and current measurements at a fixed station. [M. Eng. thesis, Faculty of Engineering and Applied Science, Memorial University of Newfoundland, 1976].

Venkatesh, S., EL-Tahan, M. and Mitten, P.T., (1985). An Arctic iceberg deterioration field study and model simulations. Annals of Glaciology, Vol. 6. (In press).

White, F.M., Spaulding, M.L. and Gominho, L. (1980). Theoretical estimates of the various mechanisms involved in iceberg deterioration in the open ocean environment. U.S. Coast Guard report NO. CG-D-62-80, pp 126.

TEMPERATURE, SALINITY AND DENSITY PROFILES AROUND ICEBERGS IN THE LABRADOR SEA

DAVE E. PEARSON
PETRO-CANADA RESOURCES

JANUARY 1986

INTRODUCTION

Past laboratory studies coupled with limited field work have confirmed that icebergs drifting in seawater will cool and freshen the surrounding water column (Allison 1984, Foldvik 1980, Josberger 1980). However, the nature and extent of this process must be clearly understood to model the degradation of icebergs around offshore platforms. To this end, a small survey was conducted in the Northern Labrador Sea during August 1984 to examine the local microclimate created by melting icebergs. Temperature and salinity profiles of the water column were acquired around several icebergs using a Neil Brown DRCM-2 current meter deployed from the research vessel MV Polaris V. This paper will examine the data obtained from two of these icebergs which are considered to be representative of the dataset.

INSTRUMENTATION

All temperature and salinity measurements were made with a Neil Brown DRCM-2 current meter. This instrument records the ocean current speed and direction in addition to the hydrostatic pressure, water temperature ,conductivity, ocean salinity and instrument tilt as a function of depth. The current meter was deployed in a vertical mode over the side of the Polaris V using an electric winch to raise and lower the meter in the water column and a five metre boom to minimize any localized effect of the ship. The temperature and salinity values were available in real time using a direct readout control unit onboard the vessel.

METHODOLOGY

Prior to conducting the salinity and temperature measurements around each iceberg, a control profile was obtained in an icefree region at a range of 2 kilometers from the iceberg. Wind and wave information along with barometric pressure and air temperature were recorded at the beginning of the program and every thirty minutes throughout the study. Ocean currents were not recorded during the control profiles since there there was no way for the ship to maintain position during the cast.

Following the acquisition of a control profile, each iceberg was surveyed to determine its physical size and drift trajectory. Photographs were taken at the four major compass points around the iceberg and a range finder and a sextant were used to determine iceberg size. A conductivity/temperature/depth (CTD) cast was then initiated on one of the compass headings as close to the iceberg as safety would permit. The initial observation was made at a depth of between 2 and 5 metres beneath the sea surface. Subsequent observations for the same profile were made at 10 metre intervals to a depth of about 90 metres. At each water depth the instruments were permitted to stabilize before a reading was made.

Following the acquisition of one profile , the vessel steamed outward on the same bearing to a point about 200 metres away from the initial profile. A second temperature and salinity profile was then made using the same method described above. When the profiles approximated the ambient oceanic conditions recorded by the control profile, the vessel steamed to a new compass heading and began profiling outward from the iceberg. A total of five independent surveys were conducted over a five day period. However, for this paper the results from only two of the surveys are presented. Sixteen CTD casts were made around these two icebergs. Greater detail is provided in Table 1 and 2 below.

TABLE ONE
ICEBERGS SURVEYED

Date	Location Lat/Long (deg/min)	Iceberg Number	Iceberg Length (metres)	Estimated Mass (tonnes)	Number of Sides Profiled
Aug 10	5831/6241	1	40	40000	4
Aug 14	5839/6240	4	118	700000	4

TABLE TWO
ICEBERG PROFILE INFORMATION

Iceberg Number	Side/ Orientation	Range to Iceberg (metres)	Time (GMT)	Seas (to)	Currents (from)
1	Control	1852	2230	North	-----
	1 North	82	1645	North	East
	1 North	183	1730	North	East
	2 East	12	2130	North	South
	3 South	9	1900	North	West
	3 South	183	2000	North	East
	4 West	70	1530	North	West
	4 West	183	1830	North	West
4	Control	2222	1630	South	-----
	1 East	61	1320	South	West
	1 East	137	1402	South	West
	2 South	46	1436	South	South
	2 South	275	1530	South	East
	3 West	91	2100	SE	South
	4 North	70	1700	South	West
	4 North	183	1730	South	SW

RESULTS

ICEBERG ONE: Iceberg One was a small tabular iceberg with an estimated draft of 35 metres. The iceberg was drifting freely throughout the survey with both the surface winds and the seas from the northwest. The averaged currents in the top fifty metres of the water column were oriented to the southwest. The largest temperature and salinity variance from the control profile were observed to the west and north of the iceberg on the windward side.

Figure 1 shows the temperature profile of the water column at two ranges from the iceberg. In the near surface region of the profile, the apparent warmer temperatures near the iceberg are attributed to localized surface heating between profile measurements. A comparison of the two profiles obtained near the iceberg (ie. at a range of 90 and 200 metres from the iceberg) indicate that the surface water is in fact 0.3°C colder at a range of 90 metres from the iceberg.

Beyond the surface layer, the water column near the iceberg was cooled to a depth of 30 metres. At greater depths both casts near the iceberg indicate slightly warmer conditions to a depth of 60 metres. At this water depth, both casts approach the ambient ocean conditions recorded by the control profile and become isothermal with depth.

At a range of 90 and 200 metres north of the iceberg, the maximum difference in water temperatures were 1.5°C and 1.4°C colder than the control profile. However when median temperatures are derived for the top fifty metres of the water column, water temperatures at ranges of 90 and 200 metres from the iceberg were 0.6°C and 0.4°C colder than ambient conditions. Thus, as expected the amount of cooling decreases with increasing distance from the iceberg. Assuming this influence decreases linearly away from the iceberg, the cold water influence might extend to a range of 500 metres north of the iceberg.

Figure 2 depicts the corresponding salinity profiles recorded near Iceberg One just north of the target. The surface salinity at a range of 90 metres from the

FIGURE 1

WATER TEMPERATURE PROFILE NEAR AN ICEBERG IN THE LABRADOR SEA

ICEBERG ONE - SIDE ONE LATITUDE 58 33N LONGITUDE 62 20W
PROFILE RECORDED ON AUGUST 10, 1984

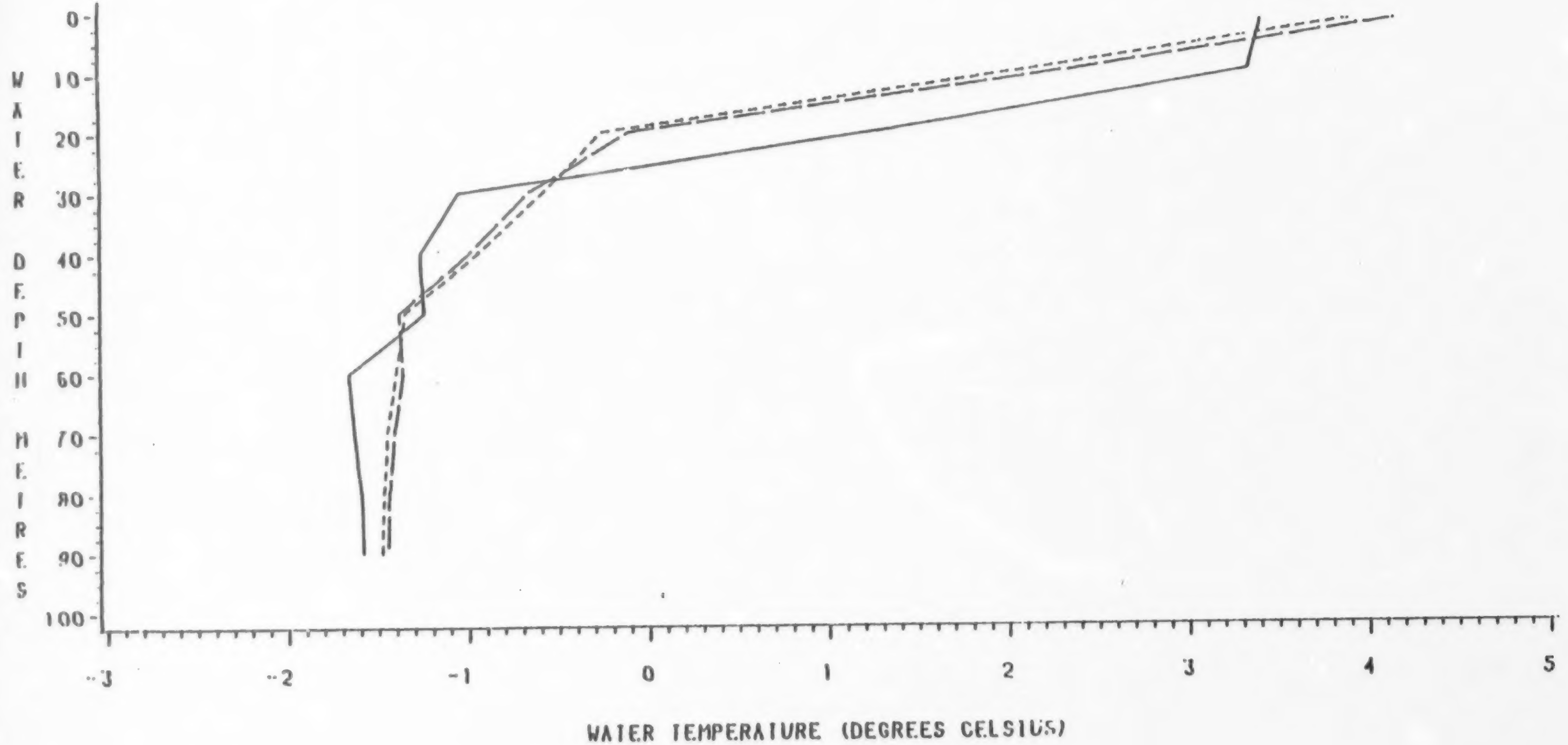

SOLID LINE = CONTROL PROFILE
DOTTED LINE = RANGE OF 90 METRES
DASHED LINE = RANGE OF 200 METRES

FIGURE 2

SALINITY PROFILE NEAR AN ICEBERG IN THE LABRADOR SEA

ICEBERG ONE - SIDE ONE LATITUDE 58 33N LONGITUDE 62 20W
PROFILE RECORDED ON AUGUST 10, 1984

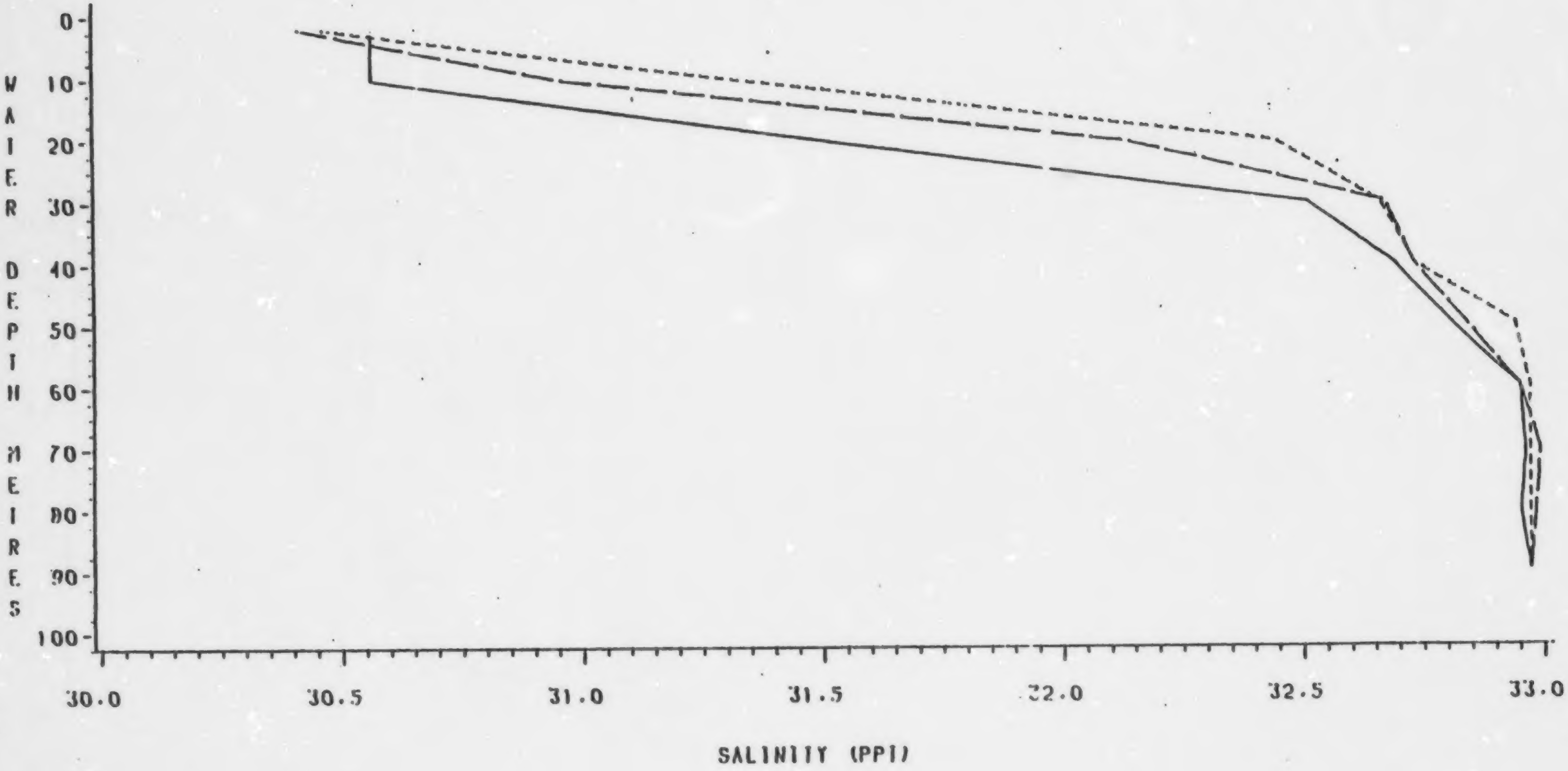

SOLID LINE = CONTROL PROFILE
DOTTED LINE = RANGE OF 90 METRES
DASHED LINE = RANGE OF 200 METRES

iceberg is roughly 0.3 ppt lower compared to the control profile. However, beyond the surface layer, the presence of the iceberg has raised the salinity of the water column to a depth of 60 metres. This increase in salinity suggests convection along the sides of the iceberg which brings colder, more saline water from depth to the surface. At a water depth of 60 metres all three salinity profiles converge and remain isothermal with depth.

Salinity profiles recorded near the iceberg show that at a range of 90 metres from the iceberg a maximum salinity increase of .92 ppt. was observed while at a range of 200 metres a maximum increase in salinity of .61 ppt. was reported. Similarly, a comparison of the median values for the two casts (90 and 200 metres) near the iceberg show that median salinities are 0.09 ppt. and 0.04 ppt. above ambient conditions. This again indicates that salinity values decrease toward ambient conditions with increasing distance from the iceberg.

Figure 3 depicts the corresponding density profiles recorded near Iceberg One. These curves are very similar to the salinity profiles of Figure 2 and indicate that the density in the upper 55 metres of the water column increases toward the iceberg. Additionally the pycnocline depth decreases toward the iceberg. This again is consistent with convection near the iceberg.

The comparison of all temperature/salinity curves for Iceberg One shown in Figure 4 indicates that the melt water plume is situated on side four, west of the iceberg. The location of the plume is consistent with the current meter measurements which indicate that the near surface current flow is to the west. The melt water plume is most pronounced in the surface layer and extends to a depth of approximately 10 metres. The surface layer (2-10 metres) is coldest next to the iceberg and warms toward ambient conditions outward from the iceberg. Simi-

FIGURE 3

DENSITY PROFILE NEAR AN ICEBERG IN THE LABRADOR SEA

ICEBERG ONE - SIDE ONE. LATITUDE 58 33N LONGITUDE 62 20W

PROFILE RECORDED ON AUGUST 10. 1984

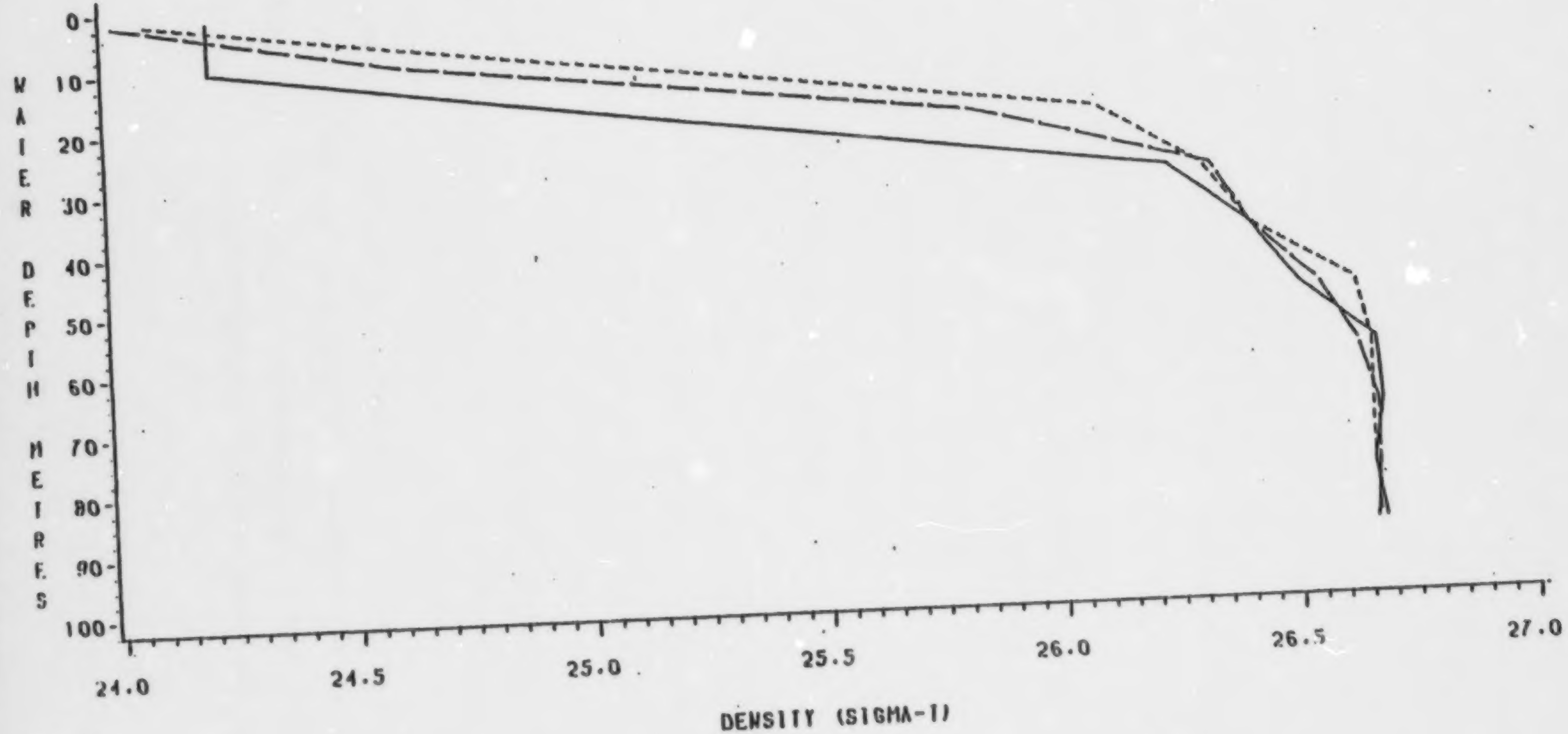

SOLID LINE = CONTROL PROFILE
DOTTED LINE = RANGE OF 90 METRES
DASHED LINE = RANGE OF 200 METRES

FIGURE FOUR

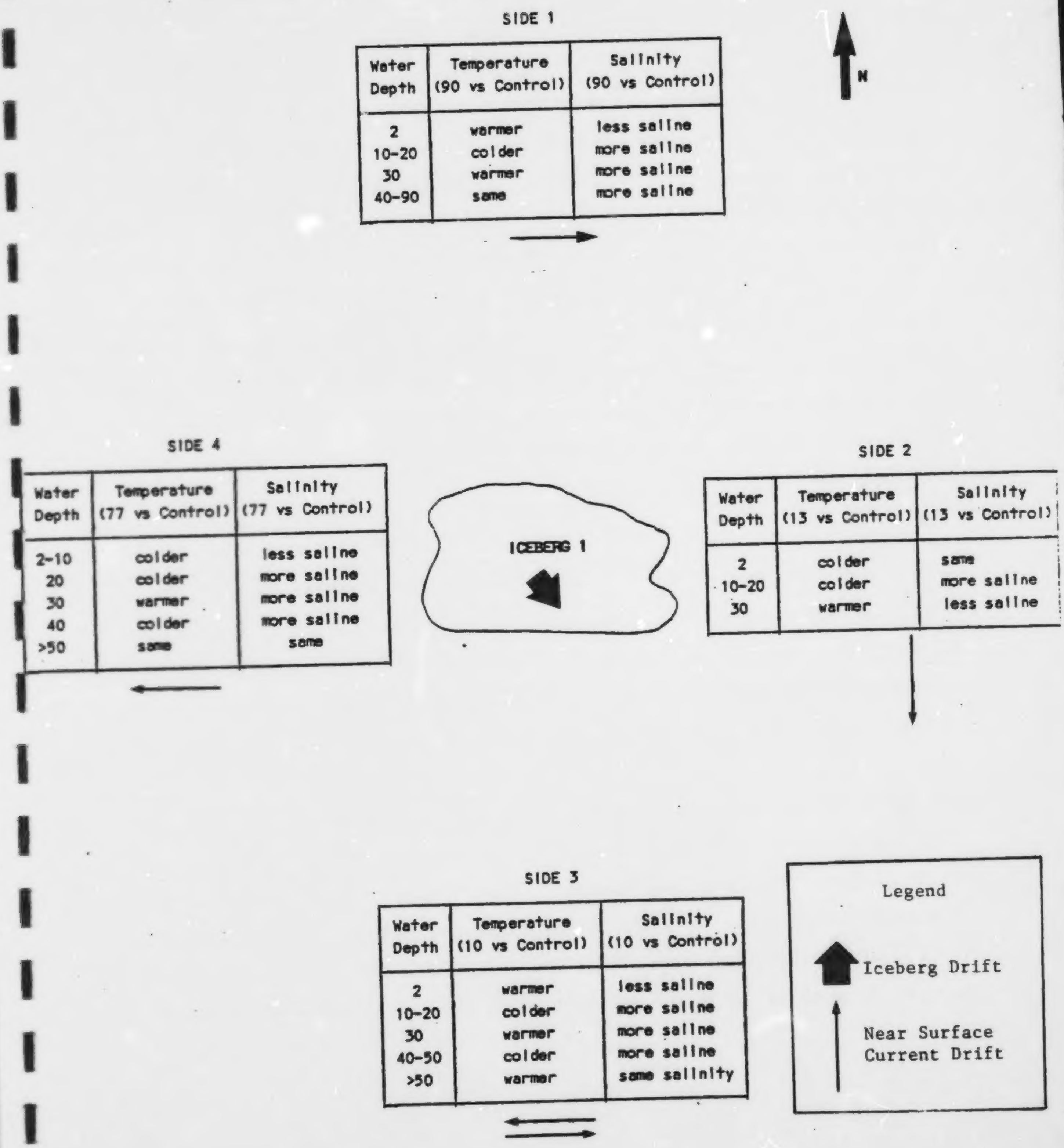

SIDE 1

Water Depth	Temperature (90 vs Control)	Salinity (90 vs Control)
2	warmer	less saline
10-20	colder	more saline
30	warmer	more saline
40-90	same	more saline

SIDE 4

Water Depth	Temperature (77 vs Control)	Salinity (77 vs Control)
2-10	colder	less saline
20	colder	more saline
30	warmer	more saline
40	colder	more saline
>50	same	same

SIDE 2

Water Depth	Temperature (13 vs Control)	Salinity (13 vs Control)
2	colder	same
10-20	colder	more saline
30	warmer	less saline

SIDE 3

Water Depth	Temperature (10 vs Control)	Salinity (10 vs Control)
2	warmer	less saline
10-20	colder	more saline
30	warmer	more saline
40-50	colder	more saline
>50	warmer	same salinity

larly the surface water column is less saline near the iceberg and approaches ambient conditions 200 metres from the iceberg.

At a water depth of 2 metres the water temperature at a range of 77 metres is .41°C colder than the temperature observed at 200 metres. Assuming that the water column cools linearly toward the iceberg, the water temperature next to the iceberg would be a further .3°C colder than that which was observed at a range of 77 metres. This is shown graphically in Figure 5.

Similarly at the same water depth the salinity decreases by .51 ppt. from a range of 200 to 77 metres. Assuming once again that the salinity decreases linearly toward the iceberg, the salinity at a water depth of two metres would decrease by a further .35 ppt. next to the iceberg. This is again shown graphically in Figure 6.

ICEBERG FOUR: Iceberg Four was identified as a medium tilted tabular iceberg which remained grounded throughout the survey. During the study the surface winds and seas were driven by light winds from the southwest. However, the near surface currents were oriented towards the southwest throughout the survey. Consequently the melt plume was expected to the west or south of the iceberg.

Although a clearly defined melt water plume was not observed on any of the profiles the greatest influence of the iceberg was observed on side three just west of the iceberg. The water temperature profile shown in Figure 7 indicates that at a range of 100 metres from the iceberg, the near surface water temperatures are 1°C colder than those observed at the control station. This condition exists to a depth of 25 metres at which point a reversal takes place and the

FIGURE 5

LINEAR REGRESSION OF ICEBERG TEMPERATURE VERSUS ICEBERG RANGE
ICEBERG ONE - SIDE FOUR

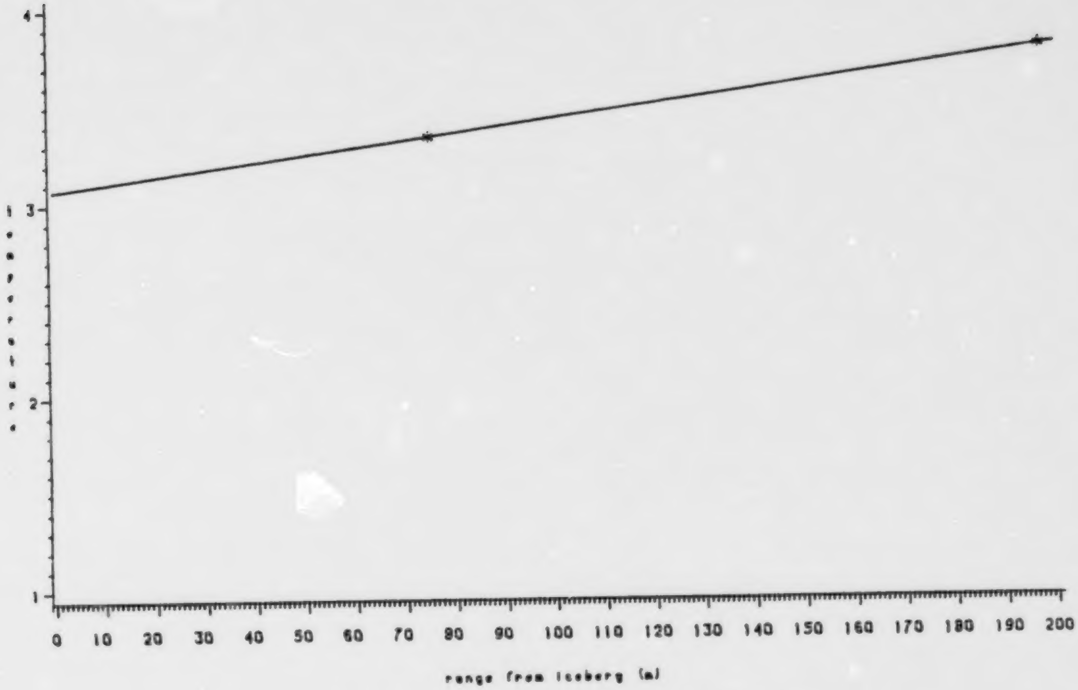

Equation: $Y = 0.003606557 * X + 3.069508$ *
Regression Line Includes 90 % Confidence Limits

FIGURE 6

LINEAR REGRESSION OF ICEBERG SALINITY VERSUS ICEBERG RANGE
ICEBERG ONE - SIDE FOUR

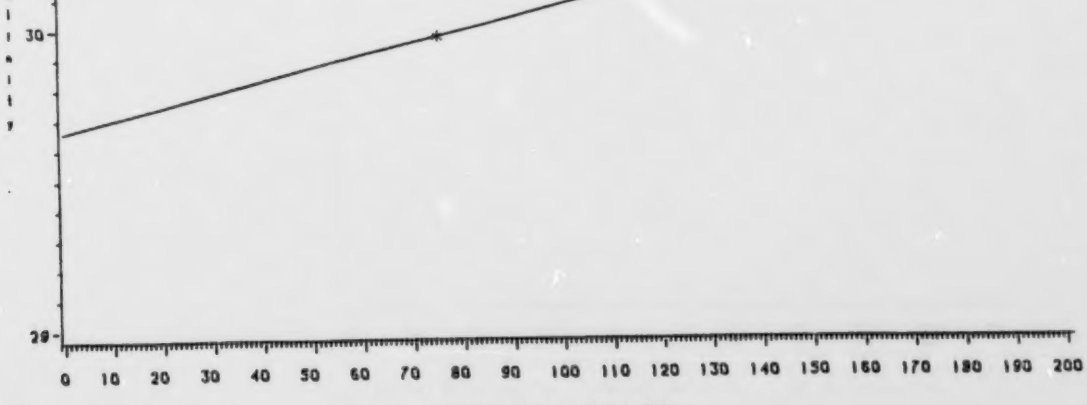

Equation: $Y = 0.004180328 * X + 29.65648$ *
Regression Line Includes 90 % Confidence Limits

Figure 7

WATER TEMPERATURE PROFILE NEAR AN ICEBERG IN THE LABRADOR SEA

ICEBERG FOUR - SIDE THREE LATITUDE 58 39N LONGITUDE 62 40W
PROFILE RECORDED ON AUGUST 14. 1984

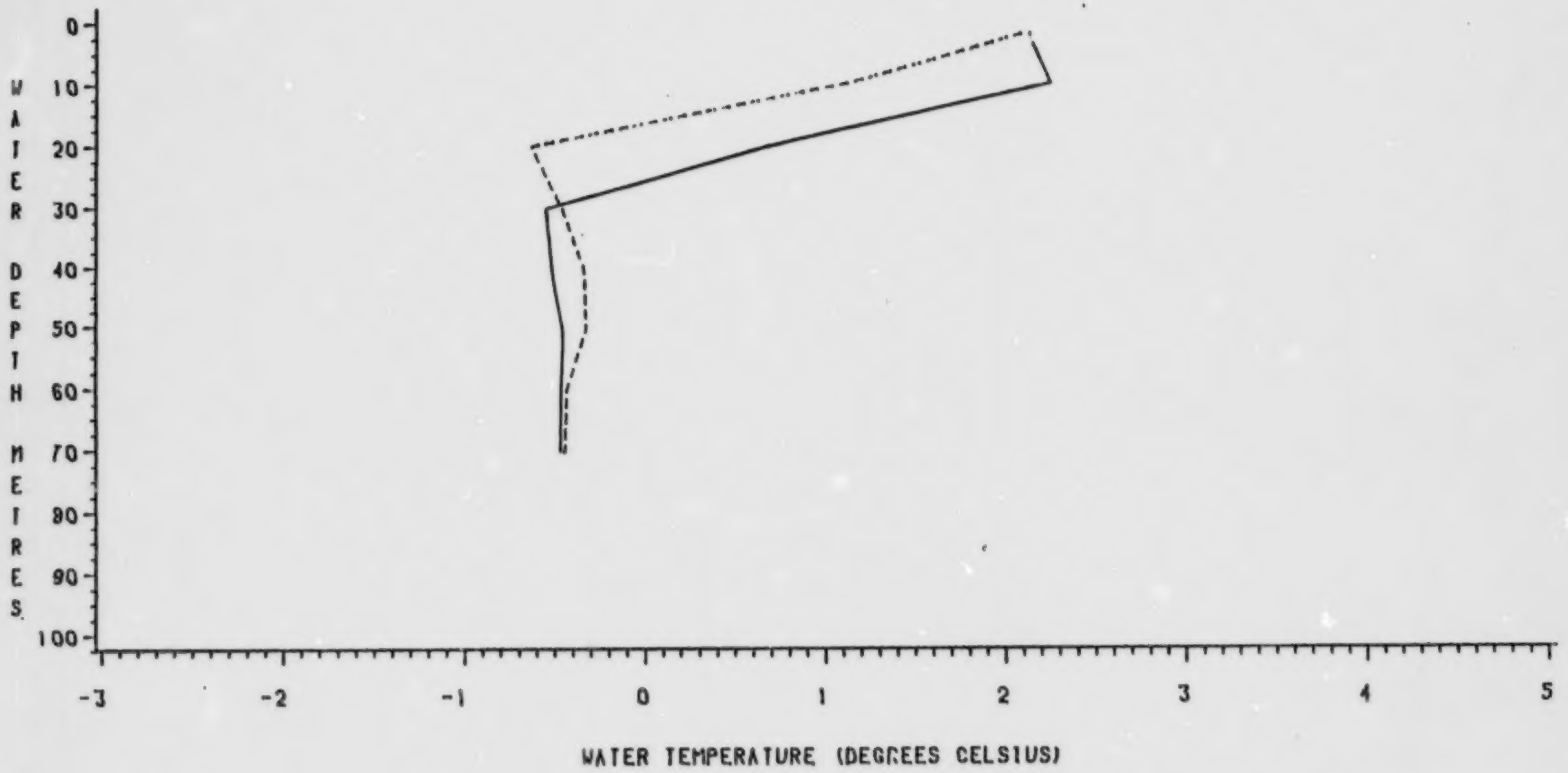

SOLID LINE = CONTROL PROFILE
DOTTED LINE = RANGE OF 100 METRES

temperatures near the iceberg actually become warmer by .2°C to a depth of 60 metres.

Figure 8 shows that the corresponding surface salinities at a range of 100 metres from the iceberg were found to be .05 ppt. lower compared with the control profile. The salinity near the iceberg then becomes .25 ppt. greater than the control from a water depth of 2 to 45 metres. Then, from a water depth of 45 to 70 metres, the water column at the control station is again slightly more saline.

The corresponding density profile shown in Figure 9 indicates that the density in the upper 40 metres of the water column increases toward the iceberg. Similarly, the pycnocline depth also decreases toward the iceberg. These two conditions support the theory of vertical convection cell development in the water column next to the iceberg. This idea is discussed in greater detail below.

DISCUSSION

Glacial ice which melts in an ocean environment will both cool the surrounding water thereby increasing its density and freshen the water column which reduces its density. However a change in salinity is ten times more effective at altering density than is a change in water temperature. Consequently, at northern latitudes, a small change in salinity is by far the more dominant component for altering the density gradient.

Laboratory and theoretical studies indicate that the melt from an iceberg can drive vertical convection adjacent to the iceberg. An analysis of this data suggests that the influence of the iceberg results in the development of small scale convection cells around the iceberg. Figure 10 provides an idealized dia-

Figure 8

SALINITY PROFILE NEAR AN ICEBERG IN THE LABRADOR SEA

ICEBERG FOUR - SIDE THREE LATITUDE 58 39N LONGITUDE 62 40W
PROFILE RECORDED ON AUGUST 14. 1984

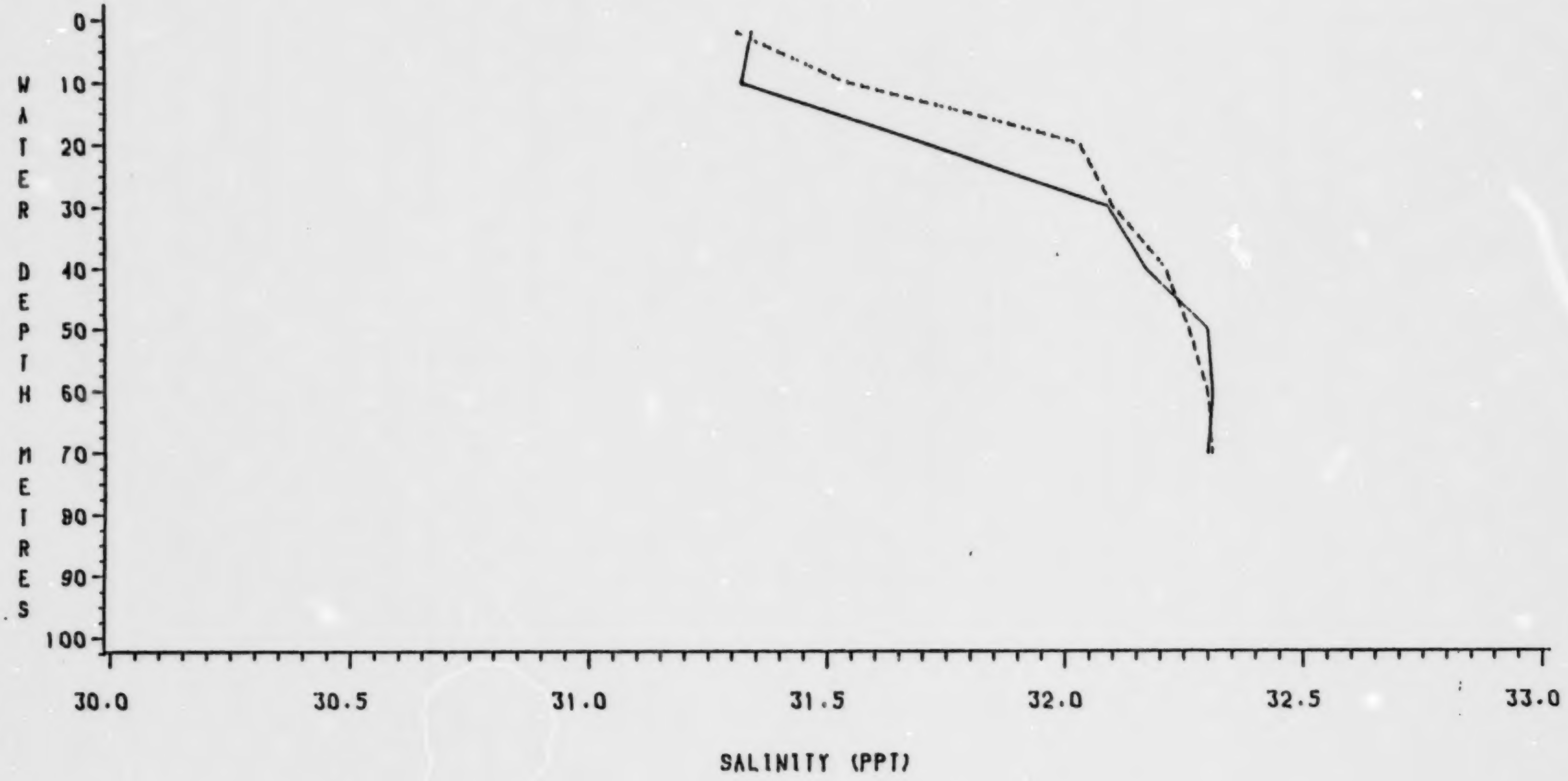

SOLID LINE = CONTROL PROFILE
DOTTED LINE = RANGE OF 100 METRES

Figure 9

DENSITY PROFILE NEAR AN ICEBERG IN THE LABRADOR SEA

ICEBERG FOUR - SIDE THREE LATITUDE 58 38N LONGITUDE 62 40W
PROFILE RECORDED ON AUGUST 14, 1984

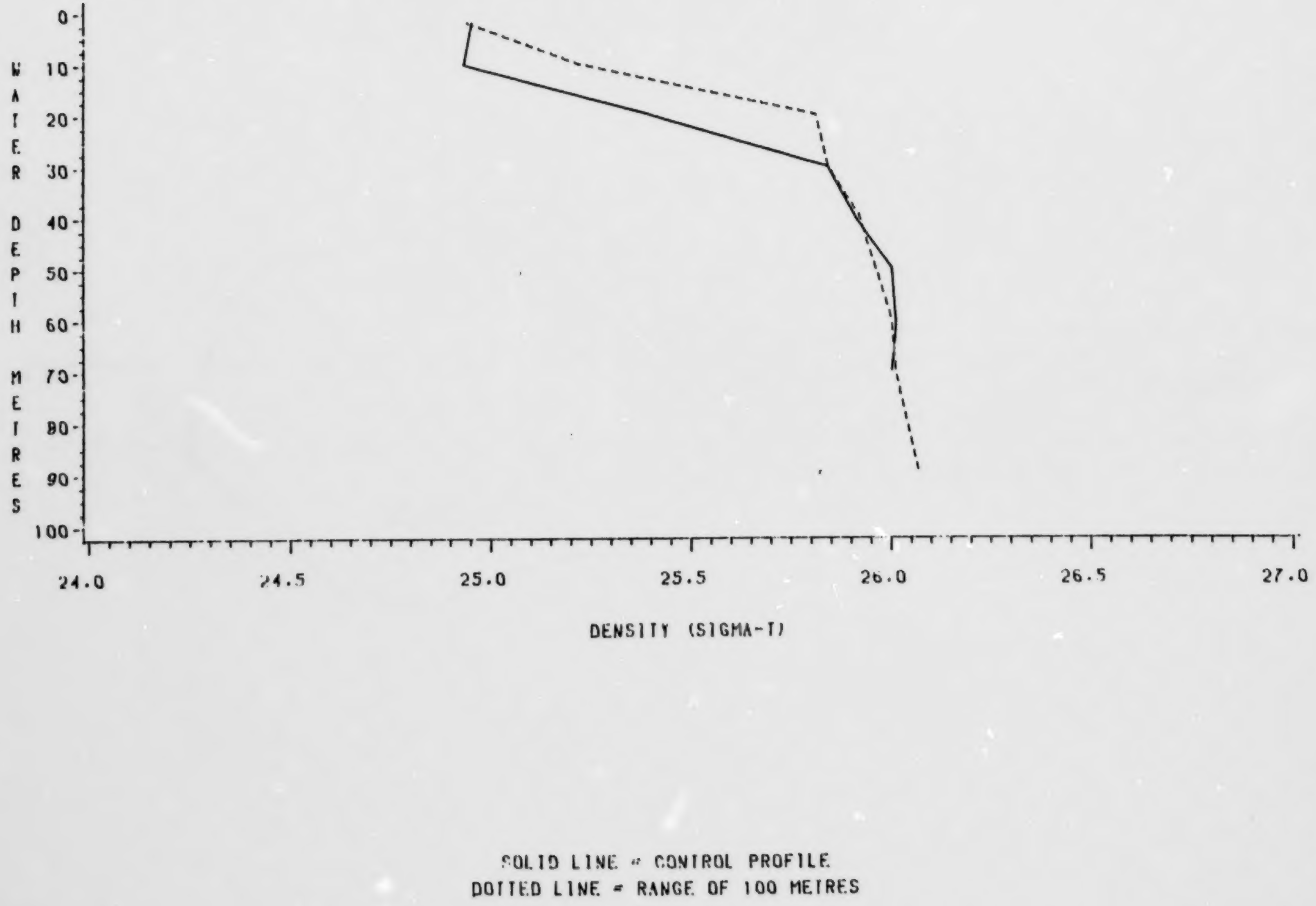

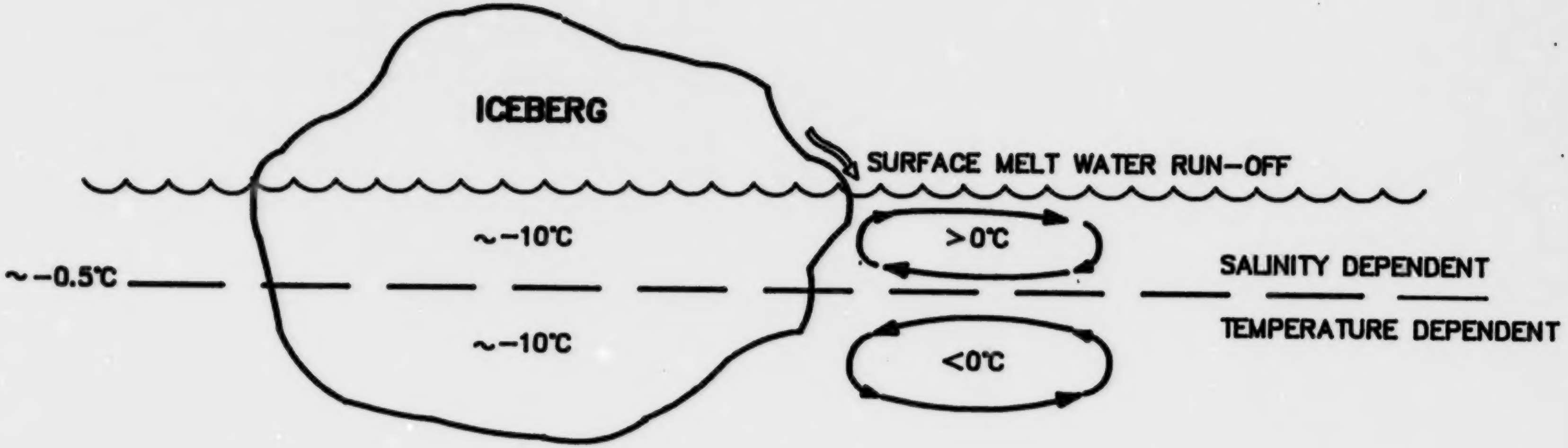

FIGURE 10

IDEALIZED CONVECTION CELL DEVELOPMENT AROUND AN ICEBERG IN THE LABRADOR SEA gram of the apparent convection process which occurs next to an iceberg during the summer period. In the near surface layer (0-5 metres) , the water column tends to be colder and less saline due to the direct runoff of melt water onto the ocean surface. This surface layer tends to be very stable and its depth will depend on the level of mixing caused by wave activity on the ocean surface.

Beneath the surface layer, a clockwise convection cell develops due to iceberg melt which releases cold, fresh water into the water column. Due to the much lower salinity of the melt water, the water column next to the iceberg will rise drawing the colder, more saline water from depth towards the surface. This convection cell occurs to a depth of 25-30 metres and is governed by the water depth below which iceberg melt becomes insignificant (-0.5°C). Below this depth an anticlockwise convection cell develops in response to a general cooling of the water column next to the iceberg. This colder water is more dense and sinks drawing warmer, less saline water to greater depths.

The results obtained in this analysis are consistent with those reported in other studies. Josberger and Neshyba (1980) reported similar findings from a field study around an iceberg along the northeast coast of Newfoundland. Similarly, Huppert and Turner (1978) identified a step-like density structure in the the water column from laboratory tests which supports the convection process around an iceberg.

CONCLUSION

The dynamic nature of the icebergs surveyed coupled with the mobility of the research vessel did restrict the collection of temperature and salinity profiles close to the iceberg. Nevertheless, the influence of the iceberg on the surrounding water column was clearly observed to a range of 300 metres from the iceberg. Icebergs trail a water plume that is slightly colder, very slightly diluted and has undergone some mixing. For example, at a range of 100 metres from an iceberg, the surface melt water from an iceberg was generally found to lower the near surface water temperature and salinity by 0.6°C and 0.4 ppt respectively. This surface layer is very stable and its areal extent is controlled by the level of mixing occuring through wave activity.

Beneath the surface layer, the temperature/salinity relationships of the water column around the icebergs suggest the development of two convection cells. A clockwise cell develops to a depth of 25-30 metres and draws colder, more saline water from depth towards the surface. Below this depth, an anticlockwise convection cell develops which draws warmer, less saline water to greater depth. The depth to which these cells develop appear to be closely related to the draft of the iceberg.

Convection created through iceberg melt does cool the water column surrounding the iceberg. This colder water column acts as an insulating layer for the iceberg against the warmer temperatures of the surrounding ocean. Consequently, when estimating iceberg deterioration, the convection process must be considered in the overall equation for iceberg melt.

ACKNOWLEDGEMENT

The author is indebted to Mr. J. Walpert and Mr. B. McVeigh of Dobrocky Seatech, Newfoundland for their diligence during the collection of this data. The assistance of Petro-Canada's East Coast Drilling Department and the Offshore Engineering Unit is also gratefully acknowledged.

LIST OF REFERENCES

Allison I., K. Kerry and S. Wright

Observations of Water Mass Modification in the Vicinity of an Iceberg. Iceberg Research, No 9, May 1985.

Foldvik A., T. Gammelsrod and Y. Gjessing

Measurements of the Radiation Temperature of Antarctic Icebergs and the Surrounding Surface Water. Annals of Glaciology, Volume 1, 1980. pg. 19-22.

Huppert H., J. Turner

Melting Icebergs. Nature, Volume 271, 1980. pg. 46-48.

Huppert H.

The Physical Processes Involved in the Melting of Icebergs. Annals of Glaciology, Volume 1, 1980. pg. 97-101.

Josberger E.

A Laboratory and Field Study of Iceberg Deterioration . In Husseiny A.A. (ed.) Iceberg Utilization. Proceedings of the First International Conference, Ames, Iowa, 1977. New York, Pergamon Press, pg. 245-264.

Josberger E. and S. Neshyba

Iceberg Melt-Driven Convection Inferred from Field Measurements of Temperature. Annals of Glaciology, Volume 1, 1980. pg. 113-117.

Keys J.R. and K.L. Williams

Rates and Mechanisms of Iceberg Ablation in the D'Urville Sea, Southern Ocean. Journal of Glaciology, Volume 30, No. 105, 1984. pg. 218-222.

Satterfield K.M., J.D. Miller and D.M. Nazarenko

Iceberg Thermal Behaviour. Petro-Canada Report. 1985.

V

REMOTE SENSING

ENHANCEMENT OF NOAA AVHRR DIGITAL DATA FOR SEA ICE ANALYSIS IN AN OPERATIONAL ENVIRONMENT

by

Bruce R. Ramsay[1] and Michael A. J. Zieger[2]

A VAX 11-750 based DIPIX Image Analysis System was used to investigate enhancement techniques which could be applied to NOAA AVHRR digital data for the purpose of enhancing and analysing sea ice features. Data was received on computer-compatible tape (CCT) from the Atmospheric Environment Service HRPT receiving stations at Toronto and Edmonton. Contrast stretching, false colour composition, interchannel arithmetic operations, principle components transformation, and a sinusoidal squeeze algorithm all provided favourable enhancements of features such as ice edges, ice pack structure, ice/cloud discrimination, and colour separation of ice types. Supervised and unsupervised classification techniques were determined to be of little value in a real-time operational analysis system due to the length of time required for processing and to the ambiguity of class definition because of the non-discrete nature of the ice data.

[1] Ice Branch, Atmospheric Environment Service, 365 Laurier Avenue West, Journal Tower South, 3rd Floor, Ottawa, Ontario K1A 0H3

[2] Undergraduate program, Department of Physics, University of Waterloo, Waterloo, Ontario N2L 3G1

1. INTRODUCTION

The Atmospheric Environment Service Ice Centre, situated in Ottawa, is responsible for the monitoring, analysis, and forecasting of floating sea ice in all navigable Canadian waters. Presently, the Ice Centre utilizes single-channel, black and white, hardcopy NOAA Advanced Very High Resolution Radiometer (AVHRR) imagery, received on Unifax-2 photo recorders, as its prime satellite data source for ice analysis and subsequent integration into the daily ice charts. With the evolution of the Ice Data Integration and Analysis System (IDIAS), these, and other, data will be received and processed in digital form on a real-time basis.

A VAX 11/750 based DIPIX Aries-II image analysis system was purchased in 1984 and is being used to evaluate digital image analysis techniques which will assist the operational ice forecasters and technicians in performing a visual analysis of these data. Colour was seen as a great assist to the analyst (Zieger, 1984) and techniques were persued that enhanced the colour separation of spectral classes. This paper will examine those digital enhancement techniques that have been found to be most useful for the analysis of sea ice from NOAA AVHRR data in an operational environment.

2. DATA SOURCE

AVHRR data was received on computer-compatible tapes from the AES HRPT receiving stations at Toronto and Edmonton. Toronto provided 5-channel, half-frame, sectorized (1024 pixels x 1024 lines) images, while the data from Edmonton had, at most, 3 channels enabled and was full-frame (2048 pixels per line). The data has a resolution of approximately 1.1 km at the satellite subpoint, at a nominal altitude of 833 kms. The following is a list of the band widths available from the AVHRR sensor on board the NOAA/TIROS-N series:

TABLE 1 : NOAA AVHRR Band Widths (micrometers)

Channel #	NOAA-6,-8	NOAA-7,-9
1	0.58-0.68	0.58-0.68
2	0.725-1.10	0.725-1.10
3	3.55-3.93	3.55-3.93
4	10.50-11.50	10.30-11.30
5	CH4 Repeated	11.50-12.50

3. ENHANCEMENT TECHNIQUES

In an operational environment, processing techniques must be found that are relatively fast and simple to use. Several enhancement techniques were found to be useful, consistent, and repeatable as a visual assist in the analysis of such ice features as: ice boundaries, ice distribution, age/stage of development, ice growth/decay, ice motion/pressure.

3.1 Contrast Stretches

Contrast stretches can be applied to the data in order to improve the dynamic range. Appropriate gain and offset values are computed from the image statistics and applied to the data intensities so as to compute new display intensities. This can be done by utilizing a linear, logarithmic, or exponential function, depending upon the original histogram spread of the data. A histogram equalization stretch assigns more display values to the more frequently - observed levels in the image data histogram. If the analysis of a specific feature is required (sea ice, for example), a special piecewise linear stretch will assign the full display range to a particular range of image values, thus providing greater radiometric detail. Figure 1 (Lillesand and Kiefer, 1979) illustrates the basic principles of contrast stretch enhancements.

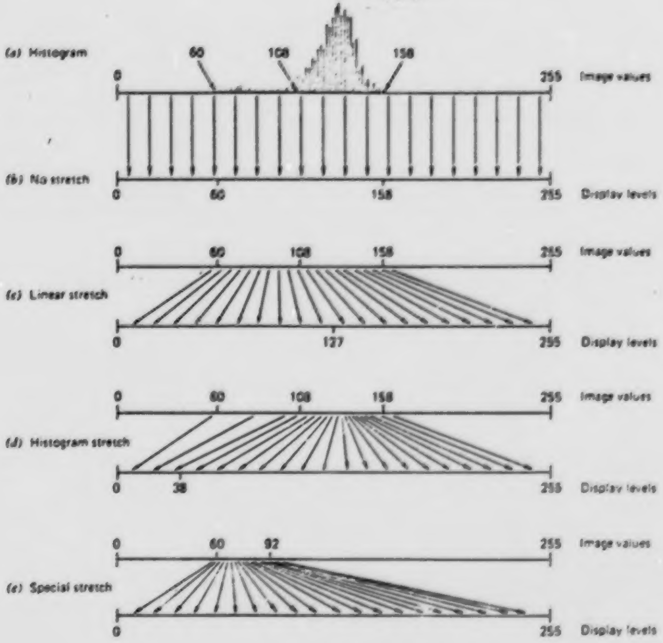

Figure 1: Principle of contrast stretch enhancement

For general purpose ice analysis, it was found that a linear stretch performed best on the 3 visual and near-infrared AVHRR channels, while a histogram equalization greatly improved the 2 thermal infrared channels (Zieger, 1985).

3.2 False Colour Composition

As mentioned earlier, the use of colour as an assist to the analyst greatly enhances his/her ability to distinguish similar class features. A false colour display is created on a digital image analysis system by loading a separate channel of data onto the red, green, and blue colour guns of the display monitor. The display intensities of each channel determine, for each pixel location, the additive mixture of the three respective primary colours. Thus, for the 8-bit NOAA AVHRR data received from the AES HRPT receiving stations, a total of 256^3 colours are theoretically displayable. For the analysis of sea ice, contrast-stretched versions of channel 1,2, and 4 AVHRR data loaded onto the red, green, and blue guns provide good colour separation between dark blue water, light yellow ice, and light blue colour. By switching channel 1 data to the blue gun, and channel 4 data to the red gun, a more pleasing combination of light blue ice and orange-red cloud is achieved (Zieger, 1984). A variety of combinations of original, and synthetically-created, channels of data can be readily flipped between the colour guns until the most effective false colour composite is created for the particular image being analysed.

3.3 Interchannel Arithmetic Operations

In order to accentuate the contrasts between different bands of image data, new channels can be created by the arithmetic combination of the pixel intensities of the original 5 bands. The following are the general purpose interchannel arithmetic operations available with DIPIX Aries-II software:

ratio	F=F(1)/F(2)
product	F=F(1) * F(2)
sum	F=F(1) + F(2)
difference	F=F(1) - F(2)
difference over sum	F=F(1) - F(2)/F(1) + F(2)
normalization	F=F1/F(1) + F(2) +...+ F(N)
arithmetic combination	F=F(1) * C(1)...(+,-,*,1)...F(N) * C(N)
Root of sum of squares	F=SQRT (F(1)**2 + F(2)**2)
Bimass index	F=SQRT (F(1) - F(2))/(F(1) + F(2) + 1.0)

By creating a series of synthetic channels and loading them onto the colour guns, more that 3 channels of data can be viewed at one time, thus taking advantage of the full range of information available from the AVHRR sensor (Ramsay, 1985).

A few of these arithmetic operations have proved to be particularly useful for specific ice analysis problems. Channel 2 (1 micron) AVHRR is very highly correlated with the channel 1 (visual) data. However, it has a significantly higher sensitivity to the ice-water interface. By computing the difference between channel 1 and channel 2 intensity values and applying an appropriate gain and offset, a new channel can be created that accentuates this difference and dramatically enhances the ice edge. Similarly, a difference over sum operation on channel 3 and channel 4 data takes advantage of the sensitivity of channel 3 AVHRR data to liquid water, to create an effective cloud mask for ice-cloud discrimination. These new channels of data can then be reapplied into false colour composites to significantly enhance the colour separation of ice/land/water/cloud classes (Zieger, 1985).

3.4 Principal Components Enhancement

If the three channels of data loaded into a false colour composite have a high degree of correlation, the resulting image is predominantly greyish, with little colour range. A principal components enhancement, however, can provide a set of component images (eigenchannels) which minimizes redundancy between channels and increases the colour separation of spectral classes (Burnstein and Lotspiech, 1983). Consider a two-dimentional data space (x1,x2), with the data distribution defined by an ellipsoid. A new coordinate system can be defined with one axis (y1) oriented in the long direction of the data, and the second axis (y2) perpendicular to the first. This is accomplished by a linear transformation of the data values in the old coordinate system, resulting in data values in the new coordinate system which have a minimum of redundancy between channels. Figure 2 (Landgrebe, 1978) illustrates these principal component axes in two-dimentional space.

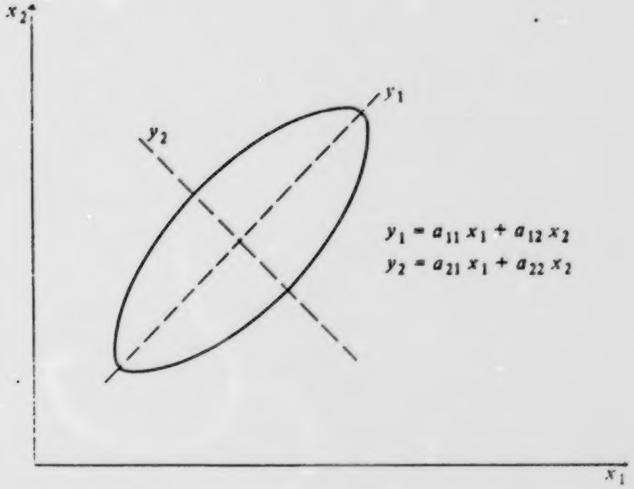
x_2
y_1
y_2
$y_1 = a_{11} x_1 + a_{12} x_2$
$y_2 = a_{21} x_1 + a_{22} x_2$
x_1

Figure 2: Principal component axes in two-dimentional space

For N-dimentional data, successive orthogonal coordinate axes can be similarly defined in the direction of the remaining data scatter, until N-principal component transformations have been completed. Each principal component is a linear combination of the original channels where the weighting coefficients are the components of the corresponding eigenvector computed from the means and the covariance matrix obtained from a training sample data set (Richards, 1984). The intensity value for each pixel of the n'th principal component is computed thusly:

$$PCn = an1\ CH1 + an2\ CH2 + \ldots + ann\ CHn.$$

The first 3 principal components can be mapped into Taylor colour space by mapping the first feature onto a "brightness" axis and the other two onto "red-green" and "blue-yellow" hue axes (Kourtz, 1978). Figure 3 illustrates the colour space developed in this way.

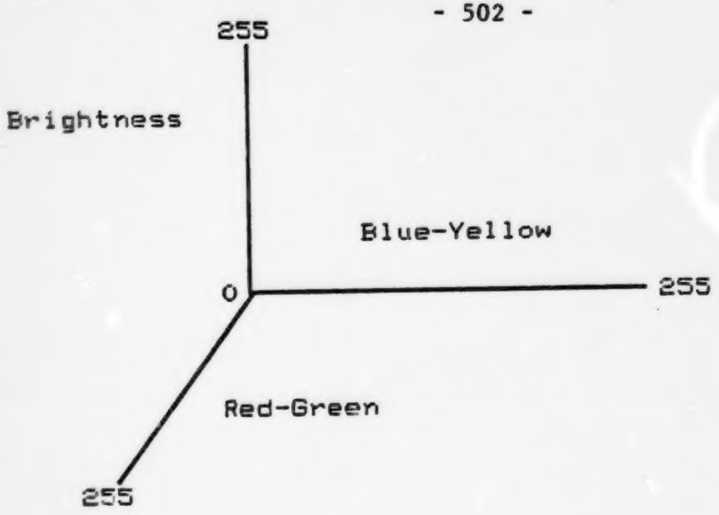

Figure 3: Taylor colour space

The three eigenchannels developed using this techniques can be "unpacked" for colour viewing by creating red, green, and blue features using the following formula available with the Aries-II software (Aries-II Users Manual,1984):

$$R = ((255 - PC2) + (.5 * PC3)) * PC1/256$$
$$G = (PC2 + PC3 + .5) * (PC1/256)$$
$$B = (255 - PC3) * PC1/256$$

Since the statistics generated from the training area will determine the nature of the transformation and therefore the resulting eigenchannels, the picking of an appropriate training area by the operator is most important (Zieger, 1985). If the training area drawn contains a representative sample of all classes in the image, a general enhancement is obtained with good colour separation between clouds, water, land, and ice. If, on the other hand, the operator selects predominantly ice pixels for his/her training area, good colour separation of ice classes is achieved, but non-ice classes are darkened out. In all images tested, the principal components transformation provided improved enhancement of the ice features deemed important by the NOAA AVHRR analysis (Zieger, 1985).

3.5 Sinusoidal Squeeze Enhancement

A special sinusoidal squeeze enhancement was developed by Thomas and Nicholas (1981) for use with LANDSAT MSS data, to colour separate Antartic ice pack classes whose spectral distributions are similar but have significantly differing intensities. This technique has been adapted to map NOAA AVHRR data to high purity colours which can be matched by a light source of a single wave length (Zieger, 1985). Figure 4 illustrates tristimulus colour space defined by red, green, and blue colour axes.

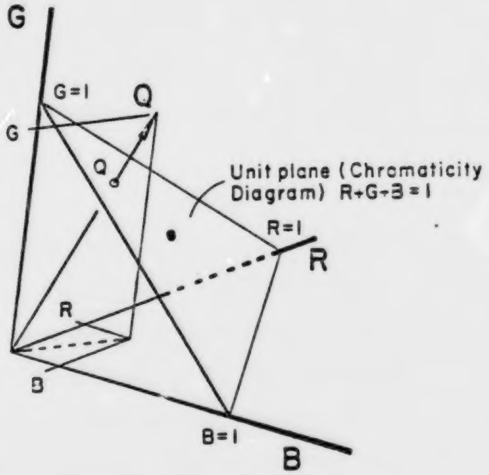

Figure 4: Tristumulus colour space

Most colours can be matched by additive mixtures of these primary colours. The unit plane through this colour space defines pure colours (Wyszecki and Stiles, 1967). Table 2 is a portion of the International Commission on Illumination 1931 Chromaticity Diagram (CIE, 1971) which equates the coordinates on the unit plane to pure colour.

Table 2

Spectral Wavelength (nm)	Colour name	Chromaticity Coordinates Red	Green	Blue
660	red	0.730	0.270	0.000
590	orange	0.575	0.424	0.001
560	yellow-green	0.375	0.625	0.002
525	green	0.114	0.826	0.060
500	green	0.008	0.538	0.453
490	blue-green	0.045	0.295	0.660
485	blue	0.069	0.201	0.731
440	purple-blue	0.164	0.011	0.825

On the chromaticity diagram, all colour hues will be transversed by going around a circle centred on white. Thus the chromaticity coordinates vary sinusoidally (the projection of circular motion on a straight line). Thomas and Nicholas (1981) developed the following sine function to map an input radiance intensity to a desired chromaticity coordinate: F = A3 + Sin (A2 + N/255 + A1). By equating radiance levels to desired chromaticity coordinates, one can solve for the constants. For example:

(255,255,255) = red = (.730,.270,.000)
(0,0,0) = purple-blue = (.164,.011,.825)

All NOAA AVHRR input radiances can then be mapped to sinusoidally squeezed radiances for 3 input channels by the following equations (Zieger, 1984):

RED = GAIN * (A3 + sin (A2 + CH1/255 * A1) * 255 + OFFSET
GREEN = GAIN * (A3 + sin (A2 + CH2/255 * A1) * 255 + OFFSET
BLUE = GAIN * (A3 + sin (A2 + CH3/255 * A1) * 255 + OFFSET

These new RED/GREEN/BLUE sinusoidally squeeze channels can then be loaded onto their respective colour guns for viewing and analysis.

The application of the transformations developed by Thomas and Nicholas (1981) for LANDSAT MSS data, to a variety of NOAA AVHRR ice scenes without regard to the spectral signatures of particular classes, produced good enhancements with a full range of colours, particularly with input channels with relatively low correlations. To map particular ice classes to a particular set of colours, the spectral signatures for each class must be predetermined by the operator, and a specific set of transformations calculated. In spite of the intense operator labour required by this methodology, the utility of the sinusoidal squeeze as a colour-classifier of ice was well demonstrated (Zieger, 1985). Further work needs to be done, however, to determine a single, simple methodology which will be applicable to NOAA AVHRR data irrespective of season and geographic location.

4. IMAGE RECTIFICATION

The previously described enhancement techniques have been developed as tools to assist the AVHRR ice analyst. For the subsequent analysis to be integratable with other data sets into the Ice Centre daily ice charts, it must be registered to a standard map coordinate system; in the case of the ice charts, this is a Lambert Conformal conic projection. Aries-II software has available an image registration package for this purpose. Using operator-identified ground control points on both the master image and slave map background, a polynomial transform is calculated. The image pixel locations are then recalculated by this transform, which effectively "rubber-sheets" the image onto the map (Aries-II Users Manual, 1984). This process provides a high degree of accuracy when a good variety of ground control points can be identified across the image. However, many AVHRR scenes of interest to the ice analyst are prodominantly ocean, with perhaps just a coastline on one side for control point selection. In this case, extreme image warping errors can play havoc to the registration (Brulé, 1985).

In order to solve the registration problem, Ice Centre is contracting the Department of Oceanography, University of British Columbia, to host NOAA AVHRR navigation and mapping software on the DIPIX by the spring of 1986. The software will use a semi-elliptical orbital model, treating the earth as an oblate spheroid, to register NOAA AVHRR images onto a subset of World Data Base-II in a Lambert Conformal projection. A "nudge" routine will enable the operator to interactively adjust for satellite timing errors. Absolute errors of no more than 1.5 km can be expected if high quality ephemeris data is used as orbital parameter inputs (Emery and Ikeda, 1984). An investigation will be conducted to see whether the substitution of NORAD TBUS orbital predict data, available on AES meteorological teletype circuits, will still provide the mapping accuracy required at the Ice Centre.

5. CONCLUSIONS

A suite of digital image enhancement techniques has been identified that assist the NOAA AVHRR analyst in the identification of significant ice features. These techniques have been applied to a variety of ice scenes with encouraging success. Further work needs to be done, however, in validating these techniques for all probable geographic locations and phases of the ice season, and in establishing standard methodologies in order to reduce operator-intensive labour. This is particularly true for the sinusoidal squeeze transformation.

In 1986, the Ice Centre will start to receive real-time, 5-channel NOAA AVHRR digital data on a 56Kbit link from the AES Satellite Data Lab in Toronto. At that time, work will begin on implementing real-time processing, geocoding, enhancement, and analysis techniques so that this data will be available to the ice forecaster for integration into the daily ice charts on an operational basis.

REFERENCES

ARIES-II V-Stream Software Version 2.2 User's Manual, May, 1985, DIPIX Systems Limited, Ottawa, Ontario.

BERSTEIN, R. and LOTSPIECH, J.B. 1983, LANDSAT-4 Images of the San Francisco Region - Results of Digital Image Enhancement and Information Extraction, IBM Palo Alto Scientific Centre, Palo Alto, California.

BRULE, A.J. 1985, Performance Evaluation of DIPIX Aries-II GCP Task Version 2.2, Ice Centre Product Development Division, Atmospheric Environment Service, Environment Canada, Ottawa, Ontario.

CIE 1971, Colorimetry - Official Recommendations of the International Commission on Illumination, Commission Internationale de L'Eclairage No. 5 (E-1.3.1), Paris, France.

EMERY, W.J. and IKEDA, M. 1984, A Comparison of Geometric Corection Methods for AVHRR Imagery, Canadian Journal of Remote Sensing, Vol. 10, No. 1, pp. 46-56.

KOURTZ, P.A. and SCOTT, A.J. 1978, An Improved Image Enchancement Technique and Its Application to Forest Fire Management, Fifth Canadian Symposium on Remote Sensing, August, 1978, Victoria, B.C., pp. 72-78

LANDGREBE, D.E. 1978, Remote Sensing - The Quantitative Approach, McGraw-Hill, p. 350.

LILLESAND T.M. and KIEFER R.W. 1979, Remote Sensing and Image Interpretation, John Wiley and Sons, pp. 562-573.

RAMSAY, B.R. 1985, Qualitative and Quantitative Interpretation of Satellite Imagery as Related to Sea Ice Analysis, Ice Centre Centre Product Development Division, Atmospheric Environment Service, Environment Canada, Ottawa, Ontario.

RICHARDS, J.A. 1984, Thematic Mapping from Multitemporal Image Data Using the Principal Components Transformation, Remote Sensing of Environment 16:35-46 (1984).

THOMAS, I.L. and NICHOLAS J.V. 1981, Special Enhancement for Antartic Mapping, LANDSAT 81 Australasian Remote Sensing Conference, 31 Aug-4 Sept 1981, Canberra, Australia.

WYSZECKI, G. and STILES, W.S. 1967, Colour Science - Concepts and Methods, Quantitative Data and Formulas, John Wiley and Sons Inc., pp. 228-252.

ZIEGER, M.A.J. 1984, Digital Enhancement Techniques for Ice Detection in AVHRR Imagery, Ice Centre Product Development Division, Atmospheric Environment Service, Environment Canada, Ottawa, Ontario.

ZIEGER, M.A.J. 1985, NOAA AVHRR Image Analysis Project Report, Parts 1, 2, and 3, Ice Centre Product Development Division, Atmospheric Environment Service, Environment Canada, Ottawa, Ontario.

Motion of ice in the Beaufort Sea from satellite and aircraft images

J.F.R. Gower[1], J.Y. Cherniawsky[2] and G.A. Borstad[2]

Abstract

To support studies aimed at improving the predictability of sea ice in the Beaufort Sea, a series of NOAA satellite AVHRR images is being analysed. These are being processed to show the movement and evolution of ice patterns over an area of 650 X 650 Km. This data provides a synoptic view of the area, but is severely limited by cloud cover, which affects most overpasses of the satellite in a way that is correlated with wind patterns and hence with the ice movement itself. Preliminary results indicate that visual images from the NOAA satellites now in orbit can provide synoptic and piece-wise continuous time series of ice compactness and velocity, and should also give data on vorticity and deformation. Examples of velocity time series are given.

A series of 125 airborne synthetic aperture radar images of sea ice cover was made available by Canadian Marine Drilling Ltd and BeauDril Ltd, for the period June 11 to December 6 1984. These give near-daily coverage of a smaller area with higher resolution, and are much less affected by weather. A video movie of this sequence has been prepared, and examples of the images are presented.

1. Institute of Ocean Sciences, Sidney B.C.
2. G.A. Borstad Ltd, Sidney B.C.

Introduction

As part of an Offshore Energy Research and Development (OERD) funded program at the Institute of Ocean Sciences (IOS) to improve the predictability of sea ice in the Arctic, we are analysing a series of satellite images which at present cover the south-east Beaufort Sea during the spring and summer of 1985. This series of data will be extended through to the end of March 1986, to cover the full expected data collection period for 6 arrays of current meters deployed in the same area in a related program at IOS. The satellite images show ice cover and surface movement. Combining this with sub-surface current meter measurements will help to determine the response of the ice to ocean currents. A third related study at IOS, reported by Topham at this meeting, is studying the detailed mechanism of this response by examining the interaction of ice keels with the water beneath it.

The satellite images show large scale patterns of ice movement down to spatial scales of a few kilometers, but are limited as to frequency of observations by cloud cover. To observe the motions on smaller scales and without the limitations imposed by weather, a series of 125 airborne synthetic aperture radar images of sea ice was employed. This was made available by Canadian Marine Drilling Ltd and BeauDril Ltd, and gave nearly daily coverage in the period June 11 to December 6 1984.

Satellite image data

The satellite images are from the AVHRR (Advanced Very High Resolution Radiometer), a scanning visible and thermal sensor on the U.S. NOAA series of weather satellites that view the earth from polar orbit. The scanner covers an angular range of 110.8 degrees (55.4 degrees to each side) across the satellite track from an altitude of about 860 Km, giving a images of a swath 3000 Km wide with a resolution of about 1 Km at nadir in the centre of the swath, degrading to more than 3 Km at the edges.

The AVHRR produces images in one spectral band in each of the visible, the reflective infrared and in the short wave thermal infrared, and in two bands in the long wave thermal infrared . Visible images require daylight and hence are not available in the Arctic winter. Thermal images can be formed in darkness from the temperature contrasts in a scene. These are often strong between ice and open water, particularly in the Arctic winter. Cloud blocks both visible and thermal imagery, and is the single greatest limitation to the use of this type of data. Data is also missed due to operational limitations at the receiving stations.

For the present study, digital satellite image data on tape were acquired from the Atmospheric Environment Service (AES) receiving station in Edmonton, Alberta. This station is far enough north to give good coverage of the study area, but is primarily concerned with weather forecasting requirements. This places a number of constraints on their ability to supply data:-

1. Data is only kept in digital, tape recorded form, for one week before the tape is re-used. A procedure was therefore arranged whereby good, relatively cloud-free scenes of the study area would be selected by an AES technician, and copied to archive tapes supplied by IOS.

2. The recorded data is degraded in that only the 8 more significant bits, of the 10 measured on the satellite for each band at each pixel, are recorded at this station. This is not a serious factor for the present study, since the contrast is high between ice and open water, but it will reduce the visibility of narrow leads.

3. Data is preserved for only 3 of the 5 spectral bands of the AVHRR, usually one visible and one in each of the short and long

wave thermal infrared bands. For this study we have used visible data when solar illumination is sufficient, and plan to use long wave thermal infrared data otherwise. The longer of the two visible wavelength bands is usually recorded. This is more suitable for this study since it gives good ice to water contrast. The 2 long wave infrared bands give nearly identical data for ice mapping, since they were designed to respond differently to (large spatial scale) atmospheric water vapour absorption.

Data processing

Table 1 shows the dates for which AVHRR data was acquired between May 29 and August 31. The sequence is far from uniformly spaced in time, reflecting cloudy periods in the area. Even in the "good" scenes some areas are obscured by cloud, as indicated by percentage and location in the table.

Before the ice motion can be measured, the images need to be geometrically corrected. The scanning pattern of the sensor, the varying azimuth of the satellite's path from orbit to orbit, and the rotation of the earth as the scene is scanned by the sensor, combine to distort the data. A typical example is shown in Figure 1a.

The navigation procedure makes use of the published orbital inclination for each satellite, and uses comparison with identified ground control points of known latitude and longitude to obtain the best fit to satellite altitude, ascending node position and the angular distance travelled round the orbit since this node. Errors due to pitch, roll and yaw of the satellite are not corrected by this procedure, except in so far as their effects can be compensated by changing the fitted parameters.

Accuracy of the fitting procedure is observed to be about 2-4 Km, when comparing positions of coast lines and other features. This is then further improved with a 3-point linear geometrical transformation, using landmarks spaced as far as possible along the coasts on the southern and eastern boundaries of the scene. The final accuracy is estimated to be about 1 Km near the coasts, increasing to 2 Km further offshore.

In Figure 1b the study area in the same image is shown corrected, or navigated, to an equi-rectangular projection in which lines of latitude and longitudeare equi-distant and parallel. The scale is equal to 1.3 Km per pixel at the centre of the scene.

A navigated image similar to Figure 1b is derived from the data for each suitable pass. The digital radiance levels are displayed in pseudo-colour on the display screen of the interactive image processor, and are enhanced by contrast stretching, so as to compensate for illumination differences between images and to maximize visibility of ice structure. Recognizable ice features are then

Table 1. Dates of relatively cloud-free satellite imagery of the study area in 1985. Time is GMT. Data is from NOAA 6,8 or 9 satellite as indicated, on ascending (A) or descending (D) orbital path. The sequences illustrated in Figures 4 and 5 are indicated by asterisks. Estimated cloud percent is for the whole scene, with most cloud concentrated in the locations indicated.

Date	Time	NOAA	A/D	Seq.	% cloud	Location
May 29	20:50	9	A	*	2	scat^{d}
May 30	20:39	9	A	*	30	W
June 1	16:06	6	D	*	10	SW
June 1	21:59	9	A	*	15	SW
June 2	17:27	6	D	*	40	S & W
June 4	19:15	9	A		20	scat^{d}
June 7	19:22	9	A		40	centre, E & W
June 8	20:53	9	A		50	centre, E & W
June 12	20:01	9	A		40	W & S
June 13	21:31	9	A		30	scat^{d}
June 15	01:45	6	A		30	SW & N
June 17	20:48	9	A	*	25	S
June 18	22:19	9	A	*	10	NE
June 19	17:17	6	D	*	0	-
June 20	16:53	6	D	*	2	scat^{d}
June 21	16:59	6	D	*	0	-
June 22	16:05	6	D	*	2	S & scat^{d}
June 22	21:36	9	A	*	2	S & scat^{d}
June 24	18:38	6	D	*	1	SE
June 25	19:28	9	A	*	0	-
June 26	16:09	6	D	*	5	SW
July 3	19:40	9	A	Not yet analysed		
July 12	09:50	9	D	Not yet analysed		
July 13	19:34	9	A	Not yet analysed		
July 26	22:17	9	A		60	scat^{d}
July 30	20:02	9	A	Not yet analysed		
Aug 2	21:01	9	A		30	centre
Aug 3	18:18	8	D		10	NW
Aug 7	21:49	9	A		0	-
Aug 8	21:39	9	A		20	scat^{d}
Aug 9	21:28	9	A		20	W
Aug 10	21:17	9	A		50	scat^{d}
Aug 14	22:19	9	A		50	N & E
Aug 18	22:33	9	A		40	N & W
Aug 19	22:22	9	A		80	scat^{d}
Aug 20	19:31	9	A		80	N
Aug 21	21:00	9	A		10	N
Aug 22	20:51	9	A		20	S
Aug 22	22:31	9	A		30	S
Aug 23	22:20	9	A		60	S
Aug 24	20:29	9	A		80	N
Aug 25	21:59	9	A		90	N

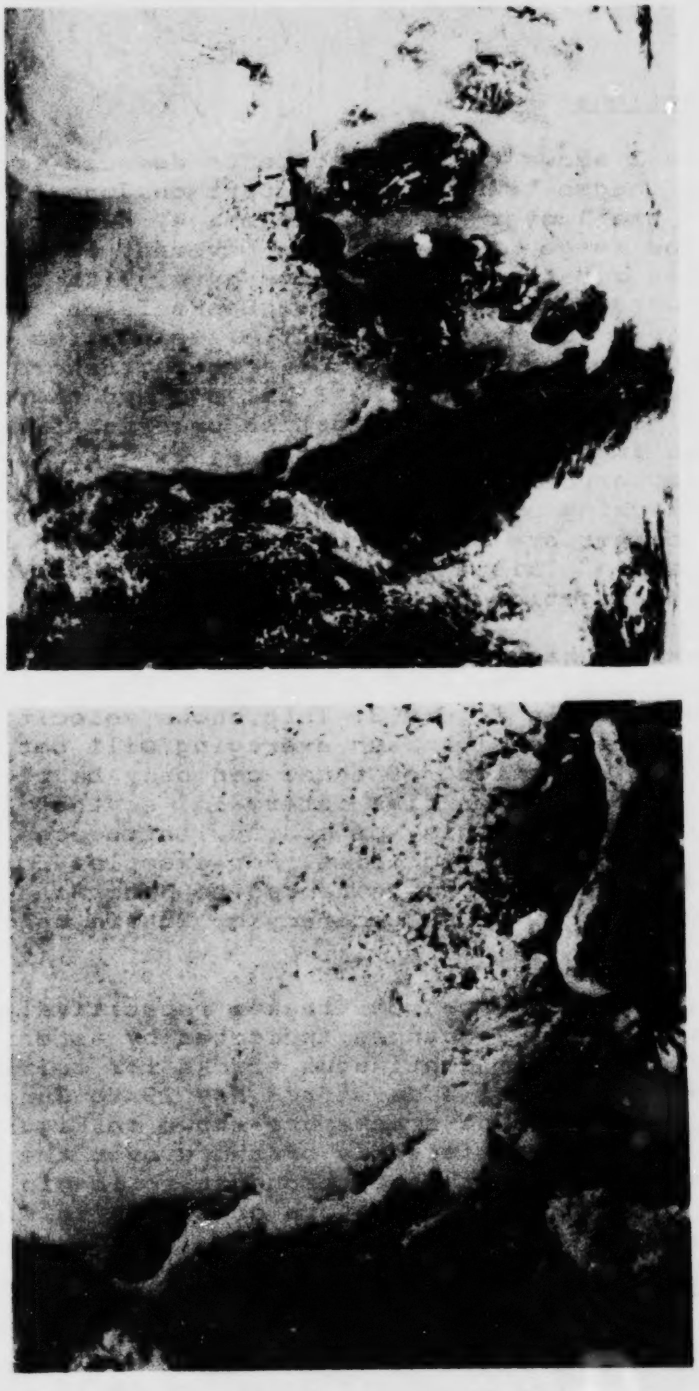

1 (a, top) Uncorrected NOAA satellite AVHRR image (visible, band 2) of the western Canadian Arctic for June 1 1985. (b, bottom) Geometrically corrected section of this image for the study area.

tracked on the display from one date to the next using interactive software developed for IOS by Arctic Sciences Ltd (1985).

Ice motions

Figure 2 shows the displacements deduced from this tracking process for two images taken one day apart on June 19 and June 20 1985. Motion is small over most of the image, but are easily measurable on the image processor. The movement is as expected for ice in the clock-wise rotating Beaufort Sea gyre, with larger motions of about 5Km southwards near the shore of Banks Island and westwards off the Mackenzie River delta. Higher outflow velocities (about 15 Km/day) occur in the mouth of Amundsen Gulf. Farther offshore the displacements are smaller, about 2-3 Km, and are therefore comparable to the expected errors due to navigation uncertainties (of 1 to 2 Km each) in the two images used. Since the pixel size in the navigated images is 1.3 Km, errors of a similar magnitude must also be expected in the manual tracking of individual features. Ice displacements in the north-west corner are small, and consistent with the motion of the gyre closer to shore. This in itself gives more confidence in the accuracy of the navigation procedure.

Errors in tracking individual features can be reduced by averaging the motions to give mean ice velocities for each square of a regular grid as shown in Figure 3. This shows velocities, plotted to show the motion more clearly. Such averaging will not, however, reduce navigation errors. The effect of these can only be reduced by comparing images over longer time intervals, so that the measured displacements are larger. This, of course, introduces a longer temporal averaging of ice velocities. For example, for errors of 1.5 Km per image, a 4 day interval is needed to determine a constant velocity of 2 Km per day to an accuracy of 25% in magnitude and 15^{o} in direction.

The same feature can be tracked repetitively over a longer period, and the two data sequences indicated by asterisks in Table 1, have been analysed to give continuous tracks for sufficiently visible features. These extend over 5 days from May 29 to June 2, and over 10 days from June 17 to 26. The tracks are shown in Figures 4 and 5. In Figure 4 the motion is consistently offshore over the whole area during the 5 day period, with the strongest motion in the mouth of Amundsen Gulf. In Figure 5 the pattern of motion in Figures 2 and 3 is seen to continue over the 10 day period.

The coast line in Figures 4 and 5 has been added from a digital atlas. Its good fit with the features in the image demonstrates the correctness of the navigation in coastal areas. Examination of the tracks in Figure 5 for the north-west area furthest from shore, shows that apparent random but spatially consistent motions of the ice about a mean track, of the type that would be introduced by navigation errors, do not exceed ±2.5 Km over the 9 day period. Since real motions of this form can occur in response to wind

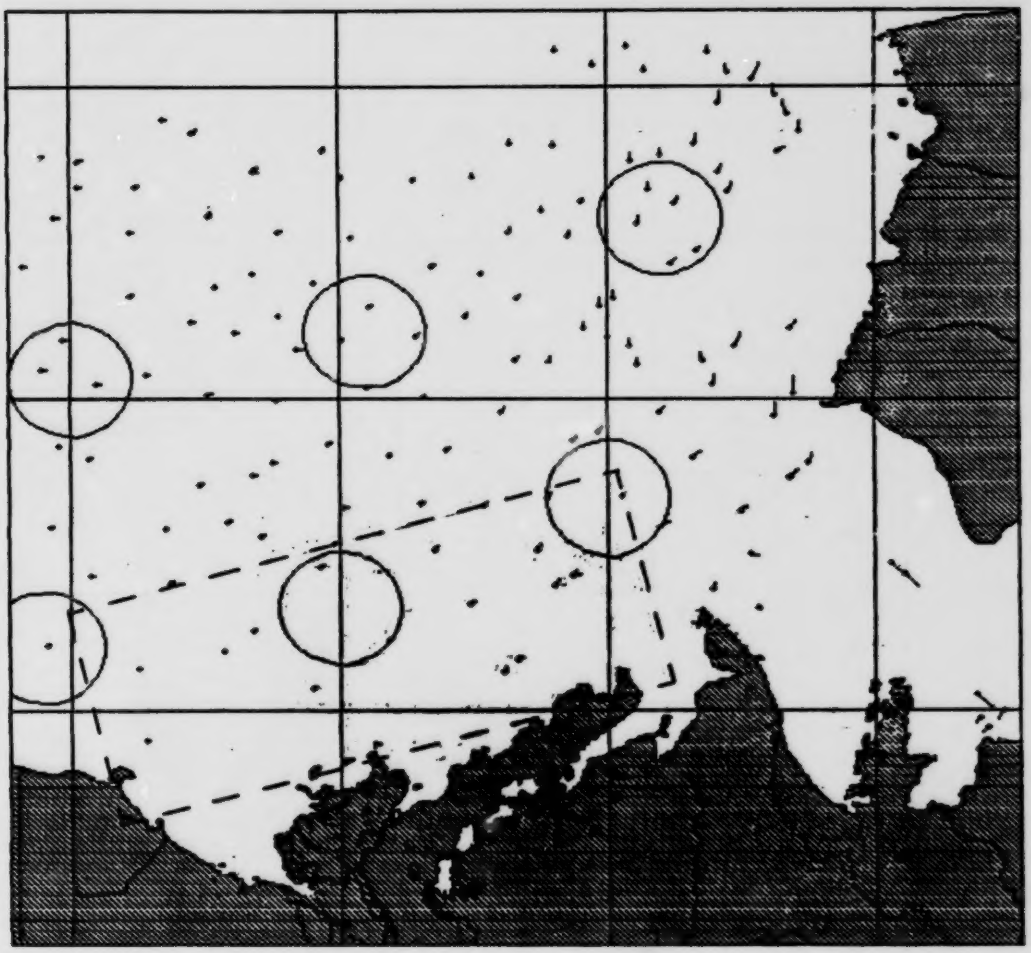

2 Displacements of identifiable ice features between June 19 1985 at 17:17 GMT, and June 20 at 16:53. Each vector ends in a small cross. The six circles of 80 Km radius are centred on the sites of current meters deployed in a related study. The dashed rectangle shows the approximate area covered by the airborne SAR images.

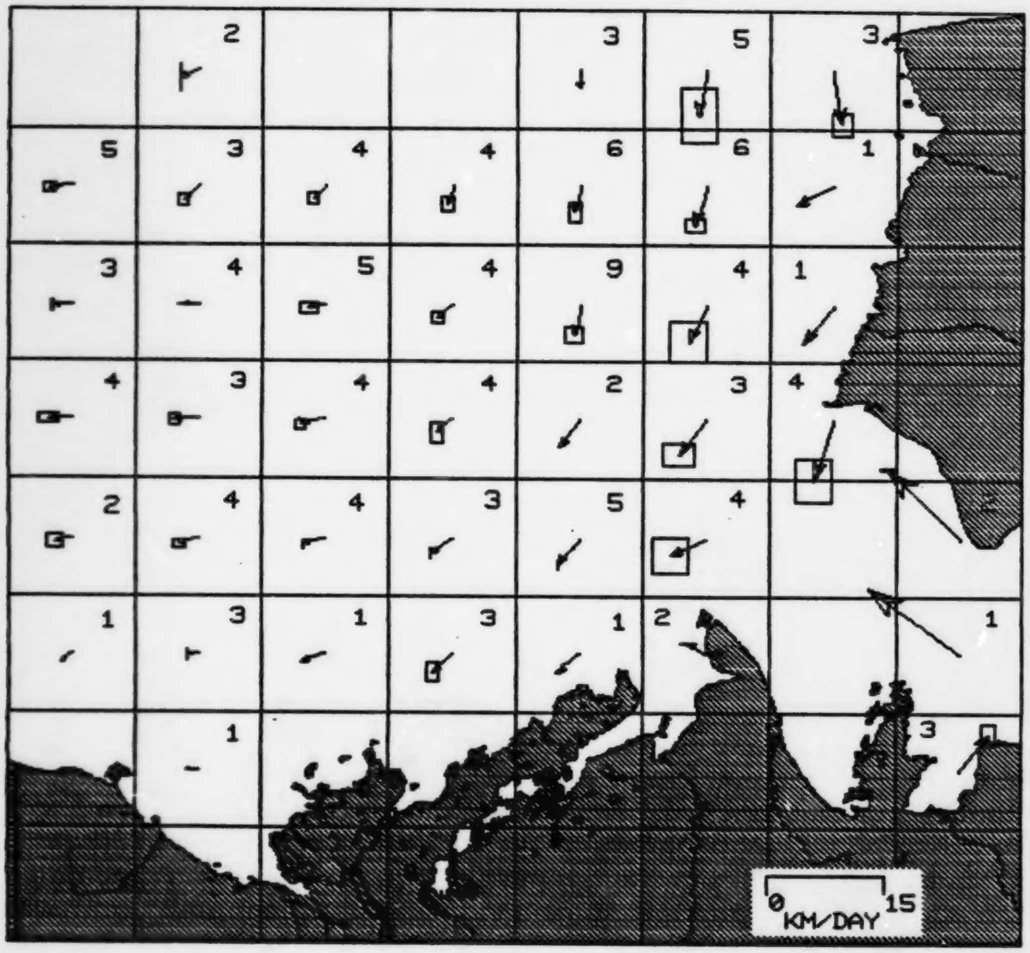

3 Velocity vectors averaged over 80 Km square areas, calculated from the displacements in Figure 2. The velocity scale is given in Km per day at the lower right. Numbers at the top right in each square show the number of features tracked in that square. The box at the end of the arrows shows the standard deviation of the north/south and east/west components of the velocities deduced from these features.

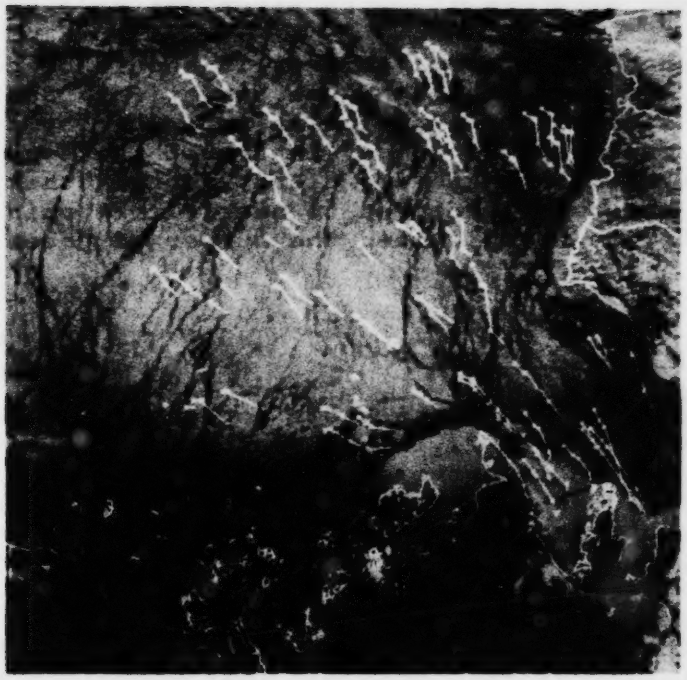

4 Tracks of identifiable ice features, as measured during the period May 29 to June 2, superposed on the image for May 29. Tracks start at the positions of features on this image. Small filled squares indicate positions on successive images.

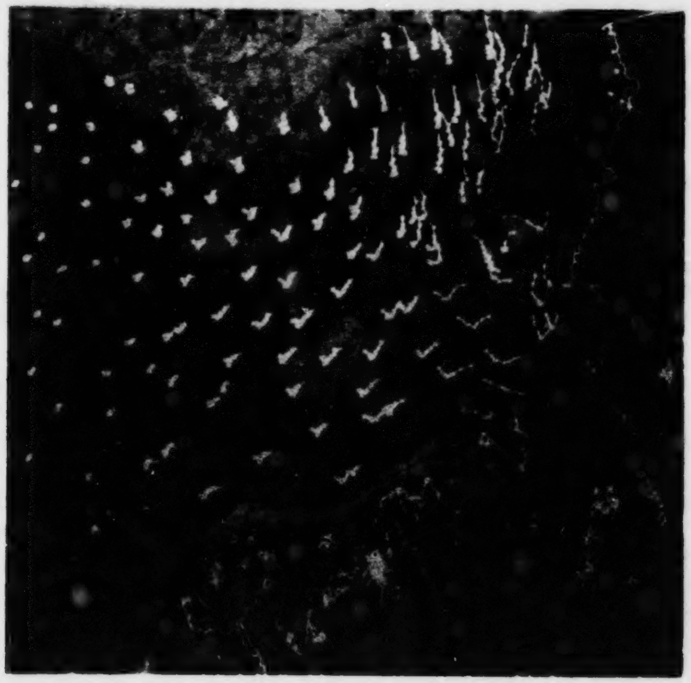

5 Tracks for the period June 17 to 26 superposed on the image for June 17.

and water forcing, this is only an upper limit to navigation errors, and is consistent with the 1 - 2 Km error estimate made above.

As can be seen from Table 1, it should be possible to extend and link these sequences through June and to form another sequence for August, if necessary using image pairs separated by longer time intervals. In some areas cloud may interrupt the sequences. July appears to have been an extremely cloudy month. Other sources of NOAA satellite data are being explored to see if constraints at the Edmonton station may have limited the number of passes we received.

Airborne SAR imagery

The airborne SAR data shows motions in the smaller area near shore, outlined in Figure 2, in a sequence that is not interrupted by cloud. The resolution is extremely high, but the navigation accuracy is relatively low, and is probably inferior to that of the satellite data. Although the resolution allows fine scale features to be tracked from image to image, the accuracy of the deduced velocities is limited by the navigation accuracy, thus greatly reducing the value of this data. Nonetheless, a SAR sequence, if available for 1985, could be compared with the present satellite data set, and would also give surface current measurements over, or near, three of the current meter sites.

The data for 1984 was in the form of photographic strips of film, one for each flight line. From 3 to 5 lines were then manually mosaiced to form the composite scene for each day. Flight line offsets can be corrected at this stage if sufficient land marks or drilling platforms are visible on the images. Images of the same features, on overlap between strips, can also be used if their movement is sufficiently slow. However, scale changes and non-linear drift errors cannot be corrected. Navigation was with reference to an inertial navigation unit which, without correction, will cause sinusoidal drift errors with average amplitudes increasing by about 1 Km per flying hour, and with a characteristic 84 minute oscillation period. Since this time is comparable with the time needed for each flight line, accurate correction is not possible with photographic methods. Digital corrections, if applied in future, should be able to reduce these errors considerably.

We were supplied with the composite SAR images for each day as a 80 by 150 cm photographic print. In order to study the ice motions shown by the sequence of prints, we arranged for them to be transferred at reduced resolution onto video tape for viewing as a time-lapse movie. The movie is partially successful in showing the changing patterns. The ice cover is sufficiently dynamic in this area that pattern correlation between days is often low, especially in the summer, when the ice is very open. The sequence is also affected by variations in radar brightness of ice from day to day (partly attributable to changing viewing geometry), by the effects of navigation, mosaicing and re-photographing errors, and by the relatvely low resolution of the video image.

A viewing speed of 10 seconds per day showed the change from one day to the next. At one second per day the longer term changes, and their variation with season, could be seen. Figures 6 and 7 show pairs of images in periods of relatively open and ice covered water. When the ice is open, the effects of small scale water motions can become visible, but often without sufficient correlation from day to day to show motions. In Figure 6, a periodic wave-like feature in the uncompacted ice edge appears north of the Mackenzie Delta, but has disappeared a day later. In Figure 7 the motion of larger floes can be followed from day to day. The pattern is highly correlated on successive days, and ice tracks as in Figures 4 and 5 can easily be deduced, but with accuracy limited by the aircraft navigation and its correction.

Conclusions

The simple navigation and manual tracking procedures used here appear accurate enough to provide valuable data on ice movement. Cloud cover in the area limits the number of good scenes, but the temporal and spatial coverage is adequate for the present purposes.

More automated methods of tracking, by digital cross-correlation of pairs of images, have now been developed, and are being used with considerable success to improve the precision and spatial resolution of velocity maps. Cross correlation measurements over land also improve the estimates of navigation errors, which can then be corrected. An uncertainty remains in propagating these corrections to regions far from the shore. Results of the automated method of ice tracking will be presented at the 10th Canadian Symposium on Remote Sensing to be held May 5-8 in Edmonton, Alberta (Cherniawsky et al. 1986).

Coverage of the satellite ice tracking could be extended to the north and west, though for some of the satellite passes the present study area is near the Edmonton receiving station's limits. Data from the U.S. station in Fairbanks, Alaska can also be used. Data from this station is archived with NOAA/NESDIS in Washington, though recent news suggests that a large fraction of the digital data has been lost.

The airborne SAR imagery demonstrates the radar's all-weather capability for imaging ice. On several occasions the high resolution showed patterns suggesting the effects of surface water movements. For tracking motion from day to day, however, the high resolution is not required, and accurate navigation is a more important requirement.

An important conclusion of this study is to demonstrate the potential value of future radar imagery from the European (ESA)

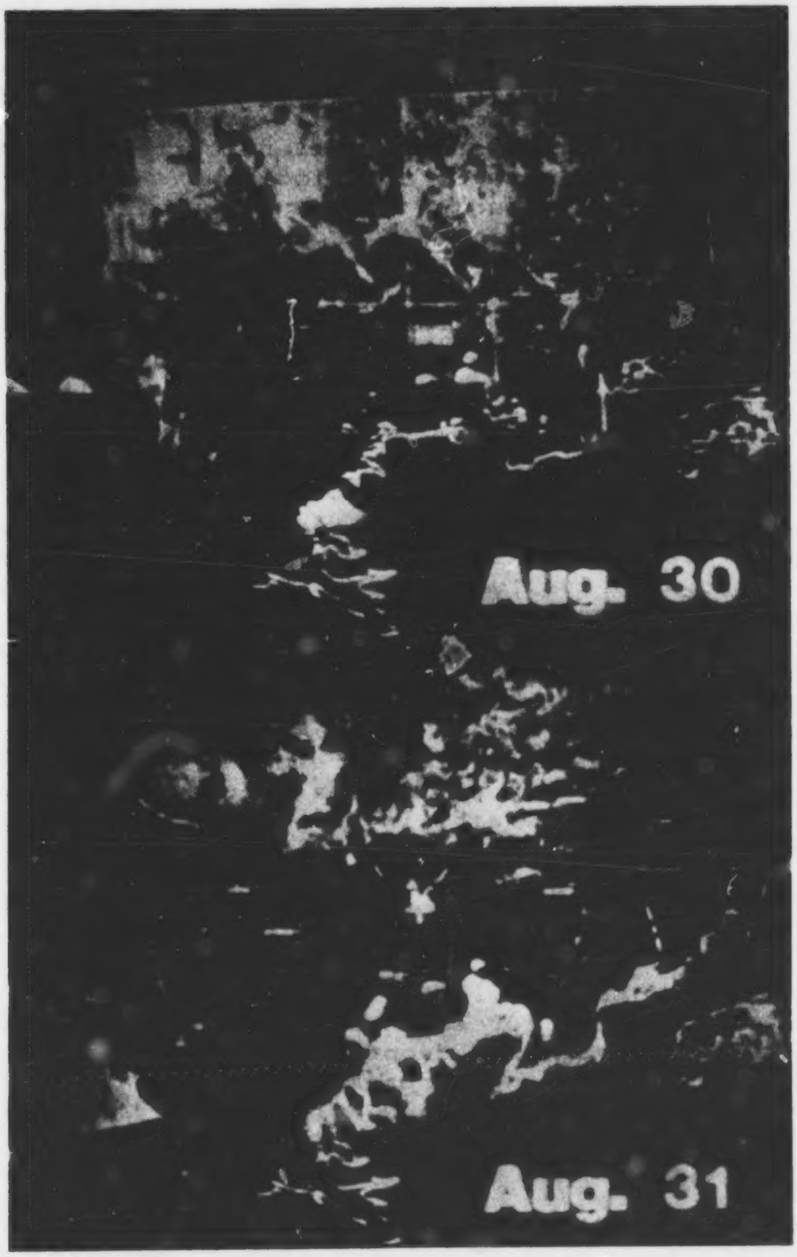

6 Examples of airborne SAR images for August 30 and 31 1984, photographed from the video time lapse movie. A wave-like feature in the ice edge is visible on August 30, but does not appear on August 31.

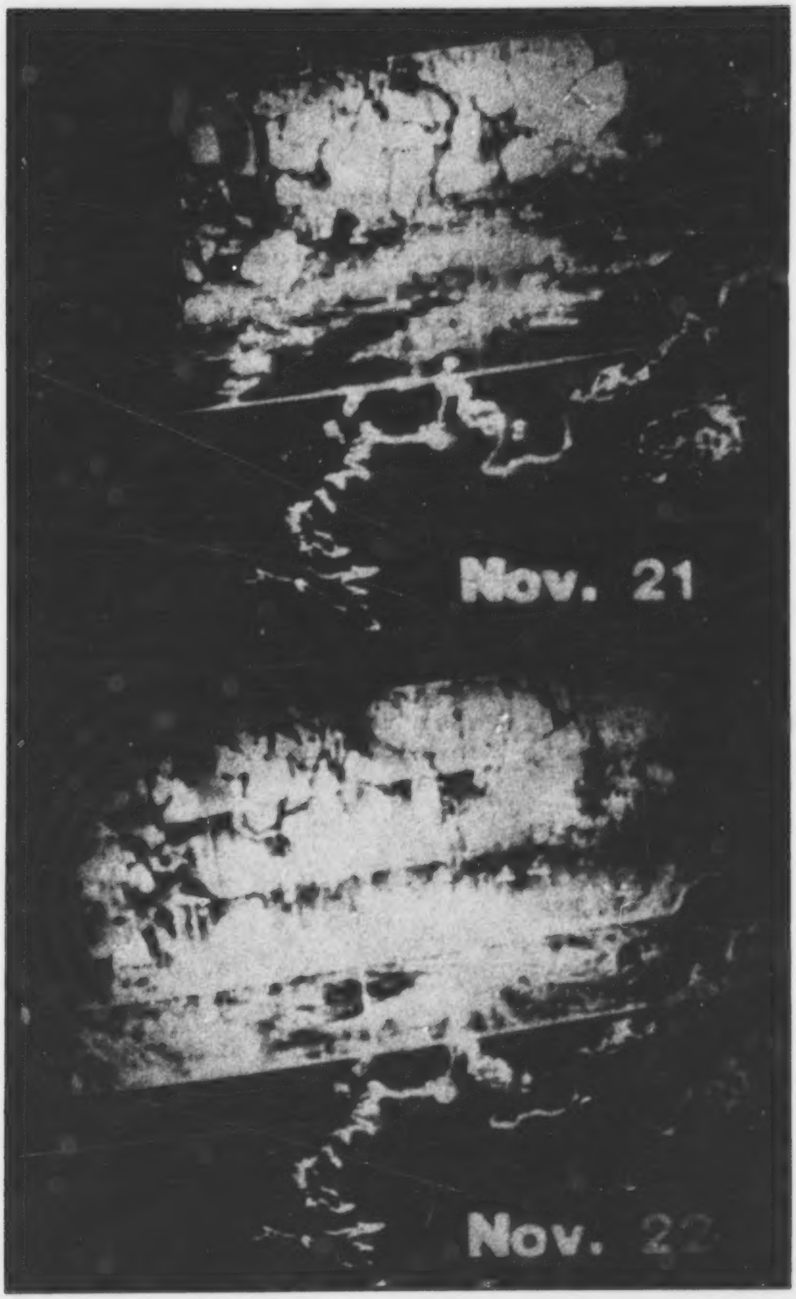

7 Examples of airborne SAR images for November 21 and 22 1984, photographed from the video time lapse movie. Motion of large ice floes can be clearly seen.

satellite ERS-1, due for launch in 1990, and the planned Canadian satellite Radarsat, planned for the 1990's. These will provide large area, all-weather imagery, with 100 meter resolution, and with good navigation accuracy.

Acknowledgements

We thank a number of colleagues at IOS for useful suggestions, especially Andrew Bennett who started the movie-making project with the airborne imagery. Also the staff at AES Edmonton who supply us with satellite imagery, especially John Bullas who oversees this process, and Jim Steen of Dome Petroleum who arranged to supply us with the airborne imagery, and made many useful comments on its application.

References

Arctic Sciences Ltd., 1985, "Development and testing of techniques for digital extraction of ice velocities from hard copy remote sensing imagery" Contractor report to IOS.

Cherniawsky, J.Y., J.F.R. Gower, H. Melling, D.N. Truax and R.C. Kerr, 1986, "Using NOAA AVHRR imagery in studies of sea ice motion in the Beaufort Sea", Paper to be presented at the 10th Canadian Symposium on Remote Sensing, Edmonton, Alberta, May 5-8, 1986

SURFACE-BASED RADAR CLASSIFICATION AND DETECTION OF ICE

by E.O. Lewis[1] and B.W. Currie[2]

This paper discusses the results of several experimental programs undertaken by the Department of Fisheries and Oceans and McMaster University to improve the classification and detection of ice at sea using a surface-based radar system. The experimental programs have been carried out from a site overlooking Lancaster Sound during periods of a full ice cover and during periods of open water.

In the most recent full ice-cover experiment, radars were operated at 3 GHz (10 cm), 9 GHz (3 cm), 16 GHz (1.88 cm) and 35 GHz (0.86 cm), with the latter three providing both like- and cross-polarized signals. Ground truth included on-ice sorties by helicopter and aerial survey photography. The various radars were operated along a set of ten 'standard' radial lines, chosen to contain a variety of ice types and features. The radar video was recorded for subsequent analysis.

In this paper, the effects of the radar parameters of resolution, frequency, and polarization are discussed, together with sample radar images. Some values of normalized radar cross-section are given for iceberg, multiyear, and first-year ice present in the landfast ice zone. Calculation of the like- to cross-polarized cross-section ratio shows that cross-polarization significantly increases the differentiation between multiyear or iceberg ice and first-year sea ice.

During an open water experiment conducted in September of 1984, a dual-polarized X-band radar and a digital recording system were used to record the radar returns from icebergs, 'bergy bits', and growlers (iceberg fragments). Based on results of previous work, emphasis was placed on the polarization properties of the return; in particular, comparison of horizontally- and vertically-polarized returns, as well as cross-polarized components. Physical measurements of the iceberg targets, sea surface, and meteorological conditions were taken. Results presented are values of the normalized radar cross-section for both like- and cross-polarized returns for a number of ice targets. The effect of the various polarizations is discussed. The nature of the returns shows the use of cross polarization enhances the ice target detection performance of the radar.

[1] Department of Fisheries and Oceans, Ocean Science and Surveys, 867 Lakeshore Road, Burlington, Ontario, Canada L7R 4A6

[2] Communications Research Laboratory, McMaster University, Hamilton, Ontario, Canada

INTERPOLATION OF NEARSHORE ICE MOTION

by R.F. McKenna, W.C. Lennox and J.F. Sykes
Civil Engineering Department, University of Waterloo
Waterloo, Ontario, Canada N2L 3G1

For pack ice in constant motion, it is seldom possible to sample the position of identifiable features on a regular grid pattern. Nevertheless, in many situations, spatial variations are best treated in this way. Interpolation is used to transform data collected at random locations in space to a well ordered pattern.

Pack ice motion was determined from aircraft radar images of the nearshore Beaufort Sea. This is an area in which the ice is primarily wind driven, subject to the influence of adjacent shorefast ice and coastal features. The field of motion was deduced from points scattered within 200 kilometers of shore. Since the time between images was 3 days, it was only feasible to consider spatial variations and not the time series of the motion.

Isotropy and homogeneity properties must be considered when selecting an appropriate interpolation method. Two major features of a spatial field are noted, the mean and the covariance structures. Methods using least squares polynomial approximations and autocovariance weighting of nearby points were compared and then integrated in an estimation scheme.

EVALUATION OF REMOTE SENSING PRODUCTS IN THE RADARSAT TIME FRAME

by L. McNutt[1], S. Venkatesh[2] and V.R. Neralla[2]

Remote Sensing data from satellites and aircraft have played a significant role in the development and testing of ice forecasting models. With the launch of ERS-1 and RADARSAT, Canada will receive operational data on a routine basis which can be used to both initialize and update forecast models for strategic ice analyses and climatological modelling. This paper describes the sensor characteristics for the instruments to be carried on the RADARSAT and ERS-1 platforms, and evaluates the data from these sensors for use in ice models currently under development. The models are then discussed in terms of the air-sea-ice parameters necessary to perform the calculations. A matrix of these parameters is developed for the various spatial and temporal scales required. A discussion follows on the use of complementary satellite, aircraft and in situ measurements which will be required to provide the most complete information possible from the data available. Finally, this matrix is used to define areas where further research and technology development are required, before the launch of these satellite systems, to ensure that the volume of remote sensing information expected can be used most effectively.

[1] RADARSAT Project Office, 110 O'Connor Street, Suite 200 Ottawa, Ontario, Canada K1P 5M9
[2] Atmospheric Environment Service, 4905 Dufferin Street, Downsview, Ontario, Canada M3H 5T4

DETERMINATION OF SEA ICE CONCENTRATION AND ICE EDGE POSITION IN THE BEAUFORT SEA USING SATELLITE PASSIVE MICROWAVE DATA

by D.R.P. Williams

Ph.D. Associates Inc.
4700 Keele St., North York
Ontario, Canada, M3J 1P3

ABSTRACT

The major aim of this paper is to evaluate the practical usage of passive microwave satellite remote sensing for monitoring sea ice in the Beaufort Sea. Using data from the Scanning Multichannel Microwave Radiometer (SMMR) on board NASA's NIMBUS-7 satellite, ice freeze-up formation is monitored from August 21 to October 4, 1983 and verified against ice charts from the Atmospheric Environment Service and AES SLAR imagery. Two sea ice algorithms; 1) the AES/Ph.D. algorithm, developed by Irene Rubinstein of Ph.D. Associates Inc., and 2) the SSM/I algorithm, developed by Hughes-U.S. Navy, that produce ice concentrations and ice edge location from the measured brightness temperatures of the dual polarized 18 and 37 GHz SMMR channels are evaluated.

INTRODUCTION

The effectiveness of passive microwave sensors in monitoring seasonal and spatial changes in sea ice has been demonstrated by a number of investigators (Gloersen, et al., 1978; Carsey, 1985; Cavalieri, 1984; and Gloersen, et al., 1977). The capability of passive microwave sensors to detect sea ice depends primarily on the large difference between the emissivity of sea ice (0.90) and of the ocean (0.45). Satellites with passive microwave instruments onboard provide 24 hour, all-weather monitoring of ice conditions on medium to large scales. Near real-time monitoring of sea ice conditions for operational purposes has been demonstrated by Ph.D. Associates Inc. using data from the Scanning Multichannel Microwave Radiometer (SMMR) onboard the NIMBUS-7 satellite (Thirkettle, 1985). With this demonstrated potential in mind, an investigation of the sea ice conditions throughout the 1983 freeze-up period detected by the SMMR are verified against AES Ice Charts and AES SLAR information. The freeze-up period was chosen since this transition from summer to winter ice conditions is an important time to monitor for drilling operations and shipping traffic through the Southern Beaufort Sea.

VALIDATION

Comprehensive developmental work with the 18 and 37 GHz data from the SMMR has yielded regionalized modelling algorithms which differentiate first year, multi-year and total sea ice concentrations (Rubinstein, et al., 1985).

Two of these models for use in the Beaufort Sea region are verified in this work. The AES/Ph.D. model (Figure 1) uses the dual polarized 18 and 37 GHz brightness temperatures (Tb) as inputs with the spatial resolution of the data being 30 km x 30 km.

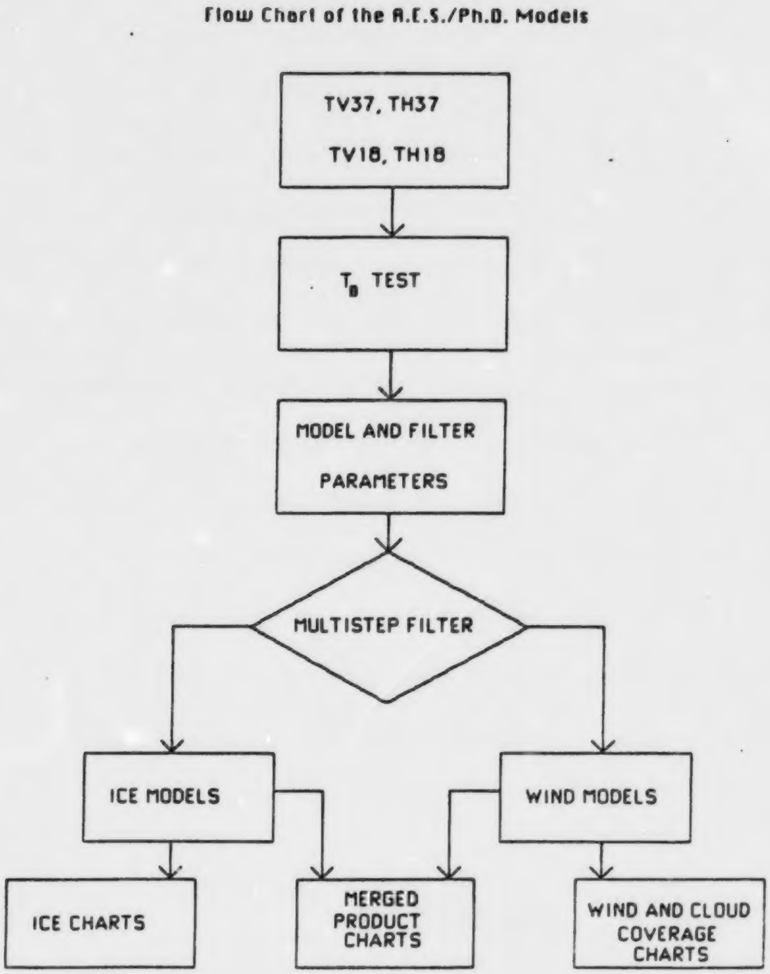

Figure 1 Flow Chart of the A.E.S./Ph.D. Model
(Ph.D. Associates Inc. Internal Report, 1985)

Brightness temperature is a measure of the product of the physical temperature and emissivity of the observed medium. These brightness temperatures are tested as to whether they fall within a reasonable range of values. The resulting data and the model and filter parameters are, then, passed through a multi-step filtering process which, among other things, corrects for atmospheric conditions such as cloud cover, and precipitation, and decides whether the data are from areas of open water or sea ice. The filtering separates the data into values used for the mapping of sea ice cover and for the calculation of windspeeds over the open ocean. The ice model used in this study calculates first year and multi-year ice concentrations to give a total ice concentration value.

The SSM/I algorithm also yields total ice concentrations but only first year or multi-year fractions. If the brightness temperatures reach a certain cut-off value, the model interprets it as being either first year or multi-year, but not a mixture of both. Both models have constants built into them whose values depend upon regional and seasonal variations in surface temperature and emissivities from different ice types. These constants require verification for the model to be used at all times of the year and in differing regions of interest.

The total ice concentrations produced by each model are computer mapped and auto-contoured at standard ice concentration levels (10, 35, 65, 85, 99 ice to water percentages used by the Atmospheric Environment Service) (Rubinstein, et al., 1985). To maintain consistency with the AES charts and SLAR, the 10% ice concentration level was taken to be representative of the ice edge. Figure 2 shows the ice edge produced by the AES /Ph.D. Model and the AES Ice Chart.

Distances in kilometers north of 70 N latitude to the ice edge were measured along every 1/4 degree of longitude between 128 W to 145 W.

Differences between corresponding measurements of the different data sources were computed on a daily basis and for the total freeze-up period (Figure 3) to determine the agreement between the models and AES map products in representing the location of the ice edge.

The overall results presented in Figure 3 include the mean, the absolute mean and the corresponding standard deviation. The mean of the differences is an indicator of the overall degree of under or overestimation. In the example of Ice Charts - SLAR, the minus sign indicates that the Ice Chart ice edge is on average, 7.5 km south of the SLAR ice edge for the total freeze-up period with an almost 23 km standard deviation.

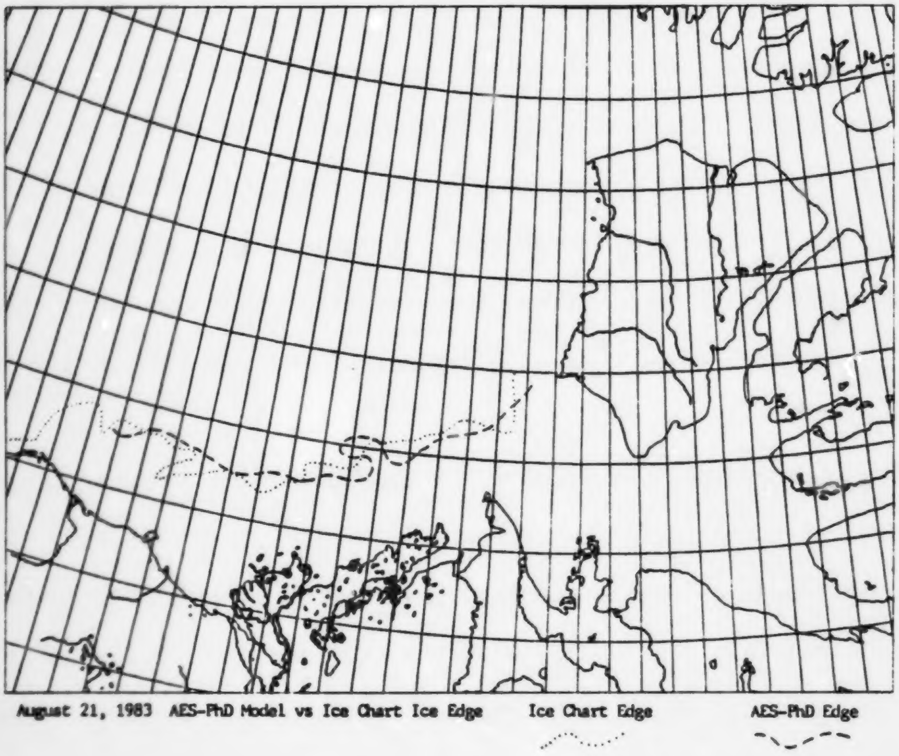

Figure 2 Ice Edge Comparison for August 21, 1983

Comparison of the Data Sources which Yield Ice Edge Location

Data Source Comparison	Mean (in km)	S.D. (±)	Absolute Mean (in km)	S.D. (±)	# of observations
Ice Charts - SLAR	-7.50	22.86	17.35	16.62	206
Ice Charts - AES-PhD Model	-4.80	24.71	19.72	15.60	294
Ice Charts - SSM/I Model	-77.63	36.78	78.03	35.93	395
SLAR - AES-PhD Model	-0.23	24.44	20.42	13.34	170
SLAR - SSM/I Model	-72.69	36.83	72.69	36.83	206

Figure 3 Data Source Comparisons

The absolute mean indicates overall the closeness of the compared ice edges regardless of the direction of the differences in position (north or south). From Figure 3, the results for the SSM/I model indicate a consistent underestimation of the ice edge by approximately two SMMR footprints. The reason for this relative northward position of the ice edge can be attributed to the seasonal constants being set at values not representative of the surface conditions. The concentration percentages tend to be underestimated to a large degree, thereby, locating the ice edge farther north.

The absolute means for the AES/Ph.D. model show the ice edge location to be generally within about 2/3 of a SMMR footprint. The best agreement was found between the AES Ice Chart and the AES SLAR ice edge locations. A graphical representation of the results is shown in Figure 4.

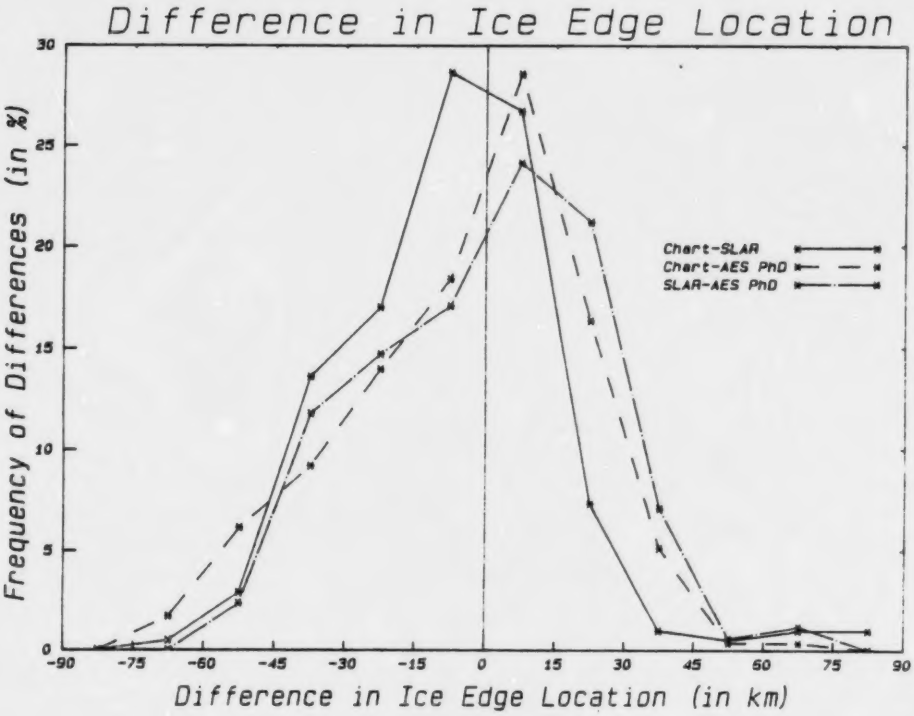

Figure 4 Frequency Distribution of Ice Edge Location Differences

Since ice edge motion is a dynamic process, the ice edge can move over spatially large areas in short periods of time. As a preliminary investigation into the causes for the differences in ice edge location between each data source, the single orbits for each day were examined.

It was surmized that one of the major causes of the ice edge location differences between data sources was the variance in time from the orbit passes and the SLAR overflights. A single orbit pass was examined which coincided exactly in time to the SLAR overflight. The results of comparing the ice edge location for each is:

DATE	MEAN (in km)	S-D (+)	ABS. MEAN (in km)	S.D. (+)	NUMBER OF OBSERVATIONS
Aug 25	0.04	16.74	12.48	10.89	27

Even though one cannot conclude much from only one day's comparison, the results do show a better agreement for the ice edge locations.

The last area of investigation pertained to the total ice concentration differences between the AES/Ph.D. model and the AES Ice Charts. For each SMMR footprint location, the total ice concentration percentage produced by the AES/Ph.D. model, was recorded along with the corresponding AES Ice Chart total ice concentration value. The differences were computed and grouped into ice concentration classes (Figure 5). The AES/Ph.D. model consistently underestimates by 20% the total ice concentration above 80%. Whereas, for the lower ice concentrations, the model performs reasonably well.

Concentration Differences Between AES-PhD Model and AES Ice Charts

Concentration Class	Mean (%)	S.D.	Absolute Mean (%)	S.D.	# of Observations
20% - 40%	3.20	± 9.45	7.83	± 6.13	89
50% - 70%	-7.98	± 11.17	10.72	± 8.54	81
80% - 100%	-20.23	± 8.28	20.23	± 8.28	202

Figure 5 Total Ice Concentration Differences Between AES/Ph.D. Model and AES Ice Charts for Freeze-Up Period

CONCLUSION

In any validation of a remote sensing tool, there is a problem in obtaining a standard data source for verification. Small scale ground-truth activities are expensive and limited spatially in coverage, hence, the validation must rely on other remote sensing techniques, each with its own inherent errors. The AES/Ph.D. model has performed well in determining the ice edge and ice concentration information for both summer and winter conditions. However, for the freeze-up period, when ice conditions and properties change rapidly, a fine tuning of the model constants is required to improve the results of the comparisons to the AES Ice Charts and AES SLAR. Another important factor in validation is to attempt to obtain the verification data products at coincident times with the orbit passes. This would negate the errors in ice concentration values caused by the rapid changes of the ice over time.

With the launch in August, 1986 of the Special Sensor Microwave Imager (SSM/I) on board the DMSP satellite, better coverage of the earth will be provided. Wider swaths, more frequent orbits over an area, and an increase in spatial resolution to 12 km x 12 km with the use of the 85.5 GHz channel, will improve the capabilities of monitoring sea ice conditions.

ACKNOWLEDGEMENTS

This work was sponsored by AES through a contract from Rene Ramseier of AES Ice Research and Development. It will be included as a portion of the author's Master's thesis in the Experimental Space Science Department at York University. Thanks is extended to Dr. Frank Bunn, Dr. Frank Thirkettle, and Irene Rubinstein of Ph.D. Associates and Rene Ramseier of AES.

REFERENCES

Carsey, F.D. (1985) Summer Artic sea ice character from satellite microwave data. Journal of Geophysical Research, Vol. 90, No.C3, p. 5015-5034.

Cavalieri, D.J., P. Gloersen and W.J. Campbell (1984) Determination of sea ice parameters with the Nimbus-7 SMMR. Journal of Geophysical Research, Vol. 89, No. D4, p. 5355-5369.

Gloersen, P., H.J. Zwally, A.T.C. Chang, D.K. Hall, W.J. Campbell and R.O. Ramseier (1977) Time-dependence of sea-ice concentration and multi-year ice fraction in the Arctic Basin. Boundary Layer Meteorology, 13, p. 339-359.

Gloersen, P., H.J. Zwally, A.T.C. Chang, D.K. Hall, W.J. Campbell, and R.O. Ramseier (1978) Time-dependence of sea-ice concentration and multi-year ice fraction in the Arctic Basin. Boundary Layer Meteorology, 13, p.339-359.

Rubinstein, I.G., F.E. Bunn and R.O. Ramseier (1985) Nimbus-7 microwave radiometry of ocean surface winds and sea-ice. Proceedings of 19th International Conference on Remote Sensing of the Environment, Ann Arbor, Michigan, October 21 - 25, 1985.

Thirkettle, F.W. (1985) A near real-time data system for satellite passive microwave ice maps. Proceedings of 19th International Conference on Remote Sensing of the Environment, Ann Arbor, Michigan, October 21 - 25, 1985.

A CLIMATOLOGICAL ANALYSIS OF EASTERN CANADIAN SEABOARD ICE CONDITIONS USING PASSIVE MICROWAVE SATELLITE DATA (1973-1985)

by

Anne E. Walker[1]

Passive microwave data from satellite microwave radiometers, Nimbus-5 ESMR and Nimbus-7 SMMR, are used to analyse ice conditions along the Canadian East Coast for the years 1973 to 1985. Maximum ice extent and ice areal coverage information are derived for the mid-February to mid-March period, and compared to climatological and oceanographic information. Interannual variation in East Coast ice cover is investigated with respect to regional climate and oceanography. Results of this analysis will be discussed, emphasizing the role passive microwave data sets can play in studies of sea ice distribution and the sea ice/climate relationship.

This research is part of the requirements of an M.A. thesis that will be submitted to Carleton University by the author.

---

[1] Ph.D. Associates Inc., 107 Fordwich Crescent, Rexdale, Ontario, M9W 2T6.

INTRODUCTION

Over the past several years, there has been an increase in offshore operations along Canada's East Coast, mainly due to oil and gas development. The presence of sea ice during the winter months can be a barrier and a hazard to these operations. Within the scientific community, there is the consensus of the need for a greater understanding of ice limits and variability (Wadhams and Lever, 1985). This paper presents results of the application of satellite passive microwave data to the study of interannual variability of sea ice extent along the Eastern Canadian Seaboard, covering the years 1973 to 1985.

Passive microwave remote sensing depends on naturally emitted radiation from the earth's surface. The main advantages are day and night sensing capability, and the ability to penetrate clouds, haze and some precipitation. These attributes make passive microwave especially suited to monitoring East Coast sea ice, where the occurrences of storms and unsettled weather during winter months may in some cases prevent visual ice reconnaissance (Mullane, 1980).

THE STUDY AREA

For the purposes of this study, the Eastern Canadian Seaboard is defined as extending from approximately 44°N to 70°N. This area includes the coastal waters known as the Gulf of St. Lawrence, East Newfoundland Waters, Labrador Sea and Davis Strait, as illustrated in Figure 1.

PASSIVE MICROWAVE DATA

The passive microwave data used in the analysis is from radiometers on board two NASA satellites:

1) NIMBUS-5 Electrically Scanning Microwave Radiometer (ESMR)
2) NIMBUS-7 Scanning Multichannel Microwave Radiometer (SMMR)

A comparison of the operation parameters of the ESMR and SMMR appears in Table 1. The main difference between the two radiometers concerns frequency. The ESMR is a single frequency radiometer operating at 19.35 GHz (horizontal polarization). The single frequency characteristic limits the amount of sea ice information that can be derived from the data. The multifrequency and dual-polarization characteristics of the SMMR provide the ability to resolve more

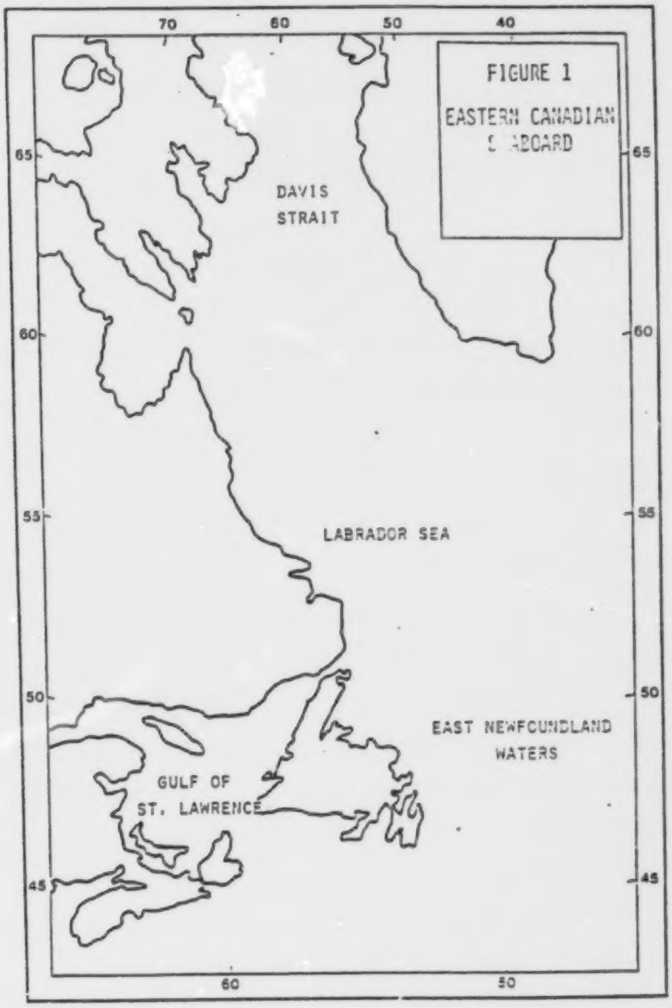

Figure 1 The Study Area

Table 1

ESMR and SMMR Operation Parameters (after NASA, 1972 and NASA, 1978)

	NIMBUS-5 ESMR	NIMBUS-7 SMMR
Resolution	30 km	30 km
Frequency	19.35 GHz	6.6,10.69,18,21,37 GHz
Polarization	Horizontal	Vertical & Horizontal
Launch Date	Dec. 1972	Oct. 1978

than one ice type from the data (Gloersen et al., 1978).

The archived radiances (brightness temperatures) measured from both the

ESMR and SMMR yield a data set covering over 13 years (December 1972 to the present). For the analysis of Eastern Seaboard ice conditions, data from the late February to late March time period were utilized. This time period corresponds to the time of maximum ice extent along the East Coast.

ICE MODELS

Ice concentrations were derived from the archived brightness temperatures (T_B's) using two computer-based algorithms, which are described below.

SIMPLE SEA ICE ALGORITHM

This algorithm was applied to the NIMBUS-5 ESMR data because of the single frequency nature of the data. It is a simple linear algorithm that derives ice concentration from an observed T_B through a linear interpolation between characteristic radiances of open ocean (0% ice) and 100% sea ice cover (Gloersen et al., 1974). Figure 2 expresses this algorithm graphically. The constants for open water and 100% ice were derived specific to the East Coast region. A value for total ice concentration is produced using this algorithm, since the single frequency measurements impede the distinguishing of different ice types. Since the Eastern Seaboard ice cover is composed primarily of first year ice with less than 10% old ice (Markham, 1980), it can be assumed that the total ice concentration value is equal to that of first year ice.

AES/Ph.D. ALGORITHM

This algorithm was derived and tested specifically with NIMBUS-7 SMMR data. Using two of the SMMR frequencies, 18 and 37 GHz , the algorithm produces first year, multiyear and total ice concentrations (Rubinstein et al., 1985). The algorithm uses regionally-specific inputs, and employs a series of filters to remove any effects of cloud, wind and precipitation that may distort ice edge location. Figure 3 presents a flowchart representation of this algorithm. Rubinstein et al. (1985) provides a more detailed description of the algorithm.

The AES/Ph.D. algorithm has been validated for East Coast ice conditions against Atmospheric Environment Service ice charts (Moreau et al., 1985). Preliminary results indicate ice concentration agreement to ±10% and ice edge agreement to ±15 km (Rubinstein and Ramseier, 1985).

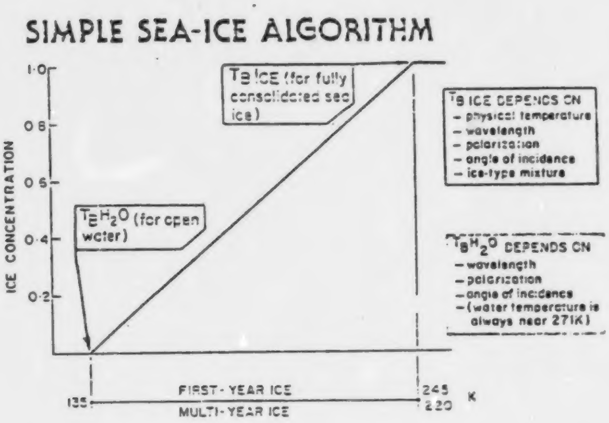

Figure 2 Simple Sea Ice Algorithm (from Ramseier, 1983)

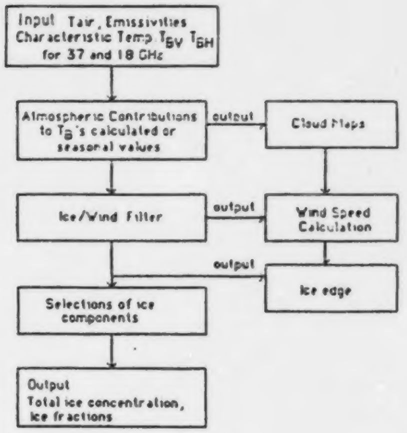
Input Tair, Emissivities Characteristic Temp TBV TBH for 37 and 18 GHz
Atmospheric Contributions to TB's calculated or seasonal values
output
Cloud Maps
Ice/Wind Filter
output
Wind Speed Calculation
output
Ice edge
Selections of ice components
Output Total ice concentration, Ice fractions

Figure 3 AES/Ph.D. Algorithm (from Rubinstein and Ramseier, 1983)

ANALYSIS OF EASTERN SEABOARD DATA

In order to investigate interannual variability in sea ice extent along the Eastern Seaboard, two methods were used to analyse the ESMR and SMMR data. A simple plotting of maximum ice extent on a map base allows for extremes in extent over the 13 year period to be identified. Derivation of values for ice extent and ice area provides a stastistical representation of the data. These two approaches are described here in detail.

ICE CONCENTRATION MAPS

The ice concentrations derived from the passive microwave data are contoured and mapped using specialized software (Thirkettle, 1985). Figure 4 presents an example of one of these plots at a reduced scale. The contours summarizing the data correspond to levels of percentage ice cover. For this analysis the levels 10%, 15%, 35%, 65%, 85% and 99% are used. Ice edge location is identified by the 15% contour.

For each year of data, weekly plots were produced covering the late February to late March time period. By overlaying these plots, the date of maximum ice extent was identified. The corresponding ice edge locations (15% contour) were transferred onto a separate overlay. This overlay, containing 13 ice edges, became a visual representation of variation in maximum ice extent. Figure 5 summarizes this overlay by presenting the extremes in maximum ice

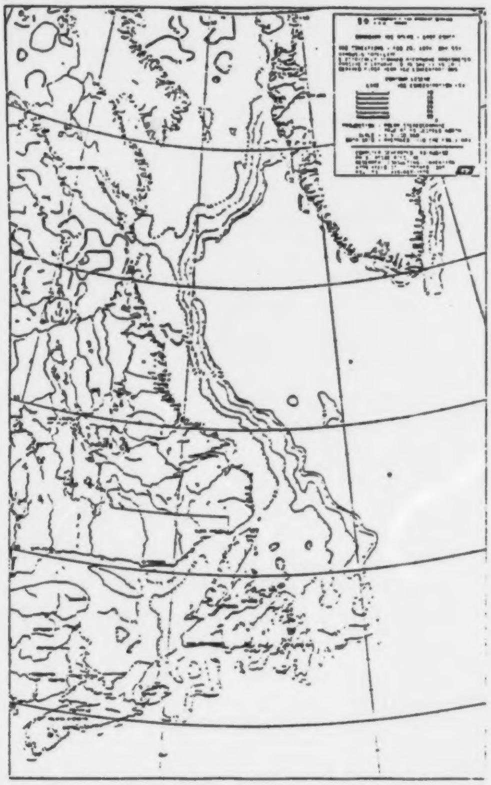

Figure 4 Ice Concentration Map (from Owens and Ramseier, 1984)

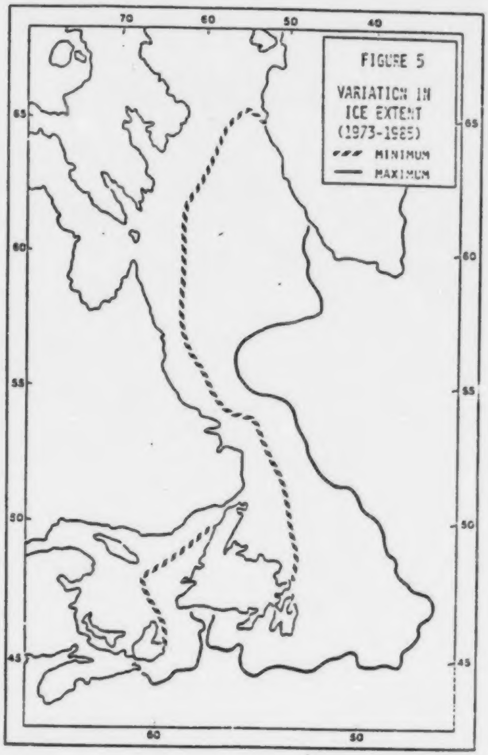

Figure 5 Extremes in Maximum Ice Extent

extent for the 1973 to 1985 period.

The results of this analysis approach revealed that maximum ice extent along the Eastern Seaboard is extremely variable from year to year. The East Newfoundland Waters and Davis Strait regions were determined to be the most variable.

STATISTICAL ANALYSIS

Before the ice concentrations are derived, the archived T_B's are remapped onto a grid using a weighted averaging technique (Thirkettle, 1985). This grid corresponds to 1/10 of the Canadian Meteorological Center (CMC) grid, with each cell measuring 38.1 km square. At each grid point, ice concentrations are computed and stored for future statistical analysis.

For the analysis of Eastern Seaboard ice conditions, 3 days of SMMR data were averaged onto the grid. The three days were necessary to obtain complete orbital coverage of the study area. Complete coverage was available with a one day average of ESMR data.

Statistics were generated for the time of maximum extent for each year in the 13 year period. Values for ice extent and ice area were generated from the gridded ice concentrations. Ice extent refers to the area of the total number of grid squares containing ice. Ice area is the actual area covered by ice, determined from the gridded ice concentrations. Ice extent represents the spatial extent of the ice, while ice area takes into account the different concentrations of ice within the pack. The value for ice extent is thus usually greater than that for ice area. The computation of these two values are summarized below:

$$\text{Grid cell area} = 38.1 \text{ km} \times 38.1 \text{ km} = 1451.61 \text{ km}^2$$

$$\text{Total ice area} = \Sigma A_n, \text{ where } A_n = \% \times 1451.61 \text{ km}^2$$

$$\text{Total ice extent} = N \times 1451.61 \text{ km}^2, \text{ where N is the total number of grid cells containing ice } (\geq 15\% \text{ concentration})$$

These values were calculated for each year in the 1973 to 1985 time period. Figure 6 presents the graphical results of this analysis, where the maximum ice extent and ice area values are plotted for each year. The resulting trend can be summarized as one of decreasing ice area and extent between 1973 and 1979, with minimum conditions existing until 1981. After 1981 an increase is noted, with a maximum for the 13 year period occurring in 1984. The maximum extent and area for 1985 are less than the values for 1984. It should be noted, that this trend represents changes in maximum extent for the Eastern Seaboard as a whole. The variation in ice extent for various subregions may differ from this trend.

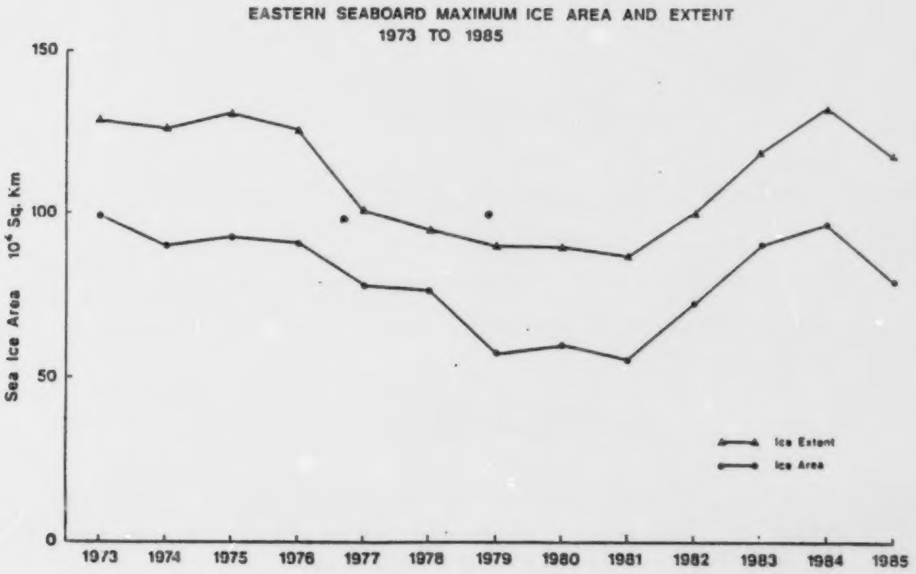

Figure 5 Eastern Seaboard Maximum Ice Area and Extent (1973-1985)

FUTURE WORK

Further work is underway to compare the results from this analysis to climatological and oceanographic data for the 1973 to 1985 time period. The aim is to account for the interannual variations observed in the passive microwave data. The results of this total research effort are in partial fulfillment of a M.A. thesis, for the Department of Geography at Carleton University.

CONCLUDING REMARKS

Satellite passive microwave data is a valuable source of ice information for studies of interannual ice variation, with extensive spatial and temporal data coverage. The method of analysis presented in this paper can be applied to any region, even the Arctic as a whole. The archived gridded ice data can be applied to climate studies and models dependent upon ice information as input. The presence of a sea ice cover on the oceans plays an important role in the global heat and energy balances. As a result, the ice area parameter is of particular significance.

The NIMBUS-7 SMMR is still operating, beyond its predicted life expectancy. The planned launch this year of the U.S. Navy's DMSP satellite containing the Special Sensor Microwave Imager (SSM/I) will ensure continued passive microwave data collection. This will extend the archived data set beyond the existing 13 years.

ACKNOWLEDGEMENTS

This research was performed under contract with Ice Research and Development of the Atmospheric Environment Service, under the guidance of Dr. R.O. Ramseier. Dr. F.W. Thirkettle of Ph.D. Associates was responsible for the computer generation of maps and statistics.

REFERENCES

GLOERSEN, P., T.T. WILHEIT, T.C. CHANG, W. NORDBERG and W.J. CAMPBELL. 1974. Microwave maps of the polar ice of the earth. Bulletin American Meteorological Society, v. 55(12): pp. 1442-1448.

GLOERSEN, P., H.J. ZWALLY, A.T.C. CHANG, D.K. HALL, W.J. CAMPBELL and R.O. RAMSEIER. 1978. Time-dependence of sea ice concentration and multiyear ice fraction in the Arctic Basin. Boundary Layer Meteorology, v. 13: pp. 339-359.

MARKHAM, W.E. 1980. Ice Atlas - Eastern Canadian Seaboard. Environment Canada, Toronto.

MOREAU, T.A., E.L. SUDEIKIS, I.G. RUBINSTEIN and F.W. THIRKETTLE. 1985. A study and report on operational ice mapping, NIMBUS-7, SMMR. Final Report for Atmospheric Environment Service, Ice Branch, Ottawa.

MULLANE, T.F. 1980. Operational use of satellite imagery in the Canadian ice program. Presented at the 6th Canadian Symposium on Remote Sensing, Halifax, Nova Scotia, May 21-23, 1980.

NATIONAL AERONAUTICS AND SPACE ADMINISTRATION. 1972. The NIMBUS 5 User's Guide. Goddard Space Flight Center, Greenbelt, Maryland.

NATIONAL AERONAUTICS AND SPACE ADMINISTRATION. 1978. The NIMBUS 7 User's Guide. Goddard Space Flight Center, Greenbelt, Maryland.

OWENS, A.E. and RAMSEIER, R.O. 1984. Ice atlas of Eastern Canada based on Nimbus-5 passive microwave data (1972-1977). Ice Research and Development Report 83-04, Atmospheric Environment Service, Ottawa.

RAMSEIER, R.O. 1983. Passive microwave remote sensing of sea ice from research to operations. Canadian Meterological and Oceanographic Society Speaking Tour 1983/84.

RUBINSTEIN, I.G. and RAMSEIER, R.O. 1985. Scientific application of passive microwave satellite data for ice monitoring and research. Proceedings of Conference on the Use of Satellite Data in Climate Models, Alpach, Austria, June 10-12, 1985: pp. 117-123.

RUBINSTEIN, I.G., F.E. BUNN and R.O. RAMSEIER. 1985. Nimbus-7 microwave radiometry of ocean surface winds and sea ice. Presented at the 19th International Symposium on Remote Sensing, Ann Arbor, Michigan, October 21-25, 1985.

THIRKETTLE, F.W. 1985. A near real-time data system for satellite passive microwave ice maps. Presented at the 19th International Symposium on Remote Sensing of Environment, Ann Arbor, Michigan, October 21-25, 1985.

WADHAMS, P. and LEVER, J. 1985. LIMEX - A Labrador ice margin experiment, Preliminary science plan. Centre for Cold Ocean Resources Engineering, Memorial University, St. John's, Newfoundland.

SIDE-LOOKING AIRBORNE RADAR DETECTION AND IDENTIFICATION OF ICEBERGS

By CDR N. C. EDWARDS, JR.
and
LTJG N. B. THAYER
United States Coast Guard
International Ice Patrol
Avery Point
Groton, Connecticut 06340-6096

ABSTRACT

The International Ice Patrol (IIP) has searched the southeastern, southwestern and southern limits of the Grand Banks of Newfoundland for hazardous icebergs using visual ship and aircraft reconnaissance techniques for seventy years. Since 1983, the AN/APS-135 side-looking airborne radar (SLAR) has been flown by HC-130 Hercules aircraft from Gander, Newfoundland to provide effective all-weather iceberg surveillance over a 35,000 nm^2 ocean area daily.

From the BergSearch '84 and the 1985 SLAR Detection experiments, SLAR detection capability has been determined. Iceberg detection decreases with increasing sea state, increasing lateral range, greater incidence angles, smaller target size and with up or down sea imaging. The typical fluctuations in iceberg target detections are +/- 10 percent and SLAR detections of small, medium and large icebergs are at the 90 percent confidence level.

Correct identification of small icebergs and slow moving ships is a real problem, for all icebergs entering the patrol area eventually become small, then growlers and many fishing vessels continue to work the Grand Banks year round. The data indicates that experienced SLAR operators can discriminate between ambiguous targets only with 60 percent confidence. Therefore, IIP has adopted specific search procedures to reduce the percentage of ambiguous targets and maintain a most effective SLAR iceberg reconnaissance program for the fog and storm laden Grand Banks.

INTRODUCTION

Following the tragic sinking of the RMS TITANIC on 15 April 1912, great international concern was raised over the safety of ships transitting the fog ladden, storm tossed waters of the Grand Banks of Newfoundland. At the first Safety of Life at Sea (SOLAS) Convention held in 1913, thirteen nations agreed to sponsor an annual ice patrol which would monitor the presence of hazardous ice near the southern, southwestern and southeastern regions of the Grand Banks. By Presidential order, the U. S. Coast Guard commenced the International Ice Patrol in 1914.

For the first thirty years, ice patrols comprised of ships locating the southernmost icebergs which drifted south from the glaciers of Greenland beyond 48°N to the Tail of the Bank. The ship maintained a watch on these pieces of glacial ice which ranged in above the surface size from a grand piano (growler at 200 tons) to a large naval vessel (very large at 10 million tons). During World War II airborne searches became a reliable technique for covering large areas, i.e.. the Ice Patrol region (40°N to 52°N and 39°W to 57°W). Since the War, IIP used primarily visual aircraft searches to detect and monitor icebergs and sea ice until 1983.

Although cutters have not been used on patrol in recent years, they have been utilized annually to collect oceanographic data and conduct iceberg research. The data has been utilized to improve the technologies of iceberg detection, drift modelling and iceberg deterioration prediction. This paper will focus on detection research conducted in 1984 and 1985.

BACKGROUND

Since 1983, the International Ice Patrol has utilized a Motorola AN/APS-135 side-looking airborne radar (SLAR) aboard HC-130 Hercules aircraft as its primary method of iceberg reconnaissance. The ability to detect icebergs with a SLAR in poor or zero visibility, plus the ability to search larger areas, i.e. 35,000 nm^2 daily, has resulted in a significant increase in the number of icebergs tracked by IIP (Thayer, 1985).

Because SLAR is used with the sea surface frequently obscurred by clouds, IIP has infrequently had visual confirmation of iceberg detections. Without visual confirmation, distinguishing between iceberg and vessels is very difficult. Research of these problems was conducted in two airborne radar detection experiments, BergSearch '84 and the 1985 SLAR Detection Experiment.

In April 1984, BergSearch '84 participants collected SLAR and synthetic aperture radar data to evaluate their ability to detect small icebergs and growlers in seas less than 4 meters. Several flights were made over the surface-truth vessel, M/V POLARIS, and selected ice targets. Results of the data analysis reported in Rossiter et al (1985) show that greater detectability is obtained with lower sea states, at lower altitudes within the operating envelop of each system and when viewing targets across rather than up or down the wind and sea. BergSearch '84 data also demonstrated that ships and iceberg generally do not display different radar target signatures on SLAR imagery.

IIP conducts iceberg reconnaissance accounting for these findings. To cover the ice limits in a vast patrol region (530,000 nm^2), a 50 km SLAR range scale setting and an 8000-foot search altitude have been routinely used. To detect visible cues on the SLAR film (target movement, wakes, brash, radar shadows, strength of return), search patterns with parallel search legs and track spacing (25 nm) equal to half the total SLAR sweep width (100 km) have been routinely used (Thayer, 1986). This type of search plan gives 200 percent coverage of the interior of the search area and offers two looks at each target.

From the BergSearch '84 results, the 1985 SLAR Detection Experiment was designed to measure SLAR's capability to detect various sized icebergs in calm and moderate sea conditions at all ranges out to 50 km and to measure the reliability of SLAR operators to correctly discriminate between iceberg and ship targets.

1985 SLAR DETECTION DATA

From Gander, Newfoundland, the CG-1504 HC-130 aircraft rendezvoused with the USCGC EVERGREEN on 30 April, 1, 2, 4, and 5 May 1985 in the vicinity of 46°N 48°W, approximately 600 km to the southeast. The aircraft made several passes each day on a medium and two small icebergs, associated growlers and the EVERGREEN while the ship recorded visually and electronically target motion, made size measurements, and observed meteorological and oceanographic conditions. Sea conditions were consistently less than 2 meters. SLAR data was collected at 2500-, 4000-, and 8000-foot search altitudes. Both 25 and 50 km SLAR range settings were utilized to test ice targets detection to 50 km, each side of the aircraft.

On 27 April, it was evident that the SLAR did a better job of tracking growlers than the CGC EVERGREEN. Seventeen growlers were detected and visually confirmed by the aircraft but only 5 were tracked by ship. Thus, a limited number of detection opportunities for growlers resulted. The growlers tracked by the CGC EVERGREEN on 30 April and 1 May ranged from 3 to 15m in length and up to 2 meters in height. Because the first iceberg, a medium dry dock (75m x 58m x 18m), broke into 7 growlers on 30 April, EVERGREEN located and remained with a small drydock iceberg (60m x 40m x 10m) which deteriorated to 35m x 25m x 6m between 1 and 5 May. On the final day, an additional small iceberg (24m x 18m x 5m) calved from the subject berg providing another ice target. The number of medium and small iceberg detection opportunities were acquired as planned (Table 1).

Target	Detection/Opportunity
EVERGREEN	90/90
Iceberg (small and medium)	132/138
Growlers	76/79

Table 1. Summary of Data

Each detection opportunity was recorded with associated lateral range (the closest point of approach between target and SLAR aircraft), wind speed, significant wave height (Hs), SLAR range setting, search altitude and target identification (Table 2). Since a post-analysis of iceberg reconnaissance flights using all cues available is normally conducted by the Ice Reconnaissance Detachment (ICERECDET), the results of this experiment closely approximate IIP search performance.

Target Type 1	Lateral Range (km)	Range^2 Scale (km)	Search Altitude (ft)	Significant Wave Height (m)	Wind Speed (m/s)
Small Iceberg	0.6 - 47.0	25 50	2500 4000 8000	0.6 - 1.8	2.0 - 12.9
Growler	0.6 - 47.0	25 50	2500 4000 8000	0.6 - 1.8	2.0 - 12.9

Note: 1. Iceberg sizes classified by IIP are growler (<5m in height, <15m in length) and small iceberg (5-15m in height, 15-60m in length).
2. 25km scale was used at 2500 and 4000 foot altitudes and 50km, at 8000-foot altitude.

Table 2. Range of Parameters Investigated During SLAR Experiment

ANALYSIS AND RESULTS

Since the CGC EVERGREEN was detected in all opportunities (Table 1), it is used as a reference point during post-flight reconstruction of ice target positions. The SLAR system detection capability was measured by correlating the manually recorded surface-truth data with the SLAR film imagery to determine detection or miss. Since this post-analysis phase used all available knowledge of concurrent target location, these data represent an upper bound on expected system detection performance.

DETECTION

The iceberg data was primarily sorted by target size (growler, small and medium) and search altitude. After detection probabilities had been computed, further analysis of medium icebergs was not necessary for as Table 3 from Robe et. al, 1985 shows all opportunities were detections. The growler and small iceberg data collected at 8000-foot and 50km SLAR were then sorted by lateral range into bins of <25km and 25 to 50km.

TARGET TYPE	SEARCH ALTITUDE/SLAR RANGE SCALE		
	2500 ft/25 km	4000 ft/25 km	8000 ft/50 km
Medium Iceberg (75 meters)	7/7 (1.00) Mean Hs = 0.8m	6/6 (1.00) Mean Hs = 0.7m	7/7 (1.00) Mean Hs = 0.6m
Small Iceberg (24 - 60 meters)	41/42 (0.98) Mean Hs = 1.4m	37/37 (1.00) Mean Hs = 1.4m	34/39 (0.87) Mean Hs = 1.3m
Growlers (3 - 15 meters)	20/21 (0.95) Mean Hs = 0.7m	46/47 (0.98) Mean Hs = 0.7m	10/11 (0.91) Mean Hs = 0.9m

Note: Ratios are number of detections/number of opportunities.
Numbers in parentheses are target detection probabilities.

Table 3. Target Detection Probabilities for Ice Target Data

The resulting detection probabilities for growlers in the near and far range were 0.86 (5 of 6 opportunities) and 1.00 (5 of 5 opportunities), respectively. Based on this limited data, no significant variation in growler detection capability appears to occur over the 50 km swath either side of the aircraft. Also, longer lateral ranges could not be linked to decreasing detection probability of small icebergs; in fact, 18 of 19 targets were detected at ranges beyond 25 km, while 16 of 20 icebergs were detected at ranges less than 25 km (Robe et al, 1986).

The small icebergs were detected on 78 of the 79 passes made at 2500- and 4000- foot altitude using the 25 km SLAR setting. Only 34 of 39 small iceberg targets were detected from 8000-foot and 50 km range. The decrease in detection of small targets at higher altitude and larger range scale is explained by a larger depression angle with increased altitude and a diminished display resolution with the wider SLAR range (Rossiter et al, 1985). Seas were less than 1 meter for all of the growler detection opportunities and detections at 2500- and 4000-foot altitudes were high with 66 for 68 opportunities. At 8000-foot, growlers were also detected on 10 of 11 opportunities.

This growler detection performance was clearly superior to that achieved in BergSearch '84. The only apparent explanation for this difference is that the 1985 data included significant wave heights (H_s) of 1 meter or less while the 1984 data were dominated by H_s values of 1.6 to 2.9 meters. No significant variation in growler detection performance with altitude is indicated in either data base.

IDENTIFICATION

From the BergSearch '84 and 1985 SLAR Experiment data bases, SLAR imagery of positively identified iceberg and ship targets was evaluated to determine the confidence level of target discrimination. All the film used in this study was collected at an altitude of 8000-foot using the 50 km SLAR range scale. The films were duplicated and targets without accompanying visual cues were selected for testing. Some targets were used more than once, but separate SLAR passes provided different looks so that each image was used only once.

Four U. S. Coast Guard Avionics Technicians from Coast Guard Air Station Elizabeth City, North Carolina, experienced as SLAR interpreters, operators and technicians during ice reconnaissance flights viewed the 74 slides (35 icebergs and 39 ships) of ambiguous targets. To simulate a post-analysis examination of the SLAR film each 2 1/4 inch photo slide provided a single target, surrounding film for background, the lateral range to the target from the aircraft and the sea conditions recorded by the ship. The technicians separately viewed the slides on a light table using an optical magnifier and identified each target as either an iceberg or a ship.

Analysis of the results reveals that too much difference in error rate and target treatment between the four observers existed to allow combining all the data (Thayer, 1986). Observers 1, 2 and 3 showed a bias toward icebergs, i.e., a tendency to identify ships as icebergs which is a reflection of their IIP experience. Observers 1 and 3 were sufficiently similar in their treatment of the targets and observer 4 showed no bias toward icebergs. Table 4 from Thayer, 1986, shows that the error rate for all targets is in the range of 40 - 45 percent. The results from observers 1 and 3 offer the most representative confidence level because of their experience and the iceberg bias, i.e. that SLAR interpreters correctly identify all ambiguous targets 60 percent of the time. Applied directly to IIP operations a possible 40 percent error rate has alarming implications, however, the targets in this study represent only a subset of IIP SLAR targets.

Observers	Error Rate
1-4	45%
1,3	40% (iceberg bias)
4	40%

Table 4. Error Rates of Identifying Ship/Iceberg Targets

First, the targets selected for this study were small or medium iceberg and ship targets of similar radar return. Small and medium icebergs represent 59 percent of the icebergs recorded by IIP SLAR in 1984 and 66 percent in 1985 (Thayer, 1986). Second, the method of this study eliminated cues, representing the most ambiguous targets available and the most difficult to identify. While data does not exist for the frequency of visual cues on SLAR targets, a conservative estimate based upon IIP experience would be that 40 to 50 percent of the targets have additional cues.

Applying a worse case error rate of 40 percent to the cueless 60 percent of the small and medium icebergs detected by SLAR, an estimated SLAR error of 14 percent in 1984 and 16 percent in 1985 is anticipated.

CONCLUSIONS AND RECOMMANDATIONS

Based upon post-flight analysis of the 1984 and 1985 data, the following conclusions reflect the AN/APS-135 system's ability to detect and identify iceberg targets.

DETECTABILITY

Estimates of detection capability consistently decrease with increasing sea state and decreasing iceberg size. Medium icebergs are detectable nearly 100 percent of the time in seas below 2.9 meters. Small icebergs are detected 90 percent of the time in similar sea states. Growlers appear to be as detectable (90%) in less than 1 meter seas but detection probability significantly drops to approximately 15 percent in seas up to 2.9 meters. The detectability of small icebergs and growlers, increases with repeated looks at the target. Typical fluctuations in iceberg target detections were determined from the BergSearch '84 data to be +/- 10 percent (Rossiter et al, 1984). To improve detection probability, IIP iceberg reconnaissance is conducted in areas of most favorable sea conditions. Since seas on the Grand Banks are less than 2 meters 64 percent of the ice season (Mortsch et al, 1985), favorable conditions are generally found during ICERECDET deployments.

Based upon data limited to less than 2 meter seas, 8000-foot altitude and 50km range setting, small icebergs and growlers are as detectable at lateral ranges between 25 to 50 km as for ranges less than 25 km. Lower altitudes decrease the depression angle on iceberg targets and improve detectability. Also, lower SLAR range settings, i.e. 25 km vice 50 km, provide a better match up between the film plotter and the 30 meter radar resolution (Rossiter et al, 1985). Since small iceberg targets are less than a single resolution cell in size, improved detection is expected. The use of two film recorders to enable

25 km range settings and 50 km area coverage should be investigated. Image enhancement using post-flight analysis of digitally recorded data to separate iceberg targets from ocean clutter could also improve detectability and identification of small iceberg targets (Rossiter et al, 1985). Further investigation of digital data analysis should be conducted.

IDENTIFICATION

With the probability of correctly identifying ambiguous SLAR targets seemingly just above chance, IIP's emphasis on obtaining cues and visual confirmation during SLAR reconnaissance is essential. Greater awareness of this identification problem has prompted improved data collection and analysis efforts. In 1984, SLAR accounted for 49.3 percent (U. S. Coast Guard, 1985) of the icebergs plotted by IIP. In 1985, with rigorous post-analysis efforts, use of supporting data from other sources and greater emphasis on visual reconnaissance, SLAR-only detections dropped to 13.3 percent (U. S. Coast Guard, 1986).

Applying this statistic to the worst-case error for unclear targets, the SLAR error rate of icebergs plotted by IIP drops from 7 percent in 1984 to 2 percent in 1985. By continuing conservative image interpretation and following the present data collection and analysis techniques, icebergs should not go undetected and the population counts should continue to be accurate.

ACKNOWLEDGEMENTS

Acknowledgements are due to the crews of the HC-130 CG-1504 and the USCGC EVERGREEN whose excellent performance resulted in a most successful data acquisition. Special recognition goes to Don Murphy, R. Quincy Robe, Iain Anderson and Gary Hover for their outstanding support and professionalism in conducting the experiment and data analysis.

REFERENCES

Mortsch, L.D., T. Agnew, A. Saulesleja and V.R. Swail (1985); Marine Climatological Atlas - Canadian East Coast; Canadian Climate Centre Rpt #85-11, Atmospheric Environment Service, Downsview, Ontario.

Rossiter, J.R., L.D. Arsenault, A.L. Gray, E.V. Guy, D.J. Lapp, R.O. Ramseier and E. Wedler (1984); Detection of Icebergs by Airborne Imaging Radars, Proceedings of the 9th Canadian Symposium on Remote Sensing, St. John's, Newfoundland.

Rossiter, J.R., L.D. Arsenault, E.V. Guy, D.J. Lapp, and E. Wedler (1985); BergSearch '84: Assessment of Airborne Imaging Radars for the Detection of Icebergs. Summary Report - Results, Conclusions and Recommendations; Environmental Studies Revolving Funds Project #099-19-03, CANPOLAR Consultants, Ltd, Toronto, Ontario.

Robe, R.Q., N.C. Edwards, Jr., D.L. Murphy, N.B. Thayer, G.L. Hover and M.E. Kop (1985); Evaluation of Surface Craft and Ice Target Detection Performance by the AN/APS-135 Side-Looking Airborne Radar (SLAR), U.S. Coast Guard, Washington, DC (unpublished).

Thayer, N.B. (1985); Effects of Side-Looking Airborne Radar (SLAR) on Iceberg Detection During the 1983 and 1984 International Ice Patrol Seasons; Report of International Ice Patrol Service in the North Atlantic, 1984 Season, CG-188-39, U.S. Coast Guard, Washington, DC.

Thayer, N.B. (1986); Iceberg/Ship Target Discrimination with Side-Looking Airborne Radar; Report of International Ice Patrol Service in the North Atlantic, 1985 Season, CG-188-40, U.S. Coast Guard, Washington, DC (unpublished).

U.S. Coast Guard (1985); Report of International Ice Patrol Service in the North Atlantic, 1984 Season, CG-188-39, U.S. Coast Guard, Washington, DC.

U.S. Coast Guard; Report of International Ice Patrol Service in the North Atlantic, 1985 Season, CG-188-40, U.S. Coast Guard, Washington, DC (unpublished).

VI

OPERATIONAL FORECASTING

THE ICEBERG INFORMATION SERVICE OF ENVIRONMENT CANADA

John C. Falkingham
Ice Centre Environment Canada

INTRODUCTION

The Expanded Ice Information Services Program that was initiated by the federal government in 1983 has two main objectives -- to extend the present sea ice information service to support year-round navigation in the Arctic and to establish an iceberg information and advisory service for the East Coast. The timetable calls for the former objective to be in place in the next decade, and for the latter to be operational in 1986. This paper specifically addresses the iceberg program being developed by the Atmospheric Environment Service (AES).

Users of the Program

When the iceberg program was first conceived, the users of the information service were identified and categorized into three main groups.

The oil and gas industry operating in the offshore areas was the primary client for the program. As a newcomer to the area, this industry was the principal driver for the program. Although these offshore operators have developed systems to meet their immediate needs for site-specific iceberg information, it was the feeling of the government that a program with a broader scope was necessary to support an increasing number of platforms operating in varied locations along the east coast. The intent was not to replace the industry programs but, rather, to supplement them with wider scale information to enhance the safety and efficiency of these operations by eliminating unnecessary surprises.

A second client for the program was the commercial shipping industry. This industry has long operated on the east coast with only the support of the International Ice Patrol to define the iceberg area. Because ships can avoid icebergs with relative ease (as compared to a drilling rig), the industry was not a prime motivator for the federal iceberg program. However, with a program in place for other reasons, ship operators can make effective use of the information to select routes which minimize the probability of iceberg collision.

The third major client is the government itself, namely, the regulatory agencies such as the Canada Oil & Gas Lands Administration (COGLA), the Environmental Protection Service and the Canadian Coast Guard, whose duty it is to protect Canadians and their environment. With vastly increased activity in the iceberg infested areas off the east coast, these agencies foresaw the need for a federally mandated, independent source of iceberg information that could be mobilized quickly to respond to their information needs in times of emergency.

Other groups such as the fishing industry and research organizations have a need for iceberg information and will undoubtedly be clients of the federal service but, for the purposes of designing the program, their requirements generally fit within those of the three major groups.

Requirements of an Iceberg Information Service

Following a survey of the potential users the following requirements were identified for the service:

a) the government should act as a clearinghouse for all iceberg reports so that users could obtain information from one source

b) iceberg reports must be available in a timely fashion; i.e. within minutes of their receipt into the system

c) forecasts must also be timely; i.e. a forecast must reach the user within the time window that decisions affected by that forecast must be made

d) the government service should concentrate on regional scale information rather than the site-specific scale; information products must span a large enough area to provide boundary conditions and planning information for the site-specific information systems operated by industry

e) in keeping with the scale of the service, normal forecasts should span timeframes longer than one day; one to five day forecasts should be the target with climatological information for longer predictions

f) the government service should have the capability of producing fine-scale site specific analyses and forecasts on an occasional basis for the regulatory agencies

g) the government service should be capable of providing iceberg information in all affected Canadian waters; operators in one area should be able to expect the same level of service as operators in another area

h) the service should include an archive of all iceberg and relevant environment data

Scope of the Federal Iceberg Program

Based on the requirements identified above, a federal program for iceberg information was designed to meet those requirements in a cost effective manner. The scope of this program is as follows:

a) the area of responsibility includes all Canadian offshore waters where icebergs pose a hazard to operations; this encompases the east coast from the Grand Banks to Baffin Bay

b) the program will operate year-round

c) regional scale information will be provided on a daily basis to public clients to assist in strategic planning in the one to five day time frame; analysis and forecast charts will typically span areas several hundred kilometres across

d) fine scale information will be provided to regulatory agencies on an irregular and infrequent basis in order to assist in tactical situation analysis for emergencies; in order to keep costs down, it may be necessary to divert resources from production of the regular daily information in order to meet this requirement

Products and Services

The products that will be issued by the Atmospheric Environment Service are still being defined and will undoubtedly undergo some modification as experience with the program is obtained. Generally, the following types of products will be available:

a) observed iceberg location charts; aircraft reconnaissance charts depicting the area of coverage and numbers of icebergs or specific iceberg locations will be prepared on board the aircraft and broadcast by radio facsimile

b) iceberg location reports; iceberg reports, including aircraft reconnaissance messages as well as ship reports, will be available from the Ice Centre in Ottawa within minutes of their reception at the Centre

c) iceberg distribution analyses; charts on a scale of 1:2M will be produced daily to cover the areas of operational interest in a similar fashion to the sea ice analysis charts produced by Ice Centre; these charts will represent a composite of all reports received at the Centre with drift and deterioration predictions to normalize these reports to a common time; information in the charts will also be available in alphanumeric form

d) iceberg distribution predictions; these will be very similar to the analyses but will applicable to some future time within the one to five day time range; the operational drift and deterioration models developed by the International Ice Patrol will be used to make these predictions initially; research and development in iceberg prediction will be supported on an on-going basis with results being incorporated into the operational program as appropriate

e) observed and predicted tracks of individual icebergs will be provided on an infrequent basis to the government regulatory agencies

Services will be provided to deliver these products and supporting information to users. Daily analysis and forecast charts will be broadcast via marine radio facsimile. Forecasters at the Ice Centre in Ottawa will be available by telephone for consultation on present and anticipated iceberg conditions. All iceberg data will be archived at the Ice Centre for retrieval by clients and for climatological analysis to support long range forecasting. All of these services will exactly parallel the similar sea ice information services that have been offered for many years.

A new service that will be provided with the advent of the iceberg program is dial-in access to computerized iceberg information. Clients with computers or computer terminals will be able to connect to the Ice Centre computer via standard data telephone lines to obtain formatted alphanumeric reports containing the same information as is depicted on the chart products. This service is specifically directed to those clients who wish to maintain their own databases of iceberg information or tailor their own products. This dial-in service will be extended to chart products in the near future allowing users to obtain standard office facsimile or computer graphic versions of the radio facsimile charts.

Elements of the Iceberg Program

There are three major elements to the new program. Aircraft reconnaissance will provide the main source of data. A new DeHavilland DASH 7 IR aircraft specially outfitted for this purpose will be available by mid-1986 to allow this reconnaissance to be carried out in conjunction with the sea ice reconnaissance presently done by the AES Electras. This reconnaissance will be carefully coordinated with that of the International Ice Patrol to avoid duplication of effort.

Analysis and prediction of iceberg distribution will be provided by the Ice Centre. The Iceberg Prediction and Analysis System (BAPS) to be installed at the Centre in May 1986 will be the central computer system that will provide many of the services listed above. The BAPS will maintain the database of iceberg reports that will be accessed by external clients and will operate the drift and deterioration models. Dual graphics workstations will allow Ice Centre personnel to plot and overlay multiple iceberg messages in order to make sense of the hundreds of reports that will be available. Graphical editing capabilities will be used on these workstations to produce the chart products described earlier. These graphical edits will be reflected in the database from which the alphanumeric products will be generated, thus ensuring compatability of various products with a minimum of human intervention. The fact that the entire forecast production system is being designed around computer compatible data allows a high degree of flexibility in designing products and will permit the Ice Centre to develop a suite of information products best suited to the user community.

The third element of the program is iceberg climatology. A computer archive of all iceberg data will be maintained at the Ice Centre. Data from this archive will be available to users and, in addition, climatological analyses will be done at the Centre to support long range statistical prediction of iceberg conditions. These analyses and other summaries of iceberg data will be regularly published. Although data archiving will commence as soon as the BAPS is installed, the full range of iceberg climatological products will not be available until 1988 when additional computer resources will be available.

Conclusion

This paper has briefly described the iceberg information program being developed by Environment Canada for implementation in 1986. The intent has been to inform the reader about the program in a general way in order to make potential users of the service aware of its scope and to spark further interest. Much of what has been described is still in the formative stage and changes in the detail will no doubt take place. The general direction is set however and those with a need for detailed information are encouraged to direct their enquiries to the Ice Centre Environment Canada in Ottawa.

ICE AND ICE MANAGEMENT ON THE GRAND BANK

J.A.N. Ransom[1]
J. R. Benoit[1]
F. J. Dello Stritto[2]

ABSTRACT

The presence of sea ice and icebergs make the Grand Bank off Newfoundland a unique offshore operating environment. Historically, ice occurrence has been intermittent and highly variable in the area. In some years, very light concentrations of icebergs or sea ice have been encountered; in others, very severe conditions have occurred. A sound ice management program, in support of hydrocarbon exploration and production, involves forecasting, surveillance, monitoring and avoidance techniques. Efficient collection and distribution of information, and effective response to that information is the core of such a program.

The ice climate of the Grand Bank is briefly described. Ice management programs for the exploration drilling and the planned Hibernia production system are reviewed. Technological developments which may substantially improve ice management capabilities are described.

INTRODUCTION

Hydrocarbon exploration and production activities on the Grand Bank must contend with sea ice and icebergs. Sea ice is formed by the freezing of the ocean surface in arctic and sub arctic areas. Icebergs are formed from massive pieces calving off northern glaciers. Both are carried south to the Grand Bank by the Labrador Current.

Exploration drilling on the Grand Bank has been conducted safely during periods of ice encroachment through a comprehensive ice management program. Throughout near-continuous drilling on the Grand Bank since 1979, no physical contact between ice and drilling rigs has occurred. As few rigs are designed to withstand impact with ice, they are moved off the site in a controlled, orderly sequence as dictated by the safety criteria of the ice management program.

Production operations on the Grand Bank require that all facilities be designed for some degree of ice loading. For the Hibernia field, a concrete GBS (gravity base structure) production platform, able to withstand any anticipated ice load, is planned. Other associated system components, such as ALP's (articulated loading platforms) and vessels, will be ice strengthened, and vessels will be moved off the site during severe ice conditions.

---

[1] Mobil Oil Canada, St. John's, Newfoundland.
[2] Mobil Research and Development Corporation, Dallas, Texas.

Ice management programs are necessary throughout the entire development of the field. Ice management for exploration drilling is currently co-ordinated among the operators on the Grand Bank. Elements of ice management are:

Surveillance:	the tracking of icebergs and sea ice, using information collated from visual and marine radar sightings from all vessels, and visual and long range radar sightings from aircraft;
Forecasting:	predicting the occurrence, arrival and severity of the iceberg and sea ice seasons, using surveillance data, forecasted weather conditions and historical data;
Monitoring:	intensive surveillance and drift forecasting for particular locations, such as well sites.
Avoidance:	deflecting icebergs by towing, or moving out of the path of ice. Procedures define timing of well suspension, well disconnect and anchor handling to move the rig off site.

Ice management technology is continually being improved. Advances which may demonstrably benefit ice management during production include:

Improved knowledge of the physical properties of ice
Improved criteria for operational limits
Improved ice surveillance by remote sensors
Improved drift predictions, particularly for icebergs
Improved iceberg towing methods
Implementation of a purpose designed ice clearing/support vessel

Operating experience and knowledge of ice gained from the exploration drilling program has increased the confidence level in ice management techniques. Such improvements will benefit Mobil during the operation of the Hibernia production system.

ICE ENVIRONMENT OF THE GRAND BANK

The occurrence and severity of ice on the Grand Bank is greatly influenced by the Labrador Current (Figure 1) and the prevailing winds, which, though they vary throughout the year, are predominantly northwest to southwest. Hibernia is located near the eastern and southern extent of the sea ice edge and is not on the main pathways of southward moving icebergs.

Sea Ice

Most sea ice on the Grand Bank forms in the north, along the Labrador and Northern Newfoundland coastlines. During a normal ice season, sea

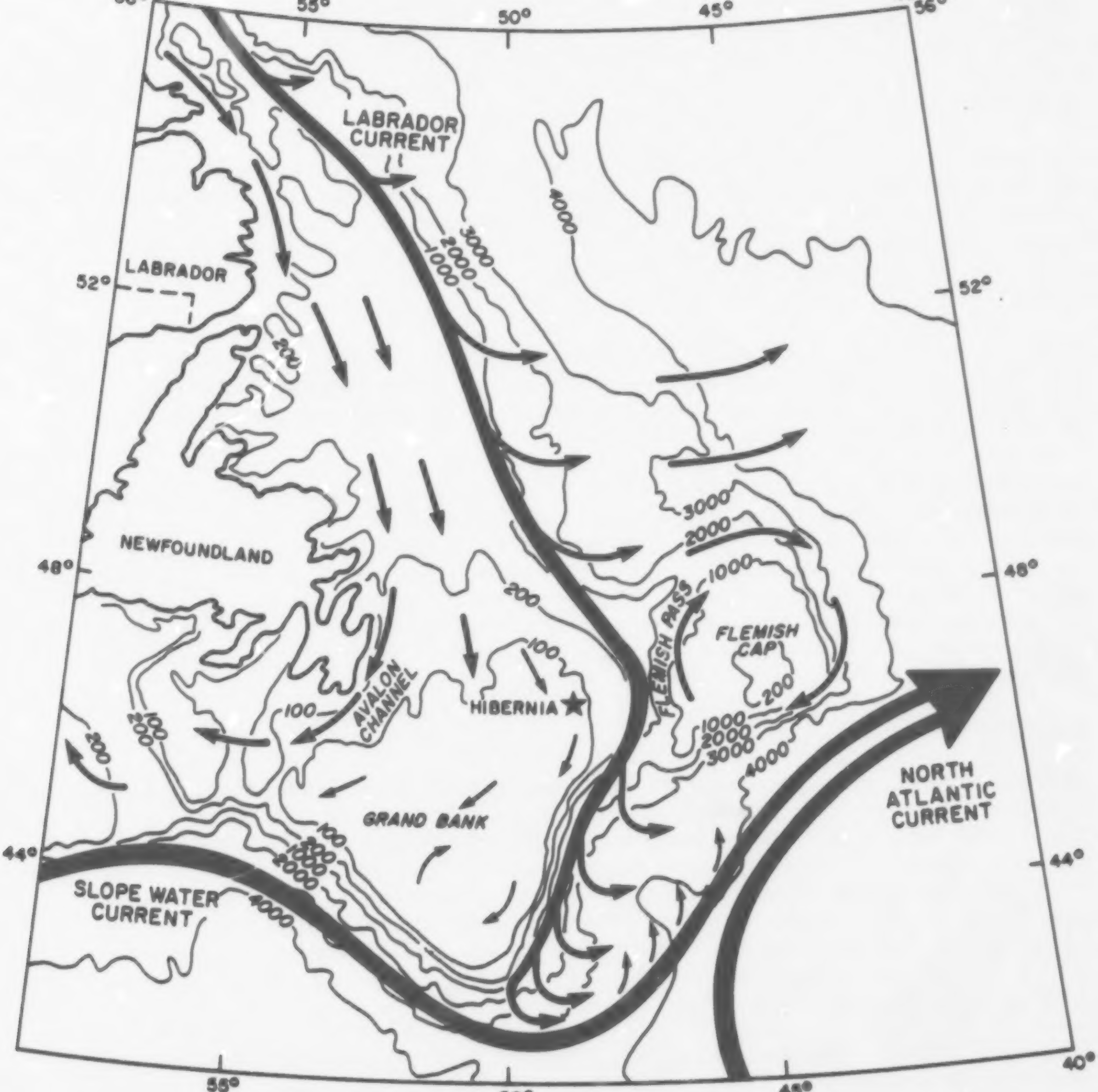

FIGURE 1 PREDOMINANT CURRENTS ON THE GRAND BANK

ice flows along the Newfoundland coastline, with a seaward (eastern) extent of about 150 miles (250 km). Mean coverage by month is shown in Figure 2. The southward advance slows by late February, and the ice edge stalls typically about 90 to 150 miles (150 to 250 km) northwest of Hibernia. It remains at that distance until late March and early April when it retreats. (Markham, 1980).

In heavy ice years, sea ice can extend well beyond the southeastern tip of Newfoundland and over 250 miles (415 km) offshore. As shown in Figure 3, in 1983 sea ice stayed near the shore and extended far to the south. In 1984 the sea ice stayed offshore. An average drift speed for Hibernia of less than 1 knot (0.51 m/s), and speeds as high as 2 knots (1m/s) are possible.

Sea ice occurs at or within 25 miles of Hibernia approximately one year in two. It has been at Hibernia as early as 4 February and as late as 23 April. The average and maximum lengths of stay were 1 week and 9 weeks, respectively.

Ice generally approaches Hibernia in strips several miles wide. Figure 4 illustrates a typical sea ice condition. Within the strips, the coverage can be near continuous, while the mean total concentration for the area is about 60 percent. The ice is typically well broken up and unconsolidated. Near Hibernia, floe sizes in the pack have an average horizontal dimension of less than 60 feet (20m) while at the ice edge, their size is less than 30 feet (10m). Average thickness is approximately 3 feet (1m). (Mobil, 1985).

Icebergs

Icebergs calve from the edges of northern glaciers and migrate southward along the flow of the Labrador Current. On reaching the northern tip of the Grand Bank, most move east and south through the Flemish Pass, a smaller number continue to move south through the Avalon Channel and an even smaller number move directly over the Grand Bank. The paths taken generally reflect the relative strengths of the two branches of the Labrador Current and the weak current over the Bank. Mean drift velocity for icebergs on the Grand Bank range from 0.2 to 1.2 knots (0.1 to 0.6m/s). (Mobil, 1985).

Figure 5 shows the annual IIP (International Ice Patrol) count of icebergs crossing the 48°N. The range is from 0 to over 2,000; the annual average is about 350. Uncertainty in the count reflects limitations in surveillance accuracy and completeness, as well as variability in visibility and other environmental conditions. Approximately 10 percent of the icebergs crossing 48°N enter the Hibernia area (i.e. between 48 and 49°W). (Mobil, 1985).

Icebergs range in mass from several thousand tons to millions of tons. Their average mass in the vicinity of Hibernia is about 0.3 million tons. Typical dimensions are 60 feet (20m) in height, 180 feet (60m) in draft and 360 feet (120m) in length. Many of the larger icebergs are

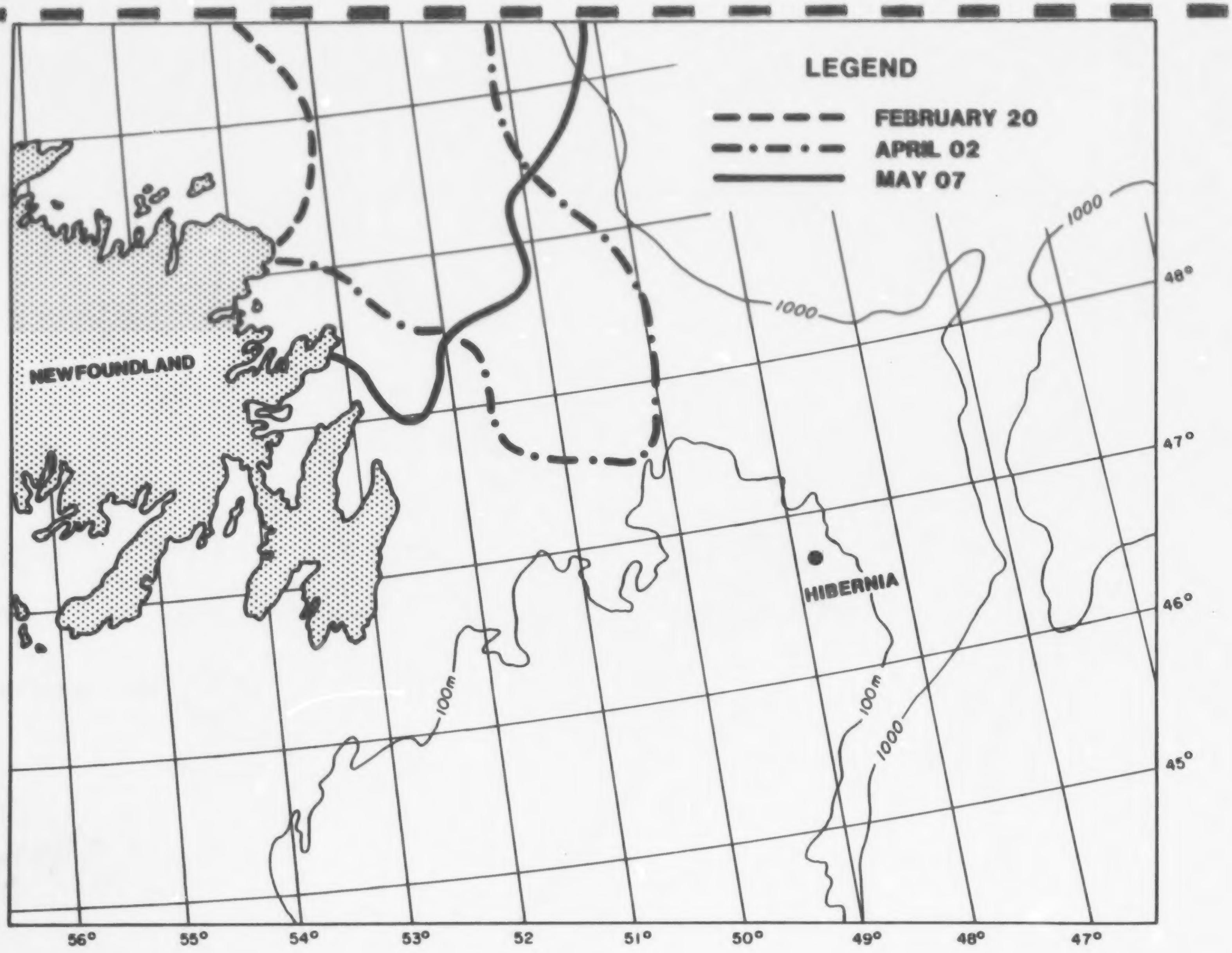

FIGURE 2 MEAN SEA ICE COVERAGE BY MONTH FOR 1964 TO 1973

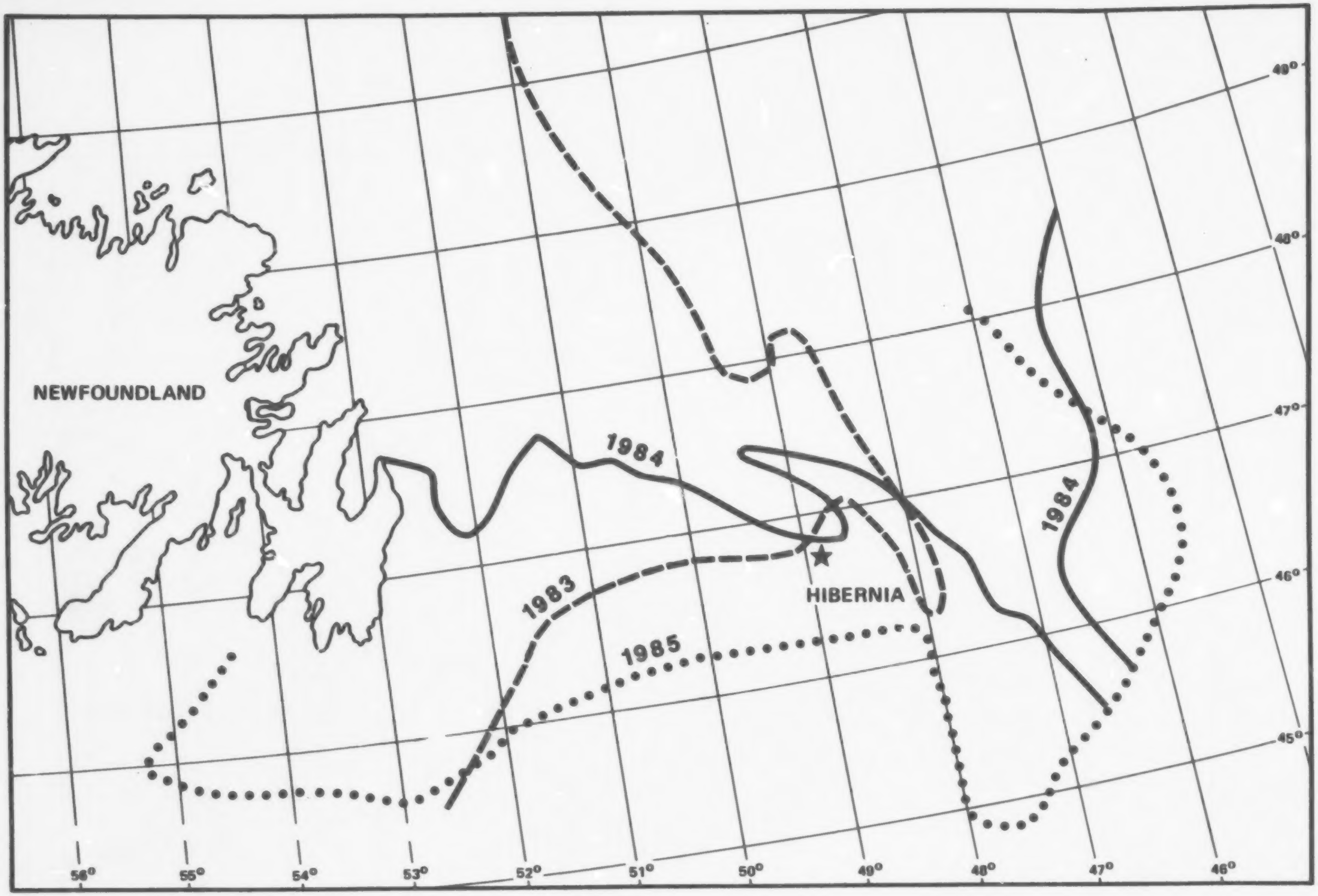

FIGURE 3 MAXIMUM EXTENT OF SEA ICE FOR 1983 TO 1985 INCLUSIVE

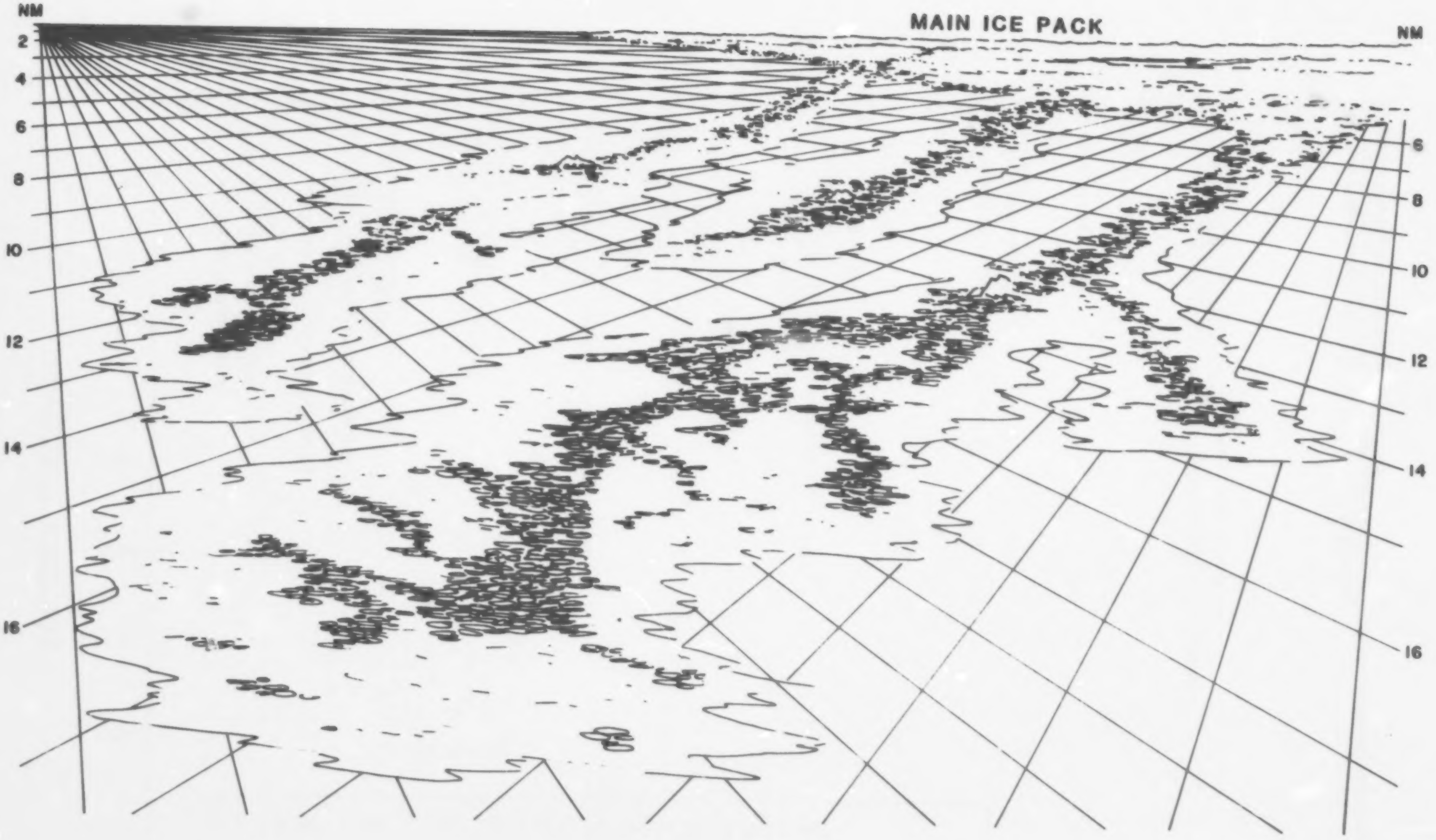

FIGURE 4 STRIPS OF SEA ICE FLOWING OUT OF THE MAIN ICE PACK COVERAGE TYPICAL OF WHAT HAS BEEN EXPERIENCED AT HIBERNIA

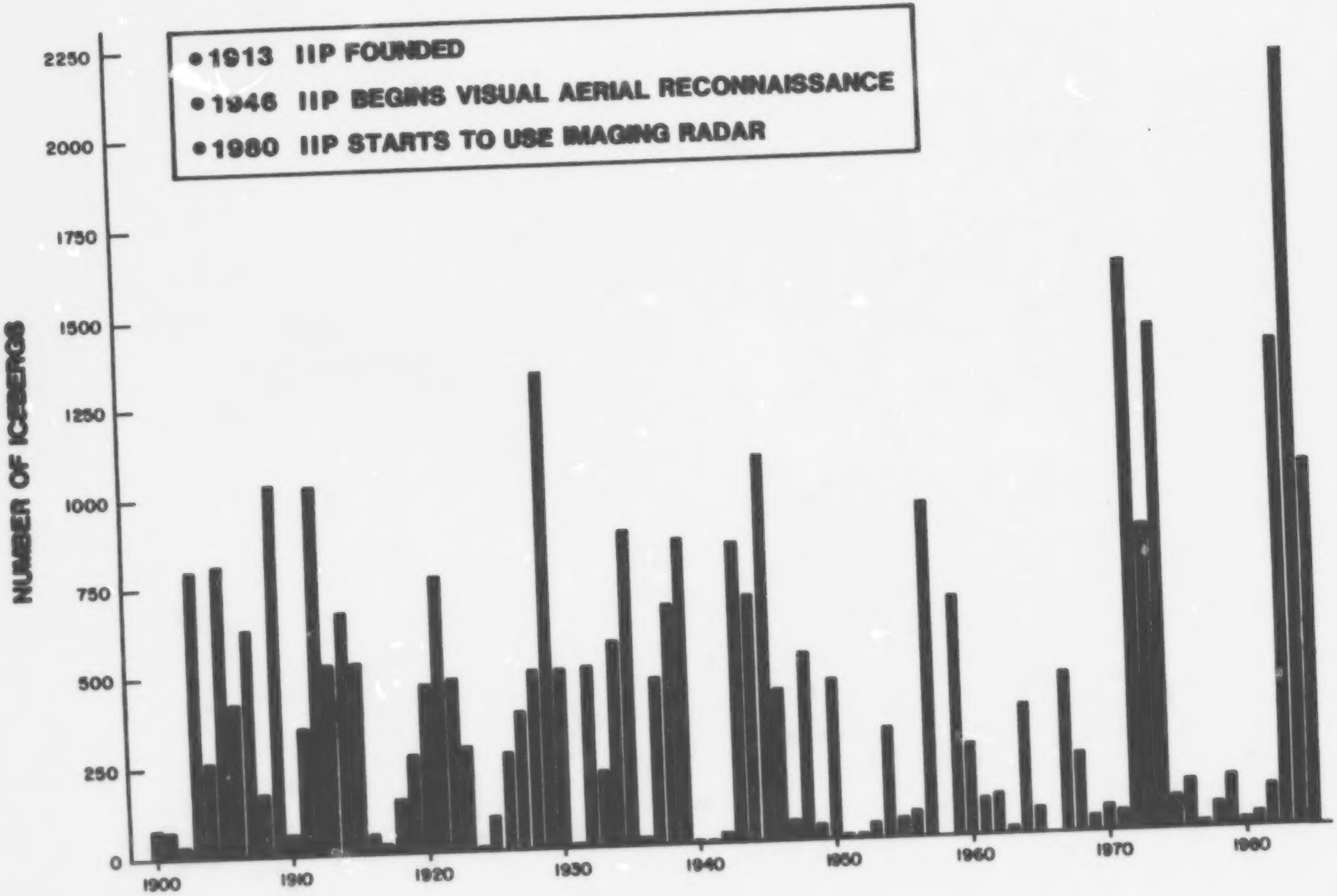

FIGURE 5 INTERNATIONAL ICE PATROL'S (IIP) YEARLY COUNT OF ICEBERGS CROSSING 48°N (LATITUDE)

prevented by water depth limitation from entering Hibernia. The largest iceberg that could threaten Hibernia is estimated to be on the order of 6 million tons.

Due to the decrease in water depth, many icebergs ground around the edge of the Bank. Icebergs with drafts near that of the water depth may scour the seafloor. Scours as deep as 5 feet (1.6m) have been measured near Hibernia, and scours in excess of 20 feet (7m) have been measured on the edge of the Bank. (Mobil, 1985).

As icebergs approach the Grand Bank, deterioration is quite rapid. They are often very smooth and deteriorated at the water line, mainly due to wave action. Growlers (up to 120 tons) and bergy bits (120 to 5400 tons) frequently shed from deteriorating icebergs. Their numbers, locations and sizes on the Grand Bank are highly variable. Due to their rapid deterioration rate, they are generally found close to the parent berg.

ICE MANAGEMENT--EXPLORATION PHASE

Ice management is a comprehensive set of procedures and guidelines for safe operations in ice-infested waters. The major components of any ice management program are surveillance, forecasting, monitoring and avoidance. Procedures for current exploration operations are based on the premise that all ice is to be avoided, since mobile drilling units are not designed for ice contact.

Surveillance

Ice surveillance is performed by both government and industry. In October of each year the Canadian government begins ice reconnaissance flights over the source areas of Grand Bank icebergs and sea ice (the Labrador coast, Labrador Sea, Baffin Bay and Davis Strait). Information from these flights is used to plot the advance of icebergs and the sea ice edge.

In January, when ice has typically reached northeastern Newfoundland, offshore operators track ice movement as reported by government reconnaissance and commercial shipping. The operators also initiate ice reconnaissance flights over the ice edge, to complement government flights. Flights are most frequent from January through June, but are necessary year-round to follow icebergs which occasionally reach the Bank in the late summer or fall.

A long range fixed-wing aircraft is used for aerial surveillance; and a trained ice observer records pertinent information. The accuracy and thoroughness of the data are limited by the often poor visibility. At Hibernia, for example, conditions for visual aerial observation exist for less than 68 percent of the time in January and for less than 40 percent in June.

When ice is within about 150 miles (250 km) of the drilling locations, flights are made on a regular basis, generally about every two days. When poor visibility is forecasted, a large area is surveyed to define the complete ice environment before the weather deteriorates. When the weather remains unsuitable for flying for sustained periods, reconnaissance is conducted by rig supply boat. The supply boat complement is increased from two to three for each rig during the ice season. Supply boats make visual observations and use marine radars.

During reconnaissance, the shapes and sizes of all icebergs are noted so bergs can be re-identified should they be sighted again before significant deterioration or rolling has occurred. These parameters also indicate whether the berg can be towed, or detected by radar.

To overcome the dependence on visual sightings, various advanced radar systems are now being evaluated to establish their effectiveness in imaging ice targets through cloud and fog. Systems such as SLAR (side looking airborne radar) and SAR (synthetic aperture radar) show promise. These systems can detect targets as small as about 100 square feet (10 sq. m) in low sea states, but their reliability in high seas requires further evaluation. These systems cannot accurately distinguish between ships and icebergs.

Starting in 1984, a dedicated SLAR (side looking airborne radar) equipped aircraft was used by the east coast operators to assist in the mapping of the ice edge during poor visibility conditions.

Forecasting

Forecasting the arrival and the extent of ice conditions is useful for planning drilling operations and for determining suitable ice management resources. Issuing bi-weekly reports of sea ice and iceberg begins several weeks before the first arrival of ice, and continues regularly throughout the season. A key input to forecasting is the ice flights. Additional inputs include historical ice and weather data and predicted global long range weather trends (for temperature and winds).

For sea ice, the bi-weekly reports for ice extent have been close to what has actually occurred, though the exact timing of events has not always been accurate. For instance in 1984, events actually occurred about two weeks ahead of their predicted time of occurrence. For icebergs, the long range forecasting effort has been only marginally successful. The forecasts have been accurate only in establishing the relative iceberg severity for the season. Attempts to improve the technique are now underway.

Monitoring

Ice monitoring is intense surveillance and forecasting for a specific location. The Grand Bank offshore operating companies coordinate ice monitoring activities as part of a joint ice management plan. Each operator appoints an ice coordinator who determines the company's specific needs and the coordinators meet at least once daily to prepare a joint plan for ice monitoring. The plan is reviewed by the operators' management committee, which allocates resources. The data thus obtained are available to each company's ice coordinator and the committee, and a new monitoring plan is then formulated. The structure of the current joint ice management scheme is shown in Figure 6.

Icebergs and sea ice near a well site are usually monitored continuously by an ice reconnaissance vessel, since detection of small ice masses in heavy seas by the drill rig radar systems currently in use is difficult. Uncertainty in detection is due to sea clutter and target size. This uncertainty makes visual monitoring of critical bergs and sea ice edges by ship indispensible.

A number of on-going programs are refining existing radar capability and developing improved types of radar. For the existing radar systems (essentially, modified marine radar), improved data processing and display systems are being developed. (ESRF, 1985)

Ice information is also available from non-industry and government sources (Figure 7). These data are combined with industry's data in a daily ice status report. Iceberg and sea ice drift forecasting is also performed using actual and forecasted environmental conditions and actual ice conditions. At present, drift forecasting is not sufficiently accurate to meet operational needs; on-going development programs are aimed at improving its accuracy. The ice status report and the drift forecast help to establish whether potential ice hazards exist, and to direct further monitoring efforts.

Avoidance

Avoidance of ice is achieved either by towing icebergs or moving the rig from the path of the ice. Supply vessels are fitted with a towing system to alter the iceberg trajectory. At present, towing is accomplished by passing a synthetic rope around the iceberg and using the vessel as a tug (Figure 8). Towing may be initiated when an iceberg is as far as 20 to 30 miles (30 to 50 km) from a rig. The success of a tow depends significantly on the shape (the stability and waterline smoothness) of the iceberg and on weather conditions. Increased towing power does not necessarily allow larger bergs to be towed. Since the center of gravity of a berg is usually below the waterline, the berg may be unstable, resulting in tow rope slippage. Due to instability, bergy bits and growlers are also often difficult to tow. For small ice

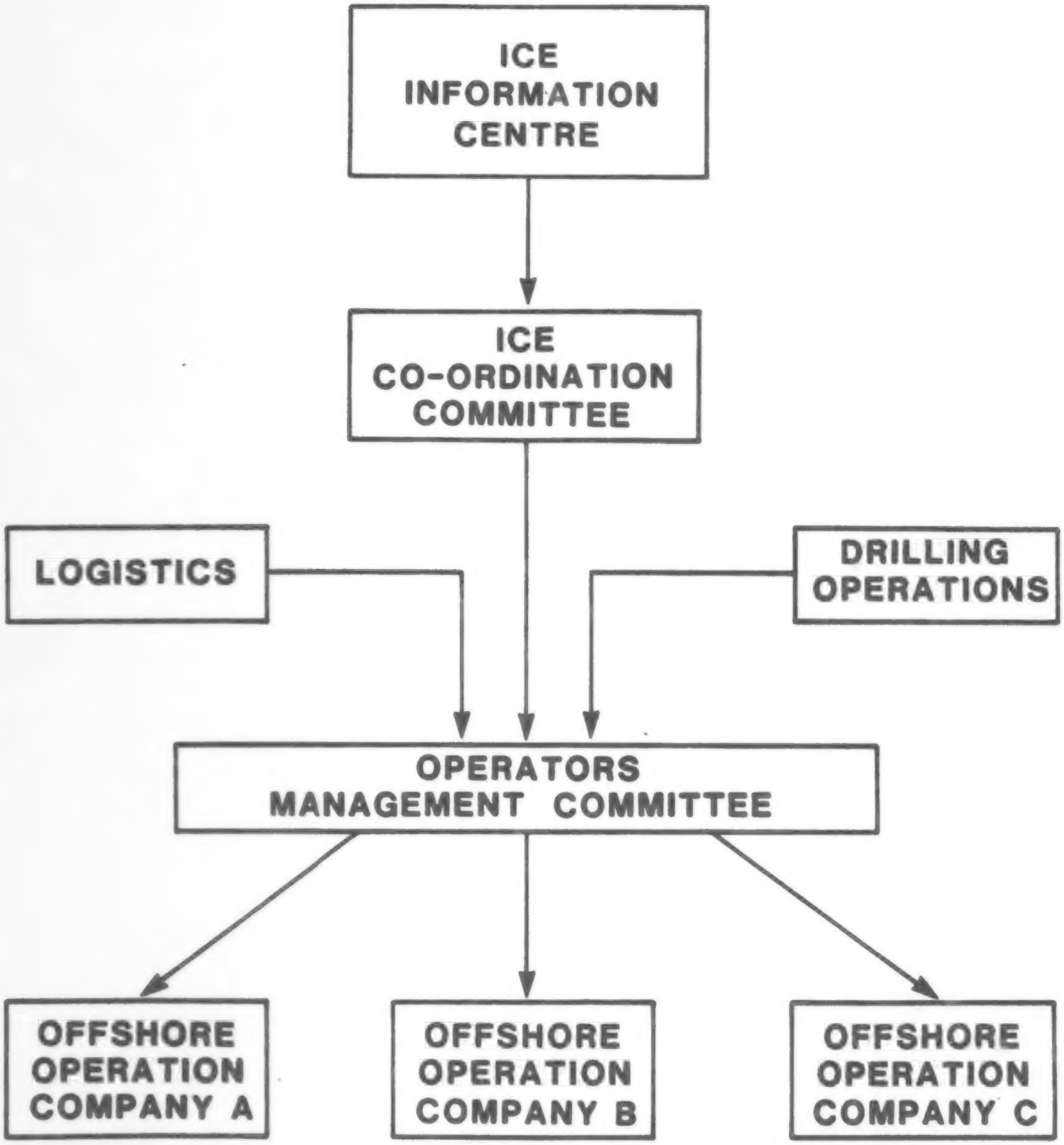
ICE INFORMATION CENTRE
ICE CO-ORDINATION COMMITTEE
LOGISTICS
DRILLING OPERATIONS
OPERATORS MANAGEMENT COMMITTEE
OFFSHORE OPERATION COMPANY A
OFFSHORE OPERATION COMPANY B
OFFSHORE OPERATION COMPANY C

FIGURE 5 JOINT ICE MANAGEMENT STRUCTURE FOR GRAND BANK OPERATIONS

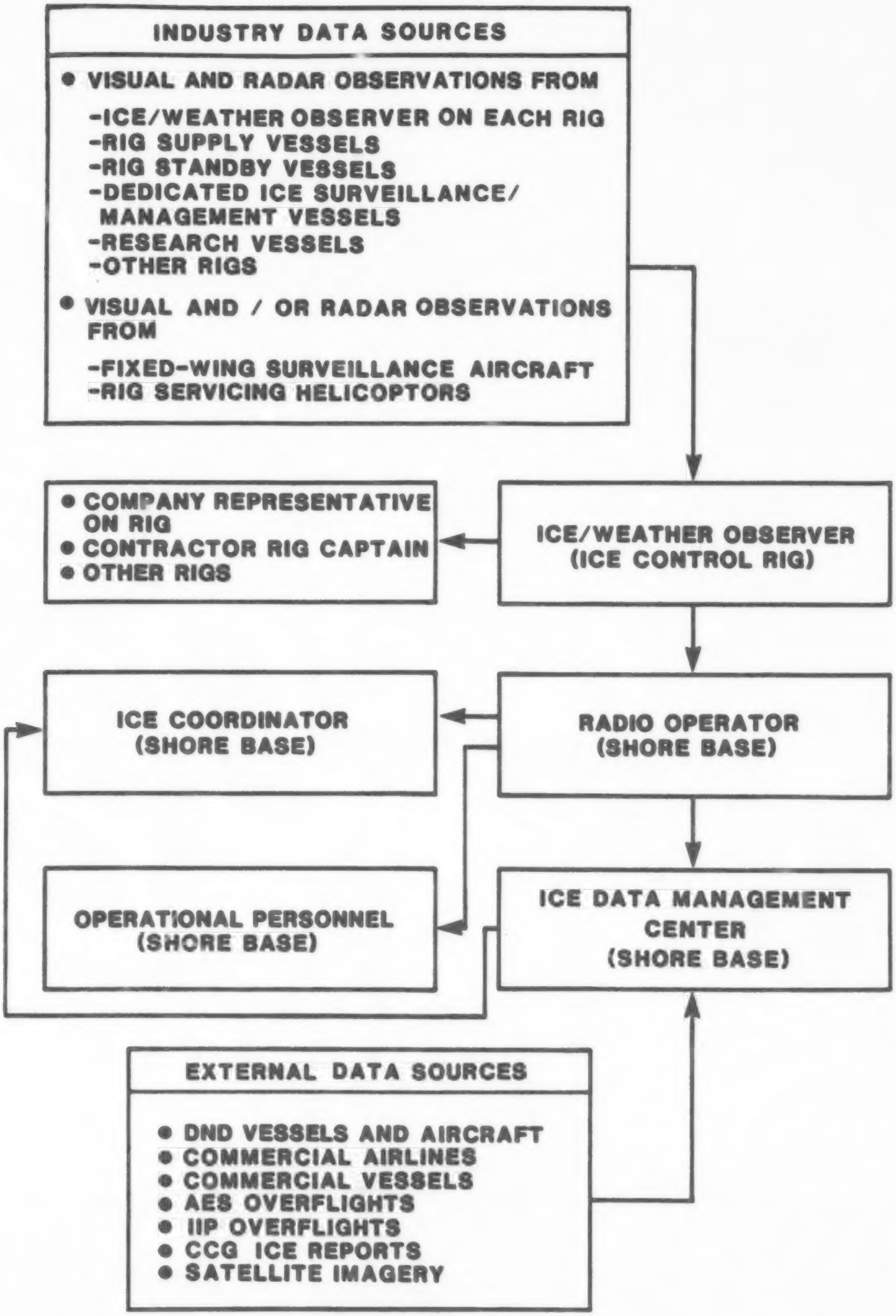
INDUSTRY DATA SOURCES
• VISUAL AND RADAR OBSERVATIONS FROM
-ICE/WEATHER OBSERVER ON EACH RIG
-RIG SUPPLY VESSELS
-RIG STANDBY VESSELS
-DEDICATED ICE SURVEILLANCE/ MANAGEMENT VESSELS
-RESEARCH VESSELS
-OTHER RIGS
• VISUAL AND / OR RADAR OBSERVATIONS FROM
-FIXED-WING SURVEILLANCE AIRCRAFT
-RIG SERVICING HELICOPTORS
• COMPANY REPRESENTATIVE ON RIG
• CONTRACTOR RIG CAPTAIN
• OTHER RIGS
ICE/WEATHER OBSERVER (ICE CONTROL RIG)
ICE COORDINATOR (SHORE BASE)
RADIO OPERATOR (SHORE BASE)
OPERATIONAL PERSONNEL (SHORE BASE)
ICE DATA MANAGEMENT CENTER (SHORE BASE)
EXTERNAL DATA SOURCES
• DND VESSELS AND AIRCRAFT
• COMMERCIAL AIRLINES
• COMMERCIAL VESSELS
• AES OVERFLIGHTS
• IIP OVERFLIGHTS
• CCG ICE REPORTS
• SATELLITE IMAGERY

FIGURE 7 SOURCES OF ICE DATA AND REPORTING FUNCTIONS

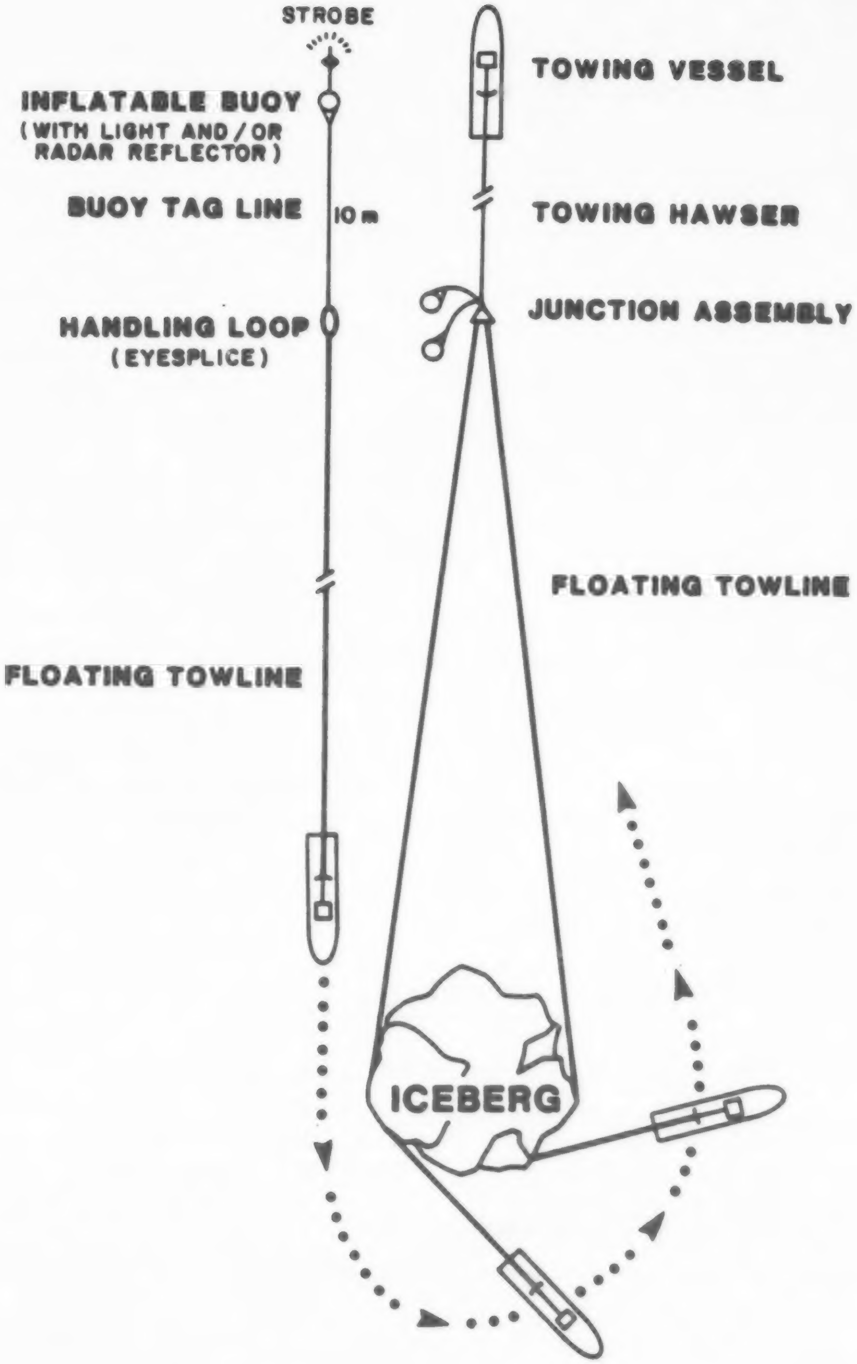

FIGURE 8 ICEBERG TOWING BY THE SYNTHETIC LINE METHOD

masses, "prop washing"-directing the vessel's propellers toward the ice to "wash it away"-may be possible. The current overall success rate for iceberg towing on the Grand Bank is about 75 percent. Developments to improve ice handling capabilities include single point tow attachment techniques, tow nets and the use of powerful water cannons.

In planning for a mobile rig move from the path of approaching ice, a series of alert zones are established around each rig. Figure 9 shows the alert zones in use during current drilling operations. These are concentric circles surrounding the drill rig; their diameters are defined by the ice's estimated minimum travel time to the rig. When high forecasted or actual winds are associated with ice, the ice alert zones are further defined by a minimum distance that ice is permitted to approach the rig.

In the yellow and orange zones the objective is to monitor the ice and, if necessary, to divert it. Activities are also undertaken to permit an orderly, efficient rig move, if necessary. The activities are as follows:

Yellow Zone:	Drilling is restricted to tasks that can be completed within 12 hours, and rig move planning begins.
Orange Zone:	Drilling operations are terminated. If the ice continues to move towards the rig, one-half of the rig's anchor complement is pulled. In the event of high forecasted or actual winds, evacuation of all non-essential personnel is considered.
Red Zone:	Remaining anchors are pulled and the rig is moved out of the path of the ice. In the event of high forecasted or actual winds, evacuation of all personnel is considered.

If sea ice or icebergs appear near the rig without prior detection, the anchor chains' quick release systems can be activated to allow for rapid retreat from the ice within hours.

The effects of ice on Mobil's drilling activities for 1983 through 1985 are shown in Figure 10. Other Grand Bank operators also experience a similar degree of downtime.

ICE MANAGEMENT--PRODUCTION PHASE

Ice management during production on the Grand Bank will be based on the principles applied during exploration, and will consist of the same major components. The following features of the proposed Hibernia system will influence the ice management program:

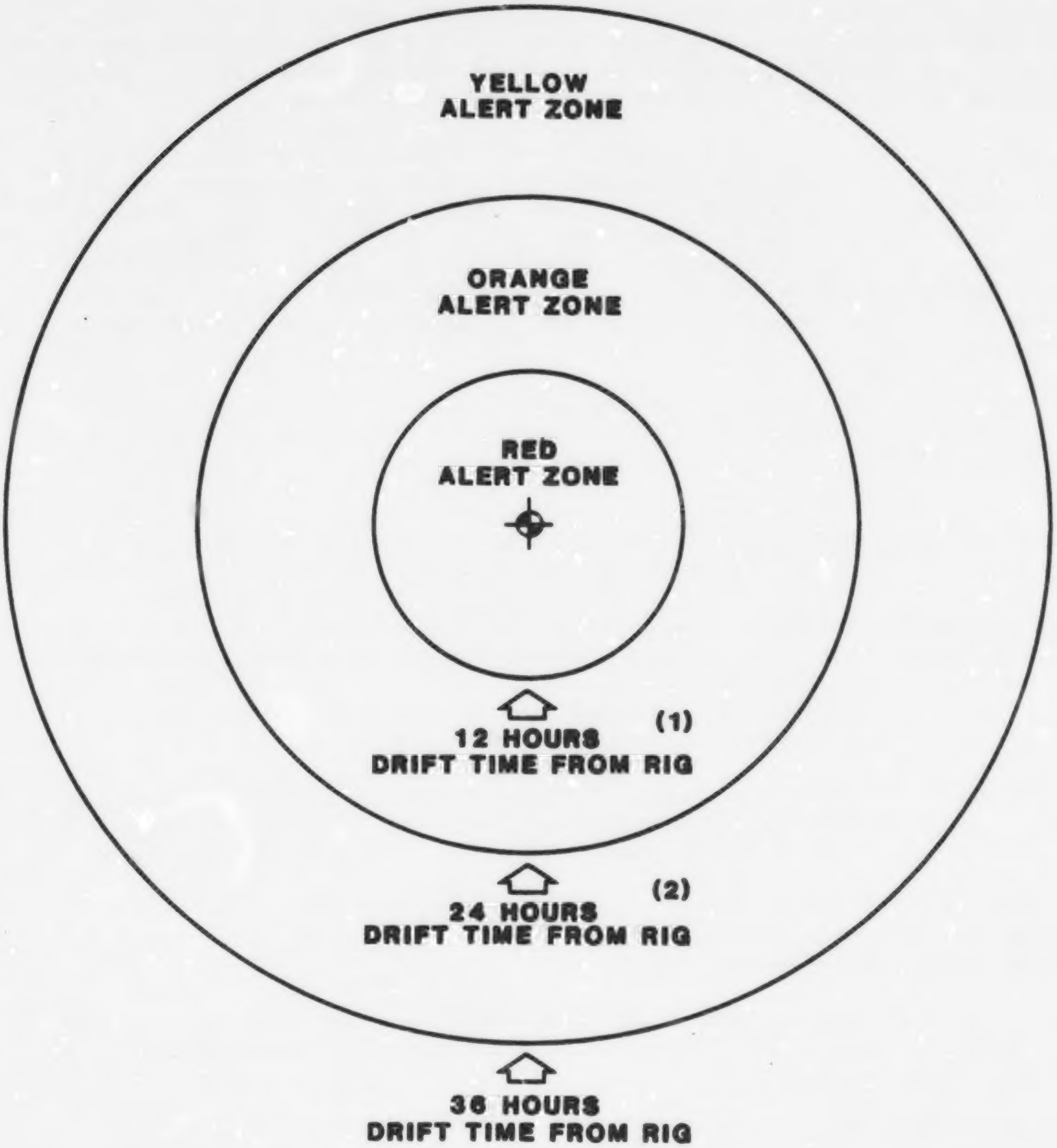

NOTES:

(1) IN HEAVY WEATHER , 12 HRS.OR 12 NM WHICHEVER IS GREATER

(2) IN HEAVY WEATHER , 24 HRS OR 24 NM WHICHEVER IS GREATER

FIGURE 9 ICE ALERT ZONES USED FOR EXPLORATORY DRILLING RIGS

	SEA ICE	ICEBERGS
1983		
NORTH DANA I-43	9	44
HIBERNIA I-46	0	24
RANKIN M-36	0	23
1984		
HIBERNIA C-96	0	23
TRAVE E-87	14	-
SOUTH MARA C-13	-	26
1985		
MARA M-54	73	-
MERCURY K-76	-	4

FIGURE 10 DOWN TIME (DAYS), DUE TO SEA ICE AND/OR ICEBERGS, EXPERIENCED BY MOBIL DURING VARIOUS WELL DRILLING PROGRAMS ON THE GRAND BANK.

1) The GBS production platform will be designed to withstand all ice.

2) ALP's will be designed to withstand ice loads below a specified threshold, and will be removed or sacrificed (to be replaced) when higher loads occur.

3) Since large icebergs may scour the seafloor and disrupt flow lines, an area around the platform of approximately 55 square miles (144 km) will be monitored.

4) Supply boats and oil shuttle tankers will be ice strengthened to allow operations in sea ice.

5) A specially designed vessel for maneuvering in and clearing sea ice, and also for iceberg towing, will be stationed in the field.

An ice management program for production has much in common with one for exploration. The sections below emphasize anticipated improvements which may be available before the Hibernia system is placed in the field (currently scheduled for 1992).

Forecasting

During production, long range forecasts (6 months) would be useful in order to permit planning for marine logistic activities during periods of concentrated ice presence.

Efforts are underway by government and industry to provide long range forecasts of sea ice and icebergs for the Grand Bank. Since iceberg flux is subject to many variables, major advancements are not expected in the short term. Improvements are expected in the next 2 to 3 years for mid-range forecasting (1 month). Sea ice movement is more easily predicted; thus the long range forecasting of sea ice severity is more successful. However, because Hibernia is located near the southern sea ice edge, it may be difficult to forecast the occurrence of sea ice there with a high level of confidence.

Surveillance

Surveillance of ice during production will consist of two components; 1) strategic or regional coverage and 2) tactical or close range coverage.

1) Strategic Coverage:

In addition to industry efforts, government agencies such as the Atmospheric Environment Services (AES) and the United States International Ice Patrol (IIP) provide intermittent regional coverage of the Grand Bank, using airborne imaging radar such as SLAR. At present, the AES mandate is to provide only sea ice reconnaissance of the area. A 5-year $37 MM program was initiated by AES in 1983 to upgrade aircraft and data processing capabilities in light of increased offshore activities. The program involves expanding the mandate to include icebergs. Owing to sensor limitations, accurate reporting of small icebergs (nominally less than 10,000 tons) will not be included. It is also expected that satellite based systems such as Radarsat will provide strategic information on ice and icebergs.

2) Tactical Coverage:

Because of the need for continuous shuttle tanker and supply vessel traffic, and because of the vulnerability of the offshore oil loading system to icebergs, accurate surveillance within a radius of 30nmi (50 km) from the production platform will be required. In light of the limitations on airborne systems, rig based marine radar will be a major component of a tactical iceberg detection system. Marine radar has been used for many years and its application to iceberg detection is regularly upgraded. The maximum detection range is nominally to 18 miles (30km).

Detection of icebergs is presently the weakest link in operational ice management. Results of a recent review (Mobil, 1984) of existing and anticipated hardware indicate that no single sensor can achieve the performance requirements dictated by the Grand Bank environment and the size and shape variability of icebergs. Numerous sensors and data sources can, however, be integrated to provide a high probability of detection in all conditions.

Industry is pursuing the development of a multi-static radar. This system, which operates in the high frequency range (HF), uses a receiver on board a rig and two or three buoy-mounted transmitters located about 12 miles (20 km) from the rig. Theoretical probabilities of detection indicate that a 3 feet (1 m) high piece of ice has a high probability of detection at a distance of 3 miles (5 km) in sea state 7.

In addition, industry is actively pursuing the development of such sensors as airborne search radars and acoustic sensors, as well as improvements to existing sensors (marine radars, imaging radars). Land-based "over the horizon" radars are also being considered to survey areas off the northern Newfoundland coast.

The RADARSAT project, initiated by the Canadian government is scheduled to launch a satellite equipped with a SAR (synthetic aperture radar) in 1992. Though the system will be capable of detecting icebergs under all atmospheric conditions, its resolution permits only the detection of large icebergs (100m). Also, the proposed orbit will provide coverage of the Grand Bank area only once every three days.

Monitoring

Constant monitoring of iceberg position and behavior will be essential to minimize both risk of impact and unnecessary downtime during production. With improved detection capabilities, icebergs can be continuously tracked as they drift through the area of concern. Drift models, used to forecast the position of icebergs, are widely recognized as inadequate for operational needs. Improvements in these models are not expected in the next few years since the parameters affecting the drift of icebergs are random and variable in space and time. Therefore, monitoring will rely primarily on continuous detection. Methods for "tagging" icebergs are being assessed. Viable "tags," such as air or ship deployable transmitters or beacons are now available, but attachment to icebergs remains a problem. Development of iceberg towing technology may offer a solution.

During production, an alert zone system will be adopted; however, as detection capabilities improve, the alert zones will be altered to reflect the greater confidence attained. For example, if an iceberg has been continuously monitored for a period of 48 hours and its drift pattern is judged predictable, the berg may be allowed to enter various zones without automatically triggering mitigative measures.

Avoidance

Once an iceberg is confirmed as a threat to a component of the production system, one or both of the following actions could be taken:

1) Towing:

Improvement of towing techniques is an area of intensive effort by both industry and government. The Canadian government's Environmental Studies Revolving Fund (ESRF) is investigating single point tow attachments to icebergs and new methods for handling small pieces of glacial ice (growlers and bergy-bits).

Current plans call for a specially designed ice clearing and support vessel to be stationed in the field. During the sea ice and iceberg season, its principal functions will be to: i) remove or break up any sea ice concentration that may threaten a component of the production system and ii) tow icebergs that may pose a similar threat. In addition, two to four logistics vessels will be under charter, each capable of towing icebergs.

2) Operations Downgrading:

In the case of Hibernia, the GBS will be designed to cope with the presence of sea ice and icebergs. Operational procedures will be developed, however, to reduce operational activity when severe ice conditions so dictate. For example, tanker loading operations may be terminated in the case of the encroachment of an unmanageable iceberg. Platform evacuation is not built into the ice management procedures, however, should it ever need to take place, it can be executed under the general platform emergency procedures contingency plan.

CONCLUSION

The key component of ice management practice during exploration drilling on the Grand Bank is ice avoidance. All components of the management program are geared to the prevention of contact between ice and offshore equipment. In more than five years of nearly continuous drilling on the Grand Bank, no physical contact between a rig and ice has occurred. This perfect safety record has been achieved, at times, at the expense of operating efficiency. Built-in redundancy has also been a factor in the success of the program: each component of the management program is a backup to another, resulting in a program which is intrinsically conservative.

An adequate ice management program for production operations can be achieved with current technology. For Hibernia, total ice avoidance will not be necessary, as the proposed system components will be designed to withstand some or all ice. The vulnerability of some components to damage from some forms of ice (e.g. scouring of flow lines or loading lines by icebergs) results in a decrease in system efficiency. A number of anticipated advances in ice management equipment and procedures should demonstrably improve this overall efficiency.

6181R

REFERENCES

1) Markham, W.E. 1980. Ice Atlas - Eastern Canadian Seaboard. Canada Department of Environment Service.

2) Sea Ice Thickness Study 1985. Report prepared for Mobil Oil Canada, Ltd. Unpublished report.

3) Hibernia Environmental Impact Statement 1985. Volume IIIa, Biophysical Assessment.

4) Iceberg Flux Evaluation 1985. Report prepared for Mobil Oil Canada, Ltd. Unpublished report.

5) Assessment of Marine Radars for Iceberg Detection 1985. ESRF Report No. 2 in press.

6) Iceberg Detection Study 1984. Report prepared for Mobil Oil Canada, Ltd. Unpublished Report.

SEA ICE DRIFT MEASUREMENTS USING SATELLITE - TRACKING BEACONS

by

Dennis M. Nazarenko and John D. Miller
Petro-Canada Resources
P.O. Box 2844
Calgary, Alberta
T2P 3E3

A 1985 program initiated by Petro-Canada, utilized satellite-tracking ice beacons to monitor sea ice motion on the Grand Banks. The objective of the program was to obtain ice drift data which would enhance our understanding of the sea ice dynamics near the southern ice limit.

Five spheroid beacons were deployed on the pack ice on February 22, 1985 in an area 150 to 250 km from the Newfoundland coast. Four of the beacons remained in the ice pack for a period of 9 to 13 days while the fifth continued to transmit positional information within the pack until March 30. In total, approximately 83 beacon days of positional information was obtained on and near the Grand Banks. On average the beacons provided positional updates 6 to 7 times per day while on the ice.

The initial positioning of the beacons resulted in motion data being collected both within the 200 metre bathymetric contour and beyond it. The resultant velocity calculations show significantly distinct motion characteristics in the two regions.

While the initial intent of the program was to gather ice motion information for oil production oriented engineering studies, the coincidence of the program with unseasonably severe ice conditions gave the program increased relevance to the Company's day to day exploratory drilling operations. The regular updates of ice drift information proved useful in assessing ice behaviour in the vicinity of the Company's wellsite locations.

INTRODUCTION

Hydrocarbon exploration on the Grand Banks requires an awareness of the special problems posed by the presence of both sea ice and icebergs. Icebergs have received widespread attention in the literature but much less has been written concerning the sea ice environment. In this paper we review some of the needs for sea ice information and discuss a study which was undertaken to meet these needs.

The occurrence of sea ice in the current drilling regions of the Grand Banks is not an annual event. During the so-called median ice year (a statistical construct and not an actual series of ice observations) ice forms along the Labrador coast in the late fall and extends to the Strait of Belle Isle by the beginning of January. The ice spreads southward reaching Notre Dame Bay by month's end. During February the ice belt broadens considerably and the southern limit reaches Baccalieu Island at the start of March. The maximum southerly limit of the ice occurs in March when it reaches 47°30'N but during this month it is generally thinner than in the previous month. At it's maximum extent the median ice edge lies some 200 km northwest of the Terra Nova wellsites. In April the melt and retreat of the ice begins reaching Fogo Island near month's end and opening the Strait of Belle Isle at the end of May (Markham, 1980).

A review of sea ice occurrences in a grid cell surrounding the Terra Nova wellsite has shown that over the twenty three year period 1963-1985 sea ice has been present in only five of those years (Petro-Canada, 1985a). Sea ice concerns thus lie somewhere in between those of annually recurring events and those designated as extreme events.

Sea ice can affect exploration and production activities in a variety of ways. Loads may be transmitted through the ice that exceed the local resistance of platform elements or the total or global resistance of the structure. Sea ice will also affect the trafficability of vessels in the area and the presence of ice interferes with iceberg control activities and may impede the operation of safety equipment. It is clear that sea ice affects both the design and the operation of a facility, impacting safety and efficiency.

For the case of design, both the local and global loads imposed by sea ice on a structure must be examined. The aim of the designer is to ensure that the structure has sufficient resistance to those loads to prevent local failure of structural members or a catastrophic failure of the structure itself. To estimate the local loads the kinetic energy of the impacting ice floe is a requirement. For the global ice loads the extent of the ice pack, its physical characteristic and the degree of momentum coupling with the ocean and atmosphere are needed.

For operations, a knowledge of the extent and concentration of the ice and the rate of advance of the ice edge is required. The areal coverage of the ice will impact upon the efficiency of supply vessels transitting from the supply base to the well location and the presence of ice at this site may necessitate the removal of the drilling vessel. Ice in the region local to the drilling vessel may impede iceberg towing operations, interfere with anchor handling and degrade the utility of safety equipment. The rate of advance of the ice edge becomes a critical element for operations as a knowledge of this variable allows the operation to achieve an optimum balance of efficiency and safety.

With these concepts in mind a program was developed to provide the sea ice speed information required to estimate ice floe kinetic energies and the rate of advance of ice floes within the pack. The program consisted of deploying 5 satellite reporting drifter buoys on ice floes within the pack and monitoring their speed and trajectory through a real time link with Service ARGOS. The information was integrated in drilling operations planning on a daily basis and post field analysis provided kinetic energy estimates for use in design applications.

METHODOLOGY

To obtain sustained sea ice motion data, it was decided to use satellite -transmitting ice buoys to provide positional information within the ice pack. Utilization of such buoys in conjunction with the Service ARGOS data collection and platform location network offered a means of obtaining position data from multiple remote locations on a regular basis.

Service ARGOS instrumentation aboard NOAA (National Oceanic and Atmospheric Administration) polar orbitting satellites receives signals from Platform Transmitter

Terminals (PTT) within view of the satellite. This information is transmitted to Service ARGOS facilities in Toulouse, France were the message is decoded and PTT positions computed using the satellite orital data combined with Doppler shift influences. The data is then stored on computer accessible files where it is available for user access. Average turn-around from data reception by the satellite to computer storage is approximately four hours.

Five buoys were utilized in the program, each capable of communicating with the ARGOS instrumentation. All the beacons were manufactured by Hermes Electronics Ltd. of Halifax, four in 1984 using the company's present spherical housing. The fifth was an older version which was refurbished specifically for the 1985 program.

Each buoy housed a PTT designed to transmit at 40 MHz, batteries for low temperature operation and an antenna. No additional sensors were configured in the package. The four spherical buoys measured 60 cm in diameter, 45 cm in height and weighed 21 kg. The older model was conical in shape with a 60 cm diameter base, stood 80 cm high and weighed 61 kg. The newer model was designed to float and to maintain its transmitting capabilities while in water.

The logistics plan called for the buoys to be deployed on the pack ice as close as possible to the Grand Banks drilling area. The 1985 ice season proved to be unusually early in its development and in retrospect, extreme in its southerly extent and persistence. As a result five semisubmersible drilling rigs were forced off location in early February. By late February the pack off the coast of Newfoundland had developed to a point where ice buoys could be deployed with a high probability of remaining on the ice for a reasonable length of time.

Plans were made to position the buoys north and west of the ice edge and to monitor their progress as they were transported towards the ice edge. The initial buoy configuration took into account reported ice conditions, expected ice deformation and local bathymetry. An array was designed to provide information concerning internal pack ice deformation in addition to ice velocity data.

The buoys were deployed on February 22 using a twin engine Bell 214ST helicopter. Positioning was done using an Omega Global Navigation System (GNS). Once over the ice pack it became apparent that the eastern ice edge had been incorrectly positioned and several of the deployment locations were in fact open water. This necessitated modification of the original deployment array to that shown in Figure 1. It can be seen that three of the buoys (ID's 4280, 4283, and 4284) were deployed beyond the 200 m bathymetric contour, a fourth (4282) almost on the 200 m contour while the fifth (4281) was deployed over water shallower than 200 m.

All five buoys were successfully activated on the ice and a positional computation made by Service ARGOS within 4 hours of their deployment. From the point of deployment four of the buoys continued to transmit regularly during the time they were on the ice. The fifth, buoy 4284, developed intermittent transmission difficulties after five days. The difficulties appeared related to the fact that the buoy was the refurbished older model. After the first five days transmission became increasingly sporadic and ceased entirely on March 5, twelve days from initial deployment.

While the data was collected from Service ARGOS on computer compatible tapes for detailed analysis, the ARGOS system was also accessed daily using standard Telex networks. The near real-time data was used in evaluating the pack ice behaviour and its influence on drilling operations.

The remaining buoys (4280 through 4283) continued to transmit signals after they left the ice pack. None were recovered by Petro-Canada and in April they were turned over to Bedford Institute of Oceanography for inclusion in their current monitoring program.

RESULTS

POSITIONING AND DATA RECEPTION

Initial signal transmission was achieved for all five ice buoys. Table 1 provides an indication of initial deployment times and position estimates using the onboard GNS system. In addition the time and calculated first positional fixes through Service ARGOS are also provided. All five buoys were deployed in a space of two hours and ARGOS positional fixes received within 3 1/3 hours on average, the maximum interval being 4 1/2 hours for buoy 4284.

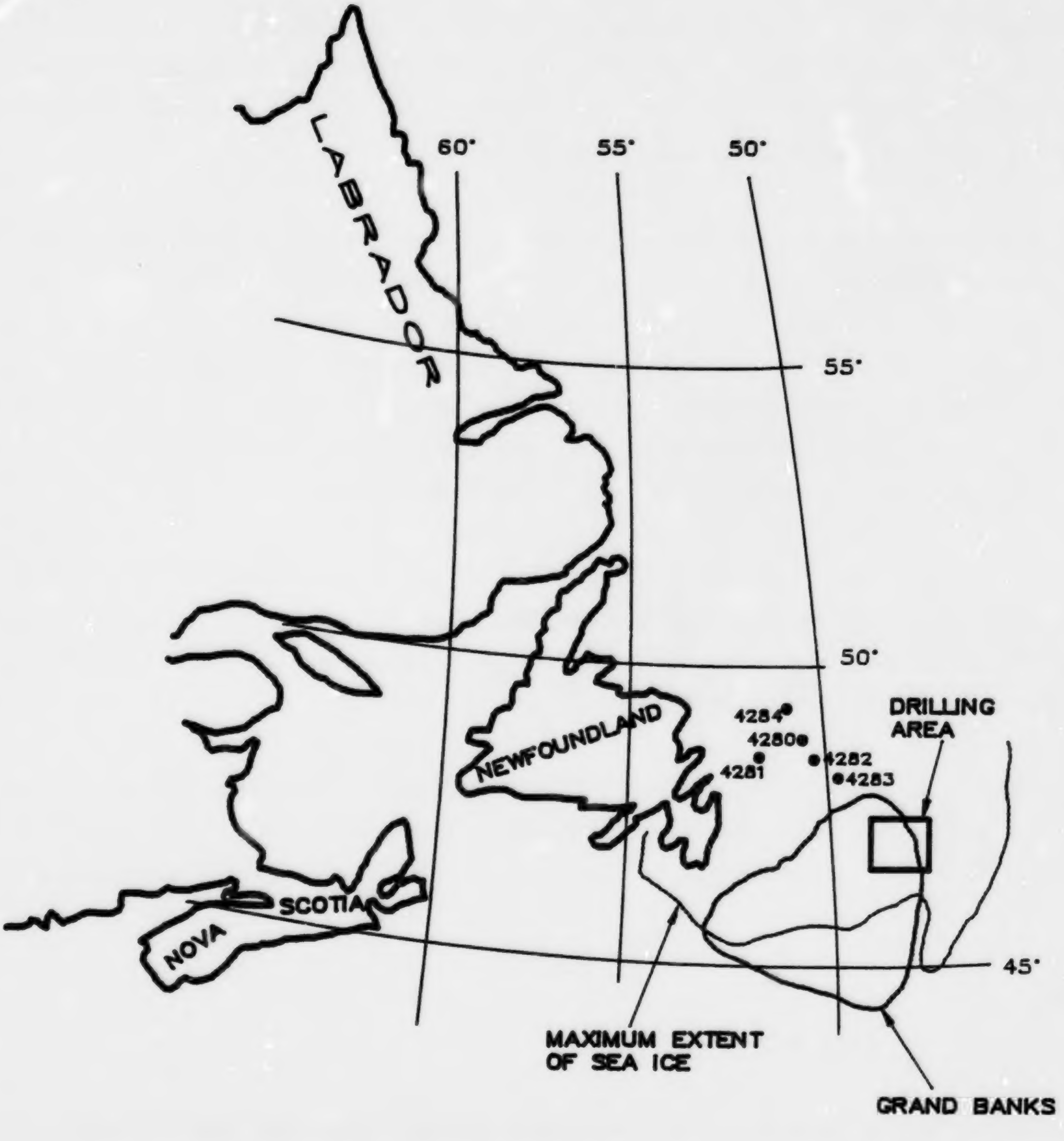

FIGURE 1

MAP SHOWING ICE BUOY DEPLOYMENT LOCATIONS

Table 1

Ice Buoy Deployment and First Computed Position Data

(Times in GMT)

Buoy ID	Deployment Time	GNS Position	First ARGOS Fix Time	Initial Fix Position
4280	1400	48° 52.90'N 50° 28.00'W	1811	48° 49.22'N 50° 24.48'W
4281	1500	48° 30.1'N 51° 31.0'W	1632	48° 28.34'N 51° 29.88'W
4282	1340	48° 32.30'N 50° 12.40'W	1632	48° 29.28'N 50° 10.74'W
4283	1300	48° 18.10'N 49° 51.00'W	1632	48° 16.26'N 49° 49.92'W
9284	1430	49° 19.40'N 50° 57.50'W	1902	49° 15.48'N 50° 48.12'W

Based on predeployment positional checks it was determined that positional accuracy for all buoys could be assumed as ± 500 m at the 95% confidence interval. The corresponding RMS velocity accuracy over six hour time intervals was equal to 0.03 m/s. Since the velocity accuracy is a function of the interval time, over shorter time periods the uncertainty increases reaching a value of 0.20 m/s for a one hour time interval.

Under ideal circumstances the combined situation of two NOAA satellites equipped with ARGOS instrumentation and the orbital configuration of the satellites results in the possibility of multiple positional fixes from each buoy in a given 24 hour period. Theoretical maximums range from a minimum of four at the equator to a maximum of 28 positions per day in the high latitudes. Other factors such as PTT performance can reduce the realized number of positional fixes from the theoretical maximum for a given area. Table 2 provides an indication of the performance of the five buoys while on the ice. For all buoys except 4284 the mean number of fixes per day was 6 to 7 resulting in an average time interval between positional updates of 3.5 to 4 hours. Buoy 4281 experienced the highest number of fixes in one day of 15 as well as the lowest of one, excluding buoy 4284. The low mean and maximum values for buoy 4284 reflect the transmission problems which plagued its short life.

Table 2
Service Argos Positional Fixes Per Day
(While Beacons Were on the Ice)

Buoy	Total on Ice Fixes	Daily Mean	Minimum	Maximum
4280	86	6	2	11
4281	279	7	1	15
4282	92	6	2	11
4283	103	7	2	12
4284	32	3	0	7

GENERAL ICE DRIFT

All five buoys exhibited a general northwest to southeast drift during the course of their life on the pack ice. Figure 2 shows the trajectories for five buoys, beginning their drift at the northern tip of the Grand Banks and travelling in a near direct line towards the Flemish Cap. Buoy 4281 deployed over shallower water than the other four, exhibited considerably more variation in both its speed and direction. These differences in ice motion suggest significant bathymetric control, an assertion which is borne out through an examination of ice speeds measured on and beyond the Grand Banks, using the 200m bathymetric contour to distinguish between the two. Figure 3 shows percent exceedence curves for ice speeds in the two regions incorporating all ice data. Beyond

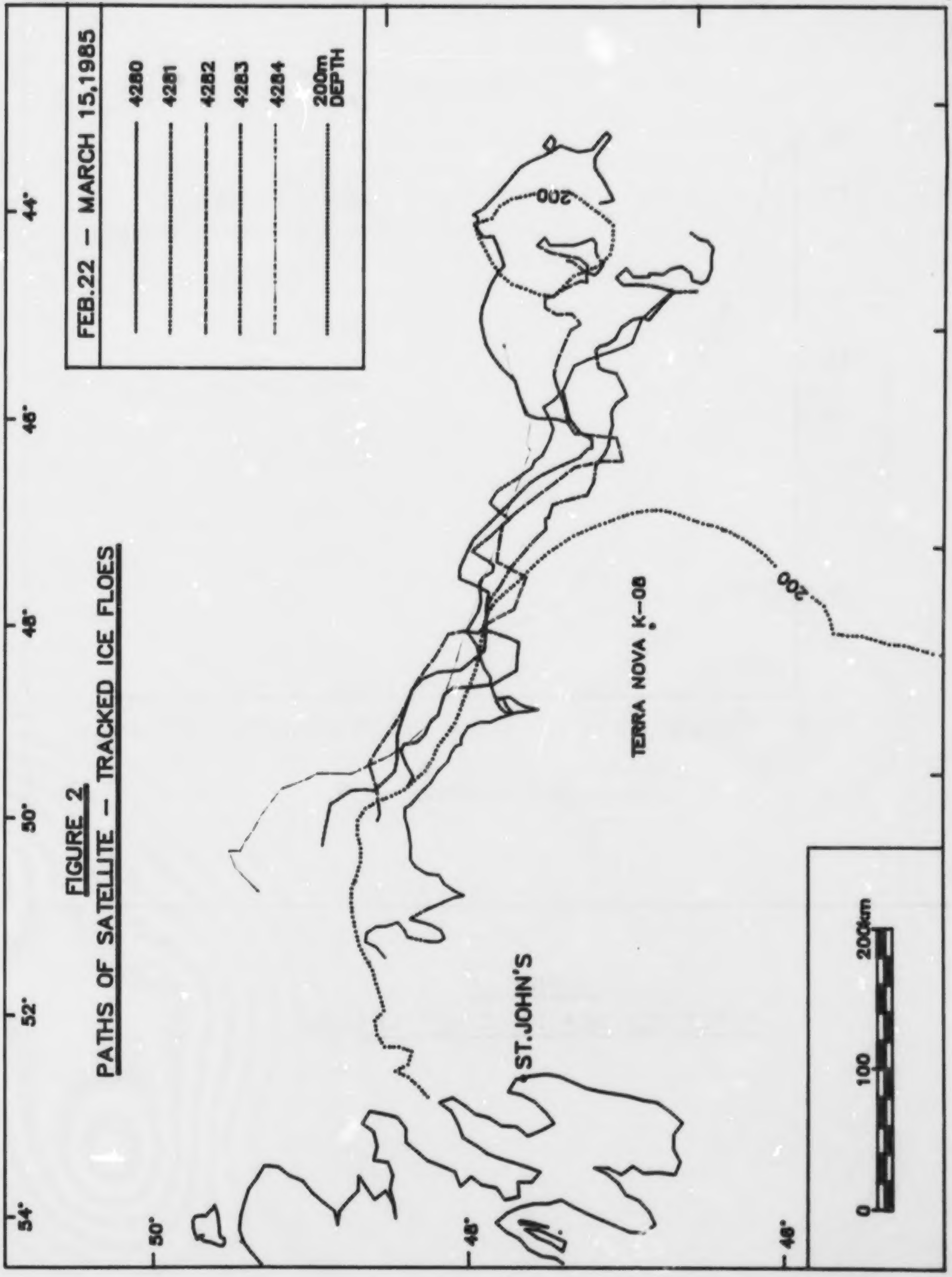

FIGURE 2

PATHS OF SATELLITE – TRACKED ICE FLOES

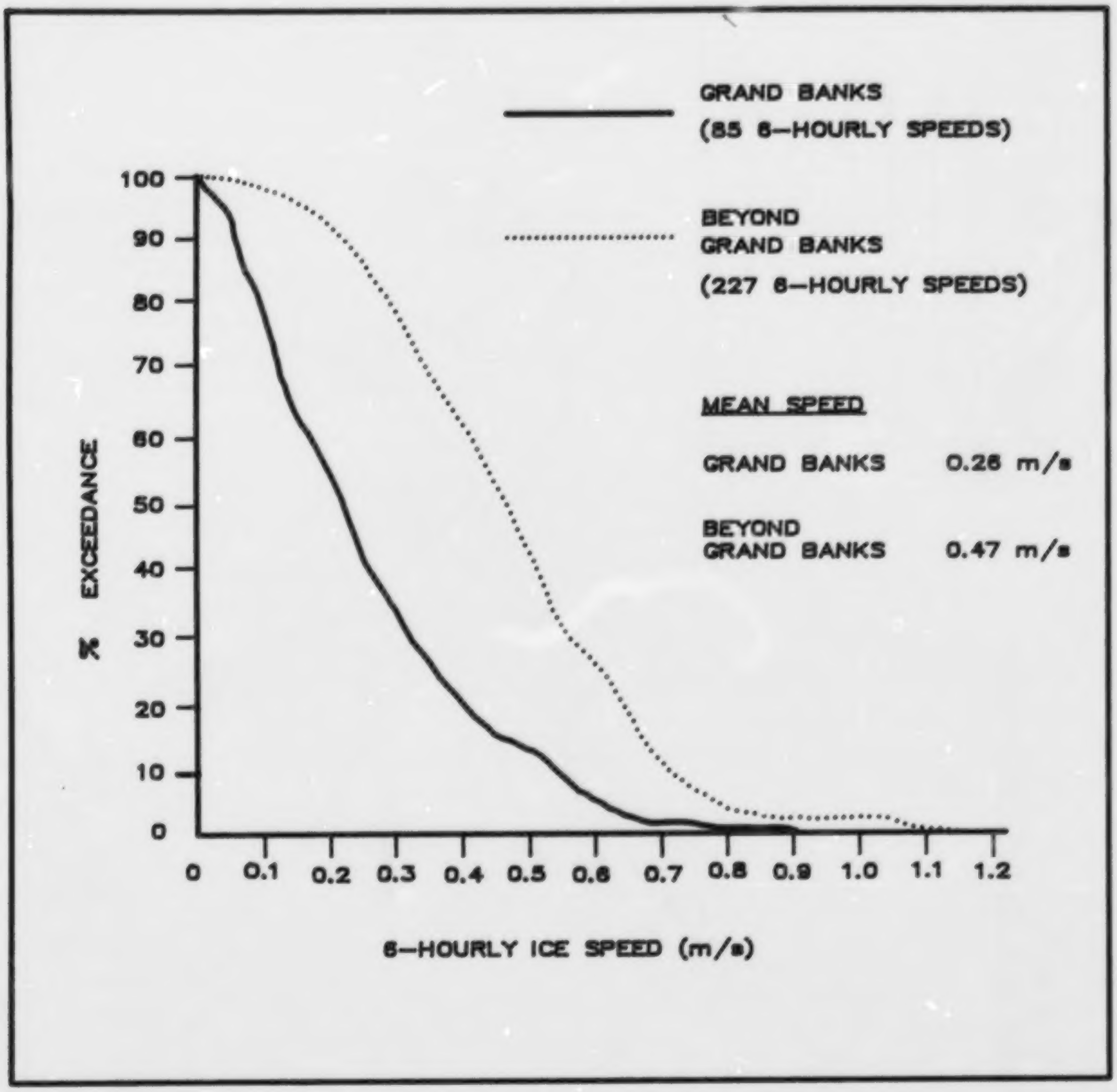

FIGURE 3

OBSERVED SEA ICE DRIFT SPEEDS

the Banks the mean ice speed (0.47 m/s) is nearly double that on the Banks (0.26 m/s). At exceedence levels below 10%, speeds in the two regions show less difference.

In addition to lower speeds over the Banks, the ice floes in this regime exhibited a greater degree of variability in the direction of ice movement. Comparison of the direction roses in Figure 4 indicates a strong tendency for ice floes beyond the Grand Banks to travel in an east to southeast direction whereas ice drift over the Banks shows much greater directional variation including substantial periods of drift to the northeast and southwest, although the dominant direction of drift is to the southeast in both ice regimes. The mean drift speed in a southeasterly direction was only half as large on the Banks as it was further offshore.

WIND INFLUENCE ON ICE MOTION

A linear regression analysis of ice velocities (V) and geostrophic winds (W) was conducted in an effort to examine the influence of wind stress on large scale sea ice motion where V=A+B*W. The results of this analysis are summarized in Table 3. In all cases, buoy 4283 excepted, the correlation coefficient exceeded 0.55 indicating that the geostrophic wind could account for some 30-44% of the total ice speed variance.

Table 3

Summary of Cross-Correlation Analysis Between Ice Velocities and Winds (Major Drift Component at 135°T)

Buoy	Ice Regime	Number of Observations	Intercept A	Slope B	Correlation R
4280	Beyond GB	32	.341	.013	.665
4281	Over GB	74	.070	.008	.567
4281	Beyond GB	56	.166	.010	.621
4282	Beyond GB	34	.254	.015	.664
4283	Beyond GB	48	.253	.007	.464

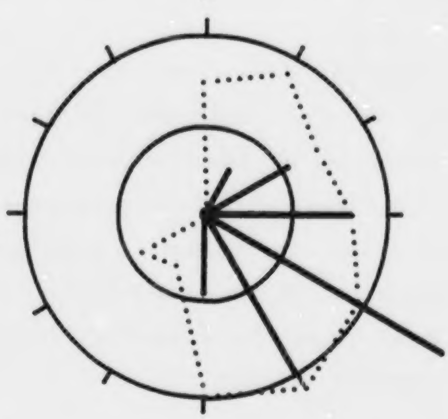

BEYOND GRAND BANKS

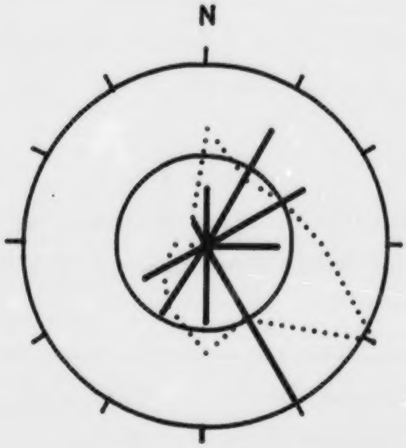

ON THE GRAND BANKS

FIGURE 4

DIRECTION ROSES OF 6-HOURLY ICE VELOCITY MEASUREMENTS

The results suggest that ice motion beyond the Grand Banks ranges from 1.0 to 1.5% of the geostrophic wind speed. In the absence of any wind, the regression analysis suggests the ice motion would range from 0.17 to 0.34 m/s, entirely in keeping with anticipated mean current speeds in the area as estimated from drifting buoy data (Petrie and Isenor, 1984).

Over the Grand Banks the coupling of ice velocity to wind speed was lower at 0.8% although the difference may not be statistically significant due to the statistical uncertainities involved. Net ice movement in the absence of wind is only 0.07 m/s, indicative of the reduced current velocities over the Banks.

DISCUSSION

The results of the cross-correlation between ice velocity and geostrophic winds, indicate that winds account for 22 - 44% of the ice velocity variance. Petrie and Isenor (1984) indicate that correlation analysis between Lagrangian velocities and winds are prone to underestimation of the correlation. This would suggest that the actual influence of wind stress on sea ice motion is higher than these results indicate, although probably not as high as that found in other areas such as off East Greenland where correlation coefficients ranging from 0.5 to 0.9 have been obtained (Johanessen et al. 1983).

Possible sources of ice velocity variance are numerous including temporal and spatial variability of the ocean both on and off the Grand Banks. Another source of ice motion variability may be spatial variations in ice stress within the ice pack itself.

In other marginal ice zone environments it has been observed that under wind forcing, ice velocities near the ice edge are greater than those further into the ice pack. If present within the Grand Banks ice pack, this characteristic would account for some of the variance in ice velocity.

APPLICATION

The project highlights described above represent those of the scientific program. The rationale for the project was to provide support for drilling operations and design engineering. A brief summary of how these support tasks were accomplished are described below.

To support drilling operations during the winter drilling period, the last position fixes were recovered twice daily by telex from Toulouse, France. The positions, speed and direction of each drifter were overlaid on a map of current ice conditions. Coupled with forecast wind conditions, these data formed the basis for predictions of ice edge advance and retreat. These data provided valuable ground truth of ice motion and helped to prevent unnecessary evacuation from the site, a time consuming and costly manoeuvre for a semi-submersible, and also helped estimate when a drilling operation, terminated due to the approach of the ice, could be re-established.

For design purposes, illustration of kinetic energy estimation of individual ice floes is provided using the data in Table 4. The velocity and thickness distributions are categorized by five points representing the 10%, 30%, 50%, 70% and 90% exceedance values. Mass estimates were obtained by assuming a floe radius of 10 metres, circular shape and a ice density of 900 kg/m^3. The kinetic energy estimate were calculated using Betz's (1970) 25 point method of estimation. Shown in Table 4 are five points on the kinetic energy (0.5 x mass x velocity x velocity) distribution. Clearly evident are the low values of kinetic energy relative to those expected for icebergs (1,000,000 - 1,000,000,000 J (Lever et al, 1984)).

Table 4
Kinetic Energy Estimation

Occurrence	Cum %	Velocity (m/s)	Thickness (m)	Kinetic Energy (J)
Very High	10	0.08	0.15	742
High	30	0.13	0.30	2,100
Average	50	0.23	0.60	4,350
Low	70	0.32	1.50	9,490
Very Low	90	0.52	2.00	30,200

This project highlights two of the needs for sea ice information for offshore development and a project undertaken to meet these needs. The authors would like to thank Petro-Canada Resources for funding the work and allowing permission to publish and K. Borysiewicz for help in preparing the manuscript. Special thanks is also given to G. Wilton, D. Fissel and J. Marko of Arctic Sciences who were involved in parts of the program from the field deployment through the data analysis. This work is dedicated to the memory of Brian Garbett who participated and assisted in many offshore ice programs over the last decade and who died last spring in an offshore helicopter crash.

REFERENCES

BETZ, D. 1970. Reservenerwartungskurven als informationsmittel und bewertungsgrundlage. Erdoel - Erdgas - Zeitsdrift, 86, pp. 249-252. (Translation - Canadian Secretary of State, Translation Bureau).

JOHANNESSEN, O.M., J.A. JOHANNESSEN, J. MORISON, B.A. FARELLY and E.A.S. SVENDSON. 1983. Oceanographic conditions in the marginal ice zone north of Svalband in early fall of 1979 with an emphasis on mesoscale processes. Journal of Geophysical Research, 88, pp. 2755-2769.

LEVER, J., E. REIMER and D. DIEMAND. 1984. A model Study of the Wave-Induced Motion of Small Icebergs and Bergy Bits. International Offshore Mechanics and Arctic Engineering Symposium (3rd), New Orleans, 282-290.

MARKHAM, W.E. 1980. Ice Atlas-Eastern Canadian Seaboard. Atmospheric Environment Service, 96 pp.

PETRIE, B. and A. ISENOR. 1984. An analysis of satellite-tracked drifter observations collected in the Grand Banks Region. Canadian Technical Report of Hydrography and Ocean Science, No. 39, 64 p.

PETRO-CANADA INC. 1985a. Sea Ice Occurrence and Icing Accretion Studies-Grand Banks Internal report prepared for Petro-Canada by Seaconsult Ltd.

PETRO-CANADA INC. 1985b. 1984/85 Ice Pack Dynamics Study. Internal Report For Petro-Canada by Arctic Sciences Ltd.

ICE MONITORING AND FORECASTING FOR THE BEAUDRIL 'KULLUK'

BY F. J. ELEY
GULF CANADA RESOURCES

INTRODUCTION

The BeauDril 'Kulluk' is a floating ice-capable drilling vessel purpose built for exploration drilling in the Beaufort Sea. It was designed to extend the drillship season from 90 days to about 160 days in the 25 to 60 m water depths in the Canadian Beaufort Sea. It is supported by a fleet of four Class IV ice-breaking supply vessels.

In order to take full advantage of the capabilities of this system, an ice monitoring program is operated in support of the Kulluk. The ice monitoring program tries to predict the potential for, or the time of occurrence of ice conditions beyond the Kulluk's capabilities, so that the rig can operate as much as possible. The system normally continues to operate until heavy ice is within 12 hours.

Due to the shallow water depths, and the consequent short coupling of the drilling system (Figure 1), rather small displacements of the vessel will stop drilling operations or damage drilling equipment. At a typical water depth of 30 m, the consequences of unannounced vessel displacements are:

1 m off	Questions are asked
5 m off	Drillers get quite upset, equipment may be damaged
20 m off	Equipment is damaged, in the drill system and possibly in the vessel moorings

The Kulluk was designed to be able to break 4 feet (1.2 m) of level ice on its own, due to the holding power of its 12-line mooring system. Experience in its operation indicates it probably could perform

FIGURE 1
KULLUK DRILLING SYSTEM
TYPICAL WATER DEPTH

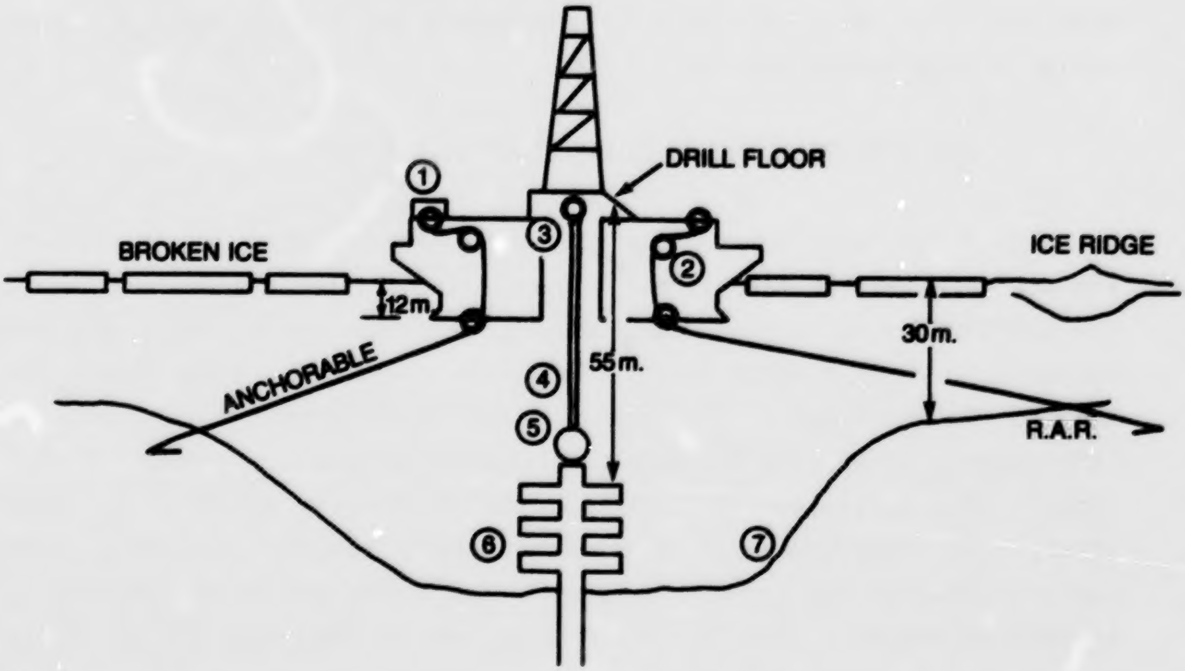

① ANCHOR WINCH
② FIXED SHEAVES – SITE OF ANCHOR TENSION SENSOR
③ UPPER BALL JOINT
④ MARINE RISER PIPE
⑤ LOWER BALL JOINT
⑥ BLOW-OUT PREVENTER STACK
⑦ 'GLORY HOLE' HIDES B.O.P. FROM ICE

that way, but that is not certain, since 1.2 m level ice does not exist in the mobile part of the Beaufort Sea. What actually happens is that ridges several meters thick form by the time the ice is 60 cm thick, and the ridges limit the Kulluk's station-keeping. On the other hand, over 9/10 of broken ice 5 m thick with thicker ridges has not stopped the Kulluk from working, when floe sizes were kept small by icebreakers and the ice was just loose enough to flow around the rig.

ICE CLIMATE OF THE CANADIAN BEAUFORT SEA

A few facts about the general ice climate of the Canadian Beaufort Sea will help to set the scene. Figure 2 shows three general ice zones. The Landfast Ice is fairly broad, usually terminated on partially grounded ridges at 15 to 20 m water depth. This zone always melts clear during the summer. The Polar Pack is the edge of Arctic Ocean permanent ice cover. By late summer, the edge is composed mainly of thick multi-year ice. In some summers this multi-year ice drifts south across the Kulluk's operating areas. The Transition Zone is the zone between Landfast and Pack, where mostly first-year ice forms, and is distorted and ridged by constant motion through the winter. This ice cover melts away in the early Kulluk season and reforms in the late Kulluk season. Figure 3 shows the short summer period when total ice concentration is usually near zero in the Kulluk operating acreage. As shown in Figure 3, the new ice usually grows to 50 cm by November 20, after which the Kulluk can only operate if the winds are not onshore.

ICE MANAGEMENT TEAM

Ice management of the Kulluk is handled under the general direction of the Vessel Superintendent (or Captain). He is assisted by technical input from Ice Observers, who keep a watch on ice and weather conditions 24 hours per day. He is also assisted by an on-board Ice Adviser who studies the general situation for the Captain, and normally acts as night ice master to relieve the Captain. Ice Advisers are engineer/scientists drawn from

FIGURE 2
SEA ICE ZONES IN THE BEAUFORT SEA

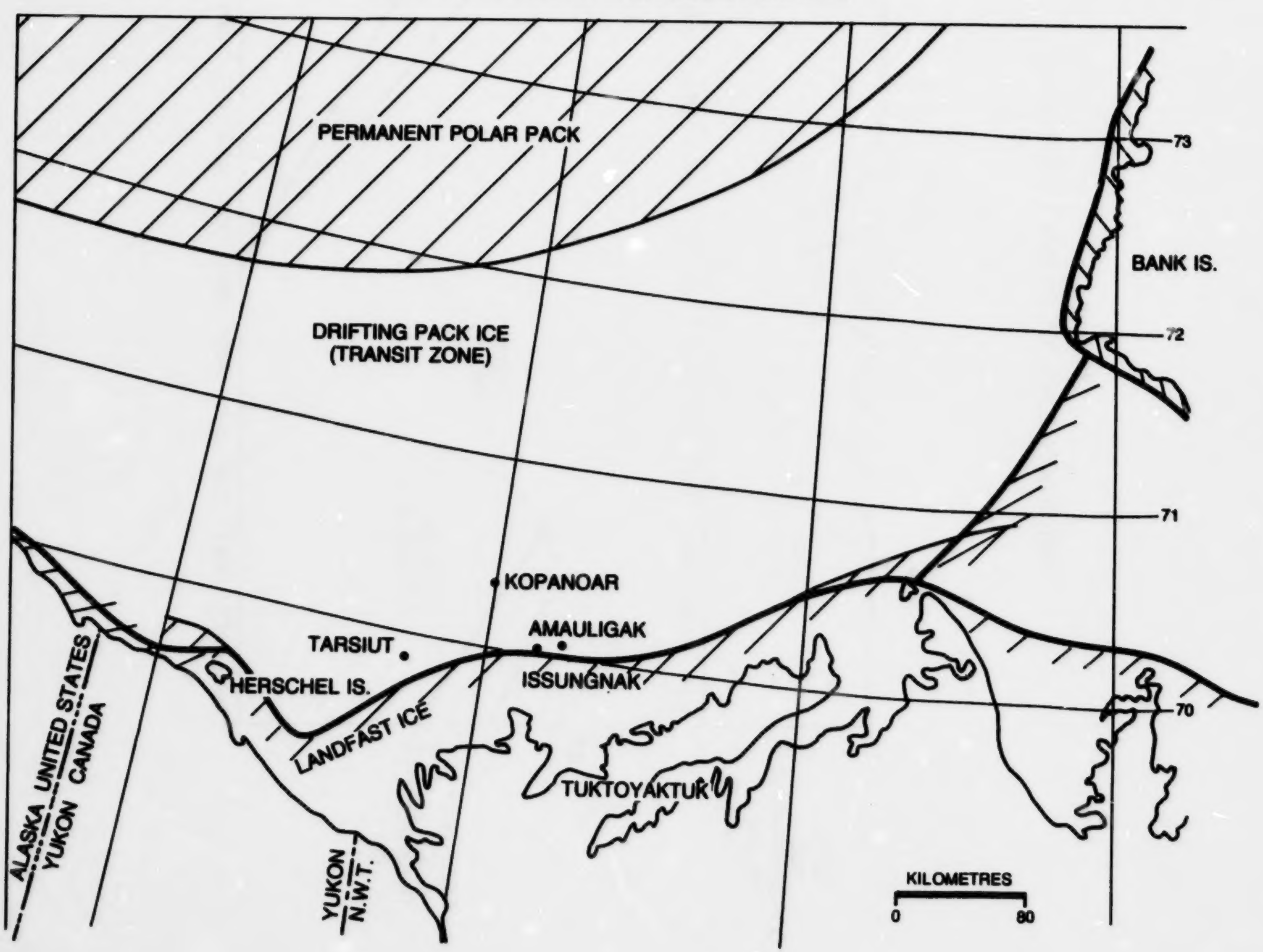

FIGURE 3

TRANSITION ZONE ICE CHARACTERISTICS

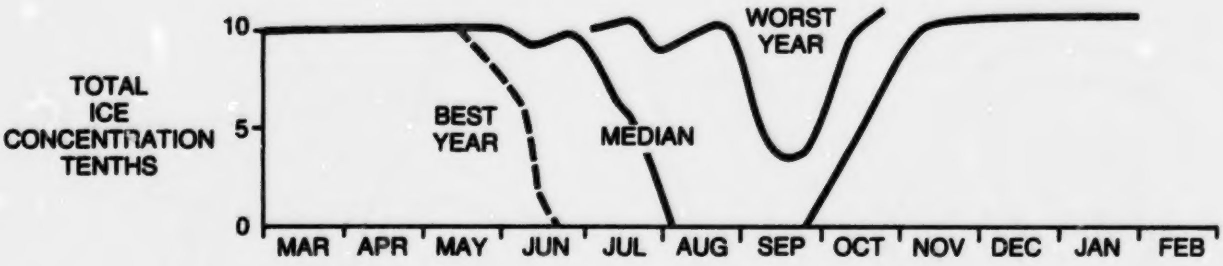

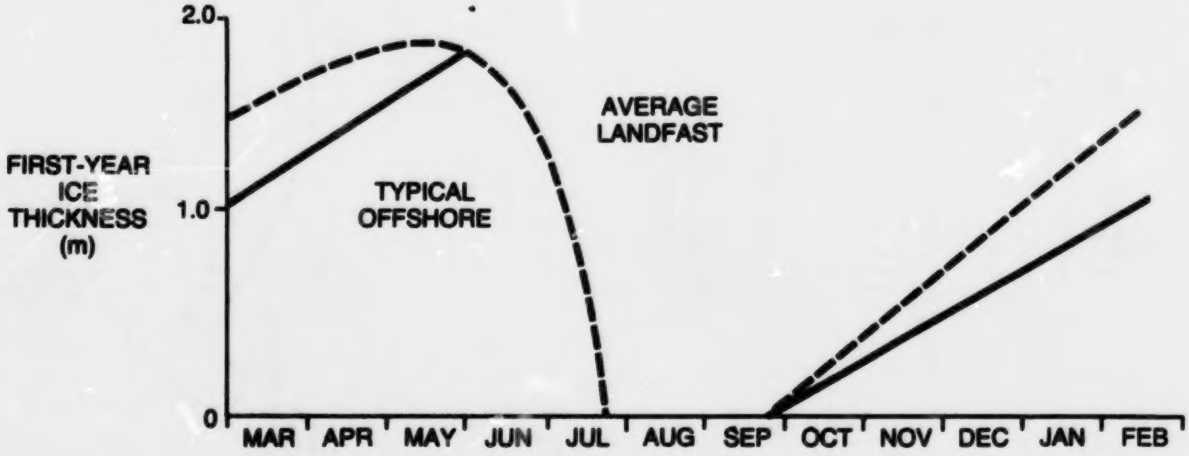

Gulf's ice expertise group. The Masters and Watchkeepers of the supporting icebreakers are active participants in Kulluk ice management. They provide reports on ice encountered and their vessel's capabilities in it, and they often recommend their own tasking. Most communication is verbal, but all vessels have telephones, and sketches are sent both ways as appropriate, via commercial office facsimile equipment.

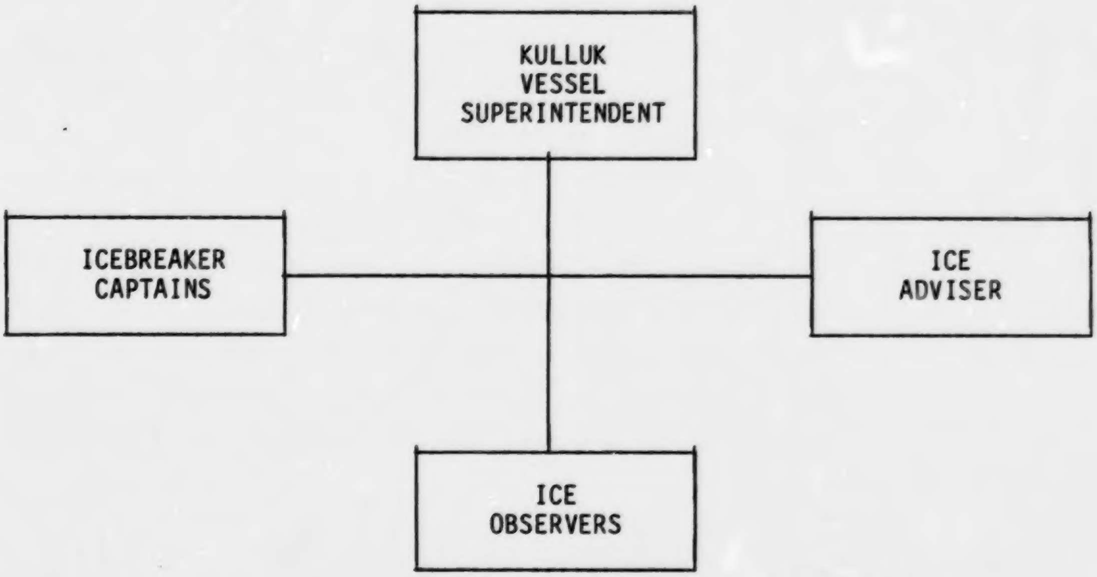

ICE INFORMATION SYSTEM

The ice information system can be conveniently seperated into regional and local, relative to the drill rig itself. The regional services are operated off the rig but for its benefit. They are generally operated from the BeauDril and Canmar bases at Tuktoyaktuk.

Regional services include the following:

1. Beaufort Weather Office - an industry operated weather office dedicated to the drill rig operations and support. With respect to Kulluk ice support, its prime function is wind

forecasting. Due to the history of Beaufort Sea offshore drilling, this office developed from pre-drilling forecast studies in 1974-75 and it has always been (seasonally) staffed by Atmospheric Environment Service personnel.

2. Ice Information Office - this is operated by Canmar Drilling and shared by BeauDril. Its prime function is handling the SAR regional reconnaissance data expeditiously for all users (up to 7 drilling systems, their support, and management at Tuk and Calgary). This office also issues twice-daily ice drift forecasts which are limited in content to 12, 24, 48 hour displacement and potential maximum drift speeds.

3. The Intera STAR-1 (SAR) radar system is used on a dedicated basis during the Kulluk operating season. It is downlinked to the Ice Office at Tuk, where it is analysed onto regional ice charts for all users. Early local analysis charts are dispatched to the drillships or needy icebreakers during the flight.

   The entire flight is also printed as a mosaic with map overlay at 1:250,000 scale and widely distributed. These image 'maps' have proven a very valuable tool in the hands of captains and managers, due to their fairly easy interpretation capability and the convenience of a proper, accurate map overlay. Wire-photo equipment routinely transmitted portions of the mosaic to Calgary. Similar transmissions to the Kulluk were treated as a 'trial' because they were not received until the first prints were run, some 8 hours after the flight.

FIGURE 4

KULLUK ICE MONITORING SYSTEM (1985)

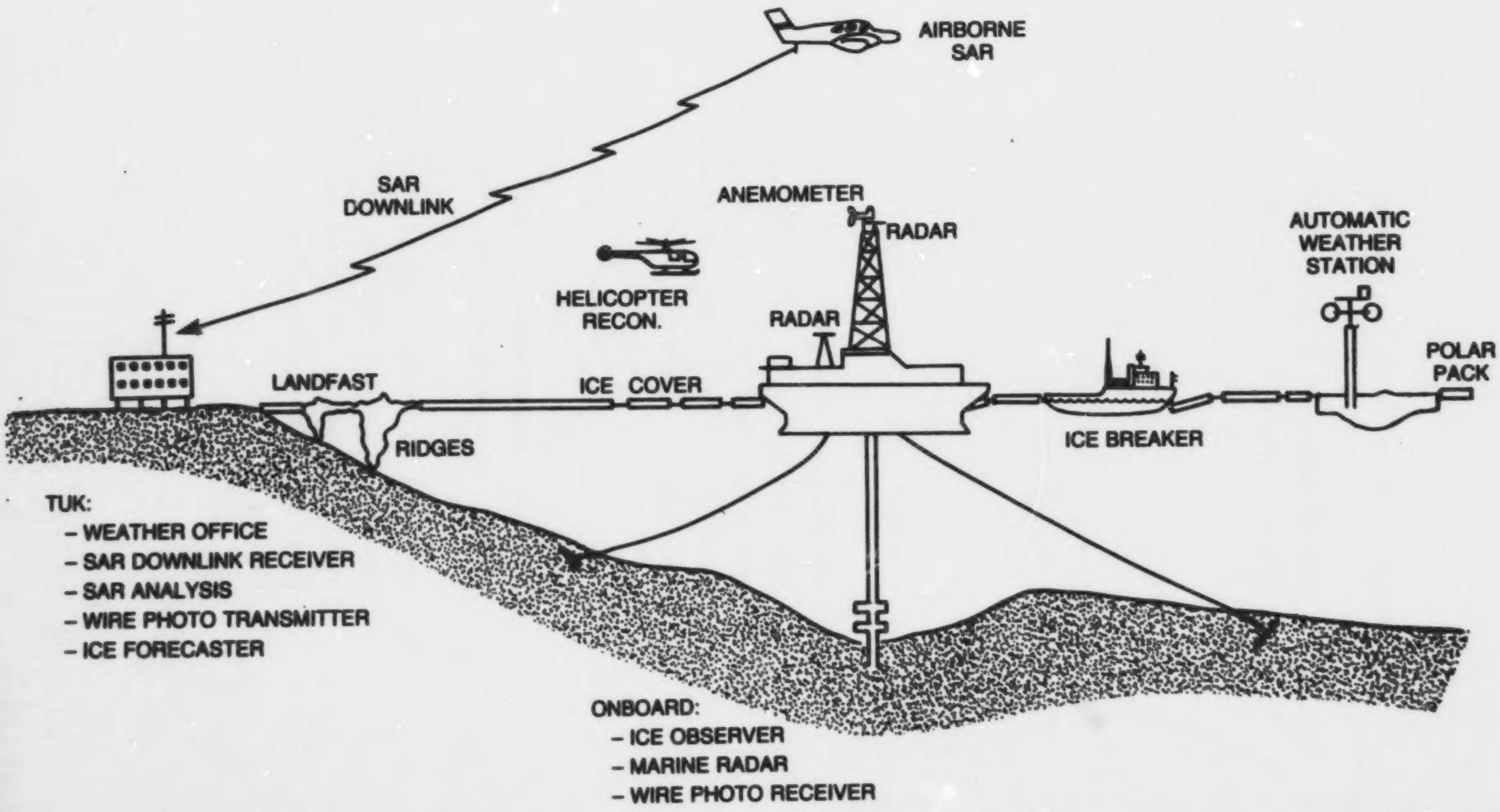

Local services on the Kulluk include:

1. Ice Observers on a 24-hour basis. They keep a continuous watch on weather, sea state and ice conditions. When necessary, they update the ice drift every 15 or 20 minutes.

   Due to the failure of all ice drift models to consistently predict, the ice observer simply reports present (most recent) drift, and icebreakers are dispatched updrift. No computers are used.

2. Ice Advisor - Usually this is one person but, as mentioned above, he usually works the night shift to watch ice management for the Captain.

3. Marine radar with a derrick - top scanner provides an effective range of 5 to 10 miles for ice detection and tracking. The prime function is ice drift tracking. Due to the Kulluk's ability to work in ice this radar's inability to distinguish ice types is seen as a serious deficiency.

   A digital radar display system is used to enhance ice tracking capability. It has a capability to flicker between two video images which has enabled tracking on a very even clutter, as opposed to normal tracking of distinct targets.

4. Helicopter ice reconnaissance from the rig is carried out as needed and possible (weather, sunlight). It has proven very useful in better informing the ice management team of conditions within 10 to 20 miles (1 to 3 days drift) of the Kulluk.

5. The anchor tension is displayed by a real-time data processor on the Kulluk. This system shows graphically and digitally the present individual line tensions, the global load vector and peaks since last reset. It also shows vessel offset and environmental data as connected, such a derrick-top wind. The system has proven invaluable in monitoring the effect of ice on the Kulluk.

ICE DRIFT FORECASTING AS APPLIED

Ice condition forecasting is dealt with on about 3 time scales: less than 3 hours, 3 hours to 3 days, and over 3 days. These time scales overlap, depending on the situation and the function.

The longest time scale deals with the progress of spring break-up and early winter freeze-up, and it is used to plan drilling support system operations to get the most out of the brief open water season. These forecasts are based on present ice conditions and the progress of the season that would develop with normal weather and with the most likely anomaly.

On shorter time scales, forecasting effort is on drift and pressure rather than melting and freezing.

For dispatch of icebreakers in heavy ice conditions (Figure 5), ice drift forecasts of only one to three hours are made. These 'forecasts' are done in the simplest possible manner by plotting ice drift and assuming it will keep moving the same way. Where enough icebreakers are available and the variability of drift warrants it, a considerable sector of updrift ice is broken or scouted.

Since typical well operations take many hours, the practical problem continually arises of how many hours are available before the Kulluk might be hit by ice conditions it could not handle (Figure 6). On this time scale of three hours to a few days, ice forecasts are based on the present

FIGURE 5
ICE BREAKER DISPATCH – TYPICAL

CASE 1

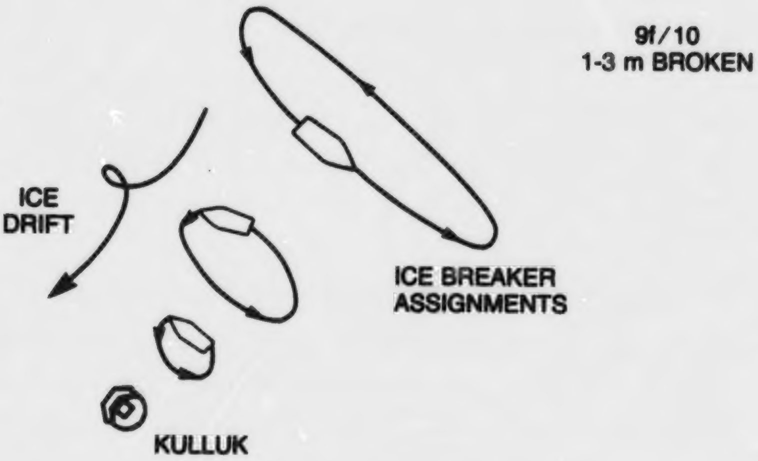

CASE 2

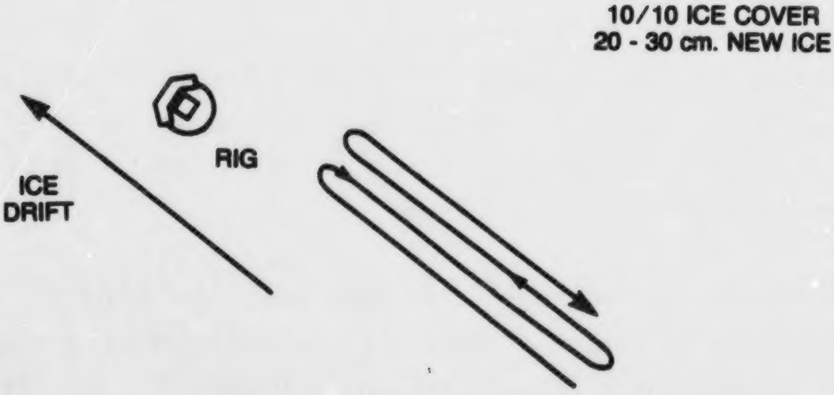

FIGURE 6
WELL OPERATIONS PLANS

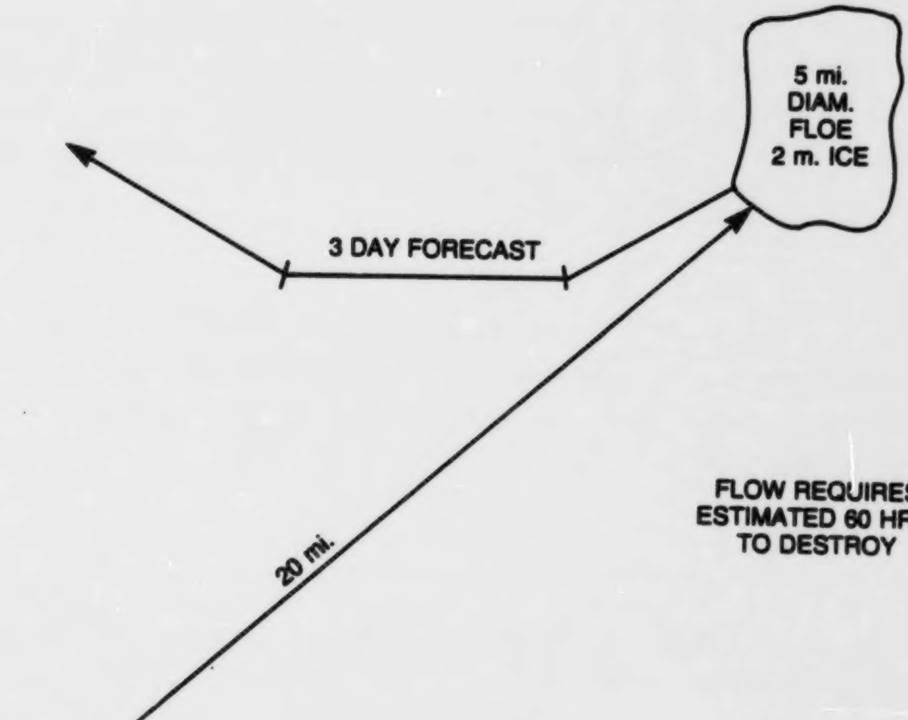

ice map and the expected wind. Ice is expected to drift downwind (not particularly right or left) and at three percent or less of wind speed. Because there is never full confidence in the wind forecast, due consideration is always given to the maximum possible drift of any hazardous ice towards the drillsite. If there are several potentially hazardous ice floes, and icebreakers could not break them all, then the big question becomes: how much confidence should be placed in the wind forecast?

ICE FORECAST VERIFICATION

Gulf ran a verification program on a series of well-designed models of Beaufort Sea ice drift, that were available to our on-board ice forecasters in 1984. The measure of accuracy was the scalar magnitude of error in position of the ice between forecast and actual drift, after each 6-hour increment, as shown in Figure 7. The three models verified were:

Model 0

Ice drift at 3% of wind speed and.20 degrees to the right of the wind. This was run on the wind as forecast and the wind as actually observed in the forecast period, to see how much of the error was due to wind forecast error.

Model 1

This model back-fits the previous 12 hours to the ice drift and wind as observed, to a model with two components: 30° right of wind and cyclic with a 12.4 hour period. The back fit determines the diameter of the circles and the ratio of wind-speed to linear component of ice drift. The model assumes an increasing ratio at ice speed to wind, as the wind speed increases.

FIGURE 7
ICE DRIFT MODELS – SCHEMATIC

MODEL 0

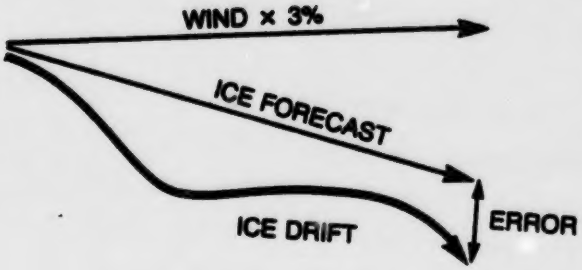

MODEL 1

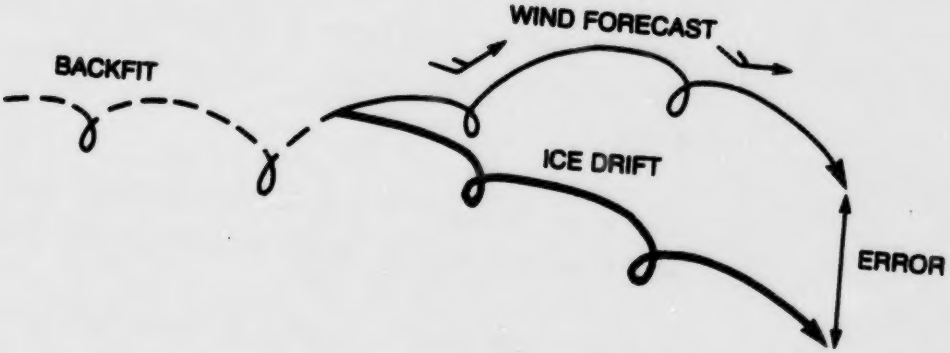

MODEL 2

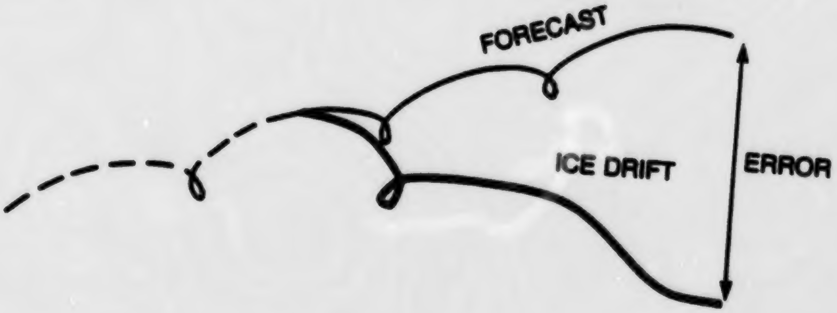

Model 2

This model ignores the wind, forecast or otherwise. It back fits the ice drift to a cycloidal pattern with a 12.4 hour period, and projects the fitted drift ahead. This may work well where wind is not very strong and it is expected to keep the same direction more or less.

The results of the verification study are plotted in Figure 8. It should be noted that mean ice drift for this period was only 7 miles per day. The final line of Figure 8 shows the mean error of forecasts issued by the Tuk Ice Office, based on the forecaster's judgement, using the same wind forecasts and ice drift models for guidance.

The main results of this sample month of mean deviation are:

i) forecast errors are large in all cases, indicating no models are adequately handling all components of forces driving ice drift.

ii) the wind forecast was a source of error but perfecting it would improve average model results by only 15-20%.

iii) straight persistence (Model 2) is a very powerful forecast model.

iv) it is possible to try too hard (Tuk Ice Office) in the situation where no physical model is adequate anyway.

FIGURE 8
MEAN ERROR FORECAST DRIFT
PITSIULAK WELLSITES JULY 1984

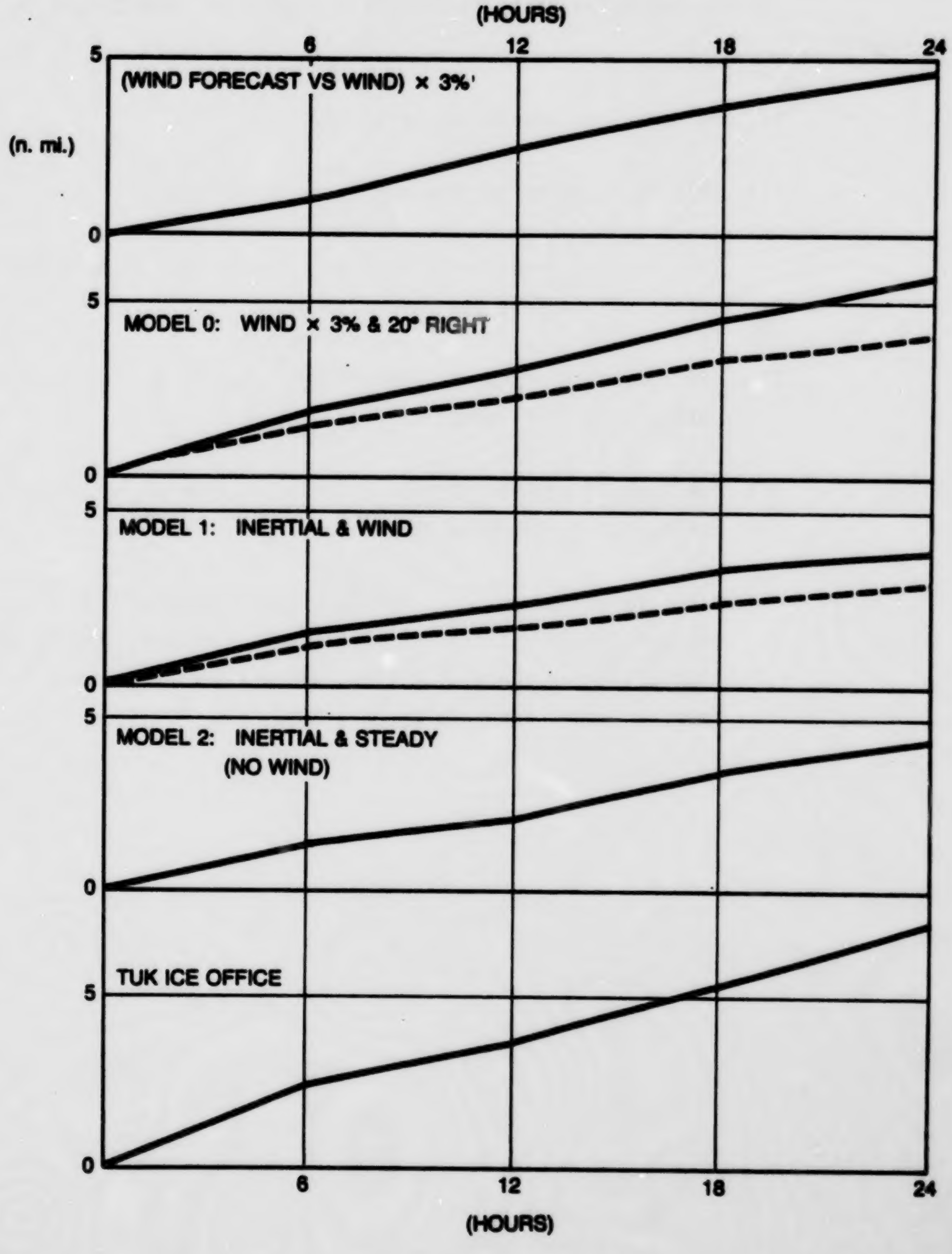

CONCLUSION

The ice drift forecasts for Beaufort drillsites were tested in two ways:

i) mathematical measure of error.

ii) what do Captains believe and actually utilize?

The results were quite similar, indicating that practical models of Beaufort Sea ice drift are:

i) for short periods, Persistence, expecting a cycloidal pattern, but not necessarily consistent.

ii) for longer periods, Downwind Drift, but with only moderate confidence in the wind forecast.

From the mathematical verification, it appears that much is unknown about driving forces (water currents, etc.) other than 12.4 hour inertial cycles, since a perfect wind forecast improved model accuracy by only 20%.

DOME-CANMAR'S OPERATIONAL ICE-FORECASTING SYSTEM FOR THE BEAUFORT SEA

BY

J. W. Steen and J. D. Trobak
Marine Systems, Environmental Operations
Canadian Marine Drilling, P. O. Box 200
Calgary, Alberta, Canada. T2P 2H8

ABSTRACT

This paper describes Beaufort Sea sea ice, its characteristics, inter-relationship with the predominant driving forces and how to derive operationally useful forecasts of its movements from attainable data.

It describes the Dome-Canmar ice forecasting system which is used by both Dome-Canmar and Gulf-BeauDril in the Beaufort Sea detailing the data that is collected, how it is handled and how it is used.

It describes the methods developed for forecasting ice movements in support of the Beaufort Sea Operations and the blending of theoretical knowledge with operational practicability.

Examples of specific forecast and the ensuing actual events outline some of the complexities involved and also treats the important subject of verification.

INTRODUCTION

The luxury of avoiding ice, of doing the easy bits, is long gone.

Our quest to add to our dwindling resource inventories has inexorably led to ever increasing activities in ice infested waters. Temporary international and domestic economic vagaries, notwithstanding, the continuation of this trend seems a foregone conclusion and is likely to be as relentless as the westward migration of the early settlers, for much the same reasons.

Our success or failure in bringing the resources for the future into our stores will be affected greatly by the knowledge available to us and our capacity to derive operational savvy from such knowledge.

However crucial we view operational experience, it will be all the better for being based on introspective and sound science. It will help to avoid costly mistakes and wasted efforts; it will help us preserve the environment, the goose that lays the golden eggs, the resources we need and seek.

Dome has developed an ice monitoring and forecasting system for its Arctic operations.

Whatever its shortcomings, it has become an essential operational service which is now subscribed to by others as well.

To reach this stage was sometimes difficult, sometimes frustrating; at all times costly.

Being the lone pioneer, Dome had to go it solo and deserves some credit for its persistent commitment.

The System was developed during the ten years Dome has been working there, not only by evolution through trial and errors, but also by applying whatever science was available.

We have had many occasions to interweave academic knowledge and technology to create practicable applications.

I say this to stress how important it is to have even the pure sciences to draw from and how important it is for us, the operational people, to recognize this.

However, it is equally important, to have some of the scientists more familiar with the applications their discoveries may serve.

The sciences and the operations must be brought to a common crossing point of the gap that sometimes separates them. Each must see where the other is, to prepare the foundations for the shortest and most direct span to bridge that gap.

We need the "purists" too, on both sides, but on their own there is too high a risk that they never find such a common crossing point. In the north, it is akin to an operational "assault party" having made a crossing into hostile territory by improvised and temporary means. They have secured a bridgehead, but will need solid and permanent support to expand this gain. The support must be directed to where they are, it will do little good if directed elsewhere.

We, the operational types, must not criticize the sciences for misdirected support if we have not let it be known where we "crossed", where we are and what we need.

You may have surmised one operational link between the sciences and the bridgehead from an earlier paper by Cherniawsky, Gower and Borstad. Indeed there is one, in this case, a longstanding relationship between the gray cells at the Institute of Ocean Sciences and the brawn at Dome (some gray cells too).

When the Institute embarked on their current programme of unlocking the enigmas of ice movements and the modelling of those, they invited us for consultation, they wanted to know what we thought would serve us. Our input would never control or compromise the total freedom for the fundamental scientific work to go wherever truth leads it. There are no strings attached. We appreciate their concern for our possible uses and we are reassured that they are looking for that common crossing point. This is a result of our relationship. It is a relationship forged by a focus on common long-term purposes; a recognition of an inter-dependency in the long term while honouring independence during each day.

There are links with others too. However, we need to expand the family, and, to this end, think it may be useful to show this august representation of the scientific world where we crossed, where we are, what we need by showing you how our improvised ice forecasting system works on the front line; its strengths and its weaknesses.

To do so, may I present my colleague and collaborator, Mr. Del Trobak. He has been instrumental in every aspect of our ice monitoring and forecasting developments. Remember as you listen to him that he has not only dealt with these problems from the sanctuaries of remote offices, laboratories and conference halls, he is one of the few of us who has had to live with the consequences of our work under fire. When we at times, find his perspectives to be different, we have long since learned to allow that that may be because of the realities that we face out there. Mr. Del Trobak!

DOME-CANMAR'S OPERATIONAL ICE FORECASTING SYSTEM FOR THE BEAUFORT SEA

Dome-Canmar has been involved in ice forecasting, in one way or another, for ten years. Initially, all forecasting was done locally on each drillship. Forecasting was limited to the immediate future; the next few hours. Only empirical rules were followed; only localized ice movements were considered. This local work is still done, but it has been augmented by general forecasts issued from a central "Ice Information Office". While site-specific forecasts are issued by the Ice Information Office, their main product describes "net" movement over longer periods of time. They smooth out the short lived local movements, leaving those for the onboard observer/forecaster to describe in detail.

The Dome-Canmar Ice Information Office, as it operated in 1985, supplied information to two drilling operators, Gulf-BeauDril and Dome-Canmar, who operate the majority of offshore drilling platforms in the Canadian Beaufort Sea. An area of some 50,000 km^2 between latitudes 69°N and 71°N; from longitude 128°W to 142°W was covered.

In addition, they supported drilling operations to a somewhat lesser extent in the American Beaufort as far west as 152° W longitude.

Before declaring themselves to be in business, at least two things must be reasonably available to the forecasters in the Ice Information Office:

(a) Data describing present conditions in the forecast area,

(b) A set of rules, or guidelines describing how those known conditions can affect the development of the conditions they try to forecast.

As the whole procedure rests, at least initially, on the use of an environmental data base, a short discussion of the data and collection methods is warranted.

Probably the most important data collected are the radar images of the ice itself. (Figure 1) These images are collected on an "as required" basis, depending upon ice conditions. For the past two seasons, these data have been provided by a Synthetic Aperture Radar (SAR) equipped aircraft flown by Intera Technologies Ltd. Daily flights are the norm when ice poses a potential hazard at any drilling location. When ice movements are extreme, or a tricky drilling operation is undertaken, the flight frequency may be increased. As the Ice Information Office supported operations in both the Canadian and American Beaufort Sea, flights of both areas were often made on the same day.

The Dome-Canmar operation has used both Side Looking Airborne Radar (SLAR) and Synthetic Aperture Radar (SAR) in recent years. The SAR imagery now used has a resolution better than 8 m by 8 m, with a swath width of about 25 km; better than 8 m by 12 m, with a swath width of about 47 km. The fact that this radar is flown at an altitude of 30 to 33 thousand feet allows the data to be telemetered reliably at ranges of 140 nm. Thus, radar images can be received, processed, analyzed and the data put to use well before the aircraft has returned to base. A typical 4 line flight as shown in Figure 1 will last about six hours from take-off to landing. Data from the first line will be available for analysis or printing during the second hour of the flight.

Even the SAR system has some shortcomings. The absolute geographic locations of shown ice features can be uncertain due to accumulated drift in the Inertial Navigation System. This problem is usually mitigated by including fixed reference points like coastlines and offshore drilling rigs in the imagery. Once the first flight line has been fixed, subsequent lines are matched to the overlap of the previous one. This also corrects for stretch in the photographic negative. The corrections are made by physically cutting the negative in locations that cause the least distortion to the imagery, particularly, in areas near drilling locations. In most cases, the finished print will have a spatial accuracy of one to two nautical miles.

The mosaiced imagery is printed on a single piece of photographic paper, usually 30" by about 60", complete with coastal features, labelled drilling locations and, in some cases, bathymetry. An average of twenty-five to thirty copies are usually ready for distribution about six hours after completion of the flight.

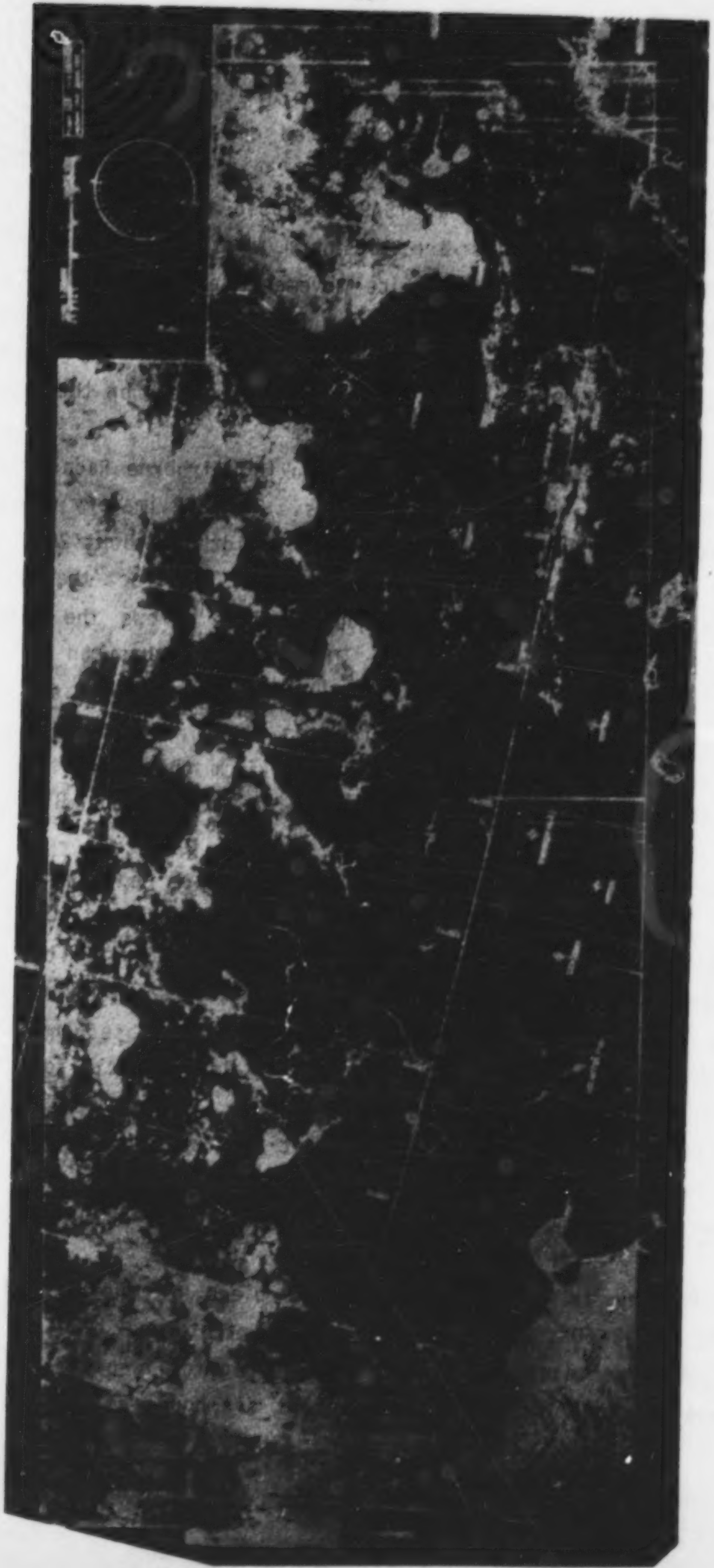

Figure 1.

The radar imagery is one of the main inputs to the ice forecasting system by locating all ice in the area, identifying floe size, ice type, amount of coverage etc. The imagery is analyzed and a full scale line drawing is made directly from the SAR mosaic. The analysis is computerized and reproduced at various scales and formats including a colour coded version. (Figures 2 and 3).

Other important data are the real-time environmental observations collected hourly at each drilling location. A full set of observations consists of aviation type meteorological reports (to SAWRS standards), a sea state report (based on MANMAR) and a section on ice (based on MANICE). This composite observing standard is the Offshore Weather Observing Station (or OWOS) standard.

With a dozen or more locations reporting observations to the shorebased Ice Information Office, a streamlined system for handling the mass of data had to be developed. Three years ago, Dome-Canmar began development of a vertically integrated computerized data handling system based on an existing IBM message switching system. The Environmental Data Acquisition and Management System (EDAMS) has reduced data handling time and increased data accuracy. It has greatly increased the accessibility of the data to users. Before this system was available, some observations were handled and transmitted up to eleven times. Some observations took up to a year to become available to interested users. An observation is now handled only once or twice and most observations are available to users immediately. The block diagram (Figure 4) outlines the system.

An observation is entered on a computer terminal. The terminal may be aboard a drilling vessel. Stations without terminals, pass the observations to the shore base by radio for entry there.

The following are immediate and automatic routines:

(a) The observation is transferred to the Calgary based mainframe where it is entered into archival file storage.

(b) The observation is reformatted into proper OWOS form and made available to the AES teletype polling circuit and the national network.

Figure 2

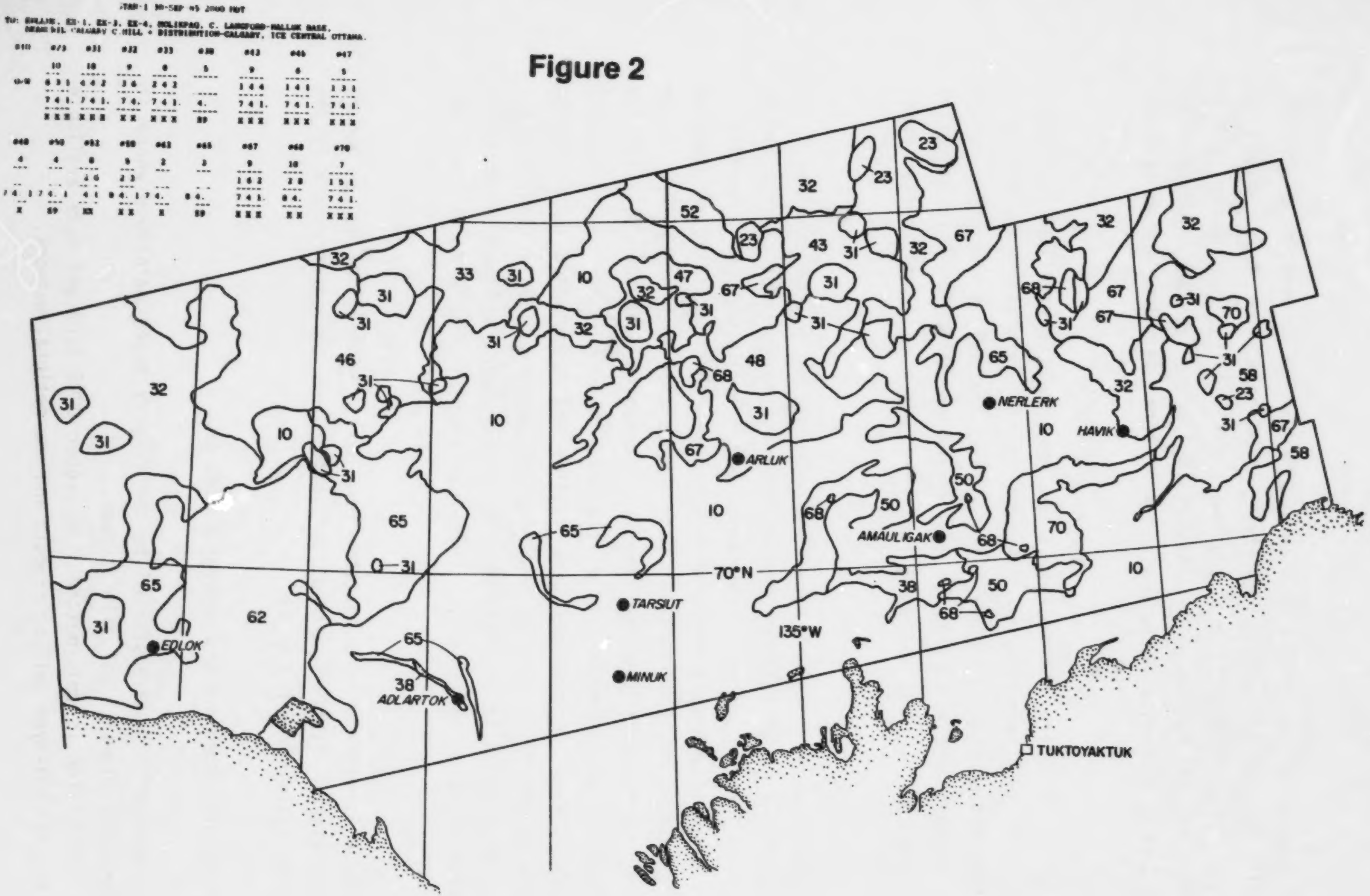
EDLOK
ADLARTOK
TARSIUT
MINUK
ARLUK
AMAULIGAK
NERLERK
HAVIK
TUKTOYAKTUK
70°N
135°W

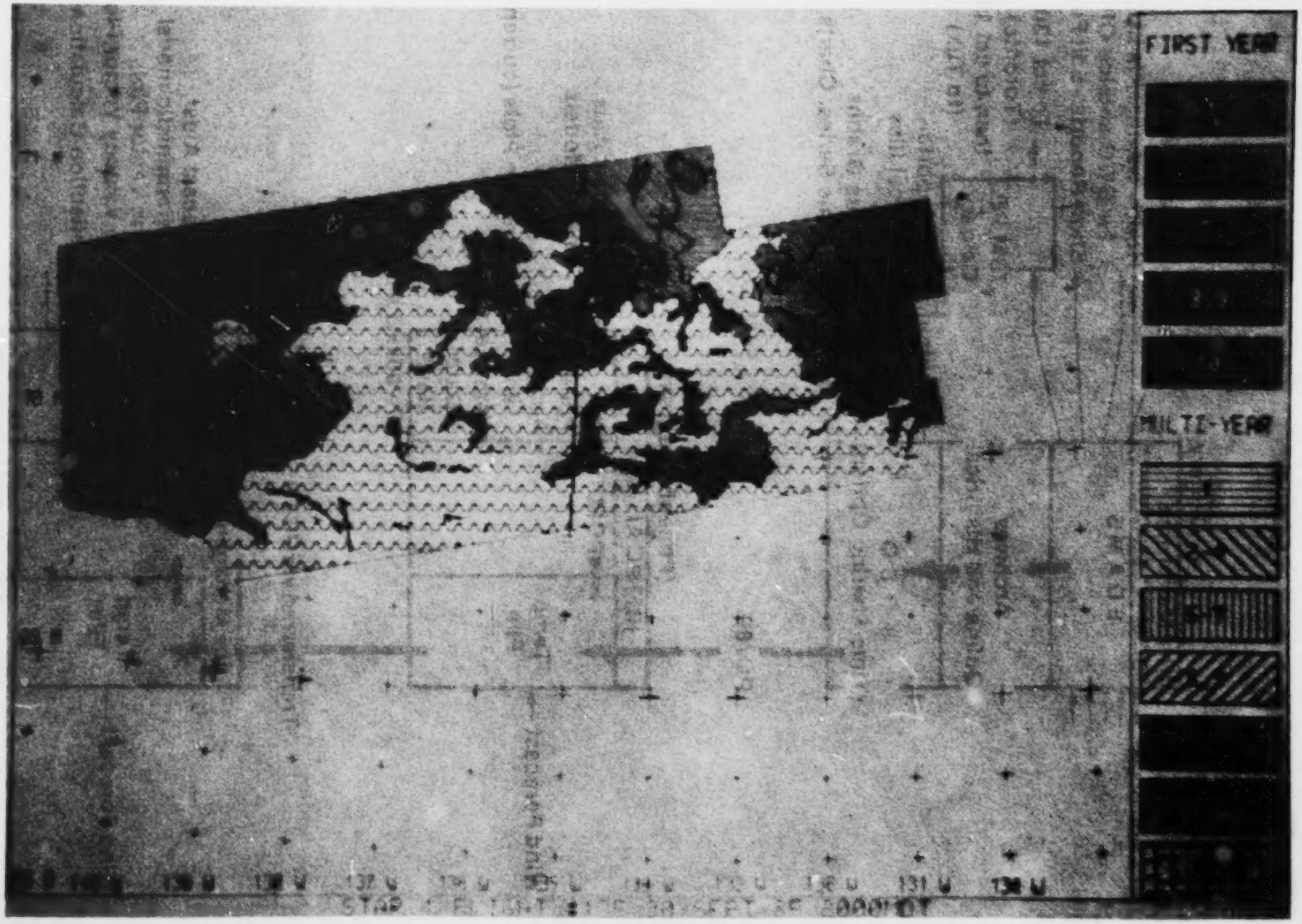

Figure 3.

Figure 4

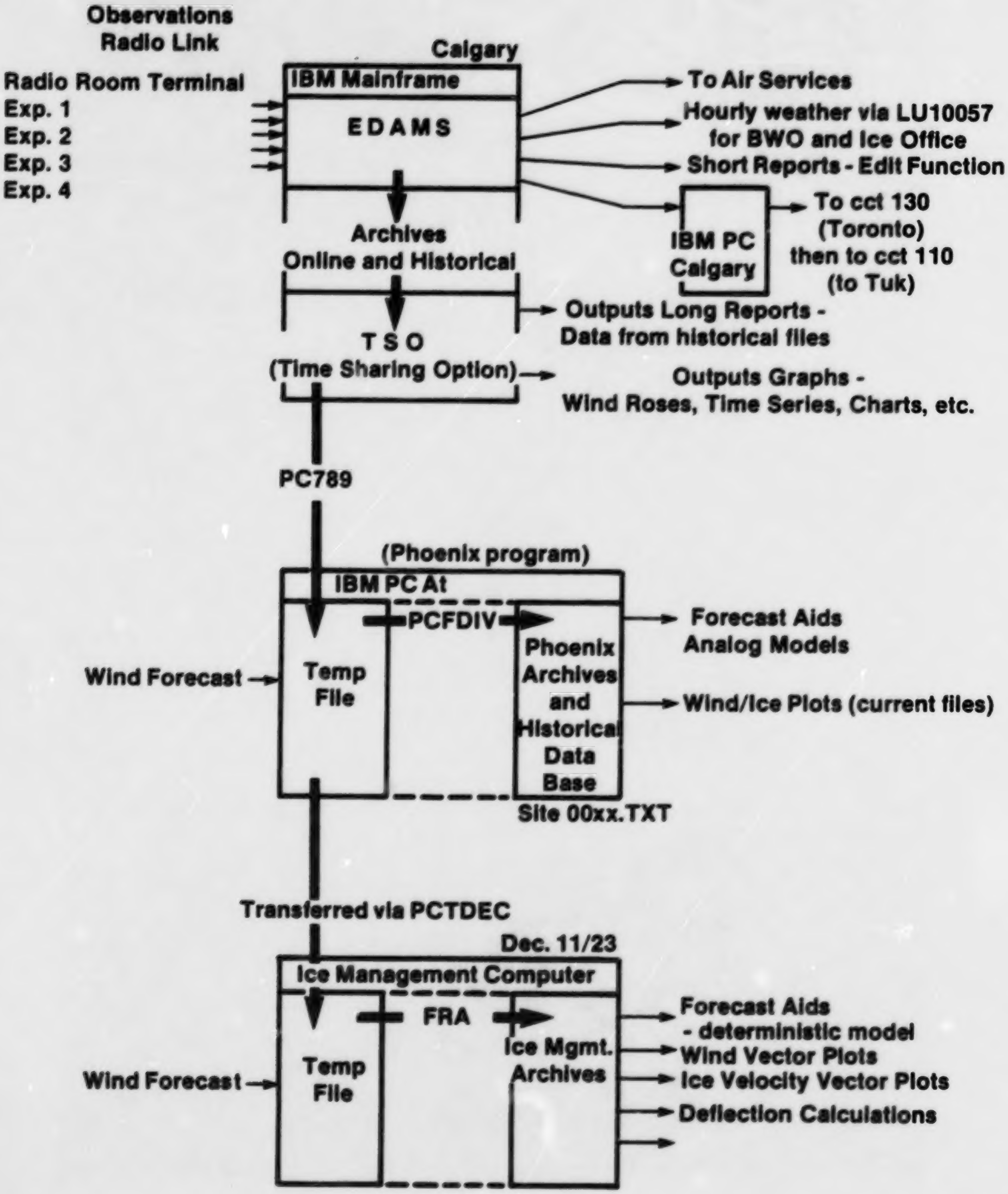
Observations
Radio Link
Radio Room Terminal
Exp. 1
Exp. 2
Exp. 3
Exp. 4
Calgary
IBM Mainframe
EDAMS
To Air Services
Hourly weather via LU10057
for BWO and Ice Office
Short Reports - Edit Function
IBM PC
Calgary
To cct 130
(Toronto)
then to cct 110
(to Tuk)
Archives
Online and Historical
Outputs Long Reports -
Data from historical files
T S O
(Time Sharing Option)
Outputs Graphs -
Wind Roses, Time Series, Charts, etc.
PC789
(Phoenix program)
IBM PC At
PCFDIV
Wind Forecast
Temp
File
Phoenix
Archives
and
Historical
Data
Base
Forecast Aids
Analog Models
Wind/Ice Plots (current files)
Site 00xx.TXT
Transferred via PCTDEC
Dec. 11/23
Ice Management Computer
FRA
Wind Forecast
Temp
File
Ice Mgmt.
Archives
Forecast Aids
- deterministic model
Wind Vector Plots
Ice Velocity Vector Plots
Deflection Calculations

(c) The observation is sent to the Beaufort Weather Office in Tuktoyaktuk where it is used by both the weather and the Ice Information Office forecasters.

(d) The observation is also reformatted into proper aviation form and made available to Air Services personnel in Tuktoyaktuk, Edmonton and Calgary where it is used in flight planning.

As the observations are entered on the data base immediately, they are available to help in answering questions about specific environmental phenomena or the relationship between events at different locations. Questions asked by the Ice Information Office are mostly about ice movements at each location over the past 12 or 24 hours. Other typical questions may be about "wave height", or "peak ice speed" during "last week's storm".

The Ice Information Office receives the weather observations in near real time. The reports are in a printed format. The data on the EDAMS system can be displayed and plotted for easier understanding. However, with data required for ice movement forecasts, such plots are usually done on either of the two ice forecasting computer systems. To facilitate this, the EDAMS system allows for data blocks to be transferred twice daily from the mainframe in Calgary to the local databases in each of the forecasting computers.

The source of the ice and oceanographic portion of the hourly observation is the ice observer at each of the reporting locations. Each drilling location has at least one trained observer reporting hourly for 12 hours a day. When ice conditions demand hourly reports 24 hours a day, a second observer is assigned to the location.

The Ice Information Office prefers 24 hourly observations per day as the continuity of data is very important when trying to establish trends. Unfortunately, the observing staff is often limited to one observer unless a significant ice hazard exists. The meteorological observations are always carried out on a 24 hour a day basis as required by aircraft operations.

The instruments used to measure environmental parameters are, mostly, standard off-the-shelf equipment. However, ocean currents have proven difficult to measure in real time with standard instruments in the presence of moving ice floes.

It has long been felt that a knowledge of real-time ocean currents could improve the ice motion forecasts and Dome-Canmar has expended considerable effort in developing an ice resistant currentmeter. In 1981, Dome-Canmar specified a currentmeter buoy which was later built for the company by Seakem Oceanography of Sydney, B.C. (Figure 5). The buoy is simple in concept. A cylindrical spar, 10 m in length, houses a Neil Brown ACM-2 currentmeter and a telemetry system. The whole unit is damped against heave and has a large righting movement. When an ice field passes the site, it is merely run over and submerged only to pop up again when the ice has gone. In many cases, this system has been submerged for hours or days at a time and survived.

The unit normally measures currents at the 5 m depth, just above the usual mixing layer in the Beaufort Sea. The telemetering system can also be used to transmit recordings from other instruments mounted lower down in the mooring. It has been used to telemeter tide gauge data.

The telemetry unit is an intelligent polling system. It will either transmit the vector averaged data at preset times or respond to requests from a master station. The transmitting range, unfortunately, is quite short as it is "line of sight". This limits the deployment area to within a few kilometres of the receiver which is normally on a drilling platform. A great deal of useful data have been collected by this system, some of which will be looked at shortly.

The last type of data used by the ice forecaster is the forecast wind velocity. This important information comes from the Beaufort Weather Office at Dome-Canmar's shore base which is staffed by Environment Canada personnel from the Arctic Weather Center in Edmonton. Forecasts are made twice a day with updates issued at six hour intervals; more often under special circumstances. Each forecast is for a 36 hour period with a further outlook. Forecasts are site-specific and cover individual drilling locations in different areas of the Beaufort Sea. During the 1985 season, the Beaufort

Figure 5

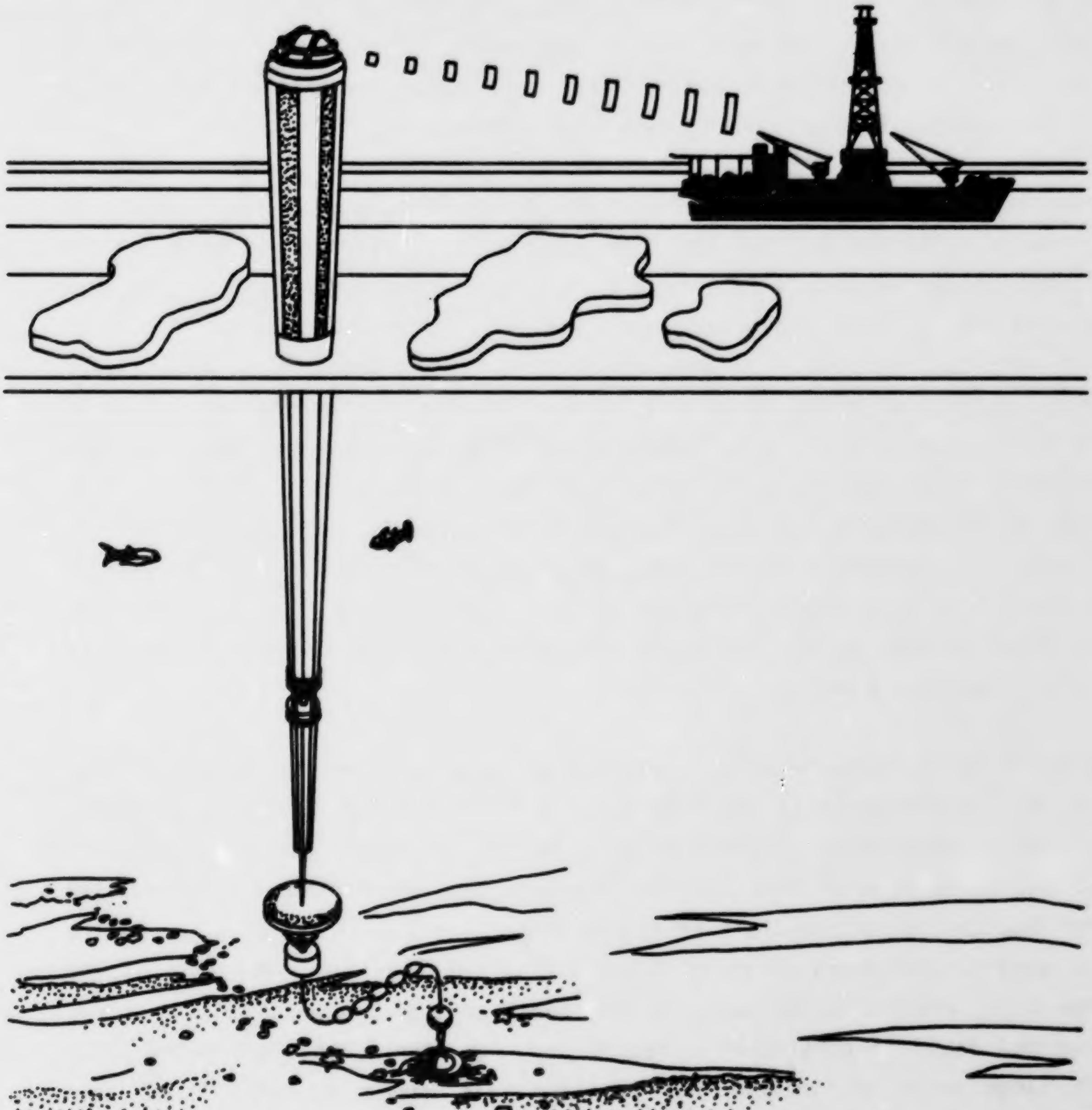

Weather Office also issued weather forecasts for areas in the American Beaufort Sea to support drilling operations there.

The wind forecasts are always important to the ice forecaster, but more so with some types of ice than others. It has been observed that sheets of ice common during the fall and winter are moved predominately by the wind. During spring break-up, when ice floes may have grown to a thickness of some 2 metres, winds still have much effect, but ocean currents play an increasing role. In late summer, with mostly first year ridge remnants or deep keeled old ice, winds play a decreasing role in ice forecasting.

Forecasting in the Beaufort Sea is difficult for the weather forecaster. It is doubly difficult for the ice forecaster who must depend, in part, on the accuracy of the weather forecast. The ice forecaster must also contend with variable short lived ocean currents, seasonal river outflows and ice types which vary in thickness from mere centimetres during freeze-up to multi-year ridges which are often 25 metres thick. If the ice forecaster is to be effective, he must learn the "rules" which affect ice movement under various conditions. He must know what ice type he is working with, and if it is likely to be affected mostly by the winds, or currents; or, perhaps, equally by both. He must take into account the ocean currents which are likely to be encountered at a specific location at that time of year. He may get some real-time current data, but most data available to him are historical in nature or must be deduced.

Figures 6 to 11 illustrate the complexities the ice forecasters face. They show the ice movements in the Beaufort Sea for a few days beginning September 22, 1985. Immediately preceeding this period, a strong sustained westerly wind had moved much of this ice into the area from the northwest. Indeed, the large floe on the extreme left of Figure 6 was located off the Alaskan coast 4 days earlier and moved about 80 miles during this period. Take note of the large floe, about 8 miles long, in the north central region. This floe was cored and found to consist of a second year ice matrix about one meter thick with large areas of thicker ice imbedded. It was code named "LULU" and remained in the area until the end of the season. Note the eddy of ice moving in a circular pattern north of Herschel Island.

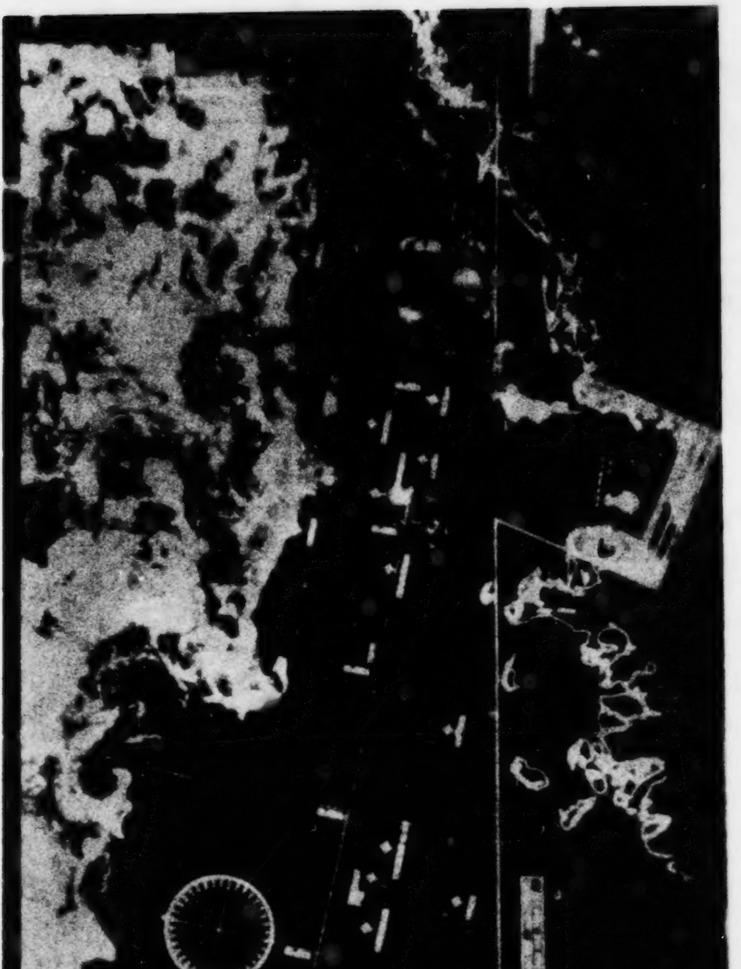

Figure 6.

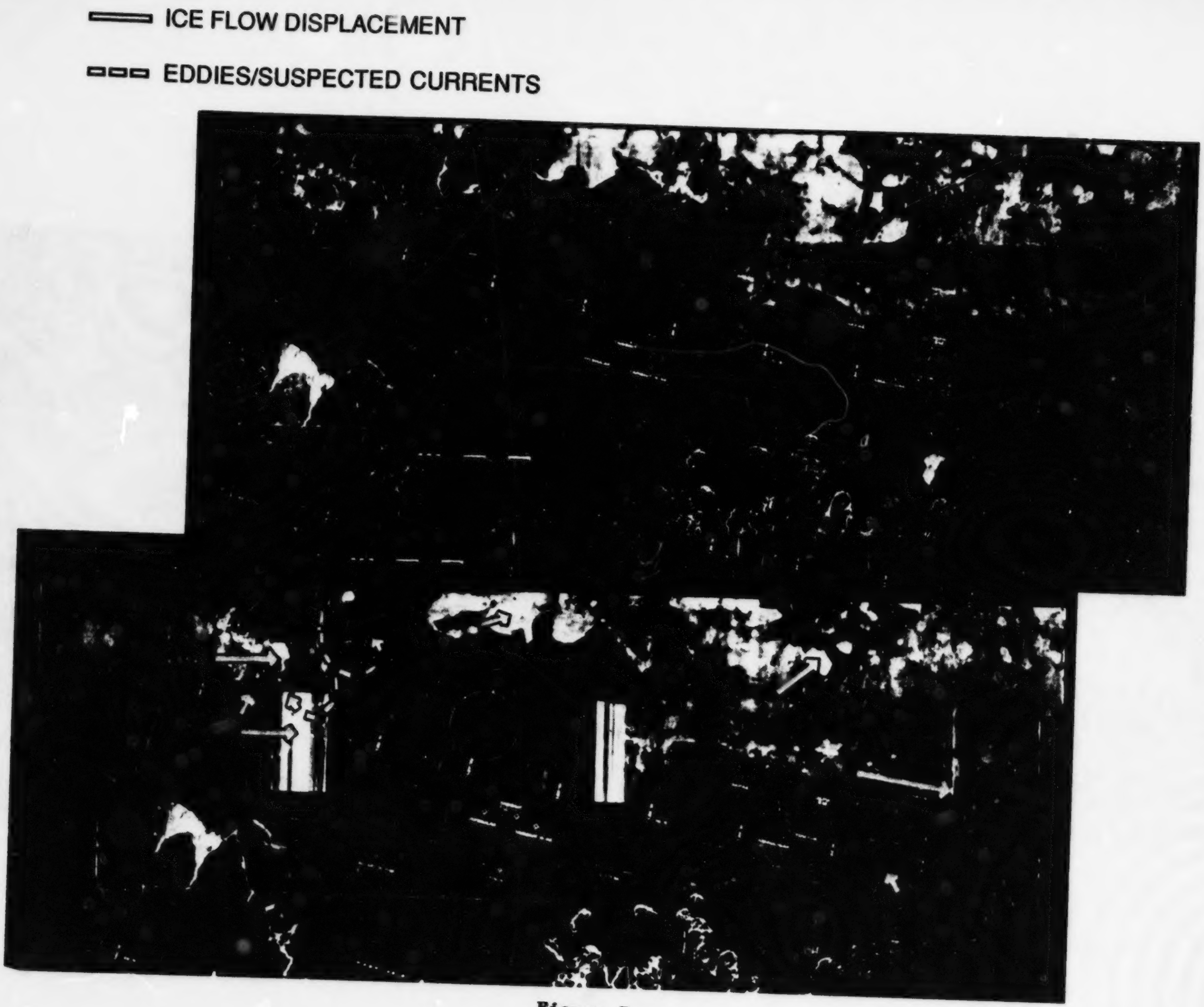

Figure 7.

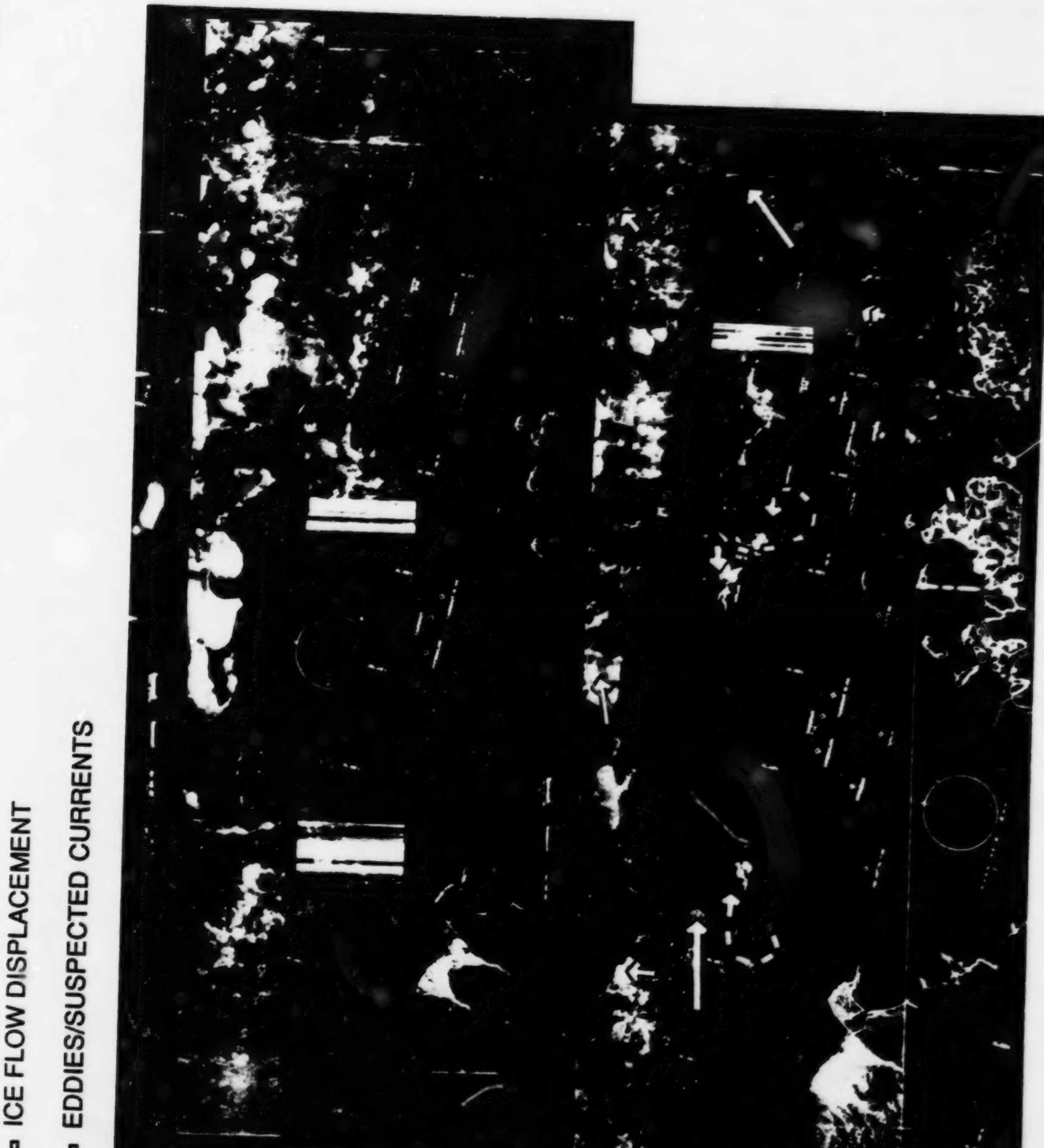

Figure 8.

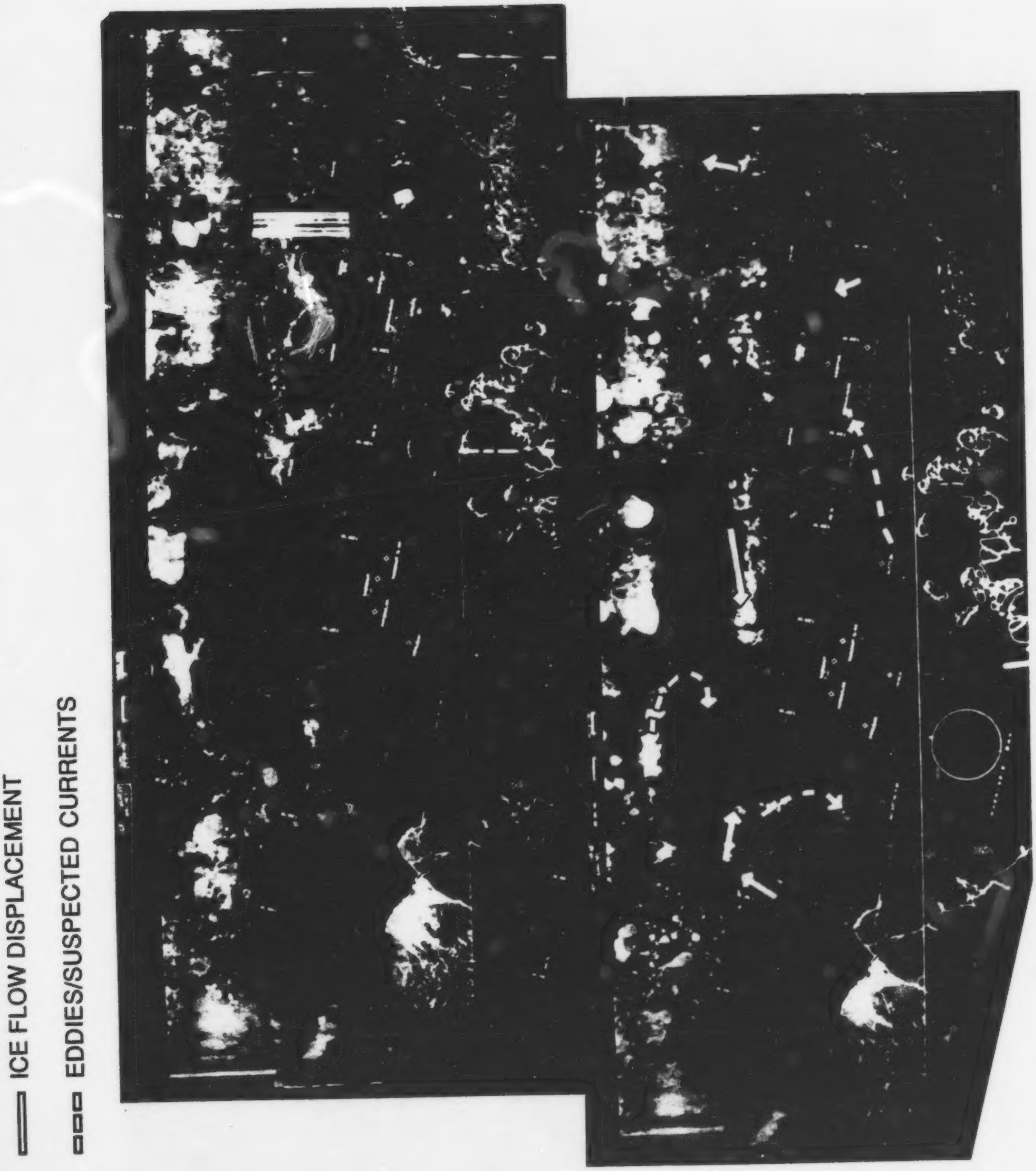

Figure 9.

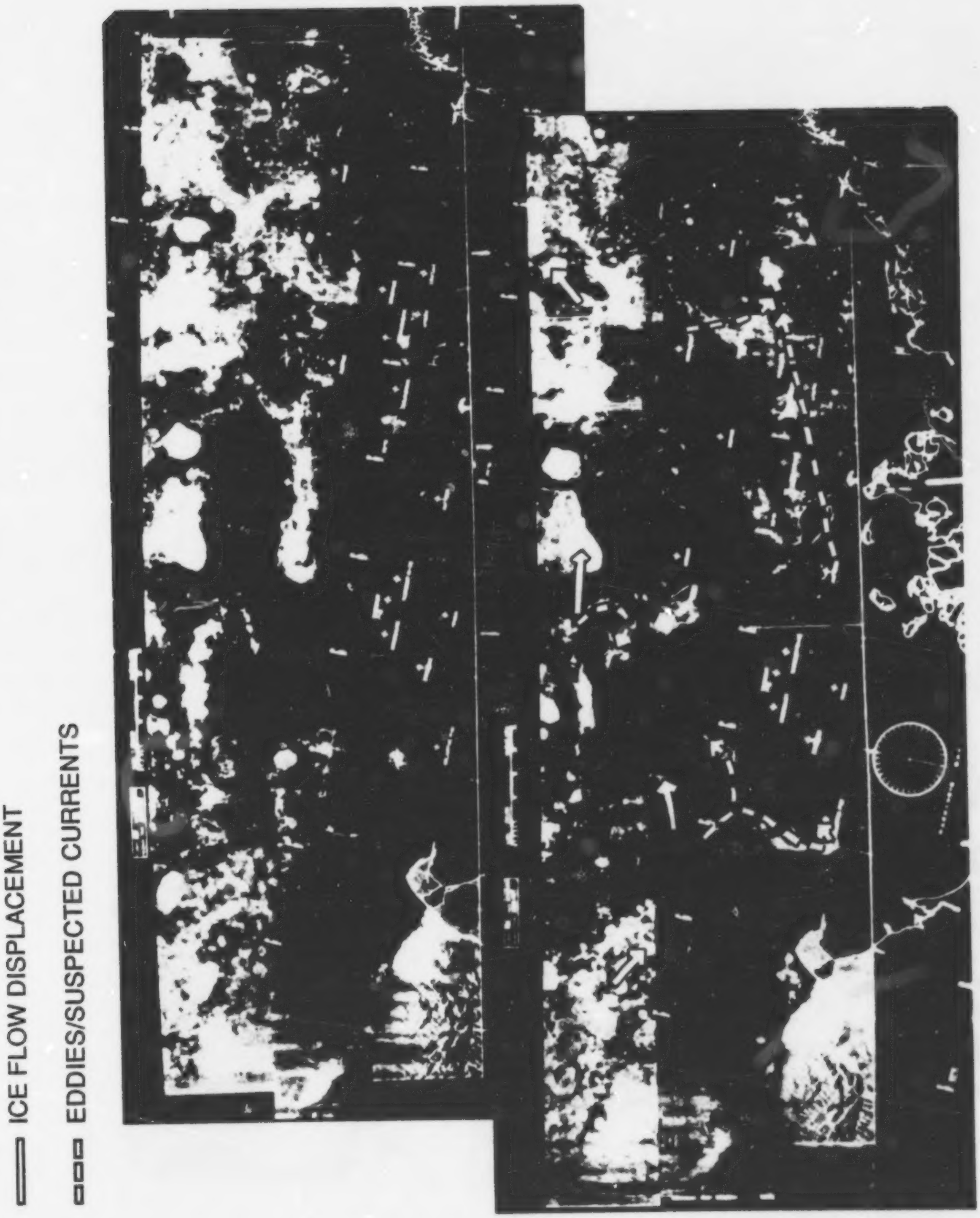

Figure 10.

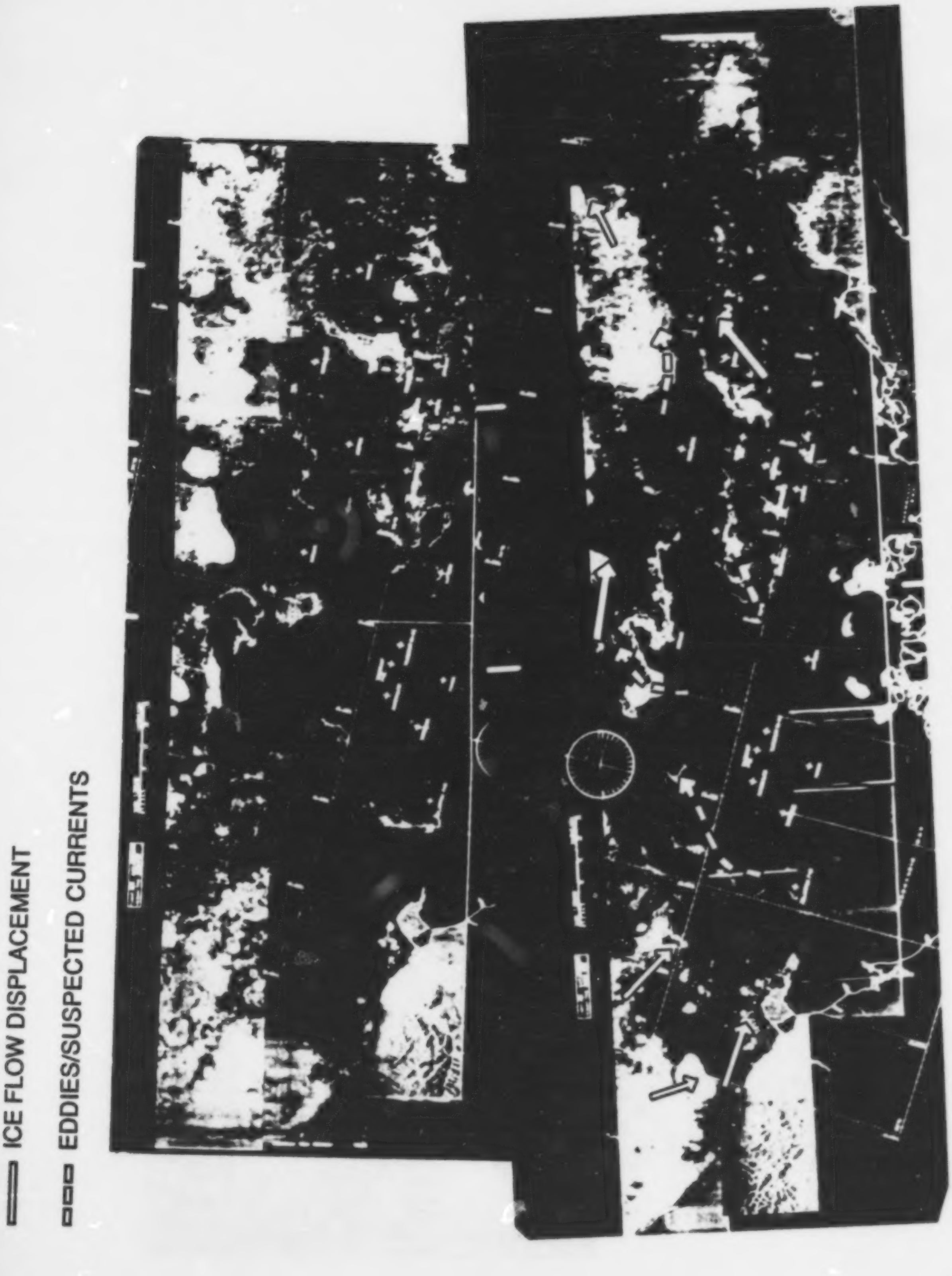

Figure 11.

Figure 7, September 23, shows "LULU" about 7 miles further east and rotated slightly counter-clockwise. The eddy had persisted, and a tongue running southward had developed. Ice movement had been generally to the eastward in the area north of Herschel Island, northeastward in the central (Akpak) area and eastward in the eastern (Havik) area. Winds during this period were fresh southwesterlies shifting to northerlies.

On September 24, Figure 8, we see that "Lulu" had continued her easterly movement another 7 or 8 miles. The ice north of Herschel Island also continued its easterly drift. The ice in the central area (Arluk) shows evidence of compacting, under the effects of the southwest winds. However in the eastern areas, (Havik) light northeasterly movement continued.

Figure 9, September 25, shows significant changes. The ice movement in the Herschel Island area continued eastward, but notice the tongue extending southward in the Adlartok area. Another tongue had developed westward across Arluk. Lulu, in the meantime, continued drifting eastward. While no measurements were made at the time, discrepancies between wind directions and ice drifts suggest a current running northeastward along Richards Island, westward across Arluk and southward over Adlartok. Winds during this period were 10 knots, backing from north to south to east and then back to north again.

September 26, Figure 10, shows a continuation of the movements begun on the 25th.

On September 27th, Figure 11, winds had shifted back to the south and increased to 20-25 knots. The ice in the western areas continued drifting eastward with Lulu moving 10 to 12 miles northeastward. The tongue which had come west over Arluk has formed an eddy and generally moved northward. The southward reaching tongue at Adlartok had dissipated and also moved northward. The characteristic tongues and eddies show that the ice in both these areas was largely current driven during the preceeding few days. The same ice became largely wind driven when wind velocities increased slightly. Lulu's course was deflected a bit to the north by the southerly winds. (Six weeks later, it was in the Amauligak area and became a potential hazard for the rig at that location.)

It is by analysis like that described briefly above that we can begin to learn the rules necessary to attempt to forecast.

At first glance, it would seem a simple matter to define a coupling algorithm by correlating wind velocity, ice type, ice movement and, if known, current velocity. Not so; when a correlation of data is attempted, the results often leave more questions than answers. For example, Figure 12 illustrates polar plots covering a 48 hour period in the central Beaufort Sea (Siuluk) in August of 1983. This plot shows wind velocity, ice velocity and 5 m currents at two locations 5 nm apart, but both within 5 nm of the drillship. Notice that the two 5 m currents bear only a slight resemblance to each other while the ice movement ties in nicely with one of them. The two meters were clearly in two separate current regimes for at least half of the 48 hour period. It appears that the meters became enveloped in the same current regime near the end of this period. This is borne out in Figure 13 which represents the next 30 hours at the same site. Note how nicely ice drift, 5 m currents and wind direction are related in this case.

Figure 14 illustrates a 34 hour period in 1984, at Arluk in the central Beaufort Sea. Here we see wind and ice velocities, along with 5 meter currents and 25 meter currents. The ice movement here was likely wind driven (fresh winds) as neither currentmeter describes the ice motion.

Figure 15 shows a 57 hour period at Orvilruk, in the western Beaufort Sea in 1982. This illustrates again quite clearly that the 5 m currentmeters were in different regimes.

Another interesting example is seen in Figure 16 where both the 5 m and 25 m currents ran opposite to the wind for 81 hours. (It was calm during the proceeding 24 hours.) It should be noted here that the 25 metre currents were generally similar to this example, easterly, for much of the summer in 1983. In fact, a large field of old, deep keeled ice moved east all the way from Prudhoe Bay in the Alaskan Beaufort Sea to the Canadian drilling area.

The four examples just discussed highlight the difficulties the ice forecasters in the Beaufort Sea face. To overcome them, they need to have:

Figure 12

Siuluk

48 hours; Aug. 3 - Aug. 5 1983

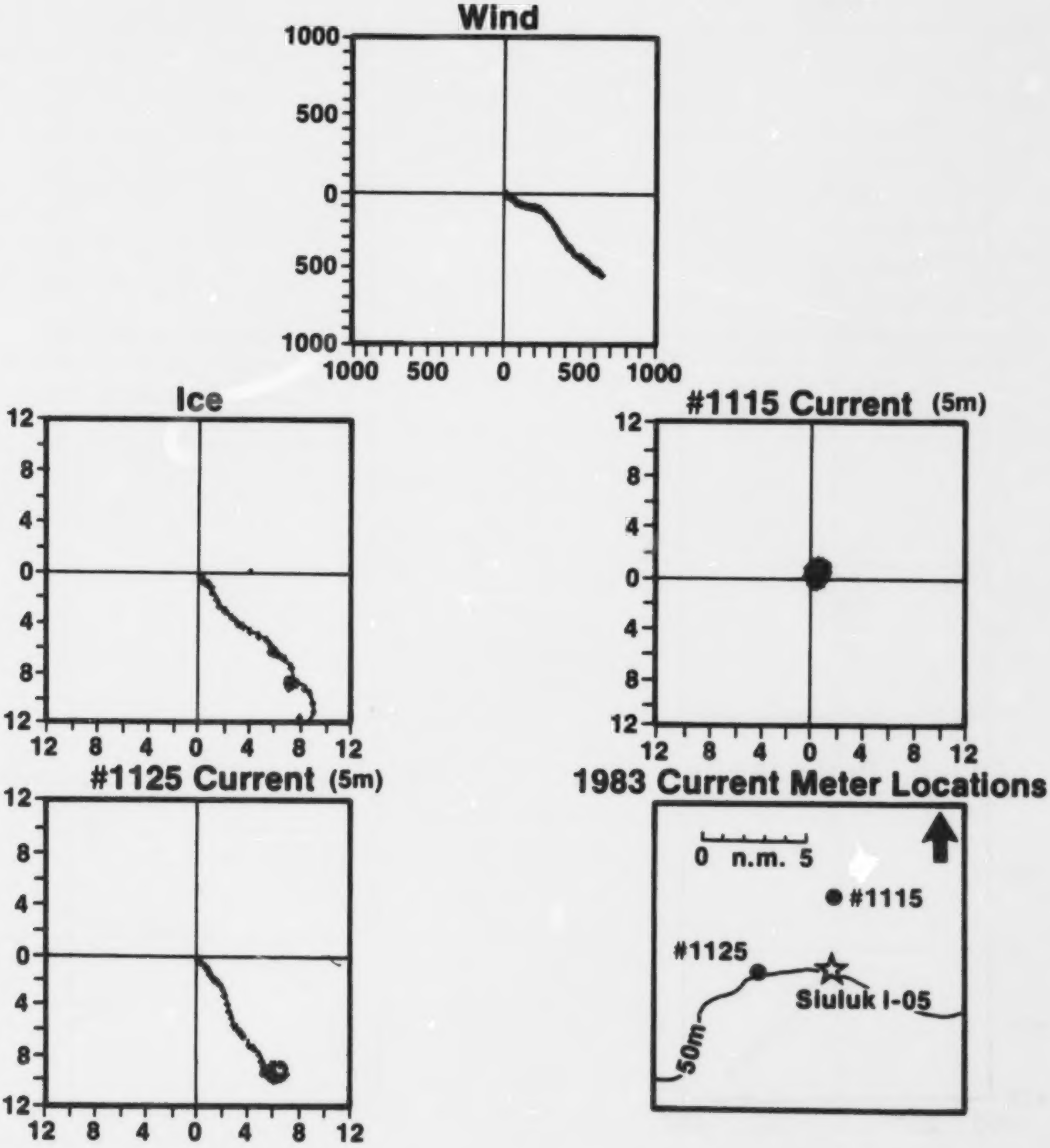

All Scales in Nautical Miles

Figure 13

Siuluk

30 hours; Aug. 4 - Aug. 5 1983

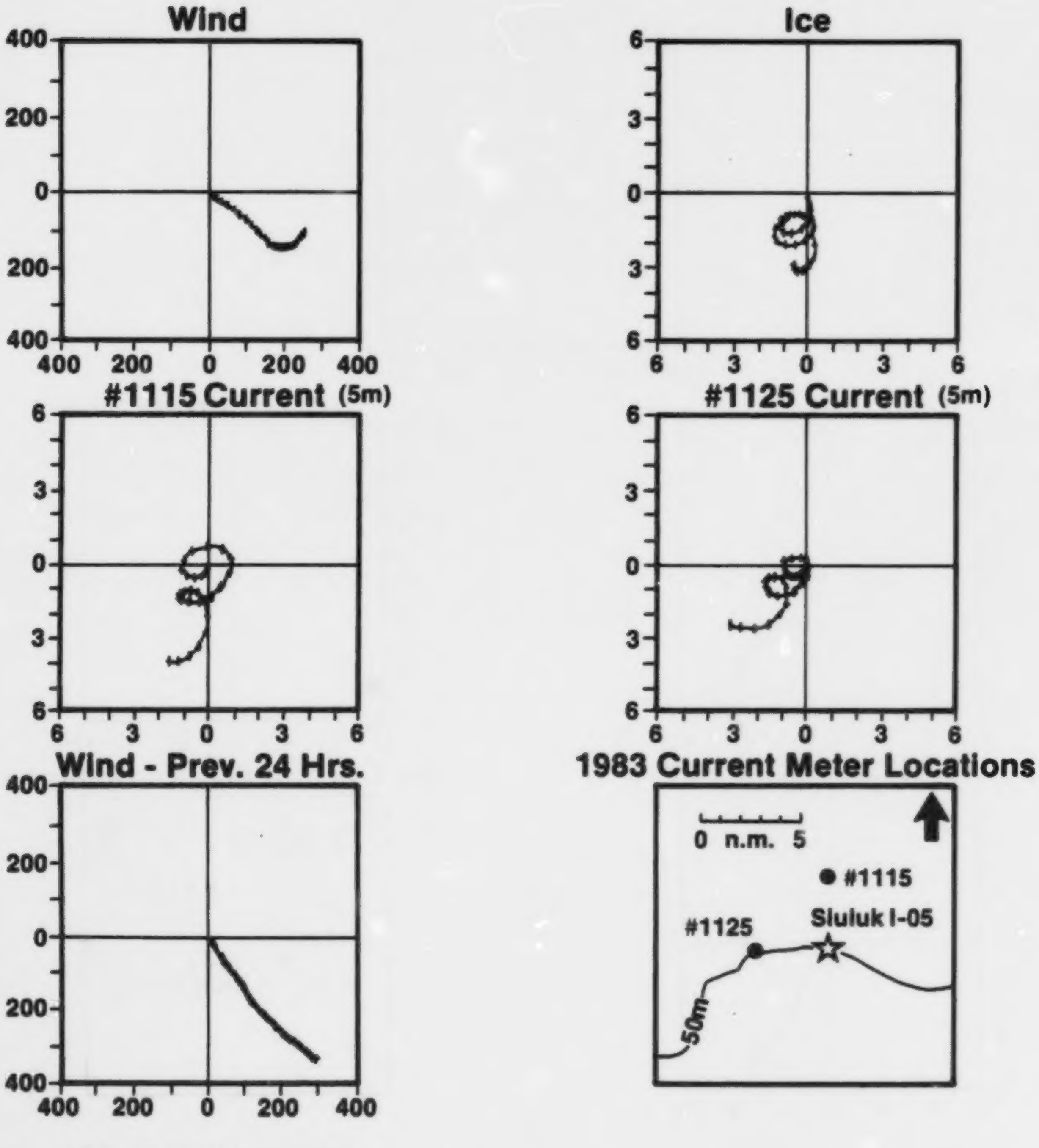

All Scales in Nautical Miles

Figure 14

Arluk

34 hours; Aug. 9 - Aug. 11 1984

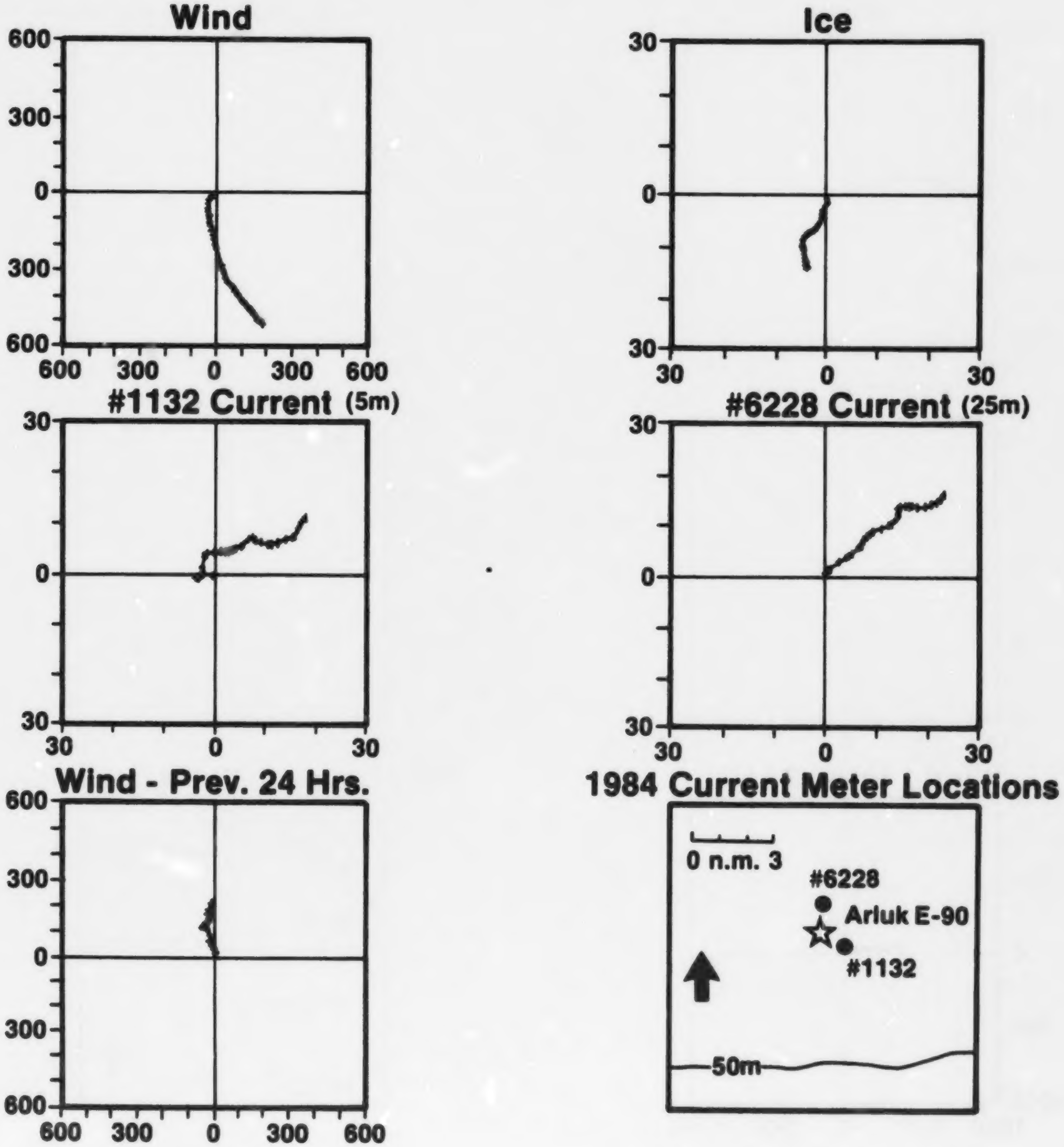

All Scales in Nautical Miles

Figure 15

Orvilruk

57 hours; Sept. 6 - Sept. 8 1982

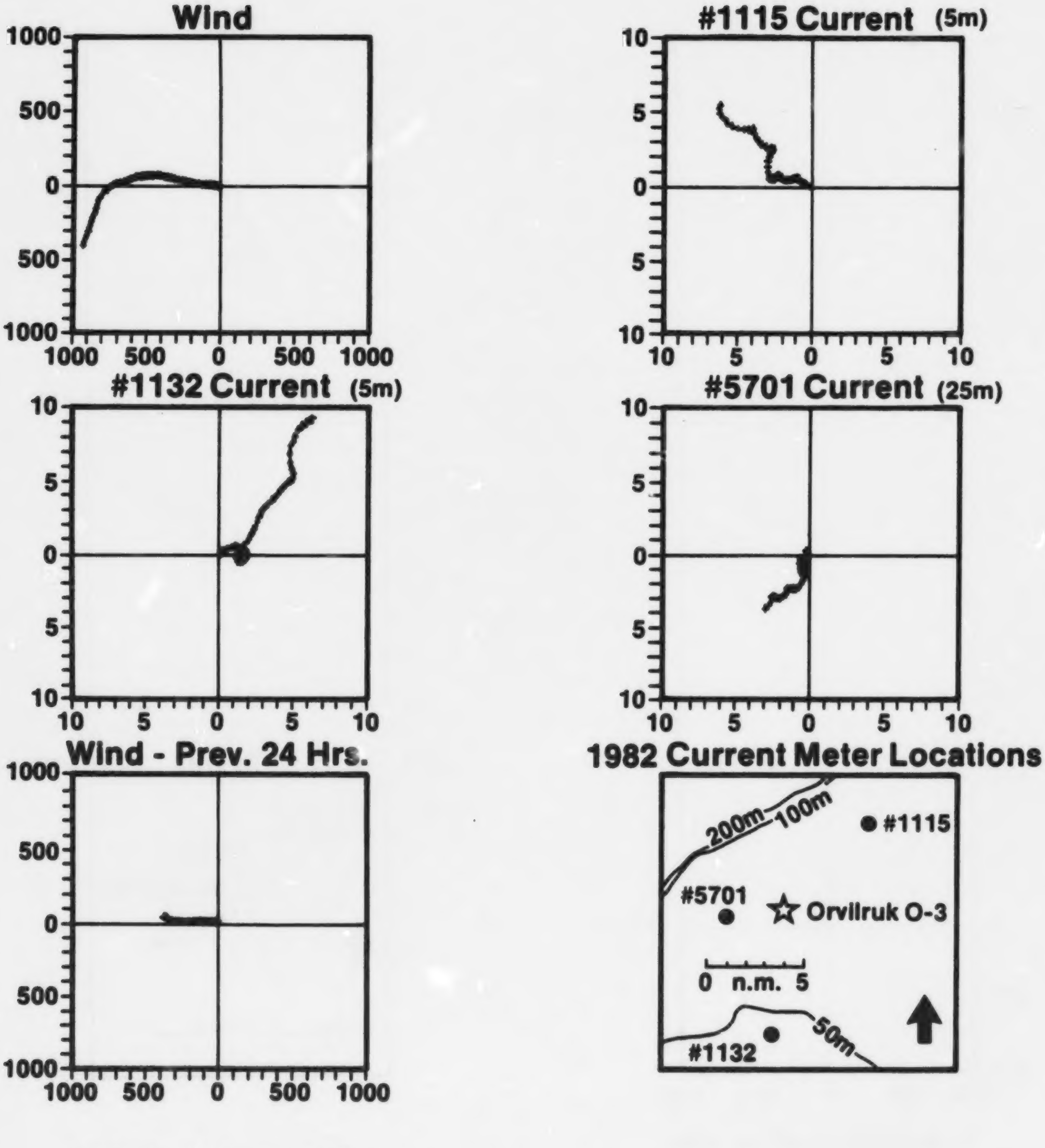

All Scales in Nautical Miles

Figure 16

Arluk

81 hours; Aug. 20 - Aug. 23 1983

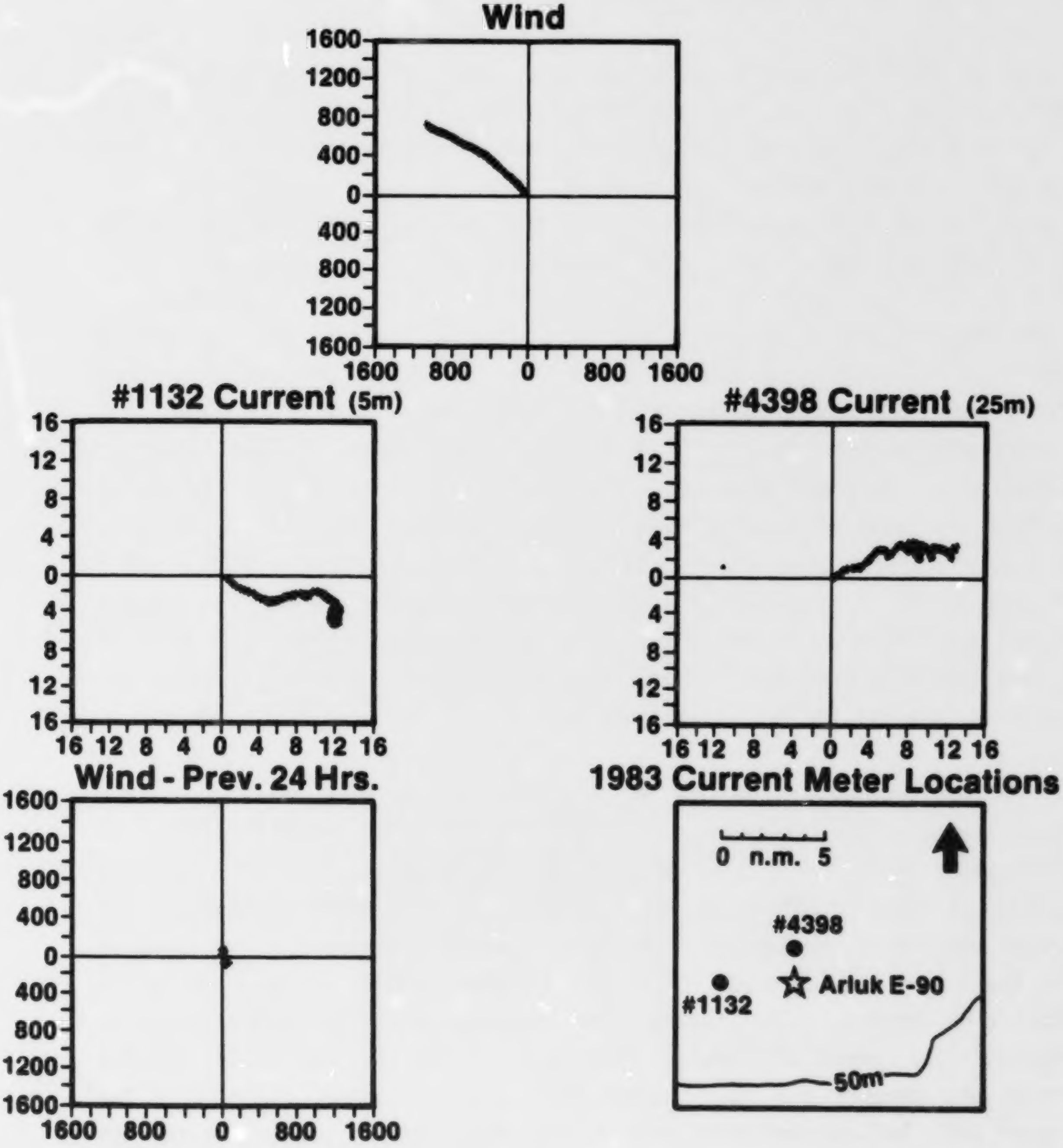

All Scales in Nautical Miles

(a) some idea of the ice thickness to determine if it will be influenced by wind, 5 m currents, 25 m currents, or by what combination thereof;

(b) an accurate wind forecast;

(c) some idea of ocean current velocities.

It can be seen from the previous examples that currents can vary greatly within 5 nm. As the cost of deploying currentmeters covering the area on a 5 nm grid pattern would be astronomical, the forecaster must make do with "deduced" current velocity. At present, this is best done by providing accurate ice velocity measurements at as many locations as possible. In the end, it may prove impracticable to do anything else.

In the Beaufort Sea, the data are used in two separate ice forecasting systems. The first system consists of a group of mathematical models of varying complexity, ranging from a simple wind driven model to one which uses all available measured data, ice drift, ice draft, ocean current velocity, observed wind, forecast wind etc. These models run on a Digital PDP series computer. For several reasons, most of them logistical, the preference is to use a deterministic model which deduces ocean currents from ice drift, rather than one which uses measured ocean current. Ocean currents, as stated earlier, are expensive to measure in real time and most reporting stations do not have the data available. Thus, the real-time data is mostly used by the observer on the rig for his "local" predictions.

A second micro-computer, an IBM PC AT, runs an analogue model. In this system, measured ice movement and the recorded wind velocities for the corresponding period have been entered into a database. The database now consists of about 26,000 hours of data from about 2 dozen locations. The operator will give the computer the latest weather forecast. The computer will then sort the database to locate 24 hour blocks of data where the historically observed wind matches the forecast wind to within specific criteria. The group of samples thus selected are further sorted by the operator who chooses the sample which best matches "todays forecast". The operator will include variables such as ice type, time of year, wind for the period prior to the 24 hour "forecast" block and geographic location when selecting the best example.

The historical data set in the analogue model is more complete than the "real-time" data set used in the deterministic model, but it does suffer from limitations. Quite often, no example can be found which matches the forecast winds within the search criteria. Also, it only has Canadian Beaufort Sea data. Its usefulness at locations in a new area like the American Beaufort Sea can only be ascertained by determining the possible similarities between a new location and any of the data sources. The variances may prove too great for the model to yield anything useful. This can only become known by experience. The analogue computer system, called "Phoenix", was assembled by Horizon Offshore of Dartmouth for Dome-Canmar and Gulf-BeauDril jointly. The original database was supplied by Dome-Canmar, using data going as far back as 1978. Data supplied by Gulf-BeauDril has now been incorporated.

Despite the fact that the ice forecaster uses two independent computer systems, the most important factor in producing a forecast is the experience and knowledge of the forecaster himself. The computer systems are tools, good tools, but they cannot stand alone. Perhaps in years to come, if a Government were to spend millions of dollars annually to measure ocean currents and expand the historical data base to millions of hours of data instead of the 20,000 or so hours Dome-Canmar has provided, a computer modelling system could become completely accurate. Until then, the forecaster's experience remains crucially important. Dome-Canmar's Ice Information Office is staffed by personnel from Horizon Offshore Services Ltd., who have nearly a decade of experience in the Canadian Beaufort.

Here are a few examples of how the forecasting system worked in 1985. Figure 17 covers a 24 hour period beginning the morning of September 01. The forecast was for the Nerlerk site in the north central Beaufort. The first polar plot is that of the wind forecast.

The weather office had forecast an east wind (blowing toward the west) of 20-25 kts decreasing to 15-20 kts. This is shown as a vector 440 nm long. The second plot is the output of the analogue Phoenix model. It suggests a 24 hour northwesterly ice movement of about 6 1/2 nm. The third plot shows the output of the deterministic model. It also shows a northwesterly movement of about 7 nm. The forecaster had examined both of these plots and had basically agreed with them; he does not always do so. He issued a forecast, plot 4,

Figure 17

Nerlerk

Sept. 1, 1985

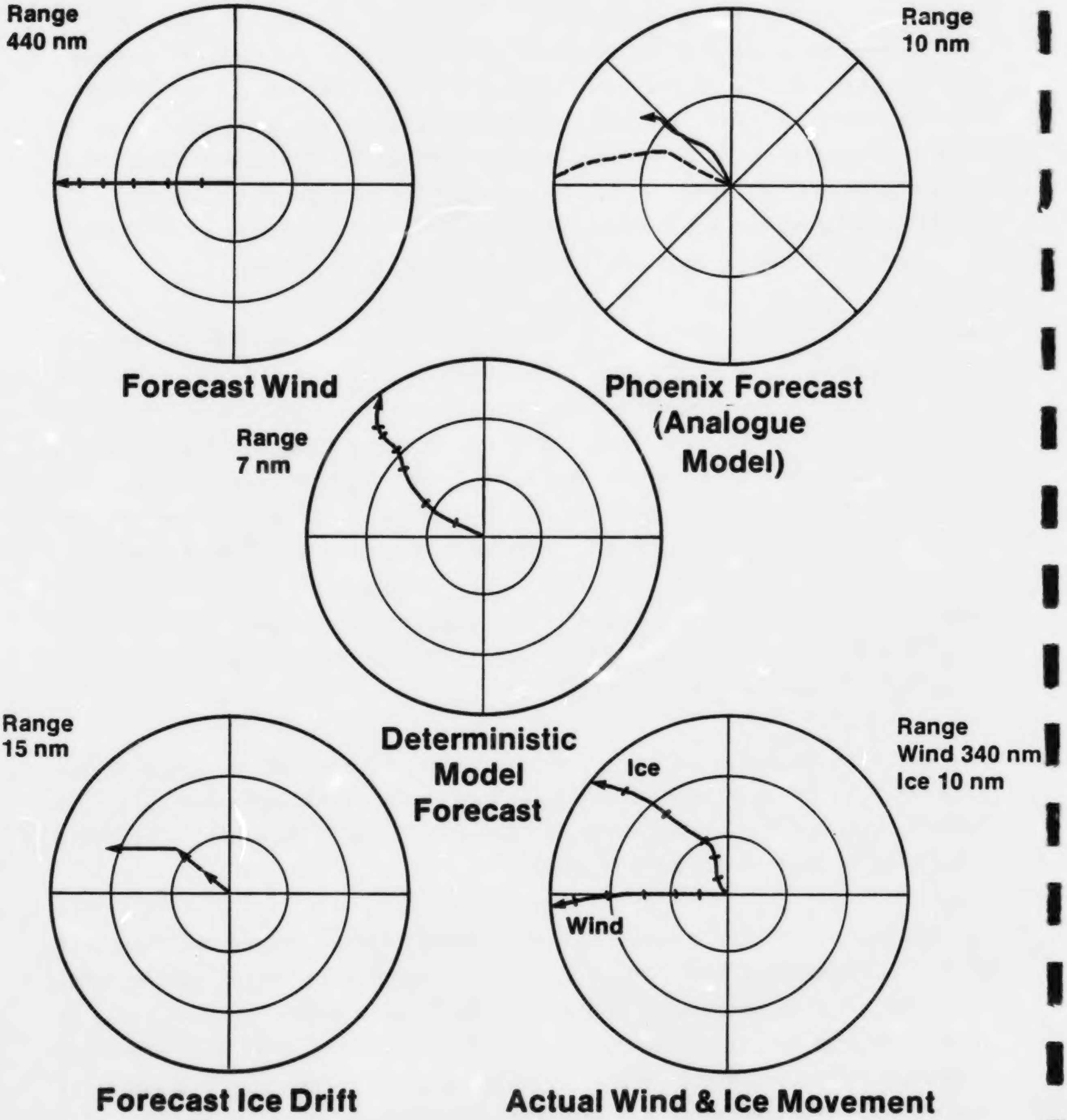

Forecast Wind

Phoenix Forecast (Analogue Model)

Deterministic Model Forecast

Forecast Ice Drift

Actual Wind & Ice Movement

which predicted a northwesterly movement of about 6 nm with an outlook for westerly drift for the second 24 hour period. When one examines what actually did happen, plot 5, it is seen that the ice movement for the 24 hour forecast period was indeed to the northwest, but 10 nm instead of 6 1/2 or 7. The ice forecaster, as well as both models, under-forecast by about 30%. In looking for a reason, it would be easy to suspect the wind forecast. However, as the wind vector shows, the weather forecast was quite accurate in direction and over-forecast the velocity by about 20%. In this case, the error in the weather forecast cannot be blamed. If anything, it reduced the error in the ice forecast. It is likely that the ice type changed slightly in the 24 hour period, that a change occurred in the ocean current, or, that the ice forecasting systems all erred by the same amount.

The next forecast example, Figure 18, is for the 23 August 85, again for Nerlerk. The first plot shows the output of the deterministic model. It forecast a west-northwesterly movement of about 6 nm. There was not a suitable sample to be found in the Phoenix database. The forecaster agreed with the computer. The actual movement, shown in plot 3, was indeed about 6 nm, but toward the north-northwest, an error of perhaps 30 degrees.

The third forecasting example, Figure 19, covers the difficult period illustrated earlier when the large circular current regime in the central Beaufort Sea resulted in ice movements of vastly different directions in areas not too widely separated.

Plots 1 and 2 illustrate the wind forecast for Arluk in the central Beaufort Sea and for Havik about 40 nm to the east. They are quite similar. There is only a slight difference in the timing of a wind shift. Plots 3 and 4 show the deterministic model outputs for the two sites. The forecast for Arluk was for a 10 nm west-northwesterly net movement while the forecast for Havik, only 40 nm away, was for over 20 nm east-northeasterly movement; almost exactly the opposite. Again, the analogue models had no data to fit this case. Plots 5 and 6 show the forecaster's interpretation. In plot 5, his forecast was west-southwesterly movement of 14 nm for Arluk. He changed the direction slightly, downplaying the inertial looping shown by the computer, and increased the distance by about 20%. Basically, he agreed with the trend. However, for the Havik site, plot 6, the forecaster reduced the distance

Figure 18

Nerlerk

Aug. 23, 1985

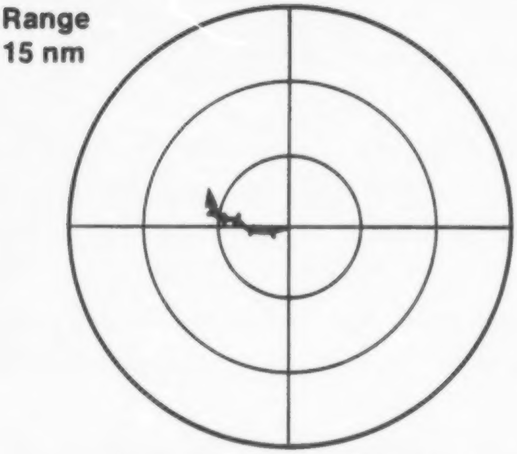

Deterministic Model Forecast

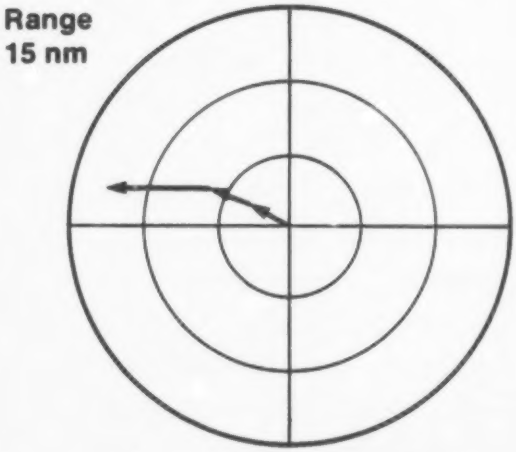

Forecast Ice Drift

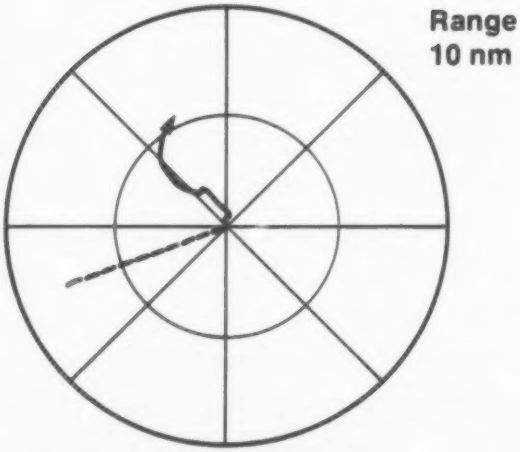

Actual Ice Movement

Figure 19

Havik - Arluk

Sept. 27, 1985

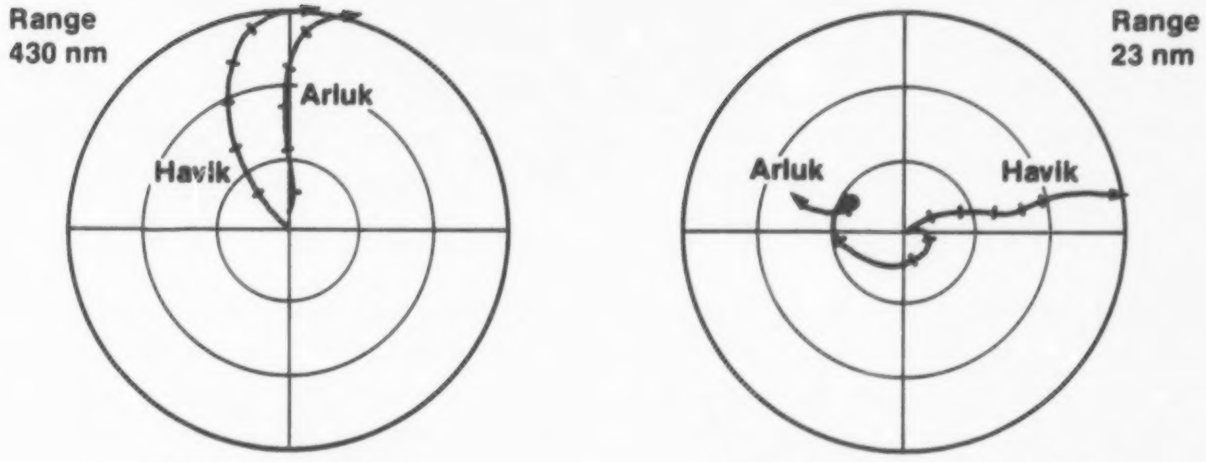

Forecast Wind

Deterministic Model Forecast

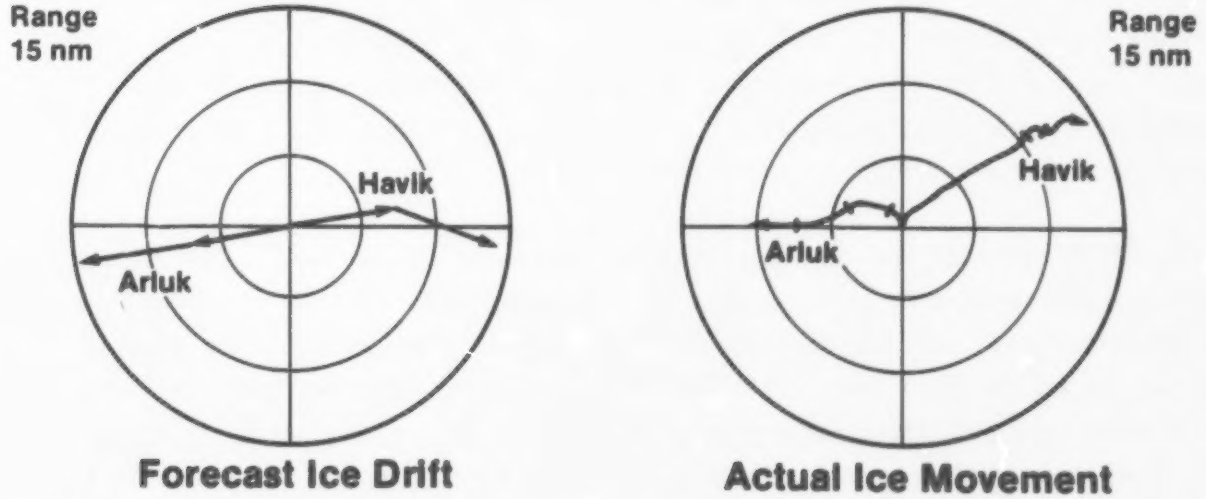

Forecast Ice Drift

Actual Ice Movement

predicted by the computer by about 30% and modified the angle slightly. Plots 7 and 8 show the actual movement recorded after the fact. At Arluk, a westerly movement of 10 nm was experienced. The computer in this case was correct in distance and only slightly off in direction. The forecaster was not quite so close having over-forecast the distance by about 20%. At Havik, a 14 nm eastnortheasterly movement was experienced. Here, the forecaster was correct in distance and off by about 45° in direction; much better than the computer. This period was, by the way, a most difficult one.

In this discussion of forecast accuracy, note the use of phrases like "over-forecast 20%" and "under forecast 30%", or an "error in forecast drift angle of 30 degrees" etc. instead of the more conventional phrases like "skill" and "persistence" to describe forecasting accuracy. There was a need for comparing the accuracy of the ice forecast to that of the wind forecast for a "cause and effect" relationship. An objective method of grading each forecast for accuracy was also required.

It became obvious that a non-standard, non-statistical type of forecast verification had to be found; something that could be used daily or weekly during the drilling season to determine whether or not any given forecast was successful and, if not, why not. A standard statistical analysis for "persistence" and "skill" did not help on a forecast-by-forecast basis. As the work on a daily basis was with vectors and as the existing computer programmes already had vector subroutines, it seemed easiest to use what was already available. Furthermore, when describing a specific forecast, all the possible types of errors, that is, errors in speed, errors in direction, or errors in the timing of a change in either of the above, can be readily discerned by examining the vectors. By linking the vectors into a polar plot, the accuracy of a forecast is immediately evident.

Figure 20 illustrates how this verification technique can be used. One of the vectors represents the ice forecast for September 22, 1985 while the other illustrates the actual ice movement in that same 48 hour period. The vectors are tested at the 12th hour, 24th hour and 48th hour. The two tests involved are simplistic, but effective. The first test compares the actual distance ice floes have moved to the distance the they were forecast to move. This test is for drift speed alone. The second test examines the vector between

Figure 20

Nerlerk

Sept. 22, 1985

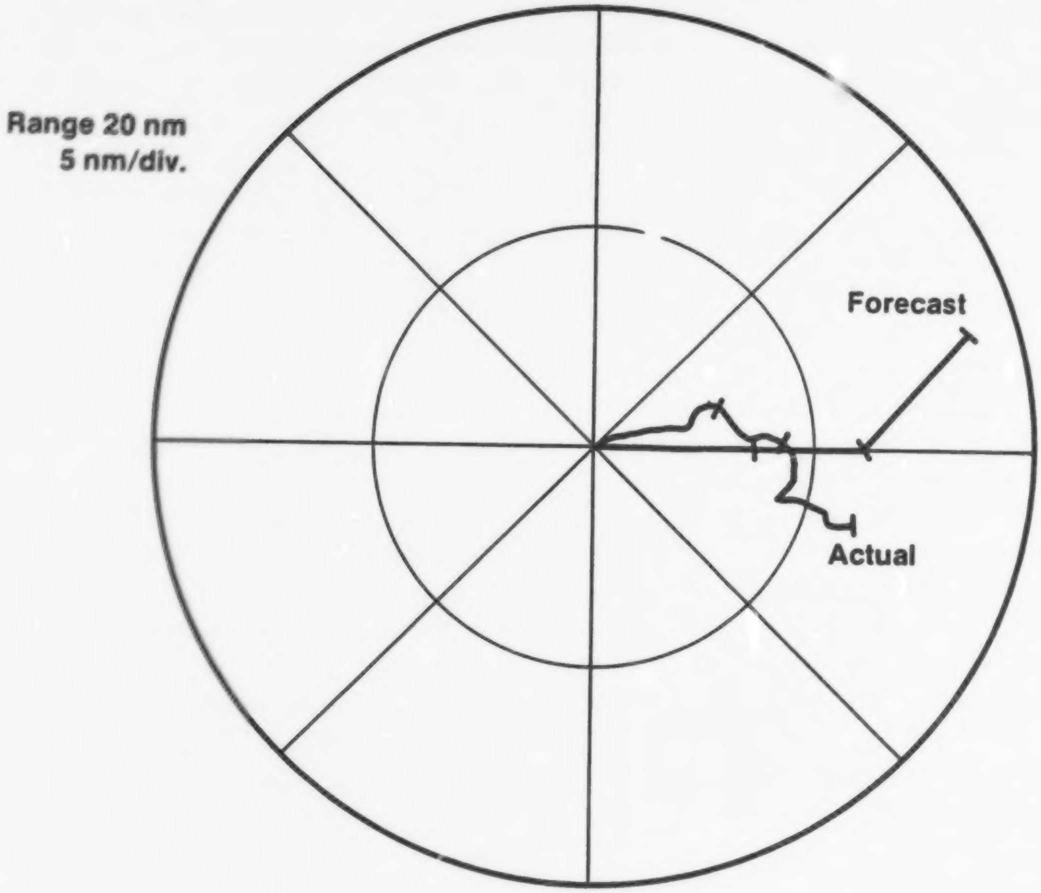

Phoenix Forecast
(Analogue Model)

the actual position of an ice floe and its forecast position. This vector represents errors in direction and timing as well as in speed. The two tests were required to detect "special cases" like ice floes ending up in the predicted locations, but having travelled the wrong path in arriving there. Seven levels of accuracy were arbitrarily chosen to describe the forecast results. These levels were not based on any magic mathematical formulae. They were based on actual observations. A level 0 represents a perfect forecast, a level 4 represents a forecast which is useful, or "better than no forecast at all" and a level 6 represents a forecast which is not only bad, but misleading in that it will cause the observer to be complacent rather than watchful for hazards. A set of wind forecasts were subjected to the same tests to relate the effect of wind forecast accuracy on individual ice forecasts.

In the above example, the scores of 1, 1 and 4 are for the periods of 0 - 12 hours, 0 - 24 hours and 0 - 48 hours respectively. A score of 1, achieved in the first two periods, is that of a very good forecast in that the net ice movement is accurately forecast, even though local looping effects are not illustrated. The 48 hour outlook is less accurate and scores a 4. This is defined as better than no forecast and will at least cause the observer to look in the right direction and it will not grossly deceive him. In this fashion, each forecast issued may be tested on its own merits and may be compared as well to the wind forecast for that period for a cause and effect relationship. While this verification technique is still under development, it is felt that its use will enable the production of better forecasts in a more reliable fashion.

This, then outlines the Dome-Canmar ice forecasting system. It was developed for pragmatic reasons and, consequently, within equally pragmatic constraints.

Some theoretical knowledge may have been missed in its development in the interest of getting a workable system into play in a timely manner.

However, far from perfect, it is operational and improvements are continually being sought and made.

It is hoped that some such improvements will emerge from ideas and work engendered at this meeting.

OVERVIEW OF PROJECT TO MEASURE ICE FORCES AT ADAMS ISLAND

by

R.M.W. Frederking,[1] J.B. Maxwell[2] and S. Prinsenberg[3]

ABSTRACT

Adams Island, a small island in the Arctic, was the site of a project designed to provide information about ice loads on structures, recognizing the two components involved: ice behaviour in relation to the environment, and loads applied by ice as a result of that behaviour. Data were collected between 1982 and 1985 concerning wind, air and ice temperatures, currents and tides, stresses, strains, and ice movement. Measuring techniques are described.

---

[1] Division of Building Research, National Research Council of Canada, Ottawa, Ontario, K1A 0R6

[2] Atmospheric Environment Service, Environment Canada, Downsview, Ontario, M3H 5T4

[3] Department of Fisheries and Oceans, Atlantic Oceanographic Laboratory, Bedford Institute of Oceanography, Darthmouth, N.S., B2X 4A2

INTRODUCTION

The determination of design ice loads on marine structures in the Arctic requires knowledge of ice behaviour, i.e. knowledge of ice behaviour in relation to the environment, and the loads resulting from that behaviour. Only by understanding both components can experience gained at one location or under a given set of circumstances be successfully applied at another site.

Available information on ice behaviour and loads on offshore structures is limited. Although extensive monitoring programs have been carried out for petroleum exploration structures in the near-shore region of the Beaufort Sea, only some of the results have been published (Metge 1976; Semeniuk 1977; Strilchuk 1977). Much more information is proprietary and only the methods of measurement have been published (Pilkington et al., 1983; Hawkins et al., 1983).

It is desirable to obtain information from other areas of the Arctic where conditions are different. For such studies small islands can take the place of man-made structures in investigations of ice/structure interaction. This approach has been used in investigations of large multi-year floe impacts on Hans Island (Danielewicz et al., 1983) and first-year sea ice rubble formation at Fairway Rock (Kovacs and Sodhi, 1981). A similar study carried out at Adams Island in Lancaster Sound is the subject of this paper.

The project involved a number of participants and extended over three winter seasons. The National Research Council of Canada coordinated the project and was involved in measurement of movements and large-scale deformations of the ice cover as well as in characterization of ice loads and behaviour. The Atmospheric Environment Service was involved with the measurement of air temperature, wind, and drag, and the Department of Fisheries and Oceans with measurement of currents and tide. C-CORE was involved with strain measurement in the ice cover and with current measurements. The Hamburg Ship Model Basin carried out in situ stress measurements in the ice cover. British Petroleum of London (BP) carried out strain measurements during the early part of the project. Technical assistance in the field was provided by the Arctic Research Establishment of Pond Inlet.

The primary objectives were to determine the response of the ice cover to climatological and oceanographic driving forces and consequent ice interaction with the island. Selected results for the winters of 1981/82, 1982/83, and 1983/84 have been reported (Frederking et al., 1983, 1984, 1986). The present paper catalogues the measurement of environmental factors such as wind, current, tide and temperatures, as well as movements, deformation, strains, and stresses in the ice cover adjacent to the island.

SITE DESCRIPTION

The area of investigation is at the intersection of Lancaster Sound and Navy Board Inlet (73° 45' N, 81° 30' W, Figure 1). Adams Island is situated about 3 km offshore from a base camp (Borden Station) on the Borden Peninsula. Established by the Department of Fisheries and Oceans, Borden Station comprises accommodation buildings, a generator house and shop, and a 300-m long airstrip, providing a base for operations in the area. The island is rocky, with steep cliffs on the north. A maximum elevation of 20 m gradually slopes to the east, south and west. The south shore is nearly vertical also, with an escarpment of about 4 m. The beaches are rocky and relatively steep. A bathymetric survey revealed that the sea bottom slopes gradually to the north and west but steeply to the southeast.

First-year ice normally forms in the middle of Navy Board Inlet in October, becomes landfast, and progresses northward up the Inlet, reaching Lancaster Sound in November. Maximum first-year ice thickness is typically 1.8 m. The island is generally at the boundary between level and ridged ice. Shear and pressure ridges make up a zone of ridged ice that becomes landfast in mid-winter to a distance of about 5 km north of the island. Even this ice can break up at any time; e.g., in March 1985 it broke away to within 100 m north of the island. During the open water season multi-year ice from the Arctic Archipelago moves through Lancaster Sound to discharge into Baffin Bay. Similarly, icebergs from the glaciers of Greenland and Ellesmere Island move about in the Sound. Some of these pass into Navy Board Inlet and are frozen into the ice cover, while others ground on the sill at the entrance to the Inlet. Typically, there can be five to ten large icebergs within 10 km of Adams Island. Multi-year ice is also frozen into the ice cover, possibly 1 to 5%. The ice pack in Lancaster Sound is generally dynamic throughout the entire winter, with a net movement from west to east. There have been occasions, however, when it has frozen over completely (Dey, 1981), as was the case for the winter of 1982/83.

ENVIRONMENTAL DRIVING FORCES

CLIMATE NETWORK

A mesoscale network was designed for the Adams Island area to permit evaluation of wind stress imposed on the surrounding sea ice (Figure 2). It was composed of two profile stations (wind and air temperature recorded at three different levels: 2.5, 5, and 10 m) located on the ice (West Profile and South Profile stations) and three stations recording at the 10-m level only, one on the ice (East Station) and the other two on land (Borden Station and Adams Island). A Campbell Scientific CR21 micrologger in an environmental enclosure recorded data at each station (Headley and

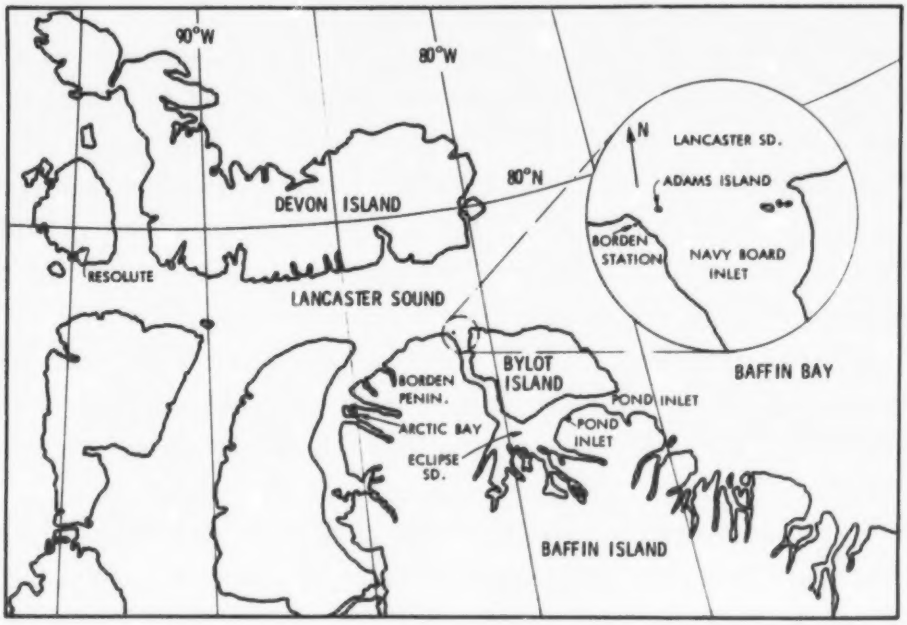

Figure 1. Location map for Adams Island area

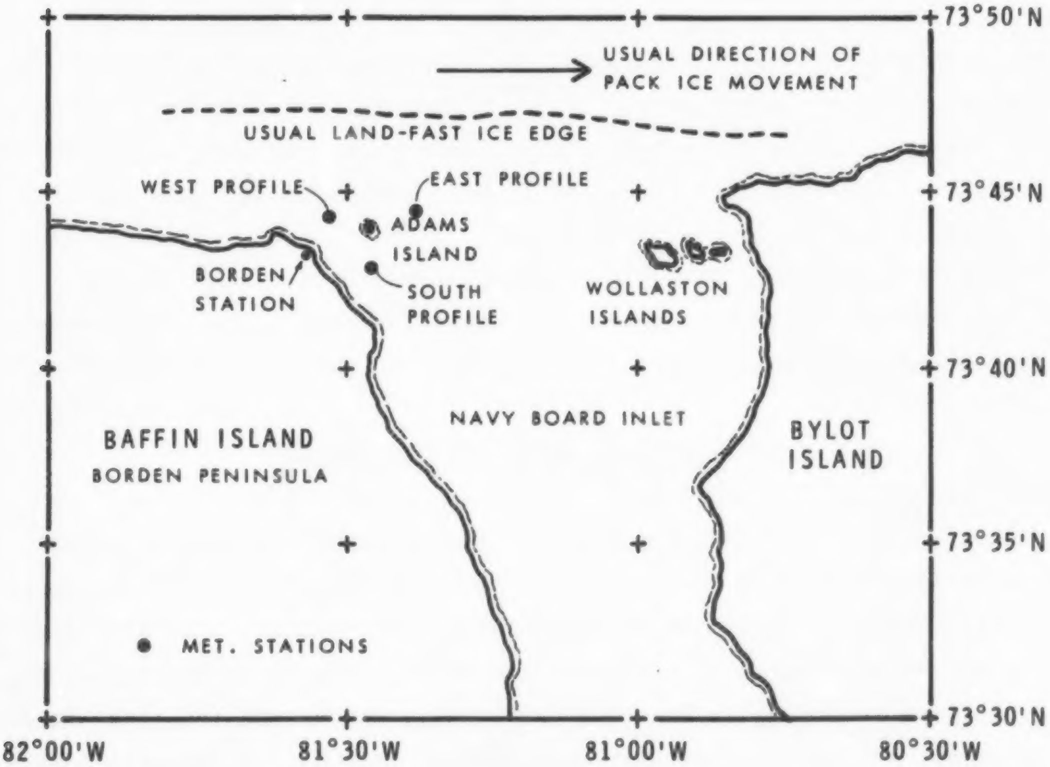

Figure 2. Location map of study area

Maxwell, 1985). The system was capable of unattended data recording for up to six months.

For the winter of 1983-84, measurements were begun in late February and were continued until late April or early May when collection ceased as a result of damage by polar bears at most sites. Only Borden Station continued in operation until the sites were inspected (and the on-ice stations were dismantled) in mid-May. During the summer (until the end of September) Borden Station and Adams Island were in operation.

For 1984-85, a sixth station was installed on the ice of Navy Board Inlet at Canada Point, about 60 km to the south. Meteorological readings were taken at the 2-m level. Temperatures were also measured at six levels in the ice cover and in the sea beneath. Data collection commenced at all six stations in early-to-mid November and continued until mid-May, with the exception of a week or so in late February at the time of mid-winter inspection and maintenance.

A package of computer programs was written for analysis of the collected data. Various tabular and graphical presentations of air temperature, wind speed, wind direction, and derived drag coefficients are possible, as illustrated in Figures 3, 4 and 5. Analysis can be done for all or any part of the data set from any station.

OCEANOGRAPHY

Ocean currents were measured with an Aanderaa RCM-4 recording current meter deployed 3 m below the surface. In 1983 the current meter was located 2 km northwest of Adams Island in an area with a water depth of 35 m. Readings were recorded at 10-min intervals for the period 16 April to 11 June. The maximum current velocity was 0.37 m/s, the predominant direction to the east; peak speeds were to the east-southeast. The currents were strongly related to tides. The east-west component of the current cycled from 0 to 0.3 m/s to the east, with a mean speed of 0.1 m/s. The north-south component cycled from 0.1 m/s to the south to 0.2 m/s to the north, with no net north-south movement.

During the 1983/84 season currents were measured continuously between 23 November 1983 and 18 May 1984. The current meter was placed 3 m below the surface about 250 m west-southwest of the island where water depth is about 15 m. Readings were taken at 10-min intervals. The currents were made up of a mean and a tidal component whose vector sum was directed predominantly in two directions: towards the north during flood tide (rising sea surface), and towards the southeast during ebbing tide. The mean current was between 9 and 12.5 cm/s in a northeasterly to easterly direction. Tidal currents are made up of diurnal ($K_1 + O_1$) and

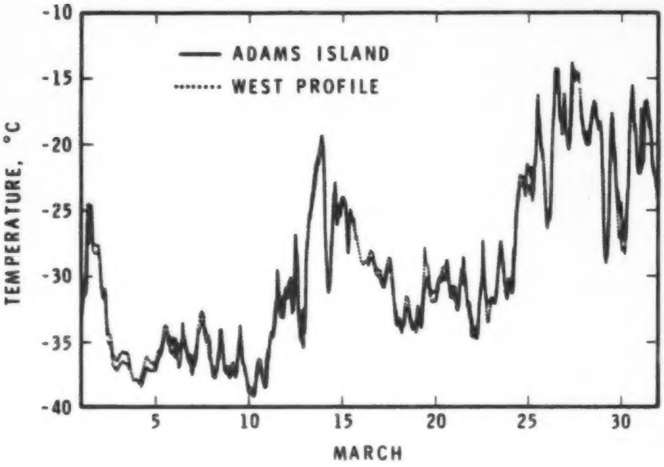

Figure 3. Comparison of air temperatures, Adams Island and West Station, 1984

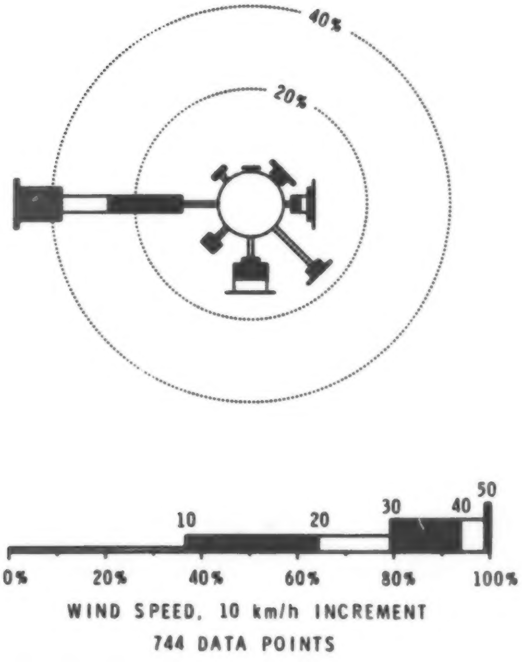

Figure 4. Borden station wind rose for 1 March 1984 to 31 March 1984

semi-diurnal tides ($M_2 + S_2$). Their amplitudes varied with the lunar cycle and reached highs of 18 cm/s for the diurnal tide and 9 cm/s for the semi-diurnal tide. Directions were in a northwest to southeast oscillating pattern that sometimes changed to a more north to south pattern. At highest tides (1.9 m) the mean northeasterly flow combined with the strong northwesterly ebbing tidal current to produce maximum current speeds of 35 cm/s towards the north. These observations duplicated closely the currents recorded during the previous field year at a location 2 km northwest of Adams Island.

No long-term current records were obtained during the 1984/85 season because of a combination of mishaps, i.e., loss of one current meter and malfunction of the other. During this season, however, C-CORE was successful in making short-term current profile measurements in November and May (Shirasawa, 1985).

An Aanderaa TC-3A tide recorder was used to measure and record tides. Each season it was installed about 1 km north of Borden Station in 5 m of water. In 1983 it was deployed from March to June, and in the 1983/84 and 1984/85 seasons from November to May. Maximum tide range was 1.9 m. The tidal regime can best be described as mixed, mainly semi-diurnal.

ICE MOVEMENTS AND DEFORMATIONS

An electronic distance measuring (EDM) instrument (Wild DI-20) coupled to a theodolite (Wild T-2) was used to measure movements of reference points on the ice cover. Prism reflectors attached to wooden stakes were used as reference points. The EDM has an accuracy of ±5 mm for distances up to 100 m, when corrections are applied to atmospheric density (barometric pressure and temperature). Horizontal and vertical angle measurements had an accuracy of ±5 s of arc. The accuracy of the surveys when checked by closure was about ±20 mm. Positions of reference points on the ice were established by measuring their distance and bearing from fixed base lines on Adams Island and at Borden Station. These base lines were tied to each other.

Two arrays of reference points were established on the ice cover in March 1983, one with 19 points around Adams Island and the other with 5 points adjacent to Borden Station. Positions of the points were measured at two-day intervals from 20 to 26 March, 27 April to 7 May, and 10 to 14 June. These measurements indicated that movements of all the reference points on the ice cover were very similar and in a north-northeasterly direction. Total movement was about 8 m, and the average rate about 80 mm/day at Borden and Adams Island.

For the 1983/84 season two arrays were again established around Adams Island and adjacent to Borden Station. They were set up in November 1983 and subsequent series of surveys were carried out in March and May 1984. For the November to March period the average rate of movement was about 80 mm/day to the northeast. For the March to May period the average rate of movement was about 90 mm/day to the north, both very similar to the previous year's measurements for the same period. Typical plots for the 1983/84 season are shown in Figure 6.

For the 1984/85 season arrays similar to those of previous years were established at Adams Island and Borden in November. At the same time an array of five reflectors was established at Canada Point, about 60 km south on Navy Board Inlet. All three arrays were re-surveyed in March and May. An additional array was set up in March about midway between Borden and Canada Point. The Borden and Adams Island arrays showed movements similar to those of previous winters. The rates at Canada Point and at the intermediate location were smaller, the predominant direction being offshore, southerly and easterly, respectively.

A wire line device supplied by Arctec Canada Ltd. was used to measure the horizontal movement of the ice cover continuously between the site visits. It comprised two wires anchored to the sea bed. Each wire was attached to a spool whose rotation could be measured. The rotation, and hence the ice movements, were measured every 15 min and logged on a battery-powered data logger. A record was obtained from March to May in 1984 and from November 1984 to May 1985. A typical record of continuous movements is presented in Figure 7. These results show that there is considerable variation in rate on a short-term basis.

STRAIN MEASUREMENTS

Surface strain meters having a gauge length of 0.3 m and arrayed as a delta were installed at the end of April 1983 by BP. The array operated for eight days before being damaged by polar bears. Strain rates of 5×10^{-9} to 10^{-8} s^{-1} were obtained. In November of 1983 C-CORE installed two arrays of surface strain meters intended to monitor long-term strain over an entire winter season. They were connected to an unattended data logger. Damage by polar bears again interrupted the records on several occasions. An average strain rate of 5×10^{-10} s^{-1} was obtained (Stander, 1985).

STRESS MEASUREMENT

STRESS PANEL

A 1-m wide × 2 m deep panel-type stress transducer ("IDEAL" supplied by Terrascience Systems Ltd.) was used to measure normal stresses in the ice cover in the late winter of 1984. The panel was divided into four equal horizontal strips so that a distribution of stresses through the ice cover could be obtained. A

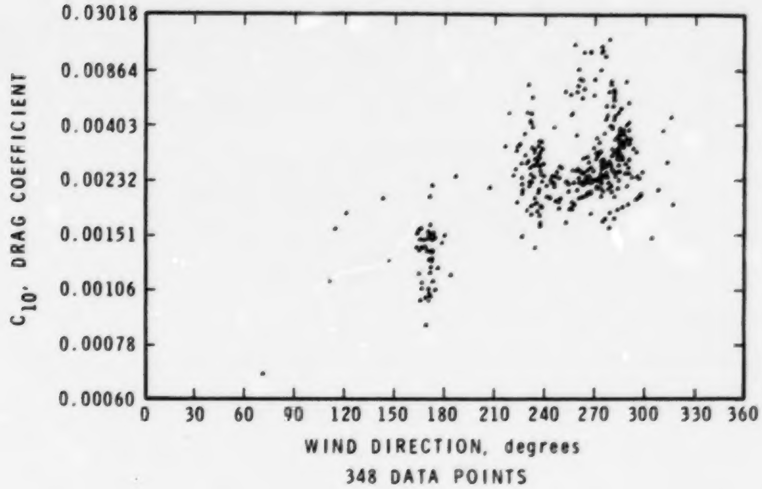

Figure 5. Drag coefficients for south profile versus wind direction, 27 February 1984 to 17 May 1984

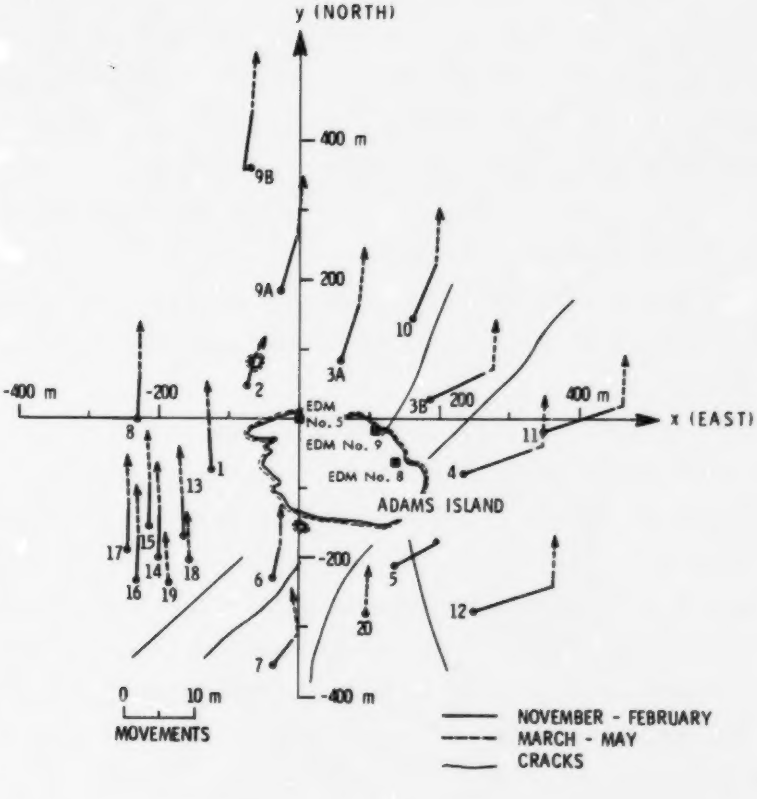

Figure 6. Ice movements at Adams Island, November 1983 - May 1984

thermistor was also located at the centre of each of the horizontal strips. The outputs were logged every 15 min on a battery-powered data logger ("ARCDATS" supplied by Arcted Canada Ltd.). The panel was located about 150 m southwest of the island. A continuous record was obtained from 6 March, when the panel was installed, until 3 May. The record of stresses versus time for each of the sectors is presented in Figure 8. Stress was not uniform, but varied through the thickness of the ice cover. The maximum was at a depth of 0.5 to 1.0 m and fluctuated between 150 and 250 kPa over the measurement period. The stress values in the top three sectors show a definite periodicity. When the results were transformed into the frequency domain, peaks were apparent at periods of 12.65 h and 6.32 h. These times correspond to the semi-diurnal tidal and half-tidal period.

In November 1984 six 1-m wide by 1-m deep panel type transducers ("IDEAL") were installed across the southern perimeter of the island, about 75 m from shore. These panels were sectored horizontally into two 50-cm deep strips. Owing to problems with the recording system no record was obtained until April 1985. From this time, however, a three week long record was obtained. It too showed a strong periodicity, but in this case peak stresses as high as 600 kPa were obtained.

BIAXIAL STRESS TRANSDUCERS

A number of small 50-mm diameter cylindrical transducers supplied by IRAD Gage (type VBS-3) were also used by personnel from the Hamburg Ship Model Basin to measure in situ stresses in the ice. These transducers are capable of determining magnitude and direction of the principal stresses in the plane of the ice cover. Controlled laboratory tests by Cox and Johnson (1983), with the transducer in ice, demonstrated that the sensor has a low temperature sensitivity (5 kPa/°C), a resolution of 20 kPa, and an accuracy of better than 10% under a variety of loading conditions.

The first deployment of these gauges at Adams Island was in April 1983. From 17 to 23 April they were deployed in two adjacent vertical arrays 120 m southwest of the island in order to obtain a profile of stresses through the thickness of the ice cover. For the period 23 to 30 April the ten gauges were re-deployed in a circumferential array around the southwest quadrant of the island about 100 m offshore. Readings were logged every 24 min. All had a 30-cm measuring depth. In each deployment there were consistent trends in the results from all the gauges. From the vertical deployment it was apparent that the majority of the stress was carried in the top quarter of the ice cover.

The second deployment of the biaxial gauges was from March to May 1984. Ten gauges were arranged round the western, southern, and eastern perimeter of the

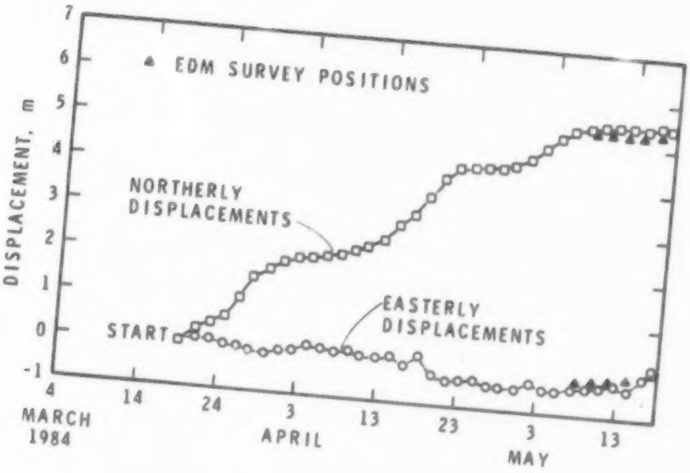

Figure 7. Comparison of horizontal movement components of ice cover measured with x-y movement recorder and EDM at reference point 14 adjacent to Adams Island for period March to May 1984

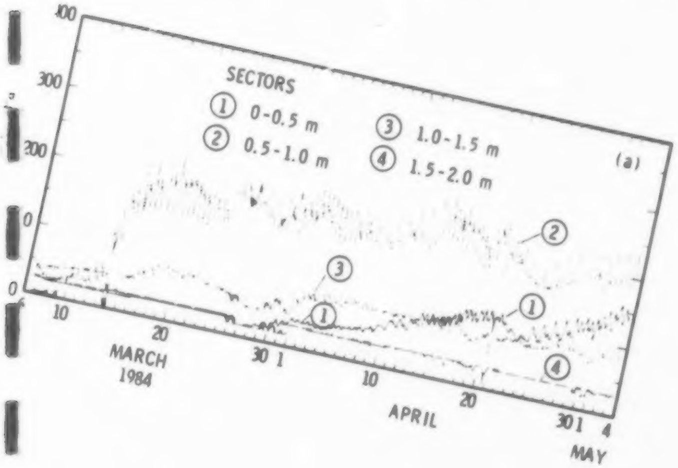

Figure 8. Stresses measured in each sector by the 1-m wide by 2-m deep ideal stress panel, Adams Island, March to May 1984

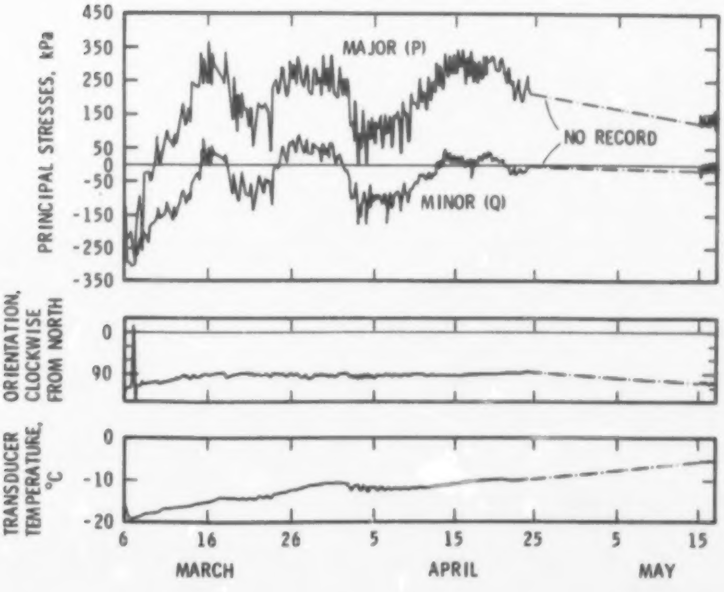

Figure 9. Principal stresses, orientation, and temperature of IRAD biaxial stress transducer 510, at 0.66-m depth in ice, Adams Island, March to May 1984

island about 200 m offshore. An unattended data logger took readings at 4-h intervals from 6 March to 26 April when the battery failed. It was re-started 15 to 17 May and logged at half-hour intervals while the transducers were removed from the ice and zero readings obtained. A typical result for a transducer at a depth of 66 cm is shown in Figure 9.

The final deployment was over the winter of 1984-85. Eight gauges were installed around the southern perimeter of the island at a distance of 80 to 100 m. Logging started on 21 November and continued at 4-h intervals until 4 December when the batteries failed. In March of 1985 seven additional gauges were installed to provide a network completely encircling the island. The logging system was reactivated on 14 March and operated until 6 April. A final set of readings at half-hour intervals was obtained 15-18 May when the gauges were removed from the ice. Although there were interruptions, a continuous record of stress was obtained from November to May. The maximum measured by an individual gauge during the three seasons of measurements was about 500 kPa. The maximum stress averaged through the thickness of the ice cover was about 150 kPa.

SUMMARY

This paper presents an overview of the data collected during the Adams Island project. Reasonably complete records of environmental data (wind, air temperature, ice temperature, current and tide) and ice sheet response (stresses, strains and movements) were obtained, the majority in an electromagnetic format. Analysis of the data focusses on establishing ice loads on the island in relation to environmental factors. Anyone interested in obtaining records is invited to contact the authors at NRC, AES, or DFO.

ACKNOWLEDGEMENTS

The financial support of the Panel of Energy Research and Development is gratefully acknowledged, as is the logistic support provided by the Polar Continental Shelf Project. The use of the facilities at Borden Station owned by the Department of Fisheries and Oceans, and the technical support in the field provided by the Arctic Research Establishment, Pond Inlet, greatly facilitated the work. Finally, the support and interest of the technical and professional staff of the NRC, AES and DFO and collaborating agencies are acknowledged.

REFERENCES

COX, G.F.N. and JOHNSON, J.G., 1983. Stress measurements in ice. U.S. Army, Cold Regions Research and Engineering Laboratory, Hanover, N.H., CRREL Report 83-23.

DANIELEWICZ, B.W., METGE, M. and DUNWOODY, A.B., 1983. On estimating large scale ice forces from deceleration of ice floes. VTT Symposium 38, 7th International Conference on Port and Ocean Engineering under Arctic Conditions, Helsinki, Finland, 4: pp. 537-46.

DEY, Balaram B., 1981. Shipping routes, ice cover and year-round navigation in the Canadian Arctic. Polar Record, 20(129): pp. 549-59.

FREDERKING, R., SANDERSON, T., WESSELS, E. and INOUE, M., 1983. Ice behaviour around a small Arctic island. VTT Symposium 28, 7th International Conference on Port and Ocean Engineering under Arctic Conditions, Helsinki, Finland, 2: pp. 875-87.

FREDERKING, R.M.W., SAYED, M., WESSELS, E., CHILD, A.J. and BRADFORD, D., 1984. Ice interaction with Adams Island, winter 1982-1983. Proceedings, IAHR Ice Symposium, Hamburg, V. 3: pp. 187-201.

FREDERKING, R. WESSELS, E., MAXWELL, J.B., PRISENBERG, S. and SAYED, M., 1986. Ice pressures and behaviour at Adams Island, winter 1983/84. Canadian Journal of Civil Engineering, V. 13(2).

HAWKINS, J.R., JAMES, D.A. and DER, C.Y., 1983. Design, construction and installation of a system to measure environmental forces on a caisson retained island. VTT Symposium 38, 7th International Conference on Port and Ocean Engineering under Arctic Conditions, Helsinki, Finland, 4: pp. 770-79.

HEADLEY, A.N. and MAXWELL, J.B., 1985. A Canadian High Arctic mesoscale surface observing project. 3rd WMO Technical Conference on Instruments and Methods of Observation, Ottawa, WMO/TO-No.50: pp. 303-308.

KOVACKS, A. and SODHI, D., 1981. Sea ice piling at Fairway Rock, Bering Strait, Alaska: Observations and theoretical analysis. 6th International Conference on Port and Ocean Engineering under Arctic Conditions, Quebec, 2: pp. 985-1000.

METGE, M., 1976. Ice conditions and ice defence at Netserk B-44 and Adgo P-25 during the winter of 1974-75. Arctic Petroleum Operators' Association, Calgary, APOA Report No. 104-1.

PILKINGTON, R., BLANCHET, D. and METGE, M., 1983. Full-scale measurements of ice forces on an artificial island. VTT Symposium 38, 7th International Conference on Port and Ocean Engieering under Arctic Conditions, Helsinki, Finland, 4: pp. 818-34.

SEMENIUK, A., 1977. Ice pressure measurements at Arnak L-30 and Kannerk G-42. Arctic Petroleum Operators' Association, Calgary, APOA Report No. 122-1.

SHIRASAWA, K., 1985. The effects of water drag and ocean currents on ice displacement at Adams Island, N.W.T., Winter, 1984/85. C-CORE Report.

STANDER, E., 1985. The measurement of horizontal and vertical strain at Adams Island, N.W.T., 11/27/1983 - 05/07/1984. C-CORE Contract Report, 15 p.

STRILCHUK, A.R., 1977. Ice pressure measurements, Netserk F-40, 1975-76. Arctic Petroleum Operators' Association, Calgary, APOA Project No. 105-1.

VII

FUTURE RESEARCH PROGRAMS

RADARSAT DATA ACQUISITION AND ANALYSIS PLANS, 1986-1991, FOR SEA ICE APPLICATIONS

by L. McNutt
RADARSAT Project Office
110 O'Connor Street, Suite 200
Ottawa, Ontario, Canada K1P 5M9

When operational satellite SAR data become available in Canada during 1989-1995, systems and algorithms for ice data extraction must already be developed which will allow users to incorporate these data into information systems currently in use or under development. To ensure that representative data sets are collected and analysed, the RADARSAT Project Office, the Data Acquisition Division, and the Applications Technology Division of the Canada Centre for Remote Sensing (CCRS) will be working together on a coordinated research plan to both collect and analyse data for sensor verification and technology enhancement. This paper presents an overview of the data collection activities through the ERS-1 and RADARSAT timeframes, and discusses these in terms of specific objectives, both scientific and operational, defined to date. It also describes these activities in relation to other research programs in this same period; i.e., SSM/I validation, and suggests some ideas for demonstration projects designed for specific user groups.

LIMEX - A LABRADOR ICE MARGIN EXPERIMENT

by J. Lever[1] and P. Wadhams[2]

It is proposed to carry out an integrated air-sea-ice investigation of the southern ice edge in the Labrador Sea in March 1987 near the time of maximum ice advance. The purpose is to understand the processes which govern the final stages of advance and initial stages of retreat, when the ice may threaten drilling operations in the Hibernia area, and when simple ice forecasting models are least reliable since the dynamics (e.g., wind-driven ice advance) and the thermodynamics (e.g., melt and breakup) act in direct opposition. The basis for the experiment will be studies of ice drift, deformation, melt rate, air-ice and ice-water boundary layers, floe size distributions, wave interactions, ocean structure and radiative fluxes in the ice edge region. It is hoped that the experiment will be carried out by a number of Canadian institutions acting in collaboration, and the 1987 study, seen as the first of a series, will involve one ice-strengthened ship with a helicopter and with support from remote sensing aircraft. The ship will also serve as a platform for ice properties studies in support of the airborne remote sensing missions, and of satellite missions in the form of the SIR-B reflight (Shuttle Imaging Radar), which is expected to occur during the experimental period.

[1]Centre for Cold Ocean Resources Engineering, Memorial University of Newfoundland St. John's, Newfoundland, Canada A1B 3X5
[2]Scott Polar Research Institute, Lensfield Road, Cambridge, CB2 1ER, England